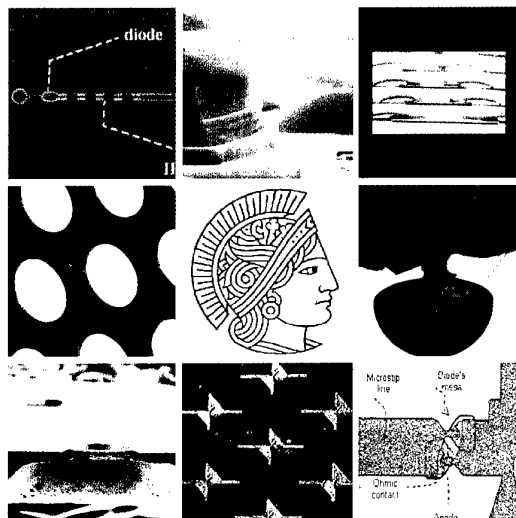
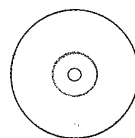


THz Conference 2000

8th International Conference on Terahertz Electronics



28 – 29 September 2000
Darmstadt, Germany



Reproduced From
Best Available Copy

mit CD-ROM

DISTRIBUTION STATEMENT A
Approved for Public Release
Distribution Unlimited



20011203 200

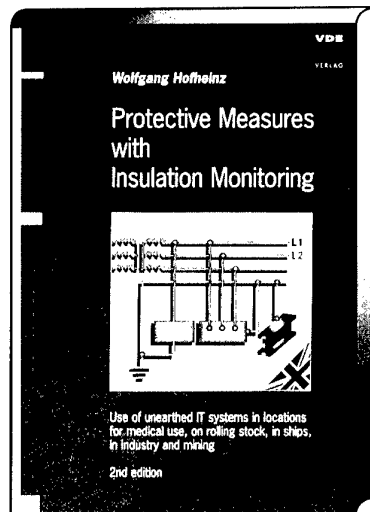
Darmstadt University of Technology

GMM

VDE

Electrical Engineering – new publication

VDE
VERLAG



Hofheinz, W.

Protective Measures with Insulation Monitoring

Use of unearthed IT systems in locations for medical use, on rolling stock, in ships, in industry and mining

2. Auflage 2000, 212 S., DIN A5, kart.

ISBN 3-8007-2516-9

38,- DM / 35,- sFr / 277,- öS / 19,43 €*

With the increasing use of unearthed power supply systems (IT systems), the selection of suitable monitoring equipment is a question of great importance. The combination of an unearthed power supply system (IT system) and insulation monitoring opens the road to a special protective technique. The advantages of this technique are increased operational reliability, increased fire protection and better accident prevention. The book describes this type of system and its application areas in locations for medical use, in ships, in industry and mining. The various techniques used in the German Federal Republic are compared to those in the United States.

Prices and information are valid at time of going to press but are subject to change.

VDE VERLAG

P.O. Box 12 01 43 · 10591 Berlin

Phone: ++/ 30/ 34 80 01-0 / Fax: ++/ 30/ 341 70 93

E-Mail: vertrieb@vde-verlag.de

Internet: www.vde-verlag.de

Werb-Nr. 000815

THz Conference 2000

8th International Conference
on Terahertz Electronics



28 – 29 September 2000
Darmstadt University of Technology
Institut für Hochfrequenztechnik/THz Conference 2000

in cooperation with:

GMM

VDE/VDE-Gesellschaft Mikroelektronik, Mikro- und Feinwerktechnik

ITG

Informationstechnische Gesellschaft im VDE

(Organizers)

and technical co-sponsored by
IEEE MTT/AP German Chapter and the IEEE German Section.

The 8th International Conference on Terahertz Electronics was supported by the Department of the Navy Grant
N000134-00-1-1104 issued by Office of Naval Research International Field Office. The United States
Government has a royalty-free license throughout the world in all copyrightable material contained herein

VDE VERLAG • Berlin • Offenbach

AQ F02-02-0270

Addresses:

Darmstadt University of Technology
Institut fuer Hochfrequenztechnik/THz Conference 2000
Merckstrasse 25, 64283 Darmstadt, Germany
Phone: ++49-6151-16 2562, Fax: ++49-6151-16 4367
e-mail: thz_conf@hrz2.hrz.tu-darmstadt.de.

Dipl.-Ing. R. Theobald (GMM)
Stresemannallee 15, 60596 Frankfurt am Main, Germany
Phone: ++49-69-6308-330, Fax: ++49-69-6312925
e-mail: GMM@vde.com

Dr.-Ing. V. Schanz (ITG)
Stresemannallee 15, 60596 Frankfurt am Main, Germany
Phone: ++49-69-6308-360, Fax: ++49-69-6312925
e-mail: ITG@vde.com

Contact Address

Program Chair: *Prof. Dr. Eng. Dr. h.c. mult. H. L. Hartnagel*
Conference Secretary: *Mr. Chih-I Lin*

Contact address:
Institut fuer Hochfrequenztechnik/THz Conference 2000
Darmstadt University of Technology
Merckstrasse 25
D-64283 Darmstadt, Germany
Phone: ++49-6151-16 2562, Fax: ++49-6151-16 4367
e-mail: thz_conf@hrz2.hrz.tu-darmstadt.de.

Die Deutsche Bibliothek – CIP-Einheitsaufnahme

Ein Titeldatensatz für diese Publikation ist bei
Der Deutschen Bibliothek erhältlich

ISBN 3-8007-2580-0

© 2000 VDE VERLAG, Berlin und Offenbach, Bismarckstraße 33, D-10625 Berlin

Alle Rechte vorbehalten

Druck: Gerhard Weinert GmbH, Berlin

0009

***Eighth International Conference on
Terahertz Electronics***

Edited by

**Dr Chih-I Lin
Manuel Rodriguez-Gironés
Dr. Victoria Ichizli**

of Institute of Microwave Techniques
Merckstraße 25
D-64283 Darmstadt, Germany

E-mail: thzuser@hrz2.hrz.tu-darmstadt.de

Home page: <http://www.hf.e-technik.tu-darmstadt.de/mwehomepage/>

Preface

The subject of this Conference is expanding very rapidly. New application areas are coming up calling for significant international research efforts. The role of such a conference is therefore to bring together all those working in this field.

After the first conference of this series was instituted eight years ago here in Darmstadt, it is a pleasure to be host of this meeting again. In the mean time it took place at many localities. Last year it was held in Nara, Japan and the two years before that in Leeds (U. K.) and Grenoble (France).

This volume contains the papers - both invited and contributed - of the THz-Conference 2000. It shows that the subject area is now covering many new developments. The authors are to be thanked for their contributions. The editors have made good efforts to make this volume of high quality - their work is gratefully acknowledged. The members of the organising committee both from the VDE/VDI-GMM (Mr. Rainer Theobald) and the VDE-ITG (Dr. Volker Schanz) as well as from the Darmstadt University of Technology (Dr. Chih-I Lin, Mr. Manuel Rodríguez-Gironés, Dr. Victoria Ichizli, Mr. Pawel Szeliga and Mr. Mustafa Saglam) have made a significant effort to make this conference a success. As Chairman of this Conference I am grateful for all this involvement.

I wish this Conference many valuable discussions and fruitful interactions between those working in this field. Anybody reading this volume later on may enjoy the descriptions contained here on new concepts and results.

Prof. Hans L. Hartnagel

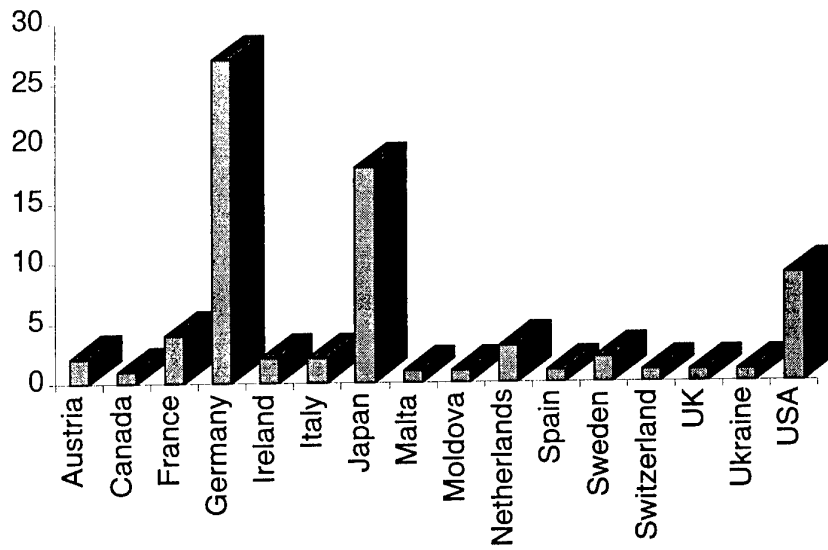
Chairman of the Eighth International Conference on Terahertz Electronics

Darmstadt University of Technology

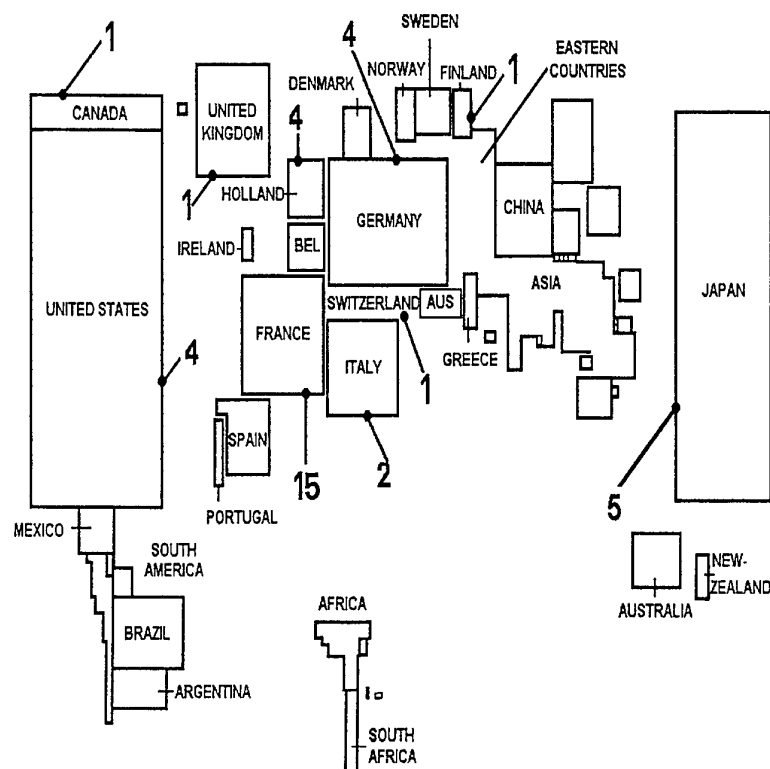
D- 64283 Darmstadt, Germany

e-mail: hartnagel@hf.tu-darmstadt.de

Statistics of Contributions



THE MILLIMETER-SUBMILLIMETER WORLD IN 2000



The domain of millimeter-submillimeter waves is a part of the electromagnetic spectrum which still remains a technological frontier. Most countries working in this field also happen to be countries involved in advanced research. The millimeter-submillimeter world can thus be represented as above, where each country is given an area which is proportional to its Gross National Product. Where does AB MILLIMETRE stand in this world? The numbers indicate how many AB MILLIMETRE MVNA-8-350 Vector Analyzers have been sold in each country since 1990. Why were these Analyzers bought? Because MVNA-8-350 can cover continuously all frequencies between 8 and 350 GHz, and up to 1000 GHz with options. What were these Analyzers bought for? MVNA-8-350s are used for characterization of antennas, other devices and materials, and also for atomic, high-magnetic-field or other kinds of spectroscopy. Who are the users? They belong to laboratories working in electrical engineering, radioastronomy, plasma physics, solid state physics, etc... Why don't YOU join us, and make the millimeter-submillimeter world even bigger?

E-mail : abmillimetre@wanadoo.fr

Web : www.abmillimetre.com

ABmm

AB MILLIMETRE
52 RUE LHOMOND
75005 PARIS France
TEL : 33 1 4707 7100
FAX : 33 1 4707 7071

Conference Program

Sources I

- SI. 1 Invited Paper**
Field Emission Studies for Microwave and Optical Wave Generation 17
 K. Yokoo, K. Okamura, H. Mimura, O. Yilmazoglu, D. Arsla, H. Hartnagel, H. Ishizuka,
 Research Institute of Electrical Communication, Tohoku University, Japan, Fiskuoaka Institute
 of Technology + TU Darmstadt
- SI. 2 Narrow-Linewidth Interwell Terahertz Intersubband Emission 21**
 B. S. Williams, B. Xu, Q. Hu, M. Melloch, MIT & Purdue University, USA
- SI. 3 Plasma Instability and Terahertz Oscillations in Resonant-Tunneling Transistors . . 25**
 V. Ryzhii, M. Shur, Rensselaer Polytechnic Institute, USA, University of Aizu, Japan
- SI. 4 Feasibility of a SiGe THz Resonant-State Laser 29**
 Y. P. Gousev, I. V. Altukhov, M. S. Kagan, V. P. Sinis, H. K. Olsson, S. G. Thomas,
 K. L. Wang, Royal Inst. of Technology of Sweden, Russian Academy of Science & Univ.
 California
- SI.5 The Copper-doped p-Ge ZHz Laser in the Voigt Configuration: Possibility
 of Mode-locked operation 33**
 J. H. Hovenier, R. M. de Kleijn, T. O. Klaassen, W. Th. Wenckebach,
 Delft Univ. of Technology, the Netherlands

Sources II

- SII. 1 Invited Paper**
THz Sources Based on Semiconductor Quantum Structures 37
 Karl Unterrainer, J. Ulrich, R. Zobl, G. Strasser, E. Gornik, Technische Universität Wien,
 Austria
- SII. 2 Thermal Receiver Detectable THz Radiation from an InAs Irradiated with
 1.04-micron Femtosecond Fiber Laser in a 2-T Permanent Magnet 41**
 H. Ohtake, Y. Suzuki, N. Sarukura, S. Ono, T. Tsukamoto, A. Nakanishi, S. Nishizawa,
 M. L. Stock, M. Yoshida, H. Endert, Science University of Tokyo, IMRA America,
 Sumitomo Sp. Metals & JASCO, Japan, Institute of Molecular Science
- SII. 3 Frequency Difference Generation in the Terahertz Region Using LTG-GaAs
 Photodetector 45**
 E. Peytavit, G. Mouret, J. F. Lampin, P. Masselin, P. Mounaix, F. Mollot, D. Lippens,
 University of Lille, France & University of Littoral
- SII. 4 Self-Generation of Ultra-Short Pulses in a Cavity with a Dielectric Mirror
 Excited by an Array of Active THz Devices 49**
 L.V. Yurchenko, V.B. Yurchenko, National University of Ireland & National Ac. Of Sciences
 (Ukraine)

Sources III

SIII. 1	Invited Paper	
	Gain and Loss in Terahertz Intersubband Emitters	53
	Jerome Faist, University of Neuchatel, Switzerland	
SIII. 2	Modelling of Micromachined Klystrons for Terahertz Operation	55
	R. E. Miles, J. J. García, J. R. Fletcher, D. P. Steenson, J. M. Chamberlain, C. M. Mann, E. J. Huq, University of Leeds, UK, Rutherford Appleton Lab., UK	
SIII. 3	Observation of Terahertz Oscillations and Efficient THz Emission from Contacted Low-Temperature-Grown GaAs Structures	59
	Ch. Steen, S. Tautz, P. Kiesel, S. U. Dankowski, U. D. Keil, G. H. Döhler, G. Segschneider, K. Siebert, H. G. Roskos, V. Krozer, Univ. Erlangen, Goethe Univ. Frankfurt & Chemnitz Univ. Technology, Germany, TU Denmark	
SIII. 4	Study of Terahertz Radiation from Narrow Bandgap Semiconductors: InAs and InSb	63
	P. Gu, M. Tani, Sh. Kono, K. Sakai, Kansai Advanced Research Centre, CRL, Japan	

Multiplication I

Mul. 1	Invited Paper	
	Solid-State Oscillators for the THz-Range	67
	Peter Zimmermann, Radiometer Physics GmbH, Germany	
Mul. 2	Frequency Tripler with Anti-Serial Schottky Diodes	69
	M. Krach, J. Freyer, M. Claassen, Technical University of München, Germany	
Mul. 3	2D Design of Schottky Diodes	73
	J. Grajal, D. Moreno, V. Krozer, Universidad Politecnica Madrid, Spain & TU Chemnitz	
Mul. 4	A Novel Evolutionary Approach for the Analysis and Optimization of THz Nonlinear Circuits	77
	M. Bozzi, M. Saglam, M. Rodríguez-Gironés, L. Perregini, H. L. Hartnagel University of Pavia, Italy & Darmstadt University of Technology	
Mul. 5	Cryogenic Operation of GaAs-Based Multiplier Chains to 400 GHz	81
	A. Maestrini, D. Pukala, F. Maiwald, E. Schlecht, G. Chattopadhyay, I. Mehdi, Caltech-JPL, USA	

Detection

D. 1	Invited Paper	
	Prospects of Compound Semiconductor Quantum Nanostructures for Terahertz Generation, Amplification and Detection	85
	Hideki Hasegawa, Research Centre for Interface Quantum Electronics, Hokkaido University, Japan	
D. 2	Ultrabroadband Detection of Terahertz Radiation up to 20 THz with an LT-GaAs Photoconductive Antenna Gated by 15 fs Laser Pulses	87
	Sh. Kono, M. Tani, P. Gu, K. Sakai, Kansai Advanced Research Centre, CRL, MPT, Japan	

D. 3	Ultrafast, Ultra-Broadband Superlattice Detector for THz Radiation	91
	E. Schomburg, F. Klappenberger, M. Krätschmer, A. A. Ignatov, K. F. Renk, W. Wegscheider, Univ. Regensburg, Germany	
D. 4	Terahertz Spectral Analysis by Frequency-Selective Incoherent Detection in High-T_c Josephson Junctions	95
	Y. Y. Divin, U. Poppe, K. Urban, O. Y. Volkov, V. V. Pavlovskii Jülich Research Centre, Germany & Russian Academy of Sciences	
D. 5	Wide Bandwidth Far-Infrared Mixing using a High-T_c Superconducting Bolometer	99
	M. Lee, C.T. Li, Bell Laboratories - Lucent Technologies & University of Virginia, USA	

Mixing I

Mil. 1	Invited Paper Technological Needs for ESA Microwave Limb Sounders	103
	Daniel Lamarre, Chung-Chi Lin, L. Marchand, T. Narhi, ESTEC / ESA, Noordwijk, the Netherlands + J. Langen, P. de Maagt, ESA, Noordwijk, The Netherlands	
Mil. 2	A Broadband, Low Noise Heterodyne Receiver at 2.5 THz	109
	K. Huber, H. Brand, L.P. Schmidt, Universität Erlangen-Nürnberg, Germany	
Mil. 3	220-320GHz Harmonic Mixer for a Full Band Sweep Vector Network Analyzer	113
	F. Mattiocco, M. Carter, B. Lazareff, IRAM, France	
Mil. 4	Performance of the Phonon-Cooled Hot-Electron Bolometric Mixer between 0.7 THz and 5.2 THz	117
	H. W. Hübers, A. Semenov, J. Schubert, G. Goltsman, B. Voronov, E. Gershenzon German Aerospace Centre, DLR, Germany & State Pedagogical University (Moscow), Max-Planck-Institut	
Mil. 5	The Design and Analysis of Antiparallel Schottky Diode Mixers	121
	J. Hesler, University of Virginia, USA	

Mixing II

Mill. 1	Invited Paper Space-Based Applications of Far-Infrared Systems	125
	Michael Gaidis, Jet Propulsion Laboratory, Pasadena, USA	
Mill. 2	Technological Developments for THz Electronics	129
	Ch.I. Lin, M. Rodríguez-Gironés, V. Ichizli, M. Saglam, P. Szeliga, H. L. Hartnagel Darmstadt University of Technology, Germany	
Mill. 3	Harmonic Mixing Effects in Schottky Diode Harmonic Mixers at THz Frequencies	133
	R. Feinäugle, H.W. Hübers, J. Hesler German Aerospace Centre (DLR), Germany & University of Virginia	

Mill. 4	SIS Receiver Noise Stability	137
	W. Kooi, G. Chattopadhyay, M. Thielman, T.G. Phillips, R. Schieder, Caltech, USA & Univ. Köln	

Multiplication II

Mu II. 1	Invited Paper	
	Progress in HBV Frequency Multipliers	141
	Jan Stake, M. Ingvarsen, L. Dillner, E. Kollberg, Microwave Electronics Laboratory, Chalmers University of Technology, Sweden	

Quasi-Optics

Q. 1	Analysis and Measurement of a Millimetre-Wave Holographic Power Combiner for 5 IMPATT Oscillators	145
	M. Hoeft, R. Judaschke, Technische Universität Hamburg-Harburg, Germany	
Q. 2	Polymeric Dielectric Mirrors for the sub-millimeter Wavelength Range	149
	T. Dobbertin, D. Turchinovich, P. Knobloch, M. Koch, Technical University of Braunschweig, Germany	
Q. 3	Coherent and Incoherent Phase Retrieval using Gaussian Beam Modes	153
	C. O'Sullivan, S. Whithington, J. A. Murphy, National University of Ireland & Cavendish Laboratory	

Passive Components & THz Circuitry

Pa. 1	Invited Paper	
	Micromachining and Integration of Terahertz Components	157
	Thomas Crowe, Dept. Of Electrical Engineering, University of Virginia, USA	
Pa. 2	Thin Film Antennas for Millimeter and Submillimeter Wave Radiation	161
	Y. Yasuoka, National Defense Academy, Japan	
Pa. 3	Low-Dispersive Coplanar Waveguides and Thin-film Microstrip Lines for Sub-mm Wave Monolithic Integration	165
	F. Schnieder, W. Heinrich, Ferdinand-Braun-Institut für Höchstfrequenztechnik (FBH), Germany	
Pa. 4	Tuneable Interferometric Bandpass and Bandstop Filters for Terahertz Applications	169
	O. Schwelb, I. Frigyes, Concordia University, Canada & Budapest University of Technology and Economics, Hungary	
Pa. 5	Micromachined Planar Antennas for D-Band Frequencies	173
	K. Duwe, S. Hirsch, R. Judaschke, J. Müller, Technische Universität Hamburg-Harburg, Germany	

Imaging & Spectroscopy

- I. 1 Invited Paper**
Imaging Technologies in the Millimetre Wave Region 177
 Koji Mizuno, Research Institute of Electrical Communication, Tohoku University,
 Sendai, Japan
- I. 2 Imaging of Photoexcited Carrier Distribution in Semiconductors by THz Beams** 181
 M. Hangyo, M. Yamashita, Y. Kitoh, M. Tonouchi, Osaka University, Japan
- I. 3 THz Imaging of Carrier Concentration and Mobility in Silicon** 185
 M. Herrmann, M. Tani, K. Sakai, R. Fukasawa, Communication Research Laboratory,
 Kansai Advanced Research Center, Japan
- I. 4 Development of a mm-Wave Imaging system for the W7-AS Fusion Experiment** 189
 S. Bäuml, G. Michel, M. Rodríguez-Gironés, H. L. Hartnagel, H. J. Hartfuß,
 Max-Planck-Inst. Plasma Physics & Darmstadt University of Technology, Germany
- I. 5 Fourier Transform THz-Wave Spectrometer Using THz-Wave Parametric Generator** 193
 J.-I. Shikata, K. Kawase, T. Taniuchi, H. Ito
 Tohoku University & Photo Dynamics Research Centre, RIKEN, Japan

Posters from 28th September to 29th September

- P. 1 A 150 GHz Fully-Integrated MMIC Schottky-Mixer Array** 197
 M. Rodríguez-Gironés, J. P. Pascual, S. Bäuml, C. I. Lin, H. L. Hartnagel,
 Darmstadt University of Technology, Germany, Universidad de Cantabria, Spain,
 Max-Planck Institute for Plasma Physics, Germany
- P. 2 Laser Micromachining of THz Components** 201
 C. Drouet d'Aubigny, C. Walker, B. Jones, C. Groppi, J. Papapolymerou,
 University of Arizona, USA
- P. 3 A One-Dimensional Photonic Bandgap System as High-Reflectivity Mirror for Microwave and THz Applications** 205
 G. W. Schwaab, Ruhr-Universität Bochum, PC II, Germany
- P. 4 An Analytical Solution to Diffraction Problems Involving Periodically Structured Objects** 209
 T. Magath, M. Akbari, Technische Universität Hamburg-Harburg, Germany
- P. 5 An Optoelectronic CW THz Source for Imaging Applications** 213
 K. Siebert, G. Segschneider, H. Quast, H. Roskos, S. Tautz, P. Kiesel, G. Döhler,
 V. Krozer, Goethe-Univ. Frankfurt, Univ. Erlangen, TU Chemnitz, Germany
- P. 6 Analysis and Design of Quasi-Optical Filters** 217
 M. Bozzi, L. Perregini, University of Pavia, Italy

P. 7	Attempt to Generate Narrow Line Width, CW Terahertz Radiation by Using Optical Frequency Comb	221
	S. M. Iftiqar, K. Sakai, M. Tani, B. Widiyatmoko, M. Kourogi, M. Otsu Kansai Adv. Res. Center, Tokyo Insti. Of Tech., Kanagawa Ac. Sci., Japan	
P. 8	Continuously Tunable THz-Wave Generation from GaP Crystal by Difference Frequency Mixing with a Dual-Wavelength KTP-OPO	225
	T. Taniuchi, J.-I. Shikata, H. Ito, Tohoku University, Japan	
P. 9	Coplanar Fed Micromachined Planar Antennas for Power Combining Applications at D-Band Frequencies	229
	S. Hirsch, K. Duwe, R. Judaschke, Technische Universität Hamburg-Harburg, Germany	
P. 10	Design and Simulation of a 600 GHz RTD Oscillator using Commercial Harmonic Balance Software	233
	J. Muscat, Ch. V. Sammut, University of Malta, Malta	
P. 11	A New Method to Measure the Shape of Short THz Pulses: Differential Electronic Gating	237
	J. N. Hovenier, R. W. Es, T. O. Klaassen, W. Th. Wenckebach, M. Krätschmer, F. Klappenberger, E. Schomburg, S. Winnerl, G. M. H. Knippels, A. F. G. van de Meer Delft Univ., The Netherlands, Techn., Univ. Regensburg, FOM Inst. Plasma Physics	
P. 12	Electrical Detection of THz Frequencies by Asymmetrically-Shaped n-n⁺-GaAs Diodes	241
	A. Suziedelis, J. Gradauskas, S. Asmontas, G. Valusis, H. G. Roskos, Vilnius Sem. Phy. Institute, Goethe-Univ. Frankfurt, Germany	
P. 13	Fast Physical Optics Simulation of the Dual-Reflector Submillimetre-Wave Telescope on the ESA PLANCK Surveyor	245
	V. B. Yurchenko, J. A. Murphy, J. M. Lamarre, Nat'l Academy of Sciences of Ukraine, Nat'l Univ. of Ireland, Univ. Paris XI	
P. 14	Few-Cycle THz Generation from Semiconductor Quantum Structures	249
	R. Bratschitsch, T. Müller, R. Kersting, G. Strasse, K. Unterrainer, Technical University of Vienna, Austria	
P. 16	From Honey-Comb to SMMIC: Schottky Diodes at TU Darmstadt	251
	C. I Lin, V. Ichizli, M. Rodríguez-Gironés, M. Saglam, P. Szeliga, H. L. Hartnagel, Darmstadt University of Technology, Germany	
P. 17	High Duty Cycle Germanium Lasers and Continuous Terahertz Emission from Germanium	255
	E. Bründermann, D. R. Chamberlin, E. E. Haller, Ruhr-Universität Bochum, Physical Chemistry, Germany	
P. 18	III-V-Material Systems for Heterostructure Barrier Varactors	259
	M. Saglam, A. Megej, J. Sigmund, M. Rodríguez-Gironés, C. K. Mutamba, V. Ichizli, C. I Lin, H. L. Hartnagel, Darmstadt University of Technology, Germany	
P. 19	IF Bandwidth of YBCO Thin Film Hot-Electron Bolometer Mixers	261
	K. Il'in, O. Harnack, M. Siegel, B. Karasik, W. R. McGrath, G. de Lange Research Ctr. Jülich, Germany, JPL & Space Research Organization Netherlands	

P. 20	An InGaAs/InAlAs Superlattice Oscillator for Frequencies above 100 GHz	263
	R. Scheuerer, E. Schomburg, A. Ignatov, K. F. Renk, D. G. Pavelev, Y. Koschurinov, V. M. Ustinov, A. E. Zhukov, A. Kovsh, P. S. Kopev, Univ. Regensburg, Germany, Nizhny Novgorod State Univ. & Ioffe Institute	
P. 21	Integrated 150 GHz Silicon IMPATT Diodes for Power Combining Applications	267
	M. Luschas, R. Ludaschke, K. Schuenemann, J.F. Luy Tech. Univ. Hamburg-Harburg, DaimlerChrysler Research Centre, Germany	
P. 22	Submillimeter-Wave Nonreciprocal Propagation Characteristics in Transversely Magnetized Image Guide and Two-Layer Parallel-Plate Waveguide Containing p- or n-InSb Slab	271
	S. Yodokawa, T. Obunai, Akita University, Japan	
P. 23	Nanotexturization of III-V Compounds for THz-Wave Generation	275
	I. M. Tiginyanu, S. Langa, K. Hjort, J. Monecke, H. L. Hartnagel Tech. Univ. Moldova, Uppsala Univ., Tech. Univ. Freiburg, Darmstadt Univ. of Technology	
P. 24	Phase Noise Estimation for THz radiation from RTDs and Other Solid-State Sources	277
	P. H. Handel, University of Missouri-St. Louis, USA	
P. 25	Power Generation in Waveguide and Quasi-Optical Technologies Using Hybrid Circuits at Millimetre Waves	281
	A. Péden. D. Bourreau, ENST Bretagne, France	
P. 26	Ridged Waveguide Bandpass Filter for Terahertz Applications	285
	G. Goussetis, D. Budimir, Westminster University, UK	
P. 27	Slot Antenna Coupled Microbolometer Arrays for THz Radiation	289
	Y. Yasuoka, Y. Hiraga, Y. Abe, National Defense Academy, Japan	
P. 28	Spatial Pattern Formation of Optically Excited Carriers in Photoconductive THz Antennas	293
	M. Bieler, G. Hein, K. Pierz, U. Siegner, M. Koch, M. W. Feise, D. S. Citrin, Phys.-Tech. Inst., Tech. Univ. Braunschweig, Germany & Washington State Univ.	
P. 29	Temperature Dependence of Low Energy Carrier Dynamics of Silicon by Terahertz Time Domain Spectoskopy	297
	S. Nashima, O. Morikawa, K. Takata, M. Hangyo Research Centre for Superconductive Photonics, Osaka University, Japan	
P. 30	THz Wave Generation by Difference Frequency Mixing in Photonic Crystal Cavity	301
	M. Tani, P. Gu, K. Sakai, H. Kitahara, M. Suenaga, M. Takeda, Kansai Advanced Res Center, Communications, Res Lab, M. P. T., Japan	
P. 31	Nonlinear Response of a Superlattice	305
	T. Flă, B. Birnir, S. J. Allen Jr.	
Author List		309

Field Emission Studies for Microwave and Optical Wave Generation

K. Yokoo, K. Okamura, H. Mimura, O. Yilmazoglu, D. Arslan, H. Hartnagel, and H. Ishizuka

Abstract - We have proposed hybrid electronics based on solid-state and vacuum electron devices for an application to relatively high power and high efficiency active devices in microwave and optical wave regions. The new electronics provides a bunched electron beam in these frequency regions and a fine beam with an extremely low electron temperature by the combination between field emission and semiconductor technologies.

The paper describes the experiments of microwave electron emission from a GaAs field emitter caused by a traveling dipole domain originated by the Gunn effect in the compound semiconductor emitter and resonant tunneling emission from a GaAs/AlAs quantum structure.

In addition, the paper describes Smith-Purcell radiation in optical wavelength using a field emitter arrays.

I. INTRODUCTION

The topic of vacuum microelectronics has been receiving a great deal of attention in the field of electron devices for the past ten years. A field emission display (FED) is a major subject in development of vacuum microelectronic devices due to an extremely large market for image media in the 21st century. However, the vacuum microelectronics is still the center of interest in high frequency electronics, because it provides relatively high power and environment hard electronics due to the advantages of vacuum as a charge transport medium. In addition, vacuum devices are generally possible to apply energy recover technique for spent electrons resulting in high efficiency.

We have proposed generation of a modulation electron beam at the frequency of microwave and in excess of millimeter wave regions and a fine electron beam with a high brightness and an extremely low beam temperature from a field emitter arrays (FEA) by applying a solid-state device technology to FEA [1]. The modulation beam provides a high efficiency in an electron beam device as expected from the operation of klystron and traveling wave tube. The cold electron beam is applicable to optical wave and further high frequency devices. These hybrid electronics based on a combination technology of solid-state and vacuum electron devices were first proposed to develop a monolithic device of FEA and an active device to control the emission current of FEA for an application to FED [2]. Then, the operation frequency is limited around several tenth and hundreds MHz. However, the concept has been expanded in the operation frequency up to microwave and THz wave regions not only by accommodating microwave transistor and applying the Gunn effect in a compound semiconductor to a FEA, but also using photomixing technique to a semiconductor FEA [3]. The cold beam without energy dispersion is produced

by using resonant tunneling behavior in a quantum structure [4].

The paper describes the basic experiments of the proposals, in which microwave electron emission based on a traveling dipole domain originated by the Gunn effect in a GaAs field emitter and resonant tunneling electron emission from a GaAs/AlAs quantum structure are discussed. Finally, the paper describes Smith-Purcell radiation in optical wavelength using a field emitter arrays.

II. ELECTRON EMISSION FROM GUNN DOMAIN

When a voltage higher than the threshold voltage is applied on a compound semiconductor diode, traveling dipole domains are generated in the diode and Gunn oscillation takes place. If the emitter tips of FEA are constructed from a compound semiconductor such as GaAs and InP and biased by suitable electric field, traveling domains are generated in the emitter and the accumulated charges in the domains are emitted into vacuum when they reach the emitter surface. The frequency of the pre-bunched electron emission is determined by the emitter size and configuration same as the Gunn diode and covers microwave and millimeter wave regions.

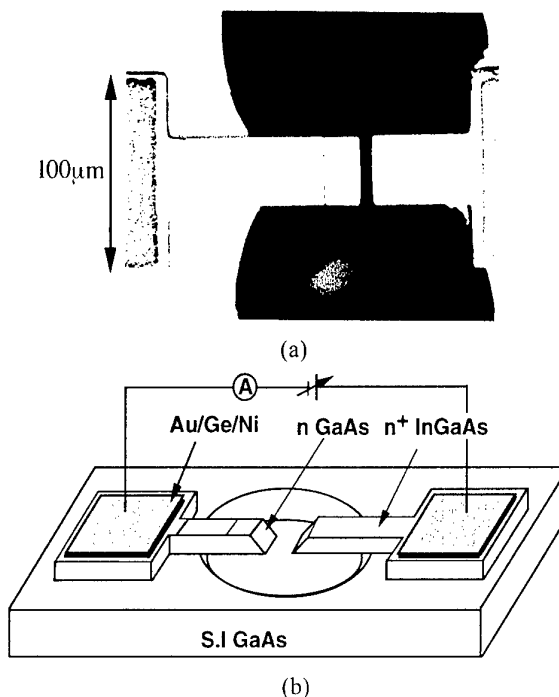


Fig. 1: SEM image (a) and its schematic structure (b) of the GaAs lateral field emitter

K. Yokoo, K. Okamura, and H. Mimura are with Research Institute of Electrical Communication, Tohoku University, Katahira, Aoba-ku, Sendai 980-8577, Japan

O. Yilmazoglu, D. Arslan, and H. Hartnagel are with Institut für Hochfrequenztechnik, Technische Universität Darmstadt, Mercksstr. 25, 64283 Darmstadt, Germany

H. Ishizuka is with Fukuoka Institute of Technology, Higashi-ku, Fukuoka 811-0295, Japan

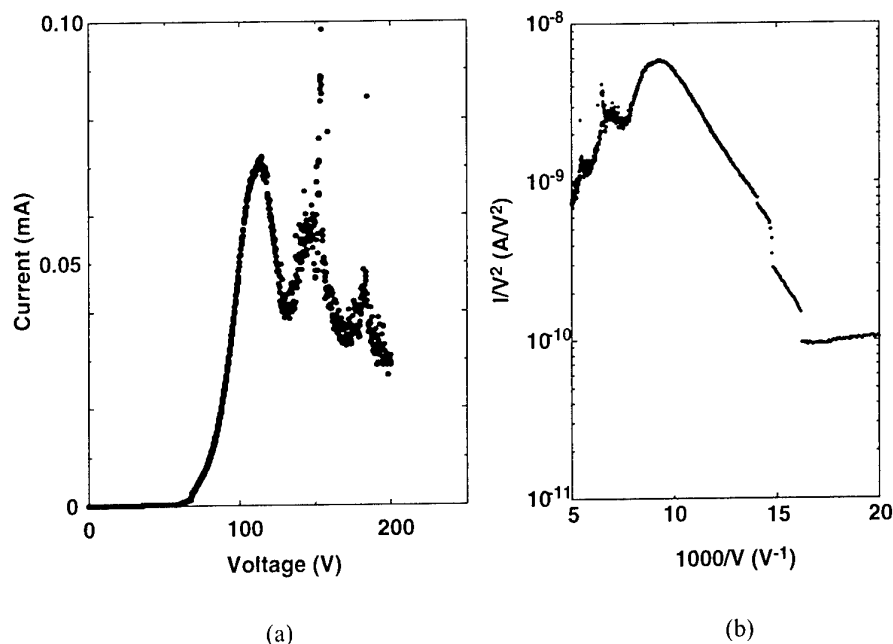


Fig. 2: Emission current-voltage characteristic of the GaAs emitter (a) and its Fowler-Nordheim plot (b)

We fabricated the GaAs field emitters with lateral structure as the first step of experiments. Figure 1 (a) and (b) show a SEM image and a schematic structure of the emitter, respectively, which are fabricated by micromachining technique using anisotropic etching of GaAs [5]. The doping concentration of the GaAs emitter is $1 \times 10^{15} \text{ cm}^{-3}$, which satisfies formation of the traveling dipole domains in the emitters. In addition, we fabricated the emitters with doping concentration of $1 \times 10^{18} \text{ cm}^{-3}$ to compare the emission characteristics of the emitters.

Figure 2 (a) and (b) show a current-voltage characteristic of an emitter and its Fowler-Nordheim plot, respectively. Electron emission occurs at about 60 V and is characterized as field emission from the slope of the straight line in the F-N plot at the low voltages less than 100 V. However, the emission current reaches the maximum value at about 110 V and it becomes unstable at the voltages above, as shown in Fig.2 (a). The current voltage characteristic of the emitter is quite similar to that of a bulk GaAs diode with Gunn oscillation except the threshold voltage around 60 V in the characteristic which does not appear in a conventional Gunn diode. On the other hand, the emission current increases monotonically with increase in voltage in the emitter with the doping concentration of $1 \times 10^{18} \text{ cm}^{-3}$, though there is the threshold voltage in its characteristic, as same as the emitter shown in Fig.2 (a). We are expecting that the electron emission is characterized by the field emission of accumulated electrons in the traveling dipole domains in the emitter.

III. RESONANT TUNNELING EMISSION

A high brightness and low emittance electron beam is very important for applications to optical wave and further high frequency electron beam devices such as a tabletop free electron laser (FEL) at optical wave and X-ray regions [6]. A cold electron beam without energy dispersion is produced by applying the resonant tunneling effect in a quantum structure to an electron emitter.

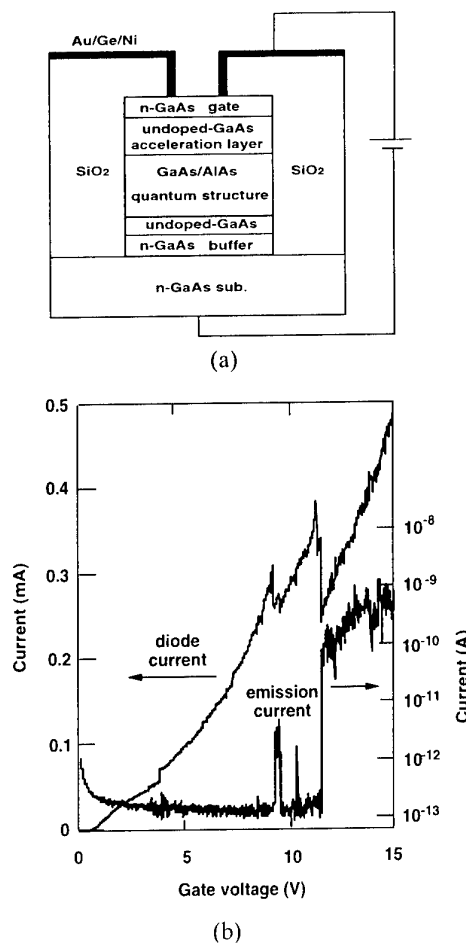


Fig. 3: Schematic diagram of a resonant tunneling cathode with GaAs/AlAs quantum-well (a) and its diode and emission current characteristics (b)

Figure 3 (a) shows the schematic diagram of a resonant tunneling cathode with GaAs/AlAs quantum-well structure fabricated by molecular beam epitaxy. Figure 3 (b) shows the diode and emission current characteristics of the cathode as a function of gate voltage. The emission current increases abruptly at some threshold voltages and has several peak values following the diode current of resonant tunneling through the sub-bands in the quantum well. The resonant tunneling electron emission is expected to be narrow enough in energy spread of emitted electrons, which improves drastically the resolution of electron microscope and electron lithograph. In addition, these cold electrons enable to produce an extremely low emittance beam and realize a new electronics such as an electron channeling free electron laser at X-ray region [7].

IV. SMITH-PURCELL RADIATION

A tabletop FEL is an attractive application of FEA, because the compact radiation system covers almost all wavelength above millimeter and submillimeter. Smith-Purcell (SP) radiation was examined at optical wavelengths of 350-750 nm by using FEA as a first step of relatively high energy beam applications of FEA.

Both single-gated Si-FEA with the number of emitter tips from 1 to 7, and double-gated FEA with 640 tips are used in the experiments, as one of SEM image of the emitter is shown in Fig. 4. An electron beam with the current higher than 10 μ A is produced from FEA and is accelerated up to 45 keV in energy by the stabilized Van de Graaff generator. The energetic electron beam flows on a grating after passing through the slit with 1 mm in width provided just in the front of the grating. The grating used in the experiments is the aluminum-coated holographic replica with the period of 0.56 μ m. Optical radiation was measured in the diffraction angle of 80° from the center of the grating.

Figure 5 shows the power spectra of radiation for several beam energy. The spectra showed good agreement with the theoretical prediction of the SP radiation, as shown in Figure 6. Diffraction orders of the radiation were -2, -3 and -4 for beam energy around 45 keV and the orders from -3 to -5 were observed at the energy around 20 keV. The radiation was relatively stable over several minutes reflecting the stable electron emission from the FEA.

These radiation experiments assure the application of FEA to a compact FEL at optical wavelength.

V. CONCLUSION

The paper described the experiments of the microwave electron emission caused by traveling dipole domains in a GaAs field emitter and the resonant tunneling emission from GaAs/AlAs quantum structure. These combination technology of solid-state and vacuum electron devices provides a new electronics especially in the field of high frequency electronics. Finally, the paper described Smith-Purcell radiation at optical wave length using a field emitter arrays and a sub-micron pitch grating which are fabricated by micromachining technique. The experiments show that FEA provides a tabletop tunable radiation source covering the wavelengths of optical and X-ray regions, which is widely applicable in the material and the biological science.

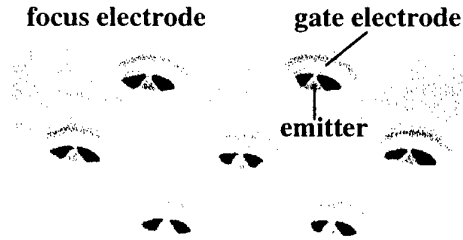


Fig. 4: SEM image of Si gated-FEA used in the experiments of Smith-Purcell radiation

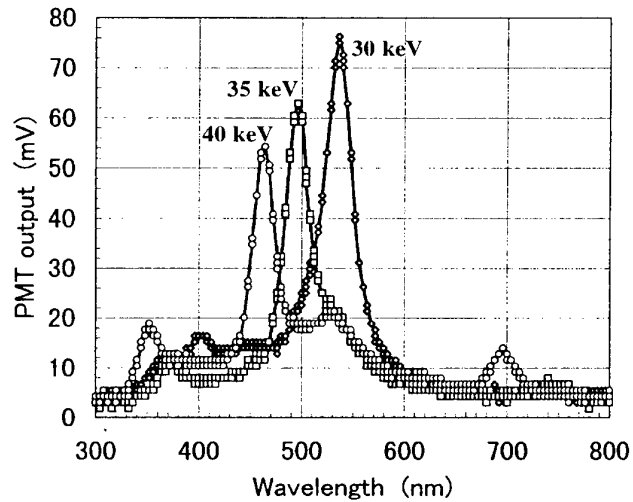


Fig. 5: Power spectra of Smith-Purcell radiations for several beam energy

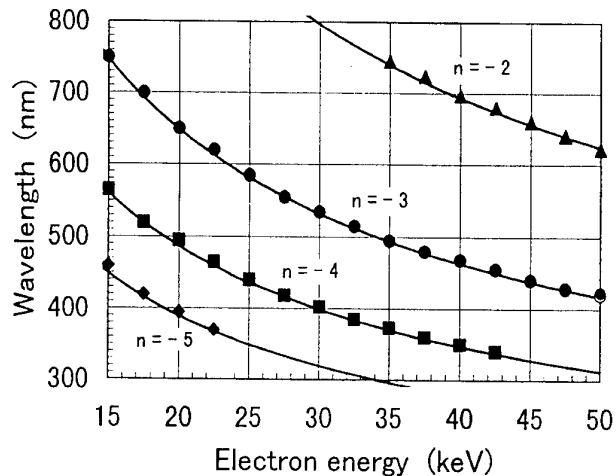


Fig. 6: Radiation wavelength for several diffraction orders observed at the diffraction angle of 80° from the center of the grating

Acknowledgment

The work was partly carried out at the Laboratory for Electronic Intelligent Systems, Research Institute of Electrical Communication, Tohoku University. Part of the work was supported by a Grant-in-Aid for Scientific Research from the Ministry of Education, Science, Culture and Sports of Japan.

References

1. K. Yokoo, Y. Neo, and H. Mimura, "New Electronics Bridging the Gap between Solid-State and Vacuum Microelectronics," 7th Int. Sympo. On Recent Advances in Microwave Technol. Proc., pp. 259-262, 1999
2. K. Yokoo, M. Arai, M. Mori, J. Bae, and S. Ono, "Active Control of the Emission Current of Field Emitter Arrays," J. Vac. Sci. Technol. B 13(2), pp. 491-493, 1995
3. K. Yokoo, "Proposal of THz FEL Using a Photomixing Field Emission Cathode," Conf. Dig. 23rd Int. Conf. on Infrared and Millimeter Waves, pp. 340-341, 1998
4. H. Mimura, Y. Neo, K. Okamura, H. Shimawaki, and K. Yokoo, "Resonant Tunneling Emission from GaAs/AlAs Quantum Structures," 12th Int. Vac. Microelect. Conf., pp. 378-379, 1999
5. H. Mimura, D. Arslan, H. Hartnagel, K. Tajima, K. Okamura, H. Shimawaki, and K. Yokoo, "Lateral GaAs Field Emitters Fabricated by Micromachining Technique," 12th Int. Vac. Microelect. Conf., pp. 146-147, 1999
6. H. Ishizuka, Y. Nakahara, S. Kawasaki, N. Ogawa, K. Sakamoto, A. Watanabe, and M. Shiho, "Design Study of mm to nm Diameter Electron Beams for Submillimeter-Wave to X-Ray Free-electron Lasers," Nuc. Instru. & Methods in Phys. Res., A 331, pp. 577-580, 1993
7. M. Strauss, P. Amendt, N. Rostoker, and A. Ron, "X-Ray Laser Gain Bragg Reflection in Relativistic Electron Beam Channel Radiation Systems", IEEE Trans. on Plasma Sci., 16, pp.548-551, 1988

Narrow-linewidth interwell THz intersubband emission

Benjamin S. Williams, Bin Xu, Qing Hu, Michael Melloch

Abstract – Narrow-linewidth terahertz spontaneous emission resulting from interwell (or diagonal) intersubband transition from an electrically pumped multiple quantum-well (MQW) structure was observed. The center frequency of the emission peak is at 2.57 THz, and its full width at half maximum (FWHM) is 0.47 THz. The emission frequency is in good agreement with the calculated intersubband transition energy of 11.3 meV (corresponding to 2.7 THz) in a three-level system, which was designed to achieve population inversion between two radiative levels using LO-phonon assisted depopulation.

I. INTRODUCTION

Spontaneous emission based on intersubband transitions was first observed in the far-infrared or terahertz (THz) frequency range[1]. However, lasers based on intersubband transitions have been developed only in the mid-infrared frequencies. In principle, intersubband lasers could be made to operate at much longer wavelengths by tailoring the design of suitable quantum-well structures. Compared to mid-infrared intersubband lasers, intersubband THz lasers require a more precise control of electron transport as well as new methods for optical mode confinement.

THz intersubband emissions with narrow linewidths (the inverse of which is proportional to the peak gain) have been measured from devices based on intrawell (vertical) intersubband transitions [2],[3],[4]. The scheme of intrawell intersubband transition is known to yield a large radiative dipole moment and a lesser sensitivity to interface roughness. Both features are advantageous to achieve a narrow emission linewidth. However, intrawell schemes also typically possess higher current densities due to faster non-radiative scattering mechanisms. Also, it is difficult to implement a three-level system utilizing LO-phonon assisted depopulation based on an intrawell transition scheme. The bottom of the lasing well must be raised relative to the rest of the structure so that the lower radiative level can be emptied by emitting longitudinal optical (LO) phonons, whose energy (36 meV or 9 THz) is at the upper end of the THz spectrum. Raising the bottom of the well would require adding aluminum to the well material GaAs, which would result in a much broader emission linewidth due to alloy scattering [5]. Furthermore, because of the uncertainty in the conduction band offset between $\text{Al}_x\text{Ga}_{1-x}\text{As}$ and GaAs and the poor accuracy in controlling the Al mole fraction for small values of $x \sim 0.05$, an accurate energy alignment between the levels in the lasing well and the rest of the structures will be difficult to achieve. Because of these issues, all

previous narrow-linewidth THz intersubband emissions were obtained from two-level systems with miniband injectors, and the population inversion will sensitively depend on the details of electron-electron scattering. In this letter, we report our measurements of narrow-linewidth THz emission that results from interwell (or diagonal) intersubband transitions from a three-level system, whose second level can be emptied by fast LO-phonon scattering.

The MQW structure is based around a core three-level system constructed from a GaAs/ $\text{Al}_{0.3}\text{Ga}_{0.7}\text{As}$ triple-quantum-well structure, as shown in Fig. 1(a). The conduction band profile, subband energies, and wavefunctions (magnitude square) were calculated by self-consistently solving the Schrödinger and Poisson equations in the effective mass approximation. The three

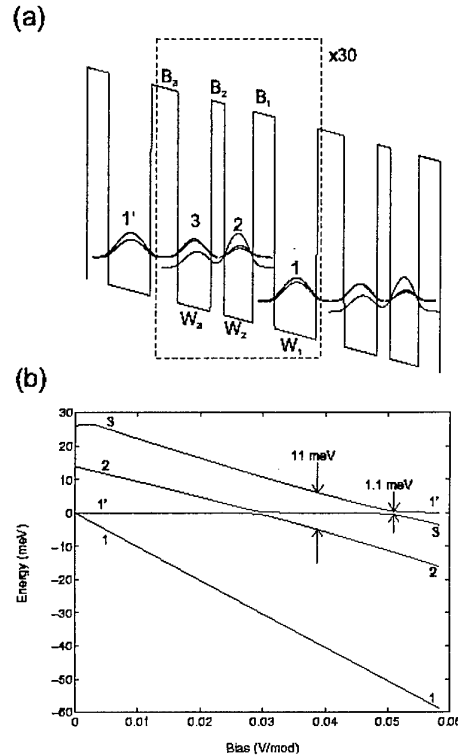


Fig. 1. (a) Numerically calculated band diagram, subband levels, and squared magnitude wave functions of two cascade-connected triple quantum-well modules under a bias of 51 mV/module. (b) Energy levels in the triple-well module vs. bias. E_1' is the injection level from the previous module and is set to zero.

barriers B_1 (4.5 nm), B_2 (2.8 nm), B_3 (5.6 nm), and three wells W_1 (8.8 nm), W_2 (5.9 nm), and W_3 (6.8 nm) form the triple-well module. E_1 , and E_2 , and E_3 are the ground

B. Williams, B. Xu, and Q. Hu are with the Massachusetts Institute of Technology, Cambridge, Massachusetts 02139.
M. Melloch is with Purdue University, West Lafayette, Indiana 47907.

states in each well, and together they form a three-level system. Thirty such three-well modules were cascaded together and grown by MBE on a n^+ GaAs substrate between n^{++} contact layers.

The designed bias for the THz emission MQW structure is 51 mV per module, at which point the ground state of a previous module E_1 is aligned with E_3 , and electrons populate the upper level of the three-level system via resonant tunneling. Electrons make a radiative transition to E_2 and emit a THz photon corresponding to the energy separation $E_{32} = 11.3$ meV (2.7 THz). At this bias, E_1 and E_3 are anticrossed and their wavefunctions are heavily mixed, which allows us to treat them as a combined doublet state. All the properties related to E_3 were calculated for the combined E_1/E_3 state. The anticrossing gap between E_1 and E_3 , determined by the thickness of B_3 , is 1.1 meV, as shown in Fig. 1(b). This anticrossing gap will broaden the THz emission spectra, since electrons will occupy both E_3 and E_1 levels under the resonant tunneling condition.

Non-radiative scattering from levels $2 \rightarrow 1$ and $3 \rightarrow 1$ is dominated by LO-phonon scattering. The LO-phonon scattering rates were calculated using the dielectric continuum model to account for the full complex phonon spectra [6],[7], including interface modes and confined modes. The energy separation between E_2 and E_1 (~ 40 meV) is designed to be slightly greater than the GaAs LO-phonon energy (~ 36 meV), so that electrons on the E_2 level can be depopulated by "GaAs-like" LO-phonon scattering with a time $\tau_{21} \approx 58$ ps. For non-zero electron temperatures, the scattering time decreases to as low as 40 ps due to activation of "AlAs-like" interface phonon modes (~ 48 meV). The parasitic scattering time from E_3 to E_1 is $\tau_{31} \approx 95$ ps, which is much longer than τ_{21} because of the reduced wavefunction overlap. These LO-phonon-scattering times are longer than the typically picosecond-scattering times seen for intrawell transitions due to the use of relatively thick barriers to keep the current density low. The scattering process from E_3 to E_2 is due to a combination of acoustic-phonon scattering, electron-electron scattering, and LO-phonon scattering of hot electrons [8],[9]. Consequently, population inversion could be achieved between E_3 and E_2 levels, if τ_{21} is made smaller than τ_{32} .

The energy separation of the two radiative subbands is designed to be close to their anticrossing gap. As a result, the wavefunctions of the E_3 and E_2 levels have a strong overlap, which yields a large radiative dipole moment ($\mu_{32} \approx 30$ Å). This results in a radiative transition lifetime of $\tau_{rad} \approx 63$ μs. Quantum efficiency $\eta \approx \tau_{31}/\tau_{rad}$ is estimated to be less than 10^{-6} . To assure full carrier ionisation and to eliminate radiative 2p-1s impurity transitions, the Si delta doping was centered in the collector barrier B_1 . The actual doping level was measured using capacitive methods [4] to be $\sim 2.5 \times 10^{16}$ cm $^{-3}$, or 8.5×10^{10} cm $^{-2}$ /module. This was slightly higher than the designed doping level of 6×10^{10} cm $^{-2}$ /module.

In order to couple out a large portion of the intersubband radiation power from a lossy cavity, we used a diffractive

metallic grating with a 15 μm period and a 50% filling factor [10]. This grating, which also served as an ohmic contact, was patterned on top of the device mesas using an annealed Ni/Ge/Au alloy. The measured grating-coupled surface emitter has an area of 415×615 μm 2 . We also processed smaller unpatterned mesas with a size of 115×115 μm 2 to measure the dc current-voltage (I - V) relation. Fig. 2 shows the dc I - V curve of the MQW structure measured at 4.2 K, along with its differential conductance.

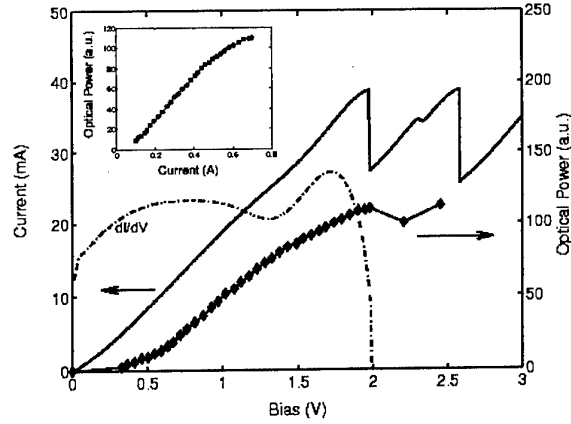


Fig. 2. Measured dc current density and conductance vs. the bias voltage of the 30 module device at 4.2 K. Also plotted is the measured intersubband output power vs. bias and current (inset), which were measured with pulsed bias with the device cooled to 5 K on the cold stage.

The conductance peaks at 1.7 V, indicating the point at which E_1 is aligned with E_3 . This is close to the designed bias of 1.53 V (30×51 mV), with the extra voltage likely due to the contact resistance. The corresponding current density at this bias is measured to be $J_0 \approx 254$ A/cm 2 . At biases greater than 2 V, E_1 becomes misaligned with E_3 , resulting in a negative differential resistance. The broader conductance peak centered at 0.7-0.8 V is likely due to the resonant tunneling process of $E_1 \rightarrow E_2$.

For emission measurements, the device was indium soldered to the cold stage in a vacuum cryostat. A free-space Fourier Transform Infrared spectrometer (FTIR) operated in step scan mode was used to resolve emission spectra. A composite silicon bolometer was used in conjunction with a lock-in amplifier to detect the THz radiation. The optical path was purged with nitrogen gas to prevent absorption by water vapor. The bias voltage across the emission device was square-wave modulated at 400 Hz with a 50% duty cycle.

Our optical spectra reveal a clear peak due to the $E_3 \rightarrow E_2$ intersubband emission. A representative spectrum taken at 5 K is shown in Fig. 3(a), which was taken at a bias of 1.6 V (close to the designed value of 1.53 V). The measured peak frequency of 2.57 THz (corresponding to 10.6 meV) is close to the designed value of 11.3 meV. Since $\Delta E = E_3 - E_2$ is designed to be close to the anticrossing gap, E_3 and E_2 track each other as the bias voltage is changed, as shown in Fig. 1(b), and we should expect to see little Stark shift of the emission frequency.

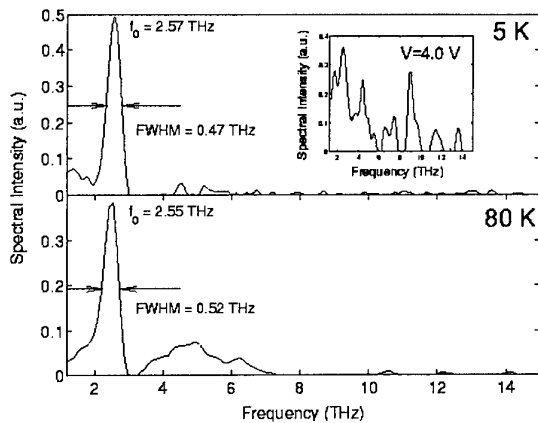


Fig. 3. Spectrally resolved THz intersubband emission taken at (a) 5 K and (b) 80 K under a bias of 1.6 V. The inset shows the spectrum under a 4.0 V bias.

This is indeed the case. In the bias range of 1.0-1.9 V, in which the level E_3 has an appreciable population, the emission spectra showed a narrow peak whose frequency barely changed with the bias voltage. The full-width half-maximum (FWHM) of the emission peak is as narrow as 0.47 THz (1.93 meV). In comparison, the anticrossing gap of E_1 and E_3 is 1.1 meV. At anticrossing, the two levels are spatially extended (as shown in Fig. 1(a)) and both contribute to the intersubband emission signals. Thus, a large fraction of the measured 1.93 meV linewidth is due to the energy splitting of the injection level E_1 and the upper radiative level E_3 . Even with 30 modules and a relatively high doping density, the total linewidth broadening due to nonuniformity, interface roughness, impurity and phonon scattering, is only ~ 0.8 meV. The spontaneous emission linewidth can be further reduced by increasing the thickness of the injection barrier B_3 that will decrease the anticrossing gap between E_1 and E_3 , provided that the injection efficiency is still limited by the lifetime τ_3 of the E_3 level [11].

In order to verify the intersubband origin of the measured emission spectra, we have measured emission spectrum at a high bias of 4.0 V at which the energy levels are severely misaligned. The spectrum is shown in the inset of Fig. 3(a), and it bears little resemblance to the main figure.

The emitted intersubband optical power is plotted versus applied bias in Fig. 2, and shows the expected behaviour. Since this power is proportional to the E_3 population, the observed power drops above 2.0 V as the subbands become misaligned. Examination of the power versus current characteristic reveals a slightly sublinear behaviour at higher currents, indicating a decrease in τ_{32} at high populations (due to $e-e$ scattering) or currents/temperatures (due to thermally assisted LO-phonon scattering). Interpretation of the $L-I$ behaviour cannot be directly compared with that from a two-level system, since at low bias, current flows through level E_2 which emits THz photons at different frequencies. The peak intersubband output power was measured to be several pW, compared with a calculated emission power

of approximately 5-10 nW. The large discrepancy is attributed to a combination of low optical collection efficiency, and free carrier losses in the upper layer.

Spectra were also taken with the cold stage cooled with liquid nitrogen to 80 K. At this elevated temperature, the $I-V$ characteristics remained principally unchanged, but the emitted optical power due to intersubband transitions was approximately a factor of 2.5 smaller. This difference is due to a reduced scattering time τ_{32} at the elevated temperature. A measured spectrum is shown in Fig. 3(b). The main peak is essentially the same as the one measured at 5 K, with a slightly broader linewidth of 0.52 THz (2.14 meV). The secondary broad feature is blackbody radiation due to device heating. The linewidth measured at 80 K is expected to be similar to that at 5 K, since nonparabolicity is negligible for THz intersubband emitters. Nevertheless, our experimental verification is encouraging for the development of intersubband THz sources at elevated temperatures.

In steady state, the relative population $n_3/n_2 = \tau_{32}/\tau_{21}$, and is a critical parameter in achieving gain. τ_{21} is due to LO-phonon scattering and can be calculated (~ 40 -58 ps). τ_{32} , however, is mainly due to electron-electron scattering and LO-phonon scattering of hot electrons. Both processes depend on the injection levels and it is difficult to accurately calculate the scattering time. Using a rate equation analysis, at design bias the current density is given by $J_0 = eN_D(\tau_{32} + \tau_{31})/((\tau_{32} + \tau_{21})\tau_{31})$. For the calculated values of τ_{21} and τ_{31} however, J_0 (254 A/cm²) only weakly depends on τ_{32} , and thus an accurate extraction of τ_{32} from experimental data is difficult. Due to the extremely thick collector barrier, and the resulting long τ_{21} , the existence of a population inversion in this particular structure is unlikely. However, in principle, our three-level systems can be easily modified to yield a greater scattering time ratio τ_{32}/τ_{21} by reducing the thickness of the collector barrier B_1 . Since this decreases the carrier transit time through a module, the doping density must be reduced to prevent an increase in current density, and a corresponding reduction in τ_{32} due to increased thermally activated LO-phonon scattering.

In summary, we have observed narrow-linewidth intersubband THz emission based on interwell (or diagonal) transitions. This intersubband-transition scheme allows a straightforward implementation of three-level systems, which can be carefully engineered to achieve population inversion at THz frequencies.

This work was supported by AFOSR, NASA, NSF, and ARO.

References

- [1] M. Helm, P. England, E. Colas, F. DeRosa, and S. J. Allen, Jr., "Intersubband emission from semiconductor superlattices excited by sequential resonant tunneling," Phys. Rev. Lett. vol. 63, pp. 74-7, 1989.
- [2] M. Rochat, J. Faist, M. Beck, U. Oesterle, and M. Illegems, "Far-Infrared ($\lambda=88\mu\text{m}$) electroluminescence in

a quantum cascade structure," *Appl. Phys. Lett.*, vol 73, pp. 3724-6, 1998.

[3] J. Ulrich, R. Zobl, K. Unterrainer, G. Strasser, E. Gornik, "Magnetic field enhanced quantum cascade emission," *Appl. Phys. Lett.*, vol 76, pp. 19-21, 2000.

[4] S. Blaser, M. Rochat, M. Beck, J. Faist, and U. Oesterle, "Far-infrared emission and Stark-cyclotron resonances in a quantum cascade structure based on photon-assisted tunneling transition," *Phys. Rev. B*, vol. 61, pp. 8369-74, 2000.

[5] K. L. Campman, H. Schmidt, A. Imamoglu, and A. C. Gossard, "Interface roughness and alloy-disorder scattering contributions to intersubband transition linewidths," *Appl. Phys. Lett.*, vol. 69, pp. 2554-6, 1996.

[6] H. B. Teng, J. P. Sun, G. I. Haddad, M. A. Stroscio, S. Yu and K. W. Kim, "Phonon assisted intersubband transitions in step quantum well structures," *J. Appl. Phys.*, vol. 84, pp. 2155-2164, 1998.

[7] S. Yu, K. W. Kim, M. A. Stroscio, G. J. Iafrate, J. P. Sun, and G. I. Haddad, "Transfer matrix method for interface optical-phonon modes in multiple-interface heterostructure systems," *J. Appl. Phys.*, vol 82, pp. 3363-3367, 1997.

[8] J. H. Smet, C. G. Fonstad, and Q. Hu, "Intrawell and interwell intersubband transitions in multiple quantum wells for far-infrared sources," *J. Appl. Phys.*, vol 79, pp 9305-20, 1996.

[9] B. Xu, Ph.D. thesis, MIT (1998), unpublished.

[10] B. Xu and Q. Hu, *Appl Phys. Lett.*, "Grating coupling for intersubband emission," vol. 70, pp. 2511-3, 1997.

[11] C. Sirtori, F. Capasso, J. Faist, A. L. Hutchinson, S. L. Sivco, and A. Y. Cho, "Resonant tunneling in quantum cascade lasers," *IEEE J. Quantum Electron.*, vol. QE-34, pp. 1722-9, 1998.

Plasma Instability and Terahertz Oscillations in Resonant-Tunneling Transistors

Victor Ryzhii and Michael Shur

Abstract—The self-excitation of plasma oscillations in a resonant-tunneling transistor structure is studied. It is demonstrated that it can give rise to the generation of transient current at frequencies in the terahertz range. The amplitudes and the frequencies of different modes of the generated oscillations are voltage-tuned.

resonance.

I. INTRODUCTION

In this paper, we study the instability of standing plasma waves in a resonant-tunneling (RT) transistor considering the nonlinear stage of their excitation and the generation of terahertz radiation at fundamental plasma frequency and harmonics. The structure under consideration consists of an undoped quantum well sandwiched by a double-barrier RT structure from one side and thick barrier layer from another side. The QW is supplied with the side contacts. This structure is sandwiched between narrow gap doped layers serving as the collector contact and the gate, respectively. The QW plays a role of the emitter channel in which a two-dimensional (2D) electron gas is induced by biasing voltages applied between the emitter channel side contacts and both the collector contact and the gate. Similar structures were proposed and realized as working devices earlier [1], [2]. However, contrary to the normal operation of these devices, we assume that the polarity and the value of the emitter-collector voltage (V_c) are chosen to provide the RT current from the emitter channel. The emitter-gate voltage (V_g) determines the electron concentration in the QW emitter channel and, in turn, the plasma wave velocity and frequencies. [3], [4], [5], [6] The conduction band profile of the RT structure under applied voltages is shown in Fig. 1. Alternatively, we can use a structure similar to a standard high-electron-mobility transistor but with a double barrier RT structure placed into the wide gap region, which separates the channel from the gate.

II. MODEL

We assume that the 2D electron gas in the QW emitter channel is degenerate. The spatio-temporal variations of electron sheet concentration $\Sigma = \Sigma(t, x)$, average lateral velocity in this channel $u = u(t, x)$, and potential of the latter $\varphi = \varphi(t, x)$ (with respect to the QW emitter channel contacts) are described by

the following set of equations:

$$\frac{\partial \Sigma}{\partial t} + \frac{\partial \Sigma u}{\partial x} = -\frac{\Sigma}{\tau_e} \Delta \left(\frac{\varepsilon_{RT}}{\Gamma} \right), \quad (1)$$

$$\frac{\partial u}{\partial t} + u \frac{\partial u}{\partial x} + \nu u = \frac{e}{m} \frac{\partial \varphi}{\partial x}, \quad (2)$$

$$\frac{W_c + W_g}{3} \frac{\partial^2 \varphi}{\partial x^2} - \frac{\varphi}{W_c} - \frac{\varphi}{W_g} = \frac{4\pi e}{\varepsilon} (\Sigma - \Sigma_i), \quad (3)$$

Here e and m are the electron charge and mass, τ_e^{-1} is the product of the try-to-escape frequency and the maximum transmission, ν is the electron collision frequency, W_c and W_g are the thicknesses of the RT structure and the emitter-gate barrier, Σ_i is the induced equilibrium concentration of electrons determined by their threshold voltage and the bias voltages, $\varepsilon_{RT} = \mathcal{E}_{RT} - \frac{1}{2}ea\varphi$ and Γ are the energy, and $a \simeq 1$ is the geometrical factor. The axis x is directed in the emitter channel plane. The RT resonance form-factor is approximated as $\Delta(z) = (1 + z^2)^{-1}$. Equation (3) is a consequence of the Poisson equation in the so-called weak non-locality approximation. This equation is more general than that often used and which corresponds to the “gradual channel” approximation [7].

We shall further assume that the span of the QW emitter potential variations is not too large that nonlinearities associated with the left-hand-side terms of

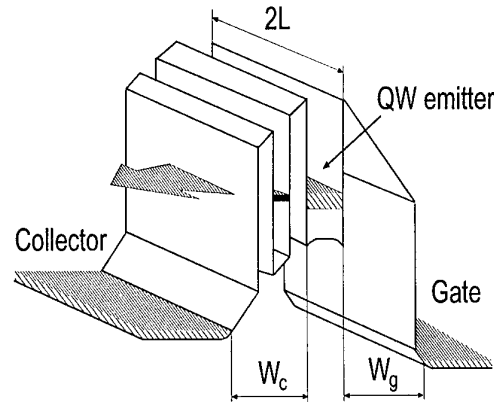


Fig. 1. Conduction band profile of the RT structure.

V. Ryzhii is with Computer Solid State Physics Laboratory, University of Aizu, Aizu-Wakamatsu 965-8580, Japan. M. Shur is with the Department of Electrical, Computer, and Systems Engineering, Rensselaer Polytechnic Institute, Troy, NY 12180-3590 USA

Eqs. (1) and (2), i.e., hydrodynamic nonlinearities, are weak. When the width of the tunneling resonance is small, so that this resonance is sufficiently sharp, the hydrodynamic nonlinearities can be neglected in comparison to the nonlinearity caused by the voltage dependence of the RT current in the right-hand side of Eq. (1). Let us choose such a value of voltage V_c to provide $\mathcal{E}_{RT} = \Gamma/\sqrt{3}$. This voltage corresponds to negative differential conductivity of the RT structure and the maximum of its modulus. Under these assumptions, the right-hand side of Eq. (1) can be expanded in powers of φ and presented as $\frac{1}{e}[j_0 - (\sigma_{RT}\varphi + \gamma_{RT}\varphi^3)]$, where j_0 is the steady-state component of the current density, $\sigma_{RT} = -(\sqrt{3}ea j_0/4\Gamma)$, and $\gamma_{RT} = (3\sqrt{3}/64)(ea/\Gamma)^3 j_0$ is the parameter of nonlinearity of the RT structure.

The boundary conditions for the potential of emitter channel are set at the side contacts:

$$\varphi|_x = \pm L = 0, \quad (4)$$

where $2L$ is the channel length (see Fig. 1). In this case, searching for the emitter channel potential in the form $\varphi(t, x) = \varphi_0(x) + \sum_n \psi_n(t) \cos k_n x$, where $\varphi_0(x)$ is the steady-state component associated with the steady-state current along the channel, $k_n = \pi n/2L$ and n is the mode index ($n = 1, 2, 3, \dots$). When the potential potential drop along the channel is small, i.e., $ea|\varphi_0(x)| \ll \Gamma$ (see the estimate below), the nonuniformity of the steady-state components of potential, electron concentration and current density can be neglected ($\varphi_0 \simeq 0$, $\Sigma_0 \simeq \Sigma_i = \text{const}$, and $j_0 \simeq \text{const}$), and Eqs. (1) - (3) give rise to the following equation:

$$\left[\left(\nu + \frac{d}{dt} \right) \left(\nu_n + \frac{d}{dt} \right) + k_n^2 s_n^2 \right] \psi_n = - \left(\nu + \frac{d}{dt} \right) \sum_{n', n'', n'''} \theta_n^{n' n'' n'''} \psi_{n'} \psi_{n''} \psi_{n'''}, \quad (5)$$

Here $\nu_n = \nu_0/b_n$, $s_n = s_0/\sqrt{b_n}$, and $\theta_n^{n' n'' n'''} = (4\pi/\epsilon) \gamma_{RT} W \delta_n^{n' n'' n'''} / b_n$, where $\nu_0 = (4\pi/\epsilon) \sigma_{RT} W = -(\sqrt{3}\pi/\epsilon)(eaW/\Gamma)j_0$, $s_0 = (4\pi e^2 \Sigma_0 W / \epsilon m)^{1/2}$, is the plasma wave velocity in the limit of small k_n , $b_n = 1 + (k_n^2 W_c W_g / 3)$, $W = W_c W_g / (W_c + W_g)$, and $\delta_n^{n' n'' n'''}$ are the coefficients determined by the overlapping integrals for different interacting plasma modes. In particular, $\delta_1^{111} = 1$ and $\theta_1^{111} = \theta_1$, where $\theta_1 = \left(\frac{3\sqrt{3}\pi}{16\epsilon} \right) \left(\frac{ea}{\Gamma} \right)^3 \frac{W j_0}{1 + (\pi^2 W_c W_g / 12 L^2)}$.

III. INSTABILITY

One can show that the state with $\Sigma = \Sigma_0$ and $\varphi = 0$ can be unstable with respect to the excitation of plasma oscillations. Indeed, in the most interesting case when $k_n^2 s_n^2 + \nu \nu_n > 0$, assuming that ψ_n is small and neglecting the nonlinear term in the right-hand

side of Eq. (5), one can arrive at the following formulas for the frequency of plasma oscillations (ω_n) and their growth rate (γ_n):

$$\omega_n = \left[k_n^2 s_n^2 - \frac{(\nu - \nu_n)^2}{4} \right]^{1/2}, \quad \gamma_n = -\frac{(\nu + \nu_n)}{2}. \quad (6)$$

One can see from Eqs. (6) that when the differential conductivity of the RT structure is negative and, hence, $\nu_0 < 0$, the uniform state under consideration can be unstable ($\gamma_n > 0$) with the excitation of different plasma modes having the frequencies ω_n . In this case, the criterion of instability has the form $\nu + \nu_n < 0$. The latter can be presented as

$$\frac{\nu_0}{\nu} < -1 - \frac{\pi^2 n^2}{3} \frac{W_c W_g}{L^2}. \quad (7)$$

As can be seen from this inequality, the instability occurs if the differential conductivity is negative and its modulus is sufficiently large. Inequality (7) yields the instability criterion different from that obtained previously. [8] The difference is due to the second term in the right-hand side of inequality (7) which reflects the effect of nonlocality. Such an effect imposes a restriction on the excited plasma modes if the ratio $|\nu_0|/\nu$ is fixed. Thus, in the situation under consideration the spectrum of the excited plasma oscillations is limited to relatively small mode indices n . An additional suppression of the instability of the modes with large indexes can be due to the nonideality of the 2D electron gas in the channel and due to the delay of electrons associated with the RT tunneling.

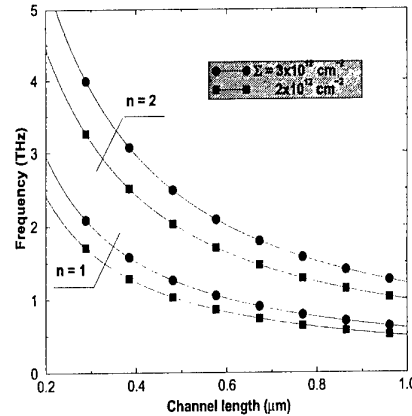


Fig. 2. Frequencies of first and second modes versus channel length for $\mu = 5 \times 10^4 \text{ cm}^2/\text{Vs}$.

Figure 2 shows the frequencies of the different plasma oscillation modes as function of the channel length for different electron concentrations. for the structure with $W_c = 2 \times 10^{-6} \text{ cm}$, The structural

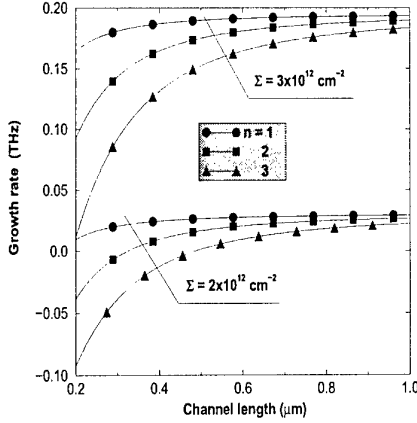


Fig. 3. Growth rate of different plasma modes versus channel length at different electron concentrations for $\mu = 5 \times 10^4 \text{ cm}^2/\text{Vs}$.

parameters used for this and subsequent figures are as follows: $W_g = 4 \times 10^{-6} \text{ cm}$, $\Gamma = 7.5 \text{ meV}$, and $\tau_e = 17.5 \text{ ps}$. One can see that at reasonable device sizes and electron concentrations, the plasma frequencies fall into the terahertz range. Figure 3 shows the dependencies of the plasma oscillations growth rate versus the channel length. As can be seen from Fig. 3, the increase in the electron concentration leads to a significant rise of the growth rate of plasma oscillations and the marked increase of the range where such a growth occurs. The use of the channel with higher electron mobility favors the instability conditions.

IV. NONLINEAR OSCILLATIONS

We shall search for the solution of Eq. (5) in the form $\psi_n(t) = A_n(t) \cos[\omega_n t - \alpha_n(t)]$, where amplitudes $A_n(t)$ and phases $\alpha_n(t)$ are relatively slowly varying functions of time. Further we shall assume that only the fundamental mode ($n = 1$) of the plasma oscillations has a positive increment. Substituting ψ_n into Eq. (5) and averaging over the period of the plasma oscillation, near the instability threshold, where $|\nu + \nu_1|$ is small, one can obtain the following equation for the amplitude of fundamental mode ($n = 1$) of plasma oscillations (compare with [9]):

$$\frac{dA_1}{dt} + \frac{(\nu + \nu_1)}{2} A_1 = -\frac{3}{8} \theta_1 A_1^3, \quad (8)$$

$$\frac{d\alpha_1}{dt} = \frac{(\nu + \nu_1)^2}{4\omega_1} + \frac{3}{16} \frac{(\nu_1 - \nu)\theta_1}{\omega_1} A_1^2, \quad (9)$$

Deriving Eqs. (8) and (9), we neglected the nonlinear effect of higher modes ($n > 1$) because such modes are assumed to be stable in the linear approximation. However, the excitation of the fundamental mode can

result in the forced excitation of the stable modes. Nevertheless, when $|\nu_1|$ barely exceeds ν , one can assume that the amplitudes of higher modes are rather small.

As follows from Eq. (9), the temporal evolution of the amplitude of the oscillations is given by

$$A_1 \approx A_1^0 \frac{\exp(-\frac{1}{2}(\nu + \nu_1)t)}{[1 + (A_1^0/A_1^\infty)^2 \exp(-(\nu + \nu_1)t)]^{1/2}}, \quad (10)$$

where A_1^0 is the initial amplitude (its fluctuational value) and A_1^∞ is the final steady-state amplitude: $A_1^\infty = [-4(\nu + \nu_1)/3\theta_1]^{1/2}$. This state is stable, because for its small perturbations Eq. (9) yields $\gamma_1 = \nu + \nu_1 < 0$. Near the stable state, the oscillation phase slowly varies. This corresponds to the following nonlinear correction of the plasma frequency: $\Delta\omega_1/\omega_1 \approx \nu(\nu + \nu_1)/\omega_1^2$.

Using the obtained amplitude of oscillations of the potential in the QW emitter channel one can arrive at the following expressions for the amplitudes of the first ($\delta J_1 \propto A_1/\Gamma$) and third ($\delta J_3 \propto A_1^3/\Gamma^3$) harmonics of the electron current from the QW emitter channel to the collector contact caused by the fundamental plasma harmonic:

$$\frac{\delta J_1}{J_0} \propto \left(1 - \frac{J_{th}}{J_0}\right)^{1/2}, \quad \frac{\delta J_3}{J_0} \propto \left(1 - \frac{J_{th}}{J_0}\right)^{3/2} \quad (11)$$

where $J_{th} = \left(\frac{2\alpha}{\sqrt{3}\pi}\right)\left(\frac{L}{W}\right)\left(\frac{\Gamma\nu}{ea}\right)$ and $J_0 = 2Lj_0$ is the dc emitter-collector current. The amplitudes of ac electron current can also be expressed via the electron concentration in the QW emitter channel: $\delta J_1/J_0 \propto [1 - (\Sigma_{th}/\Sigma_0)]^{1/2}$ and $\delta J_3/J_0 \propto [1 - (\Sigma_{th}/\Sigma_0)]^{3/2}$, where $\Sigma_{th} = \frac{2\alpha}{\sqrt{3}\pi} \frac{\Gamma\nu\tau_e}{e^2 a W}$. Going back to Eq. (5), one can find that the coupling between the fundamental (unstable) and higher (stable) modes should not result in a marked excitation of the latter if the amplitude of fundamental mode is not too large, i.e., near its excitation threshold: $(J_0 - J_{th}) < J_{th}$ or $(\Sigma_0 - \Sigma_{th}) < \Sigma_{th}$. Figure 4 shows the relative amplitude $\delta J_1/J_0$ of the established current oscillations at the fundamental frequency as a function of the electron concentration in the QW emitter channel for different electron mobilities in the latter. Due to the dependence of the induced electron concentration in the QW emitter channel on the bias voltages, particularly, the emitter-gate voltage, $\Sigma_0 \propto V_g - V_{th}$, (where V_{th} is the threshold voltage), the amplitude of ac electron current can be effectively controlled by this voltage. The emitter-gate voltage can also tune the frequency of the excited current oscillations.

Using Eqs. (1) - (3), one can estimate the potential drop along the channel as $\max e|\varphi_0| \sim J_0(\nu m L/e\Sigma_0)$. Accounting for this estimate, one can find that conditions $\max e a |\varphi_0(x)| \ll \Gamma$ (weakness of the steady-state potential nonuniformity) and $J_0 > J_{th}$ (see relationships (11)) do not contradict to each other if

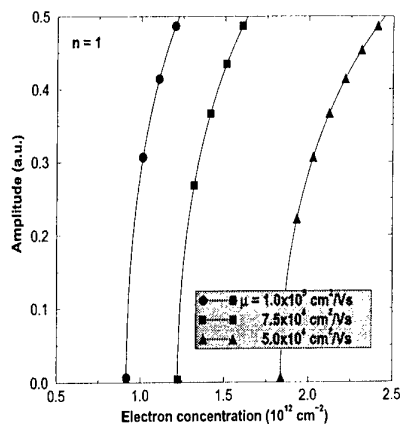


Fig. 4. Amplitude of oscillations versus electron concentration in the channel in structures with different electron mobilities and $2L = 0.3 \mu\text{m}$.

$\nu \ll s/L \sim \omega_1$. This inequality corresponds to sufficiently high electron mobility and concentration in the channel and sufficiently small length of the latter. It is typical for different devices utilizing the plasma waves (see, for example, [4], [5], [6]). Consequently, the electron drift should not lead to a marked change in the instability conditions. However, at a large potential drop along the channel, one may expect a marked change in the RT transistor behavior due to a combination of the considered mechanism and the instability mechanisms studied previously.

V. CONCLUSIONS

Using an analytical model, we studied the self-excitation of terahertz current oscillations and their nonlinear stage in a RT transistor structure associated with the plasma instability in the QW emitter channel. The criteria of the instability were found and the oscillations frequency and amplitude were calculated as functions of the structural parameters and biasing voltage.

ACKNOWLEDGMENT

The authors would like to thank I.Khmyrova and M. Ryzhii for helpful assistance. The work at RPI was partially supported by the Office of Army Research (Project Monitor Dr. Dwight Woolard) and by DARPA (Project Monitor Dr. Edgar Martinez).

REFERENCES

- [1] N. Yokoyama, K. Imamura, S. Muto, S. Hiyamizu, and H. Nishi, "A new functional, resonant-tunneling hot electron transistor (RHET)," *Jpn. Appl. Phys.* vol. 24, pp. L853-L854, 1985.
- [2] A. R. Bonnefoi, D. H. Chow, and T. C. McGill, "Inverted base-collector tunnel transistor," *Appl. Phys. Lett.* vol. 47, pp. 888-890, 1985.
- [3] S. Luryi, "An induced base hot electron transistor," *IEEE Electron Dev. Lett.*, vol. 6, pp. 178-180, 1985.
- [4] M. Dyakonov and M. Shur, "Shallow water analogy for a ballistic field effect transistor. New mechanism of plasma wave generation by DC current," *Phys. Rev. Lett.*, vol. 71, pp. 2465-2468, 1993.
- [5] M. Dyakonov and M. S. Shur, "Plasma wave electronics: Novel terahertz devices using two dimensional electron fluid," *IEEE Trans. Electron Devices*, vol. 43, pp. 1640-1645, 1996.
- [6] V. Ryzhii, "Resonant detection and mixing of terahertz radiation by induced base hot electron transistors," *Jpn. J. Appl. Phys.*, vol. 37, pp. 5937-5944, 1998.
- [7] M. S. Shur, *GaAs Devices and Circuits*. New York: Plenum, 1987.
- [8] M. N. Feiginov and V. A. Volkov, "Self-excitation of 2D plasmons in resonant tunneling diodes," *JETP Lett.* vol. 68, pp. 662-668, 1998.
- [9] A. P. Dmitriev, A. S. Furman, and V. Yu. Kacharovski, "Nonlinear theory of the current instability in a ballistic field-effect transistor," *Phys. Rev. B* vol. 54, pp. 14020-14025, 1996.

Feasibility of a $\text{Si}_{1-x}\text{Ge}_x$ THz Resonant-State Laser

Yu. P. Gousev, I. V. Altukhov, M. S. Kagan, V. P. Sinis, H. K. Olsson, S. G. Thomas, and K. L. Wang

Abstract – We report on pulsed THz emission from $\text{Si}_{1-x}\text{Ge}_x$ structures. d-doped with Boron $\text{Si}_{1-x}\text{Ge}_x$ layer was sandwiched between two Si layers grown by MBE on n-type Si substrate. Optical resonator was formed by high-accuracy polishing of lateral facets. Non-thermal emission was observed at electric field > 250 V/cm and pulse duration was < 1 μs . We believe the emission is due to the population inversion of carriers in the $\text{Si}_{1-x}\text{Ge}_x$ quantum well.

I. INTRODUCTION

Recently emerged Ge resonant-state laser (RSL) [1-5] represents, among the molecular gas laser and p-Ge (or p-Si) laser, a radiation source which can cover the entire frequency range between 2 and 10 THz. Unlike of that of the molecular laser, operation frequency of the RSL can be set to virtually any value within this range. Another feature of the RSL is that, due to the origin of population inversion, it requires relatively low electric field which gives a possibility to operate it in the cw regime [4,5]. Population inversion in the RSL is realised for the states of a shallow acceptor split under external stress. If the strain is high enough, the split-off acceptor state enters

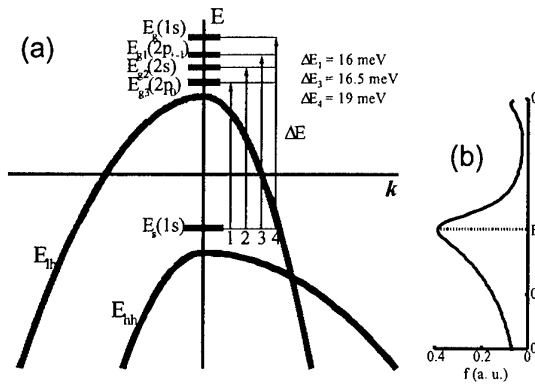


Fig. 1: Possible optical transitions and distribution function of holes under applied electric field for a case of strained Ge [4].

the light-hole branch of the valence band and creates a resonant state. For the case of Ge doped with Ga, external stress should be above ~ 3 kbar. Electric field, which is also necessary for population inversion, provides emptying the ground state due to the impact ionisation. Schematic diagram for possible optical transitions in this case is given in Fig. 1 [4]. The frequency range covered

by the RSL is determined by the threshold stress necessary for creating the resonant state, and the maximum useful stress at which optical phonon-assisted hole transitions to the valence band depopulate the resonant state. Thus, for Ga- or B-doped Ge, the operation frequency can be set to any value between ~ 2 and 10 THz.

An alternative way to realise RSL is to use a p-doped binary alloy of elements having similar to that of Ge structure of valence band, like $\text{Si}_{1-x}\text{Ge}_x$. In such an alloy, strain is induced internally due to the lattice mismatch. Therefore, acceptor levels are split without external stress, and stimulated emission can be obtained just by adding electric field.

II. HOW A $\text{Si}_{1-x}\text{Ge}_x$ LASER SHOULD FUNCTION

Population inversion mechanism in $\text{Si}_{1-x}\text{Ge}_x$ should be similar to that in Ge. However, conventional $\text{Si}_{1-x}\text{Ge}_x$ technology processes use for fabrication Si wafers which gives advantages of easier Si (unlike Ge) processing and simpler integration with Si-based electronics. In this case, x has to be relatively low, and initial position of the acceptor state in the energy gap is close to the acceptor ionisation energy in Si. Since the ionisation energy of Ga or B in Si is larger compared to that in Ge, one should induce higher strain to create the resonant state.

Ionisation energy of B is about 45 meV in Si, and about

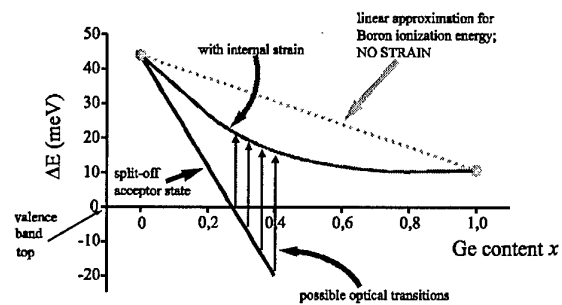


Fig. 2: Possible optical transitions for SiGe.

11 meV in Ge. An approximate diagram for acceptor energy levels in $\text{Si}_{1-x}\text{Ge}_x$ is shown in Fig. 2. Here, we assumed that ionisation energy is changed linearly with Ge content x in case of no strain is induced, and then made correction for the strain effect. In order to create a resonant state, the split-off acceptor state must enter the valence band continuum. Which means, x has to be larger than ~ 0.25 . For such a high Ge content, $\text{Si}_{1-x}\text{Ge}_x$ layer grown on Si becomes unstable, and realisation of the $\text{Si}_{1-x}\text{Ge}_x$ RSL seems problematic.

III. EXPERIMENTAL RESULTS

20 nm thick d-doped with Boron $\text{Si}_{1-x}\text{Ge}_x$ layer was

Yu.P. Gousev and H.K. Olsson are with the Royal Institute of Technology, Electrum 229, 164 40 Kista, Sweden.

I.V. Altukhov, M.S. Kagan, and V.P. Sinis are with the Institute of Radioengineering and Electronics of RAS, 103 907 Moscow, Russia.

S.G. Thomas and K.L. Wang are with the University of California, 66-147KK Engineering IV, Los Angeles, CA 90095, USA.

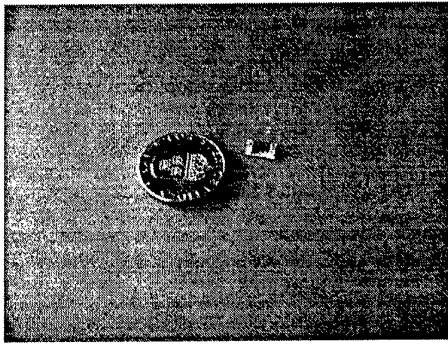


Fig. 3: Sample view. For scale, 1 Kr is shown.

sandwiched between two, 60 and 130 nm thick, Si layers grown by MBE on the n-type Si substrate; x was equal to 0.15. Ohmic contacts to the quantum well have been made by the thermal diffusion process. Lateral facets of the crystal were high-accuracy polished. Sample view is given in Fig. 3; a 1 Kr coin is shown for scaling.

Measurements of far-IR emission from the samples have been made at 4.2 K. Pulsed bias voltage up to 2000 V was applied to the sample. Pulse duration was typically about 1 μ s; repetition frequency 1 to 10 kHz. Both voltage and current applied to the sample were measured during the pulse.

Block diagram for experimental set-up is shown in Fig. 4. Emission was detected with a cooled Ge:Ga detector. To avoid RF and near-IR interference, we used a set of filters; frequency characteristics of filters are shown in Fig. 5. While the metallic mesh, used as a high-pass filter, was installed permanently, IR Teflon and black polyethylene filters were exchanged for a check if there is any contribution to the signal at frequencies above the range of interest. No IR contribution was found with an accuracy of 10 %.

Signal voltage, measured across a resistor connected in series with the detector crystal, was amplified with a low noise amplifier and registered with an oscilloscope. We found that high-intensity emission appeared at bias voltage between 250 and 700 V/cm (Fig. 6). Signal voltage up to 100 mV before amplification has been

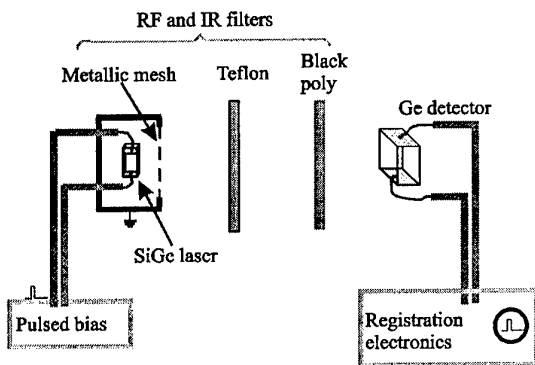


Fig. 4: Experimental set-up.

observed. We believe that difference in the threshold voltage was due to the poor quality of ohmic contacts. Above threshold voltage, intensity increased drastically

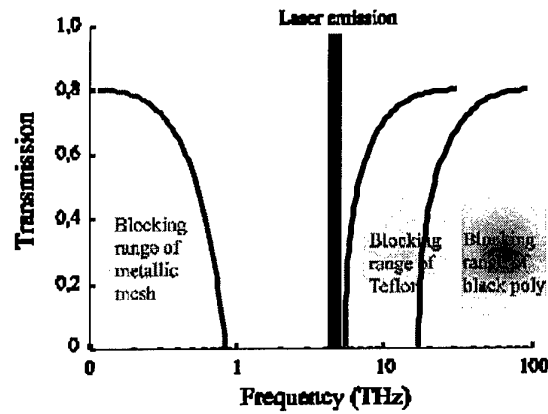


Fig. 5: Frequency characteristics of filters.

by more than an order of magnitude. Since the form of the registered intensity pulse was identical to that of bias voltage for pulse duration $< 1 \mu$ s, we suppose the emission is not due to any thermalisation process. We believe that observed signal corresponds to the stimulated emission from the $\text{Si}_{1-x}\text{Ge}_x$ layer.

The question why stimulated emission is observed at low value of x , requires further investigation. Possible explanation for the origin of population inversion follows from temperature dependence of conductivity of $\text{Si}_{1-x}\text{Ge}_x$ quantum wells presented in [6]. The resonant state can arise in the valence band at lower strain due to the tunneling of holes from the split-off acceptor state to the valence band, if a transverse electric field is present. The latter might be created by the surface charge.

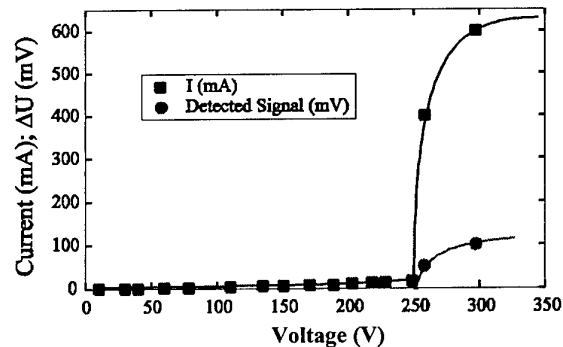


Fig. 6: Current-voltage characteristic and detected signal.

IV. CONCLUSION

We have shown that high-intensity THz emission is generated by $\text{Si}_{1-x}\text{Ge}_x$ quantum wells at low temperatures if a high-quality optical resonator is used for optical confinement. The non-thermal origin of emission proves feasibility of a $\text{Si}_{1-x}\text{Ge}_x$ resonant-state laser.

Acknowledgement

The work was supported by Wenner-Gren Foundation and by the Foundation for Strategic Research (SSF) within the High-Frequency Electronics Program.

References

1. I.V. Altukhov, M.S. Kagan, K.A. Korolev, and V.P. Sinis, *JETP Lett.*, Vol. 59, pp. 476-478, 1994.
2. I.V. Altukhov, M.S. Kagan, K.A. Korolev, V.P. Sinis, E.G. Chirkova, M.A. Odnoblyudov, and I.N. Yassievich, *JETP*, Vol. 88, pp. 51-63, 1999.
3. M. A. Odnoblyudov, I.N. Yassievich, M.S. Kagan, Yu.M. Galperin, and K.A. Chao, *Phys. Rev. Lett.*, Vol. 83, pp. 644-647, 1999.
4. Yu.P. Gousev, I.V. Altukhov, K.A. Korolev, V.P. Sinis, M.S. Kagan, E.E. Haller, M.A. Odnoblyudov, I.N. Yassievich, and K.-A. Chao, Widely tunable continuous-wave THz laser, *Appl. Phys. Lett.*, Vol. 75, No. 6, pp. 757-759, 1999.
5. I.V. Altukhov, M.S. Kagan, Yu.P. Gousev, V.P. Sinis, K.A. Korolev, H.K. Olsson, Yu.M. Galperin, M.A. Odnoblyudov, I.N. Yassievich, and K.-A. Chao, Continuous stimulated terahertz emission due to intra-center population inversion in uniaxially strained germanium, *Phys. B*, Vol. 272, pp. 458-460, 1999.
6. M.S. Kagan, I.V. Altukhov, K.A. Korolev, D.V. Orlov, V.P. Sinis, S.G. Thomas, K.L. Wang, K. Schmalz, and I.N. Yassievich, *Phys. Status Solidi (b)*, Vol. 210, pp. 667-669, 1998.

The copper-doped p-Ge THz laser in the Voigt configuration: possibility of mode-locked operation

J.N. Hovenier, R.M. de Kleijn, T.O. Klaassen and W.Th. Wenckebach,

Department of Applied Physics and Delft Institute for Microelectronics and Submicron Technology (DIMES), Delft University of Technology, P.O. Box 5046, 2600 GA Delft, The Netherlands, and D. R. Chamberlin, E. Bründermann and E. E. Haller, UC Berkeley and Lawrence Berkeley National Laboratory, Berkeley, CA 94720, USA.

Abstract - We have constructed a copper-doped germanium hot hole THz laser and studied its performance under normal - pulsed - operation, in order to investigate the possibility to create very short "quasi monochromatic" pulses through active mode-locking. The E and B field region for which normal "long pulsed" laser emission occurs, emission wavelength as a function of B field and the temporal shape of the laser pulse have been studied. The results indicate that the performance of this Ge:Cu crystal can not yet compete with that of an earlier studied Ge:Ga laser under similar conditions. Nevertheless active mode-locking has already been observed.

I. INTRODUCTION

The p-Ge hot hole laser is a solid state laser with a strong and tunable Terahertz emission [1]. The acceleration of holes in crossed electric- (E) and magnetic- (B) fields at cryogenic temperatures leads to population inversion either between the light- and heavy hole band, leading to intervalence band lasing, or between subsequent light hole Landau levels (cyclotron resonance lasing). We have shown recently that mode locked operation of such a laser can be achieved by applying an ac electric field *parallel* to B at half the cavity round trip frequency. Quasi monochromatic THz pulses as short as 60 ps have been created with that technique [2,3,4].

Most of the investigations on the p-Ge laser have been performed on Ga doped material. However, the ionization energy of this single acceptor is about 11 meV, and the finite population of the acceptor levels under lasing conditions results in strong absorption of emitted light, leading to a large gap in the laser emission around 75 cm^{-1} . Moreover it has been proposed that laser emission at certain wavelengths would be intimately related to the presence of these acceptor levels, interfering therefore with easy wavelength tunability. [5] The presence of different kinds of laser levels possibly also causes the peculiar time dependence of the emission wavelength during a laser pulse, that was found to complicate the creation of reliable mode locked pulse trains [4].

To avoid the gap in the emission spectrum, recently the double acceptors Be and Zn, and the triple acceptor Cu have been used as dopants [6,7]. Because the ionization energies of those acceptors is larger than the highest

emission energy of the Ge laser, they should not in any way interfere with the laser action. Although, the experimental evidence so far seems to indicate that Ge:Be is the best laser material, we have chosen to explore in more detail the Ge:Cu material. The reason for that being the fact that copper doped Ge can easily be fabricated in many different concentrations by simple diffusion of copper in pure Ge, whereas Ge with other dopants have to be Czochralski-grown from a doped melt. That offers a good opportunity for a detailed optimization study of this laser, for (quasi-) CW as well as for mode locked operation.

II. SAMPLE FABRICATION

As starting material we have used a 5 mm thick slice, perpendicular to (100), of Czochralski-grown ultra-pure germanium from Union Minière Electro-Optical Materials. It has a dislocation density of less than 3000 per cm^2 and a p-type impurity concentration of less than 10^{12} cm^{-3} . For the fabrication of the doped samples we followed the recipe outlined in reference [7].

Hall effect samples ($1 \times 5 \times 7\text{ mm}^3$) to test the Cu diffusion technique in the system set up at Delft University were prepared, with crystal faces normal to the (100), (011) and (0-11).

Also a $5 \times 7 \times 10\text{ mm}^3$ bar-shaped sample for a preliminary study of stimulated emission was made, with the HV contacts such that $E \parallel (011)$. For the final laser performance study a $5 \times 7 \times 50\text{ mm}^3$ sample was made (see Fig. 1.), the same size as the Ge:Ga sample on which earlier pulsed and mode lock experiments were

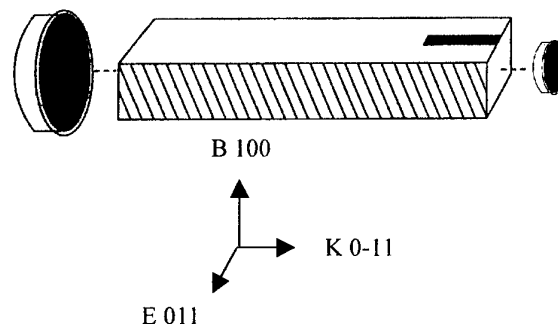


Fig. 1: Sample + cavity.

performed [2,3,4]. The copper diffusion for both lasing crystals was performed at 700 °C for 24 hours, because our results on the Hall samples showed that in that case the resulting copper concentration, after rapid quenching of the crystal to room temperature, would be about $1.5 \times 10^{15} \text{ cm}^{-3}$.

After diffusion, the sample was polish-etched and the 5x7 end faces were made parallel to each other within 30". The high voltage excitation contacts, covering the full 5x50 sides, and the 1x10 modulation contacts at the 7x50 surfaces, were made from gold on palladium, after boron implantation. Etching could not be used to define the electrical contact areas, as it destroys the optically polished end faces. Therefore, during implantation and evaporation, the *non-contact* areas were covered with pieces of silicon wafer. In order to remove implant damage and fully activate the boron, the samples were given a post-implant anneal. Copper wires were soldered on the contact areas with Indium.

III. EXPERIMENTAL SET UP

The small laser crystal with only HV contacts and no external cavity was mounted in a Helium cryostat in the bore of a superconducting solenoid. Experiments were performed with the B-field in various directions with respect to the crystal axis, but keeping B always perpendicular to E. Emission under pulsed HV excitation was measured with a fast cryogenic Ge:Ga detector, placed near to the laser crystal.

The large laser crystal is mounted in a cryostat with tail window. Two flat gold mirrors evaporated on quartz substrates, are pressed to the end faces and isolated from the crystal by 10 μm Teflon films, to form a simple cavity. The crystal is studied in the Voigt configuration, i.e. both E // (011) and B // (100) are perpendicular to the (0-11) optical axis of the laser cavity, see Fig. 1. The diameter of one of the cavity mirrors is smaller than the end face, and light leaking out alongside this mirror, through the cryostat window, is detected using a variety of room temperature detectors. Instead of this small outcouple mirror, also a capacitive outcouple mesh has been used to enable the observation of the light emitted across the full end face of the laser crystal [8]. This results also in a larger signal intensity.

The magnetic field, generated by a homogeneous room temperature electromagnet with a maximum field of 1.3T, can be rotated with respect to E to optimize lasing conditions. Both the HV excitation field and the RF modulation field are applied in pulses of a few microseconds long to avoid excessive heating of the crystal.

The THz emission is studied using either a relatively slow pyroelectric detector, or a very fast mm-wave Schottky diode or a GaAs/AlGaAs heterostructure detector. Using a simple reflection grating set up, the wavelength of the emitted light can be measured. The signals are monitored with either a 500 Mhz digitizing oscilloscope scope or with a single shot 6 GHz bandwidth oscilloscope.

IV EXPERIMENTAL RESULTS

The experiments on the $5 \times 7 \times 10 \text{ mm}^3$ crystal reveal pulsed THz emission that follows closely the high voltage excitation pulse, see fig. 2. As evident from fig. 3, the emission also shows the peculiar dependence on the applied E and B field, with a maximum intensity centered around an E/B ratio of about 1.3kV/T. Those observations prove that the emission is not due to ohmic heating of the crystal, which increases monotonously towards higher E and B fields, but originates from the population inversion created by the crossed E and B

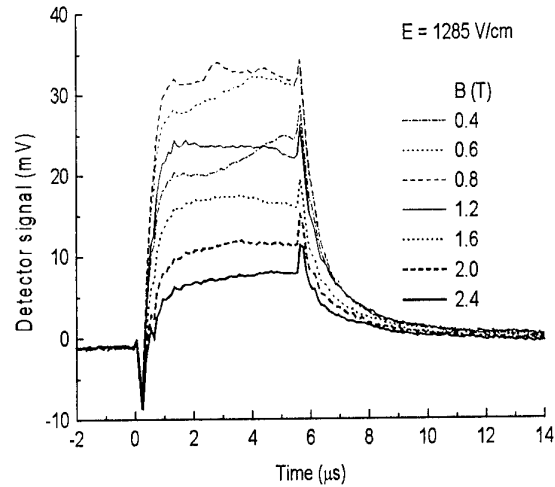


Fig. 2: Pulsed (spontaneous ?) emission from the small laser crystal.

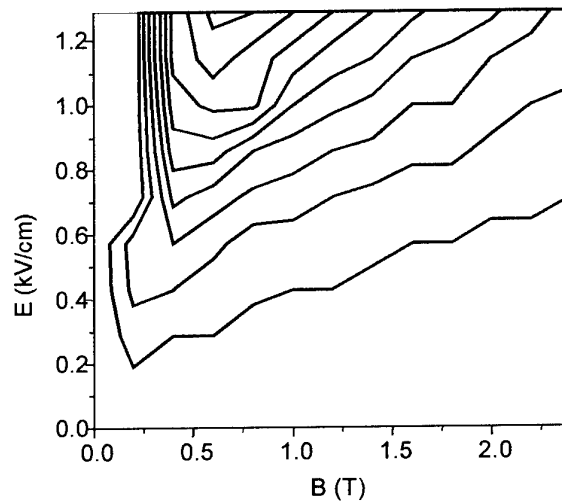


Fig. 3: E-B emission region of small crystal ; each contour line is a 4 mV signal increase ranging from 4 to 36 mV.

field excitation. In view of the rather low signal intensities and the absence of sharp emission boundaries, we deal here most probably with spontaneous rather than with stimulated emission. This result shows that the low temperature density of ionized

acceptors is of the right order of magnitude- $\approx 10^{14} \text{ cm}^{-3}$, about 7% of the Cu density [7] - to create population inversion.

Introductory experiments on the $5 \times 7 \times 50 \text{ mm}^3$ sample were performed also using a Ge:Ga detector near the crystal. In fig. 4 the pulsed emission signals at $B=0.9 \text{ T}$ and $E=1.4 \text{ kV/cm}$ are shown for various directions of B ; a clear minimum of the delay between start of HV excitation pulse at $t=0$ and start of laser action, together with the steepest growth of signal intensity is seen for $\phi \approx 4^\circ$. This direction, for which E and B are perfectly perpendicular, is independent of the magnitude of B , showing the absence of a "parallel Hall" effect, as observed earlier in Ge:Ga crystals cut along low symmetry crystal directions.

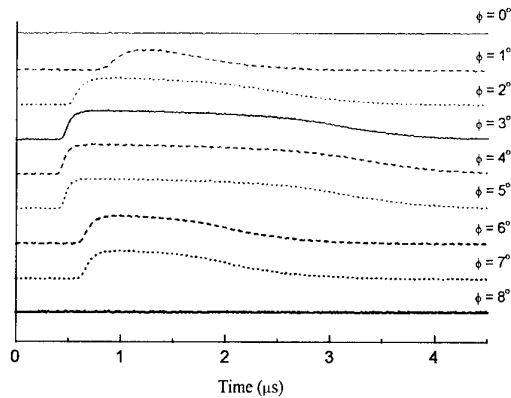


Fig. 4: Shape of the emission pulse as function of the direction of B and E .

In fig. 5 the E/B field region is shown for which stimulated emission is observed using a room temperature pyroelectric detector. With the mirror outcoupler, a smaller emission region is observed than with the mesh outcoupler, just as was found earlier for the Ge:Ga laser [8]. The E/B ration for the emission region agrees with expectations [7].

In fig. 6 emission spectra with a resolution of about 2 cm^{-1} are shown for a few B fields. Although these spectra differ from those reported by Reichertz et al [9]

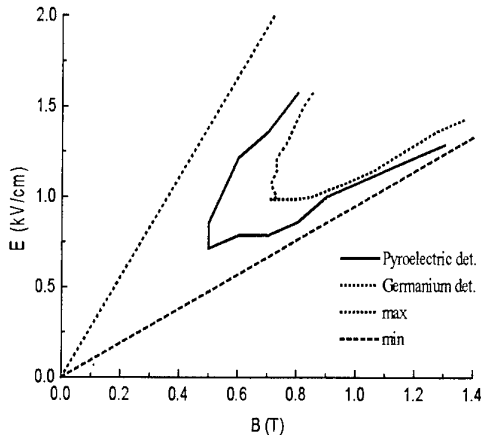


Fig. 5: E - B field region of laser action.

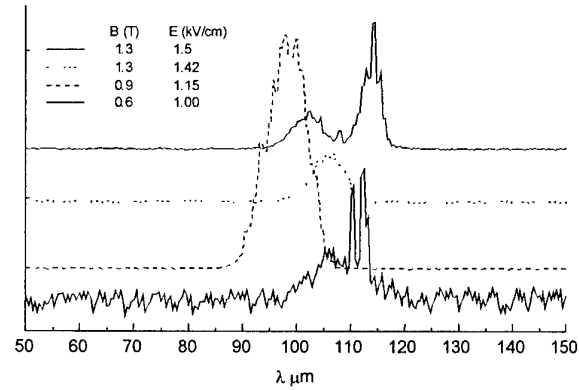


Fig. 6: Emission spectra at various B fields.

for the Be and the Cu doped Ge lasers - operated in the Faraday configuration - it is conceivable that the broadband emission originates from intervalence band transitions. It is to be investigated whether these spectral differences stem from the different laser configurations used.

Some preliminary time resolved experiments have been performed. The peculiar pulse shape shown in fig. 7 strongly resembles those observed in the Ge:Ga laser and suggests that also in the Ge:Cu system a variation in emission wavelength *during* the laser pulse occurs. The intensity variations on a 25 ns timescale are related to beating between different transverse laser modes.

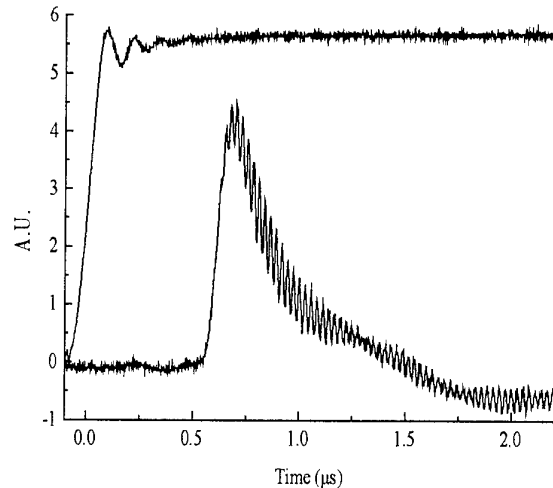


Fig. 7: Time resolved laser output at $B=0.78 \text{ T}$ observed with a fast Hetrostructure detector and the high voltage pulse.

In general, it is found that in this Ge:Cu laser the time delay between start of the high voltage excitation and start of laser action is larger, the small signal gain is smaller, and the maximum pulse duration is shorter than observed in the Ge:Ga laser. Moreover lasing action starts at a larger B field. So, these first data on long pulsed operation indicate that lasing conditions in this

crystal are less favorable than in our earlier reported Ge:Ga crystal. Experiments on other Ge:Cu crystals, also with different Cu concentrations, have to be performed to reach a more general conclusion on this point.

We have applied an RF electric field to the modulation contacts at half the cavity roundtrip frequency, to modulate the laser gain at the round trip frequency, a necessary prerequisite for mode-locking. Inspection of the electronic system showed that the Q-value of the circuit involving the modulation contacts was rather low, possibly preventing the RF field to reach its optimum value. It is not clear whether this is due to bad contacts or to an intrinsic material property. Nevertheless, in these first experiments we have succeeded in operating this laser under mode locking conditions. In fig. 8 a typical result of the optical output is given. A train of pulses at a 1.3 ns time interval, the cavity roundtrip time, is observed. However, the modulation depth is not very large; Improving on the amplitude of the RF field might possibly lead to better results and shorter pulses.

In summary we have shown that the copper doped germanium laser can be operated under mode-locking conditions; the present overall performance, however, does not yet equals that of the Ge:Ga laser.

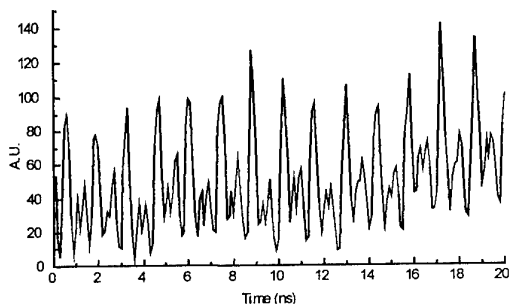


Fig. 8 Pulse train under mode-locking conditions. The 1.3 ns pulse separation equals the cavity roundtrip time.

Acknowledgement

This work is part of the research program of the European TMR Network "InterEuropean Terahertz Action (INTERACT)". The authors thank the group of prof. Renk at the Regensburg University, Germany for the use of their GaAs/AlGaAs heterostructure detector and M.J. Vermeulen, Delft Interfaculty Reactor Institute, for the use of the 6-GHz scope.

References

1. E. Gornik and A.A. Andronov, *Opt. Quantum Electron.* 23 (1991).
2. J.N. Hovenier, A.V. Muravjov, S.G. Pavlov, V.N. Shastin, R.C. Stribos, W.Th. Wenckebach, *Appl. Phys. Lett.* 71 (1997) 443.
3. J.N. Hovenier, T.O. Klaassen, W.Th. Wenckebach, A.V. Muravjov, S.G. Pavlov, V.N. Shastin, *Appl. Phys. Lett.* 72 (1998) 1140.
4. J.N. Hovenier, M.C. Diez, T.O. Klaassen, W.Th. Wenckebach, A.V. Muravjov, S.G. Pavlov and V.N. Shastin, *IEEE Transactions on Microwave Theory and Techniques* 48(2000)670.
5. S.V. Demihovsky, A.V. Murav'ev, S.G. Pavlov and V.N. Shastin, *Semicond. Sci. Technol.* 7 (1992). B622.
6. E. Bründermann, A.M. Linhart, L.A. Reichertz, H.P. Röser, O.D. Dubon, G. Sirmain, W.L. Hansen, E.E. Haller, *Appl. Phys. Lett.* 68 (1996) 3075.
7. G. Sirmain, L.A. Reichertz, O.D. Dubon, E.E. Haller, W.L. Hansen, E. Bründermann, A.M. Linhart and H.P. Röser, *Appl. Phys. Lett.* 70 (1997) 1659.
8. T.O. Klaassen, J.N. Hovenier, W.Th. Wenckebach, A.V. Muravjov, S.G. Pavlov and V.N. Shastin, *EOS/SPIE International Symposia: Conference on Terahertz Spectroscopy & Applications*, 16-18 June 1999, Munich, Germany. SPIE vol. 3828(1999) 58.
9. L.A. Reichertz, O.D. Dubon, G. Sirmain, E. Bründermann, W.L. Hansen, D.R. Chamberain, A.M. Linhart, H.P. Röser, E.E. Haller, *Phys. Rev. B* 19 (1997) 12069.

THz Sources Based on Semiconductor Quantum Structures

K. Unterrainer, J. Ulrich, R. Zobl, G. Strasser, and E. Gornik

Abstract – We present a study on spontaneous THz emission from semiconductor quantum structures. THz emission from parabolically graded AlGaAs/GaAs quantum wells driven by an in-plane electric field has been measured. We have analyzed the grating coupled radiation in the temperature range from 20 K to 240 K. The peak emission corresponds to the intersubband plasmon in the parabolic potential. From a quantum cascade structure we observe spontaneous THz emission, based on carrier injection into the excited state of a 26 nm quantum well. We have measured luminescence at a photon energy of 17.3 meV with a full linewidth at half maximum of 1.3 meV.

I. INTRODUCTION

For the development of electrically driven semiconductor sources emitting in the far-infrared wavelength region several concepts have been pursued. A far-infrared laser based on radiative transitions of holes in p-doped Germanium between Landau levels was demonstrated [1]. Sources operating without a magnetic field can be constructed employing intersubband transitions in heterostructures. THz intersubband electroluminescence

has been observed in parabolic quantum wells [2], in superlattices [3], and more recently in quantum cascade structures [4,5].

We studied the electroluminescence from two different structures. The first structure is a parabolically graded quantum well and the second one is a quantum cascade structure.

II. THz EMISSION FROM PARABOLIC QUANTUM WELLS

Parabolic quantum wells are promising candidates for THz sources operating above liquid nitrogen temperature, because their emission frequency is independent of the electron distribution and concentration in the well. In absorption and emission spectroscopy [6], coupling between the radiation and the electron system has been observed at only one frequency. This is the harmonic oscillator frequency, solely determined by the width and the energetic depth of the quantum well. These observations confirmed the validity of the generalized Kohn theorem [7] in parabolic quantum wells, stating that long wavelength radiation (as compared to the width of the well) only couples to the center of mass co-ordinate

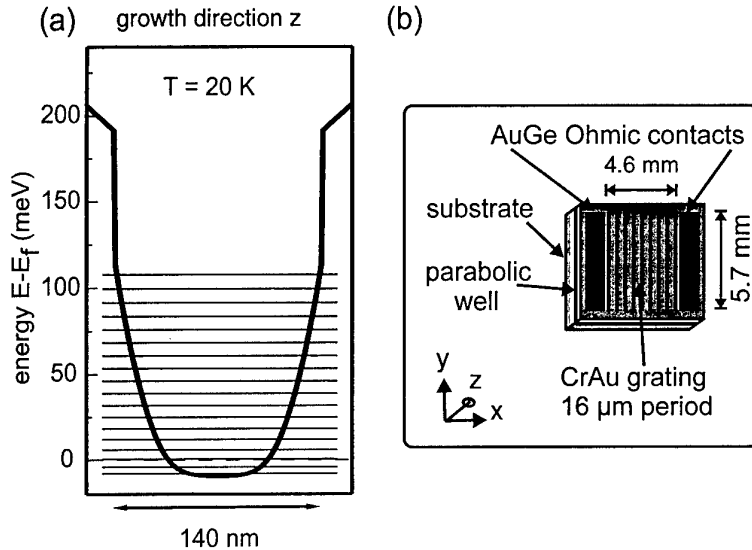


Fig.1: a) Self-consistent calculation of the band diagram of the 140 nm well. The horizontal lines denominate the energy levels in the graded part of the well. b) Device geometry of the 140 nm well sample.

K. Unterrainer, J. Ulrich, and R. Zobl are with the Institut für Festkörperelektronik, G. Strasser and E. Gornik are with the Mikrostrukturzentrum, Technische Universität Wien, A-1040 Wien, Austria.

of an electron system confined in a parabolic potential.

Two samples were examined: one with 140 nm, the other one with 200 nm well width, both with 167 meV energetic well depth. The samples were grown by molecular beam epitaxy using a digital alloy technique.

The electron concentration in both wells was determined by Hall measurements. In the 140 nm well, the electron concentration varies from $3.8 \times 10^{11} \text{ cm}^{-2}$ at 20 K to $5.1 \times 10^{11} \text{ cm}^{-2}$ at 240 K. In the 200 nm well, the corresponding values are $2.7 \times 10^{11} \text{ cm}^{-2}$ at 20 K, $3.4 \times 10^{11} \text{ cm}^{-2}$ at 240 K. The energy band diagram of the 140 nm well is displayed in Fig. 1a.

Fig. 1b shows the device geometry schematically. The wells are contacted with two AuGe Ohmic contact stripes. In order to couple out the intersubband radiation, that is polarized with its electrical field perpendicular to the layers, a metallic CrAu grating of $16 \mu\text{m}$ ($50 \mu\text{m}$) period, with its stripes parallel to the contacts, was evaporated between the contacts.

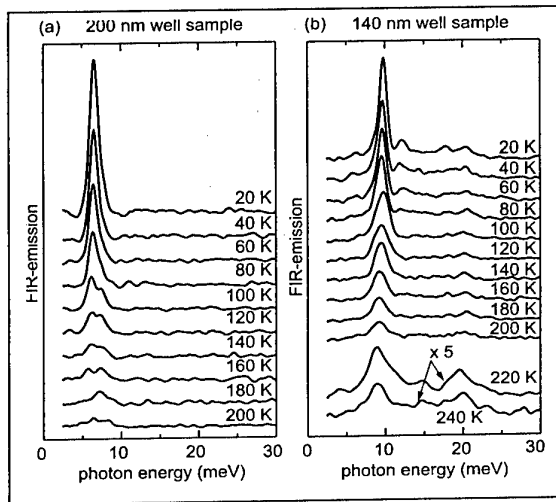


Fig. 2: Emission spectra a) of the 200 nm well sample and b) of the 140 nm well sample for various temperatures as indicated. The spectra of the two highest temperatures in (b) are shown enlarged by a factor of five.

We measured the electroluminescence of the parabolic quantum wells using a Fourier-transform infrared spectrometer in the step scan mode with a spectral resolution of 0.5 meV. The sample was mounted on the cold finger of a helium-flow cryostat. The emitted radiation was collected by an off-axis parabolic mirror with an $f/2$ aperture, transmitted through the spectrometer, and then focussed on a helium cooled Si-bolometer. The whole beam path was purged with dry nitrogen gas to minimize the far-infrared absorption by water vapor. The electron gas in the well was excited by application of a pulsed electric field between the Ohmic contacts at a frequency of 411 Hz and 50 % duty cycle. A lock-in amplifier was employed to detect the bolometer signal.

In Fig. 2a, spectra of the 200 nm well at various temperatures are displayed. The peak emission is observed at a photon energy of 6.6 meV for all temperatures. This value corresponds to the harmonic oscillator energy, calculated from the well dimensions as 6.0 meV. In agreement with the generalized Kohn theorem, the emission energy is unaltered by the temperature-induced variation of the electron distribution in the well. The spectra of the 140 nm well in Fig. 2b

show a 20 K emission peak at 9.8 meV (calculated as 8.4 meV) that is slightly shifted to lower energies (9.1 meV), as the temperature is raised up to 240 K. The full width at half maximum of the emission line of both samples ranges from 1 meV at low temperatures ($T < 100 \text{ K}$) to 2 meV in the high temperature regime ($T > 100 \text{ K}$) [8].

III. TERAHERTZ-ELECTROLUMINESCENCE IN A QUANTUM CASCADE STRUCTURE

Investigations of intersubband electroluminescence [3,4,5] have been performed aiming at an electrically driven coherent terahertz emitter based on intersubband transitions. In the mid-infrared wavelength region a quantum cascade laser has been demonstrated by Faist et al. [9]. We are trying to downscale the concept for emission of radiation with a photon energy below the LO-phonon energy in GaAs (36 meV). In that case, the upper state lifetime is not limited by LO-phonon scattering.

Our structure is made up of 50 periods of a chirped $\text{Al}_{0.15}\text{Ga}_{0.85}\text{As}/\text{GaAs}$ superlattice, as seen in Fig. 3. The radiative transition occurs in the widest (26 nm) quantum well. At an appropriate electric field (22 mV/period), electrons are resonantly injected from the first miniband of the injector (4 wells) into the second state (E_2) of the transition well. The electrons escape from the ground state (E_1) via fast resonant tunneling whereas tunneling from E_2 downstream is inhibited by the minigap of the adjacent injector. The second miniband at the operation bias is Wannier-Stark localized and does not contribute to carrier transport. The two center wells of the injector are lightly doped ($n = 1 \times 10^{16} \text{ cm}^{-3}$) to insure a constant electric field across the structure.

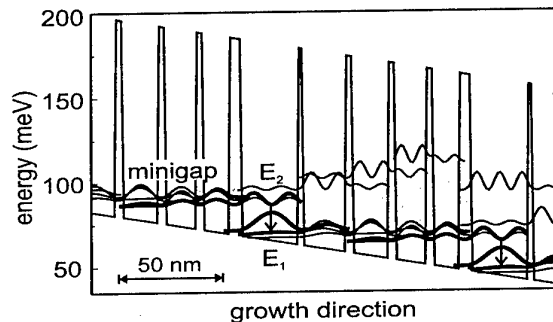


Fig. 3: Part of the band structure of a quantum cascade structure designed for emission of terahertz radiation. It has been calculated by selfconsistently solving Schrödinger's and Poisson's equation.

The layer system is grown by molecular beam epitaxy on an n^+ doped substrate that is used as the electrical bottom contact. One sample ($1300 \mu\text{m} \times 250 \mu\text{m}$) was prepared with a $16 \mu\text{m}$ period Au-grating on top that serves as the electrical top contact and as the optical outcoupler at the same time. In a second sample with a larger period grating ($50 \mu\text{m}$) the layer system was removed between the Au-stripes by reactive ion etching, leaving 7 ridges of

1300 μm length and 25 μm width emitting radiation from the edges.

In order to detect the terahertz luminescence of the samples we have employed two different spectrometers. The first one is the Fourier spectrometer described in the previous section. Our second electroluminescence set-up contains an InSb-cyclotron resonance detector which is tunable by a magnetic field. The sample is located in a second magnet in order to screen the field. The radiation is guided from the sample to the detector in a closed light pipe. The whole optics is immersed in liquid He, so that room temperature background radiation cannot reach the detector nor the sample.

We observe terahertz-emission at 17.3 meV as displayed in Fig 4. This is consistent with the calculated energy difference $E_2 - E_1$ of 17.1 meV. The linewidth is 1.3 meV, see Fig 4 (a). The linewidth of 2.2 meV in the InSb-detector spectra in Fig 4 (b) is not the true linewidth of our sample because the InSb-detector has an intrinsic linewidth of 1.5 meV. We do not observe emission from transitions other than $E_2 - E_1$. There is a monotonous increase of signal with the injection current up to the breakup of the first miniband. The increase of light output with current is sublinear. This is an indication /5/ that the non-radiative scattering rate increases with the injection current and with the population of the E_2 excited state, as it is the case for electron-electron- or Auger-scattering processes.

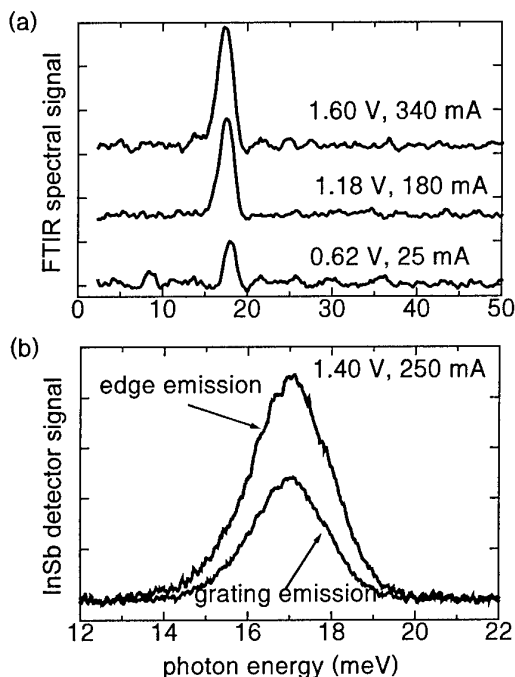


Fig. 4: (a) Emission spectra recorded with the Fourier-transform spectrometer at three different biases. (b) Emission spectra recorded with the InSb-detector spectrometer, comparing grating coupled and edge emission at the same current.

the InSb-setup, i. e. the high spectral resolution (0.25 meV) the large spectral range (0 - 50 meV), we have used the InSb-setup for its higher signal to noise ratio and for the absence of distortion of the signal by room temperature background radiation. The comparison of the two differently processed samples shown in Fig. 4 (b) yields: The edge outcoupling is about twice as efficient as the grating coupled surface emission. We attribute this difference to strong absorption in the highly doped top contact layer /10/.

IV. CONCLUSION

We have demonstrated electrically driven THz emission of parabolic quantum wells up to a temperature of 240 K. At high temperatures, the thermal energy $k_B T$ exceeds the photon energy by a factor greater than two. The electron distribution in thermal equilibrium varies significantly in the temperature range of interest. However, we observe single frequency emission, and the impact of high temperatures on the frequency and the line shape is small. The emission efficiency is limited by the temperature dependent decrease of intersubband life time. From the quantum cascade structures we observe a narrow (1.3 meV) spontaneous emission line at 17.3 meV. The efficiency of edge emission is higher than that of grating coupled emission.

Acknowledgement

This work has been supported by the Austrian Science Foundation (START Y47, Wittgenstein Award) and by the EU-TMR Program (INTERACT).

References

1. K. Unterrainer, C. Kremser, E. Gornik, C. R. Pidgeon, Y. L. Ivanov, E. E. Haller; Phys. Rev. Lett. 53, 1714 (1988).
2. K. D. Maranowski, A. C. Gossard, K. Unterrainer, E. Gornik; Appl. Phys. Lett. 69, 3522 (1996).
3. M. Helm, P. England, E. Colas, F. DeRosa, S. J. Allen, Jr.; Phys. Rev. Lett. 63, 74 (1988).
4. B. Xu, Q. Hu, M. R. Melloch, Appl. Phys. Lett. 71, 440 (1997).
5. M. Rochat, J. Faist, M. Beck, U. Oesterle, M. Illegems, Appl. Phys. Lett. 73, 3724 (1998).
6. A. Wixforth, M. Kaloudis, C. Rocke, K. Ensslin, M. Sundaram, J. H. English, A. C. Gossard; Semicond. Sci. Technol. 9, 215 (1994).
7. L. Brey, N. F. Johnson, B. I. Halperin Phys. Rev. B 40, 647 (1989).
8. J. Ulrich, R. Zobl, K. Unterrainer, G. Strasser, E. Gornik, K.D. Maranowski, A.C. Gossard; Appl. Phys. Lett. 74, 3158 (1999).
9. J. Faist, F. Capasso, D. L. Sivco, C. Satori, A. L. Hutchinson, A. Y. Cho, Science 264, 553 (1994)
10. J. Ulrich, R. Zobl, K. Unterrainer, G. Strasser, E. Gornik; "Magnetic field enhanced quantum cascade emission"; Appl. Phys. Lett. 76, 19 (2000).

Thermal receiver detectable THz radiation from an InAs irradiated with 1.04- μm femtosecond fiber laser in a 2-T permanent magnet

Hideyuki OHTAKE, Yuji SUZUKI, Nobuhiko SARUKURA, Shingo ONO, Takeyo TSUKAMOTO, Akio NAKANISHI, Seiji NISHIZAWA, Michelle L. STOCK, Makoto YOSHIDA and Heinrich ENDERT

Abstract – Thermal receiver detectable THz radiation is generated from an InAs irradiated with 1.04- μm , 80-fs, 180mW fiber laser in a 2-T field by a compact permanent magnet. The THz radiation is monitored by a pyroelectric thermal receiver that is Deuterated Triglycine Sulfate (DTGS). DTGS operates at room temperature and it neither require time-gating adjustment nor cryogen cooling operation using liquid helium. The size of THz-radiation emitter system becomes almost the same as the conventional notebook computer size including the excitation laser head.

I. INTRODUCTION

There have been numerous necessities for intense, compact, and simple THz(terahertz)-radiation sources which can be applied for sensing [1], imaging [2], and time-resolved spectroscopy [3]. The basic THz-radiation source is photoconductive antenna irradiated with ultrashort laser pulses[5,6]. The average power of THz-radiation from these kinds of antenna has been microwatt level at most, mostly limited by the electric break-down of the photo conductive antennas. An intense, compact, and simple light source is required for applications in sensing or imaging. Concerning intense THz-radiation source, Zhang et al. reported the enhancement of THz-radiation power from GaAs irradiated with femtosecond laser [7]. The enhancement mechanism of THz-radiation power is explained carrier acceleration by magnetic field, therefore, it shows quadratic magnetic field dependence of THz-radiation power up to 0.3 T. We also reported the significant enhancement of THz-radiation power from InAs in a magnetic field irradiated with femtosecond optical pulses, owing to quadratic magnetic field and quadratic excitation intensity dependence of THz-radiation power [8,9]. The advantage to utilise InAs as a THz emitter is approximately one-order higher efficiency of THz-radiation power compared with the GaAs case due to its smaller effective mass [8]. To design practical

THz-radiation sources, it is strongly required to examine the scalability of THz-radiation power with this magnetic field enhancement scheme. Previously, we have reported saturation of THz-radiation power from femtosecond-laser irradiated InAs in a high magnetic field and magnetic field dependence of THz-radiation spectra [9]. After ref. [9], THz-radiation power has been reached sub-milliwatt level to sophisticated magnetic field and incidence angle of the excitation laser [10]. In this presentation, we report thermal receiver detectable THz radiation from an InAs irradiated with 1.04- μm 80-fs, 140-mW fiber laser in a 2-T field by a compact permanent magnet. The THz radiation is monitored by a pyroelectric thermal receiver that is Deuterated Triglycine Sulfate (DTGS). DTGS operates at room temperature and it neither require time-gating adjustment nor cryogen cooling operation using liquid helium. The size of THz-radiation emitter system becomes almost the same as the conventional notebook computer size including the excitation laser head. Compared with the THz-radiation spectrum measured by a bolometer, the same spectrum is obtained even using the DTGS where water vapour absorption lines are clearly observed.

II. EXPERIMENT

The experimental setup is shown in Fig. 1. A 48-MHz repetition-rate mode-locked fiber laser delivers nearly-transform-limited 80-fsec pulses at 1.04 μm . (IMRA Wattlite 1040 nm version)

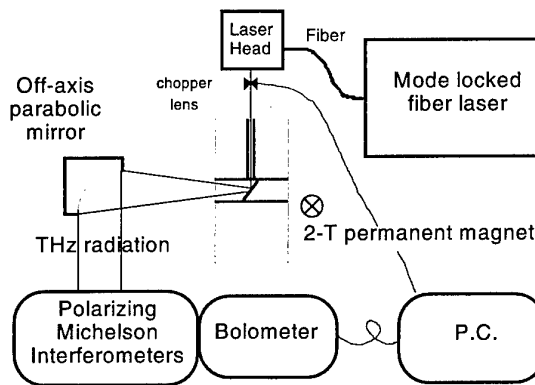


Fig. 1 Experimental setup. Laser beam is focused on the sample with 1-mm diameter.

Hideyuki OHTAKE, Yuji SUZUKI, and Nobuhiko SARUKURA are with Institute for Molecular Science, Myodaiji, Okazaki, Aichi 444-8585, JAPAN.

Shingo ONO and Takeyo TSUKAMOTO are with Science University of Tokyo, Kagurazaka, Shinjuku, Tokyo 162-8601, JAPAN.

Akio NAKANISHI is with Sumitomo Special Metal Co., Ltd, Egawa, Shimamoto-cho, Mishima-gun, Osaka 618-0000, JAPAN.

Seiji NISHIZAWA is with JASCO Corporation, Ishikawa, Hachioji, Tokyo 192-8537, JAPAN

Michelle L. STOCK, Makoto YOSHIDA and Heinrich ENDERT are with Imra America, Inc. JLO, Kojiritsuki, Hitotsugi-cho, Kariya, Aichi 448-0000, Japan

The mode-locked fiber laser is a completely turn-key system. Compared with previous Femtolite which operates at 1.55 μm , the improvement of Wattlite is significant increase of average power with use of Yb fiber amplifier [11]. The sample is undoped bulk InAs with a (100) surface. The average power for excitation is about 140 mW with 1-mm spot size in diameter on the sample. The sample is undoped bulk InAs with a (100) surface. Since the band gap of InAs at room temperature is about 3.5 μm (0.354 meV), 1.04- μm operating wavelength of Wattlite is short enough to create photoexcited carriers. A small 2 T permanent magnet consists of eight Nd-Fe-B magnet pieces. Each of pieces is magnetised in different ways as shown in Fig. 2. The remanence magnetic field of the Nd-Fe-B material itself is 1.3 T (NEOMAX-44H). Owing to the suitable magnetic circuit design [12], the magnetic field in the center exceeds the remanence magnetic field. The permanent magnet only weighs about 5 kg. The 2-T permanent magnet unit is cylindrical in shape, 128-mm diameter and 56-mm thick, which makes it smaller and much lighter than an electromagnet.

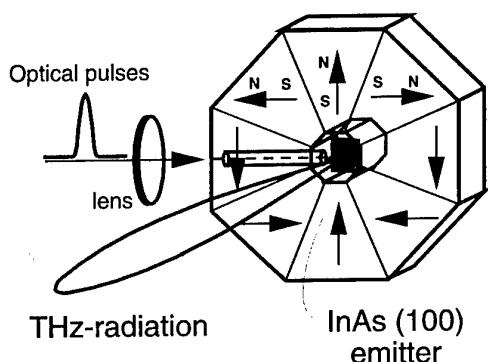


Fig. 2 2-T permanent magnet. The magnet consists of 8 pieces which have different magnetic field directions. The magnetic field reaches 2 T due to the vector sum of magnetic moments.

In the far field, the vector sum of magnetic moments is close to zero. Therefore, the magnet has a very small leak magnetic field owing to the new magnetic circuit. This is an advantage of this radiation source for further system integration. Furthermore, we are planning to increase magnetic field up to 3 T just scaling this design.

III. RESULTS AND DISCUSSIONS

The photograph of THz-radiation system are shown in Fig. 3. The size of THz-radiation system is almost the same as the A4 paper including the laser head, the magnet, and the emitter. This system is much smaller than our previous system [13]. In Fig. 4, we show typical THz-radiation spectra. These spectra are taken by Polarizing Michelson interferometer with a liquid-helium-cooled silicon bolometer and a pyroelectric thermal receiver, respectively. In this condition, the THz radiation can even be observed by a pyroelectric thermal receiver. Unlike time-gated detectors, there is no requirement of timing adjustment and it does not require cryogen cooling for operation. Such a qualitative advance in emitters will certainly widen the application field

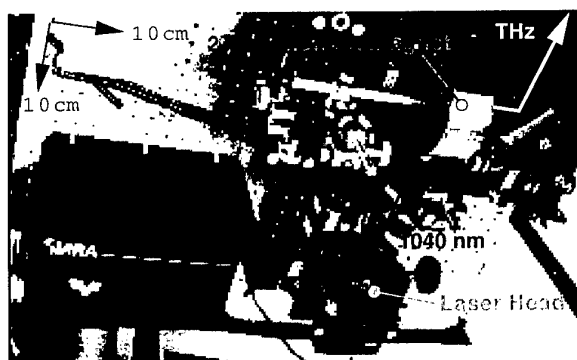


Fig. 3 Photograph of THz radiation system. Laser beam is focused on the sample with 1-mm diameter.

of THz radiation. A typical pyroelectric thermal receiver for detecting THz radiation is deuterated triglycine sulfate (DTGS). DTGS is the best material applied as a sensitive element in pyroelectric sensors due to its high pyroelectric coefficient, reasonably low dielectric constant, and best quality factor. DTGS is uniformly sensitive to radiation in wavelength from ultraviolet to far infrared due to its higher Curie temperature. Compared with the THz-radiation spectrum measured by a bolometer, we obtain the same spectrum where water vapour absorption lines are clearly observed as shown by closed blue circles in Fig. 4 [2].

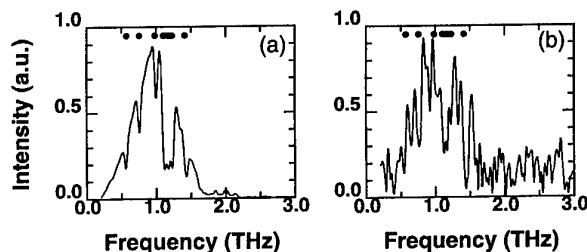


Fig. 4 THz-radiation spectra taken by different detectors. (a) a liquid-helium-cooled silicon bolometer, (b) Deuterated triglycine Sulfate (DTGS). In both cases, clear water vapor absorption lines (closed blue circles) are observed.

IV. CONCLUSION

We have demonstrated thermal receiver detectable THz radiation from an InAs irradiated with 1.04- μm , 80-fs, 180-mW fiber laser in a 2-T magnetic field provided by a compact permanent magnet. The THz radiation is observed by DTGS which operates at room temperature and it neither require time-gating adjustment nor cryogen cooling operation with liquid helium. The size of THz-radiation emitter system is almost the same as the conventional notebook computer size including the excitation laser head.

Acknowledgement

This research was partially supported by Grant-in-Aid for Scientific Research on Priority Areas (11231204) and Grant-in-Aid for Encouragement of Young Scientists (12750046) from The Ministry of Education, Science, Sports and Culture, NEDO Japan Small and Medium

Enterprise Corporation, Creative and Fundamental R&D Program for SMEs, "Research for the Future (RFTF)" of Japan Society for the Promotion of Science (JSPS-RFTF 99P01201), Research foundation for Opto-Science and Technology, and the Sasakawa Scientific Research Grant from The Japan Science Society.

References

1. for example, D. M. Mittleman, S. Hunsche, L. Boivin, and M. C. Nuss, *Opt. Lett.* **22**, 904 (1997).
2. for example, M. Exter, C. Fattinger, and D. Grischkowsky, *Opt. Lett.* **14**, 1128 (1989).
3. for example, B. I. Greene, J. F. Federici, D. R. Dykaar, A. F. J. Levi, and L. Pfeiffer, *Opt. Lett.* **16**, 48 (1991).
4. I. Brener, D. Dykaar, A. Frommer, L. N. Pfeiffer, J. Lopata, J. Wynn, K. West, and M. C. Nuss, *Opt. Lett.* **21**, 1924 (1996).
5. D. H. Auston, *Appl. Phys. Lett.* **43**, 713 (1983).
6. D. Krokel, D. Grischkowsky, and M. B. Ketchen, *Appl. Phys. Lett.* **54**, 1046 (1989).
7. X. -C. Zhang, Y. Lin, T. D. Hewitt, T. Sangsiri, L. E. Kingsley, and M. Weiner, *Appl. Phys. Lett.* **62**, 2003 (1993).
8. N. Sarukura, H. Ohtake, S. Izumida, and Z. Liu, *J. Appl. Phys.* **84**, 654 (1998).
9. Hideyuki OHTAKE, Shingo ONO, Masahiro SAKAI, Zhenlin LIU, Takeyo TSUKAMOTO, and Nobuhiko SARUKURA, *Appl. Phys. Lett.* **76**, 1398 (2000).
10. Shingo ONO, Takeyo TSUKAMOTO, Takayuki YANO, Hideyuki OHTAKE, and Nobuhiko SARUKURA, submitted to *Appl. Opt.*
11. for example, M. Jiang, G. Sucha, M. E. Fermann, J. Jimnez, D. Harter, M. Dageais, S. Fox, and Y. Hu, *Opt. Lett.* **24** 1074 (1999).
12. H. Zijlstra, *Philips J. Research*, **40** (5) 259 (1985).
13. Shingo ONO, Takayo TSUKAMOTO, Masahiro SAKAI, Zhenlin LIU, Hideyuki OHTAKE, Nobuhiko SARUKURA, Seiji NISHIZAWA, Akio NAKANISHI, and Makoto YOSHIDA, *Rev. Sci. Instrum.* **71**, 554-556 (2000).

FREQUENCY DIFFERENCE GENERATION IN THE TERAHERTZ REGION USING LTG-GaAs PHOTODETECTOR

¹E. Peytavit, ²G. Mouret, ¹J. F. Lampin, ²P. Masselin, ¹P. Mounaix, ¹F. Mollot and ¹D. Lippens

¹Institut d'Electronique et de Microélectronique du Nord
Université des Sciences et Technologies de Lille
Avenue Poincaré, BP 69, 59652 Villeneuve d'Ascq Cedex

²Laboratoire de Physique des Composants de l'Atmosphère
Université du Littoral
145 route du Pertuis d'Amont, 59140 Dunkerque

Abstract—We demonstrated Terahertz generation by optical frequency difference with a continuous tuning between 0.2 (~1 μ W) and 3 THz (~1 nW). To this aim, high speed photodetectors with an interdigitated photoconductor scheme on a submicron scale, loaded by THz log-periodic antennas, were deposited on a 1 μ m-thick Low Temperature Grown (200 °C) GaAs epilayer. Two Ti:Sapphire laser beams (~30 mW) focused onto the device yield Terahertz radiation collimated through Silicon lens and detected by means of lock-in bolometer detection. The generated power and frequency, consistent with semiconductor and circuit time constants, are discussed in the prospects of antenna arrays and optical cavities.

Key words: Terahertz, photomixing, LTG GaAs

I INTRODUCTION

Optical generation in the Terahertz gap by photomixing [1]-[3] of two Ti:Al₂O₃ or semiconductor lasers was made possible owing to the remarkable properties of Low Temperature Grown (LTG) Gallium Arsenide [4]-[5]. Such a semiconductor, grown at typical temperatures between 180 °C and 250 °C under non stoichiometric conditions, exhibits a large number of defects, often in excess of 10¹⁹ cm⁻³ in such a way that charge carriers, created by photoexcitation, are rapidly trapped, in most case at subpicosecond scale. As a consequence, the mobility lifetime of photoexcited electrons in the conduction band is extremely short blocking any photoconductivity process inside the sample.

Basically, the photomixing experiments aforementioned rely on the energy detection principle of a fast photodetector. The fact that the response is proportional to the square of the incident electric field enables the generation of frequency difference component when two optical beams, with a frequency offset, are impinging the sample. The intermediate frequency component, to use the terminology of heterodyne systems, is subsequently converted into a Terahertz radiation via radiating elements, such as dipole or slot antennas which are either broadband or resonant at a certain frequency.

It was early recognized that the frequency dependence of the conversion between the optical beams and the

Terahertz radiation was governed by two time constants. Firstly, the life-time of the photoexcited carriers which is an intrinsic property of the active layer of the photodetector. On the other hand, owing to the utilization of an optoelectronic device instead of a full optical device, some extra circuit limitations have to be taken into account. On this basis the key figure of merit was the RC time constant of the circuit constituted by the photodetector and the Terahertz antennas.

In this paper, we show the possibility to use such a principle to down-convert two optical signals around 800 nm at an intermediate frequency in the far infra-red spectrum. One of the laser was continuously tuned so that an optically monochromatic tunable source can be fabricated. The output power achieved in the present work compares with the best data published in the literature under the same broadband conditions. They also fit reasonably the expected frequency dependence on the basis of RC and life-time constants. The analysis is supported by material-based experiments such as X-Ray rocking curve and time resolved photoreflectance carried prior to the conversion experiment on the LTG GaAs samples, reported in section II. Design rules and fabrication techniques are explained in section III while the frequency and voltage dependence along with some prospects and concluding remarks are given in section IV.

II LOW TEMPERATURE GROWN GaAs EPILAYER

The epitaxial material used for all the experiments was grown by Gas Source Molecular Beam Epitaxy. Starting from a Semi-insulating (100) GaAs substrate, a buffer layer was firstly grown at the nominal temperature of 600 °C followed by the growth of a 1 μ m thick LTG GaAs with in situ control by RHEED diffraction pattern. For the LTG layer, the growth temperature was around 200 °C estimated via a thermocouple. All epilayers are nominally undoped. The samples were not annealed.

In order to assess the arsenic excess concentration of the capping LTG layer, X-Ray diffraction patterns were systematically recorded for all the samples. Figure 1 displays a typical X-Ray rocking curve. Two peaks due to the Bragg reflection are shown.

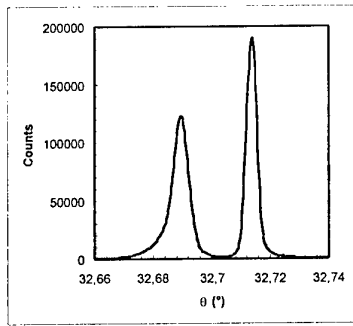


Fig. 1 X-Ray Rocking curve of the sample grown at 200 ° C

The main peak at 32.714° corresponds to the substrate and buffer layers whereas the satellite one at 32.69 ° is characteristic of the LTG epilayer with a large number of Ga antisites (As_{Ga}). The mismatch ($\Delta a/a$) between the substrate and the non-stoichiometric LTG GaAs was 6.5×10^{-4} . It was previously shown [6] that the determination of this mismatch could also be used for estimating the number of defects. Following this approach for the present technology, we found $5 \times 10^{19} \text{ cm}^{-3}$. Also, the defects characteristics in LTG GaAs can be compared to those of EL2 defects and such a finding can be useful to have a first estimate of the capture time (τ) within the semiconductor which is a key figure of merit as discussed above. With a typical value for the cross-section of $5 \times 10^{-14} \text{ cm}^2$ and a thermal velocity of 10^7 cm/s we calculated $\tau = 400 \text{ fs}$.

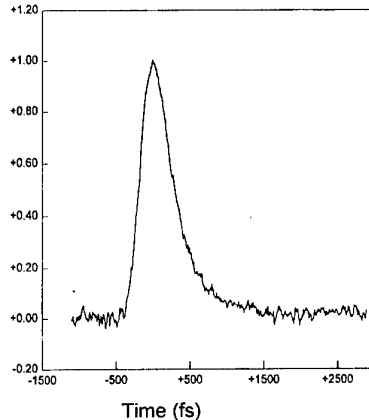


Fig. 2 Time resolved photoreflectance

Experimentally the capture time, which can be compared to a mobility lifetime, was measured by means of time-resolved photoreflectance measurements [7]-[9]. These experiments were also performed at IEMN laboratory. A typical time dependence of the reflectivity signal is given in Figure 2. For this experiment, 100 fs optical pulses near 800 nm were used with a repetition rate of 78 MHz. After a steep increase in the reflected signal in accordance with the build-up time of the optical pulse, an exponential rolloff is observed with a short time constant in the 500 fs scale.

III DESIGN AND FABRICATION

The design of the fabricated devices relies first of all on the calculation of the photodetector and then of the radiating antenna. For the former, the guidelines are the achievement of a low capacitance level so that the RC time constant of the overall system can be kept as low as possible while maintaining a reasonable transit time with respect to the photocarrier life-time. These considerations have motivated the choice of an interdigitated scheme on a submicron scale. On the other hand, shadowing effects by the metal fingers have also to be alleviated. To satisfy the corresponding trade-off we thus decided to implement a nominal pattern consisting of $0.2 \mu\text{m}$ -width finger with an interspacing of $1.8 \mu\text{m}$. Figure 3 is a Scanning Electron Micrograph of this pattern after the metallisation stage. With this geometry the capacitance ($8 \times 8 \mu\text{m}^2$) of the photodetector can be calculated by means of the model published in reference [10]. A value of 0.4 fF is representative of such a technology.

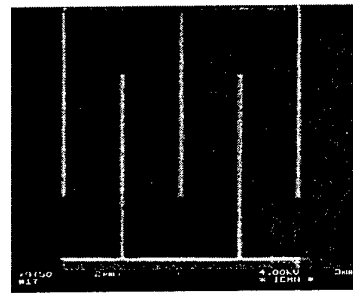


Fig. 3 SEM of the interdigitated capacitance scheme

The second stage in the design was dealing with the radiating elements. As discussed in introduction either a broadband or a resonant antenna can be chosen depending on the targeted project. For the present work aimed at assessing a broadband source, we have designed log spiral antennas. In practice, the design was carried out by means of Momentum and High frequency Structure Simulator by Hewlett Packard [11]. The outcome is the input impedance, which permits one to assess the circuit time constant as a function of frequency.

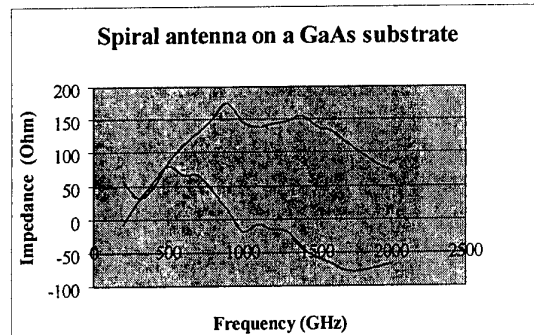


Fig. 4 : Real and Imaginary part of the log-spiral antenna impedance as a function of frequency

Starting from the epitaxial material outlined in section II, the fabrication of the devices was made by combining e-beam patterning (LEICA HR PG) and photolithography techniques. The former was required to write, in electron sensible resist (PMMA), the mould for subsequent metallisation. Conversely, photolithography was used for patterning the antennas, which necessitates a large portion of the wafer. Metallisation was made by evaporation with a 50 nm-thick Ti/300nm-thick Au metal contact. Despite the fact that the LTG layers were non-intentionally doped with non-annealing processes, let us recall that the metal/semiconductor contacts deposited on LTG are ohmic. Figure 5 is a scanning electron micrograph of the completed device with a zoomed view of one of the photodetectors in inset.

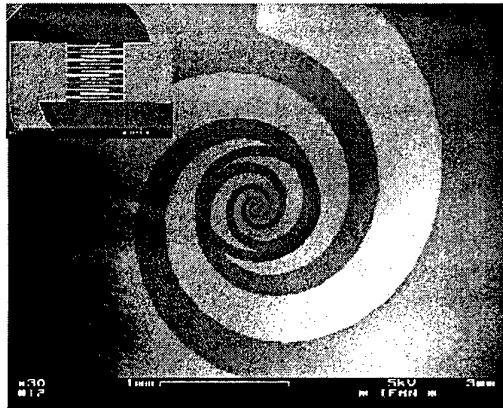


Fig. 5 SEM of the devices including the log periodic antennas

The last stage in the fabrication consists in mounting the half-size wafer onto a dielectric substrate in order to interconnect the devices to bias pads.

IV RESULTS

A schematic overview of the THz photomixing generation experiment is shown in Fig 6. Two CW Ti: Sapphire lasers (899-29 Autoscan, Coherent Inc.), tunable from 700 to 810 nm and 790 to 910 nm, were both pumped by a 23 W Argon laser. For the present demonstration, the wavelength of the two lasers was around 800 nm. A half wave plate and a polarizer were used to adjust carefully lasers pump power. Two laser beams were spatially overlapped by a beam splitter and focused by a lens onto the THz photomixer. THz emission was precollimated by the Silicon lens attached on the back side of the chip and focused with a parabolic mirror onto a Ge bolometer which operates at 4.2 K. The output signal from the detector was fed to a lock-in amplifier.

The Terahertz beam is preferentially radiating in the substrate due to the difference in the permittivity constants between air and the semiconductor. The trapping within the substrate is however avoided by the high resistivity Silicon hyperhemispherical lens (Diameter 10 mm).

Special attention was paid to the alignment of the various elements notably the silicon lens which was

mounted on the backside on a X,Y,Z translation stage. For the measurement of the absolute power we have used the calibration factors given by the manufacturer.

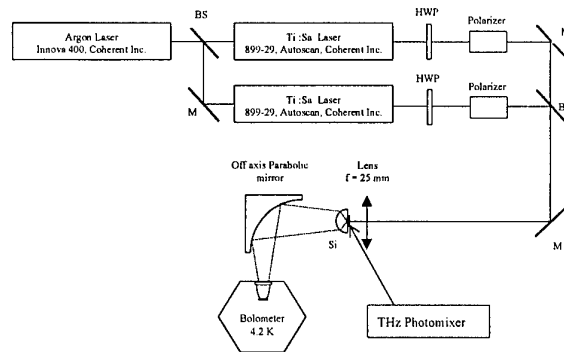


Fig. 6 Experimental setup of a tunable coherent cw – THz radiation system, HWP : Half Wave Plate, BS : Beam Splitter, Si : Collimating hyperhemispherical Silicon Lens

The first step for the experiment was to record the dark and photo currents as a function of bias voltage. It should be emphasized that the LTG samples were not annealed. Generally such a thermal treatment is used for forming Arsenic precipitates improving dramatically the resistivity of the sample. In counterpart a degradation of the life-time can be pointed out at the detrimental of the frequency capability. The ratio between the dark and photocurrent was found in excess of 10:1, with typically a photocurrent of 125 μ A at 9V.

Then, we have recorded the detected voltage of the bolometer at various bias voltages. As expected a quadratic relation ship was found in accordance with early experiments.

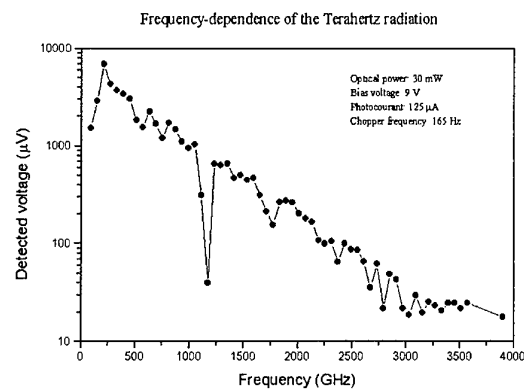


Fig. 7: Frequency-dependence of the Terahertz radiation

At last, we have systematically changed the frequency of one of the laser. Owing to their remarkable purity (500 kHz) and stability, the frequency difference (intermediate frequency) was weakly fluctuating with time so that confident data can be measured without the requirement of an external stabilization. Figure 7 shows the detected

voltage on the lock-in detection plotted in semi-logarithmic scale as a function of frequency. By translating this voltage information in terms of radiating power (10 kV/W) we obtained about 1 μ W in the lower part of the submillimeter wave spectrum and about 2 nW at 3 THz. This results compare with those obtained by the MIT group [12]–[13] under comparable conditions.

The typical optical power impinging the photodetector was about 30 mW. For higher optical levels, saturation can be observed and hence no benefit in terms of delivered power. Further improvements can be expected using the high pump power capabilities of the two autoscan lasers (500mW). On this basis it could be useful to envisage an array of broadband antennas in a fashion similar to that employed for high power amplification or source systems.

Another way of improvement concerns the use of optical cavity such as those which are widely used for photodetectors. Indeed, the efficiency of the photodetector is mainly limited by the very shallow high electric field layer despite the fact that carrier absorption takes place within a 1 μ m depth. Such a limitation was recently recognized for high speed photomixer [14] and could be implemented via membrane-like or microcavity devices.

As a last point, the recent work about the absorption of LTG material below the gap permits one to consider the operation of the devices at long wavelengths (1.3 and 1.55 μ m)[15].

CONCLUSION

High-speed interdigitated photodetector loaded by broadband log spiral Terahertz antennas were fabricated on a Low Temperature Grown GaAs epilayer. By tuning continuously the difference between two Ti:Sapphire lasers it was shown the possibility to generate a Terahertz signal with high spectral purity and significant power. Numerous degrees of freedom still exist for further improving the results notably with the implementation of an array of antenna or of optical cavities.

ACKNOWLEDGEMENTS

We would like to thank D. Vandermoere for the mounting of he devices along B. Bocquet for the fabrication of the sample post.

REFERENCES

- [1] E. R. Brown, K.A McIntosh, K. B. Nichols, and C.L. Dennis, Photomixing up to 3. 8 THz in Low-temperature Grown GaAs, *Applied Physics Letters*, **66**, p. 285 (1995)
- [2] K. A. Mc Intosh, E. R. Brown, K. B. Nichols, O. B. McMahon, W. F. DiNatale, and T. M. Lyszczarz, Terahertz photomixing with diodes lasers in LTG GaAs, *Applied Physics Letters*, **67**, p. 3844 (1995)
- [3] S. Matsuura, M. Tani, and K. Sakai, Generation of coherent terahertz radiation by photomixing in dipole photoconductive antennas, *Applied Physics Letters*, **70**, p. 559 (1997)
- [4] G. Mouret, W. Chen, D. Boucher, R. Bocquet, P. Mounaix, D. Théron, and D. Lippens, High power Terahertz radiation from a high repetition rate large aperture photoconducting antenna, *Microwave and Optical Technology Letters*, **17**, p. 23 (1998)
- [5] G. Mouret, W. Chen, D. Boucher, R. Bocquet, P. Mounaix and D. Lippens, GaAs filter correlation instrument for air monitoring at submillimeter wavelengths, *Optics Letters*, **24**, p. 1 (1999)
- [6] X. Liu, A. Prasad, J. Nishio, E. R. Weber, Z. Liliental-Weber, and W. Walukiewicz, Native point defects in Low-temperature-grown GaAs, *Applied Physics Letters*, **67**, p. 279 (1995)
- [7] S. D. Benjamin, H. S. Loka, A. Othonos, and P. W. Smith, Ultrafast dynamics of non linear absorption in LTG GaAs, *Applied Physics Letters*, **68**, p. 2544 (1996)
- [9] K. A. Mc Intosh, K. B. Nichols, S. Verghese and E. R. Brown, Investigation of ultrashort photocarrier relaxation times in Low Temperature-Grown GaAs, *Applied Physics Letters*, **70**, p. 354 (1997)
- [10] Y. Chin Lim, and R. A. Moore, Properties of alternately charged coplanar parallel strips by conformal mappings, *IEEE Trans. On Electron devices*, **15**, p. 173 (1968)
- [11] Momentum and High Frequency Structure Simulator TM Hewlett Packard
- [12] S. Verghese, K. A. Mc Intosh, and E. R. Brown, Highly tunable fiber-coupled photomixers with coherent Terahertz output power, *IEEE Transactions on Microwave theory and Techniques*, **45**, p. 1301 (1997)
- [13] S. Verghese, K.A. McIntosh, S. Calawa, W. F. Diatale, E.K. Duerr and K. A. Molvar, Generation and detection of coherent terahertz waves using two photomixers, *Applied Physics Letters*, **73**, p. 3824 (1998)
- [14] E. R. Brown, A photoconductive model for superior GaAs THz photomixers, *Applied Physics Letters*, **75**, p. 769 (1999)
- [15] H. Erlig, S. Wang, T. Azfar, A. Udupa, H.R. Fetterman, and D.C. Streit, LT GaAs detector with 451 fs response at 1.55 μ m via two photon absorption, *Electronics Letters*, **35**, p. 173 (1999)

Self-Generation of Ultra-Short Pulses in a Cavity with a Dielectric Mirror Excited by an Array of Active THz Devices

Lidiya Yurchenko, Vladimir Yurchenko

Abstract – We report on computer simulation of electromagnetic self-excitation in a cavity with a dielectric mirror and an array of active THz devices. Assuming the devices are sufficiently fast, we observed either continuous nonlinear oscillations or the trains of ultra-short pulses depending on the thickness and refractive index of the dielectric mirror.

I. INTRODUCTION

We study self-excitation of electromagnetic oscillations in a cavity with a dielectric mirror and an array of active devices (Fig. 1). The array is simulated as a continuous layer of an active medium specified by its current-voltage characteristic of N-type similar to GaAs Gunn diodes (Fig. 2).

The devices are assumed operating in the THz band so that their response to electromagnetic oscillations is instantaneous if the typical frequency of oscillations is below 1 THz.

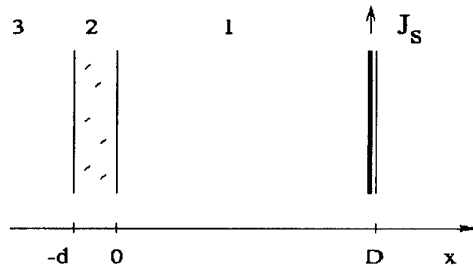


Fig. 1: Geometry of the problem

Coupling of the devices to the electromagnetic field is supposed to be sufficiently strong. In the case of an active layer, coupling is specified by the value of the surface current J_s excited in the layer by the electric field in the cavity E_z .

In reality, coupling is more complicated, and the layer can represent different kinds of devices such as a matrix of diodes, FET transistors, semiconductor superlattices, Josephson junctions, etc [1].

When electromagnetic coupling is strong, self-excitation of anharmonic oscillations with transition to dynamical

chaos is possible in the nonlinear system of this kind [2, 3]. It may have many applications, e.g., as a source of oscillations in emerging radar technologies such as a wide-band millimeter-wave noise radar [4].

In this paper, we present the results of our simulations of nonlinear oscillations in a cavity with a dielectric mirror. The latter is used for transmitting the electromagnetic signals from the cavity into the outer space. The dielectric mirror is also operating as a resonant filter when reflecting the electromagnetic field back into the cavity or transmitting it into the free space. So, the actual effect of the mirror is more complicated than simply providing the window for the electromagnetic radiation.

II. FORMULATION

We consider one-dimensional model of the cavity (Fig. 1) assuming the cavity width A being much greater than the length D .

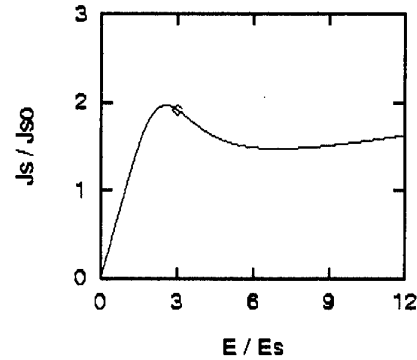


Fig. 2: Current-voltage characteristic of the devices

Nonlinear current-voltage characteristic of the active layer (Fig. 2) is approximated as

$$J_s = J_s(E) = J_{s0} G(E) = J_{s0} \left[\frac{E + 0.2E^4}{(1 + 0.2E^4) + 0.05E} \right] \quad (1)$$

where $E = E(t) = E_z(D, t)/E_s$ is the normalized electric field in the layer. The parameters are $J_{s0} = 50 \text{ A/cm}$ and $E_s = 1 \text{ kV/cm}$ where the carrier density $n = 10^{15} \text{ cm}^{-3}$ and the frequency

Lidiya Yurchenko and Vladimir Yurchenko are with the Institute of Radiophysics and Electronics, National Academy of Sciences of Ukraine, 12 Proskura St., Kharkiv, 61085, Ukraine
Vladimir Yurchenko is also with the National University of Ireland, Maynooth, Co. Kildare, Ireland

$f = 10 \text{ GHz}$ have been used to estimate the skin-layer thickness and hence the value of J_{s0} given above.

In the case of an array of active devices, we assume that the spacing between the devices is sufficiently small and the external voltage $V_0(t)$ is applied to every device in such a way that we can introduce the equivalent bias electric field $E_{z0}(t)$ directed along the array. Then, we can consider the equivalent surface current density $J_s(t)$ that arises due to the total field $E_z(D, t) = E_{z0}(t) + E_{z1}(D, t)$ where $E_{z1}(D, t)$ is the microwave field excited at the wall $x = D$.

The electric field in the cavity, $E_z(x, t)$, is a solution to the one-dimensional wave equation subject to the initial and boundary conditions. The boundary condition at the active layer $x = D$ is nonlinear and takes on the form

$$\left. \frac{\partial E_z}{\partial x} \right|_{x=D} = - \left(\frac{W_0}{c} \right) \left(\frac{\partial J_s}{\partial E_z} \right) \left. \frac{\partial E_z}{\partial t} \right|_{x=D} \quad (2)$$

where c is the speed of light, W_0 is the free-space impedance, and $J_s = J_s(E)$ is the surface current density defined above.

Eq. (2) follows from the generic boundary condition

$$H_y(D+0) - H_y(D-0) = J_s \quad (3)$$

where $H_y(D+0) = 0$, H_y is the y component of the magnetic field that, due to the Maxwell's equations, satisfies the relation

$$\mu_0 \left(\frac{\partial H_y}{\partial t} \right) \Big|_{x=D} = \left(\frac{\partial E_z}{\partial x} \right) \Big|_{x=D} \quad (4)$$

Notice that the nonlinear factor dJ_s/dE_z in Eq. (2) is the differential conductance of the active layer. The latter is negative when the total field $E_z(D, t)$ falls in the negative differential resistance region.

Boundary conditions at the both sides of the dielectric mirror are linear and follow from the continuity of the tangential components of the electric field at the dielectric surfaces.

For the further analysis, we follow [2] and make use of the Riemann solution available to the one-dimensional wave equation. By considering the field in the cavity ($i=1$), in the dielectric mirror ($i=2$), and in the free space ($i=3$), we take the solutions

$$E_z^{(i)}(x, t) = f_i(v_i t + x) - g_i(v_i t - x) \quad (5)$$

where $f_i(\cdot)$ and $g_i(\cdot)$ are unknown functions, $v_{1,3} = c$ and $v_2 = c/n$, and apply boundary conditions

at the active layer, at the surfaces of the dielectric mirror, and at infinity.

In this way, we arrive at the multiple delay difference equation as follows

$$f(\tau) = \left\{ G \left[E_0^{(0)} \right] - (C_0/n_1) G \left[E(t, \tau, \tau_1, \tau_2, \tau_3) \right] \right\} + E_1(\tau_1, \tau_2, \tau_3) \quad (6)$$

where

$$E(t, \tau, \tau_1, \tau_2, \tau_3) = E^{(1)}(\tau, \tau_1, \tau_2, \tau_3) + E^{(0)}(t), \quad (7)$$

$$E^{(1)}(\tau, \tau_1, \tau_2, \tau_3) = n_1 [f(t) - \eta^2 f(\tau_1) - \eta f(\tau_2) + \eta f(\tau_3)], \quad (8)$$

$$E_1(\tau_1, \tau_2, \tau_3) = \eta^2 f(\tau_1) - \eta f(\tau_2) + \eta f(\tau_3), \quad (9)$$

$E(t, \tau, \tau_1, \tau_2, \tau_3)$ is the total electric field in the active layer at the moment $t = (n\tau - D)/c$, $E^{(1)}(\tau, \tau_1, \tau_2, \tau_3)$ is the microwave field in the layer, $E^{(0)}(t)$ is the bias field defined by the Kirchhoff law of the bias circuit (if the latter contains the source E_{ext} , the load resistor R , and no reactive components, $E^{(0)}(t)$ is defined by the equation $E + RJ_s(E) = E_{ext}$), $E_0^{(0)}$ is the initial value of $E^{(0)}(t)$, $G_0 = W_0 J_{s0}/E_s$ (for the parameters given above, $G_0 \leq 20$), $\tau_1 = \tau - h$, $\tau_2 = \tau - L$, $\tau_3 = \tau - L - h$, $h = 2d$, $L = 2D/n$, $n_1 = n + 1$, and $\eta = (n - 1)/(n + 1)$.

The initial value of the field in the cavity, $E_z(x, 0)$, is chosen to be zero. The oscillations appear in response to a small fluctuation of the bias field $E^{(0)}(t) = E_0^{(0)} + E_1^{(0)}(t)$ where $E_1^{(0)}(t)$ is the given fluctuation function ($E_1^{(0)}(t) \neq 0$ when $t > 0$).

When the solution of Eq. (6) found, the normalized radiation field transmitted through the dielectric mirror is obtained as

$$U_1(t) = (n/n_1) f(\tau - 0.5L - d) \quad (10)$$

and the current in the active layer is computed as

$$J_s(t) = J_{s0} [G(E_0^{(0)}) + J_1(t)] \quad (11)$$

where

$$J_1(t) = n_1 [f(\tau) - E_1(\tau_1, \tau_2, \tau_3)]. \quad (12)$$

III. NUMERICAL RESULTS

We simulated the process of self-excitation of electromagnetic oscillations in the cavity with a strong coupling of electromagnetic field and active devices

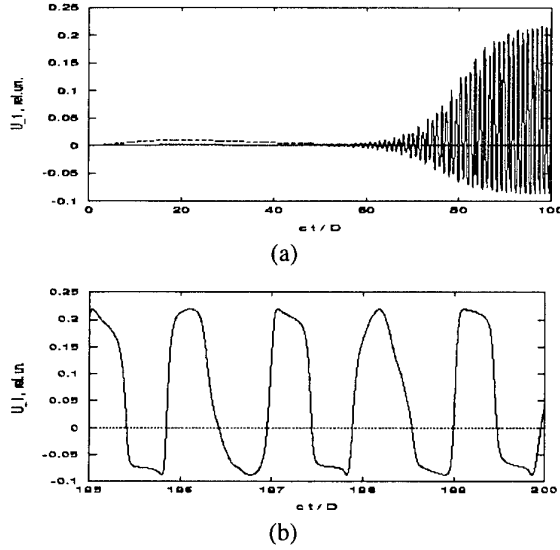


Fig. 3: Radiation field in the case of a thick mirror

when the coupling constant $G_0 \sim 1 \dots 3$. In terms of Eq. (1), it corresponds to rather large values of the surface current density $J_{s0} \sim 3 \dots 10$ A/cm in the active layer that requires sufficiently dense packaging of the powerful micro-devices in the active array.

In the case of a thick dielectric mirror, the electromagnetic field is efficiently confined in the cavity and the coupling of the field to the active layer is very strong. In this case, the continuous anharmonic oscillations are typically excited when some initial fluctuation of the bias field is applied.

Fig. 3 shows an example of such oscillations when $D = 15$ mm, $d = 5$ mm, $n = 2$, $G_0 = 2$ and $E_0^{(0)} = 3$. The basic frequency of oscillations is about $f_0 = 20$ GHz. The initial fluctuation $E_1^{(0)}(t)$ of the bias field $E^{(0)}$ is shown by the dashed curve.

On the contrary, in the case of a thin dielectric of a small refractive index chosen to be just sufficient to support self-oscillations, a train of ultra-short radio pulses is generated. The train of pulses radiated from such a cavity is shown in Fig. 4. It arises when $D = 15$ mm, $d = 0.15$ mm, $n = 2$, $G_0 = 2$ and $E_0^{(0)} = 3$ providing the pulse repetition frequency $f_p = 10$ GHz and the carrier frequency $f = 500$ GHz.

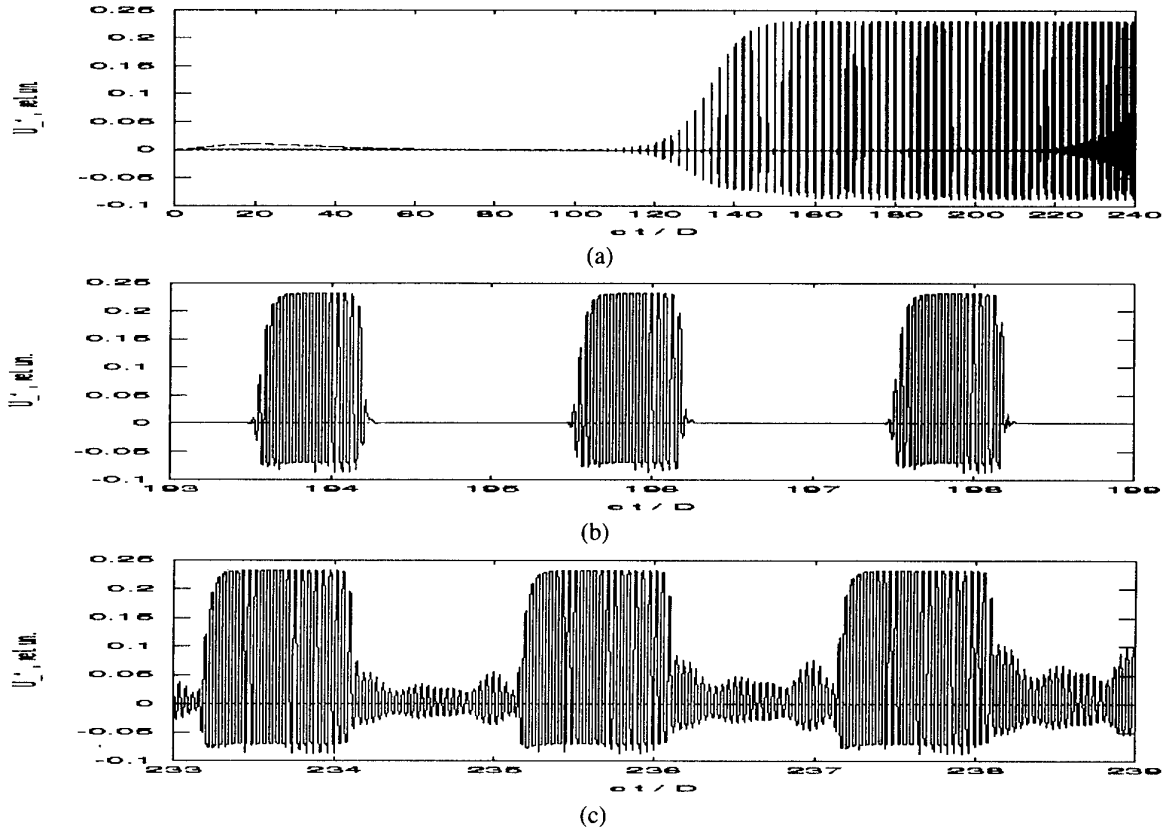


Fig. 4: Radiation field in the case of a thin mirror

The period of pulsing t_p is equal to a single round trip of the field in the cavity, $t_p = 2D/c$. Meantime, the carrier frequency of each pulse, f , is defined by the thickness d and the refractive index n of the dielectric mirror as $f = c/(2nd)$.

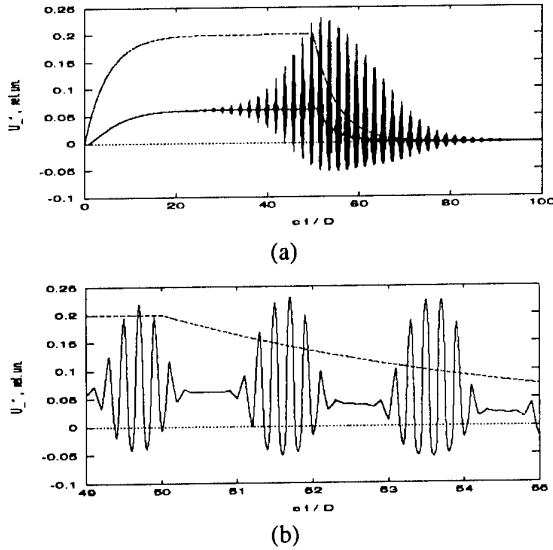


Fig. 5: The train of ultra-short pulses generated by the pulse of external voltage $E_1^{(0)}(t)$ added to the initial bias $E_0^{(0)}$. The parameters are $D = 15 \text{ mm}$, $d = 0.8 \text{ mm}$, $n = 1.4$, $G_0 = 2.8$, $E_0^{(0)} = 2.8$ and $E_1^{(0)}_{\text{max}} = 0.2$ providing the frequency of the pulse repetition within the train $f_p = 10 \text{ GHz}$ and the carrier frequency of each pulse $f = 100 \text{ GHz}$. Duration of the bias pulse is $T_p = 2.5 \text{ ns}$ while the period of pulsing within the train is $t_p = 0.1 \text{ ns}$.

The frequency f depends on d and n in such a way that the half wavelength in the dielectric is equal to d . The carrier frequency increases with decreasing d and can be up to a hundred times greater than the frequency of the pulse repetition $f_p = 1/t_p$. For example, in the case shown in Fig. 4, we have $f/f_p = 50$, with the pulse duration $t_0 = 0.4 \times 10^{-10} \text{ s}$.

The pulses gradually extend and overlap if the oscillations continue for a long time (Fig. 4, b and c). So, in order to obtain the clear train of pulses, one has to turn off the excitation at some moment by decreasing the bias voltage below the threshold value and then turn on it again by increasing $E^{(0)}$ when the pulses have been radiated from the cavity (Fig. 5).

Thus, the bias voltage has to be periodic as well, with the period T_p being much greater than the period of pulses t_p generated within the train.

The process of the excitation of ultra-short radio pulses discussed above is analogous to the generation of short pulses in optics by means of periodic pumping of a short-pulse laser by another laser providing the pump pulses of greater duration.

IV. CONCLUSION

Numerical simulation of the process of electromagnetic field excitation in a one-dimensional cavity with an active layer and a dielectric mirror has shown a possibility of ultra-short pulse generation in the system.

A solution found for the cavity of the length $D = 15 \text{ mm}$ with the dielectric mirror of thickness $d = 0.15 \text{ mm}$ and of refractive index $n = 2$, shows the generation of the train of such pulses. The repetition frequency of the pulses within the train is $f_p = 10 \text{ GHz}$ while the carrier frequency of each pulse is $f = 500 \text{ GHz}$, with the pulse duration $t_0 = 0.04 \text{ ns}$.

The excitation of the perfect trains of pulses requires periodic variation of the bias voltage around the threshold value in order to avoid the overlap of pulses within the train. The period of variation is typically large as compared to the duration of a single pulse. So, the train may contain a long sequence of ultra-short pulses.

References

1. J. C. Wiltse, J. W. Mink, "Quasi-Optical Power-Combining of Solid-State Sources", *Microwave J.*, Vol. 35, pp. 144-156, 1992
2. K. A. Lukin et al., "Method of Difference Equation in the Resonator Problem with a Nonlinear Reflector", *Soviet Physics - Doklady*, Vol. 34, pp. 977-979, 1989
3. L. V. Yurchenko, V. B. Yurchenko, "Noise Generation in a Cavity Resonator with a Wall of Solid-State Power-Combining Array", *The 11th Int. Microwave Conf. MIKON-96, Warsaw, Poland*, Vol. 2, pp. 454-458, 1996
4. K. A. Lukin, "Noise Radar Technology for Short Range Applications", *The 5th Int. Conf. on Radar Systems, Brest, France*, Vol. 'Oral Sessions', Session 2.11-2, 1999

Gain and loss in Terahertz Intersubband Emitters

Jerome Faist

Abstract – We will report our latest investigation in terahertz intersubband quantum cascade structures. Namely, the systematic study of gain and loss in such structure embedded in a so-called double plasmon waveguide has already enabled to show waveguide losses of about 100cm^{-1} and a differential gain of 20cm^{-1} . In an other line of research, the electroluminescence enhancement obtained by the application of a strong perpendicular

magnetic field in the quantum limit (cyclotron energy larger than the intersubband transition energy) will be discussed.

University of Neuchatel, Switzerland

At the time of publication the final manuscript was not available.
--

Modelling of Micromachined Klystrons for Terahertz Operation

Robert E Miles, Joan Garcia, John R Fletcher, D Paul Steenson, J Martyn Chamberlain, Christopher M Mann, Ejaz J Huq

Abstract-- The use of silicon and ultra-thick photoresist micromachining for the fabrication of terahertz frequency klystrons is discussed and a Monte Carlo based model of the device physics is presented. The model is shown to be an accurate representation of the electron flow in the device and it is demonstrated how it can be used as a design tool to optimise the geometry and operating conditions. An estimate of the power levels to be expected by the proposed devices is given.

Index Terms-- Klystron, terahertz, micromachining

I. INTRODUCTION

The klystron is a high frequency vacuum tube device, originally developed in 1939 [1] by the Varian brothers and derived from the Heil Tube of 1935. Sixty years on klystrons are still in production for uses such as radar where high power (kW) microwave radiation is required and as millimetre wave oscillators. However, as the frequency of operation increases, the device dimensions progressively decrease and their manufacture by conventional machining becomes ever more difficult. The advent of micromachining techniques in both silicon and ultra-thick photoresists now puts us in command of a precision technology which we are using to scale down the dimensions of the klystron for operation at terahertz frequencies. The klystron is nevertheless a "transit time" device (see below) and in common with other such devices (e.g. field effect transistors, FETs) the power is expected to fall off with increasing frequency. However, the klystron has a larger conducting cross section than the FET giving higher current levels and consequently more power than the solid state device and therefore a useful power level in the region of 1 mW at THz frequencies is expected.

There are a number of trade-offs in klystron operation involving both the dimensions and operating voltages and therefore an accurate simulation is required to aid in the design of an optimised device.

Robert E Miles, Joan Garcia, John R Fletcher, David Paul Steenson and J Martyn Chamberlain are with The School of Electronic and Electrical Engineering, The University of Leeds, Leeds LS2 9JT, UK.

Christopher M Mann and Ejaz Huq are with the Rutherford Appleton Laboratory, Chilton, Didcot, Oxfordshire OX11 0QX, UK

II. PRINCIPLE OF KLYSTRON OPERATION

With such a long history, the klystron is a well understood device with its own extensive literature (see for example [2,3] and more recently [4]). However, for convenience, the principle of operation of the reflex klystron (i.e. the form of the device considered in this paper) will be summarised here. A stream of electrons (conventionally produced by a heated cathode electron gun) passes through a pair of metal grids which form part of a tuned cavity as shown in Fig. 1. The stream is subsequently reflected back along its original path by a negatively charged electrode. Random fluctuations in the beam current give rise to an oscillating

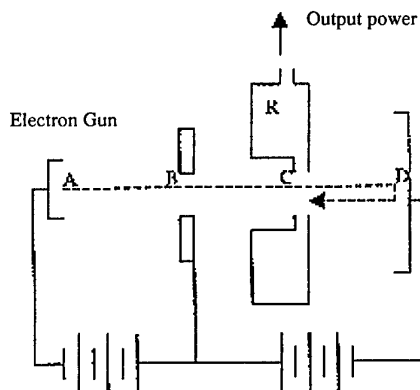


Fig. 1. Schematic diagram of a reflex klystron (B is the electron accelerating anode, C the grids, R the resonant cavity and D the repeller electrode).

electromagnetic field in the cavity which results in a corresponding periodic potential difference between the grids. This potential variation has two effects. The first is to modulate the velocities of the electrons in the beam causing them to form up into bunches in the drift region and secondly if, after reflection by the retarding potential, the bunches return to the grids at the point in the cycle when the right hand grid is positive, power is transferred to the cavity. The electrons therefore constitute a feedback mechanism to the cavity and the conditions for oscillation to start spontaneously require the power transferred from the beam to the cavity to be at least equal to the combination of the losses that occur in the cavity and the

useful power delivered to an outside load (expressed in terms of the loaded Q or "quality factor of the system).

III. MICROMACHINED IMPLEMENTATION

At terahertz frequencies the typical cavity dimensions in a reflex klystron are determined by the wavelength λ of the radiation i.e. around 300 μm . A further critical dimension is the distance between the grids which must be $< \lambda/10$ to ensure that there is a very small voltage phase change as an electron bunch passes through i.e. the "transit time limit. It is these small feature sizes that make the manufacture of THz klystrons by conventional machining very difficult, especially as the metal surfaces require a high quality surface finish in order to reduce electrical losses to a minimum. On the other hand, the required dimensions are well within those obtainable by micromachining which also results in a high quality surface finish. This implementation of the klystron also takes advantage of another development of micromachining, the silicon cold cathode field emission tip. (Fig 2) [5,6,7]



Fig. 2. A micromachined silicon field emission tip.

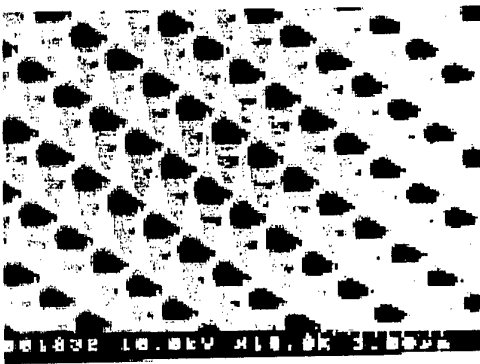


Fig. 3. An array of Si field emitter tips

Arrays of these electron emitting tips (Fig. 3.) are capable of producing higher beam current densities than heated filaments and at significantly lower temperatures. This low temperature operation is essential if ultra-thick photoresists are used to form the resonant cavities and it also relaxes the

vacuum requirements. Field emitter arrays developed for plasma display purposes have been shown to have an operating lifetime of up to 1000 hours. The construction of a micromachined device is shown in Figure 4.

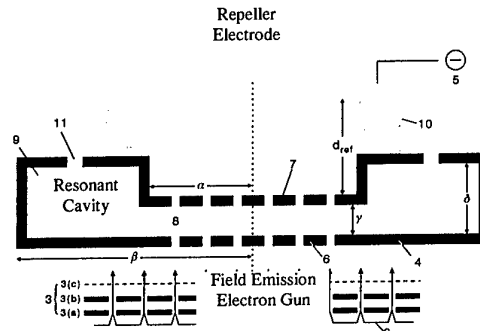


Fig. 4. Proposed construction of a micromachined klystron

IV. MODELLING

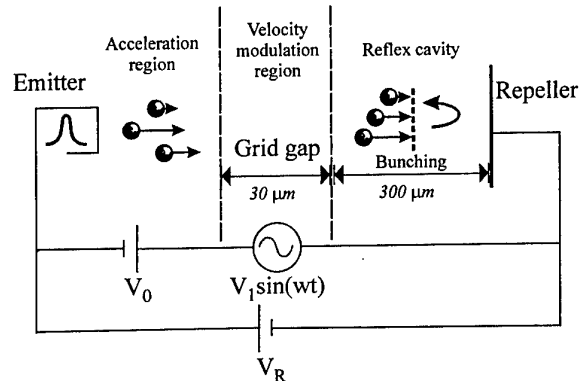


Fig. 5. Diagram of the 1-D geometry used for the physical simulation.

Figure 5 shows the structure that has been used for the modelling in this work. The electron beam is emitted from the cold cathode structure on the left and is assumed to have a Gaussian distribution of velocities. The voltage V_0 applied to the field emission tips is taken to be 80V. The periodic potential difference generated between the grids by the electromagnetic field in the cavity is simulated by applying a periodic potential difference ($V_1 \sin(\omega t)$) between them. This is in fact a very good approximation because for the high Q cavities, which are necessary for the operation of these devices, any harmonics of the fundamental frequency are at a very low level. The resultant effect therefore is essentially a simple sinusoid. This implementation also avoids the necessity of electromagnetic field modelling and allows us to use a 1-D model. Some typical dimensions are shown in the figure

but it is a simple matter to vary the grid spacing, repeller electrode position and the magnitudes of the applied voltages in order to study their effect on the device operation. The left hand grid in the figure is electrically earthed which, as far as the model is concerned, means that any electrons arriving from the direction of the repeller disappear from the particle list in the plane of this grid. The "wires" in the grids are accounted for by assuming that a certain fraction of the electrons (anything between 50% and 20%) are lost as they transit each grid. Carefully aligned grids will of course reduce the losses as electrons will only be lost as they pass through the first grid on which they are incident.

At the time of writing it is assumed that the electrons are in sufficiently low densities such that they have (i) a negligible effect on the potential distribution in the device and (ii) do not collide with each other. The main particle interactions in the Monte Carlo model are therefore those with the time varying fields and the physical structure.

On starting, the program assumes that the device is empty of electrons and that they are then supplied from the field emitter gun. The simulation must therefore be run for 2 or 3 cycles before a steady state is reached.

V. RESULTS

Figures 6 and 7 illustrate an electron bunch travelling back through the grids having been reflected by the repeller electrode. Figure 6 is a plot of charge density and Figure 7 of current, both as a function of position in the device. The double peak is a well known feature of the bunching process.

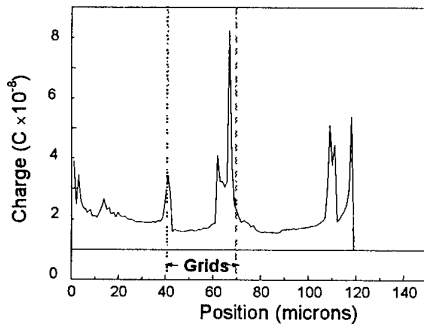


Fig. 6. Charge density as a function of position showing an electron bunch moving into the space between the grids after reflection at the repeller electrode.

The snapshot in time depicted in Figs. 6 and 7 represents the point where a charge bunch is just beginning to feed power into the cavity. Figure 8 shows the relationship between the current flowing through the device and the potential difference across it. It can be seen that the optimum phase relationship between current and voltage is not achieved under the conditions applied in this case but nevertheless the power transferred is estimated to be in the

region of 1 mW (albeit for a frequency of only about 0.02 THz in this simulation). The figure does however serve to illustrate the behaviour of the device. A preliminary study has also been carried out on the best value to choose for the magnitude of V_0 and it would appear that the electron bunching is a maximum at around 15V which is the value used in the simulations shown here.

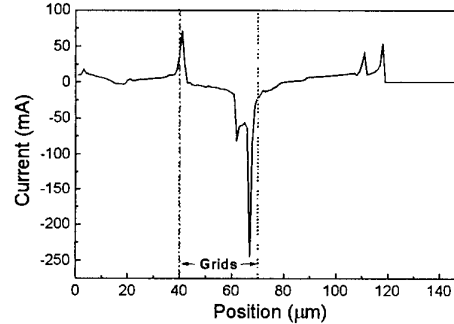


Fig. 7. Particle current against position corresponding to Fig. 6. (Note; a negative current represents electrons travelling from right to left).

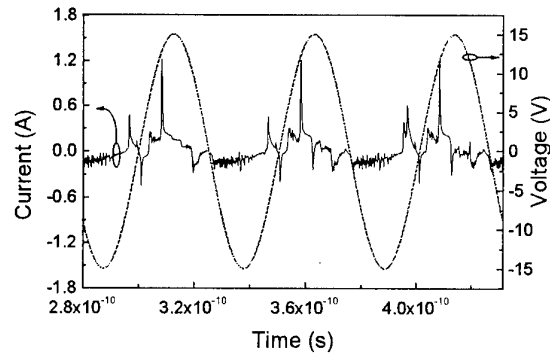


Fig. 8. Current and voltage for the simulated device.

VI. CONCLUSION

Recent developments in micromachining, particularly in cold cathode field emission arrays and ultra-thick photoresists have brought the klystron oscillator, operating at terahertz frequencies, a step closer to being realised. However there are still some formidable hurdles to overcome in arriving at an optimised device. There are a number of design parameters involving device geometries and operating conditions that can be varied but there is a strong interaction between them. An accurate physical model such as the one being developed here is therefore an essential design aid. This is particularly the case for these new devices where the fabrication technology is still under development.

ACKNOWLEDGEMENTS

The authors would like to thank the Engineering and Physical Sciences Research Council (EPSRC) and the European Union "INTERACT" project for supporting this work.

REFERENCES

- [1] R.H.Varian and S.F.Varian, "A High Frequency Oscillator and Amplifier," *J. Appl. Phys.*, vol. 10, pp 321-327, May 1939.
- [2] K.R.Spangenburg, "Vacuum Tubes," McGraw-Hill Electronic and Electrical Engineering Series, Ed. F.E.Terman, 1948.
- [3] S.Y.Liao, "Microwave Devices and Circuits" Prentice-Hall, 1985.
- [4] M.J.Smith and G. Phillips, "Power Klystrons Today," Research Studies Press Ltd. (John Wiley), 1995.
- [5] D.Peters, I.Paulus, and D. Stephani, "Field Effect Emitters for Display Systems," *J. Vac. Sci. Technol.*, Vol. B12 (2), pp. 652-656, 1992.
- [6] S.E.Huq, G.H.Grayer, S.W.Moon and P.D.Prewett, "Fabrication and Characterisation of ultra sharp silicon field emitters," *Materials Science & Engineering*, Vol. B51 pp. 150-153, 1998.
- [7] B.J.Kent, E.Huq, J.N.Dominey, A.D.Morse and N.Waltham, "The use of microfabricated emitter arrays in a high precision mass spectrometer for the Rosetta mission," *3rd Round Table on Micro/Nano Technologies for Space*, ESTEC Noordwijk, The Netherlands. 15-19th May 2000.

Observation of THz oscillations and efficient THz emission from contacted low temperature grown GaAs structures

Christian Steen, Sönke Tautz, Peter Kiesel, S. U. Dankowski, Gottfried H. Döhler,
Ulrich D. Keil,
Gregor Segsneider, Karsten Siebert, and Hartmut G. Roskos,
Viktor Krozer

Abstract – We have performed femtosecond differential transmission experiments in low temperature grown GaAs (LT-GaAs) layers under high electric fields. The fields were induced by voltages up to 60 V applied to interdigitated contacts with a few μm period. Up to about 10 oscillations of the field-induced transmission changes with a period of $T = 2.2$ ps were detected in a structure where the high-frequency effective length of the contacts was kept short. The large amplitude of the AC component of the differential transmission signal indicated that the amplitude of the light pulse induced oscillating electric field has to be of the same order of magnitude as the applied DC field. Thus the same has to be true also for the AC voltage between the fingers. In order to test this interpretation we have performed photomixing experiments. They yield a maximum emitted rf power of about 60 nW at a beat frequency of $\nu = 1/T = 0.44$ THz, at only 10 mW of incident optical laser power. Computer simulations yield the same frequency for the contact structure considered as a microstrip patch antenna.

I. INTRODUCTION

GaAs grown by molecular beam epitaxy (MBE) at unusually low temperatures (200 to 350°C) (LT-GaAs) exhibits, after suitable thermal annealing, both very short lifetimes for photo-generated carriers (down to the sub-ps range) and very high specific resistance (close to the value for intrinsic GaAs) [1-2]. These properties are attributed to fast recombination and/or capture of the photo-generated electrons and holes by a high density of deep traps. Due to these properties LT-GaAs has proven as a very promising material for efficient THz generation by photomixing [3-5]. In photomixers high DC fields are present in the active region between the contacts, which spatially separate electrons and holes close to the contacts. In order to investigate the influence of these fields on the relaxation and recombination kinetics we have performed fs differential transmission experiments on LT-GaAs layers with interdigitated metal-

semiconductor-metal (MSM-) contacts as a function of applied DC bias. We have found two important results. First, we have observed a rather strong increase of the recombination or trapping times with increasing bias. This is, of course, an effect which negatively affects the performance of photomixers. Due to a decreasing recombination rate the DC component of the carrier density increases in comparison to the AC component. Therefore, the ratio of the THz component of the photocurrent to the (purely dissipative) DC photocurrent decreases accordingly. Secondly, however, we observed oscillations of the differential transmission signal with periods in the low ps range. These oscillations were particularly pronounced in sample structures with a large capacitance, which were specifically designed to contain a sufficiently large reservoir of charge to feed the photocurrent generated by the pump beam without causing a collapse of the applied voltage. From an analysis of the time-resolved transmission oscillations we have deduced an AC field amplitude which is of the same order of magnitude as the applied DC field, indicating that this sample structure should represent an efficient THz oscillator under photo-mixing conditions. Therefore, we have also performed photomixing experiments as a function of difference frequency of the two lasers. In fact, we observed a high efficiency for the emission of radiation at a resonance frequency of about 0.44 THz with a FWHM of about 12%. In order to understand these findings in detail and in order to further improve the design of the sample structure in the future, we have performed computer simulations of the device in terms of a micro-strip patch antenna. These calculations yield excellent agreement with the experimental findings.

In Section II of this paper we sketch the design of the sample. In Section III we report on the Differential transmission measurements. The results of the photomixing experiments and of the simulations of the antenna are described in Sections IV and V. We conclude with a brief outlook in Section VI.

II. SAMPLE

The 1.4 μm thick LT-GaAs layer was grown by MBE at 250 °C and annealed ex-situ at 600 °C for two minutes. Interdigitated Ti/Au contacts (finger width of 1 μm , finger length of 20 μm and finger spacing varying

C. Steen, S. Tautz, P. Kiesel, S. Dankowski and G. Döhler are with the Institut für Technische Physik I, Universität Erlangen-Nürnberg, Erwin-Rommel-Str.1, D-91058 Erlangen
U. Keil is with the Microelectronic Centre, Technical University of Denmark, DK-2800 Lyngby
G. Segsneider, K. Siebert, and H.G. Roskos are with the Physikalisches Institut, J.W. Goethe Universität, Robert-Mayer-Str. 2-4, D-60054 Frankfurt
V. Krozer is with the Fakultät für Elektrotechnik und Informationstechnik, TU Chemnitz, Reichenhainer Str. 70, D-09126 Chemnitz

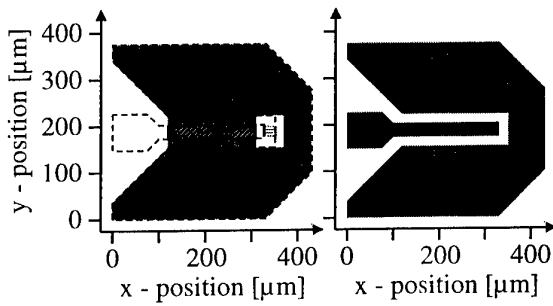


Fig. 1: Device structure. The left graph depicts the „bottom“ Au layer, which also contains the interdigitated contacts (within the window). The upper layer, shown in the right part, is separated from the bottom layer by a 1 μm thick polyimide layer. The latter one has an opening in the window region and the hatched area (see also text).

between 3 and 6 μm) and the „bottom contact layer“ (depicted on the left hand side of Fig. 1) were deposited by photolithography and metal evaporation (200 Å Ti/1500 Å Au). Except for the interdigitated contacts and the hatched area shown in Fig. 1, the sample was covered by an approximately 1 μm thick polyimide layer. On top, another Ti/Au layer (200 Å/1500 Å) was deposited with the shape shown on the right hand side of Fig. 1. This way, a patch antenna is formed. The center stripe is connected to the „bottom contact layer“ and to the left one of the interdigitated contacts on the LT-GaAs layer. The U-shaped part, which forms the „top contact layer“, establishes the metallic connection to the right side of the finger contacts. The capacitor formed by the two Ti/Au layers with the polyimide layer as a dielectric ($\epsilon = 4$) in between is 4.3 pF. 1150 Å of SiO_x, evaporated at the area with the interdigitated finger contacts, serve as surface passivation and anti reflection coating. Finally, the whole sample was removed from the substrate by the „epitaxial lift-off“ technique [6] and glued onto a 0.2 mm thick glass substrate. For the epitaxial lift-off process a 50 nm thick „sacrificial“ AlAs layer had been grown on the GaAs substrate prior to the growth of the LT-GaAs layer.

III. DIFFERENTIAL TRANSMISSION MEASUREMENT

The differential transmission experiments were performed with a mode-locked Ti-Sapphire laser providing pulses with a FWHM of 100 fs at a repetition rate of 76 MHz. The photon energy $h\nu$ of the pulses was tunable (simultaneously for pump and probe beam) from 1.4 to 1.5 eV, i.e. from below the band gap energy of GaAs ($E_g = 1.42$ eV at room temperature) to values substantially above. In Fig. 2 the relative transmission changes, measured at a photon energy of 1.43 eV = $E_g + 10$ meV (i.e. less than the thermal energy kT above band gap) taken for different applied voltages are shown as a function of the delay time of the probe beam. The density of electron hole pairs generated in the LT-GaAs layer by a single pulse was estimated to be about $2 \times 10^{18} \text{ cm}^{-3}$. At zero volt the relative transmission $\Delta T/T$ increases due to bleaching of the absorption resulting from a high carrier density near the band edges. After

reaching a maximum of 0.52 % the transmission signal decays with a time constant of about 700 fs. At finite fields there are two effects contributing to the transient transmission changes. First, the high fields induce heating of the electron hole plasma, resulting in a fast decay of the bleaching effect near to the band edge, which was very pronounced at zero volt. The second contribution is due to the Franz-Keldysh effect. At the photon energies used in this experiment the absorption

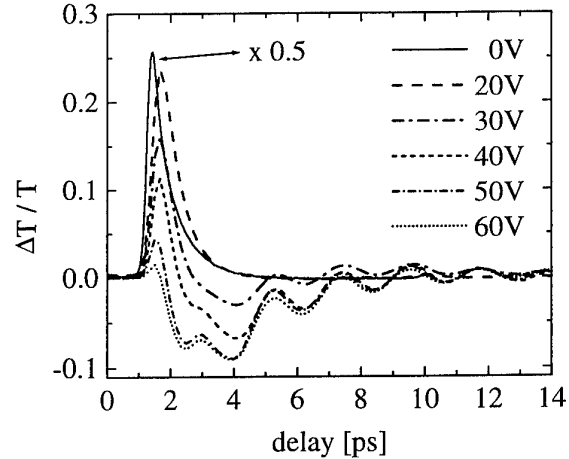


Fig. 2: Differential transmission at $h\nu = 1.43$ eV for $U = 0, 20, 30, 40, 50$, and 60 V. For $U > 20$ V the transmission signal exhibits an AC component with a period of 2.25 ps. (The curve for $U = 0$ is reduced by a factor 2).

decreases with increasing electric field. Therefore, a transient decrease of the electric field results in an increase of absorption and, hence, a transmission lower than in the dark case. A decrease of the electric field can be caused by internal screening due to mobile or trapped carriers, which become spatially separated by the electric field. But it can also originate from a break-down of the voltage at the finger contacts due to the high transient photoconductivity [7]. If the contacts are part of a resonant system (electromagnetic circuit or antenna) the latter effect will lead to (attenuated) oscillations of the field in the sample. This is exactly, what is observed in our device when a DC bias is applied (Fig.2). At increasing voltages the bleaching signal becomes more and more suppressed and the transient transmission signal is dominated by the Franz-Keldysh absorption. The AC component of this signal exhibits a voltage-independent period of about 2.25 ps. The decay of this component is significantly slower ($\tau_{AC} \approx 5$ to 10 ps) than the decay of the DC component of the transient transmission changes ($\tau_{FC} \approx 3$ ps), which reflects the time constant for return of the electric field in the sample to its original value in the dark state, when the photo-induced electrons and holes have disappeared due to extraction at the contacts or due to trapping or recombination within the LT-GaAs layer. The fact that the AC signal persists even after the DC signal has disappeared, its voltage-independent period and, last but not least, the large amplitude observed for the special design of this sample indicate that the potential between

the fingers performs (rather weakly attenuated) electromagnetic oscillations after each pulse. In order to confirm this assumption we have tested the performance of our sample under periodic excitation conditions, as described in the following section.

IV. PHOTOMIXING EXPERIMENTS

The photomixing experiments were performed with a two color cw-Ti:Sapphire laser [8]. With this system we are able to tune each color in the spectral range from 750 nm to 850 nm independently. We illuminate the device from the backside with a spot size of 15 μm . The generated THz radiation was focused with a teflon-lens onto a helium cooled InSb bolometer. The setup is

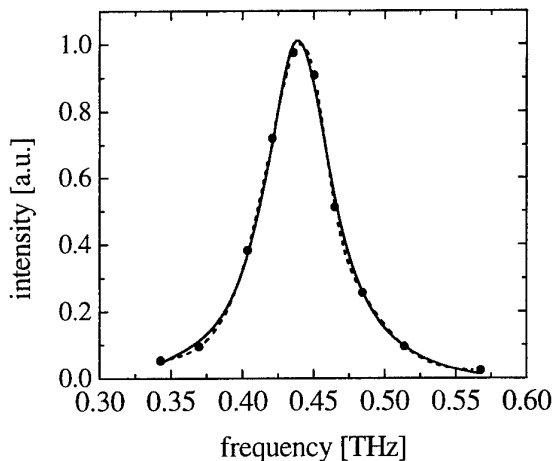


Fig. 3: Output power as a function of difference frequency. The full line depicts the Lorentzian fit.

described in detail in [9]. Fig. 3 shows the normalized power spectrum of the emitted THz radiation of the device in z direction (perpendicular to the plane of the metallizations). An electric field of 95 kV/cm was applied. The average incident optical intensity was 4.5 mW. We obtained a center frequency of about 0.44 THz and a line width (FWHM) of 54 GHz with a Lorentzian data fit. Assuming a $\delta(t)$ -like excitation this corresponds to a damping constant of about 6 ps. At an incident optical intensity of 10 mW, we measured an output power of 60 nW. Considering reflection losses

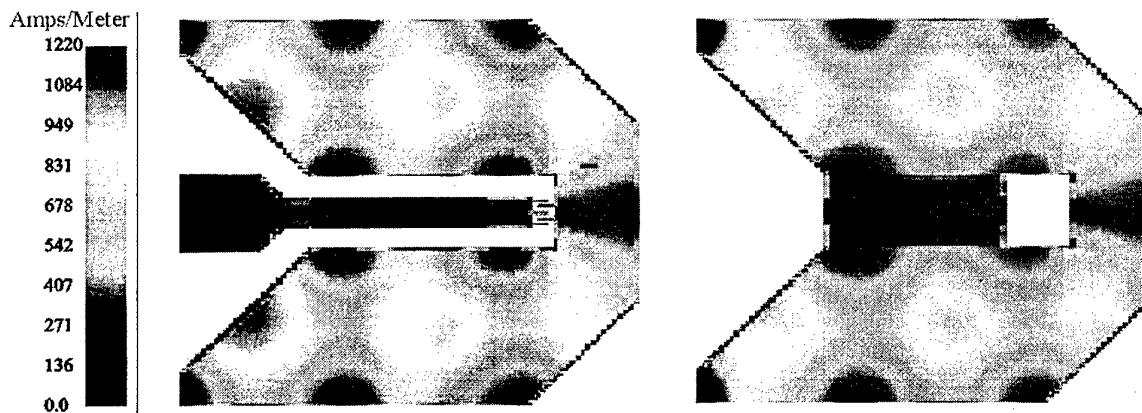


Fig. 4: Calculated current distribution of the device structure at the resonance frequency.

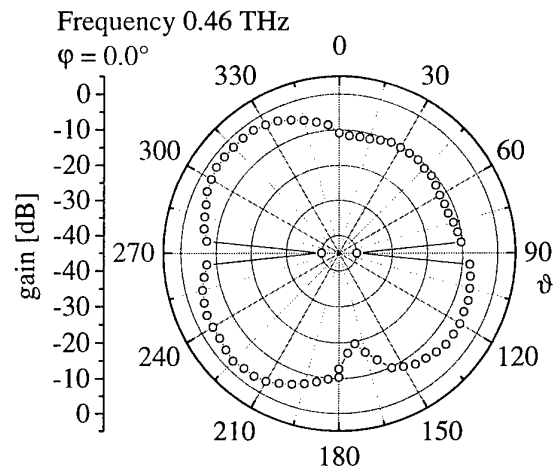


Fig. 5: Angular distribution of the calculated emitted power.

at the teflon lens we get an output power of 0.1 μW . Higher input intensities destroyed the devices glued on glass due to the poor thermal conductivity of the adhesive and the glass. Considerably higher output power should be achievable with devices attached to a heat sink.

V. SIMULATION

We have also performed electromagnetic computer simulations for the structure. For the simulations shown here, the SONNET 6.0 software has been used, assuming a resistive active area around the interdigitated fingers. The open wall boundary conditions have been used for the antenna simulations. The radiation pattern has been calculated from the current distribution. In these simulations we obtain a resonant frequency of 0.46 THz, which is in excellent agreement with the measured values. Fig. 4 shows the current distribution of our device structure. The current in the top and bottom plates indicates that the device contact structure operates as a microstrip patch antenna. Clearly three extrema of the current density are observable in Fig. 4 in x-direction. The center finger is used for DC bias supply and therefore does not exhibit appreciable THz signal. The angular distribution of the radiated output power is depicted in Fig. 5. From this figure we expect a

maximum output power in $\pm 5/4\pi$ direction, respectively. However, our photomixing measurements above were taken at an angle of $\pi/2$. Hence, the measurements were not performed in the optimum configuration. Angle dependent simulations are in progress to test this assumption. From the simulated results we deduce that the device delivers higher output powers by at least a factor of 2 to 3 because of the radiation pattern.

VI. CONCLUSIONS AND OUTLOOK

Our pump & probe measurements, photomixing experiments and computer simulations yield efficient high-field oscillations at the same frequency of 0.44 THz for the investigated sample. We expect that the relatively high output power of the photomixer of presently 0.1 μ W and the frequency can still be considerably increased by optimized design of the antenna structure, of the LT-GaAs material, and, in particular, by taking care of a better heat dissipation (no lift-off from the substrate, or attachment to a heat sink, e.g.).

References

1. S. Gupta, J.F. Whitaker, and G.A. Mourou, "Ultrafast carrier dynamics in III-V semiconductors grown by Molecular Beam Epitaxy at very low temperatures", *IEEE J.Quantum Electron.*, Vol. 28, p. 2464, 1992.
2. P. Kordos, A. Förster, J. Betko, M. Morvic, and J. Novák, "Semi-insulating GaAs layers grown by molecular-beam epitaxy", *Appl. Phys. Lett.*, Vol. 67, p. 983, 1995.
3. K. A. McIntosh, E. R. Brown, K. B. Nichols, O. B. McMahon, W. F. DiNatale, and T. M. Lyszczarz, "Terahertz measurements of resonant planar antennas coupled to low-temperature-grown GaAs photomixers", *Appl. Phys. Lett.*, Vol. 69, p. 3632, 1996.
4. S. Matsuura, M. Tani, and K. Sakai, "Generation of coherent terahertz radiation by photomixing in dipole photoconductive antennas" *Appl. Phys. Lett.*, Vol. 70, p. 559, 1997.
5. S. Matsuura, G. A. Blake, R. A. Wyss, J. C. Pearson, C. Kadow, A. W. Jackson and A. C. Gossard, "A travelling-wave THz photomixer based on angle-tuned phase matching", *Appl. Phys. Lett.*, Vol. 74, p. 2872, 1999
6. E. Yablonovitch, T. Gmitter, J.P. Harbison, and R. Bath, "Extreme selectivity in the lift off of epitaxial GaAs films", *Appl. Phys. Lett.* Vol. 51, p. 2222, 1987.
7. A detailed pump & probe study of the electric field effects on the dynamic relaxation and recombination kinetics of photogenerated carriers in LT-GaAs, using different photon energies, can be found in: U. D. Keil, J. Hvam, S. Tautz, S. U. Dankowski, P. Kiesel, and G. H. Döhler "Femtosecond differential transmission measurements on low temperature GaAs metal-semiconductor-metal structures", *Appl. Phys. Lett.*, Vol. 70, p. 72, 1997
8. F. Siebe, K. Siebert, R. Leonhardt, H.G. Roskos, "A fully tunable dual-color Ti:Al₂O₃ laser", *IEEE Journ. Quantum Electronics*, Vol. 35, p. 1731, 1999
9. K. Siebert, H. Quast, G. Segschneider, H. Roskos, S. Tautz, P. Kiesel, G. Döhler, V. Krozer, "An Optoelectronic CW THz Source for Imaging Applications", proceedings of 8th International Conference on Terahertz Electronics

Study of terahertz radiation from narrow bandgap semiconductors: InAs and InSb

Ping Gu, Masahiko Tani, Shunsuke Kono, and Kiyomi Sakai

Abstract — We investigated THz radiation from narrow bandgap semiconductors: n-type, p-type InSb and InAs were investigated using a time-resolved THz detection system. As a reference, THz radiation from InP (a wide bandgap semiconductor) was also measured. From the polarity of the waveforms we concluded that the ultrafast build-up of a photo-Dember field is the main emission mechanism for both InAs and InSb.

I. INTRODUCTION

It is known that THz radiation can be generated by irradiation of ultrashort laser pulses on semiconductors surface [1]. Besides optical rectification of ultrafast laser pulses [2], two processes are known to contribute to the THz radiation in bulk semiconductors. In semiconductors with a wide bandgap, such as InP, the generation of THz radiation is based on the ultrafast screening of the surface depletion field by the photoexcited carriers [3]. For the narrow bandgap semiconductors, on the other hand, the depletion field is generally not so strong, and the emission of THz radiation due to the depletion-field screening is not expected to be efficient. However, for the narrow bandgap semiconductors, such as Te and PbTe, it have been shown that the ultrafast build-up and relaxation of the photo-Dember field can be an efficient mechanism for generation of THz radiation. It is because that the high temperatures of photo-excited carriers due to the large excess energy and the small absorption depth (~ 100 nm) for the near infrared light cause a strong surface

field by the much faster diffusion of electrons than that of holes at the sample surface (photo-Dember effect) [4]. InSb is a narrow bandgap semiconductor, that is a unique and important material because of its high carrier mobility and small bandgap energy (Table 1). It is expected that THz emission efficiency of InSb should be comparable to or better than that of InAs because of its smaller effective electron mass and larger electron mobility than that of InAs. However, in a previous reports, we observed that the radiation power of n-InSb is approximately one-hundredth of n-InAs at room temperature [5]. In order to explain this difference, it is crucial to study the radiation mechanism of InSb and InAs.

In this work we investigated the azimuthal angle dependence of the THz radiation amplitude and THz radiation waveforms of n-type, p-type InSb and InAs using a time-resolved detection system in the same experimental condition. From the polarity of the waveforms we concluded that the ultrafast build-up of the photo-Dember field is the main radiation source for both InAs and InSb.

II. EXPERIMENTAL

The experiments were performed using a mode-locked Ti: sapphire laser pulses with an 80-fs pulse width and the 78-MHz repetition rate at a 800-nm wavelength. The laser beam was split into two parts. One part with an

Table 1: Sample properties

Sample	InSb	InAs	InP
Bandgap: E_g	0.17eV	0.36eV	1.34eV
Electron mobility: μ_e	76000 cm ² V ⁻¹ s ⁻¹	30000 cm ² V ⁻¹ s ⁻¹	4000 cm ² V ⁻¹ s ⁻¹
Hole mobility: μ_h	3000 cm ² V ⁻¹ s ⁻¹	240 cm ² V ⁻¹ s ⁻¹	650 cm ² V ⁻¹ s ⁻¹
Electron mass: m_e^*	0.0133 m_e	0.028 m_e	0.07 m_e
Hole mass: m_h^*	0.18 m_e	0.33 m_e	0.40 m_e
Surface depletion field: $\phi_s \sim E_g/2$	0.085eV	0.18eV	0.67eV
Refractive index ($\lambda = 800$ nm)	4.47	3.73	3.47
Refractive index ($f = 1$ THz)	1.93	3.78	3.52
Absorption depth: d ($\lambda = 800$ nm)	94 nm	142 nm	305 nm
Excess Energy: E (eV/T)	1.38eV/10500K	1.18eV/ 9000K	0.21eV/5000K
Electron temperature: T_e	9800K	8300K	1250K
Hole temperature: T_h	700K	700K	250K

Ping Gu, Masahiko Tani, Shunsuke Kono, and Kiyomi Sakai are with Kansai Advanced Research Center, Communications Research Laboratory, MPT, Japan588-2 Iwaoka, Nishi-ku, Kobe 651-2401, Japan

averaged power of 80 mW illuminated the sample surface at an incident angle of 45° to generate THz radiation. The other part (10 mW) gated the photoconductive dipole antenna detector to measure the THz radiation waveform. The polarization of the excitation laser beam was p-polarized and the direction of the dipole antenna was also in the same direction. The excitation laser pulses were focused onto the n- and p-InSb and -InAs surface to a spot size with a diameter less than 1 mm. The THz radiation from the sample in the optical reflection direction is collected and focused on the antenna detector with a pair of off-axis parabolic mirrors. The time-resolved waveforms of the radiation were obtained from the DC photocurrent in the antenna detector by varying the delay time between the pumping and gating pulses. The detector is a dipole photoconductive antenna having a length of 30 μm fabricated on low-temperature-grown GaAs. All experiments were performed at room temperature.

We used samples of a n- and p- InSb (100) with a residual carrier concentration of $n \sim 10^{16} \text{ cm}^{-3}$, of a n-InAs (111) and p-InAs (100) with a residual carrier concentration of $n \sim 10^{18} \text{ cm}^{-3}$, and of a n- and p- InP (100) with a residual carrier concentration of $n \sim 10^{18} \text{ cm}^{-3}$.

III. RESULTS AND DISCUSSION

Figure 1 shows the azimuthal angle dependence of the THz radiation in the present experimental configuration (a) for n- InAs (111) and (b) for n- InSb (100). Taking the surface normal as x-axis and the reflection plane as x-y plane, the electronic polarization induced in the semiconductors due to the optical rectification for (111) and (100) surface is expressed by Eq. (1) and (2), respectively:

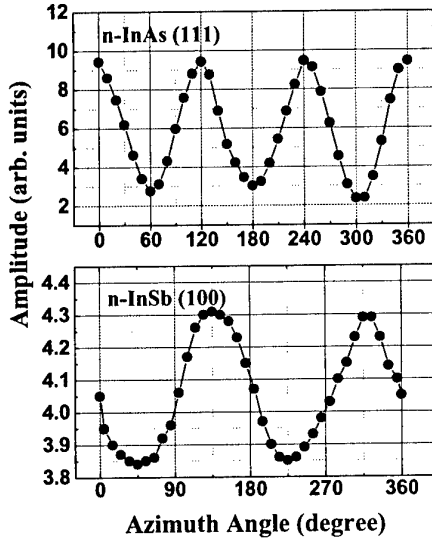


Fig.1: Azimuth angle dependence of THz radiation amplitude from semiconductors with (a) n-InAs (111) and (b) n-InSb (100) surface at a 45° incident angle of the excitation light on the sample. The solid line is only to guide the eyes.

$$P = d_{14} E^2 \begin{pmatrix} -\frac{1}{3} \cos^2 \phi + \frac{2}{\sqrt{3}} \sin^2 \phi \\ \frac{2}{\sqrt{6}} \cos^2 \phi \cos 3\theta - \frac{2}{\sqrt{3}} \cos \phi \sin \phi \\ \frac{2}{\sqrt{6}} \cos^2 \phi \sin 3\theta \end{pmatrix} \quad (1)$$

$$P = d_{14} E^2 \begin{pmatrix} \cos^2 2\phi \sin 2\theta \\ \sin 2\phi \sin 2\theta \\ \sin 2\phi \cos 2\theta \end{pmatrix} \quad (2)$$

Here, ϕ is the angle between the surface normal and the excitation laser beam inside the sample, and θ is the azimuthal angle around x-axis. As the THz radiation was detected in a reflection geometry for p-polarization, the observed THz field amplitude is expected to be proportional to

$$-p_x \sin \phi_{\text{THz}} + p_y \cos \phi_{\text{THz}}, \quad (3)$$

$$\sin 45^\circ = n_{\text{THz}} \sin \phi_{\text{THz}},$$

where ϕ_{THz} is the refraction angle for THz radiation at the interface of the sample surface and air, and n_{THz} is the refractive index of THz radiation. For the laser wavelength of 800 nm, ϕ is 10.9° , 9.0° , and 11.8° for InAs, InSb, and InP, respectively. For THz radiation ϕ_{THz} is estimated to be 10.9° , 21.5° , and 11.9° for InAs, InSb, and InP, respectively. Using these values, the angle

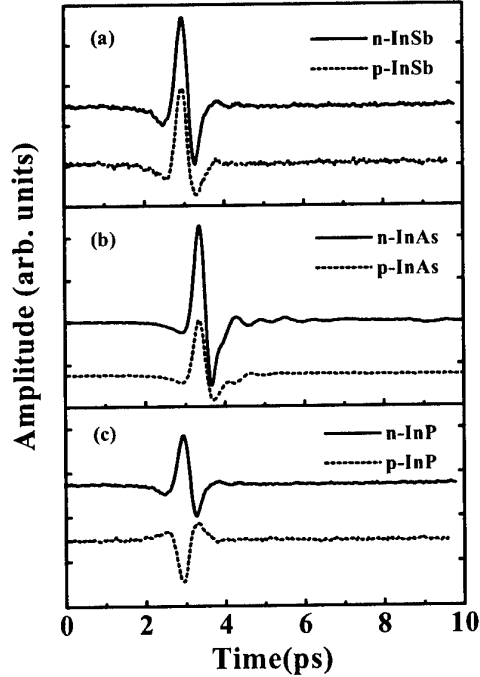


Fig. 2: Time-domain waveforms of the THz radiation from n- and p- (a) InSb, (b) InAs and (c) InP.

dependence of the radiation amplitude thus can be written as follows:

$$E \propto 0.773 \cos 3\theta - 0.153 \quad \text{for InAs (111),} \quad (4a)$$

$$E \propto 0.182 \sin 2\theta \quad \text{for InAs (100),} \quad (4b)$$

$$E \propto -0.069 \sin 2\theta \quad \text{for InSb (100),} \quad (4c)$$

$$E \propto 0.199 \sin 2\theta \quad \text{for InP (100).} \quad (4d)$$

As shown in Fig.1 the angle dependence of the radiation has a dc offset, which is attributed to the real surge current at the sample surface except for InAs (111), for which both the nonlinear process and the surge current can contribute to the dc offset. To suppress the component of THz emission resulting from optical rectification, we measured the THz radiation at azimuthal angle 26° for n-InAs (111), and 90° for p-InAs (100), and n-, p-InSb (100), where the components due to the optical rectification effect is expected to be null according to Eq. (4a)-(4d). The results are shown in Fig. 2(a) and 2(b). We also show the THz radiation waveforms of n- and p-InP in Fig.2(c) for comparison. It is known that the generation of THz radiation from InP originates mostly from the ultrafast screening of the surface depletion field by the photo-excited carriers [3]. The THz radiation due to the screening of the surface depletion field flips its polarity for the different type of doping due to the reversal of the direction of the surface depletion field, as is clearly shown in Fig.2(c). However, when the THz radiation is emitted by the ultrafast build-up and relaxation of the photo-Dember field, which originates from the different diffusion coefficients of electrons and holes, the polarity of the THz radiation remains the same for n-type and p-type semiconductors because the diffusion coefficient of electrons is always bigger than that of holes due to the small effective mass, irrespective to doping type of the semiconductor. The THz waveforms of n-, p-InSb and -InAs have the same polarity as shown in Fig.2 (a) and (b). This indicates that the excitation mechanism for the THz radiation in InSb and InAs is due to the ultrafast build-up and relaxation of the photo-Dember field. The radiation amplitude of the n-type InAs and InSb is a little larger than that of p-type. We suggest that there might be an enhancement of THz radiation due to the surface depletion field because the direction of the surface depletion field and the photo-Dember field is the same for n-type semiconductors.

By considering the sample properties, as listed in Table 1, we are able to have more insight into the THz emission

mechanisms. The surface depletion field of InAs and InSb should be much smaller than that of InP due to their small band gap energy. Consequently, the screening of surface depletion field should not be a strong source of THz radiation for InSb and InAs. On the other hand, because the photo-Dember field results from the different diffusion coefficients of electrons and holes, the build-up of the Dember field should be large for semiconductors with higher electron mobility. The short absorption depth of the laser light for the narrow bandgap semiconductors also helps to enhance the photo-Dember field because the photo-Dember field is proportional to the gradient of the carrier density. For 800-nm light the absorption depth of InAs and InSb is calculated to be 94 nm and 142 nm, while that of InP is 304 nm, respectively. In addition, the electron mobility and the excess energy of InSb and InAs is much bigger than InP due to the small effective mass and the narrow band gap. All these conditions are suggestive of a large Photo-Dember field for InAs and InSb with the optical excitation. Thus, we conclude the main source of THz radiation for InAs and InSb is the photo-Dember field, not the screening of the surface depletion field.

IV. CONCLUSION

By observing the polarity of the THz radiation from n- and p- InSb and -InAs, the main excitation mechanism of the THz radiation in the investigated narrow-band gap semiconductors, that is InSb and InAs, was concluded to be the ultrafast build-up and relaxation of the photo-Dember field. The detailed analysis of the ultrafast build-up of photo-Dember field at the narrow bandgap semiconductors will be given in the Conference.

References

1. For review paper, see for example, X.-C. Zhang, B. Hu, J. Darrow, and D. Auston, Appl. Phys. Lett. 56, 1011 (1990). D. Dykaar and S. Chuang, Optics Lett. 11, 2457 (1994).
2. S. L. Chuang, S. Schmitt-Rank, B. I. Greene, P. N. Saeta, and A. F. J. Levi, Phys. Rev. Lett. 68, 102 (1992).
3. X.-C. Zhang and D. Auston, J. Appl. Phys. 71, 326 (1992).
4. T. Dekorsy, H. Auer, H. J. Bakker, H. G. Roskos and H. Kurz, Phys. Rev. B 53, 4005 (1996).
5. S. Kono, P. Gu, M. Tani and K. Sakai: to be submitted to Applied Physics B.

Solid-State Oscillators for the THz-Range

Peter Zimmermann

Radiometers Physics GmbH, Germany

At the time of publication the final manuscript was not available.

Frequency Tripler with Anti-serial Schottky Diodes

M. Krach, J. Freyer, and M. Claassen

Abstract—In this paper a new type of frequency-multiplier from 70 GHz to 210 GHz [1] is presented which combines the advantages of a varactor with symmetrical capacitance-voltage characteristic and the low leakage current of Schottky diodes. The varactor structure consists of two inhomogeneously doped Schottky diodes in anti-serial connection which are quasi-monolithically integrated into a microstrip circuit on quartz. A theoretical description of the Schottky diode tripler is given and first experimental results are presented which show an rf-output power of 2 mW at 210 GHz.

I. INTRODUCTION

Frequency multipliers use non-linear devices to generate harmonics from fundamental oscillators. They are applied as practical rf-power sources above 200 GHz since power generation of fundamental oscillators normally is too low at these frequencies. The single Schottky diode is the most commonly used device though its application e. g. for frequency triplers is more complex as compared to varactors with symmetric capacitance-voltage characteristics, as the single-barrier varactor [2, 3]. In this case, the rf-circuit can be less complicated since no bias and idler circuits are necessary. However, the disadvantage of the single-barrier varactor is the relatively high leakage current which limits the rf-modulation.

In this paper, we present a new type of varactor structure with two inhomogeneously doped anti-serial Schottky diodes exhibiting a symmetric capacitance-voltage characteristic with relatively low leakage currents. The devices and the rf-circuit are fabricated quasi-monolithically on quartz substrate and are tested as frequency-multiplier from 70 GHz to 210 GHz.

II. NONLINEAR DEVICE

Bradley et al. [4] have shown that two anti-serial Schottky diodes with constant doping cannot be applied as varactors. This is due to the fact that with changing total charge, the

space-charge region of the reverse biased diode increases by the same amount by which the space-charge region of the forward diode is reduced. Thus, no non-linear total capacitance-voltage characteristic appears. This is, however, not valid if the doping concentration in the depletion layer is non-uniform. Then the space-charge region variations of the forward and the reverse diode differ from each other resulting in a variable total capacitance with respect to the total voltage. Due to opposite self-biasing, both diodes operate in a range of low conduction current [5].

The layer sequence of the applied Schottky diodes is schematically shown in Fig. 1. A large barrier height is realised by the use of an undoped 10 nm thick AlGaAs layer below the Schottky contact. The remaining depletion zone is split up into two layers with stepwise constant doping concentration followed by a highly n-doped zone for ohmic contact.

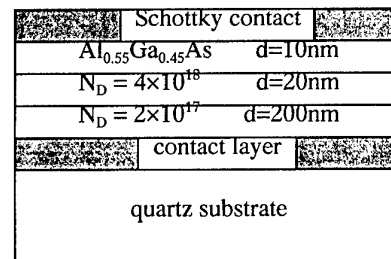


Fig. 1: Schematic layer sequence of the investigated Schottky diodes

The authors are with the Walter Schottky Institut, Technische Universität München, D-85748 Garching, Germany.

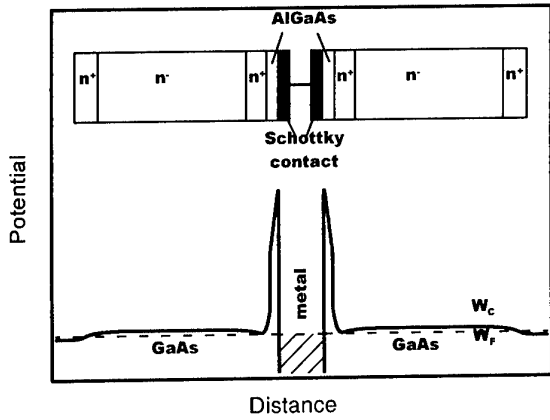


Fig. 2: Schematic layer sequence and band edge diagram of the anti-serial Schottky diodes

The symmetric varactor is realised by an anti-series connection of the two diodes with common Schottky contact schematically shown in Fig. 2.

III. SIMULATION

To determine the device properties, a simulation programme was developed which considers space-charge fields, thermionic field emission, tunnelling and impact ionisation. Capacitance-voltage and current-voltage characteristics of a single Schottky diode are calculated as follows:

Energy-band diagrams in the direction perpendicular to the layers of the structure are calculated by solving Poisson's equation self-consistently while requiring overall charge neutrality across the structure and satisfying the following boundary conditions:

1. The semiconductor properties are bulk-like.
2. With zero bias, the Fermi level remains constant throughout the entire structure and under applied bias V_a , the Fermi levels on the left and right hand side of the Schottky barrier must differ by eV_a (applied voltage).

Due to high charge densities, in some regions the Fermi level can be energetically higher than the conduction band edge. Therefore, the Fermi distribution function has to be applied to calculate the space-charge density.

The energy-band diagrams for different applied voltages may then be used to calculate the I-V characteristics of the Schottky diodes. Thermionic emission of electrons over the barrier and tunnelling of electrons through the barrier is computed using the model of Tsu and Esaki [6], in which the current density in the z direction is given by:

$$J_T = \frac{em^*k_B T}{2\pi\hbar^3} \cdot \int_0^\infty dE T(E) \ln \left(\frac{1 + e^{(E_F - E)/k_B T}}{1 + e^{(E_F - E - eV_a)/k_B T}} \right), \quad (1)$$

where m^* is the effective mass for electrons in the conduction band, e the elementary charge, E_F the Fermi level in the metal, V_a the applied voltage and E the kinetic energy of the electron due to the motion in the z direction. The transmission probability $T(E)$ is computed using WKB approximation [7]. For high voltages also impact ionisation has to be taken into account. This additional contribution to the conduction current can be implemented by the use of an impact ionisation coefficient [8].

The capacitance versus voltage behaviour of the device is calculated from the change of electric field with applied voltage:

$$C = \epsilon_r \epsilon_0 A \frac{dF}{dU}, \quad (2)$$

where F is the electric field and A the area of the diode.

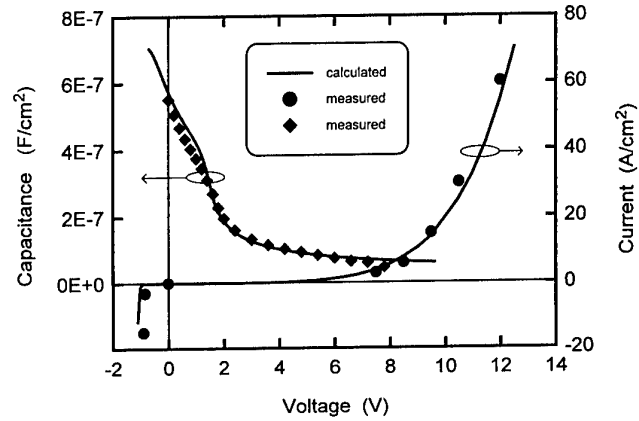


Fig. 3: Experimental and theoretical capacitance-voltage and current-voltage characteristics of a single Schottky diode (see Fig.1)

The capacitance-voltage and current-voltage characteristics of the investigated structure are depicted in Fig. 3 for a single Schottky diode showing good agreement of measured and simulated data.

The dynamic capacitance voltage characteristic of the anti-series connection of two diodes, which determines the efficiency of the tripler, can be calculated from the capacitance-voltage characteristic of a single Schottky diode. For this purpose the charge-voltage characteristic of a single diode is calculated by integrating the capacitance-voltage characteristic of the device. With this charge-voltage characteristic and the charge displacement due to the self-biasing, which is rf-voltage amplitude dependent, the total charge-voltage characteristic of the anti-series connection of two diodes can be computed. The differentiation of the total charge-voltage characteristic provides the rf-capacitance voltage characteristic of the multiplier device [5]. As an example, the resulting total rf-capacitance-voltage characteristic of two anti-serial

Schottky diodes with doping profile from Fig. 1 and characteristics from Fig. 3 is depicted in Fig. 4.

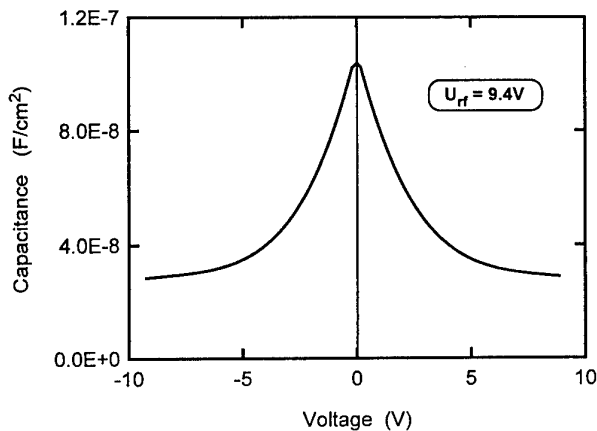


Fig. 4: Rf-capacitance-voltage characteristic of the symmetric varactor with two anti-serial Schottky diodes with a doping profile according to Fig. 1 and an rf-voltage of 9.4 V

The rf-voltage is 9.4 V in this case. It can be seen that the inhomogeneous doping profile in the depletion zone results in a strong non-linearity of the capacitance-voltage characteristic which enables application in frequency multipliers.

IV. RF-CIRCUIT

The tripler with the two devices was quasi-monolithically integrated into a microstrip tripler circuit on quartz substrate. The anti-serial Schottky diodes are connected in series via air-bridges between input and output circuit. The initial material is grown on GaAs substrate by MBE technique and after the removal of the substrate, the entire rf-circuit including the varactor is fabricated on quartz substrate using standard photoresist technology. The quartz chip with the rf-circuit, which consists of the nonlinear device, a low-pass filter, and input as well as output coupling, is placed into a split waveguide mount with two symmetrical halves. Details can be found elsewhere [9, 10]. Tuning of the tripler is obtained by backshorts at both input and output waveguide (see Fig. 5). The design of the whole circuit was carried out by the help of microwave analysis programmes (ADS, HFSS) [11].

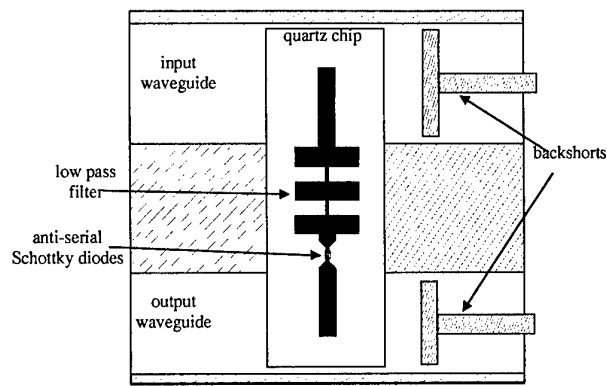


Fig. 4: Schematic view of the waveguide mount and quartz chip including the rf-circuit with quasi-monolithically integrated diodes

V. EXPERIMENTAL RESULTS

The current-voltage characteristic of the investigated Schottky diodes indicates relatively low leakage currents for reverse voltages up to 13 V. The diodes have a diameter of 10 μm and a series resistance of about 6 Ω . Tripler performance was tested at a fundamental frequency of 70 GHz. First experimental results achieved an rf-output power of 2 mW at 210 GHz with a flange to flange conversion efficiency of over 3 %. Up to this output level, saturation neither of efficiency nor of power has been observed. It should be noted that the structure of the diodes and the circuit are not yet optimised. Further work will focus on this field to increase the performance of the tripler.

VI. CONCLUSION

A new anti-series Schottky diode frequency tripler with an output frequency of 210 GHz, fabricated on quartz substrate, is reported. A theoretical description of the multiplier device as well as first experimental results are given. The rf-circuit with the nonlinear device was tested in a split full height waveguide mount. Considering the non-optimised structure for the Schottky diodes and the circuit, the achieved result of 2 mW output power is encouraging and shows the potential of this new tripler concept.

VII. ACKNOWLEDGEMENT

This work is supported by the Deutsche Forschungsgemeinschaft (SFB 348). The authors would like to thank H. Grothe for supplying the high-quality epitaxial materials.

VIII. REFERENCES

- [1] M. Krach, J. Freyer, and M. Claassen, 'Schottky Diode Tripler for 210 GHz', *Electron. Lett.* 36, pp. 858-859, 2000
- [2] E. Kollberg and A. Rydberg, 'Quantum-barrier-varactor diodes for high-efficiency millimeter-wave multipliers', *Electron. Lett.*, 25, p. 1696, 1989
- [3] J. Freyer, R. Meola, M. Claassen, and F. Neugebauer, 'Design of GaAs/GaAlAs Single-Barrier Varactors (SBV) for mm-Wave Frequency Multipliers', *Proceedings of 23rd Int. Conference on Infrared and mm waves*, Colchester, UK, 1998
- [4] R. F. Bradley and A. R. Kerr, 'Why Don't Back-to-Back Abrupt Junction Frequency Tripler Work?', *Proceedings of eight International Symposium on Space Terahertz Technology*, Harvard University, 1997
- [5] J. Freyer, M. Claassen, and M. Krach, 'Frequency Tripler with anti-serial Schottky Diodes', to be published
- [6] R. Tsu and L. Esaki, 'Tunnelling in a finite superlattice', *Appl. Phys. Lett.* 22, p. 562, 1973
- [7] C. B. Duke, *Solid State Physics*, 'Tunneling in Solids', Academic Press, New York, 1969
- [8] C. Benz, D. Liebig and M. Claassen, 'Tunnelling and impact ionization at high electric fields in abrupt GaAs p-i-n structures', *J. Appl. Phys.* 81 (7), p. 3181, 1997
- [9] A. V. Räisänen, D. Choudhury, R. J. Dengler, J. E. Oswald, and P. Siegel, 'A novel Split-Waveguide Mount Design for Millimeter- and Submillimeter-Wave Frequency Multipliers and Harmonic Mixers', *IEEE Microwave and Guided Wave Letters*, 3 (10), pp. 369-371, 1993
- [10] R. Meola, J. Freyer, and M. Claassen, 'Improved frequency tripler with integrated single-barrier varactor', *Electronics Letters* 36, pp. 803-804, 2000
- [11] R. Meola and J. Freyer, 'Design and Characterisation of an Integrated Frequency Tripler on GaAs Substrate', *Proceedings of 23th EuMC*, 2, pp. 189-192, München, 1999

2-D Design of Schottky Diodes

Jesús Grajal, Daniel Moreno and Viktor Krozer

Abstract— The optimization of Schottky diode operation together with the design of circuits based on these devices can be accomplished with a developed 2-D drift-diffusion simulator. Evaluation of the impact of different geometries on the device performance and study of limiting processes like velocity saturation at high frequencies are analysed with this simulation tool.

I. INTRODUCTION

GaAs Schottky barrier diodes continue being the key elements for mixers (heterodyne receivers) and frequency multipliers (all-solid-state power sources) for millimeter and sub-millimeter bands. The key points in the progress of the performance of circuits based on Schottky diodes have been the enhanced physical insight into and the optimization of submm-wave Schottky diode operation [1], the improvement in frequency multiplier and mixer analysis methods, and in physical analytical Schottky diode models [2], [3], as well as numerical physical device models [4]. The last milestone in this progress is the coupling of numerical physical models and circuit simulators which enables the co-design of circuits and devices [4], [5]. These advanced tools can only be effective with accurate physical models which allow the analysis of different structures without empirical adjustment parameters. Furthermore, these models must account for the limiting mechanisms at high frequency and high power operation. Besides, these simulators must be able to evaluate the impact of different geometries on the device performance. This is not possible using an 1-D simulator developed in the past [5].

We have developed a 2-D numerical simulator based on the drift-diffusion theory which incorporates the accurate physical model considered in the 1-D numerical simulator: impact-ionization, non-constant recombination velocity, self-consistent incorporation of the tunnelling and image-force effects. The geometrical aspects are included by the two-dimensional nature of the simulations. Figure 1 shows the different structures (half of the device exploiting axial or plane symmetry) which can be analysed with this simulator. It is also clear that it is possible to study planar diodes with the ohmic contact at the top of the device (ohmic contact identified with symbol (0), figure 1), and Whisker and quasi-vertical planar diodes with the ohmic contact at the rear (ohmic contact identified with symbol (1), figure 1).

This simulator was validated by comparison of simulated device characteristics with experimental results obtained

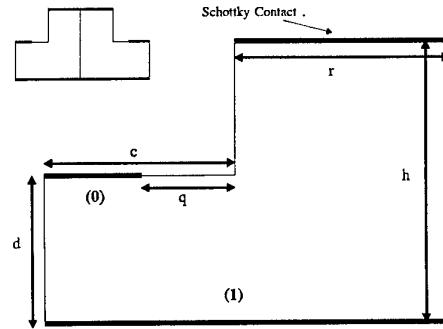


Fig. 1. Possible geometries in the 2D simulator. (i) identifies the position of the ohmic contacts.

for submm-wave Schottky diodes fabricated at the University of Darmstadt (TUD). After this initial step, we focused on the impact of different geometries on the device electrical characteristics and also on the study of some limiting physical processes at high frequencies like velocity saturation. The objective of this paper is to show that this simulator is an appropriate tool for both the study of physical properties of these devices and the design of real devices.

TABLE I
PARAMETERS FOR SCHOTTKY DIODES FROM TUD AND UVA.

Diode	Epitaxial Layer		$V_{bd,DC}$ (V)
	doping (cm^{-3})	length (μm)	
D1038	3×10^{17}	0.560	-8
UVa 6P4	3.5×10^{16}	1.0	-20
D1038	subs. doping: $2 \times 10^{18} cm^{-3}$ length: 80-100 μm		

II. GEOMETRICAL ASPECT OF THE DESIGN OF SCHOTTKY DIODES

Impact of the geometry on the series resistance R_s and the capacitance C of Schottky diodes can be directly studied with this simulator. These parameters are important because their optimization can improve the frequency performance of these devices, which is often measured by the cut-off frequency: $f_{co} = \frac{1}{2\pi R_s C_{j0}}$, where $C_{j0} = C(V_{bias} = 0)$.

Figure 2 shows the series resistance of a cylindrical Schottky diode, D1038, whose doping profile is described in table I. The ohmic contact is at the rear of the device and the radius of the Schottky contact is $r_{SC} = 5 \mu m$ ($\phi = 2 \cdot r_{SC}$ in figure 1) for different substrate lengths and radii of the ohmic contact ($r_{ohmic} = c + r_{SC}$ in figure 1). It

Jesús Grajal and Daniel Moreno are with the ETSIT, Universidad Politécnica Madrid, Ciudad Universitaria s/n, 28040 Madrid, Spain, email:jesus@gmr.ssr.upm.es

Viktor Krozer is with the Lehrstuhl für Hochfrequenztechnik, TU Chemnitz, Reichenhainerstr. 70, D-09126 Chemnitz, Germany, email: vkrozer@infotech.tu-chemnitz.de

is important to notice that the distribution of the current in the substrate changes depending on the relationship between h ($h \approx L_{\text{substrate}}$) and r_{ohmic} (figure 1), and this is the origin in variations of the series resistance. For short substrates the resistance does not depend on the radius of the ohmic contact. We have also concluded that the resistance does not depend on the size of ohmic contact, regardless the length of the substrate for $c \geq (3-4) \cdot r_{SC}$. Similar results apply for another Schottky diode with $r_{SC} = 2.5 \mu\text{m}$ as can be observed in figure 3.

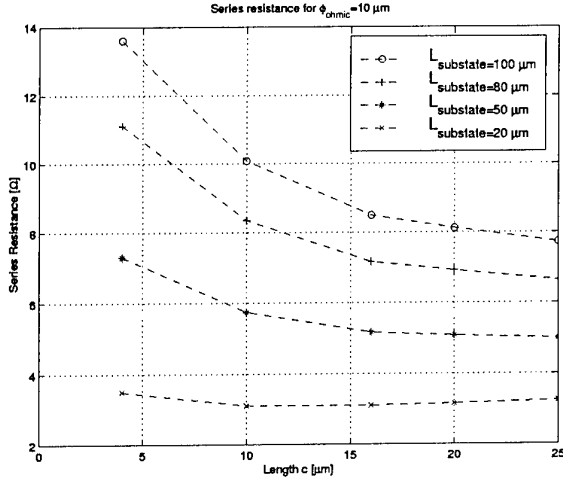


Fig. 2. Series resistance vs. radius for the ohmic contact for different substrate lengths. The ohmic contact is at the rear of the device and radius of the Schottky contact is $r_{SC} = \frac{\phi}{2} = 5 \mu\text{m}$.

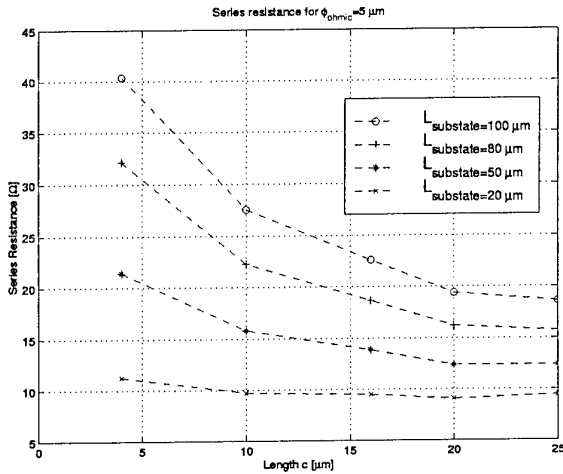


Fig. 3. Series resistance vs. radius for the ohmic contact for different substrate lengths. The ohmic contact is at the rear of the device and radius of the Schottky contact is $r_{SC} = \frac{\phi}{2} = 2.5 \mu\text{m}$.

A similar study has been performed for this device with the ohmic contact at the top for different substrate lengths and distances between the contacts: $c = 3 \mu\text{m}$, as can be seen figure 4. For this structure, the series resistance decreases for increasing substrate lengths because the area

for the current flux increases. The differences among the analysed structures are nearly negligible for distances between contacts less than $5 \mu\text{m}$.

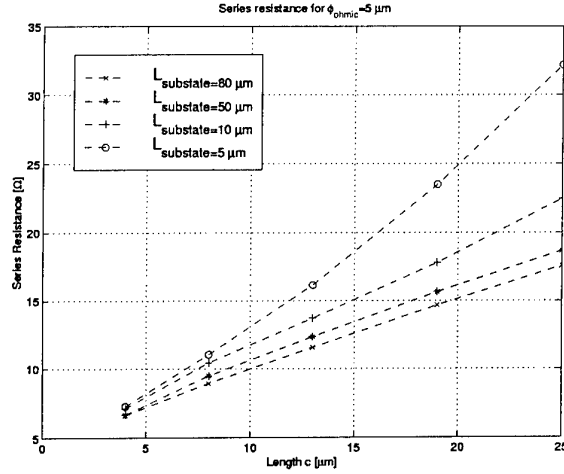


Fig. 4. Series resistance vs. distance between contacts ($c = 3 \mu\text{m}$, figure 1) for different substrate lengths. The ohmic contact is at the top of the device with radius $r_{\text{ohmic}} = 3 \mu\text{m}$. The radius of the Schottky contact is $r_{SC} = \frac{\phi}{2} = 2.5 \mu\text{m}$.

The capacitance of a small-area submillimeter-wave diode is strongly affected by the edge effects as has been pointed out by several researchers [6]. Figure 5 presents the correction factor γ_C for the capacitance due to edge effects [6] as a function of the radius of the anode for several doping densities in the epitaxial layer. It is clear that the edge effect only impacts on the characteristics of the device if the radius is small enough compared to the length of the epitaxial layer W_{epi} ($\frac{r_{SC}}{W_{\text{epi}}} < 3-4$), which is typical for submillimeter varactors. Of course, the influence of the edge effects also depends on the doping density of the diode as can be observed in figure 5.

The accurate calculation of the capacitance is fundamental for the design of varactors working as frequency multipliers, where the basic non-linearity for generating harmonics is the capacitance. Besides, the design of the device geometry in order to reduce the series resistance will impact dramatically on the efficiency of a multiplier.

III. HIGH FREQUENCY LIMITING MECHANISMS: VELOCITY SATURATION

Besides geometrical aspects, a numerical simulator is also a useful tool to gain physical insight into the diode operation. High frequency operation of Schottky diodes working as frequency multipliers or mixers is limited by the velocity saturation effect [1]. It has been outlined in [7] that the current saturation mechanism should not occur for well designed diodes at all operating frequencies. This can be achieved by choosing a sufficiently high doping density in the device $N_D \geq J_{\text{disp}}/qv_{\text{max}}$ with J_{disp} being the displacement current and v_{max} the maximum velocity of electrons in the epi-layer region outside the space charge region. Ho-

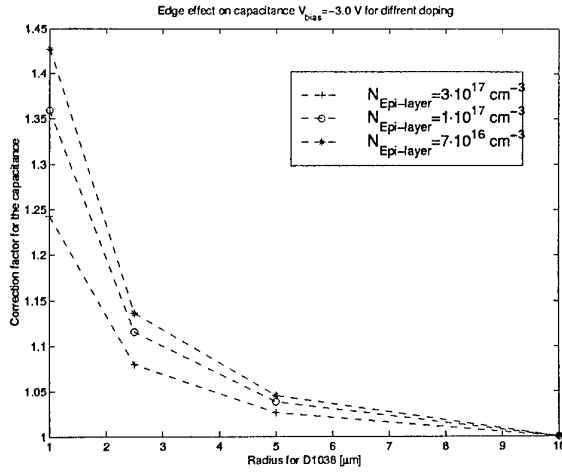


Fig. 5. Correction factor γ_c [6] for several anode radii and doping densities. Other parameters for this diode are from table I D1038. The ohmic contact is at the rear of the device with a radius of $r_{SC} + 4 \mu m$.

wever, this has an adverse effect on the breakdown voltage. The impact of saturation velocity on the performance of diode *UVa-6P4* from the University of Virginia, table I, has been demonstrated in [4] at a fundamental frequency of 100 GHz. This diode suffers from velocity saturation at this frequency because of its low doping concentration in the epi-layer.

This effect is also observed in highly doped devices at higher frequencies as illustrated in figure 6, where the edge of the depletion region can follow the voltage waveform at 100 GHz, but cannot follow the RF voltage waveform at 700 GHz. The diode contact is at right-hand side in figure 6. The diode is similar to *D1038* with $R_{SC} = 2.5 \mu m$, but with different epi-layer doping. This point can be better observed in figure 7 through contours of the space charge region edge for 100 GHz and 700 GHz. The velocity saturation effect produces a smaller modulation of the space-charge region during one period of the exciting signal, which in turn leads to a smaller capacitance modulation, with the corresponding decrease in the efficiency in frequency multipliers. Therefore, a maximum frequency for the pump signal can be defined at which velocity saturation effects become important. It is also interesting to point out that the modulation of the space charge region has hysteretic behaviour under high frequency pumping [8].

Figure 8 presents the maximum pump frequency versus doping concentration calculated with the analytical model presented in [7] and with the numerical model introduced here. The analytical model is based on simple equations for depletion layer depth, critical electric field, and the avalanche breakdown voltage (the voltage swing is selected such that it sweeps from the breakdown to forward conduction $V_{RF} = (V_D - V_{bd,DC})$). In the numerical model, the calculated maximum pump frequency is defined as the frequency where the amplitude of the calculated current is 25 % less than the extrapolated amplitude for lower frequencies. Gi-

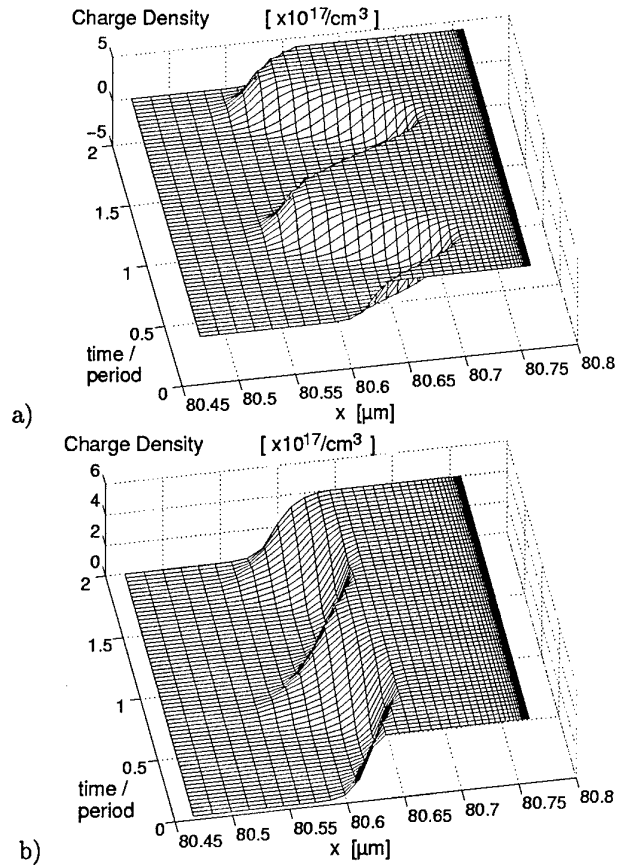


Fig. 6. Variation of the edge of the depletion region with applied RF voltage at a) signal frequency of 100 GHz, b) signal frequency of 700 GHz. The epi-layer doping is $N_{epi} = 4 \cdot 10^{17}/cm^3$, the epi-layer thickness is $t_{epi} = 560 nm$, and the substrate length is $80 \mu m$ (the Schottky contact is on the right-hand side).

ven a doping concentration of $N_{epi} = 2 \cdot 10^{17}/cm^3$ the maximum pump frequency without velocity saturation effects is found to be $f_c \leq 210 GHz$.

It is possible to increase the maximum pump frequency by decreasing the magnitude of the bias voltage. For a given doping concentration, the maximum pump frequency can be varied by changing the bias voltage and the RF voltage swing as can be demonstrated in figure 9 both for the analytical and numerical method. This implies that velocity saturation effects can be avoided by decreasing the bias voltage for a given doping concentration.

IV. CONCLUSIONS

Two-dimensional simulator is a helpful tool for the design and optimization of Schottky diodes both from the geometrical point of view and from physical considerations. The two-dimensional simulator allows to minimize parasitics like series resistance by a proper design of the geometry. Besides, a more accurate computation of the capacitance taking into account edge effects will result in a more accurate design of frequency multipliers.

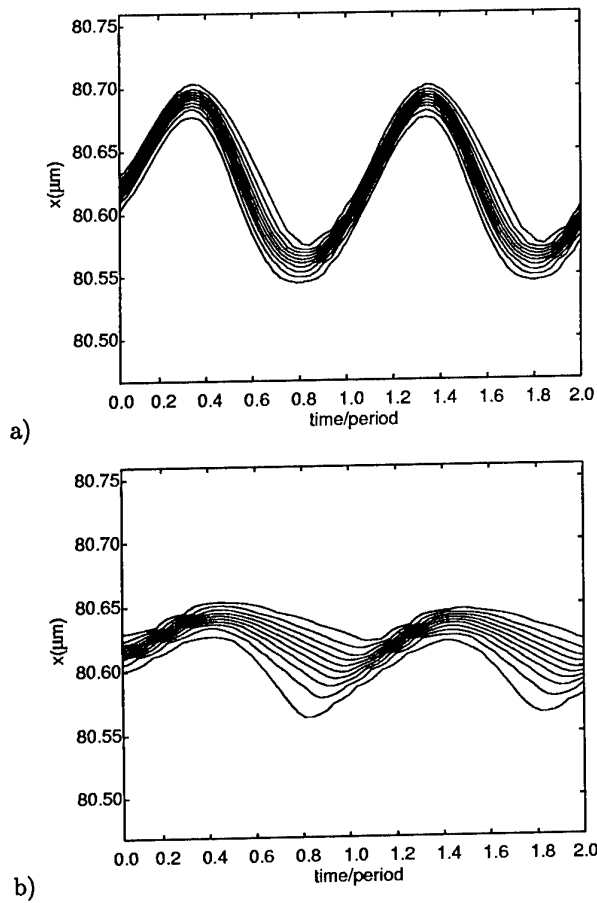


Fig. 7. Time waveforms of the depletion region edge corresponding to figure 6 a) signal frequency of 100 GHz, and b) signal frequency of 700 GHz.

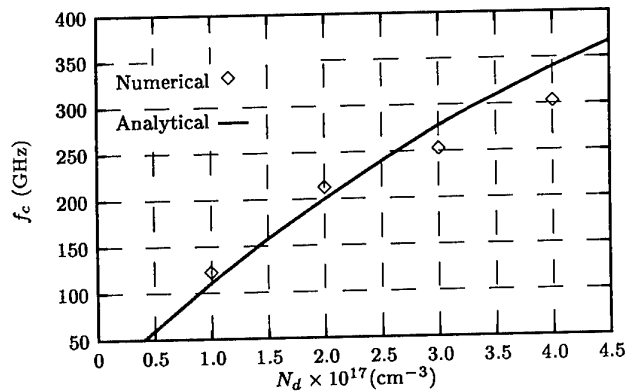


Fig. 8. Maximum pump frequency versus epi-layer doping concentration for optimum operation.

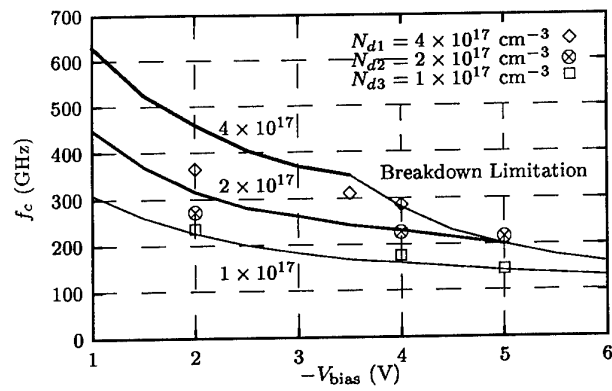


Fig. 9. Maximum pump frequency versus bias voltage V_{bias} for three different doping profiles. The RF swing is chosen as $V_{RF} = 2 \times (V_D - V_{bias})$. The continuous lines are analytical results from [7].

The limiting mechanisms for high frequency operation of Schottky diodes have been discussed. It has been demonstrated that saturation velocity effects could be omitted for well designed diodes at all operating conditions.

ACKNOWLEDGMENTS

This work was supported by Project TIC1999-1172-C02-01 of the National Board of Scientific and Technological Research (CICYT). Viktor Krozer is indepth for the financial support of the Ministerio de Educación y Cultura Madrid, Spain for financial support within the "Programa Nacional de Formación de Personal Investigador".

REFERENCES

- [1] E. L. Kollberg, T. J. Tolmunen, M. A. Frerking, and J. R. East. Current saturation in submillimeter wave varactors. *IEEE Trans. Microwave Theory and Techniques*, 40(5):831-838, May 1992.
- [2] A. Jelenski, A. Grüb, V. Krozer, and H.L. Hartnagel. New approach to the design and the fabrication of THz Schottky barrier diodes. *IEEE Trans. Microwave Theory and Techniques*, 41(4):549-557, April 1993.
- [3] J. T. Louhi and A. V. Räisänen. Optimization of the Schottky varactor for frequency multiplier applications at the submillimeter wavelengths. *IEEE Microwave and Guided Wave Letters*, 6(6):241-242, June 1996.
- [4] R. E Lipsey, S. H. Jones, J. R. Jones, T. W. Crowe, L. F. Horvath, U. V. Bhapkar, and R. J. Mattauch. Monte Carlo Harmonic-Balance and Drift-Diffusion Harmonic-Balance analyses of 100-600 GHz Schottky barrier varactor frequency multipliers. *IEEE Trans. Electron Devices*, 44(11):1843-1849, November 1997.
- [5] J. Grajal, V. Krozer, E. González, F. Maldonado, and J. Gismero. Modeling and design aspects of millimeter-wave and submillimeter-wave Schottky diode varactor frequency multipliers. *IEEE Microwave Theory and Techniques*, 48(4):700-711, 2000.
- [6] J. T. Louhi. The capacitance of a small circular Schottky diode for submillimeter wavelengths. *IEEE Microwave and Guided Wave Letters*, 4(4):107-108, April 1994.
- [7] C.I. Li, V. Krozer, J. Grajal, A. Simon, and H. L. Hartnagel. Schottky varactor diode optimization for frequency multipliers. In *5th Intern. Workshop on Terahertz Electronics*, Grenoble, France, 1997.
- [8] J. T. Louhi and A. V. Räisänen. Dynamic shape of the depletion layer of a submillimeter-wave schottky varactor. *IEEE Trans. Microwave Theory and Techniques*, 44(12):2159-2165, December 1996.

A novel evolutionary approach for the analysis and optimization of THz nonlinear circuits

M. Bozzi, M. Saglam, M. Rodriguez-Girones, L. Perregrini, H. L. Hartnagel

Abstract – This paper presents a novel approach for the analysis of the nonlinear circuits derived from the modeling of THz frequency multipliers. This method combines the rapidity of the Harmonic Balance technique with the reliability of the Genetic Algorithm. For this reason, it has been used within an fully automatic optimization procedure, which determines the maximum conversion efficiency attainable with a device for a given pump power level, as well as the optimal impedance needed at all the harmonic. As an example, we report the analysis and design of frequency triplers based on Heterostructure Barrier Varactors, and operating at 255 GHz.

I. INTRODUCTION

The design of frequency multipliers operating in the mm-wave region requires circuit simulators: they are codes able to analyze lumped-element nonlinear circuits, derived from the electromagnetic analysis of frequency multipliers (see Fig. 1) [1].

Many analyses are required in the design process of a frequency multiplier, in order to determine the most suitable device and the optimal embedding impedance Z_L , for given operating frequency and pump power level. Since a large number of analyses is required, such nonlinear simulators should be fast and reliable. The reliability is mandatory if the design is based on automatic optimization procedures, where no human intervention is possible.

Many methods have been proposed for the analysis of nonlinear circuits [2,3]: most of them are based on the Harmonic Balance (HB) technique [4–6]. Even if they are typically fast, their use requires the tuning of a number of parameters for each specific nonlinear device. Therefore, these simulators can hardly be used in a completely automatic optimization tool.

Recently, a genetic approach to the analysis of nonlinear circuits has been proposed [7]: the application of the genetic algorithm (GA) leads to circuit simulators very stable and not device-dependent, but usually quite slow.

A novel method for the analysis of nonlinear circuits, derived from the modeling of THz frequency multipliers, was recently proposed [8]. It is based on a hybrid approach, which combines the standard HB technique with the GA. This method takes advantage from both the reliability of the evolutionary approach and the rapidity of the HB technique.

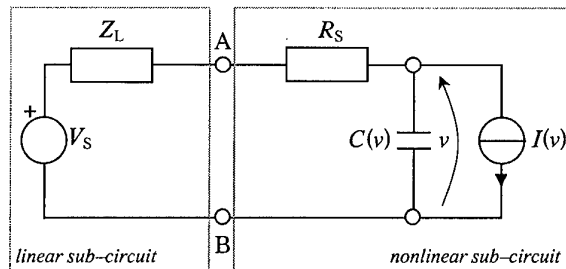


Fig. 1: Lumped element equivalent circuit of a frequency multiplier operating in the mm-wave range.

This method has been applied to the analysis and design of frequency triplers, operating at 255 GHz. Such triplers are based on Heterostructure Barrier Varactors (HBVs), fabricated and measured at the Technical University of Darmstadt. The optimization process of the multiplier and the optimal performance are discussed in this paper.

II. STANDARD HARMONIC BALANCE ANALYSIS

The HB technique is a well-established iterative method for the analysis of nonlinear circuits operating in the mm-wave range [2–6]. This technique is based on the splitting of the circuit into two parts, one containing the nonlinear elements and the other only linear components, modeled by a Thevenin equivalent circuit (Fig. 2). The analysis of the linear sub-circuit is performed in the spectral domain, whereas a time-domain analysis is applied to the nonlinear sub-circuit.

The aim of this analysis is the calculation of the voltage V_N across the terminals of the nonlinear device and of the current I_N flowing through the same device (Fig. 2). The source voltage V_S at the fundamental frequency ω_0 and the linear impedance Z_L are known, as well as the characteristics of the nonlinear device.

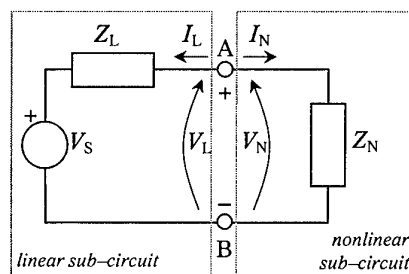


Fig. 2: Nonlinear circuit considered in the Harmonic Balance analysis. Z_N represents the impedance of the nonlinear sub-circuit.

Maurizio Bozzi and Luca Perregrini are with the Department of Electronics, University of Pavia, V. Ferrata 1, 27100 Pavia (Italy) (e-mail: m.bozzi@ele.unipv.it).

Mustafa Saglam, Manuel Rodriguez-Girones and Hans Ludwig Hartnagel are with the Institut für Hochfrequenztechnik, Merckstr. 25, 64283 Darmstadt (Germany).

In the HB analysis, a set of tentative voltages $V_N = (v_{N,1}, \dots, v_{N,P})$ at P harmonic frequencies (at $\omega_0, 2\omega_0, \dots, P\omega_0$) is arbitrarily chosen and applied to the terminals A–B of the nonlinear sub-circuit. By using a time-domain analysis and the Fourier transform, the set of currents $I_N = (i_{N,1}, \dots, i_{N,P})$ entering the nonlinear sub-circuit is determined. The same current set (apart from the sign) $I_L = -I_N$ is applied to the linear sub-circuit, and the set of voltages $V_L = (v_{L,1}, \dots, v_{L,P})$ is determined. This set of voltages V_L is compared with the tentative voltage V_N , and an error ε is calculated as the Euclidean distance between V_L and V_N

$$\varepsilon = \frac{|V_N - V_L|}{|V_N|}$$

If the error ε is larger than a prescribed value ε_{MAX} , the iteration proceeds with the estimation of a new V_N , which is obtained as a weighted summation of V_L and the old V_N .

$$V_N^{new} = p V_N + (1-p) V_L$$

This weight p , called “convergence parameter,” determines the convergence rate and must be properly chosen.

The HB technique typically permits to obtain a rapidly converging algorithm, but presents some drawbacks: an initial guess of the voltage V_N is required, and the criterion for the choice of the convergence parameter p is not easy. Moreover, the optimal convergence parameter is typically device-dependent and the convergence often depends on the initial guess.

These drawbacks reduce the effectiveness of this method, especially when the analysis code is embedded in an automatic routine for the optimization of nonlinear circuits. In this case, the aim of the design is the determination of the most suitable nonlinear device, for given operation frequency and pump power level. Therefore, different devices are considered, with different embedding impedance Z_L . Since no human intervention is possible, the analysis code must be reliable, so that the solution is found in any operation condition.

III. NOVEL GENETIC ALGORITHM/ HARMONIC BALANCE TECHNIQUE

To overcome these drawbacks, a novel algorithm was recently proposed [8]: it is based on the combination of the GA [9] with a standard HB technique [4]. The structure of our method is sketched in the block diagram of Fig. 3.

As a first step, we apply the GA: an initial population of C chromosomes [9] is generated. The chromosomes are coded as strings of real genes, each of them containing the real part or the imaginary part of the voltages V_N at all the harmonics of interest ω_p , $p = 1, \dots, P$. The number C of chromosomes is related to the number P of harmonics considered in the simulations: as a rule of thumb, we used $C = 20 \div 30 P$. The initial value contained in the genes is randomly generated, typically in the range $\pm 3V_S$.

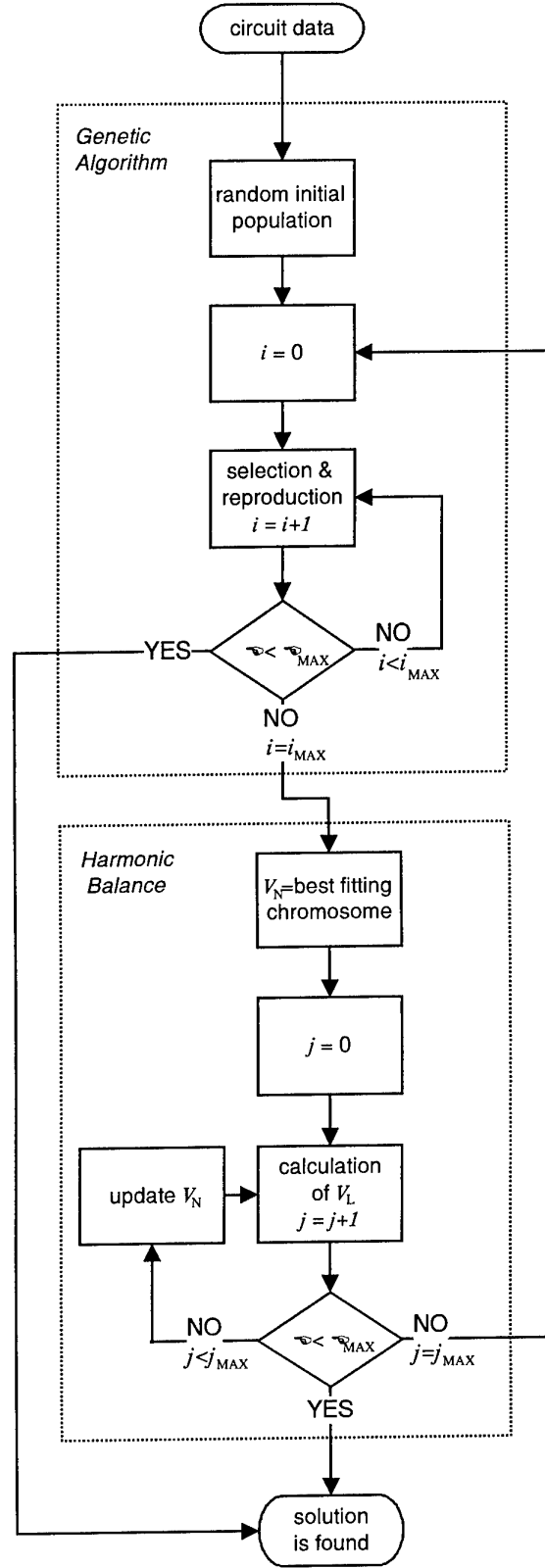


Fig. 3: Block diagram of the combined Genetic Algorithm/Harmonic Balance technique: the algorithm repeatedly switches between GA and HB, until the convergence is reached.

New generations of the population are then created: the survivors are the best fitting chromosomes, selected through a binary tournament, while the new chromosomes are obtained by applying both crossover and mutation [9]. The "fitness" of a chromosome depends on the Euclidean distance ϵ between the voltage V_N (represented by the chromosome) and the voltage V_L , determined in the same way as previously described for the HB technique. Of course, the lower is the value of ϵ , the better the fitness of the chromosome.

The algorithm stops and the solution is found if a chromosome of the current population satisfies the requirement in fitness ($\epsilon < \epsilon_{MAX}$); otherwise, a new population is generated.

If the GA does not find the solution in a fixed number i_{MAX} of generations (say $i_{MAX}=500 \div 1000$), the code switches to the HB technique. The best fitting chromosome is taken as the initial guess V_N for the HB technique. Since the values of the best chromosome are taken as initial guess, this typically represents a reasonably good choice; moreover, the user is not required of providing any information.

If the HB fails to converge after a fixed number j_{MAX} of iterations (say $j_{MAX}=100 \div 200$), the algorithm switches again to GA and proceeds for additional generations. This procedure continues, repeatedly switching between GA and HB, until the convergence is reached.

IV. OPTIMIZATION OF A 255 GHz HBV FREQUENCY TRIPLER

The analysis method presented above was applied to the optimization of a frequency tripler operating at 255 GHz based on Heterostructure Barrier Varactors (HBVs).

HBV diode is a suitable device for direct tripling since the C-V characteristic is evenly symmetric and I-V characteristic is anti-symmetric, so that only odd harmonics are generated [10]. Therefore, one of the applications where HBV diodes show a great potential is quasi-optical tripler arrays [11]: in fact, these varactor devices require less design complexity compared to Schottky diode tripler circuits since no DC bias circuitry and no idler circuit at second harmonic is required.

$Al_{0.7}Ga_{0.3}As/GaAs$ HBV structures were grown with Molecular Beam Epitaxy on SI GaAs substrate at the University of Darmstadt [12]. HBVs with diameters of 10, 20 and 40 μm were fabricated in the form of two columns with a total of four barriers. The measured C-V and I-V characteristics of the HBVs are shown in Fig. 4.

The design of the frequency tripler requires the choice of the most suitable device among the available ones, and the determination of the optimal embedding impedance, which depends on the pump power available at the fundamental frequency.

In the analyses of the HBVs, the maximum conversion efficiency of the devices was calculated, with the pump power ranging from 1 to 30 mW. For each pump power level, the optimal embedding impedance Z_L was determined.

As an example of the GA/HB technique, the analysis of the HBV with 10 μm diameter, with 20 mW pump power, is reported: Fig. 5 shows the error ϵ vs. the number of

iterations: after 1000 GA iterations, the HB analysis was inserted and reached the convergence in 104 additional steps.

From the optimization process resulted that the most suitable device in the considered pump power range was the HBV with 10 μm diameter, which achieved a conversion efficiency better than 4% and an output power larger than 1.2 mW (Fig. 6). The optimal embedding impedance at the fundamental frequency (85 GHz) and at the output harmonic (255 GHz) is reported in Fig. 7.

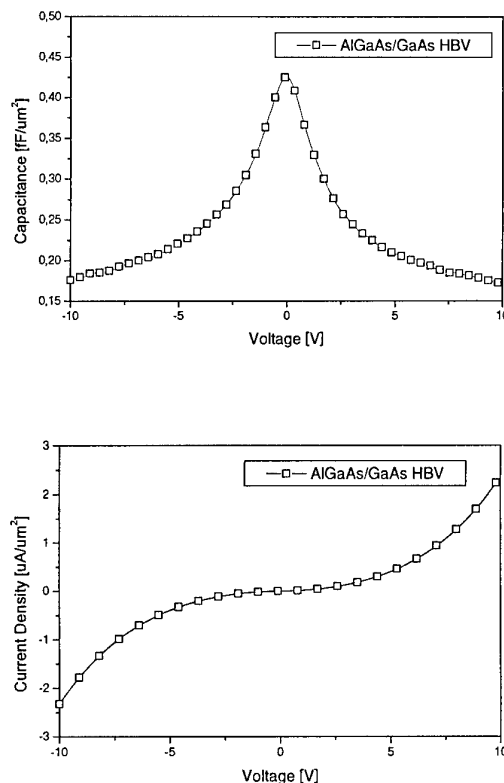


Fig. 4: Measured C-V and I-V characteristics of the $Al_{0.7}Ga_{0.3}As/GaAs$ HBVs.

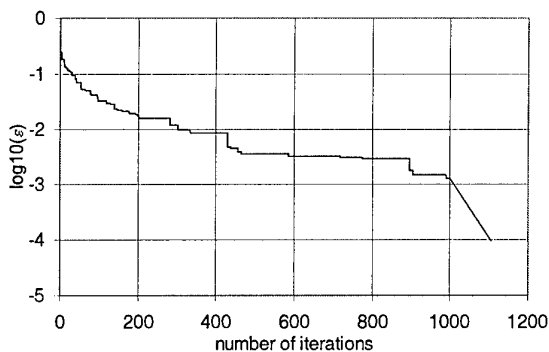


Fig. 5: Variation of the residual error ϵ vs the number of iteration in the GA/HB analysis of the 10 μm HBV. The convergence limit is fixed at $\epsilon_{MAX}=10^{-4}$. The convergence is obtained in 1000 GA iterations and 104 HB additional steps.

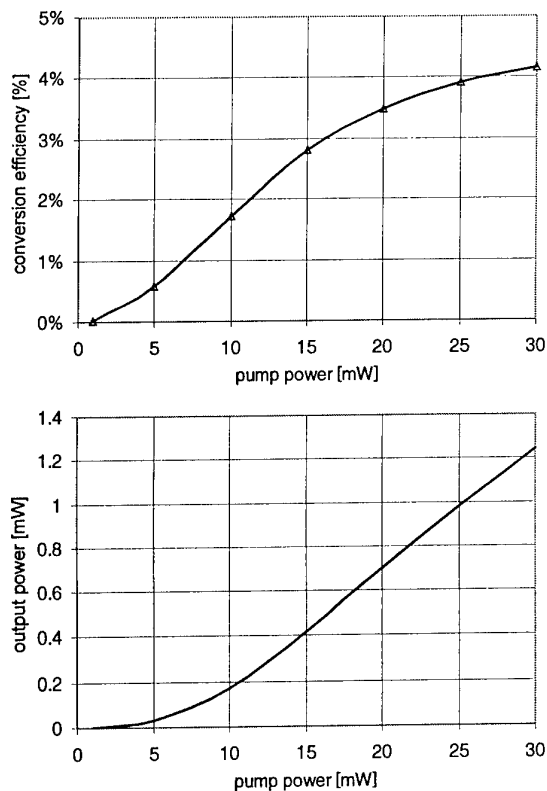


Fig. 6: Maximum conversion efficiency and output power at 255 GHz of the HBV versus the pump power level at the fundamental frequency (85 GHz).

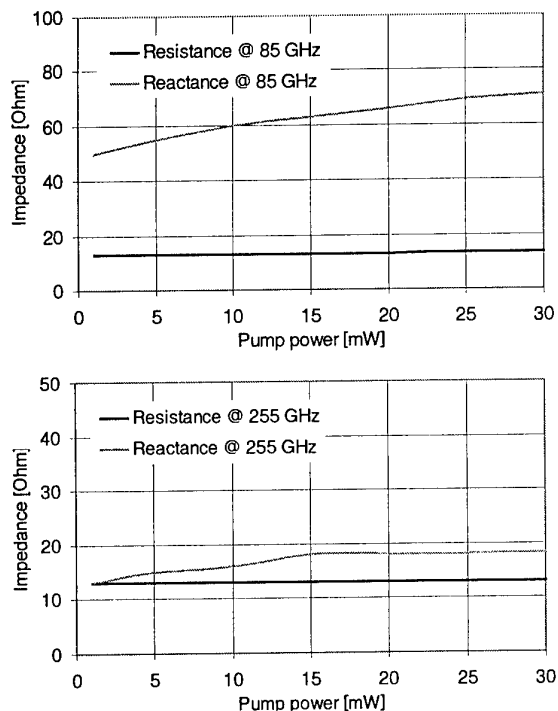


Fig. 7: Optimal embedding impedance of the 10 μm HBV vs the pump power level, at 85 GHz (fundamental frequency) and 255 GHz (output frequency)

V. CONCLUSION

We presented a novel approach for the analysis and optimization of the nonlinear circuits operating as frequency multipliers in the THz region. The method, which is an hybrid between the Harmonic Balance technique and the Genetic Algorithm, is very reliable, reasonably fast and does not require any human intervention. It was applied to the analysis and design of 255 GHz frequency triplers based on HBVs with diameters ranging from 10 to 40 μm . The results showed that the HBV with the smaller diameter exhibits good conversion performance in the considered pump power range (up to 30 mW). Conversely, HBVs with larger diameters are not suitable for operation with limited pump power level.

Acknowledgement

The authors would like to thank Ana Ruiz Laso for her contribution in the implementation of the GA/HB code. Work supported by the European Commission under the TMR Programme contract n. ERBFMRXCT960050.

References

1. P. Arcioni, M. Bozzi, G. Conciauro, and L. Perregrini, "Design and Optimization of Quasi-Optical Frequency Multipliers," *Intern. Journal of Infrared and Millimeter Waves*, Vol. 20, pp. 913-928, 1999.
2. S. A. Maas, *Nonlinear Microwave Circuits*, IEEE Press, 1997.
3. V. Rizzoli and A. Neri, "State of the Art and Present Trends in Nonlinear Microwave CAD Techniques," *IEEE Transactions on Microwave Theory & Techniques*, Vol. 36, pp. 343-365, 1988.
4. R. G. Hicks and P. J. Khan, "Numerical Analysis of Nonlinear Solid-State Device Excitation in Microwave Circuits," *IEEE Transactions on Microwave Theory & Techniques*, Vol. MTT-30, pp. 251-259, 1982.
5. G. B. Tait, "Efficient solution method for unified nonlinear microwave circuit and numerical solid-state device simulation," *IEEE Microwave Guided Wave Letters*, Vol. 4, pp. 420-422, 1994.
6. J. Grajal de la Fuente *et al.*, "Modeling and design aspects of millimeter-wave Schottky varactor frequency multipliers," *IEEE Microwave & Guided Wave Letters*, Vol. 8, pp. 387-389, 1998.
7. S. Iezekiel and A. Feresidis, "Application of genetic algorithm to sample balance analysis of nonlinear circuits," *IEE Electronics Letters*, Vol. 34, pp. 2080-2082, 1998.
8. M. Bozzi, L. Perregrini, and A. R. Ruiz Laso, "Analysis of mm-wave Nonlinear Circuits by Combining Genetic Algorithm and Harmonic Balance Technique," *Digest of the International Microwave Symposium (IMS2000)*, Boston, MA, USA, 2000.
9. D. E. Goldberg, *Genetic algorithm in search, optimization and machine learning*, Addison-Wesley Publishing Company, 1989.
10. E. L. Kollberg and A. Rydberg, "Quantum-barrier-varactor diode for high efficiency millimeter-wave multipliers," *IEE Electron. Letters*, Vol. 25, pp. 1696-1697, 1989.
11. S. Hollung *et al.*, "A 141-GHz Quasi-optical HBV Diode Frequency Tripler," *IEEE AP-S Int. Symposium and USNC/URSI National Radio Science Meeting*, Orlando, 1999.
12. M. Saglam, M. Bozzi, C. Domoto, M. Rodriguez-Girones, L. Perregrini, and H. L. Hartnagel, "AlGaAs HBV Performance in Frequency Tripling at 255 GHz," *Proc. of the European Gallium Arsenide And Other Semiconductors Application Symposium (GAAS 2000)*, Paris, France, October 02-03, 2000.

Cryogenic operation of GaAs based multiplier chains to 400 GHz

A. Maestrini, D. Pukala, F. Maiwald, E. Schlecht, G. Chattopadhyay, and I. Mehdi

Caltech – Jet Propulsion Laboratory

MS 168-314

4800 Oak Grove dr.

Pasadena, CA 91109

818-354-5892 - maestrin@merlin.jpl.nasa.gov

Abstract – The FIRST/HIFI mission allows for the local oscillator frequency multiplier chains to be cooled to 120-150 K in order to increase available output power. This paper will discuss the implication of cooling on GaAs based planar Schottky diode varactors for flight applications. A robust testbed that has been built to measure output power over a wide range of frequencies will be described. Preliminary measurements at cryogenic temperatures done on individual multipliers at 200 GHz along with multiplier chains to 400 GHz will be presented. In a 182-212 GHz designed balanced doubler the peak efficiency at 201 GHz improves from 17% to 30% upon cooling from 300 K to 50 K. When this stage is used to pump a 362-424 GHz designed balanced doubler the efficiency of the two-stage chain increases from less than 0.8% to 3%. This represents an increase in efficiency of 6 dB.

I. INTRODUCTION

GaAs based planar Schottky diode varactor frequency multipliers are being developed at the Jet propulsion Laboratory for the Heterodyne Instrument of the far Infrared and Submillimeter Space Telescope (FIRST-HIFI). The planned FIRST mission will be the only space facility covering the largely unexplored but scientifically significant spectrum from 80 μm to 670 μm [1]. The multiplier technology that is being developed for this mission has been outlined previously [2,3]. A better understanding of multiplier circuits coupled with recent advances in the fabrication of the circuits and planar devices has resulted in tremendous progress towards building planar Schottky diode varactors. Planar Schottky diode multipliers have now been demonstrated up to 400 GHz with excellent performance [4,5,6]. A number of advantages of utilizing planar diode technology for space applications have been described [7]. One advantage that is perhaps not so apparent is the ability of well-designed planar technology to withstand cooling and thermal cycling. In principal whisker contacted circuits can be cooled but the inherently mechanically sensitive approach to the building of whisker contacted circuits does not readily lend itself to thermal cycling.

It has been established that cooling of multiplier circuits can have considerable influence on the output power and efficiency of GaAs multipliers [8,9]. However, what has not been fully explored is the intricate tradeoff between the various diode parameters when one is designing for low-temperature high input-power applications. Only minor temperature dependence is expected in the circuit

losses and embedding impedances. However, the electron mobility in GaAs is strongly temperature dependent. There is a peak in the electron mobility near 100 K for an epitaxial doping of $1.10^{17} \text{ cm}^{-3}$ [10]. Because series resistance is inversely proportional to electron mobility, an increase in multiplier efficiency is expected at cryogenic temperatures. However, a better understanding of electron transport in doped GaAs as a function of temperature is required to take full advantage of the cooling. Moreover, in high input power applications the anode area is substantially hotter than the ambient temperature and accurate thermal models of the chips are required to optimize the anode characteristics for a given frequency, input power and temperature. Work is still under way to obtain a realistic diode model that includes all of these effects and will be reported in the future. This paper will present measured power and efficiency data for a high input-power 200 GHz multiplier circuit. Cryogenic data on a 400 GHz multiplier chain will be also presented. Finally, a robust setup that utilizes a quasi-optical approach for the measurement of output power has been designed and tested to 400 GHz and will be described.

II. DESCRIPTION OF THE TEST SETUP

The test setup consists of an 87-108 GHz continuously tunable source, a cryostat in which the multipliers under test are installed and a Thomas Keating power meter as shown in Figure 1. The source is composed of a 75-115 GHz BWO followed by an 87-108 GHz power amplifier chain that can deliver up to 280 mW at 92 GHz [11]. Power is adjusted by an attenuator and/or a ferrite modulator that also isolates the BWO from the amplifier chain. Frequency is monitored by a microwave counter via a harmonic mixer. A cross-waveguide coupler and a low-offset, low drift power meter are used to monitor the power delivered by the source.

A low loss wide-band isolator is located inside the cryostat, between the coupler and the multiplier chain, to avoid any load pulling effects that can affect the accuracy of the monitoring of the input power. The temperature of the multipliers is adjustable to within $\pm 1 \text{ K}$ in the 35-325 K range using a controller, two temperature sensors, a 25 W resistor and a bracket that mechanically connects the chain to the 15 K cold plate of the cryostat. The vacuum window on the output side is made of a one-mil thick by two-inch diameter Mylar shield. IR radiation going through the window is partly blocked by two 25 μm -thick layers of Zitex 135 material.

We measured the power produced by the multiplier chain with a Thomas Keating power meter. A single 25 μm -thick layer of Zitex 135 material is used to protect the membrane of the Thomas Keating sensor from air-borne acoustic vibration, as well as visible and IR radiation. In addition, the Thomas Keating sensor is installed on an anti-vibration-plate with a 0.16 Hz cut-off frequency to eliminate the low frequency vibration produced by the cryogenic generator, the BWO, the chopper and the vacuum pumps. The RF output beam is focused on the membrane of the Thomas Keating sensor by an oversized elliptical mirror that reduces the sensitivity to the optical misalignments. The beam is chopped by a two-blade wheel by ten-inch diameter wheel operating at 20 ± 0.2 Hz. The modulated signal detected by the Thomas Keating sensor is pre-amplified and filtered by a high-rejection, 10-30 Hz band-pass filter. The signal is finally measured by both a high-performance dual-channel digital lock-in amplifier and by the data acquisition card of the Thomas Keating power meter.

We found that the combination of the band-pass filter and the dual-channel lock-in amplifier greatly improves the sensitivity of the Thomas Keating power meter. $10 \mu\text{W}$ could be confidently detected with a measurement noise of $\pm 1 \mu\text{W}$, whereas the standard configuration results in a $\pm 10 \mu\text{W}$ noise floor.

Calibration procedure: A power meter that does not need to be calibrated monitors the input power. A second power meter, calibrated carefully by the manufacturer, is connected to the last waveguide bend before the multiplier chain, inside the cryostat. Recording at different frequencies the ratio between these two power levels defines a calibration chart. The output power is calibrated automatically by the Thomas Keating control program. RF losses produced by the IR filters and the Mylar film were measured around 200 GHz and 400 GHz. We found a total absorption of less than 7% at 375 GHz. The preliminary data reported in this paper does not correct for these losses. Broadband measurements of these losses are planned and will be used to improve the accuracy of the calibration.

Measurements at cryogenic temperatures: Only modulated signals are taken into account by the Thomas Keating power meter. Therefore, in order to modulate the RF signal produced by the frequency multiplier chain, we decided to use a two-blade chopper wheel. This wheel is located outside the cryostat at room temperature. When the RF beam is cut, the Thomas Keating sensor receives only the IR radiation of the blades that can be considered as a black body at 300 K. When the RF beam is not cut, the Thomas Keating sensor receives the RF signal as well as part of the IR radiation emitted by the metallic components located inside the cryostat. This is because the IR radiation is only partially absorbed by the IR filters at the output window of the cryostat. When operating at cryogenic temperature, this IR radiation is more or less the emission of a cold black body. As the Thomas Keating sensor is very broadband, it detects a modulated IR signal in addition to the

modulated RF signal produced by the frequency multipliers. This IR signal is 180° out of phase with the RF signal and, therefore, it is subtractive.

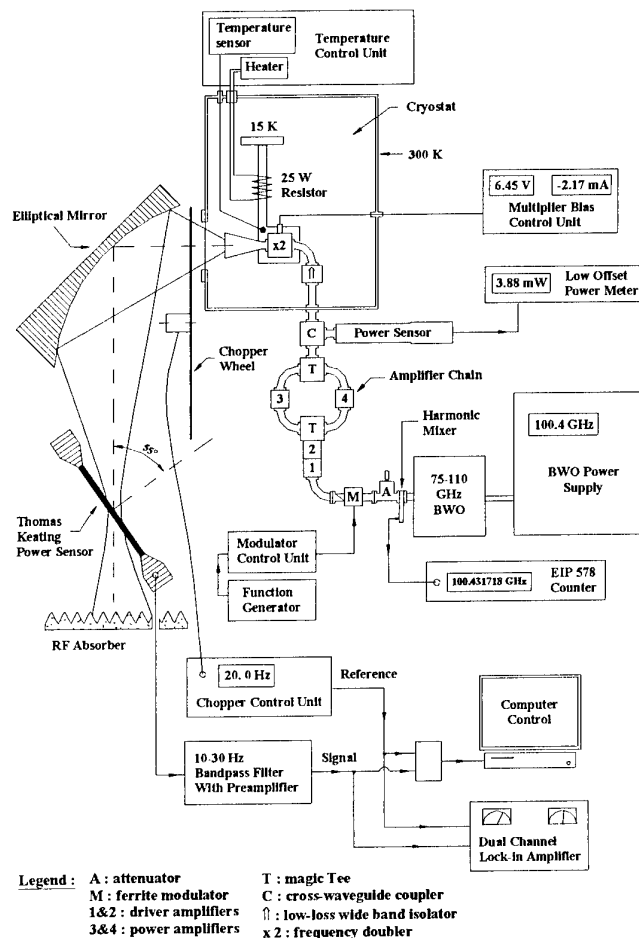


Fig. 1: LO chain power measurement test setup.

In the configuration shown in Figure 1, at around 100 K, this IR radiation has a signal strength of about $150 \mu\text{W}$. Consequently, at low RF power levels it can have a significant effect on the measurement. Accurate measurement of this IR signal must be taken and the data must be systematically corrected. One possible solution is to use a better IR filter but this might produce additional RF losses and standing waves. Another solution is to modulate the input power of the multiplier chain. The chopper wheel is removed and the modulation of the IR radiation is eliminated. The validity of this approach was ascertained by making a number of pulsed measurements with the amplifiers and the multipliers. We found that the amplifiers give slightly more power (+4% maximum) when driven with a 50% duty ratio square wave than when driven in CW. This increase of power is taken into account since the input power is monitored with a coupler and a power meter. The measurements show also that the frequency multiplier diodes reach their thermal equilibrium in less than $100 \mu\text{s}$. Hence, modulating the

input power of the doubler at 20 Hz does not produce any change in the behavior of the multiplier chain.

III. RESULTS AND DISCUSSION

The 184-212 GHz balanced planar doubler has been described in more detail in [12,13]. It is a 6-anode array with each anode being $1.5 \times 14 \mu\text{m}$. The doping in this chip was $1.10^{17} \text{ cm}^{-3}$. The performance of this doubler as a function of temperature and output frequency is shown in Figure 2. Significant improvement in the efficiency of the multiplier is obtained by cooling from 300 K to 50 K. However, it can be noted that the basic shape of the efficiency curve remains consistent. The measured output power at 201 GHz was 32 mW and 44 mW respectively at 300 K and 50 K. It is interesting to note that the efficiency for all frequencies is still improving at 50 K even though the theoretical mobility versus temperature data for GaAs indicates a peak around 100 K. This can be explained by the fact that the anode area is much hotter than the ambient temperature and thus the efficiency is still improving.

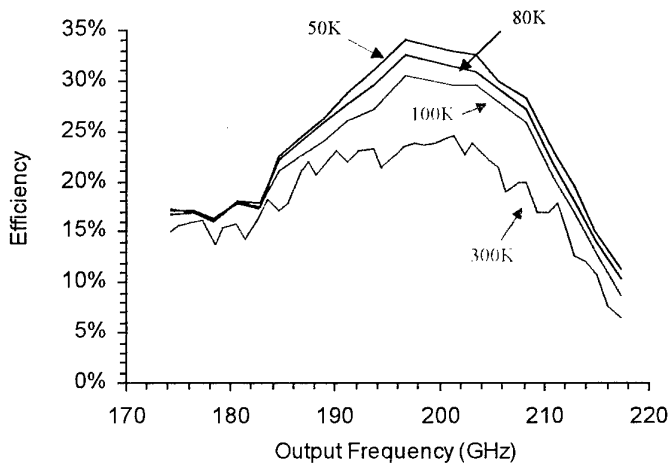


Fig. 2: Multiplication efficiency of a planar diode doubler as a function of output frequency for different block temperatures.

Figure 3 shows the performance of this multiplier as a function of input power. Though this multiplier was designed for high input power, the saturation occurs around 50-75 mW of total input power. However, upon cooling no significant change in the saturation is observed.

The 368-424 GHz balanced planar doubler has been described in some detail in [5]. This is a 4-anode array with each anode $1.5 \times 5.4 \mu\text{m}$. The doping used for this chip is $2.10^{17} \text{ cm}^{-3}$. This doubler utilizes a novel technology that greatly simplifies the assembly and design of multiplier stages. Cryogenic measurements done on the cascaded multiplier stages are shown in Figures 4 and 5. No isolator was used between the two-multiplier stages. The performance of the chain as a

function of input power to the first stage multiplier is shown in Figure 4 for the case of 382 GHz. It is interesting to note the strong dependence of the output power on the input power

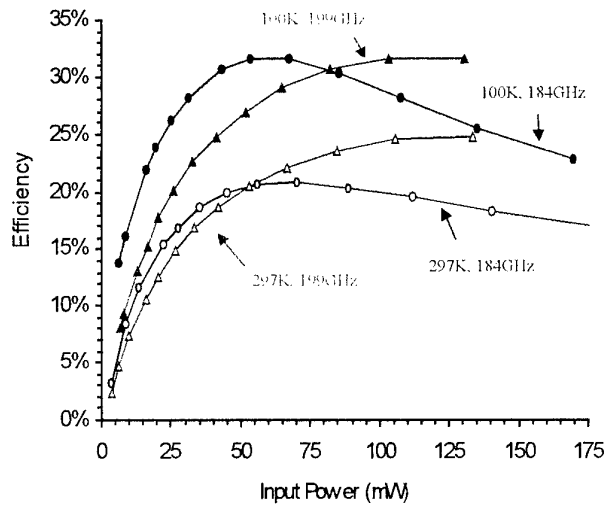


Fig. 3: Conversion efficiency of a planar diode doubler versus input power at different frequencies & different temperatures

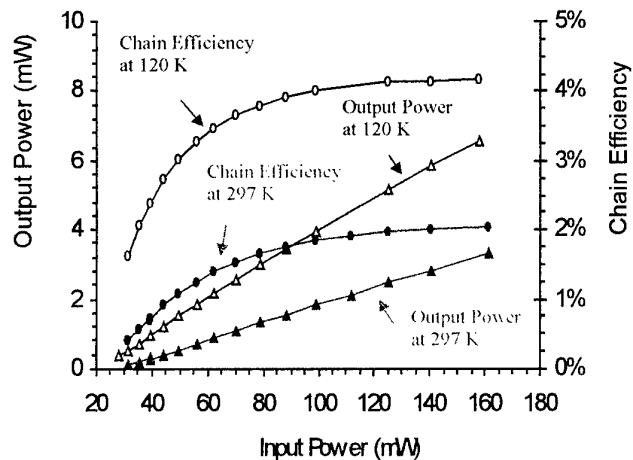


Fig. 4: Output power and chain efficiency at 382 GHz versus input power at 120K & 297K.

Figure 5 shows the output power and efficiency of the chain as a function of block temperature for two different frequencies. An improvement of 3 dB at 382 GHz and an improvement of 6 dB at 402 GHz is achieved in the efficiency of the chain, when cooling from 300 K to 50 K. It should be pointed out that at room temperature the first stage multiplier is under-pumping the second stage multiplier. Thus, cooling the multiplier chain improves significantly its performances since the first stage

multiplier is putting out more power and the second stage is getting more efficient with increased input power.

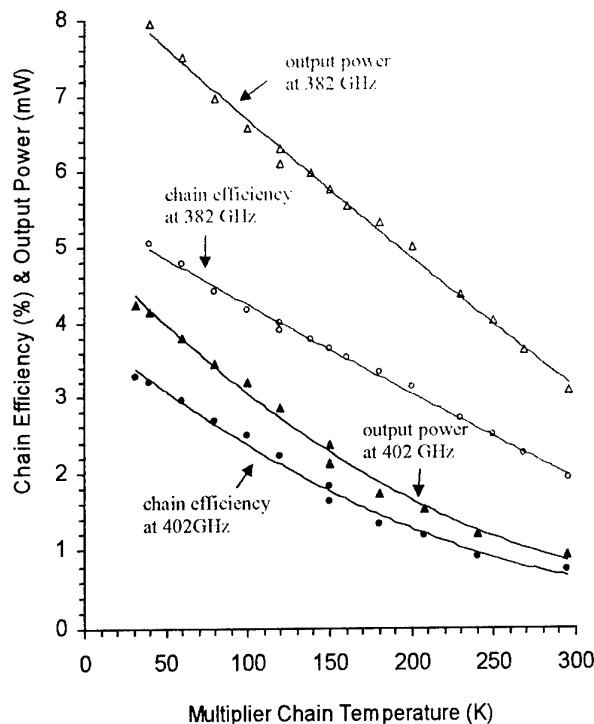


Fig. 5: Output power and chain efficiency at 382GHz & 402GHz versus temperature.

IV. CONCLUSION

A robust cryostat testbed that allows accurate calibrated measurements of power and frequency for a considerable frequency range has been described. Results presented have shown that the multiplier efficiency continues to improve beyond 100 K due to the possible heating of the anode chip in high input-power multipliers. A fix tuned multiplier chain to 400 GHz (x2x2) cooled to 50 K shows an improvement of over 3 dB.

Acknowledgements:

Technical support from L. Samoska, T. Gaier, S. Martin, B. Nakamura, and A. Fung are greatly appreciated. Technical discussions with J. Bruston, A. Skalar, P. Siegel, N. Erickson and P. Zimmermann are also acknowledged. The research described in this publication was carried out at the Jet Propulsion Laboratory, California Institute of Technology, under a contract with the National Aeronautics and Space Administration.

References:

1. G. Pilbratt, "The FIRST mission," *Proc. ESA Symp., The Far Infrared and Submillimetre Universe 1997*, ESA SP-401.

2. N. R. Erickson, R. P. Smith, S. C. Martin, B. Nakamura, and I. Mehdi, "High Efficiency MMIC Frequency Triplers for Millimeter and Submillimeter Wavelengths," *IEEE MTT Symposium*, Boston, June 2000.
3. N.R. Erickson, "Diode Frequency Multipliers for Terahertz Local Oscillator Applications," *Proc. SPIE*, vol. 3357, pp. 75-84, *Advanced Technology MMW, Radio, and Terahertz Telescopes*, T.G. Phillips, Ed., July 1998.
4. J. Bruston, E. Schlecht, A. Maestrini, F. Maiwald, S.C. Martin, R.P. Smith[†], I. Mehdi, P.H. Siegel, and J. Pearson "Development of 200 GHz to 2.7 THz Multiplier Chains for Submillimeter-wave Heterodyne Receivers," *Proc. SPIE UV, Optical, and IR Space Telescopes and Instruments*, SPIE 4013, Munich, Germany, March 2000.
5. E. Schlecht, J. Bruston, A. Maestrini, S. Martin, D. Pukala, R. Tsang, A. Fung, R. P. Smith[†], I. Mehdi, "200 and 400 GHz Schottky Diode Multipliers Fabricated with Integrated Air-Dielectric 'Substrateless' Circuitry", *11th International Symposium on Space Terahertz Technology*, Ann Arbor, Michigan, May1-3, 2000.
6. Peter Zimmermann, RPGmbH, *personal communication*.
7. P.H. Siegel, R.P. Smith, S. Martin and M. Gaidis, "2.5 THz GaAs Monolithic Membrane-Diode Mixer", *IEEE Trans. Microwave Theory and Tech.*, v. 47, no. 5, May 1999, pp. 596-604.
8. J. T. Louhi, A. V. Raisanen, and N. R. Erickson, "Cooled Schottky Varactor Frequency Multipliers at Submillimeter Wavelengths," *IEEE Trans. MTT*, vol. 41, pp. 565-571, 1993.
9. D. Porterfield, "Millimeter-Wave Planar Varactor Frequency Doublers," Ph.D. thesis at the University of Virginia, August 1998.
10. J. Ruch and W. Fawcett, "Temperature Dependence of the Transport Properties of Gallium Arsenide Determined by a Monte Carlo Method," *J. Applied Phys.*, vol. 41, no. 9, pp. 3843-3849, 1970.
11. L. Samoska, T. Gaier, A. Peralta, S. Weinreb, J. Bruston, I. Mehdi, Y.C. Chen, H.H. Liao, M. Nishimoto, R. Lai, H. Wang, Y.C. Leong, "MMIC Power Amplifiers as Local Oscillators for FIRST," *Proc. SPIE UV, Optical, and IR Space Telescopes and Instruments*, SPIE 4013, Munich, Germany, March 2000.
12. I. Mehdi, E. Schlecht, A. Arzumanyan, J. Bruston, P. Siegel, R. Peter Smith, J. Pearson, S. Martin and D. Porterfield, "Development of millimeter and submillimeter-wave local oscillator circuits for a space telescope," *Proc. SPIE*, vol. 3795, pp. 329-337, *Terahertz and Gigahertz Photonics*, R.J. Hwu, K. Wu, Eds., October 1999.
13. D. Porterfield, "A 200 GHz Broadband Fixed-Tuned, Planar Doubler," *Proc. Tenth International Symposium on Space THz Technology*, Charlottesville, VA, March 1999, pp. 466-474.

Prospects of Compound Semiconductor Quantum Nanostructures for Terahertz Generation, Amplification and Detection

Hideki Hasegawa

Abstract – In view of applications to imaging and near object analysis, remote sensing, ultra wide band/ultra high speed telecommunications etc., the present paper reviews the present status and future prospects of compound semiconductor quantum nanostructures for generation, amplification and detection of terahertz signals. Since the spectrum range falls in between the microwave/millimeter wave region and the optical region, the approach is two-fold, i.e., the electron device approach and the opto-electronic device approach. The talk will cover nano-Schottky diodes, heterostructure barrier varactors, FETs, HBTs, lasers and detectors using intersubband transitions in quantum

nanostructures, and use of novel and unexplored phenomena such as plasma waves, excitonic polaritons, and spin related transitions.

Research Centre for Interface Quantum Electronics, Hokkaido University, Japan

At the time of publication the final manuscript was not available.
--

Ultrabroadband Detection of Terahertz Radiation up to 20 THz with an LT-GaAs Photoconductive Antenna Gated by 15-fs Laser Pulses

Shunsuke Kono, Masahiko Tani, Ping Gu, and Kiyomi Sakai

Abstract – We report on the ultrabroadband detection of terahertz radiation with a low-temperature grown GaAs photoconductive dipole antenna gated with 15-fs laser pulses. The detected spectral frequency exceeds 20 THz. This is the highest frequency detected with a photoconductive antenna reported so far.

I. INTRODUCTION

Since the invention of the photoconductive (PC) antenna gated with ultrashort optical pulses, the generation and detection of terahertz (THz) radiation have been intensively studied during the last decade. The pulse width of commercially available mode-locked Ti:Sapphire lasers is approaching 10 fs. With such ultrashort pulses, a wider detection bandwidth is expected to be possible. Coherent detection of THz radiation based on a photoconductive antenna, however, was reported to be lower than 5 THz [1,2]. This limitation has been explained to be a result of the finite carrier lifetime and the RC time constant of the PC antenna. Therefore, interest in ultrafast detection of the radiation has recently shifted to the free-space electro-optic (EO) sampling technique because EO crystals are considered to have an instantaneous nonlinear response, and most of them are transparent in the regime from far to mid-infrared radiation. By exploiting these advantages, ultrabroadband detection of THz radiation based on EO sampling has been reported [3,4]. To obtain high-frequency response using EO sampling, the EO crystals should be thin enough to reduce the group velocity mismatch between the near-infrared probe beam and the THz radiation. However, even with a PC antenna fabricated on slow carrier lifetime semiconductors, such as semi-insulating (SI) GaAs or SI InP, the detection of relatively broadband (~ 3 THz) THz radiation was reported [5,6]. This detection with a slow carrier lifetime was possibly due to the fast-rising edge of the carrier injected by the ultrashort optical pulses. This suggests that the detection bandwidth is not strongly restricted by the carrier lifetime and is possibly extended by using shorter laser pulses. Thus, it is worthwhile to investigate the high-frequency limit of a PC antenna gated with ultrashort optical pulses whose width is close to 10 fs.

In this article, we demonstrate an ultrabroadband detection of electromagnetic radiation with a PC antenna fabricated on a low-temperature-grown GaAs (LT-GaAs) substrate and gated with 15-fs laser pulses. The detected

radiation frequency exceeded 20 THz. This is the highest frequency observed with PC antennas reported so far.

II. EXPERIMENTAL

A mode-locked Ti:Sapphire laser generated 12-fs laser pulses at a center wavelength of 800 nm and with a spectrum width of 90 nm (FWHM). The average output power of the laser was 320 mW. The laser beam was divided into pump and probe beams by a 1-mm glass-plate beam splitter. The average power of the pump beam was about 110 mW. The pump beam was collimated onto a SI InP (100) wafer by a silver-coated off-axis parabolic mirror with an incident angle of 45 degrees. The THz radiation from the emitter was collected in the reflection angle of the incident pump beam by a pair of off-axis parabolic mirrors and then focused on the PC detector. A silicon hemispherical lens was attached to the back side of the PC antenna to collimate the THz radiation.

The PC antenna was a 30- μm long dipole antenna with a 5- μm gap at the center, fabricated onto an LT-GaAs. The carrier lifetime of the LT-GaAs was estimated to be about 1.4 ps by a transient photo-reflectance measurement. The probe beam was focused onto the photoconductive gap with a reflection-type objective lens to avoid broadening of the optical pulses due to the dispersion and color aberration typically caused by an ordinary glass lens. The timing between the THz pulses and the probe pulses was scanned by the time delay line in the path of the probe beam with a corner reflector on a high-precision motorized translation stage.

The laser pulses were negatively chirped at the exit of the laser due to a multiple reflections between the pair of chirped mirrors. Even after the chirp of the laser pulses were positively compensated by the insertion of the beam splitters and neutral density filters, the pulse width on the semiconductor emitter and PC antenna was approximately 15 fs. The photo-current signal from the PC antenna was preamplified with a low-noise current amplifier and then detected with a lock-in amplifier referenced to an optical chopper (2 kHz) in the pump beam path.

III. RESULTS AND DISCUSSIONS

Figure 1(a) shows the waveform of THz radiation from a SI-InP (100) emitter for a single scan. The time constant of the lock-in amplifier was 0.1 sec, and the scanning time for a 3-ps time window was about 3 minutes with a 1- μm step resolution in the delay-line translation stage. There was a single THz pulse centered around 0.5 ps,

S. Kono, M. Tani, P. Gu, and Kiyomi Sakai are with Kansai Advanced Research Center, Communications Research Laboratories, MPT, 588-2 Iwaoka, Nishi-ku, Kobe, 651-2492, Japan

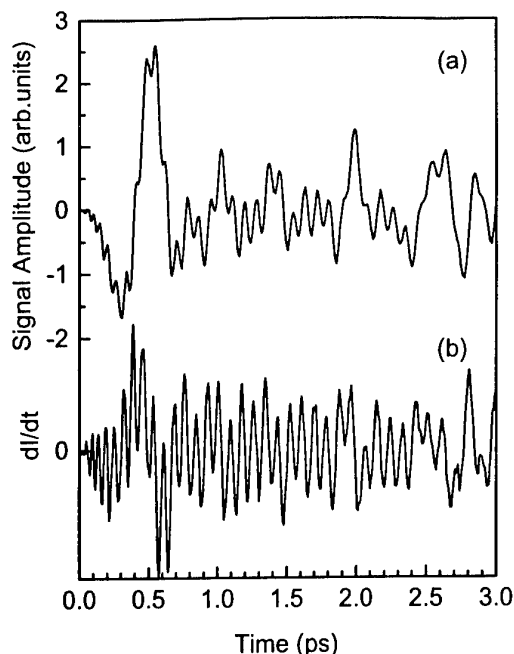


Fig. 1 (a) Time-resolved waveform of THz radiation from InP (100) surface. (b) Calculated time-derivative of the waveform (a).

which is attributed to the radiation due to the real current modulation at the emitter surface. Very fast oscillations were superposed on this pulse. The shortest oscillation period was about 45 fs. These fast oscillations were attributed to the radiation generated by the optical rectification effect in the emitter. Figure 1(b) shows the calculated first time-derivative for the waveform in Fig. 1(a). The fast oscillations are clearly visible in Fig. 1(b) because the slow component was suppressed while the fast oscillation component was enhanced by differentiation. The ringings after the first single and large cycle of oscillation were mainly attributed to dispersion and absorption in the GaAs substrate of the detector and absorption by water vapor in the ambient air. Figure 2 shows the Fourier transformed spectrum of the THz radiation waveform shown in Fig. 1(a) for a longer time window. The spectrum was extended more than 20 THz. This bandwidth is four times wider than the widest bandwidth achieved by a PC antenna ever reported. The absorption band from 7 to 9 THz was due to the phonon resonance in the 0.4-mm thick GaAs substrate of the PC detector (Reststrahlen band). The peak at 10.5 THz corresponds to the LO phonon frequency of InP. Many of the absorption lines observed in the spectrum were due to the water vapor in the ambient air.

It is rather surprising that the bandwidth of the PC antenna exceeded 20 THz. We need to explain the origin of this ultrabroadband band response. It has been reported that a PC antenna with a very long carrier lifetime (~ 100 ps) was able to detect THz radiation with almost the same detection bandwidth of a PC antenna with a subpicosecond carrier lifetime. The fast temporal response of a slow photoconductive antenna can be explained by the fast rise of its photocurrent on excitation by the ultrashort laser pulse. As described in Ref. [5,6], if the response function of the PC antenna with a slow carrier lifetime is a step-function, the PC antenna works as a sampling detector in

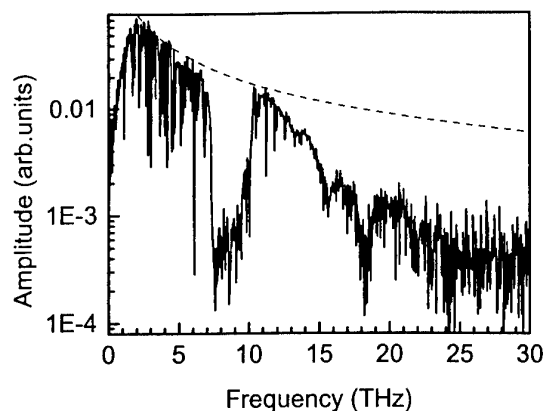


Fig. 2 Fourier transformed spectra of THz radiation wave form in Fig. 1 (a) for a longer time window. The dashed line represents the RC response function with the RC time constant of 0.2 ps.

an integration mode. This appears to be the case in the present experiment: the carrier lifetime of the LT-GaAs (~ 1 ps) was much longer than the gating pulse width. The fact that the time derivative of the THz waveform shown in Fig. 1(b) is similar to that of Ref. [3] also supports our interpretation. The physical origin of the fast photocurrent within the time scale of ~ 100 fs still needs to be investigated. However, it may be explained by the ballistic transport of the photo-excited electrons in the biased electric field, which was reported by Hu et al. in the same time range [7].

In addition to the carrier lifetime, the RC constant of the antenna is an important parameter in determining the frequency response. In a previous report, we estimated an RC time constant for the same type of antenna to be of the order of subpicoseconds (~ 0.2 ps) [8]. This finite RC time constant restricts the bandwidth of the PC antenna and reduces its responsivity at higher frequencies. The frequency response of the PC antenna was approximated by the equation of the differential circuit $G(\omega) = X_c / \sqrt{R^2 + X_c^2}$, where $X_c = 1/\omega C$, R is the resistance of the PC antenna, and C is the capacitance formed between the antenna electrodes. For example, for a 0.2 ps RC time constant, the cut-off frequency was calculated to be about 0.8 THz. The responsivity of the antenna at 5 and 10 THz respectively decreases to 25 and 13 % of that at the cut-off frequency. The circuit response function in the frequency domain calculated with an RC time constant of 0.2 ps is indicated by the dashed line in Fig. 2. The RC response function reproduces the spectral profile at the frequency range lower than 5 THz. In spite of the reduction of the circuit responsivity due to the carrier lifetime, this slow decay of the frequency response can be one of the reasons of our observation of radiation at unexpectedly high frequencies with a PC antenna. Other factors, such as the emitter bandwidth and absorption or reflection loss, will be necessary for better reproduction of the overall spectral profile.

IV. CONCLUSION

In conclusion, we demonstrated that a PC antenna gated with 15-fs laser pulses was capable of ultrabroadband detection up to 20 THz. This is the highest frequency detected with PC antennas than ever reported. PC antenna is also promising for ultrabroadband detection as well as the EO sampling technique. In the EO sampling technique, the strong absorption and dispersion at the phonon resonance frequencies of EO crystals is a disadvantage. Although we also observed the strong phonon absorption in GaAs substrate, this problem can be avoided by fabricating the LT-GaAs on another substrate material, such as high resistivity silicon.

References

1. N. Katzennellenbogen and D. Grischkowsky, "Electrical characterization to 4 THz of N- and P-type GaAs using THz time-domain spectroscopy," *Appl. Phys. Lett.* 61, 840-842 1992
2. M. Tani, R. Fukasawa, H. Abe, S. Matsuura, K. Sakai, and S. Nakashima, "Terahertz Radiation from Coherent Phonons Excited in Semiconductors," *J. Appl. Phys.* 83, 2473-2477 1998
3. Q. Wu, and X.-C. Zhang, "Free-space electro-optics sampling of mid-infrared pulses", *Appl. Phys. Lett.* 71, 1285-1287 1997
4. A. Leitenstorfer, S. Hunsche, J. Shah, M. C. Nuss, and W. H. Knox, "Detectors and sources for ultrabroadband electro-optic sampling: Experiment and theory", *Appl. Phys. Lett.* 74, 1516-1518 1999
5. F. G. Sun, G. A. Wagoner, and X.-C. Zhang, "Measurement of free-space terahertz pulses via long-lifetime photoconductors," *Appl. Phys. Lett.* 67, 1656-1658 1995
6. M. Tani, K. Sakai and H. Mimura, "Ultrafast Photoconductive Detectors Based on Semi-Insulating GaAs and InP" *Jpn. J. Appl. Phys.*, 36, L1175-L1178 1997
7. B. B. Hu, E. A. de Souza, W. H. Knox, J. E. Cunningham, M. C. Nuss, A. V. Kuznetsov, and S. L. Chuang, "Identifying the distinct phases of carrier transport in semiconductors with 10 fs resolution", *Phys. Rev. Lett.* 74, 1689-1692 1995
8. Shuji Matsuura, Masahiko Tani and Kiyomi Sakai, "Generation of coherent terahertz radiation by photomixing in dipole photoconductive antennas," *Appl. Phys. Lett.* 70, 550-561 1997

Ultrafast, ultra-broadband superlattice detector for THz radiation

E.Schomburg, F.Klappenberger, M.Krätschmer, A.A.Ignatov, K.F.Renk, and W.Wegscheider

Abstract – We report on a novel detector for THz radiation. It consists of a GaAs/AlAs superlattice mesa device mounted in a corner cube antenna system. The detector shows a current-voltage characteristic with a negative differential conductance. Under the influence of THz radiation, the dc current through the superlattice mesa is reduced; this is caused by a THz field-induced modulation of Bloch oscillating miniband electrons in the superlattice. A fast detector response (several tenths of picoseconds, limited by the electronics) and a high responsivity is demonstrated in a frequency range 0.7-7 THz.

I. INTRODUCTION

Semiconductor superlattices, as proposed by Esaki and Tsu [1], show non-linear electrical transport properties due to their unique bandstructure consisting of minibands along the superlattice axis. It has been found that a doped superlattice showed a negative differential conductance [2] and that THz radiation applied to a superlattice by an antenna resulted in a reduction of the direct current [3, 4]. In this contribution, we report on the use of a GaAs/AlAs superlattice mesa device mounted in a corner cube antenna system as THz detector and discuss results of temporal resolution, responsivity and dynamical range. All experiments were performed with the detector at room temperature.

II. THE DETECTOR

The main element of the detector is a superlattice device fabricated from a n-type doped GaAs/AlAs superlattice (doping level $1 \cdot 10^{17} \text{ cm}^{-3}$), which was grown by molecular beam epitaxy on a n^+ GaAs substrate. For our study, we used different superlattices, which typically consisted of 100 periods; a period contained a GaAs and a AlAs layer. The thickness of these layers was chosen that a miniband width in the order of 100 meV was obtained. The device (area: $200 \times 200 \mu\text{m}^2$) consisted of superlattice mesas (diameter about $4 \mu\text{m}$) in a honeycomb-like arrangement on the GaAs substrate. Each mesa was covered by an ohmic contact. An additional ohmic contact was made on the n^+ GaAs substrate.

The superlattice device was mounted in a corner cube antenna system (Fig.1). A single superlattice mesa was

contacted with a gold wire connecting the mesa to ground for the direct current. The wire acted as a long wire L-antenna for the THz radiation and was placed in a 90-degree corner cube reflector. A second contact to the superlattice mesa was established by connecting the substrate contact to the inner wire of a coaxial line. The coaxial line was used to couple the detector response to an oscilloscope (input impedance 50Ω) and to apply a constant voltage to the superlattice. Outside the detector, detector response and bias voltage were separated by a bias tee. In order to test the detector, we used radiation from the FELIX free electron laser. For a lower frequency (700 GHz), a backward-wave oscillator was used.

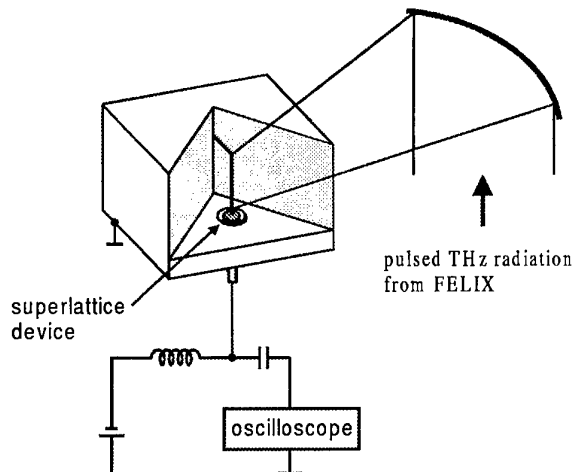


Fig. 1: Experimental set-up.

III. RESULTS

The current-voltage characteristic (Fig.2) of a superlattice mesa showed ohmic behaviour for small voltages and had a negative differential conductance for higher voltages. The current maximum corresponded to a current density of about 100 kA/cm^2 .

The coupling of THz radiation to a superlattice mesa leads to a reduction of the current. This current reduction is the basis of the detector response monitored by the oscilloscope. As example, the signal for a radiation pulse at 7 THz and a duration of 6 ps is given in Fig.3. The detector signal has a duration (halfwidth) of about 30 ps; the temporal resolution was limited by the electronics, mainly the bandwidth of the oscilloscope and the jitter in the trigger.

Recently, it was shown [5] using a differential electronic gating technique developed by a group at the Delft

E.Schomburg, F.Klappenberger, M.Krätschmer, A.A.Ignatov, K.F.Renk, and W.Wegscheider are with the Institut für Angewandte Physik, Universität Regensburg, D-93040 Regensburg, Germany. Electronic mail: ekkehard.schomburg@physik.uni-regensburg.de

University of Technology (N.Hovenier et al.) that our superlattice detector can temporal resolve 10-ps THz pulses (the measurements were performed at frequency of about 2 THz) from the FELIX free electron laser.

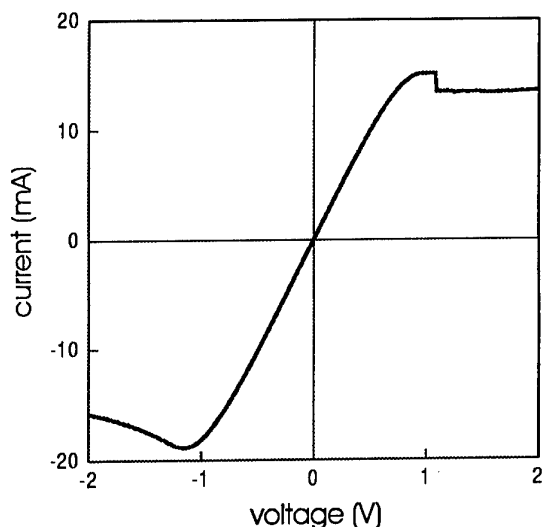


Fig. 2: Current-voltage characteristic of a superlattice mesa.

The dynamical range of the superlattice detector, i.e. the range in which the detector signal is proportional to the radiation power, is several orders of magnitude. For a superlattice (miniband width 105 meV) at 2.5 THz the smallest power registered from a cw laser was below 100 μ W, while the largest power detected from a FELIX pulse was about 5 W before the detector starts to saturate.

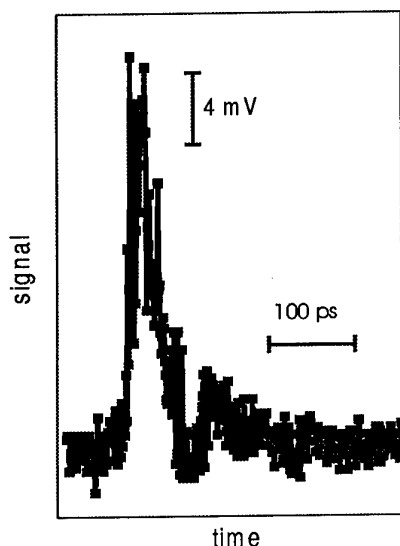


Fig. 3: Signal of a superlattice detector in response to a FELIX pulse (duration: 6 ps; energy: 2 nJ) at 7 THz.

An overview of the voltage responsivity (which is the signal voltage corresponding to the current reduction at a 50 Ω load impedance) of superlattice detectors, with miniband widths of the order of 100 meV, is given in Fig.4. The superlattice mesas were biased near the current maxima, where the highest responsivity was found. The

responsivity was proportional to f^4 , where f is the radiation frequency. For comparison, Schottky diodes [6] mounted in a similar corner cube antenna system has a much higher responsivity (more than an order of magnitude at 700 GHz and about three orders of magnitude at 2.5 THz). However, Schottky diodes can be destroyed by intense THz radiation pulses. The superlattice detector was irradiated with THz-laser pulses (duration 5...10 ps) of the order of kilowatts without being destroyed. In comparison to the interband detector [7] and the photon drag detector [8], which have a similar robustness against high power levels and comparable time resolution, the superlattice detector has a responsivity being several orders of magnitude higher.

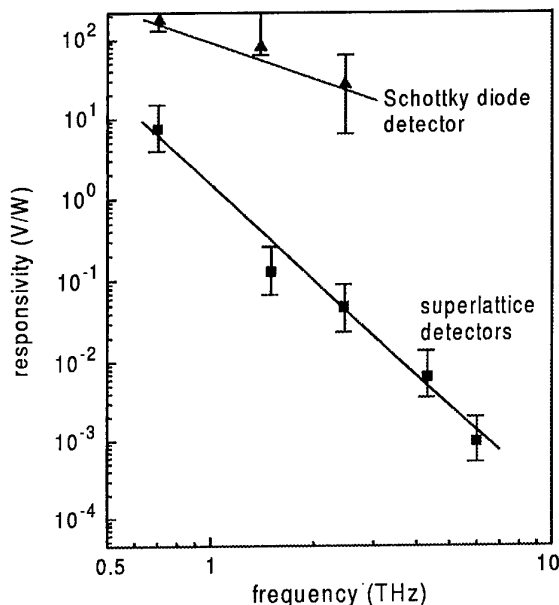


Fig. 4: Responsivity of superlattice detectors (squares) and Schottky diode detectors (data taken from [6]).

IV. THE PHYSICS OF THE DETECTOR

The current along the superlattice is mainly carried by electrons in the energetically lowest miniband. The negative differential conductance indicates that miniband electrons perform Bloch oscillations. According to the Esaki-Tsu model [1] of miniband transport, the negative differential conductance occurred for fields larger than a critical field $E_c = \hbar/(e a \tau)$, where e is the elementary charge, \hbar Planck's constant, a the period of the superlattice and τ the intraminiband relaxation time. An analysis of current-voltage characteristics of different superlattices with wide minibands indicated a value of the order of 10^{-13} s for the intraminiband relaxation time. Thus, for the THz frequency range, the condition of a dynamical interaction ($2\pi f \tau \geq 1$) of the miniband electrons with the THz field is fulfilled. An earlier study [4] showed that the response of a superlattice to THz radiation corresponded to classical rectification for $2\pi f \tau < 1$ and to dynamical interaction for $2\pi f \tau \geq 1$. In the case of dynamical interaction the miniband electrons perform frequency-modulated Bloch oscillations; the modulation frequency is equal to the frequency of the

THz radiation and the modulation degree is determined by the amplitude of the THz field inside the superlattice. The modulation leads to a reduction of the spatial amplitude of the Bloch oscillations corresponding to a dynamical localisation of the miniband electrons. The localisation causes the reduction of current and, therefore, leads to the detector response. Intrinsically, the characteristic response time of a superlattice to a change in the THz field is governed by the intraminiband relaxation time.

An analysis of the responsivity of a superlattice detector [9] indicated a decrease of the responsivity with the fourth power of the frequency, which is in good agreement with our experimental results. Furthermore, the analysis showed that the responsivity is proportional to the maximum current density of the superlattice and is inversely proportional to the cross-section of the superlattice mesa. Therefore, an increase of the doping level in the superlattice and a reduction of the mesa area should lead to an increase of responsivity.

V. CONCLUSION

A new room temperature THz detector was described. The detector has an intrinsic response time of the order of 10^{-13} s, a large range of response (from smaller 0.7 THz to 7 THz) and a large dynamical range. The detector is robust against intense radiation pulses. Our detector is most suitable for the characterisation of intense ultrashort THz radiation pulses.

Acknowledgement

This research was supported by the Deutsche Forschungsgemeinschaft. We gratefully acknowledge the

assistance of the Stichting voor Fundamenteel Onderzoek der Materie (FOM) in providing required beam time on FELIX and greatly appreciate the skilful assistance by the FELIX staff.

References

1. L. Esaki and R. Tsu, IBM J. Res. Dev. **14**, 61 (1969).
2. A. Sibille, J.F. Palmier, H. Wang, J.C. Esnault, and F. Mollot, Appl. Phys. Lett. **56**, 256 (1990); F. Beltram, F. Capasso, D.L. Sivco, A.L. Hutchinson, S.-N.G. Chu, and A.Y. Cho, Phys. Rev. Lett. **64**, 3167 (1990).
3. A.A. Ignatov, E. Schomburg, K.F. Renk, W. Schatz, J.F. Palmier, and F. Mollot, Ann. Physik **3**, 137 (1994).
4. S. Winnerl, E. Schomburg, J. Grenzer, H.-J. Regl, A.A. Ignatov, A.D. Semenov, K.F. Renk, D.G. Pavel'ev, Yu. Koschurinov, B. Melzer, V. Ustinov, S. Ivanov, S. Schaposchnikov, and P.S. Kop'ev, Phys. Rev. B **56**, 10303 (1997).
5. J.N. Hovenier, R.W. van Es, T.O. Klaassen, W.Th. Wenckebach, F. Klappenberger, M. Krätschmer, E. Schomburg, S. Winnerl, G.M.H. Knippels, and A.F.G. van der Meer, submitted to Appl. Phys. Lett. (2000).
6. H.-W. Hübers, G.W. Schwaab, and H.P. Röser, J. Appl. Phys. **75**, 4243 (1994).
7. S.D. Ganishev, E.V. Berulin, and I.D. Yaroshetskii, Proc. SPIE **1985**, 523 (1993).
8. S.D. Ganishev, Ya.V. Terent'ev, and I.D. Yaroshetskii, Sov. Tech. Phys. Lett. **11**, 20 (1985).
9. A.A. Ignatov and A.-P. Jauho, J. Appl. Phys. **85**, 3643 (1999).

Terahertz Spectral Analysis by Frequency-Selective Incoherent Detection in High-T_c Josephson Junctions

Yuri Divin, Ulrich Poppe, Knut Urban, Oleg Volkov, Valery Pavlovskii

Abstract – The detector response of YBa₂Cu₃O_{7-x} Josephson grain-boundary junctions to monochromatic radiation with the frequency f in the range from 60 GHz to 5 THz has been studied. Odd-symmetric resonances near the voltages $V = hf/2e$ in the responses $\Delta I(V)$ of these junctions to radiation with different frequencies f have been observed in a decade of spectral range for any operating temperature between 30 to 85 K. The spectral range of this selection detection has scaled with the $I_c R_n$ -product of the Josephson junction, so decreasing the junction temperature from 85 to 30 K one can perform the spectral analysis in two decades. A prototype of terahertz Hilbert-transform spectrum analyzer based on high-T_c Josephson junction integrated into a Stirling cooler has been developed. A resolving power $\delta f/f$ of around 10^{-3} has been demonstrated in the spectral analysis of output radiation from optically-pumped far-infrared CH₃OH laser.

I. INTRODUCTION

One of the promising applications of superconducting junctions is the detection of electromagnetic radiation. Among them, the detectors using the ac Josephson effect can give an information on the spectrum of incident radiation [1]. A frequency-selective detection takes place in Josephson junctions due to an interaction of internal voltage-controlled Josephson oscillations and external signals. The corresponding detectors based on low-T_c Josephson junctions have been studied earlier [2-5], and only after some progress in junction fabrication, the first evaluations of high-T_c Josephson junctions for this application have been carried out [6-8]. Recently, we have demonstrated a selective Josephson detection in a decade of the spectral range with the highest frequency of 3.1 THz [9].

Frequency-selective Josephson detection of electromagnetic radiation is the basic principle of Hilbert-transform spectral analysis [1]. Spectral measurements of millimeter- and submillimeter-wave radiation by Hilbert-transform technique have been carried out using both low-T_c and high-T_c Josephson junctions [1, 10-16]. The laboratory prototypes of Hilbert-transform spectrometers and spectral analyzers cooled by cryogenic liquids have been developed [1, 11, 13, 16].

A necessity to use cryogenic liquids for cooling is considered as a main obstacle on the way of superconducting electronics into the market, and a

replacement of them by cryocoolers is required [17]. Here, we report on the characteristics of a Hilbert-transform spectrum analyzer based on high-T_c Josephson detector integrated into a Stirling cooler.

II. THEORY

In the simple resistively shunted junction (RSJ) model [18], the response $\Delta I = I(V) - I_0(V)$ of a Josephson junction to weak monochromatic radiation with the frequency f is equal to [18]

$$\Delta I(V) = I_s \left(\frac{2e}{h} \right) \frac{I_c^2 R_n^2}{8 I_0 V} \left[\frac{(f_j + f)}{(f_j + f)^2 + \left(\frac{\delta f}{2} \right)^2} + \frac{(f_j - f)}{(f_j - f)^2 + \left(\frac{\delta f}{2} \right)^2} \right], \quad (1)$$

where I_c is the critical current of the junction, R_n is the normal-state resistance of the junction, I_s – is the amplitude of the radiation induced current ($I_s < I_c$), I_0 is the dc current flowing through the junction, $V = R_n(I_0^2 - I_c^2)^{1/2}$ is the voltage across the junction, $f_j = 2eV/h$ is the voltage-controlled frequency of internal Josephson oscillations and δf is the Josephson oscillations linewidth.

The response $\Delta I(V)$ (Eq. 1) is quadratic with the signal amplitude I_s . At low voltages $V \ll hf/2e$ in the limit of small δf , the response $\Delta I(V)$ approaches the value

$$\Delta I_0 = - (I_s^2 R_n / 2) (2e/h) (f_c / 2f^2), \quad (2)$$

where $f_c = (2e/h) I_c R_n$ – is a characteristic frequency of the Josephson junction. This low-voltage response is actually a suppression of the critical current of the junction by external radiation.

At the voltages V , where the Josephson frequencies f_j are close to the frequency f of the incident radiation, the response $\Delta I(V)$ shows an odd-symmetric resonance. The maximum amplitude ΔI_{max} of this resonance at $V = (h/2e)[f + (\delta f/2)]$ is inversely proportional to the Josephson linewidth δf :

$$\Delta I_{max} = (I_s^2 R_n / 2) (2e/h) [f_c^2 / 4(f_c^2 + f^2)^{1/2} \delta f]. \quad (3)$$

For broadband thermal fluctuations with a noise temperature T and $kT \ll eV$ (equilibrium case), the Josephson linewidth is equal to [18]

$$\delta f = 4\pi (2e/h) kT (R_d^2 / R_n) \left[1 + \left(I_c^2 / 2 I_0^2 \right) \right], \quad (4)$$

where R_d is the dynamic resistance of the junction. The dynamic resistance $R_d(V) = dV/dI = R_n(V^2 + I_c^2)^{1/2} / V$ is

Y. Y. Divin, U. Poppe, K. Urban are with the Institute of Solid-State Physics, Juelich Research Center, 52425 Juelich, Germany
O.Y. Volkov, V.V. Pavlovskii are with the Institute of Radioengineering and Electronics, Russian Academy of Sciences, 103907 Moscow, Russia

equal to the normal-state resistance R_n at high voltages $V > I_c R_n$, and at small voltages $V < I_c R_n$ it is inversely proportional to the voltage. So, the linewidth and the width of the odd-symmetric resonance in the response $\Delta I(V)$ (Eq. 1) will decrease with the increase of the frequency f at low frequencies $f < f_c$ and will be frequency independent at high frequencies $f > f_c$.

One can expect from Eq. 3 and Eq. 4, that the amplitude ΔI_{max} of the selective response should rise linearly with the increase of the frequency f at low frequencies $f < f_c$, reach a maximum at $f = f_c$ and fall down inversely proportional to f^2 at high frequencies $f > f_c$. This conclusion is valid, provided the same current amplitudes I_s are induced by radiation with different frequencies f . But, due to the different power level of the radiation sources and frequency-dependent coupling of radiation to the junction, the requirement of a constant I_s is difficult to fulfill experimentally.

We have solved this problem by a selfcalibration procedure, when we normalize each of the measured response curves $\Delta I(V)$ to its value ΔI_0 (Eq. 2) at low voltages [5]. The maximum amplitudes ΔI_{max} of the resonances in these normalized responses are proportional to f^3 at low frequencies $f < f_c$ and independent of the frequency at high frequencies $f > f_c$. The last circumstance just reflects the frequency-independent behavior of the amplitude of Josephson oscillations in the RSJ model. With this normalization, each set of data can be compared with the others, measured for different frequencies, and deviations from the RSJ-behavior can be easily detected.

The Josephson junctions which are close to those of predicted by RSJ model are good candidates for the Hilbert-transform spectral analysis [1]. Within the framework of the resistively-shunted-junction (RSJ) model, the small-signal response $\Delta I(V) \ll I_0(V)$ was calculated for radiation with an arbitrary spectrum, inducing currents through the junction with the spectral density $S_i^2(f)$. The calculated response $\Delta I(V)$ with the accuracy of smooth experimentally measured functions was found to be proportional to the Hilbert transformation of the spectral density $S_i^2(f)$, so the unique deconvolution of $S_i^2(f)$ from the experimental data is possible. The exact solution of the problem was found to be [1]

$$S_i^2(f) = \left(\frac{1}{\pi} \right) \cdot \int_{-\infty}^{+\infty} \frac{H(f_j)}{(f_j - f)} \cdot df_j \quad (5)$$

where $f_j = 2eV/h$ is the voltage-controlled frequency of the Josephson oscillations, $H(V)$ is a normalized response function

$$H(V) = (8/\pi)(h/2e)[\Delta I(V)I(V)V/I_c^2 R_n^2], \quad (6)$$

consisting of the product of the response $\Delta I(V)$, the current-voltage characteristic $I(V)$ and the voltage V . I_c is the critical current and R_n is the normal-state resistance of the Josephson junction. The principal value of integral should be taken in Eq. 1. So, to get spectrum of radiation, one should measure the $I(V)$ - curve of Josephson junction, its response $\Delta I(V)$ to this radiation and perform

the Hilbert transformation of normalized response function $H(V)$. Actually, the spectral resolution of HTS is determined by the linewidth δf of the Josephson radiation (Eq.4).

III. EXPERIMENT

A laboratory prototype of spectrum analyzer based on high- T_c Josephson junction has been developed. A frontend of this analyzer is shown in Fig. 1. High-quality $\text{YBa}_2\text{Cu}_3\text{O}_{7-x}$ grain-boundary junctions fabricated on untwinned $2 \times 14^\circ$ (110) NdGaO_3 bicrystal substrates [19] have been used in the experiments. The widths of the junctions were in the range 1-3 μm . The $I_c R_n$ -products of these junctions were up to 330 μV at 78 K, and the values of resistances R_n varied from 1 to 8 Ohm. A broadband $\text{YBa}_2\text{Cu}_3\text{O}_{7-x}$ log-periodic antenna has been integrated with each junction on the substrate.

The substrate with the Josephson junction was mounted in a vacuum chamber on the coldfinger of a Stirling cooler [20]. Junction temperatures in the range from 30 to 90 K have been achieved in this cryogenic environment. The measurements at any of these temperatures could be carried out during several hours with a reasonable drift of 1-2 K. The compressor of the Stirling cooler and the vacuum chamber were magnetically shielded by several layers of mu-metal foil.

An optically-pumped far-infrared laser and a backward-wave oscillator with a multiplier were used as sources of monochromatic radiation in this study. With this combination we were able to deliver radiation in the

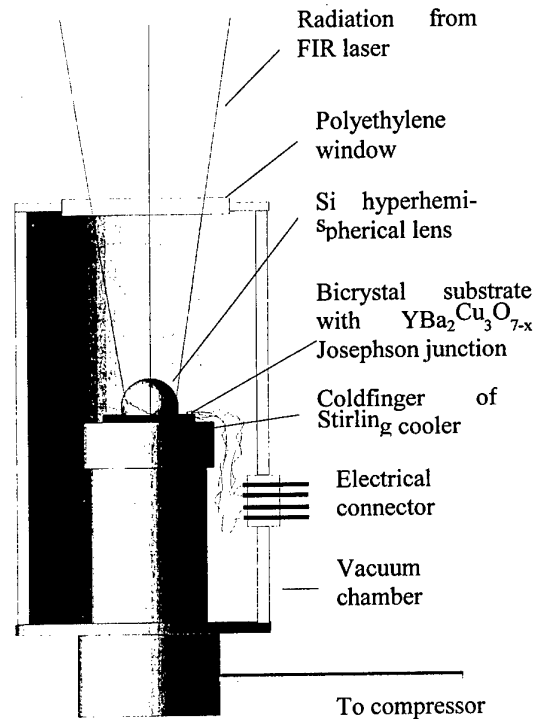


Fig. 1. Frontend of terahertz spectrum analyzer based on high- T_c Josephson junction integrated into a Stirling cooler.

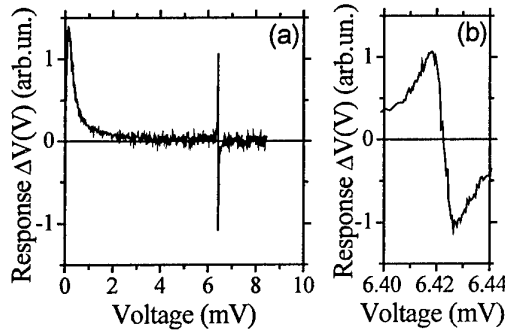


Fig. 2. a) The response $\Delta V(V)$ of $\text{YBa}_2\text{Cu}_3\text{O}_{7-x}$ bicrystal Josephson junction to far-infrared laser radiation with the frequency of 3.106 THz. b) The same response near the resonance at the voltage $V=6.423$ mV. The junction resistance $R_n = 1$ Ohm and the temperature $T = 34$ K.

frequency range from 60 GHz to 5 THz. Absorption attenuators were placed between the radiation sources and the Josephson junction to guarantee a low level of radiation for square-law detection by the Josephson junctions. Radiation was focused to the junction antenna by a parabolic mirror through a polyethylene window in the vacuum chamber and a hyperhemispherical Si-lens on the substrate (Fig. 1).

IV. RESULTS

The response $\Delta V(V)$ of a $\text{YBa}_2\text{Cu}_3\text{O}_{7-x}$ Josephson junction to 3.1 THz radiation is shown in Fig. 2 [9]. The Josephson junction has a resistance of $R_n = 1$ Ohm and quite high $I_c R_n$ -product of 1.5 mV at 34 K. The shape of the response $\Delta V(V)$ (Fig. 2a) is very close to that of the RSJ model in the voltage range from 0 to 8.5 mV. The response ΔV demonstrates a very sharp odd-symmetric resonance around the voltages near $V = hf/2e = 6.423$ mV. The width of this resonance is around 8 μV (Fig. 2b), which corresponds to the Josephson linewidth δf of 3.9 GHz. So, it follows from the measured response that a resolving power $\delta f/f$ of the order of 10^{-3} might be achieved with selective detection by high- T_c Josephson junctions.

To obtain a normalized response $\Delta I(V)/\text{abs}(\Delta I_0)$, as it was discussed in the introduction, the current response $\Delta I(V) = -\Delta V(V)/R_d(V)$ was calculated and the value of ΔI_0 was determined by extrapolation of the low-voltage behavior of $\Delta I(V)$ to $V=0$. A set of the normalized current responses $\Delta I(V)/\text{abs}(\Delta I_0)$ of a Josephson junction with $R_n = 7$ Ohm to monochromatic signals with the frequencies from 0.404 THz up to 4.25 THz are shown in Fig. 3. With an increase of frequency f , the amplitude of the odd-symmetric resonances at $V=hf/2e$ also increases, then, when the frequency is around $2f_c$ (and the voltage is around $2I_c R_n$), reaches the maximum, and falls down with further increase of frequency.

For each temperature in the range of 30 – 85 K the selective response is observed at least in one decade of frequency bandwidth [9]. The middle frequency of this

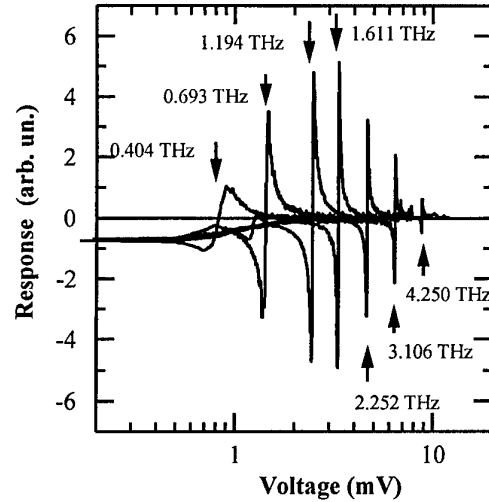


Fig. 3. Normalized responses $\Delta I(V)/\Delta I_0$ of the $\text{YBa}_2\text{Cu}_3\text{O}_{7-x}$ Josephson junction to monochromatic far-infrared radiation with different frequencies. The junction resistance $R_n = 7$ Ohm and the temperature $T = 34$ K.

bandwidth scaled with the characteristic frequency $f_c = (2e/h)I_c R_n$ so the total bandwidth of selective detection, which was covered by one Josephson junction at different temperatures, was around two decades.

The low-frequency cut-off of the appearance of the resonances in responses $\Delta I(V)/\text{abs}(\Delta I_0)$ in Fig. 3 is in accordance with the RSJ behavior. It is the result of the low-voltage increase of the linewidth of Josephson radiation and a corresponding decrease of the resonance amplitude according to Eq.3. The high-frequency fall-down of the selective response was attributed to Joule heating [9] and it might be shifted to higher frequencies by increasing the junction resistance and/or further decreasing the operation temperature. As we can see from Fig.3, the increase of the resistance to 7 Ohm results in the increase of highest frequency to 4.25 THz. In the case of high-ohmic junctions the high-frequency cut-off might be also due to capacitive shunting of the junction.

V. APPLICATION

An example of application of the developed Hilbert-transform spectrum analyzer is demonstrated in Fig. 4. Radiation to the spectrometer came from a far-infrared CH_3OH laser, pumped by 9P36 line of CO_2 laser. The length of the FIR laser cavity was slightly changed from one position (a) to the other (b). In the case (a), two odd-symmetric resonances appeared at the response $\Delta I(V)$ of the spectrometer. An application of Hilbert-transformation to the normalized response $\Delta I(V) \cdot I(V) \cdot V$, according to the Eq.5, gives the spectrum of incident radiation. Two lines, the main at 2.523 THz and the competing one at 1.758 THz, are clearly visible in the spectrum. The intensities of laser lines are inside the dynamic range of the spectrum analyzer and no artificial line at the difference frequency has appeared in the spectrum. Changing the length of

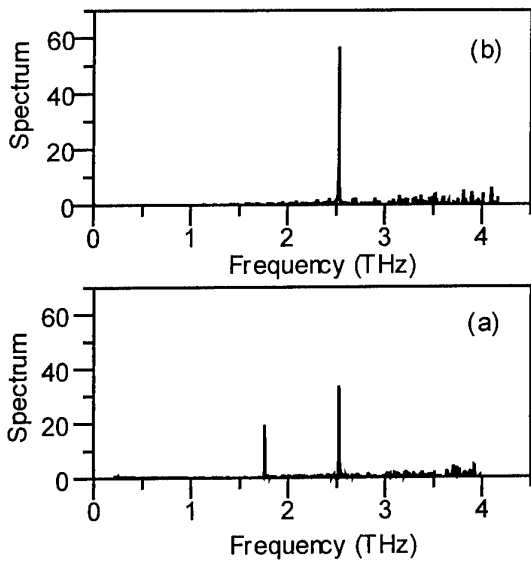


Fig. 4. Spectra of radiation from optically-pumped CH_3OH laser recovered by Hilbert-transform spectrum analyzer. The pump line of CO_2 laser is 9P36. Spectra (a) and (b) have been measured for different lengths of laser cavity.

laser cavity and controlling the spectrum of laser radiation it is possible to get a single-line operation of the optically pumped laser (b). The measurement time of around 10 seconds has been achieved with this analyzer.

VI. CONCLUSION

We have demonstrated a decade bandwidth of the selective detection of terahertz radiation by $\text{YBa}_2\text{Cu}_3\text{O}_{7-x}$ Josephson junctions for any junction temperature in the range of 30 - 85 K. The bandwidth scaled with the $I_c R_n$ -product of the junction, and using one junction at different temperatures one can cover up to almost two decades with a selective detection. A prototype of Hilbert-transform spectrum analyzer have been developed based on high- T_c Josephson detector integrated into a Stirling cooler. An application of this spectrum analyzer for optimization of single-line operation of far-infrared optically-pumped CH_3OH laser has been demonstrated. Broadband operation of Hilbert-transform technique [1] in the terahertz range with a resolving power of around 10^{-3} might be achieved according to these experiments.

Acknowledgement

Support by the German BMBF (project 13N7335/8) is gratefully acknowledged.

References

1. Y.Y. Divin, O.Y. Polyanski, A.Y. Shul'man, *Sov. Techn. Phys. Lett.* **6**, 454 (1980)
2. H. Kanter, F.L. Vernon, *J. Appl. Phys.*, **43**, 3174 (1972)
3. Y. Y. Divin, F.Y. Nad', *Sov. Techn. Phys. Lett.*, **4**, 785 (1978)
4. D. A. Weitz, W. J. Skocpol, M. Tinkham, *Phys. Rev. B*, **18**, 3282 (1978)
5. Y. Y. Divin, N. A. Mordovets, *Sov. Techn. Phys. Lett.*, **9**, 108 (1983)
6. Y.Y. Divin, J. Mygind, N.F. Pedersen, P. Chaudhari, *Appl. Phys. Lett.*, **61**, 3053 (1992)
7. P. A. Rosenthal, E. N. Grossman, *IEEE Trans. Microwave Theory Tech.*, **42**, 707 (1994)
8. K. Nakajima, J. Chen, H. Myoren, T. Yamashita, P. Wu, *IEEE Trans. Appl. Supercond.*, **7**, 2607 (1997)
9. Y.Y. Divin, U. Poppe, O.Y. Volkov, V.V. Pavlovskii, *Appl. Phys. Lett.*, **76**, 2826 (2000)
10. U. Stumper, J.H. Hinken, W. Richter, D. Schiel, L. Grimm, *Electronics Lett.* **20**, 540 (1984)
11. J. H. Hinken et al. *Proc. 18th Europ. Microwave Conf.* pp 177-182 (1988)
12. Y.Y. Divin, S.Y. Larkin, S.E. Anischenko, P.V. Khabaev, S.V. Korsunsky, *Int. J. Infrared & Millimeter Waves*, **14**, 1367 (1993)
13. M. A. Tarasov, A.Y. Shul'man, G.V. Prokopenko, V.P. Koshelets, O.Y. Polyanski, I.L. Lapitskaya, A.N. Vystavkin, *IEEE Trans. Appl. Supercond.* **5**, 2686 (1995)
14. S.Y. Larkin, S.E. Anischenko, V.V. Kamyshev, P.V. Khabayev, *Proceedings SPIE*, **2842**, 607 (1996)
15. Y. Y. Divin, H. Schulz, U. Poppe, N. Klein, K. Urban, V.V. Pavlovskii, *Appl. Phys. Lett.*, **68**, 1561 (1996)
16. Y.Y. Divin, O.Y. Volkov, V.V. Shirov, V.V. Pavlovskii, U. Poppe, P. Schmueser, M. Tonutti, K. Hanke, M. Geitz, *Proc. SPIE*, **3465**, 309 (1998)
17. J.M. Rowell, *IEEE Trans. Appl. Supercond.* **9**, 2837 (1999)
18. K. K. Likharev, *Dynamics of Josephson Junctions and Circuits*, Gordon and Breach, New York, 1986
19. Y.Y. Divin, I.M. Kotelyanskii, P.M. Shadrin, O.Y. Volkov, V.V. Shirov, V.N. Gubankov, H. Schulz, U. Poppe, *Proceedings of EUCAS 97*. Ed.: H. Rogalla and D.H.A. Blank, IOP Publishing Ltd., 1997, Bristol, p.p.467-470.
20. Model SL-200, AEG INFRAROT-MODULE GmbH, D-74001 Heilbronn, Germany

Wide Bandwidth Far-Infrared Mixing using a High- T_c Superconducting Bolometer

Mark Lee, Richard C.-T. Li

Abstract – We report on the gain bandwidth and noise characteristics of far-infrared mixers using high- T_c superconducting YBa₂Cu₃O₇ (YBCO) thin films. The YBCO films are patterned into lattice-cooled hot-electron bolometers (HEBs) coupled to an integrated antenna and transmission line. Heterodyne and homodyne down-conversion using LO frequencies of 115 GHz and 585 GHz show a device conversion gain of as high as -9.5 dB at 66 K using 1 μ W of LO power. Y -factor noise measurements show a double-sideband noise temperature of 3400 K at 66 K. Both gain and noise bandwidths show a single-pole roll-off with -3 dB point near 10 GHz.

I. INTRODUCTION

Gershenson, *et al.* [1] first proposed the design of a lattice-cooled superconducting hot-electron bolometer (HEB) for use as a low-power, wide-bandwidth heterodyne mixer at millimeter and submillimeter-wave frequencies. In principal, HEB mixers have several very attractive properties, including wide LO and IF bandwidths, low LO pump power requirements, reasonable noise figures, ease of fabrication, and freedom from capacitive parasitics. The lattice-cooled idea was first successfully implemented using NbN [2], which showed a conversion gain up to -15 dB using 1 μ W of LO power at a temperature of 4.2 K.

The ultimate speed and bandwidth of a lattice-cooled HEB is determined by the electron energy relaxation rate, which in metals is presumed to be the electron-phonon scattering rate. For this reason, Gershenson [3] suggested that the high normal-state resistivity of the high- T_c superconductor YBa₂Cu₃O₇ (YBCO) implied a very fast electron inelastic scattering rate and so make this material an ideal candidate to produce a very wide instantaneous bandwidth lattice-cooled HEB operating near liquid nitrogen temperatures. The first reports of such mixers at 1.5 μ m (Ref. 4) and 9.6 μ m (Ref. 5) wavelengths showed a very low intrinsic conversion gain of -77 dB (excluding coupling losses) using a relatively large 0.3 mW of absorbed LO power. However, the gain bandwidth showed a two-plateau structure. A low frequency plateau near -77 dB rolled off near 1 GHz IF but gave way to a second plateau near -90 dB that extended to at least 18 GHz, the upper limit of the measurement.

Karasik, *et al.*, [6] did extensive calculations on the conversion gain and noise properties of lattice-cooled HEB mixers using a two-temperature model. They found that the conversion gain increases and noise temperature

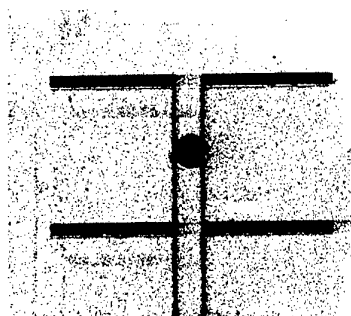


Fig. 1: SEM micrograph of a YBCO HEB coupled to a 585 GHz double-slot antenna and a co-planar transmission line. The 1 μ m x 2 μ m HEB itself is at the intersection of the two tapers in the center of the picture. The width of the antenna arms is 175 μ m.

decreases for smaller bolometer volumes. The gain bandwidth of the HEB is determined by the time it takes to remove heat from electrons via electron-phonon scattering and the escape of phonons from the bolometer. The latter is the slower time scale and is determined primarily by the bolometer thickness, with thinner bolometers leading to faster response times. The first roll-off in the reported two-tiered bandwidth structure was interpreted as a consequence of the phonon escape time from the HEB, and the upper limit of the second plateau interpreted as caused by the electron-phonon relaxation rate. Time-resolved measurements⁷ of the electron-phonon relaxation rate in YBCO show a relaxation time $\tau = 1.5$ ps, leading to an upper IF bandwidth limit of $f_c = 1/2\pi\tau$ in excess of 100 GHz.

II. DEVICE STRUCTURE AND MEASUREMENT

Our HEB devices began with sputter-deposited (001)-oriented YBCO thin films nominally 100 nm thick covered with > 2 penetration depths (> 200 nm) of a gold overlayer, all on MgO substrates. A double-slot antenna and coplanar transmission line were then lithographically patterned and etched into the YBCO/Au using an Ar ion beam (see Fig. 1). A window over the area of the HEB was patterned, and the Au overlayer over the HEB was then removed using a non-aqueous iodine-based selective Au etch, which did not affect the superconducting transition temperature or width of the underlying YBCO film. The nominal dimensions of the HEB were 1 μ m (width) x 2 μ m (length) x 100 nm (thickness). The width and length dimensions were measured in an optical microscope. In practice, DC resistance measurements suggested that the thickness of the film was less than 100 nm, perhaps due to some etching into the YBCO film during the Au etch. Finished bolometers had room

Mark Lee is with Bell Laboratories – Lucent Technologies, 600 Mountain Ave., Murray Hill, NJ 07974 USA.
Richard C.-T. Li is affiliated with the University of Virginia, Dept. of Physics, McCormick Rd., Charlottesville, VA 22903 USA.

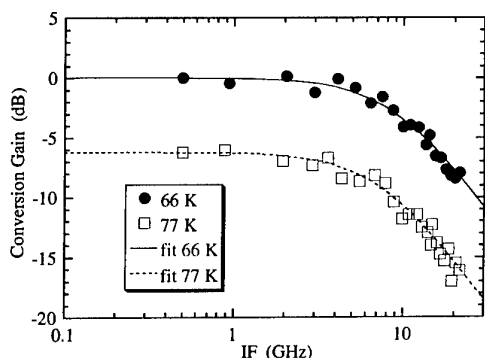


Fig. 2: Measured conversion gain bandwidth at two sample temperatures for 115 GHz LO frequency using $1.5 \mu\text{W}$ LO power. Data are normalized to the low-frequency gain at 66 K. The fits are simple Lorentzians, with -3dB points of 9 GHz (66 K) and 7.5 GHz (77 K).

temperature resistances of 100 to 300Ω , transition widths of 1 to 2 K at around 85 K, and nominal critical currents at 77 K of $\sim 0.1 \text{ mA}$.

All measurements were done quasi-optically. The HEB devices were clamped onto a high-resistivity silicon hyper-hemispherical lens and heat sunk to a copper block. Sample temperature could be varied from 66 to 93 K. For direct heterodyne conversion gain measurements, two tunable Gunn oscillators (115 to 145 GHz) were used. The LO was kept fixed at 115 GHz, and the rf source was varied. Attenuators kept the total incident power $< 1 \text{ mW}$, with the rf power typically $\sim 10 \text{ dB}$ below the LO power. At 585 GHz LO frequency, homodyne response was measured by using a Schottky diode in a corner cube to generate amplitude modulated sidebands onto the beam from a molecular gas laser. Sidebands could be detuned up to 20 GHz off the laser line. Sideband power (1 to $10 \mu\text{W}$) was calibrated using a known Schottky diode receiver. In both cases, the intermediate frequency generated by the HEB was amplified using a cooled microwave amplifier with bandwidth of 20 GHz.

III. DATA AND ANALYSIS

Fig. 2 shows the measured conversion gain bandwidth at two different temperatures for one of the YBCO HEBs using $1.5 \mu\text{W}$ of LO power at 115 GHz. The rf power was kept at $0.1 \mu\text{W}$ and was tuned upward from the LO. Data are normalized to the low-frequency gain at 66 K. Estimating a coupling loss of 9 dB from pumped and unpumped I - V curves, [8] the device conversion gain is to is approximately $\sim 9.5 \text{ dB}$ at the lowest frequencies at 66 K. The conversion gain is slightly lower and has a lower frequency roll-off at the higher temperature. At both temperatures, the data are well fit by a simple Lorentzian with -3 dB roll-off of 7.5 GHz at 77 K and 9 GHz at 66 K. Fig. 3 shows similar gain bandwidth data in a homodyne measurement at 585 GHz LO frequency. The device conversion gain here is $\sim 11 \text{ dB}$ at the lowest frequency, with a -3 dB point of 7 GHz.

Fig. 4 shows the IF output vs. DC bias current data from a Y-factor noise temperature measurement. The LO

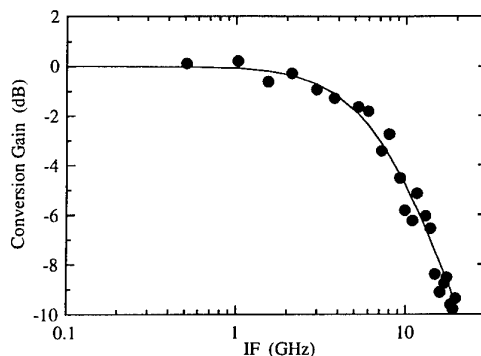


Fig. 3: Homodyne conversion gain bandwidth at 66 K for 585 GHz LO frequency using $1 \mu\text{W}$ LO power. Data are normalized to the low-frequency gain at 66 K. The fit is a Lorentzian, with -3dB point of 7 GHz.

is 585 GHz. The rf signal is derived from one of two blackbody radiators, one at room temperature (300 K) and the other at 77 K. The IF signal is amplified by a cooled 2.0 GHz tuned low-noise amplifier (noise temperature of 45 K operating at 77 K) and measured with a tuned power meter. Note that the IF output of the bolometer mixer is zero for any bias smaller than the critical current. The inset shows the time-domain IF power signal when the rf is chopped between the two blackbodies at 35 Hz. The DC bias is set to maximize the signal. From the difference in the IF output power, we obtain the double-sideband noise temperature at the input of the device to be about 3600 K.

Fig. 5 shows the calculated two-tiered conversion gain bandwidth for a YBCO HEB with the nominal physical dimensions of our device, using the model of Ref. 6. The low-frequency plateau shows a maximum device conversion gain of $\sim 12 \text{ dB}$, dropping to $\sim 50 \text{ dB}$ at the second plateau. The first, lower frequency roll-off reflects the phonon escape rate from the film to the substrate heat sink. Because of the relatively large (100 nm) nominal thickness of the films used, the slow phonon escape lifetime leads to an f_l of only 55 MHz. The

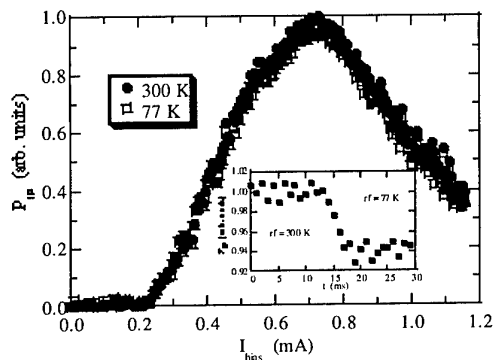


Fig. 4: Hot/cold load response of HEB mixer at 585 GHz LO. Shown is the output power at 2.0 GHz IF using rf blackbody sources at 300 K and 77 K. Inset: time domain response to a chopped 300 K / 77 K rf source.

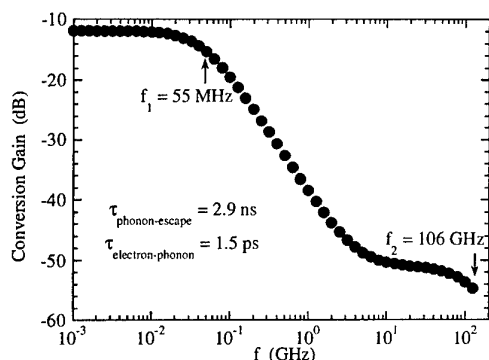


Fig. 5: Numerical calculation of YBCO HEB conversion gain bandwidth using the model of Ref. 6 and the nominal physical dimensions of our device. The phonon escape time is set primarily by the film thickness. The electron-phonon scattering time is taken from the reported data of Ref. 7.

second, higher roll-off f that is due to electron-phonon scattering is well beyond the measurement bandwidth of our experimental apparatus.

Clearly, the data measured for our HEB mixer is inconsistent with the numerical results. First, the maximum device conversion gain measured is larger by roughly a factor of two than that predicted. More importantly, the roll-off frequency measured is over 100 times higher than the f calculated based on the HEB's nominal dimensions. The larger conversion gain can be explained by an effective device thickness somewhat smaller than the nominal dimension. However, because the roll-off frequency increases approximately linearly with a decrease in film thickness in this model, there is no way the effective thickness can be made small enough to account for the factor of 100 discrepancy in 3 dB frequency between model and measurement. A 1 nm effective film thickness is smaller than the unit cell lattice constant in the (001) direction and would not superconduct at all. Some mechanism other than phonon escape is thus responsible for the observed roll-off frequency, but what this might be is currently unknown.

IV. CONCLUSION

Superconducting YBCO hot-electron bolometers have been demonstrated for use as far-infrared mixers operating near liquid nitrogen temperatures. These mixers have a device conversion gain as high as -9.5 dB, gain bandwidths near 10 GHz, and input noise temperatures around 3600 K at 585 GHz LO and 1 μ W pump power. The gain bandwidth is much higher than models of the HEB mixing predict, but the origin of the discrepancy is currently unknown.

Acknowledgement

The authors would like to express their acknowledgements to Prof. R. M. Weikle of the University of Virginia for useful technical advice and to Prof. C.-B. Eom of Duke University for synthesizing the YBCO thin films. Work at the University of Virginia

was supported in part by the U. S. National Science Foundation through grant ECS-9623893.

References

- 1 E. M. Gershenzon, G. N. Gol'tsman, I. G. Gogdize, Y. P. Gusev, A. I. Elant'ev, B. S. Karasik, and A. D. Semenov, *Sov. Phys. Supercond.* **3**, 1582 (1990)
- 2 J. Kawamura, R. Blundell, C. E. Tong, G. Gol'tsman, E. Gershenzon, B. Voronov, and S. Cherednichenko, *Appl. Phys. Lett.* **70**, 1619 (1997)
- 3 E. M. Gershenzon, G. N. Gol'tsman, Y. P. Gousev, A. L. Elant'ev, A. D. Semenov, and I. M. Pirogovskaya, *IEEE Trans. Magnetics* **27**, 1317 (1991)
- 4 M. Lindgren, M. A. Zorin, V. Trifonov, M. Danerud, D. Winkler, B. S. Karasik, G. N. Gol'tsman, and E. M. Gershenzon, *Appl. Phys. Lett.* **65**, 3398 (1994)
- 5 V. A. Trifonov, B. S. Karasik, M. A. Zorin, G. N. Gol'tsman, E. M. Gershenzon, M. Lindgren, M. Danerud, and D. Winkler, *Appl. Phys. Lett.* **68**, 1418 (1996)
- 6 B. Karasik, W. R. McGrath, and M. C. Gaidis, *J. Appl. Phys.* **81**, 1581 (1997)
- 7 F. Hegmann, D. Jacobs-Perkins, C.-C. Wang, S. H. Moffat, R. A. Hughes, J. S. Preston, M. Curre, P. M. Fauchet, T. Y. Hsiang, and R. Sobolewski, *Appl. Phys. Lett.* **67**, 285 (1995)
- 8 H. Ekström, B. Karasik, E. Kollberg, and S. K. Yngvesson, *Microwave Guided Wave Lett.* **4**, 253 (1994)

Technological Needs for European Space Agency's Microwave Limb Sounders

D. Lamarre, J. Langen, C.-C. Lin, L. Marchand, P. de Maagt, T. Narhi *

Abstract – Since they present good capabilities for the detection of important trace species for atmospheric chemistry, the European Space Agency (ESA) has, in recent years, investigated a number of limb sounding instrument principles. These feasibility studies have provided baseline concepts which have helped to grasp the main features of these instruments and to identify their critical aspects. A number of scientific and technical activities have then followed, dedicated to specific topics, from retrieval simulations to developments of antennas, calibration loads, mixers, support to campaigns, etc. To make observations in the upper troposphere and lower stratosphere (UTLS), where they are the most urgently needed, the ESA limb sounder concept is called MASTER (Millimetre-wave Acquisitions for Stratosphere/Troposphere Exchange Research), which counts five broad detection bands, hence five receivers, from 200 to 500 GHz. The main channels of MASTER for UTLS sounding, which detect in priority ozone, water vapour and carbon monoxide, are centered near 300, 325 and 345 GHz.

I. INTRODUCTION

ESA's strategy concerning earth observation is now spearheaded by its Earth Observation Envelope Programme (EOEP). The programme is managed and executed within the Directorate of Applications. Within EOEP, work related to the definition of future earth observation missions takes place mainly at the European Space Research and Technology Centre (ESTEC, The Netherlands), and is performed by the Future Programmes Department.

A candidate for a new mission can be classified either as a Core Earth Explorer, an Opportunity Earth Explorer, or an Earth Watch. An Earth Explorer is defined as a scientific or demonstration mission, deemed to be financed primarily by ESA, possibly aided by other space agencies, while an Earth Watch has a commercial or operational potential and assumes a large financial contribution from an interested partner, such as the private sector or the European Union. A proposed scientific mission which would require substantial funding, such as many instruments aboard a large platform, would be proposed as a Core Explorer. A small scientific mission, requiring technology deemed readily available, would be presented as an Opportunity Explorer. The selection process for the implementation of Explorers involves and depends mainly upon the European and Canadian scientific community. The scientists themselves identify which missions they want to see implemented, while ESA acts as a facilitator and

provides technical expertise and recommendations concerning programmatic aspects.

At the time of writing of this paper, a Call for Ideas for Core Earth Explorers has been initiated by ESA. It is expected that a proposal will be made by the atmospheric chemistry community for a new mission which could include a millimetre-wave limb sounder, and possibly also submillimetre-wave and far infrared (or THz) limb sounders. The time frame for the launch of such a next Core Explorer is not earlier than 2008.

Table 1: Instrument Requirements

Band	MASTER		
	Spectral Range (GHz)	Noise Temp. (K)*	Vertical Resolution (km)**
A	200.5-209	4000	4.5
B	294-305.5	6000	3
C	316.5-325.5	6000	3
D	342.25-348.75	6000	3
E	497-506	6000	2

Spectral resolution: 50 MHz nominal

3 MHz in specific intervals

*: SSB detection, with ca 30 dB image attenuation

**: Interval, at the limb, containing 85% power

Band	SOPRANO		
	Spectral Range (GHz)	Noise Temp. (K)*	Vertical Resolution (km)**
A	497.5-504.75	5000	4
B	624.6-629	6000	4
D	952-955	10000	4

Spectral resolution: 3 MHz nominal

0.3 MHz in specific intervals

*: SSB detection, with ca 20 dB image attenuation

**: Interval, at the limb, containing 85% power

Targeted OH Line	PIRAMHYD	
	Spectral Range (GHz)	Noise Temperature (K)*
@ 2.5 THz	2508.5-2511.5	20000
	2512.8-2515.8	20000
or @ 3.5 THz	3532-3535	30000
	3540-3545	30000
	3549-3552	30000

Vertical resolution: 2 km (FWHH at the limb)

Spectral resolution: 1 MHz

*: SSB detection, with ca 20 dB image attenuation

*: Authors are with the European Space Research and Technology Centre (ESTEC) of the European Space Agency (ESA): ESTEC/ESA, Keplerlaan 1, 2200 AG Noordwijk ZH, The Netherlands

II. INSTRUMENT CONCEPTS

During the last decade, ESA has conducted a considerable number of activities concerned with microwave limb sounding for atmospheric chemistry: Scientific studies, instrument studies, technology breadboarding, support to airborne measurement campaigns. Many activities are currently on-going and others are planned in the near future. This interest is justified by the capability of microwave limb sounding to provide concentration profiles of important species with high vertical resolution, and that down to relatively low altitudes.

ESA has defined three microwave limb sounder concepts: MASTER (Millimetre-wave Acquisitions for Stratosphere/Troposphere Exchange Research), SOPRANO (Submillimetre-wave Observations of Processes in the Atmosphere Noteworthy for Ozone), and PIRAMHYD (Passive Infra-Red Atmospheric Measurements of HYDroxyl). These are passive instruments, ie they simply detect the radiation emitted

relying on the use of frequencies at the upper end of the millimetre-wave range, the high vertical resolution required for the retrieval of species in the upper troposphere translates into an antenna with a large diameter. Figure 2 shows an artist's impression of MASTER. The large 2.2 m diameter of the antenna is oriented along the vertical. MASTER is a big instrument, weighing about 300 kg, and consuming about 350 W of power. It operates at room temperature.

Stratospheric depletion of ozone is the main topic addressed by SOPRANO measurements. Ozone, chlorine monoxide, hydrogen chloride and nitric oxide are the main target species. SOPRANO is shown on figure 3, and its main requirements are also listed in table 1. The higher frequencies and the more relaxed vertical resolution requirements allow for a much smaller antenna, with a vertical diameter of only 1 m. The instrument is still big, weighing about 150 kg, and consuming about 300 W. At the time of the last SOPRANO study, it was still deemed necessary to

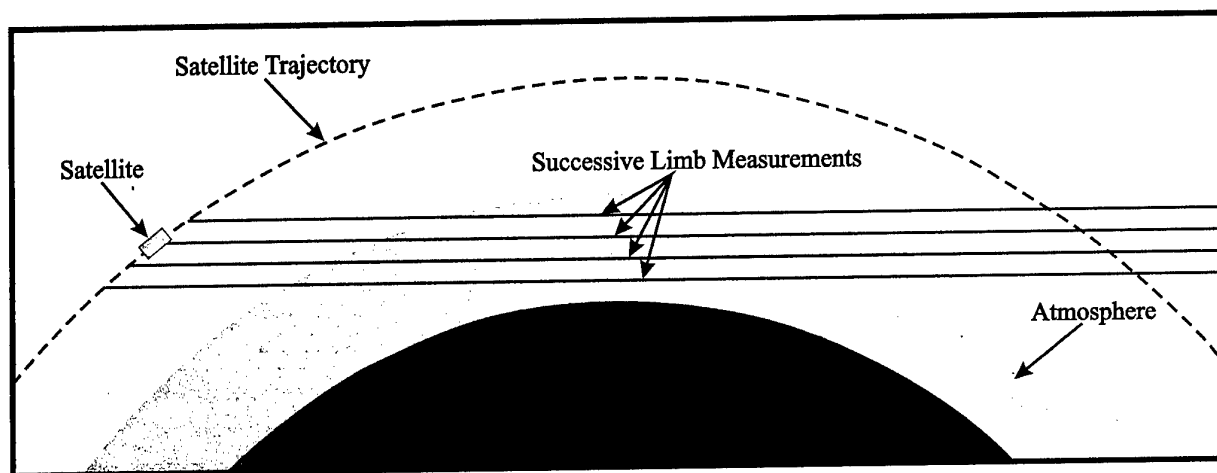


Figure 1: Limb Sounding Geometry

by the atmosphere itself. The geometry of limb sounding is shown on figure 1. The instruments observe the atmosphere tangentially, against the deep space background. MASTER, SOPRANO and PIRAMHYD have a single instantaneous viewing direction, so that successive measurements have to be taken to gather sufficient information from all desired altitudes. A single measurement gives mostly information on the lowest height region viewed by the line of sight (LOS). Figure 1 shows a special case where the timing of the scan is such that successive measurements have parallel LOS, which yields a vertical locus of tangent points. Generally, limb sounders may adopt different scan patterns, so that tangent points of a given elevation scan may not at all rest close to a vertical line.

MASTER targets mainly the detection of water vapour, carbon monoxide and ozone in the UTLS. High resolution maps of these species are needed for appropriate modelling of atmospheric effects related to global changes, such as radiative forcing, exchanges between the stratosphere and the troposphere, and upper tropospheric chemistry. MASTER is shown on figure 2, and its main requirements are listed in table 1. Although

actively cool its D receiver to 80 K to achieve the required sensitivity. Note that band A of SOPRANO is covered by band E of MASTER. Should both instruments be destined to fly on the same platform, some simplifications could be envisaged.

ESA investigations have been relatively modest on the subject of hydroxyl detection. This radical is a main player in many chemical reactions, and considerable insight into atmospheric processes would be gained by providing measurements of hydroxyl in the UTLS. Unfortunately, measurements below 20 km are very difficult, since, as one goes to lower altitudes, water vapour renders the atmosphere increasingly opaque, and since the hydroxyl concentration itself diminishes.

Three quite different instrument principles can be considered for PIRAMHYD. One could attempt to detect hydroxyl either using a Fabry-Perot interferometer, a microwave receiver, or a Fourier transform spectrometer. Each technique has, as always, its advantages and disadvantages. In the case of the microwave receiver, heterodyne detection offers good performance even at 300 K operating temperature, with high spectral

resolution and relatively good spectral coverage. However, the local oscillator is quite complex. Table 1 also contains the requirements for the microwave receiver version of PIRAMHYD. Still, a choice has to be made between detection of hydroxyl either at 2.5 THz or 3.5 THz. For spectroscopic reasons the 3.5 THz version is preferred, if technology allows [ref.1].

The priority having been given to MASTER and SOPRANO in the last years, the microwave version of the PIRAMHYD instrument has not yet been the subject of comprehensive ESA activities with the space industry.

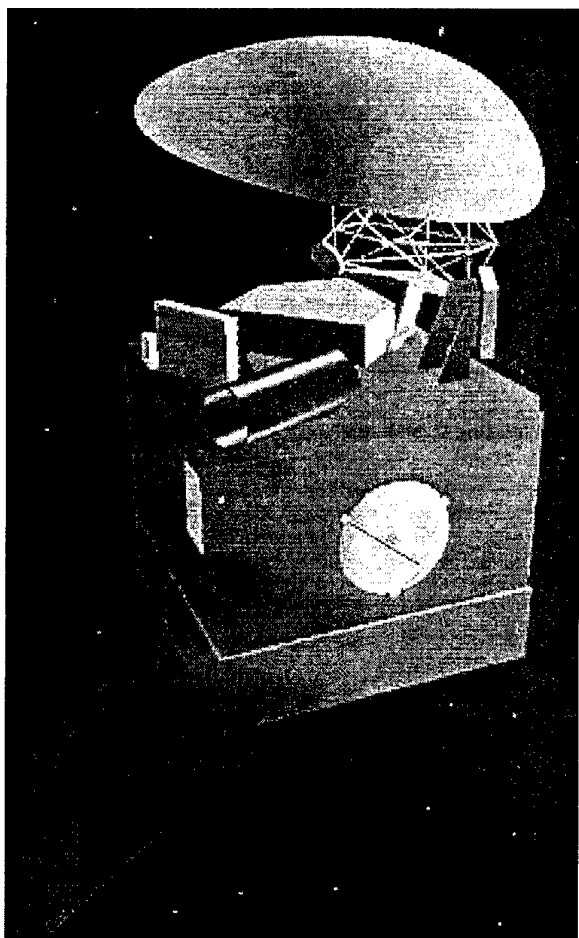


Figure 2: MASTER on a Small Satellite [ref.6]

ESA involvement in this domain has been limited to scientific studies and to the development of a 2.5 THz mixer [ref.3]. Hence, the rest of the discussion will be limited to sub-THz, ie MASTER and SOPRANO. These two instruments are quite similar. Putting aside the more common subsystems such as pointing mechanism, computer, coolers, and power supply, MASTER and SOPRANO have three main parts: Antenna, receivers, spectrometers.

III. ANTENNA

The work on the antenna subsystem is typical of the way ESA has conducted its investigations on these limb sounders. Eight years ago, the first instrument studies started on sets of specifications which were based on various assumptions, many of them concerning the

sensitivity of retrieved profile accuracies to instrumental parameters and instrumental errors. These industrial activities were then followed by scientific investigations involving retrieval simulations, the latter using as inputs many results of the industrial studies, which then yielded refined sets of specifications for the instruments. This process was iterated once more, ie other industrial studies [ref.5-8] followed by other scientific studies [ref.9-12].

It was assumed, at the beginning of this process, that the surface accuracy of the main reflectors of the antennas had to be quite high, and that only very low side-lobes could be tolerated. The measurement of the antenna pattern was deemed important but not critical. It turned out, however, that the accuracy of the manufactured surface and the level of the side-lobes can be relaxed, as long as the antenna pattern is precisely measured and that the antenna shape, of course, does not change afterwards. This relaxed requirement on side-lobes offers the degree of freedom of weakening the illumination taper, with the goal of either reducing the antenna size or reducing the beamwidth, the latter of which would improve the precision of the retrieved profiles. The emphasis in the development of this subsystem has thus shifted from a difficult manufacturing tolerance to a serious stability requirement, and from a highly efficient beam to a highly accurate measurement of the antenna pattern.

The stability requirement for the antennas is on the order of 10 microns peak to peak. This means, basically, that the shape of the reflectors, once in orbit and taking measurements, shall not differ by more than 10 microns from the shape that the reflectors had when the antenna patterns were being measured in the test facility on earth. This is deemed feasible with a reflector made of CFRP (carbon fibre reinforced polymer). A study [ref.5] concluded surprisingly that partial shielding might be preferable to complete shielding of the reflectors from sun illumination, since the former could translate into low temperatures which would distort the reflector more than thermal gradients caused by the latter.

Retrieval simulations [ref.9-12] were done to assess the required accuracy of the measurement of the antenna patterns. It turns out that an accuracy of -50 dB is needed, relative to the boresight. This requirement assumes that any noise rectification occurring at the -50dB level is properly taken out. If not, the accuracy requirement is then -65 dB. This is difficult but possible. Currently, no facility exists in Europe to perform these measurements on 2 m diameter antennas.

IV. RECEIVERS

As shown on the MASTER and SOPRANO requirements in table 1, the wide bandwidths of these instruments constitute a predominant feature. Another one is single side-band detection (SSB). This mode has been preferred over double side-band detection (DSB) to avoid the problems of characterization and stability of the relative response. Although the requirements of table 1 do not seem outrageously demanding, their simultaneous achievement remains to be demonstrated. Using room temperature receivers, except for receiver D of SOPRANO (at 80 K), it is difficult to reach the desired

sensitivity and image rejection over such wide bandwidths.

The receiver subsystems can be broken down into mixer (including feedhorn), quasi-optics (QO), local oscillator (LO), and intermediate frequency (IF) amplifier. Here follows a summary of the main conclusions of the various tradeoff studies. *Mixer:* Schottky diodes are chosen for

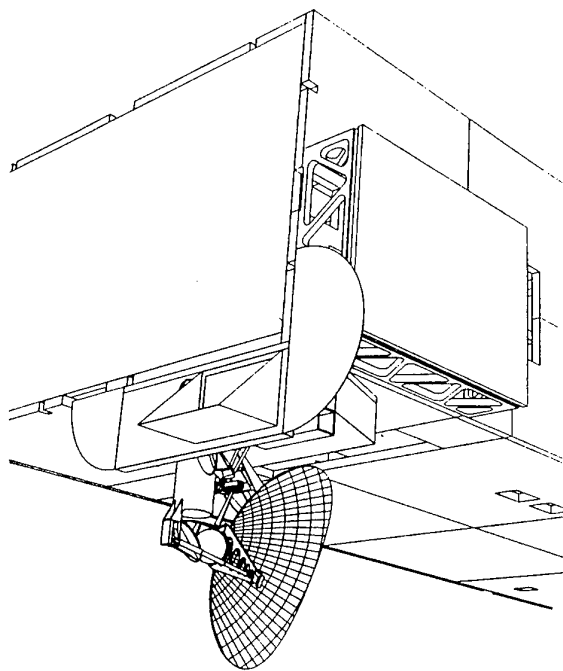


Fig.3: SOPRANO on ENVISAT-Type Platform [ref.7]

operation at room temperature. For reliability, reproducibility, and quality control, whisker contacted diodes are avoided where possible. Planar technology is preferred. Waveguide mixers using corrugated feedhorns are still preferred over open structure mixers. The configuration of the receiver is mainly determined by the type of mixer, ie either fundamentally-pumped (FP) or sub-harmonically pumped (SHP). At the time of completion of the instrument studies, however, an SHP configuration was deemed premature for receiver D of SOPRANO (950 GHz). If FP still keeps a performance edge over SHP, the latter is now preferred, since, among others, it simplifies the LO and its injection. *QO:* To perform frequency separation, single side-band rejection, and LO injection (for FP), polarizers and various kinds of dichroic plates can be used. For SOPRANO, where bandwidths are not as wide, and where image rejection requirements are less stringent, Martin-Puplett interferometers can also be considered. Whatever the solution, the combination of the requirements of low loss and high image band rejection results in a high IF. *LO:* Solid state oscillators are possible over this frequency range, and so consist of a Gunn diode source and multipliers (eg based on heterostructure barrier varactors). Phase locked loops are used. *IF amplifier:* Because of the high frequency range, 15 to 35 GHz, and of the poor conversion efficiency of the mixer, even low noise amplifiers (eg based on high electron mobility

transistors) contribute significantly to the overall system noise temperature.

A note concerning the calibration of the instrument: A high radiometric accuracy is required, ie about 0.5 K in absolute brightness temperature. To achieve this, a two-point characterization method is required, where deep space and an internal calibration blackbody constitute respectively the cold and hot loads. A switching mirror allows to take characterization measurements in three ways: Deep space viewed through the whole antenna, deep space viewed through the switching mirror, blackbody viewed through the switching mirror. The combination of antenna reflector temperature readings and characterization measurements yield the calibration information. The current design of the blackbody relies on the principle of a cone-shaped cavity and specular reflection [ref.3].

V. SPECTROMETERS

The spectral requirements included in table 1 are achieved in a straightforward manner with acousto-optical spectrometers (AOS)[ref.3], except for the high resolution channels of SOPRANO, which can be taken care of by either digital auto-correlation spectrometers [ref.4] or chirp-transform spectrometers [ref.2]. However, if an AOS offers excellent performance, its 2.2 GHz bandwidth limitation necessitates a large number of units and considerable IF circuitry. Development of a spectrometer which would analyse simultaneously a 12 GHz bandwidth could greatly simplify the instruments and reduce mass and power consumption.

VI. CURRENT AND PLANNED ACTIVITIES

ESA is currently pursuing several activities related to needed technologies for microwave limb sounders. KASIMIR aims at achieving a competitive 650 GHz mixer performance with planar diodes and an open structure architecture. Related to KASIMIR are activities related to improving quality and process control in diode fabrication. ADMIRALS aims at fabricating and testing a MASTER flight representative antenna, both mechanically and electromagnetically representative, and upgrading an existing antenna test facility to allow its use up to 500 GHz. In MARSCHALS, an airborne simulator of MASTER will be fabricated, with the aim of performing measurement campaigns from either a stratospheric balloon or the russian Geophysika aircraft. These measurements would demonstrate the capability of MASTER to retrieve concentration profiles with the desired accuracy and vertical resolution in the UTLS. A technology breadboarding activity has been started to demonstrate the feasibility of the MASTER receiver B requirements.

In the near future, ESA will initiate activities on wide-band (12 GHz) spectrometers and on the development of mixer diodes. The latter counts in its objectives a contribution towards a competitive european capability. Upon reception of proposals for the Call for Ideas for Core Earth Explorers, it is possible that further activities related to microwave limb sounding for a future atmospheric chemistry mission will be defined.

VII. CONCLUSION

The context and the main conclusions of the ESA activities related to microwave limb sounding have been presented. Emphasis has been put on sub-THz investigations, ie for MASTER and SOPRANO. The main technological challenges still remaining concern the accurate measurement of the antenna pattern, the stability of the antenna structure, and the simultaneous achievement of receiver requirements: Sensitivity, bandwidth and image rejection. These challenges and the demonstration of limb sounding capabilities are being addressed by ESA.

Acknowledgement

The authors would Chih-I Lin and Victoria Ichizli (T.U. Darmstadt) for reviewing early material for this paper.

References

1. "PIRAMHYD Retrieval Study: OH Profiling by Far Infrared Limb Sounding", Final Report, ESA CR(P) 4195, by SERCO, SRON, IROE-CNR, RAL, DLR, 1998
2. "Submillimetre-wave Limb Sounder Technology Breadboarding", Summary Report, ESA Contract 8742/90/NL/PB(SC), by DASA, T.U. Chalmers, U. Bremen, Observatoire de Paris-Meudon, RPG, RAL, U. Bern, 1995
3. "Submillimetre-wave Limb Sounder Technology Breadboarding", Summary Report, ESA Contract 8742/90/NL/PB, by DASA, T.U. Chalmers, U. Bremen, Observatoire de Paris-Meudon, RPG, RAL, U. Bern, AEA Technology, MMS, Max Planck Institute for Aeronomy, 1999
4. "Digital Autocorrelation Spectrometer Study & Design", Final Report, ESA Contract 11211/94/NL/CN, by Omnysis Instruments, 1996
5. "MASTER Extension Study", Executive Summary, ESA CR(P) 4181, by MMS UK, MMS F, RAL, Observatoire de Paris-Meudon, 1998
6. "MASTER 2nd Extension Study", Executive Summary, ESA Contract 11159/94/NL/CN, by MMS UK, 1999
7. "Limb Sounder Pre-Phase A Study Extension", Executive Summary, ESA CR(P) 3971, by MMS UK, RAL, 1995
8. "MASTER Pre-Phase A Extension", Executive Summary, ESA CR(P) 4136, by Alenia Aerospazio, DSS and RPG, 1994
9. "SOPRANO Extension Study", Executive Summary, ESA Contract 10612/93/NL/SF, by Daimler-Benz Aerospace, RPG, Observatoire de Meudon, 1996
10. "Study on UTLS Sounding", Final Report, ESA Contract 12053/97/NL/CN, by SERCO, U. Bremen, RAL, U. Berne, 1998
11. "The Retrieval of Data from Submillimetre-wave Limb Sounding", Final Report, ESA Contract 11979/NL/CN, by U. Bremen, RAL, U. Berne, 1999
12. "Critical Assessments in Millimetre-wave Limb Sounding", Draft Final Report, ESA Contract 13348/98/NL/GD, by SERCO, U. Bremen, RAL, not released yet
13. "An Extension to the Study on The Retrieval of Data from Submillimetre-wave Limb Sounding", Draft Final Report, ESA Contract 11979/NL/CN, by U. Bremen, U. Bordeaux, not released yet

A Broadband Low Noise Heterodyne Receiver at 2.5 THz

K. Huber, H. Brand, L.-P. Schmidt

Abstract—A 2.5 THz low noise heterodyne receiver with an IF bandwidth of about 7 GHz operating at room temperature is presented. Its main component is an open structure Schottky diode mixer with a substrateless Schottky diode designed and fabricated at the IHFT Darmstadt. The weak IF-signals are amplified by a noise-matched IF-amplifier in a frequency range from 6 to 13 GHz, covering the emission lines of several important molecules involved in the stratospheric ozone chemistry. The local oscillator signal (provided by a CO₂-laser-pumped methanol FIR-laser) is fed to the mixer together with the received signals via a Fabry-Perot type diplexer, which allows for significantly reduced signal loss compared to commonly used Martin-Puplett diplexers especially at the band edges. System noise temperatures as low as 16000 K (DSB) have been achieved up to the moment.

I. INTRODUCTION

The 2.5 THz heterodyne receiver setup is depicted schematically in Fig. 1. It consists of a local oscillator subsystem, quasi-optical circuitry for calibration and diplexing and an open structure Schottky mixer combined with a noise matched IF-amplifier.

The local oscillator laser described previously [1] is capable of delivering a maximum output power of about 50 mW at 2522.8 GHz when powered by a 20 W CO₂-laser beam ($\lambda \approx 9 \mu\text{m}$).

K. Huber, H. Brand and L.-P. Schmidt are with the Lehrstuhl für Hochfrequenztechnik, Universität Erlangen-Nürnberg, Cauerstr. 9, D-91058 Erlangen

The main objectives of the radiometer are broadband imaging radiometry as well as spectroscopy of molecules involved in the stratospheric ozone chemistry. Both areas of application mentioned above benefit from a large IF-bandwidth, by a shorter measurement time in the broadband case and by a larger amount of specific emissions detectable in the spectroscopy application (for example OH, H₂O and O₃).

Thus, special care has been taken on broadband noise match of the first amplifier as well as on broadband operation of the diplexer.

II. DIPLEXER

Fig. 2 shows a photograph of the Fabry-Perot diplexer. It consists of two total reflectors, one of them being a refocusing mirror, and two partial reflectors. As most of the dielectric materials commonly used as beamsplitters in millimeter wave systems are quite lossy at 2.5 THz, wire grids have been used as partially reflecting mirrors. The tungsten wires have a diameter of 10 μm and a grid spacing of 50 μm and were fabricated at the mechanical workshop of the "Lehrstuhl für Hochfrequenztechnik" (LHFT).

The free spectral range (FSR) of the diplexer has been chosen to be approximately 1.88 GHz, thus the receiver IF bandwidth limited by the mixer-amplifier chain is split

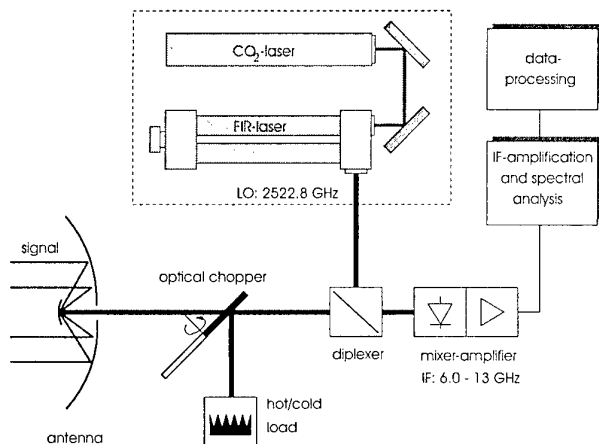


Fig. 1. Simplified schematic view of the radiometer

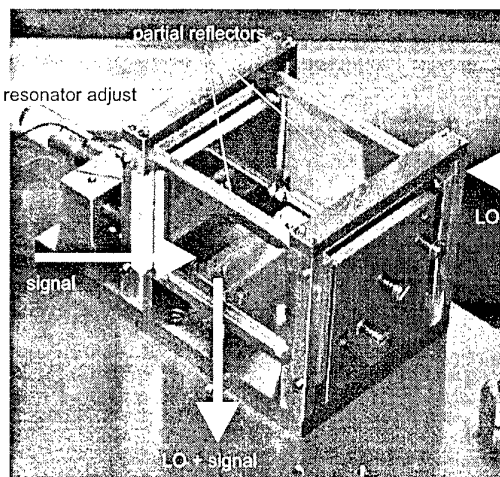


Fig. 2. Photograph of the 2.5 THz Fabry-Perot diplexer

into four subbands with center frequencies of 6.6, 8.4, 10.3 and 12.2 GHz, covering the emission spectra of various molecules involved in the stratospheric ozone chemistry [2]. For continuous covering of the entire receiver band, as desirable in broadband radiometry applications, the FSR of the Fabry-Perot would have to be increased (i. e. the dimensions of the diplexer have to be decreased) or a Martin-Puplett type diplexer must be used.

The LO-path loss has been measured to be about 4 dB whereas the signal-path loss is only about 0.5 dB. These values are slightly worse than predicted by theory, which is assumed to be due to the preceding transformation of the LO-beam and the resulting beam distortions and due to non-ideal adjustment of the diplexer.

III. MIXER-AMPLIFIER COMBINATION

At frequencies in the Terahertz or far infrared (FIR) regime the junction capacitance of mixer diodes has to be kept well below 1 fF in order to provide a good conversion efficiency. This means anode diameters of $0.5 \mu\text{m}$ or even less have to be realized. As the bias current necessary for optimum conversion is not affected by the diode area, the current density inside the junction rises with decreasing anode diameters and reaches values of several thousand A/mm^2 . Measurements of the noise contribution of small area Schottky diodes have proven that the available noise power of forward biased diodes exceeds the value predicted by the classical formula by far [3]. The so called excess noise is assumed to be mainly due to hot electrons and interfacial traps [4]. Fig. 3 shows the noise temperature of an $0.5 \mu\text{m}$ substrateless Schottky diode compared with the noise temperatures of an ideal

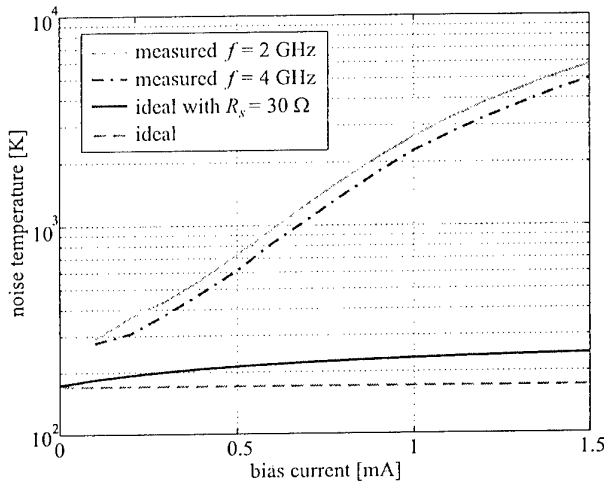


Fig. 3. Measured noise temperatures of an $0.5 \mu\text{m}$ substrateless Schottky diode compared to the noise temperature of an ideal Schottky diode without and with a series resistance of 30Ω , respectively

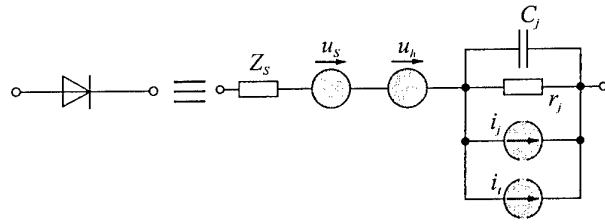


Fig. 4. Modified equivalent circuit of the Schottky diode

Schottky diode without series resistance and with a series resistance of 30Ω , respectively.

Based on the measurement results, a modified model for the Schottky diode according to Fig. 4 has been derived and implemented in a harmonic balance simulation of the mixer (with HP microwave design system). In the equivalent circuit Z_s is the complex impedance of the diode substrate, C_j is the bias dependent capacitance and r_j the dynamic resistance of the junction. The noise sources u_s , u_h , i_j and i_t represent the thermal noise of the series resistance, the hot electron noise, the shot noise and the trap noise, respectively. The values of the unknown quantities u_h and i_t have been derived by least squares fits of various noise power measurements of substrateless diodes with anode diameters of $0.5 \mu\text{m}$ and epi-layer doping concentrations of $3 \cdot 10^{17} \text{ cm}^{-3}$.

It has been found, that the optimum diode bias current ranges between $150 \mu\text{A}$ and $300 \mu\text{A}$ depending on both the available LO power and the diode noise parameters.

The mixer diode, a substrateless Schottky diode fabricated by the IHFT in Darmstadt, has been soldered directly to the mixer block. The 4λ antenna is connected to the amplifier via a 90° bend and a 1.5 mm horizontal wire section (see Fig. 5).

The resulting IF path of this configuration is extremely short and thus eases a broadband noise match of diode and amplifier.

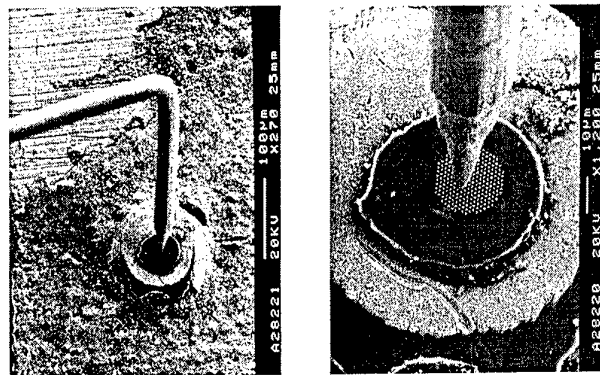


Fig. 5. SEM photographs of a contacted diode

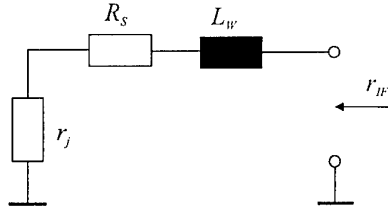


Fig. 6. Equivalent circuit of diode and whisker antenna at IF frequencies

In Fig. 6, the equivalent circuit of the diode including the whisker antenna at IF frequencies is depicted. The element values are:

- diode and whisker series resistance $R_S = 30 \Omega$
- junction resistance at optimum operating point $r_j = 300 \Omega$
- whisker inductance $L_W = 1.5 \text{ nH}$

As the resulting IF-impedance of the whiskered diode is far from a value of 50Ω , the noise contribution of commercially available 50Ω amplifiers exceeds the value given in their datasheets when connected directly to the mixer. Instead of adding a passive IF-transformer between the mixer and a commercial 50Ω amplifier, a noise-matched, two stage, uncooled HEMT-amplifier with FHX45X chips (Fujitsu) with an integrated bias supply for the mixer diode has been designed. Fig. 7 shows a photograph of the mixer-amplifier combination with the adjustable rooftop of the mixer's corner cube antenna and the integrated bias supply circuit.

In Fig. 8 the simulated and measured effective noise temperatures of the amplifier are shown. As it is difficult to measure the noise figure of the amplifier connected to the mixer, the amplifier noise for a source impedance r_S of 50Ω has been simulated and compared to the measured

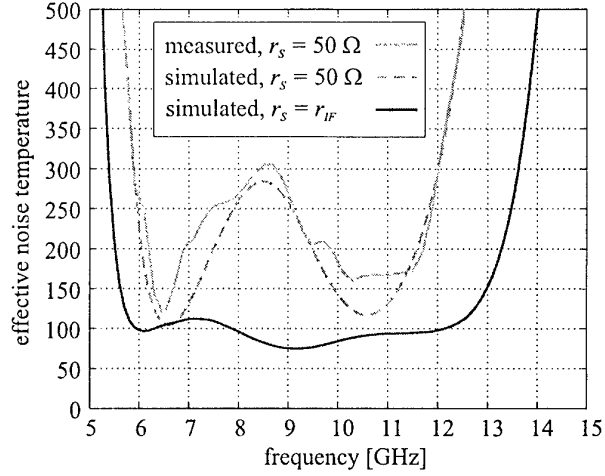


Fig. 8. Noise temperature of the IF-amplifier

values for this source impedance. The simulation of the actual noise temperatures of the amplifier connected to a source with $r_S = r_{IF}$ indicates values of about 100 K within a frequency range of 6 to 12.5 GHz.

IV. SYSTEM PERFORMANCE

In Fig. 9 the measurement setup for the determination of the DSB noise temperature of the system is displayed. The LO passes a variable attenuator and the Fabry-Perot diplexer and is then focused on the corner cube antenna of the mixer. The signal path is continuously switched between a hot and a cold load, the resulting IF-signal is then amplified, filtered and rectified by a diode detector. From the ratio between dc voltage V_{dc} and ac voltage \hat{V} and the corrected effective noise temperatures of the hot and cold load at 2.5 THz (T_h^* , T_c^*) the system noise temperature is calculated.

$$T_{sys} = (T_h^* - T_c^*) \cdot \frac{V_{dc}}{2 \cdot \hat{V}} - \frac{T_h^* + T_c^*}{2} \quad (1)$$

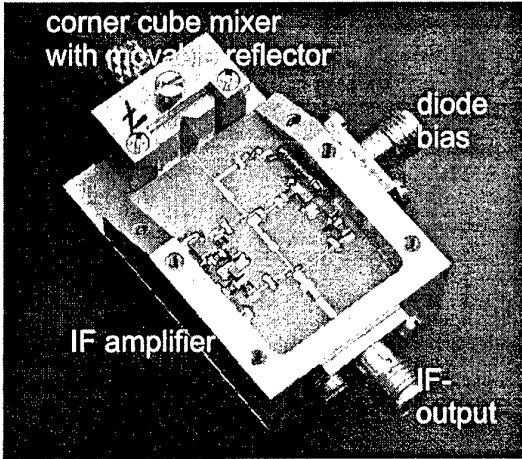


Fig. 7. Photograph of the mixer-amplifier combination

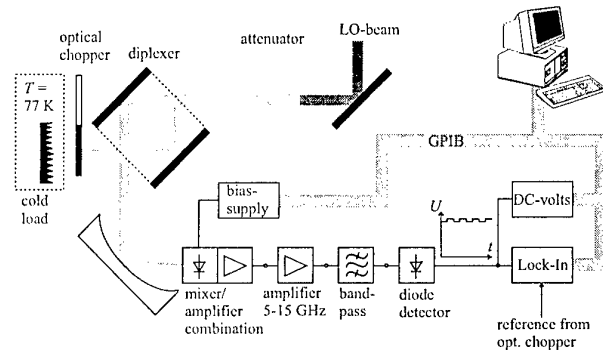


Fig. 9. Schematic view of the system noise temperature measurement setup

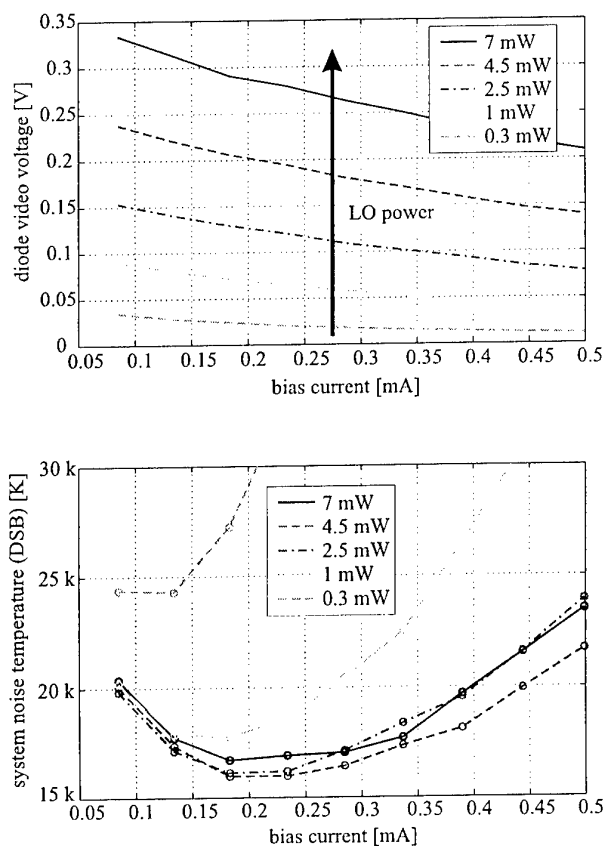


Fig. 10. Video voltage and DSB system noise temperature versus bias current for different LO power levels

Fig. 10 shows the results for the 8.5 ± 0.5 GHz channel of the receiver for different LO power levels which have been adjusted by various attenuators brought into the LO path. In the upper viewgraph the mixer diode video voltage is displayed, in the viewgraph below the DSB system noise temperature is shown.

The best noise temperature of about 16000 K could be achieved for a bias current of 0.2 mA just as expected from the harmonic balance simulation results. Another important result is that the optimum system performance is not achieved at the maximum LO power of about 7 mW (measured after the diplexer) but at a level of about 3-4 mW.

V. CONCLUSIONS

A 2.5 THz heterodyne receiver with a large IF bandwidth and a system noise temperature of 16000 K (DSB) has been presented. Key to the low noise operation at room temperature is the combination of an open struc-

ture mixer with a substrateless Schottky diode and a noise matched HEMT amplifier with an effective noise temperature as low as 100 K.

Diode improvement as well as optimization of the passive receiver components will certainly lead to a further decrease in system noise temperature.

ACKNOWLEDGMENTS

The authors would like to thank the technical staff of the LHFT for the fast and precise fabrication of mechanical components. The authors would also like to express their thanks to Dr. Chih-I Lin and the other members of the "Institut für Hochfrequenztechnik" of the Technical University of Darmstadt for supplying Terahertz Schottky diodes [5].

REFERENCES

- [1] M. Raum and K. Huber, "Standard design of SMMW laser ring resonators with optical pump beam guiding," in *Proceedings of the 6th IEEE International Conference on Terahertz Electronics*, (Leeds, United Kingdom), September 1998.
- [2] S. Miller, M. Birk, F. Schreier, and D. Hausamann, "Airborne far-infrared heterodyne remote sensing of stratospheric OH: A feasibility study," *International Journal of Infrared and Millimeter Waves*, vol. 13, no. 9, pp. 1241 - 1268, 1992.
- [3] G. Rehm, K. Huber, and S. Martius, "Excess noise in Schottky diodes for THz applications," in *Proceedings of the 6th IEEE International Conference on Terahertz Electronics*, (Leeds, United Kingdom), September 1998.
- [4] A. Jelenski, A. Grüb, V. Krozer, and H. L. Hartnagel, "New approach to the design and the fabrication of THz Schottky barrier diodes," *IEEE Transactions on Microwave Theory and Techniques*, vol. 41, pp. 549 - 557, April 1993.
- [5] C. I. Lin, A. Simon, and H. L. Hartnagel, "Fabrication of substrateless Schottky diodes for THz applications," in *Proceedings of the 4th International Workshop on Terahertz Electronics*, (Erlangen, Germany), September 1996.
- [6] K. Huber, R. Hillermeier, H. Brand, C. I. Lin, A. Simon, M. Rodriguez-Girones, and H. L. Hartnagel, "2.5 THz corner cube mixer with substrateless Schottky diodes," in *Proceedings of the 5th International Workshop on Terahertz Electronics*, (Grenoble, France), September 1997.
- [7] K. Huber, R. Engelbrecht, R. Hocke, M. Raum, H. Brand, S. Martius, and L.-P. Schmidt, "A broadband, low noise heterodyne receiver for stratospheric measurements at 2.5 THz," in *Proceedings of IGARSS 99*, (Hamburg), June 1999.
- [8] K. Huber, G. Rehm, and N. Richt, "Numerical simulation of the base impedance of long wire whisker antennas," *International Journal of Infrared and Millimeter Waves*, vol. 20, pp. 265 - 278, February 1999.

220 - 320 GHz Harmonic Mixer for a Full Band Sweep Vector Network Analyzer.

François Mattiocco, Matthew Carter, Bernard Lazareff.

Abstract –This paper presents the design and characterization of a fixed tuned 220 - 320 GHz harmonic mixer employing commercial Schottky beam lead diodes in an antiparallel configuration. A diplexer provides distinct ports and matching for the subharmonic LO (26-40GHz) and the IF (20 MHz) . The conversion loss was measured using a Gunn + tripler or quadrupler source calibrated with an absolute bolometer. We have built a 220 - 320 GHz full band sweep Vector Network Analyzer (VNA) using two WR3 waveguide couplers and three identical harmonic mixers (transmitter, reference, and receiver) pumped by two synthesizers (13-20GHz) followed by active doublers. The available dynamic range is 60 dBc/Hz over most of the band.

I. INTRODUCTION

The VNA is a versatile and highly sensitive instrument to test the devices and material, transmission and reflection properties in the microwave domain. Receiver fabrication for radio astronomy has involved the development of millimeter VNA which work in a frequency range up to 1THz. Above 200 GHz, the transmitter sources used in these systems are made with phase locked Gunn oscillators followed by reactive multipliers, carcinotrons [1], or harmonic resistive multipliers associated with synthesizers [2]. Gunn oscillators associated with multipliers and carcinotrons work up to 1 THz but are expensive. The Gunn phase locked band is narrow at each frequency, and the carcinotron life time is limited. The low cost resistive 220- 320 GHz harmonic multiplier or harmonic mixer we have built for the VNA can be pumped by sweep synthesizers over 40 % of the band.

II. MIXER BLOCK

The mixer block is split in two blocks in a plane perpendicular to the input waveguide as is shown in Fig.1. The input WR3 waveguide is formed using spark erosion. Two beam lead Schottky diodes are bonded with silver loaded epoxy in an antiparallel configuration on a suspended microstrip quartz substrate (shown in Fig. 2) where the following circuits are defined: the waveguide to microstrip transition, the RF and the LO matching, the low pass rejection circuits, and the bias ground return. Input LO and output IF access are made through a K connector.

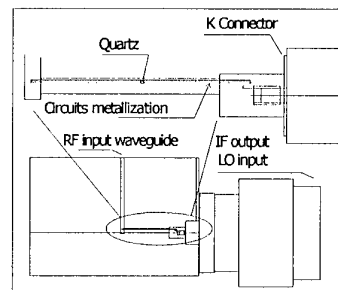


Fig. 1: Structure of the harmonic mixer bloc.

III. MIXER DESIGN

The WR3 waveguide to microstrip transition was designed using an analytic model [3]. Figure 3 shows the real and imaginary part antenna impedance at the microstrip input as a function of the antenna length L when the antenna width w is 0.24mm and the waveguide short is at 0.34mm from the antenna. The antenna length $L= 0.250$ mm gives an impedance real part between 45 and 50 Ohms in most of the waveguide band .

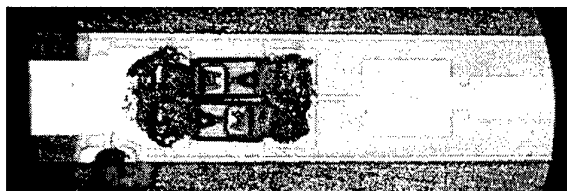


Fig. 2: Beam Lead diodes bonded on a 0.420 mm width quartz substrate of 80µm thickness.

The mixer was optimised for the best performance in the frequency range 250-300 GHz which corresponds to one of IRAM's receiver bands. The quartz substrate of 0.420 mm width was chosen to allow the integration of two diodes (0.2 x 0.15mm) and the ground return filter circuit. The first Longitudinal Section Magnetic mode (LSM) cutoff frequency given by the crystalline quartz and channel dimensions is 320 GHz [4].

Table 1: Beam lead diode specifications

Device	Cjo	CT	Rs
SBL-016	3 fF	8 fF	13 O

The matching and filtering of the RF, LO, IF and bias circuits were designed with a simple model using only the reactive and resistive impedance associated with the diode model. Table 1 shows the pair matched beam lead diode parameters [5]. The wire anode to connecting pad

F. Mattiocco, M. Carter and B. Lazareff, are with IRAM Institut de Radio Astronomie Millimétrique, 300 Rue de la Piscine, Domaine Universitaire 38406 Saint Martin d ' Heres France.

inductance L_s is 0.01 nH [6]. The differential resistance R_d which is given by the LO level was taken as a variable in the model.

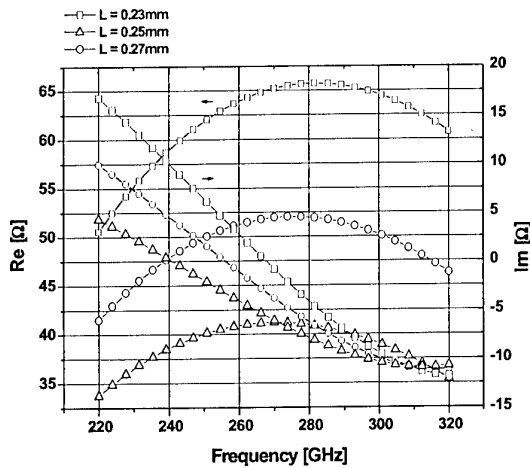


Fig. 3: Transition antenna impedance variation with the antenna length.

The RF return loss variations with the differential resistance R_d computed using the software Libra Series IV (Fig.4) are lower than -10 dB when $R_d < 150$ Ohms. The computation gives the RF to LO isolation of the order of 10 dB and the LO return loss stayed below -10 dB between 26 and 40 GHz.

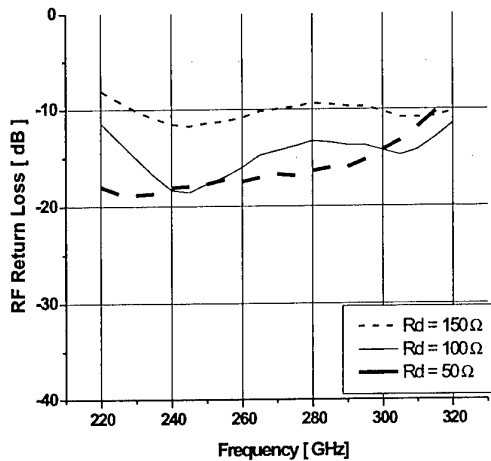


Fig.4: Computed input RF Return Loss variations with the differential resistance R_d .

IV. MIXER CHARACTERISATION

A. Conversion Losses

The conversion loss was measured using an association of phase locked Gunn oscillators, a tripler and a quadrupler as transceiver. The output power measured with a total power bolometer [7] and a corrugated horn at the multiplier output was of the order of -10 dBm. The local oscillator for the measured mixer is made by a 13 - 20 GHz synthesizer followed by an active doubler. The

synthesizer 10 MHz internal reference was used to lock the the Gunn oscillator PLL. A diplexer provided a distinct port for the LO and the IF. The 20 MHz IF signal level was measured with a spectrum analyzer. The conversion loss given by the ratio of the 20 MHz IF output power over the RF input power using the 8th LO harmonic is shown in Fig. 5. The conversion losses are between 40 and 50 dB over most of the band 220 to 320 GHz.

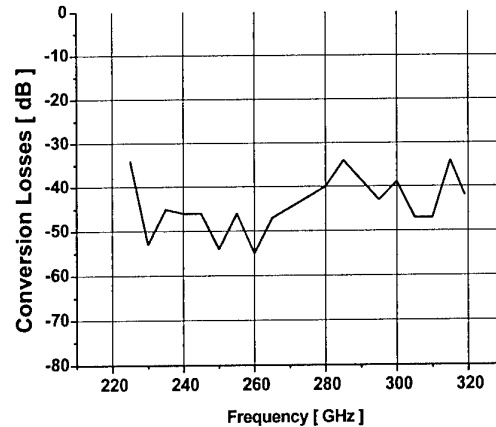


Fig. 5: Harmonic mixer conversion losses.

B. LO Return Loss.

The LO Return Loss measured between 26 and 40 GHz using an HP8510 VNA associated with a waveguide Test Set extension is below -7 dB between 26 and 35 GHz as shown in Fig. 6.

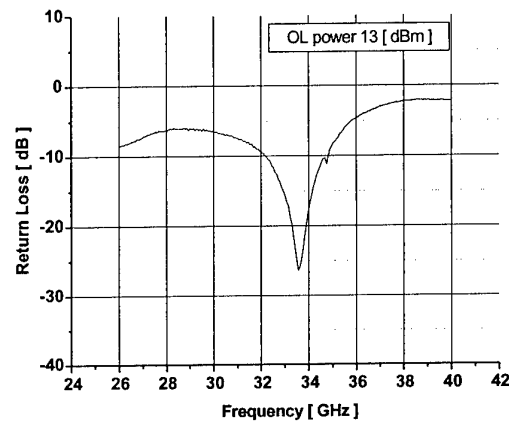


Fig.6: LO Return Loss measured with 13 dBm input signal power.

V. APPLICATION TO THE VNA

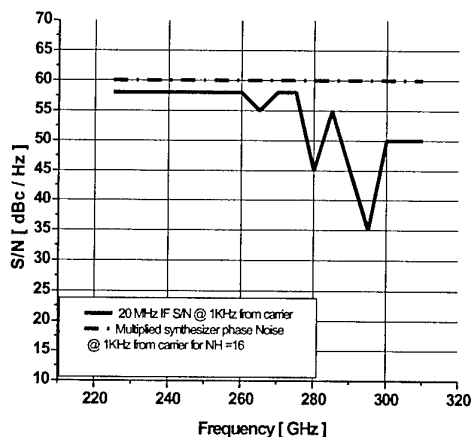
A. VNA System

The 220-320 GHz full band sweep VNA system is identical to the one described in the reference [2]. The performances were improved using the new WR3 harmonic mixer and the WR3 waveguide coupler. A second synthesizer was added to a 20 GHz basic HP8510

Network Analyser. The 20 MHz beat signals given by the reference, the transmission, and the reflection harmonic mixers after amplification and filtering are analysed by the HP8510 four channels 20 MHz receiver. The reference, transmission and the reflection signals were taken using two in-house made WR3 15 dB waveguide broad-wall multi-hole couplers whose reverse coupling is 35 dB. The 20 MHz IF and the 26 to 40 GHz LO are coupled to the receiver mixers via diplexers. The mixers are self-biased.

B. IF Signal and Noise

The 20 MHz IF signal given after emission and reception between a resistive harmonic multiplier and a harmonic mixer is observed with a spectrum analyser. The IF Signal to Noise ratio was measured after amplification at 1KHz from the carrier with a 100 Hz input filter resolution. Figure 7 shows the comparison between the 20 MHz IF S/N and the transceiver synthesizer signal / phase noise level after multiplication by a factor of 16 and degradation of 24 dB. Below 270 GHz both are of the same order of magnitude (about 60 dBc/Hz), in this case, the phase noise is limited by the transceiver synthesiser phase noise. Above 270 GHz, the typical dynamic is 40 dBc/Hz, which is reduced below the synthesizer signal/phase noise ratio by the emission-reception conversion losses degradation. However the corresponding phase noise fluctuations stays below 1.5



degrees over the band.

Fig.7: 20 MHz IF S/N variation.

C. Dynamic Range

The transmission through a waveguide attenuator was measured to test the dynamic range. Figure 8 gives the transmission for three attenuation values over a dynamic of 30 dB between 220 and 320 GHz. Figure 9 gives the transmission through two attenuators over 60 dB dynamic range between 254 and 320 GHz.

D. Calibration and typical measurement:

The VNA is calibrated with WR3 waveguide references : short, delay-short and load. Figure 10 shows the low loss measurement of the transmission through a WR3 H-bend followed by a WR3 coupler of the same type as the one

used in the VNA.

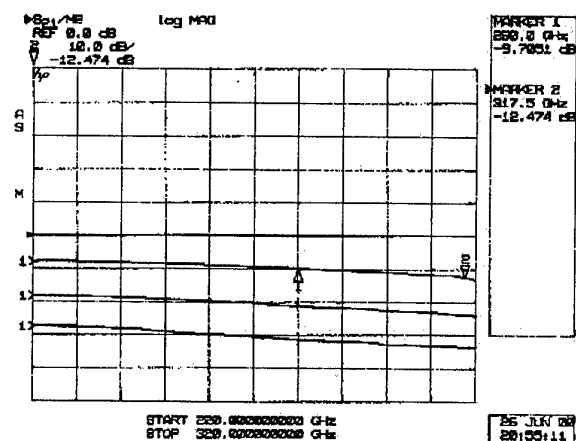


Fig.8: Transmission through one WR3 waveguide attenuator. Scale: 10 dB / Div between 220 - 320 GHz.

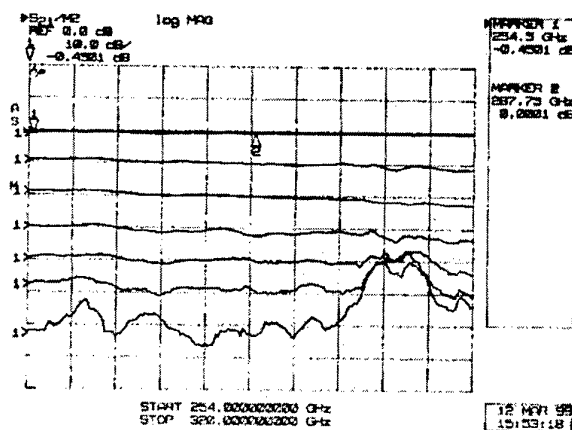


Fig.9: Transmission through two WR3 waveguide attenuators. Scale: 10 dB / Div between 254 - 320 GHz.

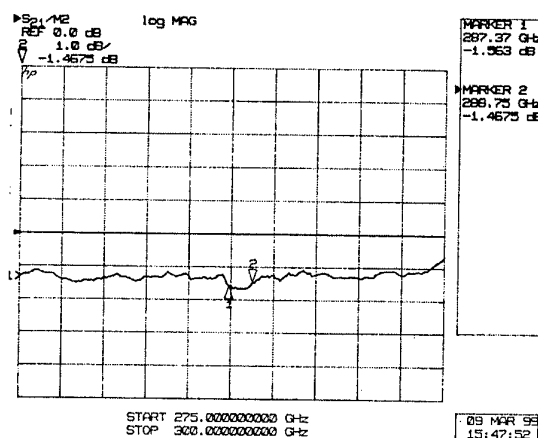


Fig.10: Low loss measurement of the transmission through a WR3 H-Bend and a WR3 coupler. Scale: 1 dB / Div between 275 to 300 GHz.

Figure 11 shows the measurement of the input reflection S11 parameter of a harmonic mixer between 220 and 260 GHz.

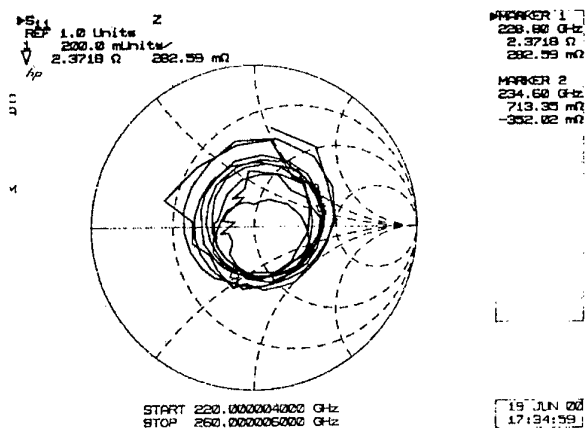


Fig.11 Input reflection S11 parameter from a harmonic mixer between 220 to 260 GHz.

VI. CONCLUSION

A 220-320 GHz fixed tuned harmonic mixer was designed built and characterised. The mixer was used to build a 220 to 320 GHz full band sweep VNA which gives 60 dB of dynamic range in a 44 seconds sweep time over most of the band. That analyser can be used to qualify a large number of devices operating in this frequency range.

Acknowledgement

The authors would like to express their acknowledgements to S. Halleguen and V. Grigis, both at IRAM, for their technical assistance.

References

1. P. Goy, M. Gross, AB Millimetre, 52 rue Lhomond 75005 Paris, France.
2. F. Mattiocco, M. Carter, "80-360 GHz Very Wide Band Millimeter Wave Network Analyser", International Journal of Infrared and Millimeter Waves, Vol. 16, No. 12, pp 2249-2255, 1995.
3. G. Yassin, S. Withington, "Analytical Expression for the Input Impedance of a Microstrip Probe in Waveguide", International Journal of Infrared and Millimeter Waves, Vol. 17, No.10 pp 1685-1705, 1996.
4. M. V. Schneider, "Millimeter-wave integrated circuits" presented at the *GMTT Int. Microwave Symp.* June 16-18, 1973.
5. Faran Technology Ltd, Product Catalogue, 1996. Ballincollig, Cork, Ireland.
6. I. Kneppo, J. Fabian, "Microvawave integrated cicuits" Published by Chapman & Hall.
7. Thomas Keating Ltd, Station Mills, Billingshurst, West Sussex, RH149SH, England.

Performance of the Phonon-Cooled Hot-Electron Bolometric Mixer between 0.7 THz and 5.2 THz

Heinz-Wilhelm Hübers, Alexei Semenov, Josef Schubert,
Gregory Gol'tsman, Boris Voronov, Evgeni Gershenzon

Abstract – We report on the phonon cooled NbN hot electron bolometer as mixer in the terahertz frequency range. Its hybrid antenna consists of a hyperhemispheric silicon lens and a logarithmic-spiral feed antenna. Noise temperatures have been measured between 0.7 THz and 5.2 THz. A quarter wavelength layer of Parylene works as antireflection coating for the silicon lens and reduces the noise temperature by about 30%. It was found that the antenna pattern at 2.5 THz is determined by the feed antenna and not by the diameter of the lens.

I. INTRODUCTION

A number of on-going astrophysical and atmospheric research programs are aimed to the Terahertz (THz) spectral region. Projects which involve THz heterodyne receivers are the Stratospheric Observatory for Infrared Astronomy (SOFIA) [1] and the Far-Infrared and Submillimetre Telescope FIRST [2]. Many important emission lines which will be observed with these observatories are between 1 THz and 5 THz. Examples are the CII fine structure line at 1.6 THz, the OH rotational transition at 2.5 THz and the OI fine structure line at 4.75 THz. These applications require a receiver with the noise temperature close to the quantum limit. Recent studies have shown that superconducting hot-electron bolometric (HEB) mixers are able to satisfy such requirement [3,4]. Since in a sufficiently small superconducting HEB mixer only the electrons are heated by the incoming radiation the response time of the HEB is of the order of the electron-phonon interaction time. This results in low noise temperatures, low local oscillator (LO) power requirement, and intermediate frequencies (IF) of several GHz. In this paper we present the design and performance of a NbN phonon-cooled HEB mixer in the frequency range from 0.7 THz up to 5.2 THz.

II. MIXER DESIGN

Devices were fabricated from 3.5 nm thick NbN films which typically had a room temperature resistivity of $220 \mu\Omega\cdot\text{cm}$ and a superconducting transition temperature of about 10 K. Films were deposited in a nitrogen atmosphere by dc reactive magnetron sputtering of Nb on 350 μm thick optically polished substrates from pure silicon. Details of the process are described elsewhere [5]. A planar two-arm complementary logarithmic-spiral

antenna was used to couple the signal and the LO radiation with the mixer. The log-spiral antenna belongs to a family of frequency independent antennas, i.e. impedance and beam pattern are to a large extent frequency independent. The winding of our antenna can be characterized by the angle $\phi = 70^\circ$ at which a radial line from the origin of the antenna intersects a spiral arm. The central part of the antenna was patterned from a 250 nm thick gold film using electron beam lithography while the outer part was defined by conventional UV photolithography. The layout of the antenna is shown in Fig. 1. The circle inside which the antenna arms form inner terminals has a diameter of 2.2 μm . The diameter of the circle that circumscribes the spiral structure is 130 μm . Between these circles, the antenna arms inscribe 2.15 full turns. The spiral structure is terminated by a coplanar line, which was lithographed on the same substrate and had an impedance of 50 Ω . The substrate carrying the HEB, the planar antenna and the co-planar line, was glued with its rear surface onto the flat side of an extended hemispheric lens. The lens was cut off from an optically polished sphere that was made from high resistivity ($>10 \text{ k}\Omega\cdot\text{cm}$) silicon. Spheres of 6 mm and 12 mm diameter were used for this purpose. The extension of the lens together with the substrate yields a total extension length of 1.2 mm and 2.4 mm for the 6 mm and 12 mm lens, respectively. These values are very close to the extension length corresponding to the synthesised elliptic lens for which the beam pattern of the hybrid antenna is expected to be diffraction limited [6]. The mixer was mounted at the cold plate of a 1-He cryostat. A cold quartz filter was used to block the 300 K background radiation.

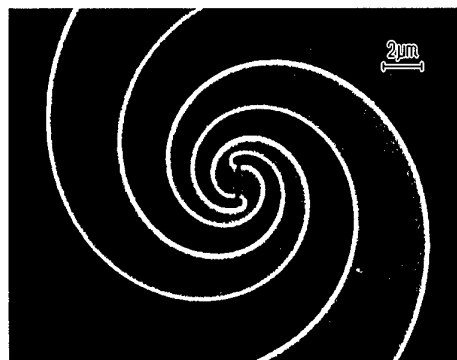


Fig. 1: Layout of the logarithmic spiral antenna. The gap in the center of the antenna has the height 1.7 μm and the width 0.2 μm . The width defines the length of the HEB.

H.-W. Hübers and A. Semenov, are with the Institute of Space Sensor Technology and Planetary Exploration of the German Aerospace Center (DLR), Rutherfordstr. 2, 12489 Berlin
Josef Schubert is with the Max-Planck Institut für Extraterrestrische Physik, Giessenbachstr., 85740 Garching
G. Gol'tsman, B. Voronov, and E. Gershenzon are with the Physical Department of the State Pedagogical University, 119435 Moscow

III. NOISE TEMPERATURE

The noise temperature was measured at several frequencies from 0.7 THz to 5.2 THz. The IF frequency was 1.5 GHz. An optically pumped far-infrared (FIR) ring laser and a transversely excited FIR laser were used as a local oscillator in the frequency ranges 0.7 THz to 2.5 THz and 2.5 THz to 5.2 THz, respectively. Results from measurements of the noise temperature at 2.5 THz were identical irrespective of which laser system was used. The double side-band (DSB) receiver noise temperature was determined by the Y-factor method making use of Eccosorb as the hot and cold load at temperatures of 293 K and 77 K, respectively. To derive the receiver noise temperature from the measured Y-factor the dissipation-fluctuation theorem in the form of Callen and Welton was used.

Table 1: DSB noise temperatures at THz frequencies.

Freq. [THz]	Device	Lens	T_{DSB} [K]	$T_{\text{DSB,corr}}$ [K]
0.623	A1	12 mm	1300	800
1.397	A1	12 mm	2000	1100
1.627	A1	12 mm	2100	1200
2.523	A1	12 mm	2600	1700
3.106	A3	6 mm	4000	2800
4.252	A3	6 mm	5600	3900
5.246	A3	6 mm	8800	6200

A major contribution to the noise temperature originates from losses in the optical elements. The main sources are the quartz filter with 1.1 dB to 1.9 dB loss and the reflection loss at the surface of the silicon lens (≈ 1.5 dB). At frequencies below 3 THz a filter made from Zitex has a lower loss than quartz [7]. The reflection loss of the lens can be reduced by an anti-reflection (AR) coating with Parylene (see section IV). The last column in Table 1 displays the DSB noise temperatures assuming a Zitex filter for the data below 3 THz and a AR coated silicon lens optimized for each frequency. Above 3 THz the improvement is only due to the AR coating since Zitex and quartz have almost the same loss. Beside the losses in the optical components there is another mechanism which contributes to the increase of the noise temperature with higher frequencies. This additional loss is caused by an increasing impedance mismatch between the HEB itself and the antenna. Due to the skin effect the rf-current in the HEB is confined to the outer region of the bridge while the central part carries less and less current with increasing frequency. A detailed investigation of this mechanism can be found in Ref. [8].

IV. PARYLENE ANTI-REFLECTION COATING

Parylene C is a good candidate as AR coating. It is a polymer with a refractive index of about 1.62 that matches closely the required value $n_{\text{Si}}^{1/2} \approx 1.84$ for a quarter wavelength antireflection layer on silicon. Beside that Parylene C is chemically inert, has a high thermal stability and has practically no water absorption. It is deposited from the gas phase. This results in films of uniform thickness and high conformity. Two lenses each with a diameter of 6 mm were made from the same silicon crystal. One of the lenses was coated with a 18.5 – 20 μm thick Parylene C layer. The improvement of the noise temperature due to a lens with this AR coating was investigated for two HEB mixers at four different

frequencies between 0.7 THz and 2.5 THz. A significant improvement of about 30% was achieved at 2.5 THz. The improvement decreases towards the smaller frequencies as expected because the thickness of the Parylene C layer corresponds to about a quarter wavelength at 2.5 THz. Fig. 2 illustrates the relative improvement, i.e. the difference in noise temperature measured with the uncoated and the coated lens divided by the noise temperature measured with the uncoated lens. Also shown (solid line) is the relative improvement as expected from transmittance measurements of plane parallel silicon samples [9]. In this case, the relative improvement is the difference in transmittance between the coated and the uncoated sample divided by the transmittance of the uncoated sample. However, the transmittance measurements have been performed at 300 K where the refractive index is 1.62. It is known that the refractive index of Parylene C decreases with temperature. The dashed line is the relative improvement of the transmittance calculated by assuming a refractive index of 1.5 for Parylene C at 4 K. It can be seen that the transmittance data and the noise temperature measurements are in excellent agreement. A detailed study of Parylene C as AR coating at THz frequencies can be found in Ref. [9].

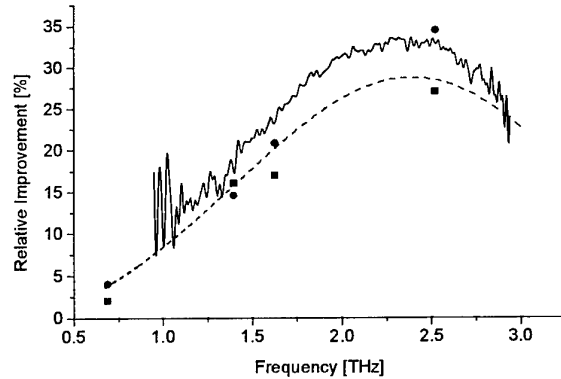


Fig. 2: Relative improvement of the noise temperature of two HEB mixers (circles and squares) due to a AR coating with Parylene C. The solid and the dashed line correspond to the relative improvement of the transmittance of a plane parallel silicon sample with the same coating at 300 K and 4 K, respectively.

V. ANTENNA PATTERN

Beam patterns of the hybrid antenna have been measured at 2.5 THz with the 6 mm and the 12 mm lens. Both lenses had no AR coating. Fig. 3 displays results for E-planes. The dashed lines represent the diffraction limited antenna patterns that were simulated for the physical diameter d of the lens according to the expression $(2J_1(v)/v)^2$, where $v = (\pi \tan(\theta) d)/\lambda$, θ is the angle and J_1 is the Bessel function of the first kind. The calculated full widths at half maximum (FWHM) are 1.19° and 0.59° while the measured profiles yield 1.65° and 0.75° for the 6 mm and the 12 mm lens, respectively. The solid lines are calculated according to the above given expression but the diameter of the aperture was set to yield the

closest match with the measured antenna pattern. The resulting diameter of the effective aperture is 4.5 mm and 9.3 mm for the 6 mm lens and the 12 mm lens, respectively. These values correspond to a 70° beamwidth (FWHM) of the log-spiral feed antenna independent of the diameter of the lens. This is in good agreement with measurements of the antenna pattern of a log-spiral antenna with the same characteristic angle but at cm-wavelengths [10]. A less tightly wound spiral with smaller characteristic angle ϕ will yield a broader pattern of the feed antenna resulting in a narrower beam. However, the pattern will be less symmetric.

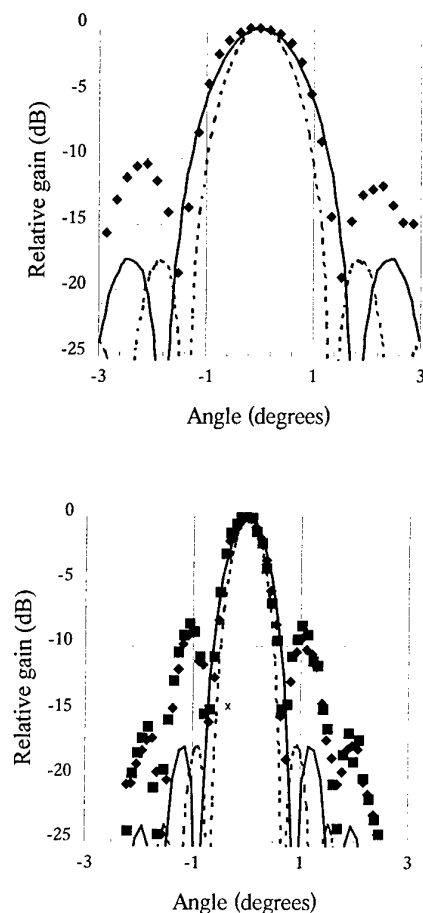


Fig. 3: Beam pattern at 2.5 THz of the hybrid antenna with a 6 mm lens (upper figure) and a 12 mm lens (lower figure). The solid lines display the closest match between theory and experiment while the dashed lines correspond to the pattern as expected from the lens diameter.

VI. CONCLUSION

We have investigated phonon-cooled NbN HEB mixers in the THz frequency range. The noise temperatures range from 1300 K at 0.7 THz to 8800 K at 5.2 THz. A major source of loss is the reflection at the surface of the silicon lens of the hybrid antenna. This can be overcome by a quarter wavelength AR coating with Parylene C. The noise temperature is decreased by about 30% due to this AR coating. It is shown that the beam pattern of the hybrid antenna is determined by the beam pattern of the feed antenna and not by the diameter of the lens.

References

1. R. K. Melugin, H. P. Röser, Proc. of SPIE vol. 4014, "Airborne Telescope Systems", 2000.
2. N. D. Whyborn, "The HIFI Heterodyne Instrument for FIRST: Capabilities and Performance", Proc. of ESA SP-401, pp. 19-24, 1997
3. J. Schubert, A. Semenov, G. Gol'tsman, H.-W. Hübers, G. Schwaab, B. Voronov, and G. Gershenzon, "Noise Temperature of a NbN Hot-Electron Bolometric Mixer at Frequencies from 0.7 THz to 5.2 THz, Supercond. Sci. Technol. 12, pp. 748-750, 1999
4. B. Karasik, M. Gaidis, W. R. McGrath, B. Bumble, and H. G. LeDuc, "A Low-Noise Superconducting Nb Hot-Electron Mixer at 2.5 THz", Proc. of the 8th Int. Symp. on Space Terahertz Technology, pp. 55-66, 1997
5. S. Cherednichenko, P. Yagoubov, K. Il'in, G. Gol'tsman, and E. Gershenzon, "Large Bandwidth of NbN Phonon-Cooled Hot-Electron Bolometer Mixers on Sapphire Substrates" Proc. of the 8th Int. Symp. on Space Terahertz Technology, pp. 245-257, 1997
6. T. H. Büttgenbach, "An Improved Solution for Integrated Array Optics in Quasi-Optical mm and Submm Receivers: the Hybrid Antenna", IEEE Trans. Microwave Theory and Tech. 41, pp. 1750-1761, 1993
7. D. J. Benford, M. C. Gaidis, and J. W. Kooi, "Transmission Properties of Zitex in the Infrared to Submillimeter", 10th Int. Symp. on Space Terahertz Technology, pp. 405-13, 1999
8. A. D. Semenov, H.-W. Hübers, J. Schubert, G. N. Gol'tsman, A. I. Elantiev, B. M. Voronov, and E. M. Gershenzon, "Design and Performance of the Lattice-Cooled Hot-Electron Terahertz Mixer", accepted for publication in J. Appl. Phys., 2000
9. H.-W. Hübers, A. Krabbe, and J. Schubert, M. Birk, G. Wagner, A. Semenov, G. Gol'tsman, and E. Gershenzon, "Parylene Anti-Reflection Coating of a Quasi-Optical Hot-Electron-Bolometric Mixer at Terahertz Frequencies", submitted to Infrared Physics and Technol., 2000
10. J. D. Dyson, "The Unidirectional Equiangular Spiral Antenna", IRE Trans. Antenna and Propagation, pp. 329-334, 1959

The Design and Analysis of Antiparallel Schottky Diode Mixers

Jeffrey Hesler

Abstract— This paper discusses the techniques developed to design integrated anti-parallel Schottky diode mixers. The use of these techniques has enabled us to efficiently design and build submillimeter wavelength mixers that are not only highly sensitive, but also have enhanced mechanical robustness and large fixed tuned bandwidth. A "coaxial probe technique" is used with a finite-element analysis program to determine the loop and external embedding impedances of the anti-parallel diode pair. Nonlinear analysis of the diode is performed to examine such issues as mixer sensitivity and LO power requirement. As a design example, a 400 GHz subharmonic mixer with state-of-the-art performance is considered..

I. INTRODUCTION

New techniques have been developed to scientifically design integrated planar Schottky diode mixers that are robust, easy to assemble, have large fixed tuned bandwidth and achieve state-of-the-art sensitivity. The diodes are integrated on a quartz circuit containing the embedding circuitry [1], which is placed in a microstrip channel. Two-sided waveguide-to-microstrip transitions are used to couple both the RF and LO signals

diode integration allows greater accuracy of computer simulations and better sensitivity and bandwidth.

The primary focus of this paper is the method used to design integrated mixers, including both the embedding circuit design and the nonlinear analysis of the Schottky diode pair. The embedding circuit design includes the waveguide-to-microstrip transitions and the diode's embedding circuitry. The "coaxial probe technique" is used with HFSS to determine the loop and external embedding impedances. As a design example, a 400 GHz subharmonic mixer with state-of-the-art performance [2] will be considered.

II. MIXER LAYOUT

The mixer block, similar to that described in [3], is split in the E-plane of the RF and LO waveguides, thus simplifying block fabrication and mixer assembly, as well as reducing the losses in the waveguides. The planar diode and mixer circuitry are fabricated on a 35 μm thick fused-quartz substrate. The circuits are then placed in a shielded microstrip channel which runs perpendicular to the RF and LO waveguides. A schematic of the mixer

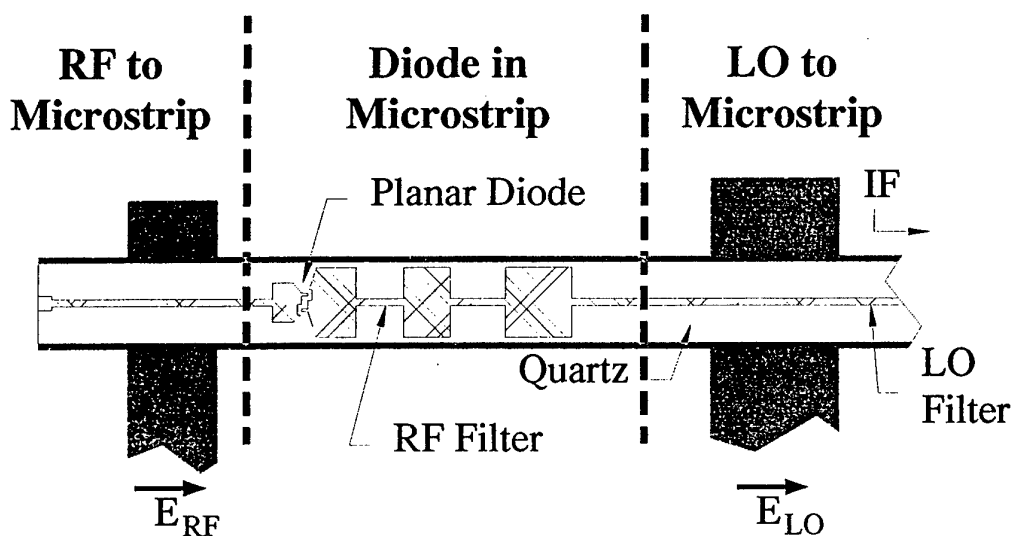


Fig. 1: Layout of the subharmonic mixer block configuration.

into the channel. The integration of the diodes with the embedding circuitry allows precise control of the circuit geometry and a reduction of parasitic elements. Thus,

J. Hesler (hesler@virginia.edu) is with the University of Virginia Dept. of EE, Charlottesville, VA 22903.

block circuit configuration is shown in Fig. 1. The diodes are located in the microstrip channel. Waveguide-to-microstrip transitions are used to couple both the RF and LO into the channel. The microstrip metallization bridges across each guide, necessitating the use of reduced height waveguide to achieve reasonable fixed-tuned bandwidths

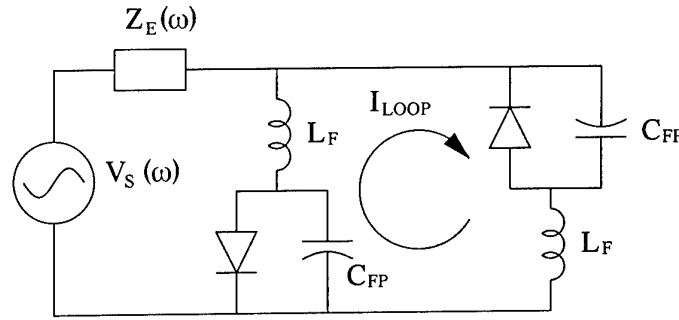


Fig. 2: Equivalent circuit of anti-parallel diodes used for the nonlinear analysis.

[4]. For this mixer, half height waveguide was used for the RF, and third height waveguide was used for the LO. A low-pass microstrip filter is used to prevent the RF signal from coupling to the LO guide, and a short-circuited half-wave stub is used to provide the LO termination.

III. NONLINEAR DESIGN

The equivalent circuit model of the anti-parallel diode used during the nonlinear design is shown in Fig. 2. The main goal of the nonlinear design is to determine the value of the external embedding impedance Z_E at the LO, RF and IF frequencies so that the external circuitry can then be tuned to present the proper impedance to the diode. In addition to this goal, the nonlinear analysis is used to look at mixer sensitivity and bandwidth, LO power requirements, and other performance issues.

In order to simulate the behavior of the nonlinear circuit it is first necessary to determine the reactance seen by loop currents. For the planar anti-parallel diodes used in this research the loop is well modelled by an inductance L_F (representing the diode finger and the lateral spacing between the diodes) and the junction fringing capacitance C_{FP} (the finger-to-pad capacitance). HFSS simulations of the anti-parallel diode mounted in a microstrip channel were performed to determine the appropriate values of L_F and C_{FP} . Coaxial ports were used at the anode junctions, as discussed in [5]. By feeding the two diode ports in phase (where this phase is referenced to the diode's polarity) we can then directly determine the loop reactance, from which we can calculate the loop inductance and capacitance. For a diode with a finger length of 20 μm and a lateral distance between fingers of 22 μm , L_F was 10 pH and C_{FP} was 2.5 fF. The same values of L_F and C_{FP} were found to match the HFSS simulations at both the LO and RF, thus giving an indication of the utility of the equivalent circuit used. In addition, L_F and C_{FP} were found to change very little when the external cavity was varied, and the same L_F and C_{FP} were found to be valid even when the diode was mounted directly in a waveguide.

Using these values of the loop parasitics, nonlinear simulations were performed for an RF of 400 GHz. The Schottky diode that was modelled had an epitaxial layer doping of $4 \times 10^{17} \text{ cm}^{-3}$ and an anode

diameter of 0.8-0.9 μm . The measured DC parameters for this diode were an ideality factor $\eta=1.32$, a saturation current $I_{SAT}=3 \times 10^{-13} \text{ A}$, and a series resistance $R_S=10 \Omega$. The zero bias junction capacitance was calculated to be 1.5 fF per anode based on the anode diameter and the epitaxial layer doping. The simulations predict a mixer conversion loss of 4.0 dB (DSB) and noise temperature of 300 K (DSB) using 1.5 mW of LO power. The optimum embedding impedance Z_E was $30+j80\Omega$ at the LO, $20+j30\Omega$ at the RF and 100Ω at the IF.

The total conductor and dielectric loss for the horn, waveguide, microstrip, and diode was estimated to be about 2 dB. Using this estimate the predicted performance is a mixer conversion loss of 6 dB (DSB) and mixer noise temperature of 650 K (DSB). The simulations predict a usable RF bandwidth of better than 20% fixed tuned.

The LO bandwidth is difficult to estimate since it is closely linked to the amount of power available from the LO source. In order to determine the effect of the LO embedding impedance on the mixer performance, a graph was made (see Fig. 3(a)) showing the required LO power as a function of LO impedance for the mixer simulated above. Fig. 3(a) was generated by realising that for a perfectly balanced subharmonic mixer the RF performance is unaffected by the LO embedding impedance as long as an equivalent amount of power is delivered to the diodes. Knowing this, we can then determine the amount of LO power required to keep the delivered power constant for a given LO embedding impedance. Fig. 3(a) shows that reasonably low LO power is required to drive the mixer over a large range of LO impedances.

IV. EMBEDDING CIRCUIT DESIGN

The LO and RF waveguide to microstrip transitions can be designed independently of the microstrip circuit around the diode. The transitions are designed to match the microstrip line to the waveguide, and can be therefore simply modelled during the microstrip circuit design. In order to achieve good fixed-tuned bandwidth the impedance of the microstrip lines running across the waveguide was set to about 100Ω .

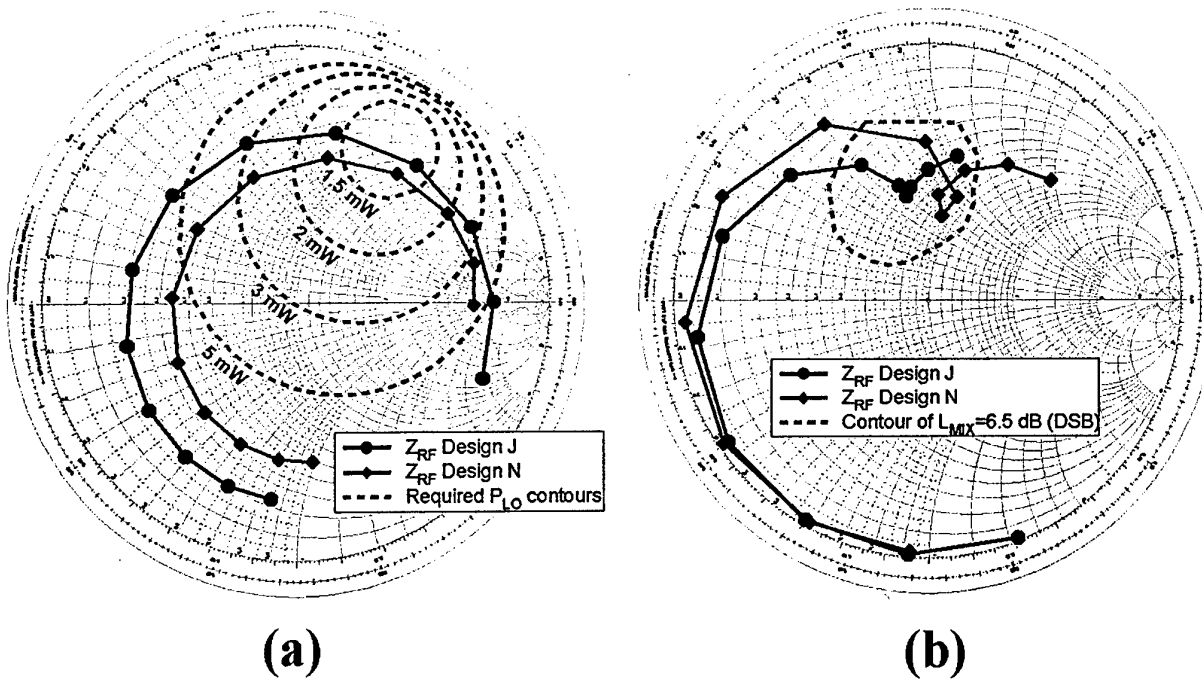


Fig. 3: Predicted embedding impedance for two circuit designs at the LO and RF. (a) LO embedding impedance, with marker spacing of 6.7 GHz, (b) RF embedding impedance, with marker spacing of 13.4 GHz.

This impedance is a compromise between bandwidth, microstrip line loss, and the effect on the diode embedding impedance. A fixed-tuned bandwidth of approximately 20% was achieved for this design at the RF and LO. Wider bandwidths could be attained at the cost of some increase in circuit complexity.

The diode embedding impedance was found using the same method that was used to determine the loop parasitics. To determine the external embedding impedance Z_E rather than the loop impedance the diodes must be fed out of phase. The length of microstrip line between the RF waveguide and the diode can be used to tune the LO impedance while not affecting the RF impedance. The length of the first section of the RF-block filter is the primary tuning element for the RF circuit. Fig. 3 shows the predicted contours for two different mixer circuit designs as modelled in HFSS. The effects of the finite bandwidth of the waveguide-to-microstrip transitions has been included in the simulation. The fixed-tuned bandwidth of the RF is predicted to be about 20%.

V. CONCLUSIONS

This research has enabled us to efficiently design and build submillimeter wavelength mixers that are not only highly sensitive, but also have enhanced mechanical robustness and large fixed tuned bandwidth. The coupling of these new analysis techniques and the new integrated diode technology can be easily extended to other circuit designs such as balanced and subharmonic mixers and frequency multipliers, and will allow the development of a new generation of SubMillimeter-wave

Integrated Circuits (SMICs) for a wide range of scientific, military and commercial applications

Acknowledgements

This work was supported by NASA-GSFC Grants No. NAG5-6507 and NAG5-4750 and by the U.S. Army National Ground Intelligence Center under contract DAHC90-96-C-0010.

References

1. S.M. Marazita, W.L. Bishop, J.L. Hesler, K. Hui, W.E. Bowen, and T.W. Crowe, "Integrated GaAs Schottky Mixers by Spin-On-Dielectric Wafer Bonding," IEEE Trans. on Electron Devices, Vol. 47, No. 6, pp. 1152-1157, June 2000.
2. J. L. Hesler, "Broadband Fixed-Tuned Solid-State Heterodyne Mixers from 183 GHz to 640 GHz," Proc. 2000 Int. Symp. On Space THz Tech., Ann Arbor, MI, May 2000.
3. A.V. Raisanen, D. Choudhury, R.J. Dengler, J.E. Oswald, and P. Siegel, "A novel split-waveguide mount design for millimeter- and submillimeter-wave frequency multipliers and harmonic mixers," IEEE Microwave and Guided Wave Letters Vol. 3, No. 10, Oct. 1993, pp. 369-371.
4. J.L. Hesler, K. Hui, R.M. Weikle, T.W. Crowe, "Design, Analysis and Scale Model Testing of Fixed-Tuned Broadband Waveguide to Microstrip Transitions," Proc. of Eighth Int. Symp. on Space THz Tech., Cambridge, MA, pp. 319-325, March 25-27 1997
5. J.L. Hesler, W.R. Hall, T.W. Crowe, R.M. Weikle, II, B.S. Deaver, Jr., R.F. Bradley, and S.-K. Pan, "Fixed-Tuned Submillimeter Wavelength Waveguide Mixers Using Planar Schottky Barrier Diodes," IEEE Trans. Microwave Theory Tech., Vol. 45, pp. 653-658, May 1997

Space-Based Applications of Far-Infrared Systems

Michael C. Gaidis

Abstract – This paper discusses the applications of space-based far-infrared/terahertz sensors and systems. It also covers the needs and desires of scientists, discusses what has been done to date, and what is planned for the future.

I. INTRODUCTION

As is the case in other spectral regions, astronomers and atmospheric scientists drive much of the cutting-edge technology development in the FIR. The dramatic attenuation of FIR radiation by water and other constituents of Earth's atmosphere forces many of the scientists' measurement platforms above the atmosphere, into space. Therefore, there is a strong correlation between the development of new FIR technology and the development of FIR spaceborne instrumentation.

Technologists working at microwave frequencies effectively utilize a "wave" and "electron" approach, while those working in the infrared effectively utilize a "particle" and "photon" approach. Unfortunately, given the state of technology today, neither approach is optimal for use in the FIR. With only marginal success, researchers toil diligently to stretch the boundaries of both wave and particle technologies to the FIR. The pessimist may complain about the state of FIR technology, but the optimist will note that this field is ripe for development, and possesses great potential for breakthrough discoveries.

Because there has been only minimal application of FIR technology in spacecraft to date, even the simplest FIR measurements offer great potential for breakthrough discoveries.

II. FAR-INFRARED APPLICATIONS

A. Astronomy

Characteristic temperatures, molecular bond strengths, and dust grain sizes are responsible for filling the heavens (and Earth!) with FIR radiation. COBE spacecraft measurements showed almost half the luminosity and 98% of the post-Big Bang *photons* in a typical galaxy lie in the FIR spectral region [1]. This is shown in Fig. 1, along with the 1.9 THz carbon line – a single spectral line responsible for 0.25% of the energy radiated by a galaxy [2]! In addition to the wealth of photons in the FIR, we find the wavelength of FIR photons is such that one can probe deeply inside regions of gas and dust that surround stars, without the dramatic attenuation typically seen by near-IR photons. This gas and dust, in many places

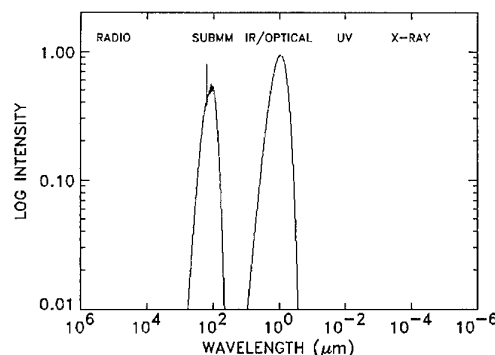


Fig. 1: COBE/DIRBE measured spectrum of the Milky Way galaxy [2]. Note the 158 μm CII line.

responsible for the birth of new stars and galaxies, is at temperatures that exhibit a peak in the Planck blackbody radiation spectrum in the FIR [3]. Using Doppler information collected by high-spectral-resolution heterodyne radiometers, the dynamics of galaxies new and old may be understood. Frequency resolution better than a part in a million is necessary for many of these studies.

With the sluggish advancement of FIR technology, there has been only one spacecraft to date which has successfully utilized FIR heterodyne radiometers: the Submillimeter-Wave Astronomy Satellite (SWAS) [4]. Launched in 1998, this spacecraft has generated impressive astrophysical measurements at frequencies near 490 and 550 GHz (where atmospheric attenuation is particularly strong). Several other spacecraft are due to launch in the near future with FIR heterodyne radiometers for astrophysical, atmospheric, and cometary studies. Most notable is the European Space Agency's Far-Infrared & Submillimeter Telescope (FIRST), which includes a significant contribution from NASA. Set to launch in 2007, it will utilize cold optics and state-of-the-art bolometers and superconducting mixers to make extremely sensitive measurements from the mm-wavelength region to frequencies exceeding 1 THz [5].

Among the more interesting possible space-based astronomy missions is a proposal for a single-aperture far-infrared (SAFIR) observatory. The National Academies' Astronomy and Astrophysics Survey Committee has recommended SAFIR as a follow-on to the Next-Generation Space Telescope (NGST) [6]. SAFIR is planned to utilize a cold 8-m space-based telescope that is diffraction limited at 30 μm , and will be more than 100 times as sensitive as FIRST. It will investigate the earliest stages of star and galaxy formation by penetrating into regions too dust-shrouded to be studied by NGST, and too warm to be effectively studied

Michael Gaidis is with the Jet Propulsion Laboratory, California Institute of Technology, Pasadena, CA91109, USA.
Email: gaidis@merlin.jpl.nasa.gov

by ground-based facilities such as ALMA (Atacama Large Millimeter Array). Given its large size, low temperature, and sensitive detectors, SAFIR's "astronomical capability" will be of order 100,000 times that of previous missions. There is obviously tremendous potential for breakthrough discoveries!

In the following decade, attention will naturally shift to the creation of a FIR interferometer in space. A 30-m class space infrared interferometric telescope (SPIRIT) has been proposed as a precursor to a 1-km baseline interferometer, the Submillimeter Probe of the Evolution of Cosmic Structure (SPECS) [2]. Poor angular resolution has been a major limitation in FIR studies of the evolution of primordial structure in the universe, and the formation of galaxies, stars, and planets. Angular resolution on the order of 0.01 arcsec is needed to resolve distant galaxies or protoplanetary systems in nearby star-forming regions. The ground-based mm-wavelength ALMA will provide such resolution, and in the FIR, SPECS would perform similarly. SPIRIT would be used as technology validation, with compelling science objectives as well. Given the large number of FIR photons available, the sensitivity of filled-aperture telescopes is only necessary for certain measurements (e.g., high resolution spectroscopic observations of distant objects), and much science can still be performed with a sparsely-filled-aperture telescope.

While direct detection holds a sensitivity advantage over heterodyne radiometry for some applications in the FIR, the longest-baseline interferometers will require the phase-coherent techniques of heterodyne measurements to allow realistic combination of the numerous telescope signals. Very-large-aperture telescopes (perhaps tens of meters in diameter, from inflatable structures) will be required to make the sensitivity of such an interferometer of practical use for many astrophysical studies.

B. Atmospheric Chemistry

We all have been touched to some extent by regulations imposed to maintain a healthy atmosphere. We may notice the effects of reduced smog levels, trends in global warming, a potentially life-saving ozone layer, or the expense of a CFC-free refrigerator, but behind the scenes, governments make extremely difficult choices in balancing economic and environmental priorities. Atmospheric scientists strive to provide governments with unequivocal data that makes these choices obvious. As fate would have it, important molecules in the Earth's atmosphere exhibit vibration and rotation spectra in the FIR. By monitoring such molecules, one can gain a better understanding of atmospheric dynamics, obtain more realistic data for atmospheric models, and provide real-time feedback on atmospheric conditions [7].

Precise observation of molecular spectral line shapes, widths, and amplitudes are critical to extracting the relevant information from measurements. Doppler and pressure-broadening of the spectral lines typically results in linewidths of order 1 to 10 MHz [8]. For sufficient accuracy in data collection, one desires spectral resolution of better than a part in a million.

The Upper Atmosphere Research Satellite, Microwave Limb Sounder (UARS-MLS) instrument began operation in 1991, and has been consistently returning useful data of this nature to the present day [9]. Although the highest frequencies observed with UARS-MLS were only in the neighborhood of 200 GHz, it has laid the groundwork for the next generation Earth Observing System, Microwave Limb Sounder (EOS-MLS). Set for launch in 2003 in NASA's AURA spacecraft, EOS-MLS is presently the largest American FIR space mission, and will observe the atmosphere in five radiometer frequency bands from 100 GHz to 2.5 THz with semiconductor-based heterodyne receivers [10]. An additional follow-on mission to launch near the end of the decade is being proposed.

FIR heterodyne receivers also find application in cloud ice crystal observations, an important part of accurate global-warming models [11]. A DC-8 airplane-based instrument is presently being built at JPL to demonstrate the usefulness of this technique, and will hopefully lead to a space-based global application. Lastly, the effects of aerosols and dust spewed into the atmosphere by volcanoes are readily observed in the FIR, and are occasionally detected by the MLS radiometers.

C. Planetary Science

Earth's atmosphere is but one of many interesting atmospheres in our solar system. Remote or in-situ FIR measurements are particularly well-suited to intriguing atmospheres like those of Venus, Mars, the gaseous planets, and Saturn's moon Titan. By learning about the atmospheric composition and dynamics on remote planetary bodies, scientists can develop models of planetary evolution and suitability for future exploration. The sensitivity of FIR radiometry to emission from water molecules may lead to missions to Mars and Jupiter's moon Europa. Missions to Mars have been proposed, and a potential FIR study of Venus' atmosphere is presently receiving much attention. The reduced size of FIR antennas with respect to their millimeter-wave counterparts also makes them attractive for in-situ "weather stations" and sensor webs.

Other solar system bodies are realistic candidates for FIR study – comets and other Kuiper Belt objects (KBOs) offer clues to understanding the creation of our solar system, and possibly life on Earth as well. The molecular gas and dust outflows from heated comets offer much information in the FIR, from identification of molecular species to the size, quantity, and albedo of the ejected debris. Rosetta, another ESA-NASA collaboration, will contain the MIRO instrument for 236 and 562 GHz remote studies of the comet 46 P/Wirtanen as it orbits the comet. The instrument will remotely measure gas volatile composition, coma temperature, gas velocity, and subsurface temperatures of the cometary nucleus to a depth of 2 cm or more. Key measurements include CO and water in the head and tail of the comet, temperatures, and isotope ratios. Launch is in 2003, and rendezvous is expected in 2011, with observations lasting at least 2 years thereafter. Future FIR studies of the albedo, size, and position of KBOs will be useful for understanding the conditions that regulated the formation and evolution of the debris that coalesced into our solar system [3].

As many signatures of life (as we know it) can be found in the molecules detectable with FIR radiometers, one would envision that space missions in the distant future will include large-aperture, large-baseline interferometers for examining the chemistry of extra-solar planets. The ratio of planet to stellar flux increases significantly as one moves from the near-IR to the FIR, another reason for working in the FIR. Although extremely large telescopes (at this time unfeasible) would be required for the necessary sensitivity, the predicted molecular species and planetary atmosphere temperatures associated with life make FIR radiometers particularly well-suited to the task of detecting extraterrestrial life.

D. In-Situ Studies

The rapid advancement of terahertz imaging, based on terahertz time-domain spectroscopy, makes feasible a portable terahertz spectrometer [12]. With improvements in spatial resolution, signal processing, and penetration depths, terahertz imagers could be valuable in remote geological studies, in-situ atmospheric spectroscopy, and as medical diagnostic tools for humans in space. Presently, the processing time and the size of the instruments is inadequate for space flight use, but a dedicated technology development effort can solve these problems with reasonable cost.

E. Non-Scientific Spaceborne Applications

The information-carrying capacity of signals with terahertz bandwidths is obviously immense. Due to atmospheric absorption, one finds few applications of free-space FIR transmission at the Earth's surface. However, satellite-to-satellite communication can be achieved with the immense bandwidths offered by the FIR. Defense applications exist here as well because of the difficulty in eavesdropping through the atmosphere. Compact, low power FIR radiation sources, detectors, and filters must be developed before such applications become economically feasible.

III. HETERODYNE DEVICES

A. Why Heterodyne?

Heterodyne technology offers highest sensitivity in the longer-wavelength region of the FIR. As wavelengths decrease, the attractiveness of direct detection instruments increases. Nonetheless, for most applications in the FIR that require high frequency resolution (a part in 10,000 or more), heterodyne receivers are most practical. While this is a useful guide, most often, the specific targeted application will make the choice of heterodyne vs. direct for you. For brevity, only heterodyne devices are discussed in this paper; we refer the interested reader to reference [13] for information on the present status of direct detectors.

B. Mixers

The highest-sensitivity applications requiring high frequency resolution utilize superconductor-insulator-superconductor (SIS) tunnel junction mixers operating at temperatures of 4 K or below. For frequencies above about 1 THz, one resorts to hot-electron bolometer (HEB)

mixers if high sensitivity is needed. Again, these operate at temperatures near 4 K. For space applications, cooling technology becomes a very important issue. Even for spacecraft operation at the friendly L2 Lagrangian location, one cannot expect passive cooling to provide temperatures below 30 K [14]. For room-temperature operation, or simplicity in low-sensitivity applications, Schottky diodes are used. The convenience of operating at room temperature typically carries a penalty of a factor of 5 to 10 in sensitivity, but new advances in planar diode technology [15] are making Schottky diodes more attractive. Figure 2 shows recent measurements from our laboratory, with uncorrected receiver noise below 6500 K, DSB. Removing the effects of atmospheric loss and IF amplifier noise in the measurement setup gives room temperature *mixer* noise close to 4000 K, DSB.

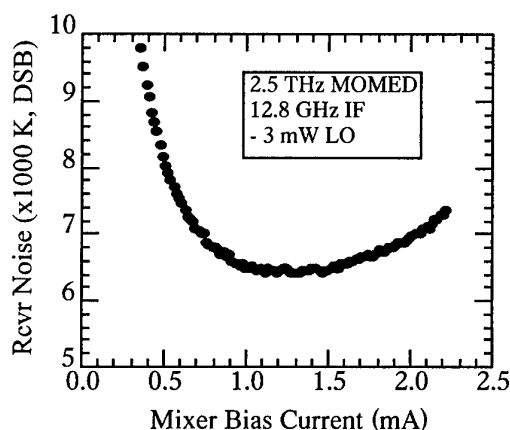


Fig. 2: Uncorrected receiver noise temperature with JPL's planar Schottky diode MOMED.

C. Local Oscillators for Spaceborne Use

Typical LO power requirements range from 100 nW (HEBs) to 1 μ W (SIS) to 1 mW (Schottky), and has enormous consequences on the applications in which these mixers are used. Inefficiencies in diplexing and optical coupling can raise the actual LO source powers needed by a factor of 5. Note that arrays of such mixers are envisioned for the future, and the aforementioned LO power must be multiplied by the size of the array (assuming a very efficient LO power distribution scheme).

SIS and Schottky mixers enjoy an advantage over HEB mixers in the power stability requirements of the LO. The SIS and Schottky mixers operate in a region where fluctuations in LO power are compressed somewhat: fractional changes in LO power correspond to perhaps ten times lower fractional changes in IF output power. HEB mixers, however, operate in a regime where such compression is much less significant, and LO fluctuations are nearly indistinguishable from signal fluctuations. Requirements on power stability are typically 1% for the SIS and Schottky, but 0.1% for the HEB mixers.

There is a division of approaches used for LO technology, with electronic techniques generally used at

frequencies below 1 THz, and photonic techniques above 1 THz. While reasonable success has been achieved in the former regime, the latter frequency regime has only rarely been able to meet the demands of use in spacecraft.

IV. SPACE FLIGHT QUALIFICATION

Lifting a radiometer into space is no easy task. The complexity and cost of such systems can easily be an order of magnitude larger than similar systems built for ground use. There must be a strong science driver and a friendly political climate to enable such missions. When given the necessary endorsement and funding, one must then take into account the need for:

1. minimal mass, volume, DC input power
2. thermal requirements and thermal stability
3. ability to withstand launch vibration, typ. 5-25 g, rms
4. radiation hardness; from ≈ 10 krad (Si) (in low Earth orbit) to > 1 Mrad (Si) (near Jupiter)
5. minimal EMI susceptibility; protection against ESD
6. adequate testing, given the improbability of repairs in space (including vacuum testing)
7. precise, careful engineering to ensure best instrument performance (justifying the cost of launch)
8. reliability and lifetime analyses and tests
9. materials choices (low outgassing, minimal mechanical stress in optics,...)
10. quality assurance, configuration control, documentation.

Although it is possible to create a low noise terahertz receiver in the laboratory, challenges exist in making it robust enough for practical use. Most electronic (but not optical) FIR components are relatively immune to launch vibration, as their small mass places resonant frequencies high above the few-hundred Hertz typical of launch vehicles. GaAs Schottky diodes are known to be relatively immune to total-dose effects resulting from the deposition of ionizing energy, but other devices now being introduced may suffer more from their use of minority carriers or nano-scale features [17]. To ensure radiometer lifetimes in excess of common 2-to-10 year mission durations, accelerated lifetests with fit to Arrhenius-lognormal or electromigration models are necessary. This is of particular importance with novel device designs and their high current densities.

V. CONCLUSION

While very few space missions have applied heterodyne FIR technology, it is quite clear that its utilization is of utmost importance in many fields of science. Many breakthrough discoveries in these fields can reasonably be expected, but are being hindered by a lack of FIR technology. Figure 3 outlines the pressing technology needs for FIR spaceborne applications.

VI. ACKNOWLEDGEMENT

We would like to acknowledge the many valuable contributions of the following people: K.A. Lee, W.R.

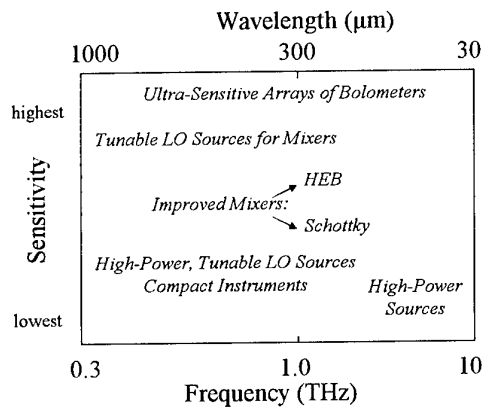


Fig. 3: Technology needs for the FIR.

McGrath, I. Mehdi, L. Samoska, P.H. Siegel, J.W. Waters, R.A. Wyss, and the continuing contributions of the Submillimeter Wave Advanced Technology team at JPL. This work is performed at the Jet Propulsion Laboratory, California Institute of Technology, under contract with the National Aeronautics and Space Administration's Office of Advanced Concepts and Technology.

References

1. <http://space.gsfc.nasa.gov/astro/specs/> and J.C. Mather et al., "The Submillimeter Frontier: A Space Science Imperative," white paper available at <http://xxx.lanl.gov/abs/astro-ph/9812454>
2. D. Leisawitz et al., to be published in *UV, Optical, and IR Space Telescopes and Instruments, Proc. SPIE*, **4013**, 2000.
3. G.H. Reike et al., "Charting the Winds that Change the Universe: Far Infrared and Submillimeter Astronomy," FIRST Science Working Group Report, June 1999.
4. see, e.g., <http://sunland.gsfc.nasa.gov/smex/swas/index.html>
5. <http://astro.estec.esa.nl/SA-general/Projects/First/bibliography.htm>
6. *Astronomy and Astrophysics in the New Millennium*, from the National Academy Press, Washington DC, 2000.
7. S. Solomon, *Rev. Geophysics*, **37**, pp. 275-316, 1999.
8. B. Carli and M. Carlotti, p. 4 in K.N. Rao and A. Weber, eds., *Spectroscopy of the Earth's Atmosphere and Interstellar Medium*, New York: Academic Press, 1992.
9. F. Barath et al., *J. Geophys. Res.*, **98**, pp. 10,751-10,762, 1993.
10. J.W. Waters et al., *J. Atm. Sci.*, **56**, pp. 194-218, 1999.
11. K. Evans & G. Stephens, *J. Atmos. Sci.*, **52**, pp. 2058-2072, 1995.
12. D.M. Mittleman et al., *Appl. Phys. B*, **68**, pp. 1085-1094, 1999.
13. M.J. Griffin, *Nucl. Inst. Meth. A*, **444**, pp. 397-403, 2000.
14. G.M. Cushman et al., *Rev. Sci. Inst.*, **68**, pp. 4596-4599, 1997.
15. P.H. Siegel et al., *IEEE Trans. MTT*, **47**, pp. 596-604, 1999.
16. S. Kayali et al., "GaAs MMIC Reliability Assurance Guidelines for Space Applications," JPL Publication 96-25 (1996).

Technological Developments for THz Electronics

Chih-I Lin¹, Manuel Rodríguez-Gironés, Victoria Ichizli, Mustafa Saglam, P. Szeliga, Hans L. Hartnagel

Abstract – Due to the lack of available power with raising frequencies, the quality and performance requirements on THz devices and circuits are especially high. Effects traditionally considered as secondary become unusually relevant and a great deal of research as well as very complex and demanding fabrication control processes are required to minimise them. In this paper we report on the recent technological efforts carried out at Darmstadt in the field of THz electronics in respect to devices as well as passive circuits elements.

I. INTRODUCTION

For the submillimetre wavelength region, devices with high cut-off frequencies over 1 THz are key active elements for both mixing and multiplying applications. Pt/n-GaAs Schottky diodes have been proven to be the best-performing devices at room temperature up to several Terahertz. In order to increase the breakdown voltage of the diode, optimisation of the passivation technique was performed. To reduce the excess noise introduced by the reactive ion etching process during the anode opening process, an investigation on the etching parameters and on post-RIE treatment methods was undertaken. Back deposition of organic etching products onto the opened area, which result in inhomogeneous deposition of Pt/n-GaAs Schottky contact, was performed. Recently, heterostructure barrier varactors have shown significant improvement in tripler performance and could be a new challenge to Schottky varactor diodes for frequency multiplication applications. With increasing interest on integration of active devices and passive circuit elements, further technological developments were carried out, which include the micro-air-bridge technique, micro-lines for coplanar as well as microstrip waveguides.

II. DEVICE TECHNOLOGIES

A. Pt/n-GaAs Schottky Diode:

The basic difference between whisker-contacted Schottky diodes and planar diodes is the usage of semiconductor area for the Schottky contact. This represents around 50% for whisker-contacted diodes and 0,2% for planar diodes. The situation is even worse for integrated circuits, where typically only one Schottky diode is realised over an area greater than 1 mm². Therefore, it is important to optimise the critical process steps in order to increase the yield of the Schottky contact. The critical steps directly related to the quality of the Schottky contact are the passivation and the anode opening using RIE.

1. Passivation Technique:

Unlike Silicon, GaAs can not be thermally oxidised on the surface to realise a good native passivation layer. Therefore, deposited SiO₂ is usually applied as the passivation layer. However, the SiO₂-layer results in a breakdown voltage of Pt/n-GaAs Schottky diode lower. The PECVD-technique can provide layers with different characteristics by combining process gases. In our investigation, we have changed the process parameters including the gas mixture, the process temperature and the process rf power. It is found that the gas flows and the rf power have the largest influence on the breakdown voltage of Schottky varactor diodes. Fig. 1 shows the dependence of the breakdown voltage on the N₂O gas flow while other gas flows are fixed to standard values. The influence of rf power is shown in Fig. 2.

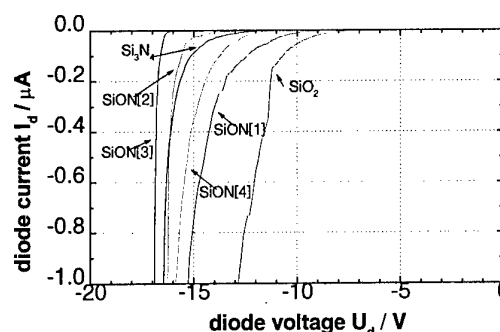


Fig.1: reverse I/V-characteristics of Schottky diodes with different passivation layers realised by changing gas mixture in the PECVD process.

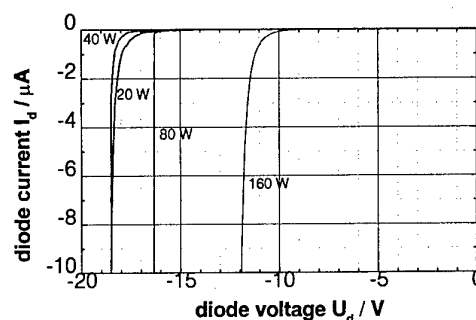


Fig.2: reverse I/V-characteristics of Schottky diodes with different passivation layers realised by varying process rf power.

¹ The authors are with the Institut für Hochfrequenztechnik, TU Darmstadt, Merckstrasse 25, D-64283 Darmstadt, Germany
E-Mail: hfmwe013@hrz2.hrztu-darmstadt.de
Home-Page: <http://www.hf.e-technik.tu-darmstadt.de/thz.html>

Both results indicate that proper passivation parameters have to be chosen to get the maximum value of breakdown voltages for given doping levels.

2. Reduction of Excess Noise Resulted from Reactive Ion Etching:

The reactive ion etching for Schottky contact area opening is the most critical step for the fabrication of Schottky diodes. It provide repeatable etch results and well-defined openings. Nevertheless, it introduces much higher excess noise which can degrade the rf performance of Schottky diodes. In our investigation, it is verified that a thermal treatment after RIE can reduce the noise temperature of Schottky diodes dramatically. Fig. 3 shows measured diode noise temperature at 1.5 GHz in dependence of overetching times. A 12-minute-etching is usually applied to exactly remove the passivation of the anode openings. One can notice that even with an overetching time of 15 minutes, a comparable noise temperature curve can be achieved when a thermal treatment is applied to the overetched sample.

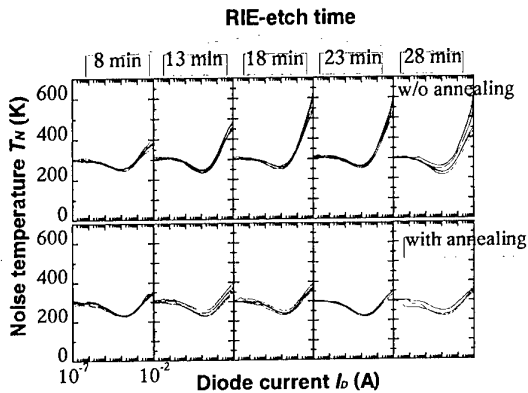


Fig. 3: Measured noise temperatures of test diodes with and without thermal treatment after the different RIE-etch times. 12 minutes of RIE are the minimum expected to remove the passivation layer.

3. Removal of Back Deposition resulting from RIE
Another disadvantage of RIE is the back deposition of etching products onto the surface which prevents homogeneous deposition of Schottky contacts and introduces a interface between the Schottky metal and the semiconductor. This layer can be effectively removed by applying AZ 400K developer directly after the RIE process. Fig. 4 shows a test sample before and after the cleaning process. Significant difference in the surface colour can be noticed.

B. Heterostructure Barrier Varactors (HBVs)

The Heterostructure Barrier Varactor (HBV) is being recently intensively investigated for direct tripling since its C-V characteristic is evenly symmetric so that only odd harmonics are generated. Because it does not need any DC bias, it is very suitable for quasi-optical power combining system. Fig. 5 shows a SEM picture of an GaAs/AlGaAs-HBV chip after completing the process and Fig. 6 the measured C/V-characteristics using a network analyser at 1 GHz.

Fig. 4: Removal of back deposition using AZ400K developer after RIE (left / bottom: before treatment, right / top: after treatment).

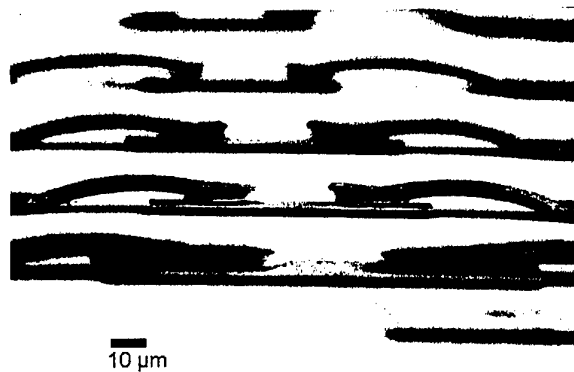


Fig. 5: SEM picture of a GaAs/AlGaAs-HBV chip after the fabrication process.

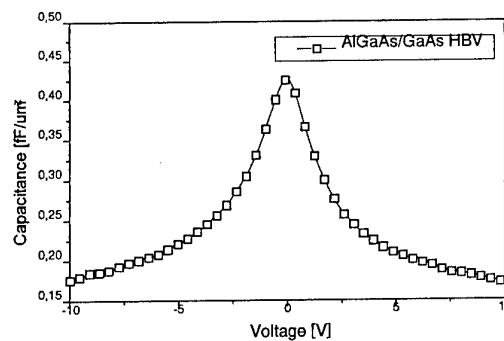


Fig. 6: at 1 GHz measured C/V-characteristics of an HBV

C. Micro-Air-Bridge Optimisation

For planar device technologies, a mechanically stable micro-air-bridge is as important as the diode itself. We have achieved high adhesion of electrolytically plated gold to a Pt/n-GaAs Schottky contact by seeding the Au layer with a sputtered Ni/Ag/Ni layer. After anode deposition and mesa formation, the needed air-bridge and pad shapes are defined photolithographically, a Ni(20nm)/Ag(80nm)/Ni(50nm) seed layer is deposited by sputtering. This enables a very dense, well-adhering layer which may be removed selectively to GaAs with different etchants. Optimisation of selective removal of this seed layer with presence of plated Gold was performed, in order to avoid large undercutting which can lead to

disconnection of the interconnects, contacting pads, etc. from the substrate. Fig. 7 shows the results achieved by the etching optimisation with minimum undercutting due to the high adhesion of the seed layer. This provides a high robustness of the micro air-bridge structure.

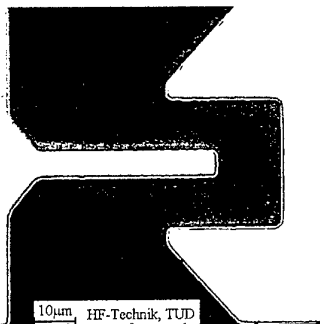


Fig. 7: Investigation of under-cutting after the process of the air-bridge. The under-cutting of the seed layer is about 1 μm .

III. INTEGRATION OF THz CIRCUIT ELEMENTS

In addition to the device developments, further technologies such as coplanar waveguides and microstrip waveguides are necessary for the monolithic integration. However, the devices as well as the circuit elements become electromagnetically large as the frequencies increase. Therefore, as opposed to the simulation and design technologies in the millimeter wave region with a relatively large tolerance in the design, sub-millimetre wave circuits have to be considered more carefully. Any discontinuity along the circuit lines can not be neglected. Therefore, 3-D electromagnetic simulators such as High Frequency Structure Simulator or Microwave Studio have to be applied to calculate their characteristics and transfer them into S-parameter for system performance optimisation. Some important technological aspects have been to be done to realise a stable fabrication process of monolithically integrated THz circuits:

1. Control of Metallisation Shape and Dimensions

With the success of MMICs, the interest to realize SMMICs is getting larger. The dimension of passive elements in SMMICs must decrease, which means that the requirements on the precision of the fabrication is higher. In addition, in mixing applications, for example, the intermediate frequency is usually several GHz, which imposes a limitation to the thinness of the metallisation (a few μm). Therefore, control of the metallisation dimensions to avoid parasitic effects resulting from any technological deviation is an important task while realizing SMMICs. Fig. 8 shows a comparison of realised 2 μm thick, 12 μm wide Au-metallised coplanar waveguide from top side as well as the bottom side to the original mask. It can be seen that the bottom side is of the same width of the mask. The top side of the metallisation is about 1 μm wider than the mask. Such variation limited by the photoresist can be considered during the simulation phase to get a more precise performance prediction.

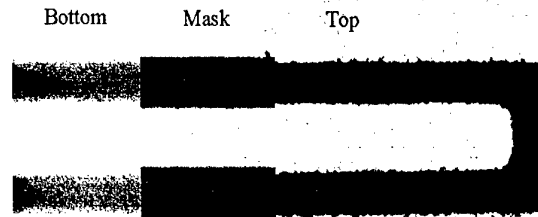


Fig. 8: Comparison of 2 μm thick Au-deposited coplanar waveguide from the top side and bottom side to the original mask. The original width of the middle line is of 6 μm . The bottom side has an identical width while the top side of about 1 μm wider than to the mask.

2. Thick Dielectrics for THz Circuits

Dielectrics are necessary for circuits using microstrip, multi-layer and planarisation of planar and integrated devices. Dielectric layers with less mechanical stress, low loss at high frequencies, good adhesion and the technological possibility to realize via-hole contact are

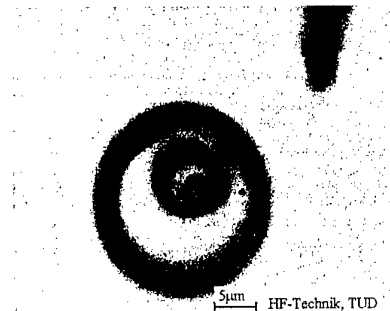


Fig. 9: Via hole through a 5- μm thick passivation layer. The 3- μm anode at the bottom of the via can be observed.

the main factors while when choosing a suitable dielectric layer. Fig. 9 illustrates a via-hole opening with a diameter of 3 μm to the Schottky diode through 5 μm thick PECVD-deposited dielectrics.

3. Process Control

A large chip area over several mm^2 is usually used in monolithically integrated THz circuits. Therefore, it is important to introduce a system of process control for THz-device fabrication to make sure that the fabrication process is executed properly. In large series production, a system of Failure Mode, Effects and Criticality Analysis (FMECA) [1] is known representing a disciplined design review technique that focuses the development of products and processes on prioritised actions to reduce the risk of product field failures, and documents those actions and the review process in large series production. In opposite to FMECA, a small production which is nowadays typical for THz-electronics, needs a separate system of control and measures adjusted to its requirements. Such system of measures includes a process identification document (PID) and a lot-

traveller (LT) for each kind of device or circuit fabricated at TU Darmstadt. PID includes full description of the fabrication process, as well as complete guidelines for the technological facilities at TU Darmstadt necessary for the fabrication process. LT accompanies each sample batch (lot) during the whole technological process. All steps are recorded by the operator according to their date and time of performance. All changes of parameters are recorded and followed. All positive or optimised changes are introduced in the new version of LT for the following batch. Apart from that a thorough system of trouble shooting (TS) is developed. It increases device yield considerably. Both LT and TS contain many images illustrating the way structures should or should not look or behave themselves electrically. The documents and the process control system described above are the first known to be used at a research university that is active in small series-production in THz-electronics.

4. <http://www.fmeca.com/>

IV. CONCLUSION

In this paper, we present the recent technological developments of THz electronics at TU Darmstadt. Pt/n-GaAs Schottky diodes have been optimised with respect to applications in the frequency range 150-2500 GHz. An improved passivation technique and post-RIE treatment leads to a significant performance improvement in the diode characteristics. The optimisation of the micro-air-bridge, the metallisation techniques and the thick dielectrics along with the optimised device technique enables a precise fabrication of SMMICs.

Acknowledgement

This work includes several research projects 'MM and Sub-MM Wave Open Structure Integrated Receiver Front-End Technology Development', 'Critical Technologies for MMW Radiometers' and 'Establish a Controlled Fabrication Process for MM and Sub-MM Wave Schottky Diode Components' funded by ESA/ESTEC, Noordwijk, as well as the MEMSTIC project funded by Deutscher Forschungsgesellschaft, and the TMR program from EU. The authors also would like to express their gratitude to the co-operation partners from Institute for Semiconductor Electronics at TU Darmstadt for the RIE and PECVD facilities and from Technical University Munich for the MBE wafers.

References

1. H. L. Hartnagel and C.-I. Lin, "Passivation of Compound-Semiconductor Surfaces For Low-Noise Terahertz Devices", *International Seminar on Semiconductor Surface Passivation*, Ustron, Poland, September 19-22, 1999
2. J. M. M. Pantoja, C.-I. Lin, M. Brandt, M. Rodríguez-Gironés, H. L. Hartnagel, J. L. Sebastian. "Influence of Reactive Ion Etching Technologies on the Microwave Noise Generated by Metal-Semiconductor Interfaces of Pt/n-GaAs Schottky Diodes", *accepted to be published IEEE Electron Device Letters in Nov. 2000*.
3. J. Stake *et al.* "Effects of Self-Heating on Planar Heterostructure Barrier Varactor Diodes," *IEEE Transactions on Electron Devices*, Vol. 45, No. 11, November 1998.

Harmonic mixing effects in Schottky diode harmonic mixers at THz frequencies

Roland Feinäugle, Heinz-Wilhelm Hübers, Jeffrey L. Hesler, *Member, IEEE*

Abstract – We report on the breakdown of IF power for certain bias voltages for single-diode Schottky mixers at THz frequencies. This dramatic loss of IF power is due to an increase of conversion loss and is governed by intrinsic and external parameters. Based on an analytical approach utilising small signal analysis, it is possible to explain the depth of the breakdown and to estimate the voltage where the breakdown occurs. Measurements for 2nd harmonic mixers show good agreement with analytical predictions.

I. INTRODUCTION

An interesting effect associated with submicron GaAs Schottky diodes has been found by several authors [1,2,3,4,5]. Deep breakdowns of intermediate frequency (IF) power have been observed when varying the DC bias voltage for Schottky diode harmonic mixers. Although this effect has been reported for some time, only recently has a theoretical explanation been given [4,5,6].

In the case of a fundamental mixer it is well understood that successively increasing the DC bias voltage or the DC bias current, respectively, yields an IF power output with a broad maximum (Fig. 1, upper curve). In contrast to that behaviour, it has been observed that under certain bias conditions the same diodes reveal a significant breakdown of IF power when operated as harmonic mixers at THz frequencies. In the case of a single-diode 2nd harmonic mixer, one IF power minimum with different depths can be observed, depending on the diode used (Fig. 2). This breakdown of IF power can be explained by small-signal analysis taking into account different mixing paths to convert power from signal frequencies into intermediate frequencies.

II. EXPERIMENTAL SET-UP

The diodes were measured in a set-up with two far-infrared (FIR) gas lasers as CW radiation sources. The FIR lasers were pumped with two CW CO₂ lasers. The laser assigned as a local oscillator (LO) was emitting at 693 GHz, whereas the 'RF' laser was operating at 1397 GHz. For comparison, the diodes were also measured as fundamental mixers with both lasers emitting at 2523 GHz and the two lasers slightly detuned yielding an IF of 1 MHz. Additionally, Schottky diodes have been measured operated as 4th harmonic mixers. Again, one laser was emitting at 693 GHz whereas the second frequency of 171.8 GHz was generated by a klystron.

R. Feinäugle and H.-W. Hübers are with the German Aerospace Center (DLR), Inst. of Space Sensor Technology and Planetary Exploration, Rutherfordstr. 2, D-12489 Berlin, Germany. Meanwhile, R. Feinäugle (email: Roland.Feinaugle@dlr.de) is with DLR's Mission Operation and Astronaut Training RB-AT, Linder Höhe, D-51147 Köln, Germany. J. Hesler is with the Department of Electrical Engineering, University of Virginia, Charlottesville, Va 22903, USA.

Table 1: Diode parameters

Diode name		117	1112	J118	1T12	1T14	1T15	1T23
Producer		UVA	UVA	MIT	UVA	UVA	UVA	UVA
Anode diameter	d_A in μm	0.8	0.45	1.0	0.5	0.5	0.25	0.25
Doping epitaxial layer	N_d in 10^{17} cm^{-3}	3	4.5	1	3	10	10	10
Thickness epitaxial layer	w_{epi} in \AA	1000	600	1000	750	450	300	300
Zero-bias capacitance	C_{j0} in fF	0.9-1.2	0.45	1.8	0.5	0.85	0.25	0.5
Series resistance	R_s in Ω	13	33	30	28	10	20	30
Ideality coefficient	η	1.3	1.4	1.15	1.22	1.5	1.5	1.6

The whisker-contacted diodes were mounted on a corner-cube reflector to couple the radiation into the submicron diameter-sized diodes. All measurements were performed at ambient temperatures. Diode parameters together with data provided by the manufacturers can be taken from Table 1. The experimental set-up is described in greater detail in [4]. Details about the Schottky diodes and their manufacturing process can be found in [7,8].

III. SMALL-SIGNAL ANALYSIS

Following the notation of [9], a 2nd harmonic mixer can be described using the admittance matrix \mathbf{Y} , which connects the small-signal voltages V_m and currents I_j at the different side-band frequencies

$$\omega_m = |m \omega_{LO} + \omega_{IF}| \quad (1)$$

with ω_{IF} the intermediate frequency. For a 2nd harmonic mixer with a RF frequency at the second upper side-band

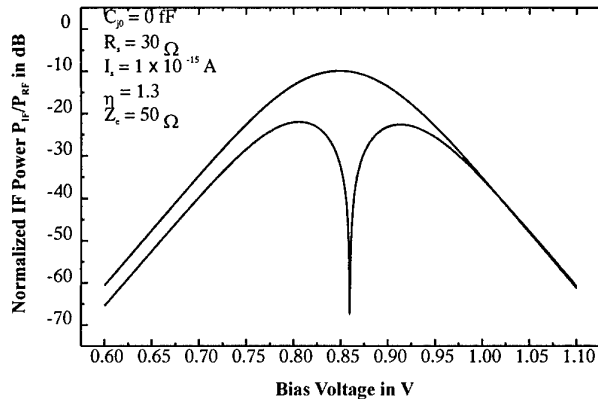


Fig. 1: Calculation of normalised IF power vs. bias voltage for a fundamental (upper curve) and a 2nd harmonic (lower curve) mixer.

of the LO frequency with all the lower side-bands ($m < 0$) as well as side-bands higher than the second upper side-band ($m > 2$) shorted out, the augmented matrix, \mathbf{Y}' , can be written as

$$\begin{bmatrix} I'_2 \\ I'_1 \\ I'_0 \end{bmatrix} = \begin{bmatrix} Y'_{22} & Y'_{21} & Y'_{20} \\ Y'_{12} & Y'_{11} & Y'_{10} \\ Y'_{02} & Y'_{01} & Y'_{00} \end{bmatrix} \begin{bmatrix} V'_2 \\ V'_1 \\ V'_0 \end{bmatrix} \quad (2)$$

For \mathbf{Y}' , the embedding impedances and the series resistances of each port are included in the network [9]. Unlike a fundamental mixer, there are no *external* currents at the LO side-bands, hence I'_1 equals zero. By eliminating V'_1 , equation (2) can thus be reduced to a 2×2 matrix:

$$\begin{bmatrix} I'_2 \\ I'_0 \end{bmatrix} = \begin{bmatrix} Y''_{22} & Y''_{20} \\ Y''_{02} & Y''_{00} \end{bmatrix} \begin{bmatrix} V'_2 \\ V'_0 \end{bmatrix} \quad (3)$$

with the elements of the reduced matrix, \mathbf{Y}'' , of the form

$$Y''_{20} = Y'_{20} - \frac{Y'_{21} Y'_{10}}{Y'_{11}} \quad (4)$$

Here, Y'_{20} represents the 'standard' mixing path for power converted from the RF frequency by mixing with the doubled LO frequency to the IF frequency. The second expression in equation (4) represents another mixing path from the RF frequency to the LO upper side-band frequency, ω_1 , and from there down to the IF frequency. If the two existing paths possess the same overall admittance the conversion efficiency will be zero. According to [9], for the case of a 2nd harmonic mixer the mixer conversion loss, L_{02} , is:

$$L_{02} = \frac{|Z_{RF} + R_{s2}|^2 |Z_{IF} + R_{s0}|^2}{4 |Z''_{02}| \text{Re}(Z_{RF}) \text{Re}(Z_{IF})} \quad (5)$$

with Z_{RF} and Z_{IF} the embedding impedances at the RF and the IF frequencies and R_{s2} and R_{s0} the respective series resistances. Z''_{02} represents the impedance matrix element connecting the exciting RF current with the IF small-signal voltage. It can be calculated by inverting equation (3) taking into account the impedance matrix, \mathbf{Z} , being the inverse of the admittance matrix, \mathbf{Y} . Z''_{02} can be calculated using

$$Y'_{mn} = G_{m-r} + i(\omega_{IF} + m\omega_{LO})C_{m-n} + \delta_{mn} \frac{1}{R_{sm} + Z_{em}} \quad (6)$$

with G_m , and C_m being the fourier coefficients of the time-dependent conductance G_j and capacitance C_j .

For known diode's I - V and C - V characteristics one can then calculate the IF power of a mixer without any numerical means. This has been done for some typical diode parameters with the zero-bias capacitance neglected (Fig. 1). As can be seen from the lower curve, a deep breakdown of the IF power appears for a harmonic mixer. This phenomenon has also been found experimentally (Fig. 2).

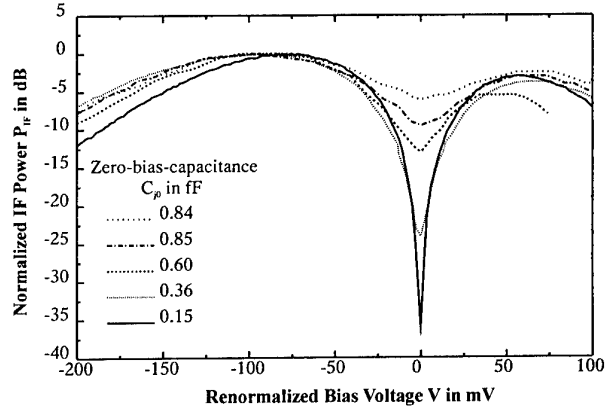


Fig. 2: Measured IF power vs. bias voltage for diodes with different zero-bias capacitances. The curves are normalised to their maximum power and overlaid at their breakdown voltage.

Now, looking at Fig. 3 gives evidence of the above stated suggestion that the two competing mixing paths lead to the breakdown of IF power. There exists a bias voltage where the two admittances have the same magnitude and are real due to the negligence of the capacitive mixing branch. This leads to an overall admittance null and thus to a null of the diode's impedance matrix element at exactly that bias voltage. On the other hand, by inserting very small diode impedances into equation (5) it is obvious that this leads to high conversion losses.

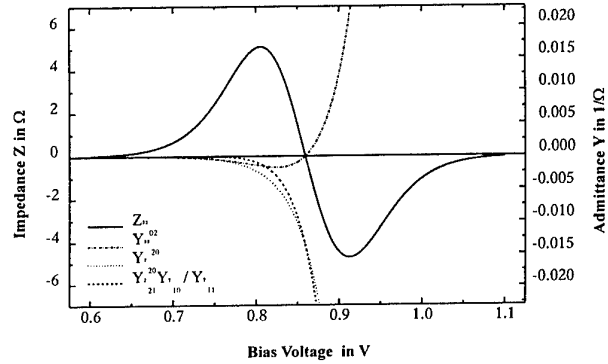


Fig. 3: Diode impedance and admittances as a function of bias voltage for a 2nd harmonic mixer.

IV. REAL DIODES

When comparing diodes with different zero-voltage capacitances, another interesting effect arises. As can be seen from Fig. 2, the depth of the measured IF power breakdown strongly depends on the zero-bias capacitance. It can be seen, in principle, that a smaller zero-bias capacitance results in a deeper minimum of the IF power. For the diode with the smallest zero-bias capacitance (0.15 fF), an overall depth of the IF power breakdown of as much as 36 dB could be measured. This phenomenon can be explained by having a closer look at the capacitive mixing branch.

Usually, the classical one-over-square-root-type C - V characteristic is assumed [9]. This yields reasonable results for small bias voltages far off the flat-band

condition. For forward bias voltages near the flat-band condition, this approach yields unreasonably high barrier capacitances. In order to avoid this singularity, an exponential diode C - V characteristic has been used that has been fitted to the so-called refined capacitance [4,5]. This refined capacitance takes into account real charge distributions through the depletion layer [10] and leads to finite barrier capacitances under flat-band conditions. Now, this approximated barrier capacitance without singularities can be used in the analytical determination of the conversion matrices.

Looking at the impedance matrix element, it can be seen that, by introducing a capacitive admittance, the impedance matrix element becomes complex. The absolute value of the impedance matrix element is not zero anymore at the IF power breakdown voltage and, therefore, the breakdown itself is not as deep as without capacitive elements.

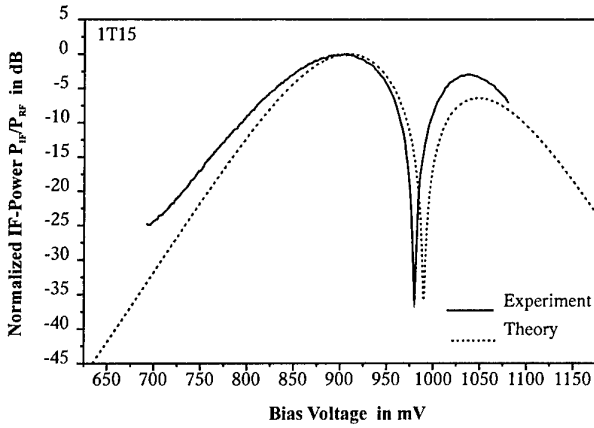


Fig. 4: Measured and calculated normalised IF power vs. bias voltage for the diode 1T15.

The reason for that behaviour can be found by looking at equation (6). It can be shown analytically that both fourier components of the conductance G_m and the capacitance C_m are either real or imaginary for the same side-band index m . Because they are connected via the complex number i , the overall admittance matrix element and, thus, the impedance matrix element is complex whenever G_m and C_m are present at the same time. The absolute value of the complex impedance matrix element, on the other hand, yields zero only if the real part as well as the imaginary part become zero for the same bias voltage. When a capacitive conductance is inserted, this still results in a minimum of the impedance matrix element but the IF power does not fall off to such an extent anymore. This now explains the experimental results of the dependency of the depth of the IF power breakdown on the zero-voltage capacitance in Fig. 2.

The results for a diode with a small zero-bias capacitance (1T15) can be seen in Fig. 4. Similar curves have been gained for all diodes. Keeping in mind the simplifications made, good matching of measured and calculated curve can be observed.

In general, all expressions in equation (6) which add an imaginary contribution to the diode's conductance have an effect on the admittance matrix element and therefore on the breakdown depth. I.e. have there been measured

deeper breakdown depths for lower LO frequencies while keeping all the other parameters constant [4].

V. VOLTAGE POSITION

After considering the depth of the IF power breakdown, an expression shall be given to estimate the bias voltage where the IF power breakdown occurs. Looking at equation (5) shows that large conversion losses and, hence, low IF power occur when Z''_{02} is small. Thus, Z''_{02} can be calculated using equations (3) and (6). From that it can be seen that Z''_{02} is small when also Y''_{20} is small. Therefore, Y''_{20} has been set to zero in order to solve this equation for the bias voltage. Again, the diode capacitance has been neglected because it only has a small effect on the IF power breakdown voltage, V_{Min} :

$$V_{Min} = \frac{\eta k T}{e} \left\{ \left(\frac{\eta k T}{e I_s} I_2 \left(\frac{e V_{LO}}{\eta k T} \right) \right) / \times \ln \left\{ \left((R_{s1} + Z_{e1}) I_1^2 \left(\frac{e V_{LO}}{\eta k T} \right) - (R_{s1} + Z_{e1}) I_0 \left(\frac{e V_{LO}}{\eta k T} \right) \frac{\eta k T}{e I_s} I_2 \left(\frac{e V_{LO}}{\eta k T} \right) \right\} \right\} \quad (7)$$

I_n is the modified Bessel function of the first kind of the n -th order and V_{LO} is the intrinsic voltage across the diode's depletion layer induced by the LO's electromagnetic field. As can be seen does V_{Min} depend on diode parameters such as ideality coefficient, saturation current, I_s , series resistance, embedding impedance as well as externally determined parameters such as the diode voltage V_{LO} . T , e and k are the temperature, the electronic charge and Boltzmann's constant, respectively.

In Fig. 5, the bias voltage at IF power breakdown, V_{Min} , has been plotted as a function of the local oscillator voltage for four different diodes. V_{LO} has been calculated from the measured bias voltage drop induced by the local oscillator when having a constant bias current source. An

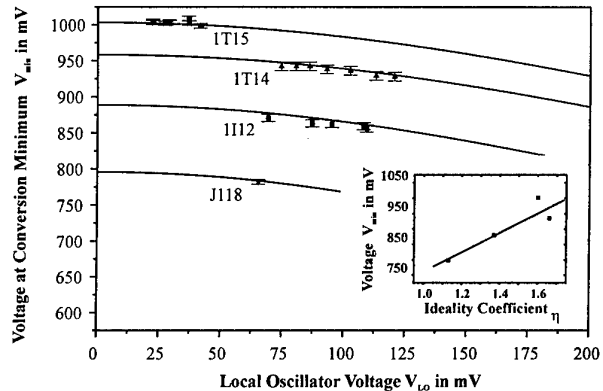


Fig. 5: Measured and calculated IF power breakdown voltages vs. local oscillator voltage.

excellent match of the predicted and the measured IF power breakdown voltages can be found, though several simplifications have been made in the theoretical model.

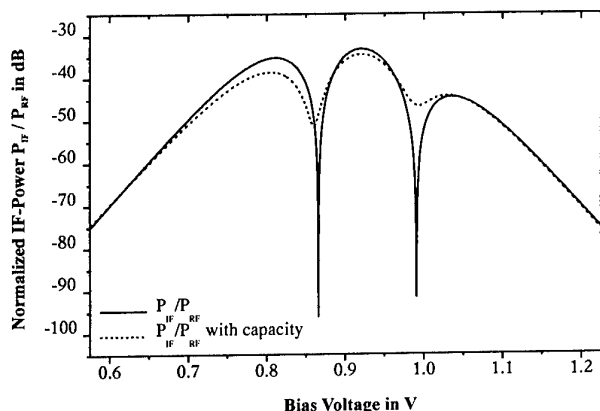


Fig. 6: Calculated IF power vs. bias voltage for a 3rd harmonic mixer.

VI. HIGHER HARMONICS

Calculating a 3rd harmonic mixer one can apply the same procedure as for a 2nd harmonic mixer. Calculations of the corresponding curves for some typical diode parameters with and without diode capacitance reveal the existence of now two IF power minima (Fig. 6). The existence of two minima for a 3rd harmonic mixer and one minimum for a 2nd harmonic mixer confirms the phenomenological law introduced in [6] that a N -th harmonic mixer produces $N-1$ IF power breakdowns. This behaviour has also been confirmed through numerical harmonic balance analysis.

Unfortunately, no appropriate FIR laser lines were available to measure these effects for a 3rd harmonic mixer. A 4th harmonic mixing experiment has been carried out instead. It can be seen in Fig. 7 that three IF power minima arise for this 4th harmonic mixer. This is a

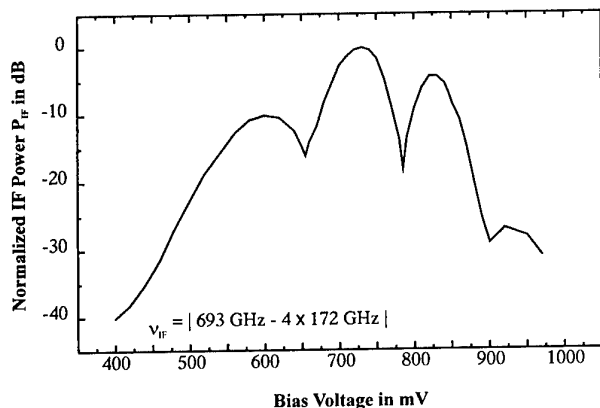


Fig. 7: Measured normalised IF power vs. bias voltage for a 4th harmonic mixer.

further strong evidence for the above-mentioned phenomenological $N-1$ law.

VII. CONCLUSION

The mixing behaviour of single-diode harmonic Schottky mixers has been investigated analytically and experimentally. It has been shown that N -th harmonic mixers produce $N-1$ IF power minima when the diode's bias voltage is varied. This has been confirmed by an analytical description for a 2nd and a 3rd harmonic mixer and through experimental results for a 2nd and a 4th harmonic mixer. The reason for these minima is a cancellation of power due to the competition of different mixing paths leading to an increased conversion loss. The depth of the IF power breakdown depends on the diode's barrier capacitance and other parameters adding to the imaginary part of the admittance. Furthermore, an approximation formula has been given with which it is possible to predict the bias voltage for the IF power minimum for a 2nd harmonic mixer. Comparison of measured and calculated curves shows good agreement.

References

1. R.U. Titz, H.-P. Röser, G.W. Schwaab, T.W. Crowe, and W.B. Peatman, "Performance of GaAs Schottky barrier diodes as mixers in the THz range", In: R.J. Temkin (editor): Conf. Digest, SPIE – The International Society for Optical Engineering, vol. 1514, Orlando, Florida, 1990.
2. R. Titz, "Untersuchung von GaAs-Schottky-Dioden mit Submillimeter-Lasern", Dissertation, Universität Bonn, 1991.
3. D.W. Porterfield, "Subharmonically pumped mixers at submillimeter wavelengths", Masters Engr., University of Virginia, 1994.
4. R. Feinäugle, "Untersuchungen zum Mischverhalten von submikron GaAs Schottky-Dioden im THz-Frequenzbereich", ISBN 3-89820-006-X, Mensch & Buch Verlag, Berlin, 1999, also Dissertation, TU Berlin, 1999.
5. R. Feinäugle, H.-W. Hübers, J.L. Hesler, and H.P. Röser, "On the Effect of IF Power Breakdowns for Schottky Diode Harmonic Mixers", submitted to IEEE Trans. Microwave Theory Tech., May 2000.
6. J.L. Hesler, D. Kurtz and R. Feinäugle, "The Cause of Conversion Efficiency Nulls for Single-Diode Harmonic Mixers", IEEE Microwave and Guided Wave Letters, 10(12), pp. 532-534, 1999.
7. T.W. Crowe, R.J. Matlack, H.P. Röser, W.L. Bishop, W.C.B. Peatman, and X. Liu, "GaAs Schottky Diodes for THz Mixing Applications", Proc. of the IEEE, 80(11): 1827-1841, 1992.
8. W.C.B. Peatman, and T.W. Crowe, "Design and Fabrication of 0.5 Micron GaAs Schottky Barrier Diodes for low-noise Terahertz Receiver Applications", Int. J. on IR and MM Waves, 11(3): 355-365, 1990.
9. D.N. Held and A.R. Kerr, "Conversion Loss and Noise of Microwave and Millimeter-Wave Mixers: Part 1 – Theory", IEEE Trans. Microwave Theory Tech., vol. MTT-26, pp. 49-55, 1978.
10. E.H. Rhoderick and R.H. Williams, "Metal-Semiconductor Contacts", Clarendon Press, Oxford, 2nd edition, 1988.

SIS Receiver Noise Stability

J.W. Kooi, G. Chattopadhyay, M. Thielman, and T.G. Phillips

California Institute of Technology, 320-47, Pasadena, CA 91125, USA.

R. Schieder

University of Koln, Dept. of Physics.

Abstract— There is a strong interest in the submillimeter astronomy community to increase the IF bandwidth of SIS receivers in order to better facilitate broad spectral linewidth and continuum observations of extragalactic sources. However, with an increase in receiver IF bandwidth there is a decrease in the mixer stability. This in turn effects the integration efficiency and quality of the measurement. In order to better understand the noise mechanisms responsible for reducing the receiver stability, we employed a technique first described by D.W. Allan and later elaborated upon by Schieder *et al.* In this paper we address a variety of factors that degrade the noise stability of SIS receivers. The goal of this exercise is to make recommendations aimed at maximizing SIS receiver stability.

Keywords— “Allan” Variance, SIS mixer stability, low noise amplifier, gain stability, bias noise, temperature fluctuation noise, acoustic vibrations, Josephson noise.

I. INTRODUCTION

RADIO astronomy receivers in general look at very weak signals deeply embedded in noise. To extract the weak signals, synchronous detection (signal on - signal off) is typically employed. This is done by either slewing the whole telescope back and forth so as to get the beam on/off the source, or by moving the secondary mirror (subreflector) of the telescope at a certain rate. The problem in both these cases is the dead time between observations, i.e., chopping efficiency. A practical lower limit for slewing the whole telescope is typically 15 seconds, while chopping the secondary mirror can perhaps be as fast as 0.2 seconds (5 Hz). Frequency switching is possible and can be at a much higher rate, but suffers from a separate set of problems not discussed here.

If the noise in the receiver system is completely uncorrelated (white), it turns out that the rate of chopping (modulation frequency) has no effect on the final signal to noise ratio. This can be deduced from the well known radiometer equation (1) which states that the noise integrates down with the square root of integration time:

$$\sigma = \frac{\langle x(t) \rangle}{\sqrt{(B * \tau_{int})}} \quad (1)$$

Here σ is the standard deviation (rms voltage) of the signal, $\langle x(t) \rangle$ the signal mean, B the effective fluctuation bandwidth, and τ_{int} is the total integration time of the data set.

However, in practice the noise in radiometers, and in particular superconductor-insulator-superconductor (SIS) receivers, appears to be a combination of low frequency

drift (correlated noise), $1/f$ electronic noise and white (uncorrelated) noise. Hence, there is an optimum integration time, known as the “Allan” stability time (T_A), after which observing efficiency is lost. In actual synchronous detection measurements “n” samples of difference data (signal on - signal off) are taken, each with a period T . These differences are then averaged so that the total observed time equals $n * (2T)$. If the period T is larger than the “Allan” stability time (T_A) of the system, then apart from loss in integration efficiency, there will be a problem with proper baseline subtraction. This manifests itself in baseline ripples at the output of the spectrometer which severely limits how well the noise integrates down with time.

In this paper an effort has been made to understand the de-stabilizing effects on a radiometer output due to:

- LNA bias noise and gain fluctuations of the cryogenic low noise amplifier (LNA) immediately following the mixer.
- Temperature modulation of the SIS mixer and low noise amplifier.
- Acoustic noise pickup by the LNA and the local oscillator (LO).
- LO pumping of the SIS mixer.
- SIS mixer bias noise and the effectiveness of suppressing the Josephson effect [5] by means of a magnetic field applied across the SIS junction.

The goal of this paper is to focus attention to the output noise stability of radiometers and SIS receivers in particular. This work is especially pertinent in light of the present trend to construct very large IF bandwidth SIS and HEB receivers for spectroscopic and continuum observations of very weak extragalactic sources.

II. THEORETICAL CONSIDERATIONS

To optimize observation efficiency, it is important to find the best secondary mirror (subreflector) chopping rate. This requires a knowledge of the nature of the receiver noise fluctuations. In practice, we have employed a method developed by Allan [2], Barnes [3], and further elaborated on by Schieder *et al.* [4].

Following Schieder’s analyses of synchronous detection, two sets of contiguous data samples are taken, each with the same integration time (T). The first measurement is the signal $s(t)$, and the second measurement is the off-source

reference signal $r(t)$. In the analysis, it is assumed that there is no dead time between the data samples. If we define the first measurement as:

$$S(T) = \int_0^T s(t) dt, \quad (2)$$

and the second measurement as:

$$R(T) = \int_T^{2T} r(t) dt, \quad (3)$$

then difference of the two measurements is

$$D(T) = S(T) - R(T). \quad (4)$$

Because we look at signals deeply embedded in the noise and are only interested in how the noise integrates down with time, we can make the simplification that there is essentially no signal present in $s(t)$. This means that on average $D(T) = 0$, and $s(t) = r(t)$.

If μ is defined as the mean of $D(T)$ and σ^2 the variance of $D(T)$ then

$$\sigma^2(T) = \langle [D(T) - \mu]^2 \rangle = \langle D(T)^2 \rangle - \langle D(T) \rangle^2 \quad (5)$$

Here $\langle D(T)^2 \rangle$ is the mean (expectation value) of the difference squared and $\langle D(T) \rangle^2$ is the squared mean of the difference. But since $\langle D(T) \rangle$ equals zero we get

$$\sigma^2(T) = \langle [R_1(T) - R_2(T)]^2 \rangle. \quad (6)$$

From [2] we find that the "Allan" Variance is defined as:

$$\sigma_A^2(T) = 1/2\sigma^2(T) \quad (7)$$

The mathematical treatment of the above expression can be found in [3] for different types of noise spectra. If the noise spectral density is represented by a power law, then

$$S(f) = f^{-\alpha}, \quad \alpha = [-1, 3] \quad (8)$$

and one finds that

$$\sigma_A^2(T) \propto T^{\alpha-1} \quad (9)$$

where $\alpha = 0$ stands for white (uncorrelated) noise, $\alpha = 1$ for "1/f" noise, and $\alpha \geq 2$ for correlated low frequency (drift) noise. Using a simple power law to characterize low frequency drift noise might not be correct. A more accurate representation would be to describe the noise by a correlation function, given by:

$$g(\tau) = \langle r(t) * r(t + \tau) \rangle. \quad (10)$$

The "Allan" variance can then be expressed as:

$$\sigma_A^2(T) = \frac{1}{T^2} \int_{-T}^T (T - |\tau|)(g(\tau) - g(T + \tau)) d\tau. \quad (11)$$

Because we are interested only in integration times less than the correlated (drift) noise time scale, the correlation

function can be expanded in a power series with only a few terms:

$$g(\tau) = g(0) - a\tau^\beta \pm \dots, \quad \beta = 1, 2, \dots \quad (12)$$

From equation (11) we get

$$\sigma_A^2(T) \propto T^\beta. \quad (13)$$

Combining equation (9) and equation (13) we find that for a noise spectrum that contains drift, white noise, and 1/f noise that the "Allan" variance takes the form:

$$\sigma_A^2(T) = aT^\beta + \frac{b}{T} + c, \quad (14)$$

where a, b , and c are appropriate constants. For short integration times, the variance decreases as $\frac{1}{T}$, as expected from the radiometer equation (1). For longer integration times, the drift will dominate as shown by the term aT^β . In that case, the variance starts to increase with a slope β which is experimentally found to be between 1 and 2. On certain occasions, it is observed that the variance plateaus at some constant level. This is attributed to the constant factor and is representative of flicker or 1/f noise in the electronics.

Plotting $\sigma_A^2(T)$ on a log-log plot demonstrates the usefulness of this approach in analyzing the radiometer noise statistics. For reference, a slope of $(\frac{1}{T})$ has been drawn in all figures. This represents the uncorrelated (white) noise part of the spectrum. The minima in the plot gives the "Allan" time (T_A), the crossover from white noise to 1/f or drift noise. For the sake of optimum integration efficiency, one is advised to keep the integration time well below the system's "Allan" time.

Finally, it is often of interest to estimate what happens to the "Allan" stability time if the IF bandwidth of the radiometer is increased. Solving equation (14) for T as a function of receiver IF bandwidth we get:

$$T_A \propto B_{IF}^{-\left(\frac{1}{\beta+1}\right)}, \quad \beta = 1 - 2. \quad (15)$$

B_{IF} presents the IF bandwidth and β the slope of the drift noise as discussed above. As the uncorrelated (white) noise component of the mixer spectral output power is reduced, the intersect between radiometric (1) and drift noise (13) equations occurs at an earlier time. Where exactly the two curves intersect depends on the statistical nature of the long term drift. It should be noted that all data presented in this paper have been taken with a 100 MHz bandpass filter.

III. MEASUREMENT SETUP AND CALIBRATION

The measurement configuration is shown in Fig. 1 and consists of a variable 0-10 dB step attenuator, a 100 MHz bandwidth filter, centered at 1.5 GHz, and a Schottky power detector. RF signal power on the detector has been kept constant to within 1 dB throughout the measurements. The whole unit is bolted to a 1 cm thick aluminum

between positions than actually taking data. On the other hand, if integrations longer than 10 seconds are allowed, baseline subtraction suffers and integration efficiency is expected to be poor. An alternative observing mode is 'on-the-fly' (OTF) mapping. Here the telescope is allowed to scan through the source while averaging the data in short (typically ~ 3 sec) bins. When atmospheric conditions are good (≤ 1 mm of precipitable water vapor) 'on' scans can last for upwards of 120 seconds before a single 'off' scan is taken, thereby minimizing the loss in time associated with slewing the telescope between 'on' and 'off' positions. However, even when the 'OTF' mapping technique is used observing efficiency and proper baseline subtraction will improve if the receiver stability is increased.

When SIS receivers are used for large continuum or low resolution extragalactic observations only fast 'beam switching' operation seems appropriate.

Finally, it should be noted that interferometers (multiple telescope's used together to synthesize a single large diameter telescope) are by their nature much more tolerant of gain fluctuations than single dish receivers. This because only correlated signals will appear at the output of the spectrometer while uncorrelated signals such as receiver instabilities will not. Note however that this does not negate the importance of high integration efficiency, and hence having receivers with suitable long stability ("Allan" variance) times.

XII. CONCLUSION

A detailed study on the output noise stability of SIS receivers is presented. We have investigated the destabilizing effects of acoustic vibrations on a low noise amplifier (LNA) and local oscillator (LO) chain, micro-phonics noise on the LNA and SIS mixer bias lines, SIS constant voltage feedback bias noise, Josephson oscillation noise, and finally thermal drift noise of the SIS mixer and low noise amplifier.

In the process we found that fundamentally the SIS mixer is stable to at least 6 seconds in a 100 MHz bandwidth. This limit is set by how well one is able to suppress the Josephson effect in the superconducting tunnel junction and possibly also by SIS mixer bias noise, which modulates the mixer gain. In practice though the Josephson effect does not limit the stability of SIS receivers, rather the stability of the receiver is set by numerous external factors.

In a passive cooled dewar we have measured "Allan" variance stability times up to 9 seconds with an above the energy gap biased SIS mixer (IF bandwidth = 100 MHz). The "Allan" variance time in this case is limited by the room temperature IF total power amplifier and measurement setup.

In an active cooled hybrid style dewar the situation was much worse. With the low noise amplifier mounted on the 15K active cooled stage we measure an "Allan" variance time of 1.5 seconds, both at the observatory and in the laboratory. Vibration isolating the low noise amplifier gives a significant stability improvement, however the exact amount of improvement is very much dependent on the

amplifier design and employed mounting scheme.

In the lab we did not observe a difference in the "Allan" variance stability time of the receiver when the junction was biased in closed feedback, or open loop mode. At the observatory, due to the large EMI/RFI noise environment, we did in fact notice a significant change.

The mixer gain of a Local Oscillator pumped SIS junction has been measured and is observed to be a strong and negative function of temperature. The mixer's peak sensitivity to temperature change appears to be at approximately 4.9 Kelvin. The low noise amplifier (GaAs HEMT's) in contrast has a small, linearly varying, and positive temperature dependence. Cooling the mixer below 3K improves the mixer gain by 10%, but even more importantly reduces the mixer's susceptibility to LHe bath temperature fluctuations. In high resolution spectrometer mode with a channel bandwidth of 100 KHz, 1 second of "Allan" stability time and an high altitude Helium bath temperature of 3.6 Kelvin, we find a maximum allowed temperature fluctuation of 106 mK/second for the LNA and 48 mK/second for the SIS mixer. At 4.2 Kelvin the allowed SIS mixer temperature fluctuation has been reduced to 13.8 mK/second. These numbers are upper limits, and for wide bandwidth continuum or coarse resolution extragalactic observations the result is much more stringent.

Finally, high mobility transistor (HEMT) gain fluctuations, if any, appear to be at least an order of magnitude below such noise sources as acoustic vibrations, bias line noise due to high EMI/RFI noise environment, and problems with Josephson noise suppression.

It is recommended that special attention be given to minimize microphonic pickup in the LNA and Local Oscillator chain. Temperature fluctuations should be kept at a minimum, especially so when the mixer is operated at a Helium bath temperature of 4.2 Kelvin. In a high noise environment such as an observatory, it may be advisable to use several different feedback loop time constants, depending on the mode of operation. And finally a resistive divider network in the SIS and LNA bias line should at all cost be implemented.

XIII. ACKNOWLEDGMENTS

We wish to thank Jonas Zmuidzinas and Frank Rice of Caltech for very helpful discussions on the fundamental physics of SIS mixers, Chris Walker of the University of Arizona, Dave Woody of Caltech, and John Carlstrom of the University of Chicago for their input regarding the implications of receiver instability to Radio Astronomy, and Sander Weinreb of JPL for his thoughts on LNA gain stability. This work was supported in part by NSF grant# AST-9615025.

REFERENCES

- [1] J.D. Kraus, "Radio Astronomy", 2nd Edition, pp7-8
- [2] D. W. Allan, "Statistics of Atomic Frequency Standards", *Proc. IEEE*, Vol. 54, No. 2, pp 221-230, 1969
- [3] A.B Barnes, "Characterization of frequency stability", *IEEE Trans. Instrument Measurements*, Vol. IM-20, No. 2, pp 105-120, 1971

- [4] R. Schieder, "Characterization and Measurement of System Stability", *SPIE, Vol 598, Instrumentation for Submillimeter Spectroscopy* (1985)
- [5] B.D. Josephson, "Possible new effects in superconductive tunneling", *Phys. Letters 1*, (1962) pp 251-253
- [6] R. Bradley, *NRAO*, Private Communication
- [7] S. Padin, "A Cooled 1-2 GHz balanced HEMT amplifier", *IEEE, Microwave Theory and Techniques*, Vol 39, No. 7, pp. 1239-1243 (1991)
- [8] *Infrared Laboratories, Inc.* 1808 East 17th Street, Tuscon, Az 85719
- [9] B.N Ellison, "A low noise 230 GHz SIS receiver", *Int. J. Infrared and Millimeter waves*, Vol. 8, pp. 609-625, June 1987
- [10] CTI-Cryogenics, Helix Technology Corporation, Nine Hampshire Street, Mansfield, MA 02048, USA.
- [11] Personal communication
- [12] G. Chattopadhyay, D. Miller, H. G. LeDuc, and J. Zmuidzinas, "A 550-GHz Dual Polarized Quasi-Optical SIS Mixer," *Proceedings of the Tenth International Symposium of Space Terahertz Technology*, Charlottesville, Virginia, pp. 130-143, March 16-18, 1999.
- [13] J. W. Kooi , M. Chan, B. Bumble, and T. G. Phillips, "A low noise 345 GHz waveguide receiver employing a tuned $0.50 \mu\text{m}^2$ Nb/ AlO_x /Nb tunnel junction," *Int. J. IR and MM Waves*, vol. 15, No. 5, May 1994.
- [14] J.W. Kooi, J. Pety, B. Bumble, C.K. Walker, H.G. LeDuc P.L. Schaffer, and T.G. Phillips, "A 850 GHz Waveguide Receiver employing a Niobium SIS Junction Fabricated on a 1um Si3N4 Membrane," *IEEE Transactions on Microwave Theory and Techniques*, Vol. 46, No. 2, pp151-161, February 1998.

Progress in Heterostructure Barrier Varactor Frequency Multipliers

Jan Stake, Mattias Ingvarson, Lars Dillner, and Erik Kollberg

Abstract – The Heterostructure Barrier Varactor diode and its performance as a varactor frequency multiplier is reviewed.

I. INTRODUCTION

The Heterostructure Barrier Varactor (HBV) diode which was introduced about ten years ago, Kollberg and Rydberg [1, 2], is a strong candidate for high power frequency multipliers at millimetre and submillimetre wave frequencies. Since the HBV has a symmetric capacitance-voltage (C-V) characteristic, it operates unbiased and will only produce odd harmonics when pumped with power at the fundamental frequency, f_p . The absence of even harmonics simplifies the realisation of higher order multiplier circuits. For the tripler case, it is possible to build a multiplier circuit considering the pump frequency and the output frequency only. As a result of the simplified circuit, design of frequency triplers and quintuplers operating over a wider frequency range is possible. An important advantage of the HBV diode compared to the Schottky varactor diode is that several barriers can be epitaxially stacked, which increases the power handling capability considerably, Krishnamurthi *et al.* [3] and Rahal *et al.* [4]. Hence, an HBV diode can be tailored for a certain application in terms of both frequency and power handling capability.

Recently, HBVs have been fabricated on a copper substrate to improve their heat sinking capability [5]. These devices can be designed to handle at least one Watt of input power and yet maintain the device temperature below 100°C. For a single twelve-barrier HBV, a realistic conversion efficiency of 10% is expected, thereby providing output power in the region of 100 mW at 250 GHz. This could then be used to drive an HBV quintupler to provide milliwatt levels of power at THz-frequencies.

II. MATERIAL SYSTEMS

The HBV consists of a high bandgap semiconductor sandwiched between low bandgap semiconductors. The high bandgap material (barrier) prevents electron transport through the structure. When the structure is biased, electrons are accumulated on one side of the barriers and depleted on the other side of the barriers. The resulting C-V is shown in Fig. 1. It is necessary that the barrier material and the depletion layer material have almost the same lattice constants to avoid lattice dislocations and inferior performance. However, it is possible to grow dislocation free layers with a small

Table I ITME 1817 layer structure

Layer	Material	Thickness [Å]	$ N_D - N_A $ [cm ⁻³]
12	InAs	100	$>5 \cdot 10^{18}$
11	In _x GaAs $x=0.53 \rightarrow 1$	} 400	$>5 \cdot 10^{18}$
10	In _{0.53} GaAs		$>5 \cdot 10^{18}$
9	In _{0.53} GaAs	4000	$3 \cdot 10^{16}$
8 x 6	In _{0.53} GaAs	200	undoped
7 x 6	In _{0.52} AlAs	50	undoped
6 x 6	AlAs	30	undoped
5 x 6	In _{0.52} AlAs	50	undoped
4 x 6	In _{0.53} GaAs	200	undoped
3	In _{0.53} GaAs	4000	$3 \cdot 10^{16}$
2	In _{0.53} GaAs	3000	$>5 \cdot 10^{18}$
1	InP		$>5 \cdot 10^{18}$
Subst.	InP		N ⁺⁺

lattice mismatch if the layers are thinner than a critical thickness. The first HBV diode was realised using GaAs/Al_{0.7}GaAs grown on GaAs [2]. The GaAs/AlGaAs material system is well characterised and relatively simple to process. A drawback with this device is the comparatively large conduction current due to a low conduction band offset and, hence, a corresponding low barrier height. The conduction current deteriorates the efficiency. It has also been shown that the temperature increases when the diode is pumped, which further increases the conduction current and leads to an even lower efficiency, Stake *et al.* [6].

The material system In_{0.53}GaAs/In_{0.52}AlAs grown on InP offers a larger conduction band offset, which results in a lower conduction current and an improved varactor performance. It is also possible to increase the effective barrier height even further if a thin layer of AlAs is inserted in the middle of the barrier. It is very difficult to grow thick epilayers of high quality on InP by MBE. Thick epilayers are needed for planar HBVs, since they use thick buried contact layers, and for HBVs with a large number of barriers. However, it has recently been shown that very good HBV material can be grown by MOVPE, Strupinski *et al.* [7]. A material grown by MOVPE is presented in Table I. The structure, originally designed for planar devices, is similar to HBV materials grown by MBE, but with larger undoped spacer layers to prevent diffusion of silicon into the barrier layers.

A lower doping concentration in the depletion layers results in a higher breakdown voltage and a low minimum capacitance. Typically a current density ≤ 0.1 $\mu\text{A}/\mu\text{m}^2$ is required for good efficiency, yielding a

The authors are with the department of Microelectronics ED, MC2, Chalmers University of Technology, SE-412 96 Göteborg, Sweden. E-mail: jan.stake@ep.chalmers.se

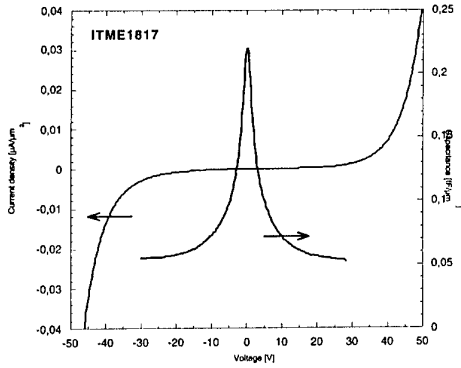


Fig. 1. Current density versus voltage and C-V characteristics for a six-barrier HBV (ITME 1817).

maximum voltage of 8 V per barrier for $N_d = 3 \cdot 10^{16} \text{ cm}^{-3}$ in the depletion layers. A drawback with a low doping concentration is that it results in a high resistivity which increases the losses and decreases the dynamic cut-off frequency. MOVPE material is now equal in performance to MBE material, Strupinski *et al.* [7], Lheurette *et al.* [8].

III. HBV DESIGN AND ANALYSIS

For a varactor multiplier, the conversion efficiency is related to the ratio of the pump frequency and the dynamic cut-off frequency $f_c = (S_{\max} - S_{\min}) / 2\pi R_s$, where R_s is the series resistance, S_{\max} and S_{\min} are the maximum and minimum elastance during a pump cycle [9]. For an HBV tripler, the maximal conversion efficiency can be estimated from the following empirical expression [10]:

$$\eta \approx \frac{100}{1 + 200 \left(\frac{f_p}{f_c} \right)^{1.5}} [\%]. \quad (1)$$

How to calculate corresponding optimal embedding impedances, input power, and theoretical limit of the bandwidth was presented by Stake *et al.* [10]. To maximise the efficiency, the above dynamic cut-off frequency should be maximised. Thus, optimum performance is a trade-off between maximum elastance swing and series resistance. The maximal extension of the depleted region is determined by the maximum electric field at breakdown or the effect of current saturation [11, 12]. Hence, the maximum elastance swing is determined by one of the following conditions:

- depletion layer punch-through;
- large electron conduction across the barrier region at high electric fields;
- large electron conduction from impact ionisation at high electric fields;
- the saturated electron velocity in the material determines the maximum length an electron can travel during a quarter of a pump cycle.

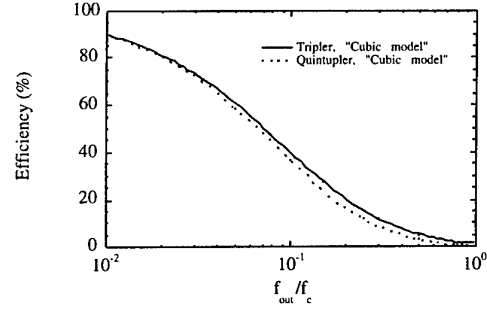


Fig. 2. Maximum tripler and quintupler efficiencies normalised to the same output frequency.

For a given application (frequency and available power) and material system, it is possible to optimise the HBV layer structure in terms of number of barriers, length and doping concentration of depletion layers, see reference [10].

It is interesting to compare quintuplers with triplers as power sources for the same output frequency. A varactor diode is usually dimensioned from the output impedance. Since the output impedances are approximately equal for triplers and quintuplers, triplers and quintuplers with the same diode capacitance can be compared. Referring to Figure 2 it is shown that the maximum efficiencies are almost equal, except for output frequencies near the dynamic cut-off frequency. This indicates that quintuplers have an advantage over triplers, since they use a lower input frequency where more powerful sources are available. The circuit is more complicated for quintuplers since the impedance at the idler frequency has to be optimised.

As discussed previously, the conduction current is a strong limiting factor for the conversion efficiency. The small signal conductance is, as the capacitance, voltage dependent. If the ratio $G_{\max} / (C_{\min} \omega_p) < 0.1$, the conductance current will not deteriorate the efficiency more than a few tenths of a dB.

Accurate quasi-static models that describe the voltage across the HBV capacitance and the conduction current have been proposed by Dillner *et al.* [13]. For detailed HBV analysis, codes combining time-dependent numerical device analysis with frequency-domain harmonic-balance analysis can be used [14, 15].

IV. HBV FREQUENCY MULTIPLIERS

The first HBV tripler experiment was performed in a crossed-waveguide mount. The single-barrier GaAs/-AlGaAs HBV was contacted with a whisker wire, Rydberg *et al.* [2]. A maximum output power of 1 mW was generated at 225 GHz and the peak flange-to-flange efficiency was 3.1 %.



Fig. 3. Planar 2x2-barrier HBV (NU2003J) design.

The first planar GaAs/AlGaAs HBV diode was tested in a crossed-waveguide frequency tripler, Jones *et al.* [16]. A maximum output power of 2 mW was generated at 252 GHz and the peak efficiency was 2.5 % for a four-barrier device. Cooled measurements on this type of HBVs showed an improvement in efficiency of a factor of three [6]. To reduce the effect of self-heating, a planar four-barrier GaAs/AlGaAs HBV diode with an improved diode geometry (Fig. 3) was fabricated. 4 mW output power and 4.8 % efficiency was obtained at an output frequency of 246 GHz, Stake *et al.* [17].

A planar four-barrier InGaAs/InAlAs HBV diode was tested in a crossed-waveguide frequency tripler, Mélique *et al.* [18]. A maximum output power of 9 mW was generated at 250 GHz and the peak efficiency was 12 %. This is the best HBV multiplier performance obtained so far.

In a new design the InP substrate is etched away and replaced with pure copper, Dillner *et al.* [19]. This offers not only a lower series resistance but also an improved thermal heat sink, which improves the power handling capacity. In a recent tripler experiment using a crossed waveguide mount, Dillner *et al.* [5] (see Fig. 4), and this new diode, a maximum output power of 7.1 mW was generated at 221 GHz with a flange-to-flange efficiency of 7.9 %.

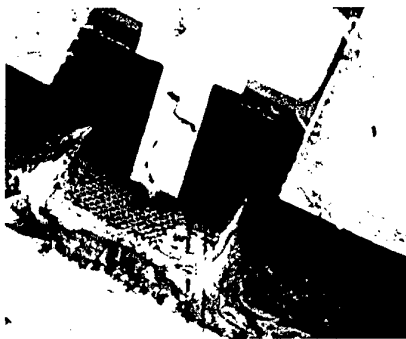


Fig. 4. HBVs on a copper substrate mounted in the output waveguide. The three-barrier HBV is contacted with a planar whisker.

In addition to the crossed waveguide multiplier, two other HBV multiplier topologies, Hollung *et al.* [20, 21], have been developed. One is a broadband distributed HBV frequency tripler consisting of a finline transmission line periodically loaded with 15 HBV diodes, see Fig. 5. This frequency tripler uses planar diodes with two barriers and exhibits 10 mW peak radiated power at 130 GHz with

more than 10% 3-dB bandwidth and 7% conversion efficiency.

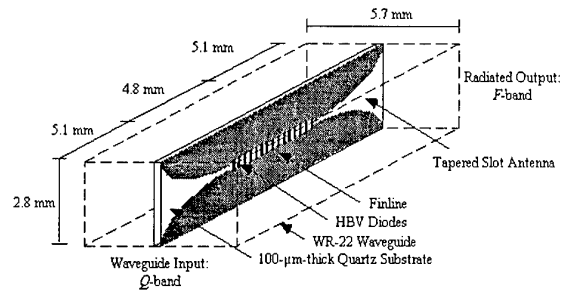


Fig. 5. Non-linear transmission line HBV tripler consisting of two tapered slot antennas and a finline loaded with 15 HBVs on a 100 μm -thick quartz substrate.

The second design is a quasi-optical HBV diode frequency tripler consisting of two slot antennas loaded with four planar HBV diodes and located at the focal plane of a dielectric lens, Fig. 6. The quasi-optical tripler demonstrates a radiated power of 11.5 mW and a conversion efficiency of about 8 %.

Single barrier InGaAs/InAlAs HBV diodes have also been tested in a crossed-waveguide frequency quintupler, Räsänen *et al.* [22]. 0.78 % efficiency was reported at an output frequency of 172 GHz.

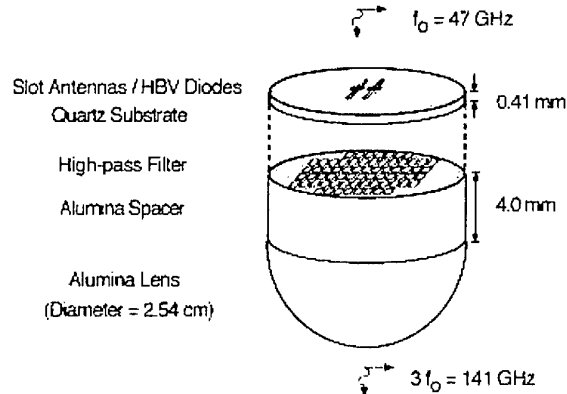


Fig. 6. Quasi-optical HBV tripler. The circuit consists of two slot antennas loaded with four HBV diodes and located at the focal plane of a dielectric lens.

V. CONCLUSION

The HBV is today comparable to Schottky varactors in terms of conversion efficiency, I-V and C-V predicts superior power handling capability, and the HBV is more suitable for high order frequency multipliers. The performance of planar GaAs/AlGaAs HBV multipliers is severely reduced due to self-heating. This problem can be solved by modifying the epitaxial structure to increase the barrier height and by improving the diode heat sink. High efficiency and wide bandwidth HBV triplers have been demonstrated. We predict that HBV quintuplers will be very competitive as high frequency power sources.

ACKNOWLEDGEMENT

The authors would like to express their acknowledgements to Dr. Chris Mann (RAL), Dr. Stein Hollung, Dr. Stephen Jones, Dr. Mohamed Henini, Mahdad Sadeghi (CTH) and Dr. Wlodek Strupinski (ITME) for good co-operation.

REFERENCES

- [1] E. L. Kollberg and A. Rydberg, "Quantum-barrier-varactor diode for high efficiency millimeter-wave multipliers," *Electron. Lett.*, vol. 25, pp. 1696-1697, 1989.
- [2] A. Rydberg, H. Grönqvist, and E. L. Kollberg, "Millimeter- and Submillimeter-Wave Multipliers Using Quantum-Barrier-Varactor (QBV) Diodes," *IEEE Trans. Electron Devices*, vol. 11, pp. 373-375, 1990.
- [3] K. Krishnamurthi, R. G. Harrison, C. Rogers, J. Ovey, S. M. Nilsen, and M. Missous, "Stacked Heterostructure Barrier Varactors on InP for Millimeter Wave Triplers," presented at Fifth International Symposium on Space Terahertz Technology, 1994.
- [4] A. Rahal, R. G. Bosisio, C. Rogers, J. Ovey, M. Sawan, and M. Missous, "A W-Band Medium Power Multi-Stack Quantum Barrier Varactor Frequency Tripler," *IEEE Microwave Guided Wave Lett.*, vol. 5, pp. 368-370, 1995.
- [5] L. Dillner, W. Strupinski, S. Hollung, C. Mann, J. Stake, M. Beardsley, and E. Kollberg, "Frequency Multiplier Measurements on Heterostructure Barrier Varactors on a Copper Substrate," *Electron Device Letters*, vol. 21, pp. 206-208, 2000.
- [6] J. Stake, L. Dillner, S. H. Jones, C. M. Mann, J. Thornton, J. R. Jones, W. L. Bishop, and E. L. Kollberg, "Effects of Self-Heating on Planar Heterostructure Barrier Varactor Diodes," *IEEE Trans. on Electron Devices*, vol. 45, pp. 2298-2303, 1998.
- [7] W. Strupinski, J. Sass, L. Dillner, K. Kosiel, R. Jakiela, J. Stake, and M. Ingvarson, "MOVPE strain layers - growth and application," presented at The Tenth International Conference on Metalorganic Vapor Phase Epitaxy, Japan, 2000.
- [8] E. Lheurette, P. Mounaix, P. Salzenstein, F. Mollet, and D. Lippens, "High Performance InP-based Heterostructure Barrier Varactors in Single and Stack Configuration," *Electronics Letters*, vol. 32, pp. 1417-1418, 1996.
- [9] L. Dillner, J. Stake, and E. L. Kollberg, "Analysis of Symmetric Varactor Frequency Multipliers," *Microwave Opt. Technol. Lett.*, vol. 15, pp. 26-29, 1997.
- [10] J. Stake, S. H. Jones, L. Dillner, S. Hollung, and E. Kollberg, "Heterostructure Barrier Varactor Design," *IEEE Transaction on Microwave Theory and Techniques*, vol. 48, 2000.
- [11] J. T. Louhi and A. V. Räisänen, "On the Modeling and Optimisation of Schottky Varactor Frequency Multipliers at Submillimeter Wavelengths," *IEEE Trans. Microwave Theory Tech.*, vol. 43, pp. 922-926, 1995.
- [12] E. L. Kollberg, T. J. Tolmunen, M. A. Frerking, and J. R. East, "Current Saturation in Submillimeter Wave Varactors," *IEEE Trans. Microwave Theory Tech.*, vol. 40, pp. 831-838, 1992.
- [13] L. Dillner, J. Stake, and E. L. Kollberg, "Modeling of the Heterostructure Barrier Varactor Diode," presented at 1997 International Semiconductor Device Research Symposium, Charlottesville, 1997.
- [14] J. R. Jones, G. B. Tait, S. H. Jones, and S. D. Katzer, "DC and Large-Signal Time-Dependent Electron Transport in Heterostructure Devices: An Investigation of the Heterostructure Barrier Varactor," *IEEE Trans. Electron Devices*, vol. 42, pp. 1393-1403, 1995.
- [15] J. Stake, S. H. Jones, J. R. Jones, and L. Dillner, "Analysis of Carrier Transport in a Heterostructure Barrier Varactor Diode Tripler," presented at 1997 International Semiconductor Device Research Symposium, Charlottesville, 1997.
- [16] J. R. Jones, W. L. Bishop, S. H. Jones, and G. B. Tait, "Planar Multi-Barrier 80/240 GHz Heterostructure Barrier Varactor Triplers," *IEEE Trans. Microwave Theory Tech.*, vol. 45, pp. 512-518, 1997.
- [17] J. Stake, C. M. Mann, L. Dillner, S. H. Jones, S. Hollung, M. Ingvarson, H. Mohamed, B. Alderman, and E. L. Kollberg, "Improved Diode Geometry for Planar Heterostructure Barrier Varactors," presented at Tenth International Symposium on Space Terahertz Technology, Charlottesville, VA, 1999.
- [18] X. Mélique, A. Maestrini, E. Lheurette, P. Mounaix, M. Favreau, O. Vanbésien, J. M. Goutoule, G. Beaudin, T. Nähri, and D. Lippens, "12% Efficiency and 9.5 dBm Output Power from InP-based Heterostructure Barrier varactor Triplers at 250 GHz," presented at IEEE-MTT Int. Microwave Symposium, Anaheim, 1999.
- [19] L. Dillner, J. Stake, and E. L. Kollberg, "Heterostructure Barrier Varactors on Copper Substrate," *Electronics Letters*, vol. 35, pp. 339-340, 1999.
- [20] S. Hollung, J. Stake, L. Dillner, M. Ingvarson, and E. L. Kollberg, "A Distributed Heterostructure Barrier Varactor Frequency Tripler," *IEEE Microwave and Guided Wave Letters*, vol. 10, pp. 24-26, 2000.
- [21] S. Hollung, J. Stake, L. Dillner, and E. L. Kollberg, "A 141-GHz Integrated Quasi-Optical Slot Antenna Tripler," presented at IEEE AP-S International Symposium and USNC/URSI National Radio Science Meeting, Orlando, 1999.
- [22] A. V. Räisänen, T. J. Tolmunen, M. Natzic, M. A. Frerking, E. Brown, H. Grönqvist, and S. M. Nilsen, "A Single Barrier Varactor Quintupler at 170 GHz," *IEEE Trans. Microwave Theory Tech.*, vol. 43, pp. 685-688, 1995.

Analysis and Measurement of a Millimeter-Wave Holographic Power Combiner for 5 IMPATT Oscillators

M. HÖFT AND R. JUDASCHKE

Arbeitsbereich Hochfrequenztechnik
Technische Universität Hamburg–Harburg
D–21073 Hamburg, Germany

Phone: +49 40 42878-3370, FAX: +49 40 42878-2755, E-mail: m.hoeft@tuhh.de

Abstract

IMPATT diodes are the most powerful solid-state devices for millimeter-wave frequencies, but their power still has to be increased to compete with vacuum tubes. This can be accomplished by combining the power of an oscillator ensemble. In the millimeter-wave region, the most efficient method to perform power combining is holography. A 65 GHz holographic power combiner for five IMPATT oscillators has been designed and experimentally investigated utilizing quasi-optical multiple-device circuit technology.

1 Classical Methods of Power Combining

Power combining, i.e. summarizing the output power from many individual sources, is a necessary means if one likes to replace vacuum tubes by all-solid-state sources in the frequency ranges of submillimeter and millimeter waves. Eliminating tube sources from many systems is, on the other hand, often inevitable if space-borne and even air-borne applications shall be met because of their inherent disadvantages of great consequence: complicated bias supply, large size and weight, and in particular limited lifetime. Although power combining seems to be a mature concept for microwaves [1], it is accompanied by a great deal of conceptual and technical problems for millimeter waves [2]. This may be explained by considering the basic requirements for any power combining circuits. An ideal method of power combining should show the following features:

- sufficient spacing for appropriate heat sinking,
- combining efficiency independent of number of sources,

- combining efficiency approaching unity,
- negligible ohmic losses,
- arbitrarily large number of sources,
- individual sources with equal (i.e. maximally available) output power,
- uniform distribution of coupling for stable mutual synchronisation,
- unlimited scalability with frequency,
- broad bandwidth performance,
- graceful degradation with respect to failure of single devices,
- low sensitivity to geometrical parameters,
- flexibility and robustness.

All hitherto known principles of power combining do not meet even one of these requirements if the frequency exceeds about 60 GHz whereas holographic power combining which is developed at our institute will fulfill all of them.

The classical methods of power combining encompass the Kurokawa circuit, ladder networks, spatial power combining [3], grid amplification, and resonant quasi-optical power combining [4]. They all suffer from undesired miniaturization with increasing frequency which limits their performance drastically. Hence one will not find any successful experimental solutions to the problem at frequencies above say 60 GHz.

In summary, there did not exist till now any principle for millimeter (or even submillimeter) wave power combining showing more than one or two of the desired twelve features which have been listed before. Moreover, the features these principles could meet have only been reached as a first approximation. Hence one can state that the problem of millimeter

wave power combining is yet unsolved. Naturally, the same statement also holds for the inverse problem of power splitting which is inherent in the realization of multiple device frequency multipliers and of down-converters for both focal plane arrays and sub-harmonic pumping.

2 Holographic Power Combining

Fig. 1 shows a typical source of Gaussian beams. It involves a horn antenna as beam launcher and a (solid-state) source of millimeter waves. As has been emphasized, a millimeter-wave source has normally a large electrical dimension. This also holds for an effective beam launcher, i.e. the diameter of the horn is a relatively large multiple of a wavelength.

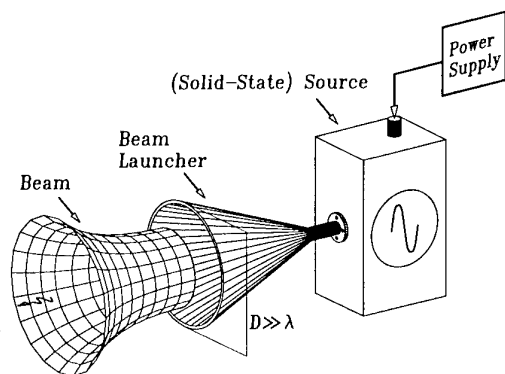


Figure 1: A millimeter-wave source along with a beam launcher

Trying to spatially combine the power output by a group of these Gaussian beam generators, we arrange a linear array of them. In regard to their dimensions and according to the theory of antenna arrays, the radiation pattern of such array contains a few grating lobes, as can be recognized from the contour plot of Fig. 2.

The reason why only a few number of grating lobes has a significant power level is the highly directive radiation of each array element, i.e. of the beam launchers. Hence the aim should be to suppress the grating lobes and deflect their power in the boresight direction.

One could explain the formation of the grating lobes by a phase deviation in the radiated wavefront as compared with a plane or a well-collimated wave. Keeping this fact in mind, one should propose

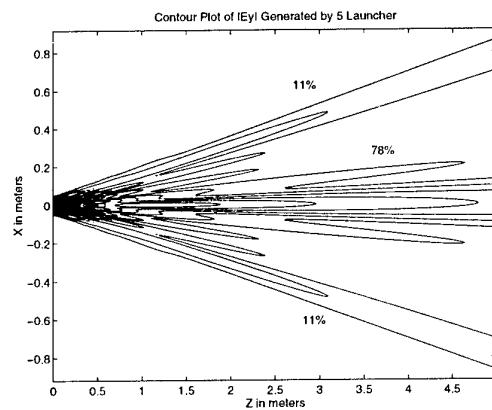


Figure 2: Radiated field by a 5-element antenna array with an inter-element spacing of 30 mm. The antennas radiate at 65 GHz.

a scheme for phase front transformation in order to eliminate the undesired grating lobes. Holography offers an appropriate solution.

It is well known that in holography for a complete reconstruction of a wave scattered by an object, i.e. the object wave, its interference with a reference wave, usually a plane wave, is recorded in a hologram. Recording can be performed by changing the local electrical characteristics of the hologram in accordance with the interference pattern. Illumination of the hologram with the same reference wave makes the reconstruction of the object wave possible.

This principle is remarkable for any type of wavefront transformation like that we are looking for. In other words, to eliminate the grating lobes, we should record the interference of the wavefront generated by the array with a plane wave. Hence illumination of the hologram with the array produces the reference plane wave which must carry the combined power. For instance, using an optimization approach, we designed a hologram for suppression of grating lobes appearing in the radiation pattern of a five-element antenna array. Fig. 3 depicts the impact of this computer-generated hologram on the radiation intensity of the array. The hologram used in this simulation is made of dielectric and has a very simple groove shape.

It can be seen that the hologram reduces the grating lobes and directs their power in the desired direction. The obtained efficiency in this process, i.e. the ratio of the total power carried by the main lobe to the total radiated power by the array, is 97%.

Fig. 4 illustrates a holographic power combiner. It is evident that this power combining approach is appli-

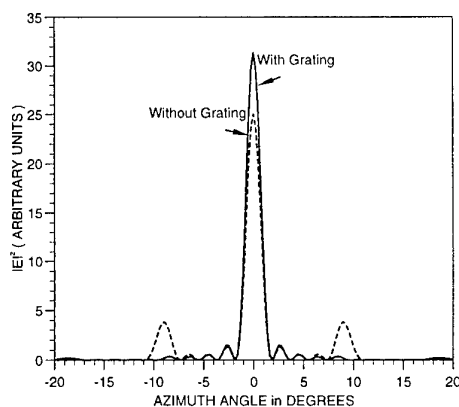


Figure 3: Reduction of the grating lobes with a hologram. The array has the same characteristics as that in Fig. 2.

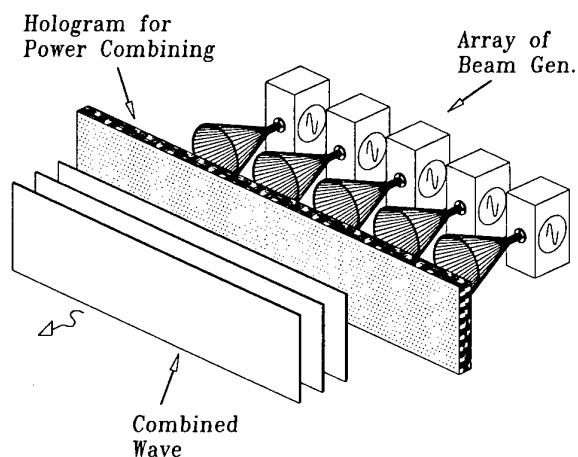


Figure 4: A holographic power combiner

cable to an arbitrary number of identical sources, and may be scaled up to extremely high frequencies. Furthermore, an optimized design of the hologram simplifies the process of mutual synchronization between the sources by a low-power reflection from the hologram, which is particularly relevant for any nonresonant power combining method. More details on this subject can be found in [5].

In order to design the holographic power combiner, one needs a powerful (i.e. a numerically efficient but still rigorous) tool. This has recently been developed in form of a model of (coupled) transmission lines [6]. Its numerical evaluation has proved that all features of ideal power combining stated above are really obtained by a holographic combiner. Hence the experimental demonstration is the only task which must still be done. It is the topic of our present work.

3 Results for a 65 GHz 1-D Holographic Combiner

We have chosen a 1-D array of 5 IMPATT oscillators operating at 65 GHz as a first example. Each diode delivered more than 100 mW of output power. In the oral presentation, we will report about the design of both the oscillator array and the combining hologram, describe its optimization, and discuss the practical problems which had to be solved. The most important and difficult of them is to perform mutual phase synchronization so that all single sources are oscillating in the in-phase mode. To this end, a partially reflecting dielectric plate of approximately half of a wavelength thickness has been located at the output side of the hologram. First experimental results show an overall combining efficiency of 84% while the theoretical limit is 97%.

References

- [1] K. J. Russell, "Microwave Power Combining Techniques," *IEEE Trans. Microw. Theo. Tech.*, vol. MTT-27, pp. 472-478, May 1979.
- [2] K. Chang, C. Sun, "Millimeter-Wave Power-Combining Techniques," *IEEE Trans. Microw. Theo. Tech.*, vol. MTT-31, pp. 91-107, Feb. 1983.
- [3] R. A. York, R. C. Compton, "Quasi-Optical Power Combining using Mutually Synchronized Oscillator Arrays," *IEEE Trans. Microw. Theo. Tech.*, vol. MTT-39, pp. 1000-1009, June 1991.
- [4] J. W. Mink, "Quasi-Optical Power Combining of Solid-State Millimeter-Wave Sources," *IEEE Trans. Microw. Theo. Tech.*, vol. MTT-34, pp. 273-279, Feb. 1986.
- [5] M. Shahabadi, K. Schünemann, "Holographic power combining: A new principle for millimeter and submillimeter-wave power combining", in *Proc. 26th European Microwave Conf.*, Prague, Czech Republic, Sept. 1996, pp. 115-119.
- [6] M. Shahabadi, K. Schünemann, "Millimeter-wave holographic power splitting/combining," *IEEE Trans. Microw. Theo. Tech.*, vol. MTT-45, pp. 2316-2323, 1997.

Polymeric Dielectric Mirrors for the sub-millimeter Wavelength Range

T.Dobbertin, D.Turchinovich, P.Knobloch, and M.Koch

Abstract – We present a simple and cheap approach to fabricate large-area stopband filters and mirrors for the THz range. This approach extends the well known concept of dielectric mirrors to the far-infrared. We use alternating layers of different materials to build a flexible all-plastic mirror. The films with a typical thickness of several tens of micrometers are arranged to form pairs of quarter-wavelength-layers. The structures are characterized by THz time-domain spectroscopy. The experimental results are in good agreement with transfer matrix simulations.

I. INTRODUCTION

THz technology is a rapidly growing field of scientific and engineering interest. The body of the work is devoted to THz spectroscopy. Besides the principles of “light”-matter interaction in the THz range, which represent problems interesting on their own right, people focus on several THz applications in the field of medical imaging and sensing in general. Another important aspect is the development of electronic devices such as Gunn, Impatt, and Schottky diodes etc [1,2,3], which could serve as emitters and receivers in future wireless short-range communication networks. Obviously those systems will also require a variety of passive devices such as stop-band and band-pass filters, which can be used for frequency selection and impedance matching.

Several approaches to fabricate the sub-mm optical filters were reported so far including metallic meshes [4,5] and photonic band-gap (PBG) crystals [6]. Metallic meshes are periodically perforated metal films. While a wire grid represents a high-pass filter, a low-pass can be realized by an array of metal squares which are separated by sections of dielectric material. An periodic array of cross shaped metal structures on a dielectric layer represents a band-pass filter, cross shaped dielectric sections in a metal film lead to a stop-band filter. Those metallic mesh structures can be produced using photolithographic etching [4] or vacuum deposition [5]. In principle this “metal film approach” can provide filters with large lateral dimensions.

Photonic band-gap structures, on the other hand, can only act as stop-band filters. They can be manufactured using micromachining. Reported are 3-dimensional structures with a wood-pile geometry [6], i.e. they consist of layers of parallel dielectric rods which are tilted by 90 degrees

from layer to layer. The overall dimensions of the structure in [6] are 2x2 cm. Such a small area will most likely be common to 3-dimensional PBG structures due to the complex fabrication process.

In this work we present an easier and cheaper method to fabricate the large area filters and mirrors. We produce dielectric mirrors for sub-mm range simply by stacking alternating $\lambda/4$ layers of polymeric materials with different refractive indices. The materials relevant for commercial dielectric mirrors should obviously satisfy the following conditions: a sufficient step in the refractive index, low absorption and dispersion, mechanical stability, processing simplicity and low cost. For a first demonstration we use commercial polymer films of polyethylene (PE), low density polyethylene (LDPE), polypropylene (PP) and Styrolux™ (SX). They satisfy the above mentioned criteria, have a thickness ranging from a few tens to more than a hundred microns and are widely available.

Material	Thickn. [μm]	Ref. ind. n	$\lambda/4$ at
PE	100	1.67	450
PE	120	1.67	375
PE	150	1.67	299
PE	100	1.73	432
PE	190	1.74	267
PP	150	1.53	326
SX	300	1.59	157
SX	100	1.8	417
SX	100	1.8	417
LDPE	60	1.7	735
LDPE	70	1.7	630
LDPE	80	1.7	551
LDPE	90	1.7	490

Table 1: Properties of the polymeric films.

II. EXPERIMENTAL SETUP

The mirrors were characterized with a THz Time-Domain Spectrometer which contains photoconductive dipole antennas. In this experimental scheme information on the sample under investigation is obtained by comparing so called THz waveforms taken with and without a sample in the THz beam. The frequency spectra obtained via a Fourier-transformation of the waveforms extend from a few tens of gigahertz to a few terahertz. This technique gives a very high signal-to-noise ratio (not less than 1000/1). For details on such a spectrometer refer see Ref [7].

T.Dobbertin, D.Turchinovich, P.Knobloch, and M.Koch are with the Institut für Hochfrequenztechnik, TU Braunschweig, Schleinitzstr. 22, 38106 Braunschweig. (e-mail: p.knobloch@tu-bs.de)
D.Turchinovich is on the leave from A.F.Ioffe Physico-Technical Institute, 194021 St.Petersburg, Russia

III. RESULTS AND DISCUSSION

To find combinations of two different films which represent a pair of $\lambda/4$ layers for a certain frequency we first estimated the refractive indices of all polymer films available. The estimation was done by measuring the time shifts introduced by the films. The refractive indices for the investigated films range from 1.5 to 1.8. They are listed in table 1.

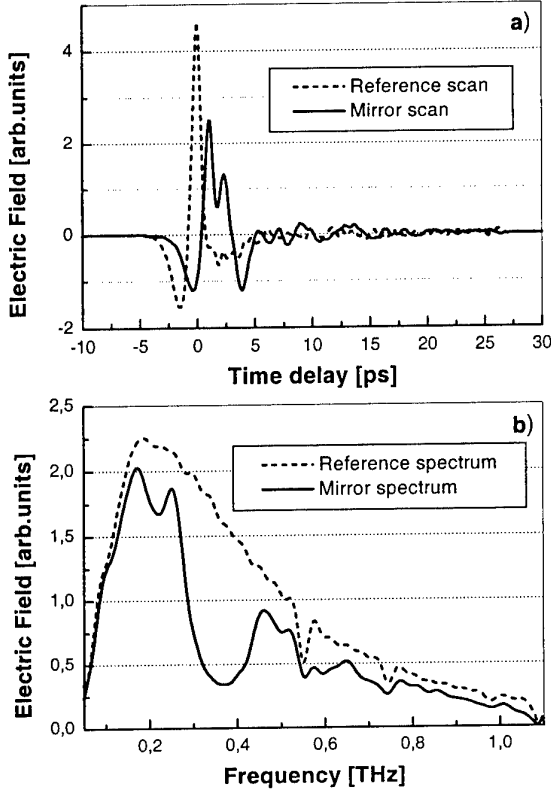


Fig. 1: a) Solid line: THz waveform after passing through an air-plastic mirror. Dashed line: free space reference scan. b) Spectra corresponding to the data in a).

Based on the results of table 1 we have fabricated several structures comprising different film combinations. To obtain a tight structure and to avoid air bubbles between the layers they were mechanically pressed together using a specially designed holder. Here we restrict ourselves to an area of 2x2 cm.

Besides all-plastic structures one can also easily assemble an air-plastic mirror. This is accomplished by using spacers with a desired thickness. In our first attempt we simply cut out some area from a plastic film to produce a spacer. The advantage of such a structure is the higher step in the refractive index between the layers.

The transmission functions of the dielectric mirrors are obtained from a comparison of a freespace reference measurement and a measurement with the sample in the beam. Fig. 1a shows the waveforms of a reference scan

(dashed line) and a scan on a structure consisting of 3.5 pairs of 100 μm PE and 200 μm air (solid line). The corresponding frequency spectra are shown in Fig 1b. The sharp dips around 0.56 and 0.75 THz, which can be seen more clearly in the reference spectrum, correspond to rotational transitions of atmospheric water vapor. The transmission spectrum obtained for this structure is shown in Fig. 2 as a solid line. At the position of the stop-band which is centered around 350 GHz the transmission is suppressed by 95%.

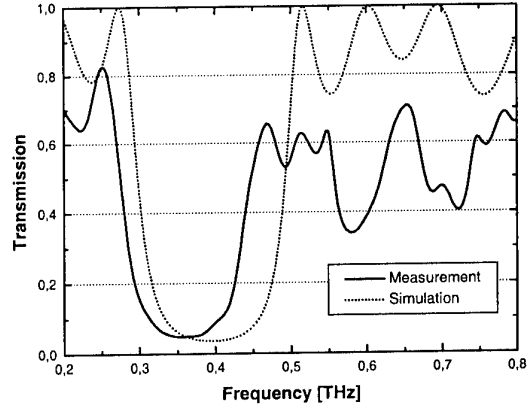


Fig. 2: Solid line: experimental transmission spectrum of a mirror consisting of 3.5 pairs of 100 μm PE films and 200 μm air films. Dashed line: simulated transmission spectrum.

The experimental data are compared to a numerical simulation based on the transfer matrix method (TMM) [8]. In TMM a characteristic transfer matrix is assigned to each layer. The overall optical properties of the whole structure are then described by a matrix obtained by multiplying the individual matrices. The result of this simulation using the experimentally determined film thickness and refractive index is shown in Fig. 2 as a dashed line. We obtain a reasonable agreement between measured and simulated data. Yet, the experimental stop-band is slightly red-shifted with respect to the theoretically predicted one. This red-shift is observed for all mirror structures we have fabricated. It may result from small random tilts of the interfaces inside the mirror structure or from slight uncertainties in values of the refractive index.

Similar results are obtained on an all-plastic mirror. The results shown in Fig. 3 are obtained for a structure that consists of 8.5 pairs of 190 μm thick PE and 300 μm thick StyroluxTM films. In the experimental spectrum (solid line) the fundamental stop-band is observed around 175 GHz together with the second order stop-band at 350 GHz. In addition, there are indications for higher order stop-bands. The latter conclusion can be drawn from a comparison of the experimental curve with the

TMM simulation (dashed line) which shows all stop-bands equally pronounced.

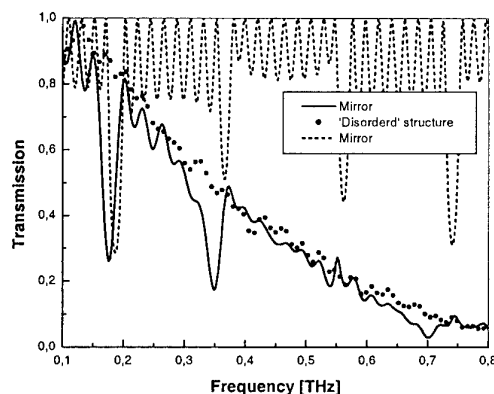


Fig. 3: Experimental transmission spectra of an all-plastic mirror (solid line) and 'disordered' structure (dots). Simulated transmission spectrum of the mirror (dashed line). The mirror consisted of 8.5 pairs of 190 μm PE and 300 μm StyroluxTM films.

Again, good agreement between both curves is found regarding the width and positions of the stop-bands. There is however a striking difference in the overall transmission. Experimentally the transmission is strongly suppressed at higher frequencies; an effect which can also be observed in the data of Fig. 2. To investigate the nature of this effect we performed measurements on a "disordered" structure which contains the same layers but without the periodic arrangement. The transmission function of the disordered structure is plotted as dots in Fig. 3. It shows the same drastic decrease with increasing frequency, yet, without the stop-bands which are typical for the mirror arrangement. Since the THz absorption of polymeric materials is quite low (typically less than a few inverse centimeters) and, in addition, does not strongly depend on the frequency, we can exclude absorption as the loss mechanism at higher frequencies. We therefore conclude, that the losses are due to scattering arising from film imperfections. In fact a profile scan of a StyroluxTM film (not shown here) reveals a micro-roughness with a typical length scale in the order of 400-500 μm . Although more profile scans and further analysis are needed, it is obvious that thickness fluctuations on this length scale should lead to strong scattering for frequencies above a few hundred GHz.

IV. CONCLUSION

In conclusion, we have presented a cheap and easy approach to build large area dielectric mirrors and filters for the sub-mm wavelength range. Even with no special but commercially available plastic films, we were able to demonstrate the main effects and to observe pronounced stop-bands. The produced structures show, however,

frequency depending losses due to film roughness. Future efforts will focus on the fabrication of high quality mirrors using smoother polymer layers. In addition, we will build a reflection setup to detect the THz radiation reflected from our structures.

The structures presented here may act as wallpaper to shield and isolate single buildings or rooms in future wireless pico-cellular networks [9].

Acknowledgement

D.Turchinovich acknowledges the financial support from the Gottlieb Daimler- und Karl Benz-Stiftung (scholarship 02-36/99).

References

1. H.Eisele, "Two-terminal Devices as Fundamental Solid-state Terahertz Oscillators", Conference on Terahertz Spectroscopy and Applications, SPIE vol. 3828, Munich 1999
2. H.L.Hartnagel, "THz Device Technology for Monolithic Integration Using III-V Semiconductors", in: Proceedings of IEEE 7th International Conference on Terahertz Electronics, p. 48-51, Nara, 1999
3. E. Schomburg, R. Scheuerer, S.Brandl, K.F. Renk, D.G. Pavel'ev, Yu. Koschurinov, V. Ustinov, A. Zhukov, A. Kovsh, and P.S. Kop'ev, "InGaAs/InAlAs superlattice oscillator at 147 GHz" Electron. Lett. **35**, pp 1491-1492, 1999
4. C. Winnewisser, F. Lewen, J. Winzierl, and H. Helm, "Transmission features of frequency-selective components in the far-infrared determined by terahertz time-domain spectroscopy" Appl. Opt. **38**, pp 3961-3967, 1999
5. T.Timusk and P.L.Richards, "Near millimeter wave bandpass filters" Appl. Opt., **20**, pp 1355- 1360, 1981
6. A.Chelnokov, S.Rowson, J.M. Lourtzioz, L.Duvillart, J.L.Coutaz, "Terahertz characterisation of mechanically machined 3D photonic crystals", Electron. Lett. **33**, pp 1981-1983, 1997
7. D.Grischkowsky, S.Keiding, M. van Exter, C.Fattinger, "Far-infrared time-domain spectroscopy with terahertz beams of dielectrics and semiconductors", J. Opt. Soc. Am. **7**, p. 2006-2015, 1990
8. M.Born, E.Wolf, "Principles of Optics"; Cambridge University Press, 1998.
9. German patent application # 100 33 259.5; July 18th 2000.

Coherent and Incoherent Phase Retrieval using Gaussian Beam Modes

Cr  dhe O'Sullivan¹, Stafford Withington² and J. Anthony Murphy¹

Abstract – Phase retrieval techniques are important at terahertz frequencies where it is often difficult to determine the phase of a field directly. In this paper we present a phase retrieval technique based on a Gaussian-Beam formalism. We show how the complex mode coefficients of a coherent field can be determined by fitting to intensity distributions at any two planes. We extend the analysis to incoherent or partially-coherent fields by working in terms of coherence matrices rather than mode coefficients. Working with the coherence matrix also allows us to vary the entropy of the field as part of the fitting process and to handle the problem of noise in the measurements more correctly. We illustrate our techniques with some simple examples.

I. INTRODUCTION

The phase retrieval problem arises when attempting to determine the phase of a complex function from measurements of intensity alone. Such situations occur frequently in fields such as microscopy and antenna design where far-field intensity patterns can most easily be measured. The complex coefficients of non-ideal horns and of antennas (e.g. planar antennas) whose mode coefficients are not otherwise known, are needed in the design of many submillimetre optical systems. Different object-plane fields can yield the same intensity in the far-field, and so to obtain a unique solution for the object-plane phase, additional information must be supplied (see e.g. Taylor[1] for an overview of the problem and possible solutions). Gerchberg and Saxton [2] suggested a technique using intensity measurements in the Fraunhofer and object planes, Misell [3] used intensity distributions in two slightly defocused images. In the case of few-moded bolometers for example, the analysis must be applicable to partially coherent fields.

Here we follow the method of Isaak et al.[4] and describe the object in terms of Gaussian beam modes (see e.g. [5]). The mean-square error between the measured (numerically simulated) and trial intensity distributions on two planes is then minimised by adjusting the complex mode coefficients. Again using the Gaussian beam formalism, we extend the technique to partially coherent fields by adjusting the elements of its coherence matrix rather than its mode coefficients. We find it useful to describe the degree of coherence of the field, using the concept of entropy, in order to constrain the solution, particularly for the incoherent case or where noise is present in naturally coherent fields.

II. COHERENT PHASE RETRIEVAL

The intensity distribution of a beam, at a distance z from the waist, can be expressed in terms of basis functions (ψ_n) appropriate to the symmetry of the source as

$$I(r, z) \propto \left| \sum_n (a_n \exp(jp_n)) \psi_n(r, z) \exp(jn\Delta\phi(z)) \right|^2, \quad (1)$$

where a_n and p_n are the mode amplitudes and phases, $\Delta\phi$, the phase slippage between modes is

$$\Delta\phi = \tan^{-1} \left(\frac{\lambda z}{\pi W^2} \right), \quad (2)$$

and W is the beam waist radius.

Table 1: Coherent phase retrieval

Actual Values		Retrieved Values	
a_i	Δp_i	a_i	Δp_i
0.78119	-	0.78125	-
0	(0.1000)	1.05055×10^{-4}	-0.6233
-0.23166	0.2000	-0.23177	0.1997
0	(0.3000)	-4.25362×10^{-4}	3.0074
0.053578	0.4000	0.053841	0.4092

So the phase retrieval problem, in the coherent case, is to determine the a_n and the p_n by fitting to intensity measurements alone. Intensity measurements on at least two planes are needed, but unlike some retrieval techniques there is no restriction on which two, since the beam can be propagated to any plane by simply changing the phase slippage term. The expression

$$\sum_k \sum_i (I_{k,i} - M_{k,i})^2 \quad (3)$$

is minimised using a suitable algorithm[†] to adjust the mode amplitude and phases. $I_{k,i}$ is the modelled intensity at point r_i on plane k and $M_{k,i}$ is the corresponding measurement. (Sampling and data-weighting issues have been discussed elsewhere [4]). As an example we have simulated the (one-dimensional) field produced by a corrugated conical horn at two planes, one close to the mouth of the horn, the other in the far-field. We sampled

C. O'Sullivan, and J. A. Murphy are with the National University of Ireland, Maynooth, Ireland.

S. Withington, is with the Cavendish Laboratory, Cambridge, UK.

[†] Minimisations were carried out using MATHEMATICA[®]'s FindMinimum routine which uses a modification of Powell's method [8].

the distributions at 11 points and attempted to recover the first 5 Hermite-polynomial modes.

The actual values used in the simulation are listed in Table 1 along with the retrieved values. The initial trial values were zero, except for the lowest-order mode amplitude which was set to 1. We found the coherent phase retrieval for examples of this type did not depend significantly on the initial values chosen. The phase retrieval process does not constrain the absolute phase and so we list the phase difference between each mode and the fundamental.

Table 1 shows excellent agreement between retrieved and simulated values. Optimisation of the choice of planes, measurement weightings and sampling may further improve the results, but in this paper we instead concentrate on extending the technique to partially coherent fields. As the method described so far relies on the field modes maintaining a fixed phase relationship, another method must be chosen for this.

An alternative approach, appropriate for both coherent and partially-coherent fields, is to work in terms of their coherence matrices rather than mode vectors. We describe such a method in the following sections.

III. THE COHERENCE MATRIX

The analysis of partially coherent fields has been described previously [6]. We summarise some of the main points here. A partially coherent field is constructed from a set of coherent diffracting free-space modes. We assume that the field under investigation is one member of an ensemble of such fields and, as with a coherent field, it can be expanded in terms of a sum of modes

$$E^i(\mathbf{r}, \omega) = \sum_m A_m^i(\omega) \psi_m(\mathbf{r}, \omega), \quad (4)$$

so long as the bandwidth is sufficiently small that the phase at one point in a member of the ensemble is well-defined in respect to the phase at any other point in the same field. The cross spectral density W is then

$$\begin{aligned} W(\mathbf{r}, \mathbf{r}') &= \langle E^i(\mathbf{r}) E^{i*}(\mathbf{r}') \rangle \\ &= \sum_m \sum_n C_{mn} \psi_n^*(\mathbf{r}') \psi_m(\mathbf{r}) \end{aligned} \quad (5)$$

where

$$C_{mn} = \langle A_n^{i*} A_m^i \rangle \quad (6)$$

are the elements of the coherence matrix. The coherence matrix characterises the form of a field at any plane, with all the second-order statistical properties being completely specified. In terms of the cross spectral density, the elements of the coherence matrix are given by

$$C_{mn} = \int W(\mathbf{r}', \mathbf{r}) \psi_n^*(\mathbf{r}') \psi_m(\mathbf{r}) ds' \quad (7)$$

where the expansion functions ψ_m form an orthonormal basis set and s is the source.

For an incoherent field of uniform intensity

$$W(\mathbf{r}', \mathbf{r}) = I_0 \delta(\mathbf{r}' - \mathbf{r}) \quad \text{and} \quad (8)$$

$$C = I_0 \mathbf{I}; \quad (9)$$

all the modes are excited equally and independently. For a completely coherent field the coherence matrix can be simply calculated from the ordinary mode coefficients as

$$C = \mathbf{A} \mathbf{A}^{*T}. \quad (10)$$

A partially coherent field can be traced through a submillimeter-wave optical system using the overall coherent-mode scattering matrix \mathbf{S} of the system. Withington & Murphy[6] have shown that

$$\mathbf{D} = \mathbf{S} \mathbf{C} \mathbf{S}^{*T} \quad (11)$$

where \mathbf{C} is the coherence matrix at the input plane of the system and \mathbf{D} is the coherence matrix at the output plane. The elements of the scattering matrix for free-space propagation to a plane a distance z away are simply

$$S_{mn} = \exp(jm\Delta\phi) \delta_{mn} \quad (12)$$

where $\Delta\phi$ is again given by (2).

Just as in the coherent case where the fields were decomposed into modes and then propagated from one plane to another, in the more general case the cross spectral density is broken down into modes and it is these modes (or elements of the coherence matrix) that are propagated. The intensity distribution of the field can then be recovered from the coherence matrix using

$$I(\mathbf{r}) = \sum_m \sum_n C_{mn} \psi_n^*(\mathbf{r}) \psi_m(\mathbf{r}). \quad (13)$$

In phase retrieval process we determine those elements of the coherence matrix that give the best fit to two measured intensity distributions. The $N \times N$ coherence matrix of a fully coherent field (given by (10)) can be constructed from $2N-1$ independent quantities corresponding to the N mode amplitudes and $N-1$ phase differences of §I. Phase retrieval results using the coherence matrix formalism were similar to the mode vector method, although it was found that for some initial trial values the minimisation routine did not converge.

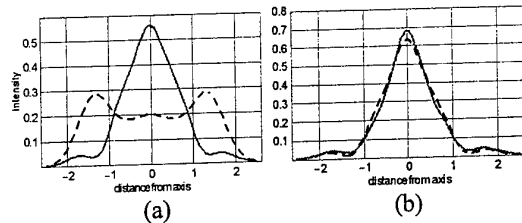


Fig. 1: Intensity (arbitrary units) as a function of off-axis distance for an incoherent beam in (a) the near- (continuous line) and far-field (dashed) and (b) in the source plane (the continuous line is the recovered intensity). 5 modes were used and the intensity was sampled at 21 points along the two planes plotted in (a).

For an incoherent or partially coherent field, however, the only restriction we have placed on the matrix is that it is

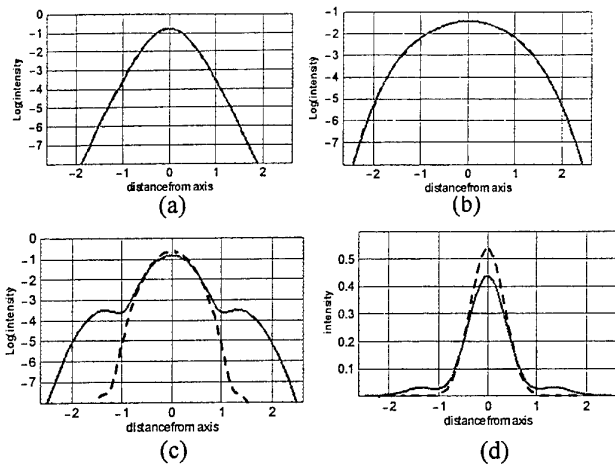


Fig. 2: Intensity (arbitrary units) as a function of off axis distance for a beam in the (a) near- and (b) far-field and in the (c)&(d) object plane. The continuous line shows the intensity derived from the recovered coherence matrix and the dashed line the actual intensity. 5 modes were used and the intensity was sampled at 21 points along two planes.

Hermitian, and the phase retrieval fitting process was carried out with respect to N^2 variables.

The coherence matrix of a fully incoherent source with an intensity distribution $I(\mathbf{r})$ can be calculated using (7) with $W(\mathbf{r}', \mathbf{r}) = I(\mathbf{r})\delta(\mathbf{r}' - \mathbf{r})$. (Despite the fact that the source itself is incoherent, correlations will exist between modes if the intensity distribution is not uniform [6]). We simulated an incoherent source with the same intensity distribution as the example in §1 and carried out the retrieval process for an Hermitian coherence matrix. The simulated intensities in the near -and far-field, along with the retrieved and simulated intensities in the source plane are plotted in Fig. 1. The elements of the retrieved coherence matrix differed from the actual values by a few percent.

Surprisingly, the success of this technique was found to decrease with increasing beam coherence. Fig.2 illustrates the results for a completely coherent beam (again making no restriction on the coherence matrix other than it be Hermitian). A coherence matrix that described the field well at the two sampled planes was found and yet this solution was not a good approximation to the original coherent field. Quite often, if the retrieval was not constrained to be a coherent field the method converged to an incoherent one. Sampling at more than two planes improved the result but since the fit to the measured data was always very good there was no way of predicting the accuracy of the reconstructed object field.

So, for completely coherent or incoherent fields we have retrieval methods that recover good approximations to the coherence matrix. For partially coherent fields, however, the minimisation must converge to the correct solution which has a beam coherence somewhere between the two extremes.

For this we need to supply information that characterises the coherence of the beam. A coherent field has a single dominant natural mode whereas for an incoherent field

power is spread evenly amongst each of the natural modes of the field. One way of describing this distribution of power amongst field modes is by the entropy of the field.

IV. ENTROPY

It turns out that the entropy of the field can be easily determined once the coherence matrix is known[9]. Since the $N \times N$ coherence matrix of the field, C , is non-negative and Hermitian, it has N real eigenvalues λ_i . Each eigenvalue corresponds to the total power in each natural mode of the field. The probability, p_i , that a detected photon belongs to the i^{th} eigenmode is given by

$$p_i = \frac{\lambda_i}{\sum_j \lambda_j}, \quad (\sum p_i = 1) \quad (14)$$

and the entropy (H) of the system becomes

$$H = -\sum_{i=1} p_i \ln p_i \quad (15)$$

where the sum is taken over all possible modes (N).

A completely coherent wavefield is specified by only one non-vanishing eigenvalue, whereas a completely incoherent field (maximum amount of disorder) has all eigenvalues the same. The entropy of a field can thus vary between 0 (fully coherent) and $\ln(N)$ (fully incoherent). As an example The entropy of the field in Fig. 2 was 1.06 (compared to a maximum possible of 1.609) which illustrates the coherence imposed on the field due to the non-uniform intensity distribution. Diagonalising the coherence matrix and finding its eigenvalues allows the entropy of the field to be determined.

Repeated diagonalisation of the coherence matrix in a minimisation routine, however, can be computationally expensive and so we use an alternative way of determining the entropy from the coherence matrix.

It can be shown that the entropy of a wavefield can also be expressed in terms of its coherence matrix as

$$H = -\text{Tr}[C' \ln(C')] \quad (16)$$

or, using the power series expansion of natural log

$$H = \text{Tr} \left[C' \sum_{r=1}^{\infty} \frac{1}{r} (I - C')^r \right] \quad (17)$$

where I is the identity matrix and C' is the normalised coherence matrix ($C/\text{Tr}[C]$).

The value of the entropy obtained using the above power series converges reasonably quickly to the value calculated by means of diagonalising the coherence matrix. To check the rate of convergence we have used both methods to calculate the entropy of a well-behaved source of variable entropy. A Gauss-Schell source[7] has a Gaussian intensity distribution (width characterised by σ_s) and a Gaussian coherence length (characterised by σ_c). By changing the relative scale factors (σ_s/σ_c) it is possible to move from having a fully coherent Gaussian through to having a fully incoherent Gaussian. We calculated the entropy of the source as a function of the

degree of coherence using both the diagonalisation and power series methods.

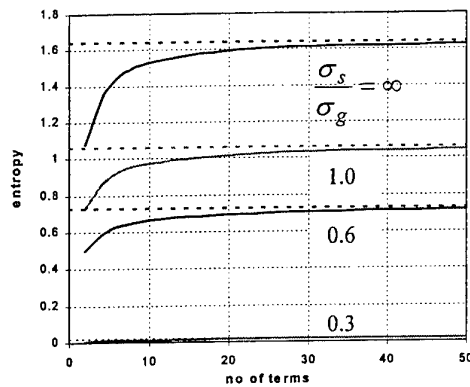


Fig. 3: Plot of entropy as a function of the number of terms in the expansion of equation (17). Entropy is calculated for four Gauss-Schell sources with different relative scale factors σ_s/σ_g (∞ for a fully incoherent source, 0 for a fully coherent source). The dashed lines show the entropy calculated by diagonalising the coherence matrix. (Since only 5 modes were used in these calculations, the maximum entropy is $\log_2 5 = 1.609$)

Fig. 3 shows that the power series expansion is a good way of getting a first-order measure of the degree of overall coherence efficiently.

V. PARTIALLY COHERENT FIELDS

Finally we look at an example of a partially coherent field. We have chosen a fully coherent horn surrounded by a sheet of perfect absorber (a fully incoherent source). The coherence matrix of the whole system is simply the sum of the individual coherence matrices for the horn and absorber [6]. Fig. 4 shows the result of starting with a uniform, fully incoherent source and minimising both the intensity difference and the entropy of the field. Without the use of entropy an excellent fit to the data was found, (total error $\sim 10^{-6}$) but the recovered field did not resemble the actual source field. Minimising the entropy as well as the intensity error gave a much improved estimate for the original coherence matrix.

VI. CONCLUSION

This paper describes numerical simulations to test phase retrieval using a Gaussian-beam formalism to represent complex fields. For coherent fields fitting for mode vectors was found to be a robust technique. We have tested both coherent and partially coherent fields using a coherence matrix method. As with other techniques, success depends on the function being minimised, sampling and the initial estimate, but one significant advantage with this method is that it does allow intensity measurements to be taken across any number of planes. Here we have restricted ourselves to two. For coherent fields it was found that local minima did not vary too much from the true value, but the minimisation did not converge for some initial trial values. For partially

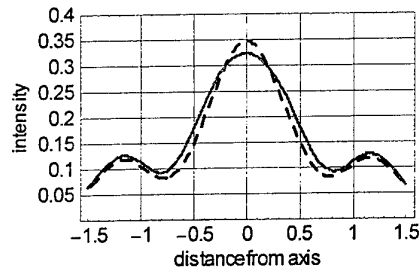


Fig. 4: Intensity (arbitrary units) as a function of off-axis distance for a coherent horn surrounded by an incoherent absorber. The continuous line shows the recovered intensity, the broken line is the actual intensity. 5 modes were used to model the field, and the intensity was sampled at 21 points along two planes.

coherent fields local minima were often found that fitted the simulated data very well but did not reproduce the object field. We found that incorporating the entropy of the beam expected into the function to be minimised improved the results.

Future work will look at the effect of measurement error on the phase retrieval technique, as well as a closer investigation of sampling, weighting of data and the best function to minimise.

Acknowledgements

The authors would like to thank the board of the JCMT and Enterprise Ireland for financial assistance.

References

1. L.S. Taylor, "The Phase Retrieval Problem", IEEE Trans. Antennas & Propagation, Vol. 29, No. 2, pp. 386-391, 1981
2. R.W. Gerchberg, W.O. Saxton, "Phase determination from image and diffraction plane pictures in the electron microscope", Optik, vol. 33, pp. 275-284, 1971
3. D.L. Misell, "An examination of an iterative method for the solution of the phase problem in optics and electron optics: I. Test Calculations", J.Phys.D, Appl.Phys, vol. 6, pp. 2200-2216, 1973
4. K.G. Isaak, S. Withington, "Phase Retrieval at Millimetre and Submillimetre Wavelengths using a Gaussian-Beam Formalism", Fourth Int. Symp. On Space Terahertz Technology, pp. 199-205, 1993
5. P.F. Goldsmith, "Quasi-optical techniques at millimeter and sub-millimeter wavelengths" in Infrared and Millimeter Waves, 8, pp. 227-343, 1982
6. S. Withington, J.A. Murphy, "Modal Analysis of Partially Coherent Submillimetre-wave Quasioptical Systems", IEEE Trans. Antennas & Propagation, Vol. 46, pp. 1650-1658, 1998
7. L. Mandel, E. Wolf, "Optical Coherence and Quantum Optics", CUP, 1995
8. S. Wolfram, "The MATHEMATICA Book", Cambridge University Press, 1999
9. S. Withington, G. Yassin, J.A. Murphy, "Dyadic Analysis of Partially Coherent Submillimetre-wave Antenna Systems" Submitted to IEEE Trans. Antennas & Propagation

Micromachining and Integration of Terahertz Components

Thomas W. Crowe

Abstract – Two recent innovations at the University of Virginia have the potential to significantly reduce the cost of terahertz mixers and multipliers. These are the integration of high-quality and low-parasitic GaAs diodes on dielectric substrates and the fabrication of terahertz waveguide circuits by micromachining. This paper reviews the basic fabrication processes and presents the most recent results.

I. INTRODUCTION

GaAs Schottky barrier mixer and multiplier diodes are used to extend the range of electronic receiver technology well into the terahertz frequency band. To date, frequency mixers have been realized to at least 5 THz and all-solid-state sources using frequency multipliers have reached slightly above 1 THz. However, these components rely on discrete diodes, often with whisker-contacts. This causes the components to be very difficult to assemble and virtually impossible to accurately model, even with the most advanced software packages. This is because the actual circuit cannot be assembled with the precision required to match the computer model. For these reasons the circuits are not particularly frequency agile and generally rely on mechanical tuners to achieve their optimum performance. Clearly, the solution to this problem is to develop integrated diode circuits that eliminate the need to handle and solder discrete devices while also ensuring that the Schottky anode is placed in the embedding circuit with micron precision. Our GaAs-on-dielectric integration process achieves this important goal.

A second major concern is the expense and delay of relying on traditionally machined waveguide housings. Although many groups in the terahertz field have developed extensive machining capabilities to fabricate terahertz waveguides and horns, this technology is simply not available to most terahertz engineers. For example, we have often been forced to wait six months or more to receive a single split-block housing from a commercial supplier or a national laboratory that was kind enough to fabricate our components. Needless to say, this delay has greatly hampered our research program. Several years ago we began to develop a process to fabricate high-quality waveguide housings on silicon wafers using standard semiconductor processing techniques. Using this process we have now fabricated state-of-the-art mixers at 585 GHz and prototype components to as high as 1.6 THz.

II. GAAS-ON-DIELECTRIC INTEGRATION

Our integration process [1,2] begins with a GaAs epitaxial wafer consisting of a heavily doped substrate and the following layers in order of growth,

- i) an AlGaAs etch stop layer,
- ii) a heavily doped GaAs buffer layer, typically about five microns thick with $n \geq 5 \times 10^{18} \text{ cm}^{-3}$,
- iii) a thin GaAs active layer designed to achieve the desired anode properties.

A SiO_2 passivation layer is deposited on the GaAs surface using atmospheric pressure chemical vapor deposition (APCVD). Circular anode wells of the appropriate diameter are then etched into the oxide to within about 50 nm of the GaAs surface by standard lithography and reactive ion etching (RIE). Next, the SnNi/Au ohmic contacts are formed, alloyed, and electroplated with additional Au to form a low resistance contact. The wafer is then mounted facedown in wax (Apiezon-W) on a silicon carrier and the bulk GaAs substrate and AlGaAs etch stop layer are removed by a wet chemical etch.

Simultaneously, a quartz wafer is similarly mounted to a second silicon wafer and thoroughly cleaned. A spin-on-dielectric (SOD) is applied to the quartz substrate and baked on a hotplate to yield a solid film about 0.5 microns thick. The GaAs and SOD/quartz surfaces are brought together and bonded under vacuum at elevated temperature. Although the temporary adhesive wax melts during this step, the wafers are held in place by pressure. After cooling, the Si carrier is removed from the front surface of the GaAs wafer by remelting the wax on a hotplate.

Processing then continues on the top surface of the GaAs epitaxial layers, which are now supported by the quartz substrate. The GaAs outside of the device areas is removed to reveal the SOD layer and the exposed SOD is plasma etched to reveal the surface of the quartz substrate. The thin SiO_2 layer protecting the GaAs anode surface is then etched in buffered oxide etchant and a thin layer of Ti/Au is electron beam evaporated over the entire wafer to form the Schottky anode contact. Photoresist is then applied to the wafer and the diode fingers and microstrip circuitry are defined and plated through the photoresist. After plating and photoresist removal, an RIE process followed by a brief wet etch removes the thin evaporated metals from areas outside of the fingers, contact pads and circuit lines. Fig. 1 shows an array of 585 GHz mixers. Note the filters are formed directly on quartz outside of the device mesa to form low loss microstrip lines. Also, excellent metal step coverage is

T.W. Crowe directs the Semiconductor Device Laboratory at the University of Virginia, Charlottesville, VA, 22903 USA. (twc8u@virginia.edu)

achieved between the GaAs mesa and the quartz substrate. The surface channel etch step is then used to form a low parasitic air bridge under the fingers and a plasma etch removes the SOD from the surface channel area. A dicing saw is then used to separate the completed circuits from the wafer. In the final devices, shown in Fig. 2, the only remaining SOD is sandwiched between the quartz and the small GaAs mesas.

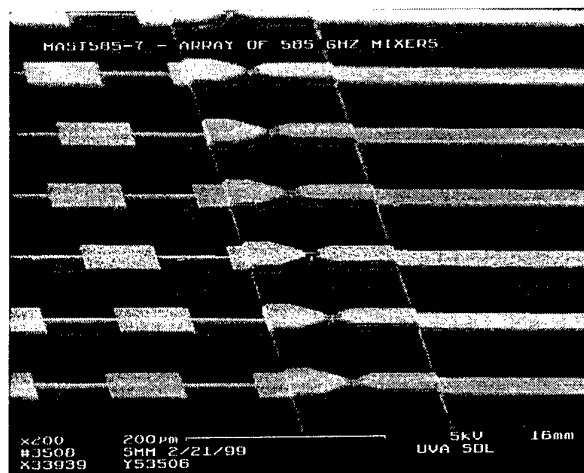


Fig. 1: An array of 585 GHz mixers. The metal circuitry is deposited directly on quartz.

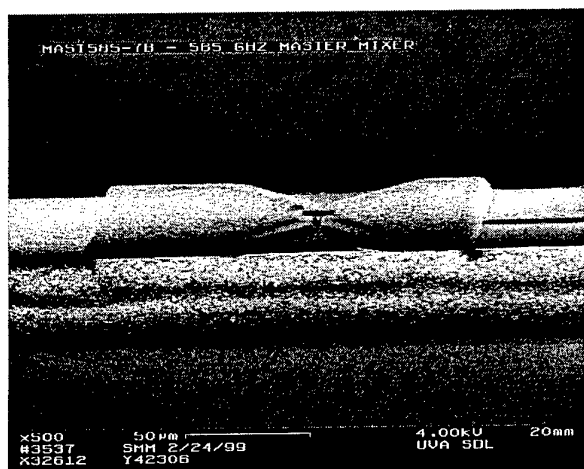


Fig. 2: An integrated GaAs-on-quartz mixer circuit after dicing. The only GaAs is the thin mesa below the metal pads in the center of the device.

The mixers were first tested in a standard metal waveguide housing as described in [3]. A molecular gas laser supplied the LO pump power and the hot/cold method was used to measure the receiver sensitivity. The results, summarized in Table I, are equivalent to the best ever reported in this frequency range at room temperature and 77 K. Also, it should be pointed out that this mixer had no mechanical tuners and the mixer assembly was simple and repeatable. These excellent results demonstrate the benefit of GaAs-on-dielectric integration over the use of discrete devices.

TABLE I
SUMMARY OF INTEGRATED MIXER
PERFORMANCE AT 585 GHz

Ambient (K)	T _{sys} (K)	T _{mix} (K)	L _{mix} (dB)	P _{LO} (mW)
300	1631	1135	6.6	1.74
300	1799	1341	6.7	0.35
77	970	880	7.2	-

III. MICROMACHINED WAVEGUIDE CIRCUITS

The fabrication process presented here is a modified version of the process reported in several previous conference publications [4,5,6] and has been described more fully in a recent paper [7]. It begins with the formation of a modified diagonal horn by selective crystal etching of a silicon wafer through a silicon dioxide masking layer. This etch creates a very suitable horn structure with easily controlled flare angle and aperture. Next, a thin layer of photoresist is spun onto the wafer and exposed to mark the precise position of the waveguide. An automatic dicing saw is then used to slit-cut the waveguide. For our 585 GHz mixer the cut had a depth of 150 µm (±5 µm) and width 205 µm (±2 µm) for each half of the block. The photoresist and oxide layers are then removed.

The next step is to form the microstrip circuit channel that runs perpendicular to the waveguide. This is achieved with an ultra-thick photoresist known as SU-8 [8]. This resist can be exposed by standard UV lithography to depths of up to 1 mm. First, the horn structure is filled with SU-8 resist. Next, a layer of SU-8 is spun on the wafer that is significantly thicker than our desired channel depth. This resist is then exposed through a mask that protects the horn, waveguide and channel areas. Both pre- and post-exposure bakes are used. After the exposure, the wafer is developed to remove the unexposed resist and hard-baked to cure the remaining SU-8 into a plastic layer that remains as a permanent part of our mixer. This plastic is then lapped to the desired thickness on a commercial wafer lapping system. Lapping allows control of the depth of the channel to within ±2 µm and eliminates any problem with the planarity of the original SU-8 surface. For 585 GHz the width of the microstrip channel was 120 µm (±2 µm).

Alignment grooves are then diced into the wafer (200µm deep by 400µm wide), the sample is coated with metal by a combination of sputtering and electroplating and the individual components are diced. Both the dicing and alignment grooves are prepatterned in the SU-8 layer to facilitate proper alignment on the wafer. A three-inch process wafer yielded twelve complete waveguide pairs and required two weeks for a graduate student. As this process is refined we expect this time to be significantly reduced. The result is shown in Fig 3. Note that the features are very crisp and the fixed backshort is defined with lithographic precision.

To date, we have assembled several 585 GHz mixers using the micromachined waveguides and the integrated diodes described above. The results have been equivalent to those obtained with the traditionally machined metal waveguides. However, we have noted that the precision of the micromachined features is far superior to any of the metal housing we have obtained. More recently we have assembled and tested prototype mixers and a sideband generator at 1.6 THz.

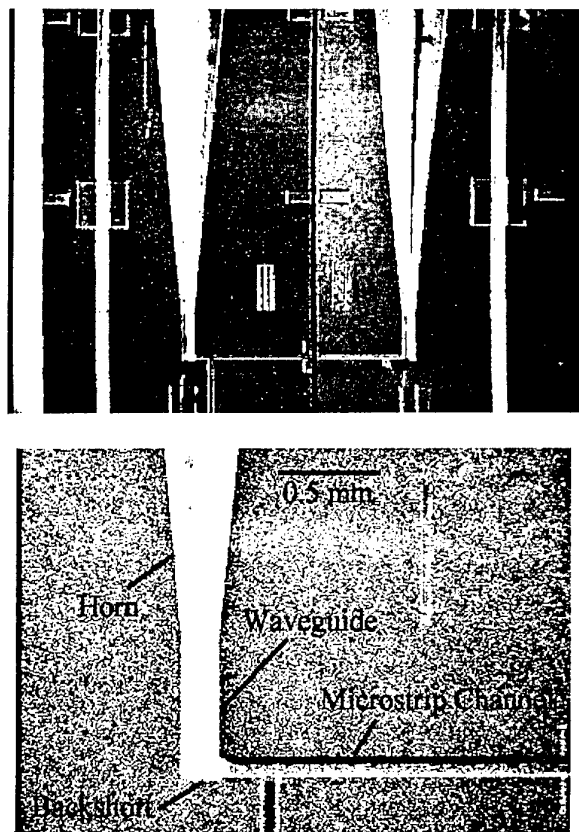


Fig. 3: Two views of the micromachined 585 GHz mixer, top: a split-block pair, and bottom: a closer view of the flared horn, waveguide and channel.

IV. CONCLUSION

GaAs Schottky diode technology continues to be a workhorse for many scientific applications in the terahertz frequency band. However, the complexity of using discrete diodes in traditionally machined waveguide circuits greatly increases the cost. This will prevent terahertz technology from ever being used in the broader array of potential military and commercial applications that are now being proposed. Through the

use GaAs-on-dielectric integration and the micromachining of waveguide circuits we hope to greatly reduce these costs. Our results to date have demonstrated that integrated terahertz circuits and micromachined waveguides can be fabricated with high precision, low cost and excellent performance.

Acknowledgement

This work was supported by the U.S. Army National Group Intelligence Center (DAHC90-96-C-0010), the Army Research Office (D. Woolard) and NASA/JPL.

References

1. S.M. Marazita, W.L. Bishop, J.L. Hesler, K. Hui T.W. Crowe, "Integrated GaAs Schottky Mixers by Spin-On-Dielectric Wafer Bonding," IEEE Trans. Electron Devices, Vol. 47, No. 6, pp. 1152-1157, June 2000.
2. S.M. Marazita, "Integrated Planar GaAs Schottky Mixers or Submillimeter Wavelength Receivers," Doctoral Dissertation, University of Virginia, Charlottesville, VA, USA, May 1999.
3. J.L. Hesler, W.R. Hall, T.W. Crowe, R.M. Weikle, B.S. Deaver, R.F. Bradley, S.-K. Pan, "Fixed Tuned Submillimeter Wavelength Mixers Using Planar Schottky Barrier Diodes," IEEE Trans. Microwave Theory and Tech., Vol. MTT-45, No. 5, pp. 653-658, May 1997.
4. C.M. Mann, D.N. Matheson, M.L. Oldfield, P.J. Koh, T.W. Crowe, W.L. Bishop, R.M. Weikle, J.L. Hesler, "A Simple Micromachining Technique for Millimeter, Submillimeter and Terahertz Waveguide Cavities," Proc. 2nd ESA Workshop on Millimeter Wave Technology and Applications, Helsinki, Finland, pp. 144-149, May 1998.
5. C.M. Mann, J.L. Hesler, P.J. Koh, T.W. Crowe, W.L. Bishop, R.M. Weikle, D.N. Matheson, "A Versatile Micromachined Horn Antenna," 20th ESTEC Antenna Workshop on Millimetre Wave Antenna Techn. And Antenna Measurements, Noordwijk, NL, June 1997.
6. T.W. Crowe, P.J. Koh, W.L. Bishop, C.M. Mann, J.L. Hesler, R.M. Weikle, P.A.D. Wood, D. Matheson, "Inexpensive Receiver Components for Millimeter and Submillimeter Wavelengths," Proc. Eighth Int. Symp. on Space THz Tech., Cambridge, MA, March 25-27, 1997.
7. K. Hui, J.L. Hesler, D.S. Kurtz, W.L. Bishop and T.W. Crowe, "A Micromachined 585 GHz Schottky Mixer," in press, IEEE Microwave and Guided Wave Letters.
8. K.Y. Lee, N. LaBianca, S.A. Rishton, S. Zolgharnain, J.D. Gelorme, J. Shaw, T.H.-P. Chang, "Micromachining Applications of a High Resolution Ultrathick Photoresist," J. Vac. Sci. Technol. B 13(6), pp. 3012-3016, Nov/Dec 1995.

Thin Film Antennas for Millimeter and Submillimeter Wave Radiation

Yoshizumi Yasuoka

Abstract – Properties of the thin film submillimeter wave single slot antenna and slot antenna arrays on the dielectric substrate were theoretically and experimentally investigated. The thin film antennas were fabricated using micro-fabrication techniques, and the receiving experiments were carried out at 700 GHz. The experimental data agree with the theoretical predictions. The power gain of 13 dBi was obtained by the two-dimensional 8 x 3 slot antenna arrays.

INTRODUCTION

The demand for millimeter and submillimeter wave systems consisting of planar antennas has recently increased in communication systems, remote sensing, radio astronomy and plasma diagnostics. Some planar antenna arrays fed by a waveguide structure for millimeter wave radiation have been reported [1], [2]. However, the waveguide structure is too complex to fabricate in the submillimeter wave region. On the other hand, a thin film antenna placed on the dielectric substrate is relatively easy to fabricate through recently developed microfabrication techniques. These techniques have encouraged the fabrication of thin film antennas, transmission lines, and detectors on the coplanar substrate. Also, new research has been done on thin film devices in the millimeter and submillimeter wave regions [3], [4].

As thin film antennas for millimeter and submillimeter wave systems, the dipole [5], slot [6], microstrip [7], spiral [8] and log periodic [9] antennas have been studied. Of these antennas, the slot antenna had a simple structure and directivity perpendicular to the substrate. These characteristics make the slot antenna a suitable antenna in the millimeter and submillimeter wave regions. The author and his group have been studying thin film slot antennas for millimeter and submillimeter wave radiation [10], [11].

In this paper, the fabrication and properties of a thin film slot antenna on a dielectric substrate and its arrays with parasitic slots, one-dimensional slot antenna arrays fed by coplanar waveguide (CPW), and two-dimensional slot antenna arrays fed by CPW at 700 GHz are discussed.

THEORETICAL ANALYSIS

Properties of thin film antennas cannot be discussed without taking into account the effects of a dielectric substrate, because the thin film antennas are always fabricated on the dielectric substrates. In the case of the slot antenna on the dielectric substrate, the power radiated from the antenna (P_0) is divided into three parts:

the power radiated into the air (air side: P_a), the power radiated into the air through the substrate (substrate side: P_d) and the power loss (P_s) captured in the substrate as a surface wave.

The P_a , P_s and P_d are calculated using the theory based on the transmission lines model [12]. Figure 1 shows the variation of P_a/P_0 , P_s/P_0 and P_d/P_0 of a single slot antenna on the dielectric substrate with substrate thickness (h). The power distribution in the region where the substrate is sufficiently thick converges to $P_a/P_0 = 0.11$, $P_d/P_0 = 0.17$ and $P_s/P_0 = 0.72$. This means that 72 % of the radiated power from the antenna is trapped in the substrate as a surface wave, and that the remaining 28 % is delivered to the power P_a (11 %) and P_d (17 %).

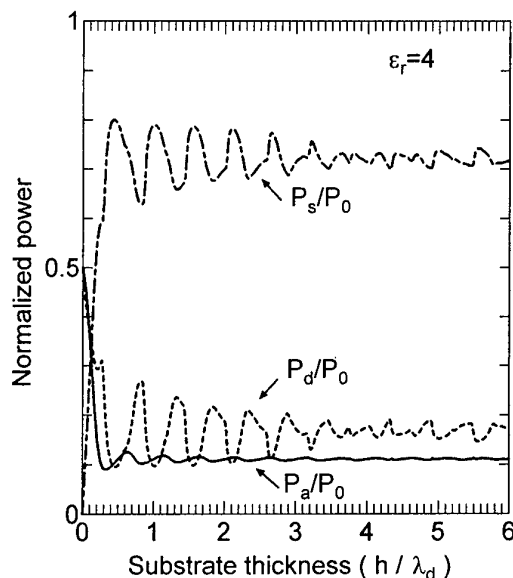


Fig.1 Power distribution of the slot antenna as a function of the substrate thickness.

The radiation pattern and the power gain of the antennas are also calculated. Here, the power gain is defined as the absolute gain in the direction normal to the substrate expressed in dBi, in comparison to a lossless isotropic point source in air. Figure 2 shows the power gain as a function of the substrate thickness. The dotted line indicates power gain on the air side while the solid line indicates power gain on the dielectric side. The gain on the air side decreases quickly until $h = 0.3 \lambda_d$ and subsequently converged to -3.7 dBi. On the other hand, the gain on the dielectric side decreases quickly until $h = 0.5 \lambda_d$ and exhibits a periodic variation with minima at even integer multiples of $\lambda_d/4$. Here, λ_d is the wavelength in the dielectric substrate given by $\lambda_d = \lambda_0/\epsilon_r^{1/2}$ in terms of the free space wavelength λ_0 .

Y. Yasuoka is with Department of Electronic Engineering, National Defense Academy, Yokosuka 239-8686, Japan (E-mail: yasuoka@cc.nda.ac.jp).

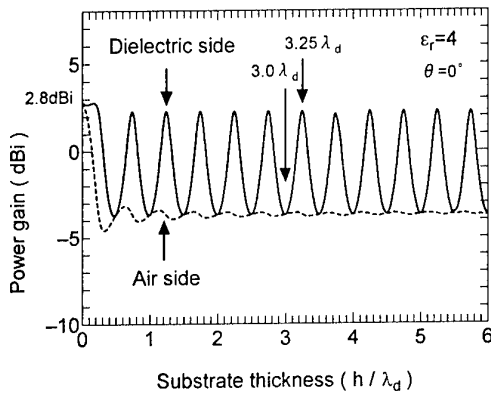


Fig.2 Power gain of the single slot antenna as a function of the substrate thickness.

Figure 3 shows the radiation patterns of the antenna on the dielectric substrate of $h = 3.0 \lambda_d$ and $3.25 \lambda_d$. Figure 3(a) shows the radiation pattern on the air side, and Fig. 3(b) depicts the ones on the dielectric side. The radiation pattern on the air side is independent of the substrate thickness. On the dielectric side, the radiation patterns for odd integer multiples of $\lambda_d/4$ ($h = 3.25 \lambda_d$) are sharper than those for even integer multiples of $\lambda_d/4$ ($h = 3.0 \lambda_d$). This sharper radiation pattern increases power gain on the dielectric side up to 2 dBi although the radiation power P_d/P_0 on the dielectric side is less than 0.2 in Fig. 1.

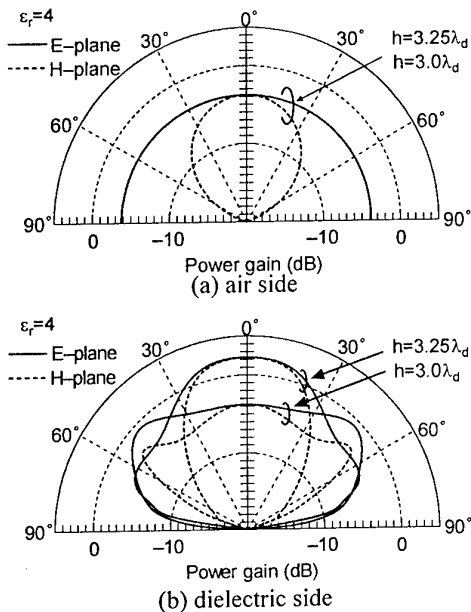


Fig.3 Calculated antenna patterns ($h = 3.0 \lambda_d$ and $h = 3.25 \lambda_d$)

A method to reduce the surface wave is to use an antenna array. A double slot antenna fed by a coplanar waveguide decreases the surface wave loss, P_s , up to 50 %, and increases the P_d up to 30 % as shown in Fig. 4. The P_s is further decreased to 36 % by using a four-slot antenna array with two parasitic slots, and power gain was improved by 5 dB over the single slot antenna at 700 GHz. It is considered that the coupling efficiency

between two parasitic slots could still be improved by coupling the slots with CPW.

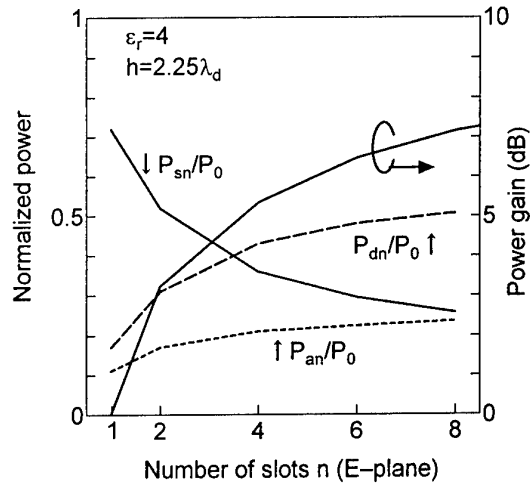


Fig.4 The relationship between the normalized power distribution and the number of slots. And the relationship between the power gain and the number of slots.

Figure 5 shows the configuration of the proposed array antennas fed by CPW. Figure 5(a) shows the one-dimensional eight-slot antenna array, and Fig. 5(b) shows the two-dimensional 8×3 slot antenna array. The length of the CPW between two slots is $1.0 \lambda_m$ in order that all the slots are excited with an equal phase, where λ_m is the mean wavelength shown by $\lambda_m = \lambda_0 / [(1 + \epsilon_r)/2]^{1/2}$.

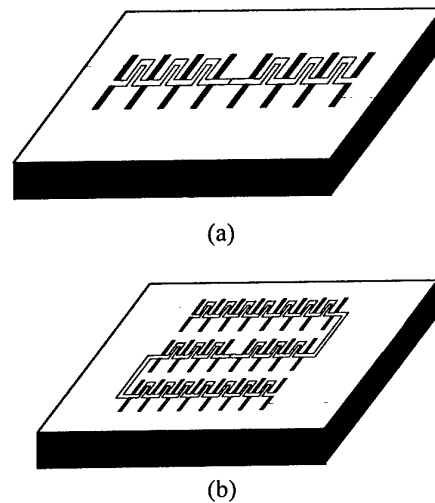


Fig.5 Configuration of the antenna arrays fed by CPW. (a) The one-dimensional eight-slot antenna array fed by CPW. (b) The two-dimensional 8×3 slot antenna array fed by CPW.

Figure 6 shows the relationship between the power gain and the number of slots in the one-dimensional n -slot antenna array and the two-dimensional $n \times m$ ($E \times H$ plane) slot antenna array. The power gain is calculated on the condition that the transmission efficiency of the CPW per λ_m is $\delta = 0.8/\lambda_m$ and that the rate of the radiated power

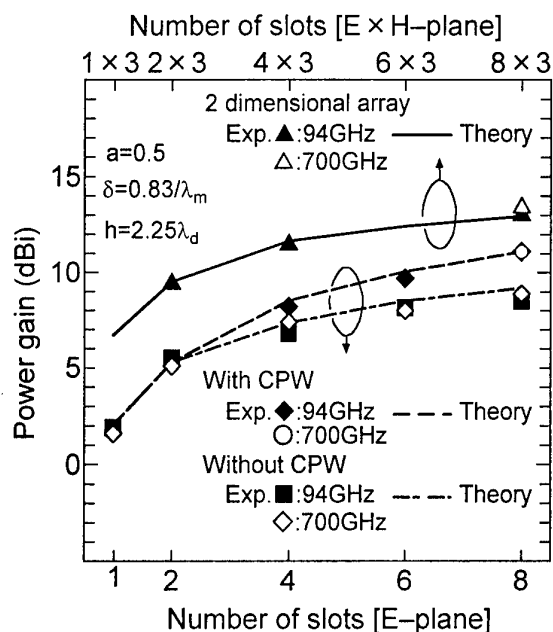


Fig.6 The relationship between the power gain and the number of slots.

from the slot antenna is $a = 0.5$. In the figure the power gain of the parasitic slot antenna array is also shown for comparison. The two-dimensional 8×3 slot antenna array on the dielectric substrate, of which the thickness is odd integer multiples of $\lambda_d/4$, will have an improved power gain of 11 dB over the single slot antenna and a power gain of 13 dBi by irradiating the signal from the dielectric side.

EXPERIMENTS AND DISCUSSION

The receiving slot antennas for 700 GHz radiation were fabricated on the fused quartz substrate using a photolithographic method. Figure 7 shows the SEM photographs of the fabricated single slot antenna, six-slot antenna array with parasitic slots and two-dimensional 8×3 slot antenna array fed by CPW. The length and width of the antenna are $0.72 \lambda_m$ and $0.08 \lambda_m$, respectively. Thickness of the substrate is $2.25 \lambda_d$. A bismuth microbolometer is used as a detector and placed at the center of the CPW. To apply the bias current to the bolometer, DC cuts (narrow slits) are inserted.

In the experiments, an HCOOH laser pumped by a CO_2 laser was used for 700 GHz submillimeter wave source. The laser beam was chopped at 1 kHz and irradiated onto the slot antenna directly or through the substrate. The power gain of the slot antenna was calculated using the measured voltage and the sensitivity of the microbolometer.

Figure 6 shows the relationship between the power gain and the number of slots in the three kinds of antennas, when the 700 GHz submillimeter wave was irradiated through the substrate. In the figure, the data measured at 94 GHz is also shown. Symbols ▲, △, ◆, ○, ■ and ◇ represent the measured power gain of the antennas. Experimental data agree with the theory based on the transmission line model [12]. It was confirmed from the figure that the two-dimensional 8×3 slot antenna array

had a power gain of 13 dBi, which was 11 dB higher than that of the single slot antenna as theoretically expected.

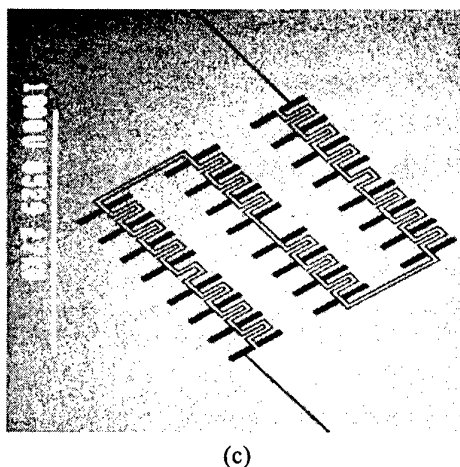
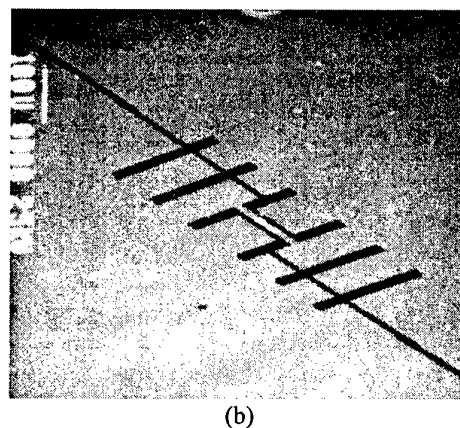
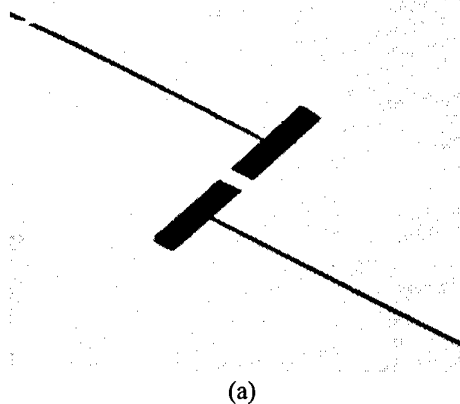


Fig.7 SEM photographs of the fabricated slot antenna and its array. (a) The single slot antenna, (b) the six-slot antenna array with parasitic slots and (c) the two-dimensional 8×3 slot antenna array fed by CPW.

CONCLUSION

Properties of the thin film single slot antenna and the antenna arrays on the dielectric substrate were discussed using the theory based on the transmission line model, in order to obtain a thin film antenna with high power gain for millimeter and submillimeter wave radiation. Theory predicted the following things:

1. It is necessary to select the thickness of the substrate odd integer multiples of a quarter wavelength of the radiated signal.
2. The signal should be irradiated through the substrate. In this case, the power gain is 6 dB higher than that on the air side, and reach 2 dBi.
3. The one-dimensional eight-slot antenna array, consisting of six parasitic slots and a double slot antenna, improves the power gain by 7 dB compared to the single-slot antenna, and the power gain reaches 9 dBi.
4. The one-dimensional eight-slot antenna array fed by CPW has a power gain of 11 dBi.
5. The two-dimensional 8×3 slot antenna array fed by CPW has a power gain of 13 dBi, which is 11 dB higher than that of the single-slot antenna.

The single-slot antenna and its arrays were fabricated using microfabrication techniques and the receiving experiments were carried out at 700 GHz. The experimental data agree with theoretical predictions.

References

1. R. S. Tahim, G. M. Hayashibara, and K. Chang, "Design and performance of W-band broad-band integrated circuit mixers," *IEEE Trans. Microwave Theory Tech.*, vol. MTT-31, pp.277-283, Mar.1983.
2. K. Sakakibara, J. Hirokawa, M. Ando, and N. Goto, "Single-layer slotted waveguide arrays for millimeter wave applications," *IEICE Trans.*, vol. E-79B, pp.1765-1772, Dec. 1996.
3. S. S. Gearhart and G. M. Rebeiz, "A monolithic 250-GHz Schottky-diode receiver," *IEEE Trans. Microwave Theory Tech.*, vol. MTT-42, pp.2504-2511, Dec. 1994.
4. M. C. Gaidis, H. G. LeDuc, M. Bin, D. Miller, J. A. Stern, and J. Zmudzinas, "Characterization of low-noise quasi-optical SIS mixers for the submillimeter band," *IEEE Trans. Microwave Theory Tech.*, vol. MTT-44, pp.1130-1139, July 1996.
5. D. F. Filipovic, W. Y. Ali-Ahmad, and G. M. Rebeiz, "Millimeter-wave double dipole antennas for high-gain integrated reflector illumination," *IEEE Trans. Microwave Theory Tech.*, vol. MTT-40, pp.962-967, May 1992.
6. B. K. Kormanyos, W. Harokopus, L. P. B. Katehi, and G. M. Rebeiz, "CPW-fed active slot antennas," *IEEE Trans. Microwave Theory Tech.*, vol. MTT-42, pp.541-545, Apr. 1994.
7. H. Legay, and L. Shafi, "A self-matching wide-band feed network for microstrip arrays," *IEEE Trans. Antennas Propagat.*, vol. AP-45, pp.715-722, Apr. 1997.
8. T. Fukutomi, Y. Yasuoka, S. Kawasaki, and S. Ito, "A printed two-arm spiral antenna operating at the 90-GHz band," *IEICE Trans.*, vol. J77-C1, pp.599-606, Nov. 1994.
9. B. K. Kormanyos, P. H. Ostdiek, W.L. Bishop, T. W. Crowe, and G. M. Rebeiz, "A plana wide-band 80-200-GHz subharmonic receiver," *IEEE Trans. Microwave Theory Tech.*, vol. MTT-41, pp.1730-1737, Oct. 1993.
10. T. Shimizu, Y. Abe, and Y. Yasuoka, "Thin-film slot antennas for 700GHz submillimeter wave radiation," *IEICE Trans.*, vol. E-78C, pp.1002-1006, Aug. 1995.
11. T. Shimizu, Y. Abe, and Y. Yasuoka, "Thin-film slot antennas for 2.5THz submillimeter wave radiation," *Jpn. J. Appl. Phys.*, vol.35, pp. L266-L268, Feb. 1996.
12. H. Kobayashi, M. Yuki, and Y. Yasuoka, "Effects of substrate thickness on the gain of millimeter and submillimeter wave slot antennas," *IEICE Trans.*, vol. J80-B, pp.54-62, Jan. 1997.

Low-dispersive Coplanar Waveguides and Thin-film Microstrip Lines for Sub-mm Wave Monolithic Integration

Frank Schnieder and Wolfgang Heinrich

Abstract – Planar sub-millimeterwave transmission-line structures suitable for monolithic integration are discussed. The results show that both miniaturized coplanar waveguides and appropriate thin-film microstrip configurations provide low-dispersive propagation properties up to 1 THz. The paper discusses radiation and dispersion effects as well as basic rules how CPWs should be designed in order to reach the desired sub-mm wave performance.

I. INTRODUCTION

Monolithic integration of sub-mm wave components is still an ambitious goal. Today, most of these systems are realized as a hybrid circuit. But any interconnect causes reflections, and already small parasitics may become critical at Terahertz frequencies. Accordingly, one tries to integrate as many elements as possible together with the semiconductor device, also in the hybrid case. For this purpose, transmission-line structures are required that offer low dispersion together with reasonably low loss. At the same time, they must be compatible with the common planar circuit geometry and processing scheme.

Particular candidates are the coplanar waveguide (CPW) and the thin-film microstrip line (TFMSL), which is realized on top of the substrate using polyimide or BCB (bis-benzocyclobutene) as dielectric layer of 1..20 μm thickness. This allows to scale down strip width and thus the total line dimensions. Our investigations show that such thin-film microstrip lines can be used up to 1 THz with excellently low dispersion. Coplanar waveguides with scaled-down dimensions achieve similar properties. Additional to the common CPW design criteria, however, one has to take into account higher-order modes and radiation loss.

II. THIN-FILM MICROSTRIP LINE (TFMSL)

In contrast to the conventional microstrip, the TFMSL is realized on top of the substrate using a thin polyimide or BCB dielectric layer. Fig. 1 shows the cross section. The fields are concentrated in the dielectric layer and the ground metalization provides shielding against the substrate. Therefore, one may use lossy material as a substrate, e.g., low-resistivity silicon. The typical BCB or polyimide thicknesses are in the range 1...25 μm . This is considerably smaller than for the conventional microstrip

case. As a consequence, the line dimensions, i.e., strip width, can be scaled down, which increases the frequency range of quasi-TEM operation well into the Terahertz region. One has to pay for this, of course, by larger attenuation due to conductor loss.

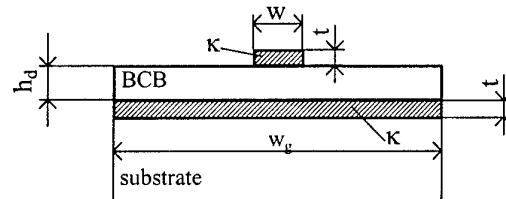


Fig. 1: TFMSL cross-section metal (κ denotes metal conductivity, the thickness is $t = 0.8 \mu\text{m}$, and ground width $w_g \gg w$, 5 Ωcm Si is used as a substrate and BCB as dielectric).

Fig. 2 presents simulated and measured results for such a TFMSL with 2.7 μm thick BCB dielectric. The 7.4 μm wide strip yields 50 Ω characteristic impedance. For simulation, the full-wave mode-matching method of [1] is applied that rigorously accounts for metal loss. The experimental data refers to electro-optic measurements at the RWTH Aachen [2].

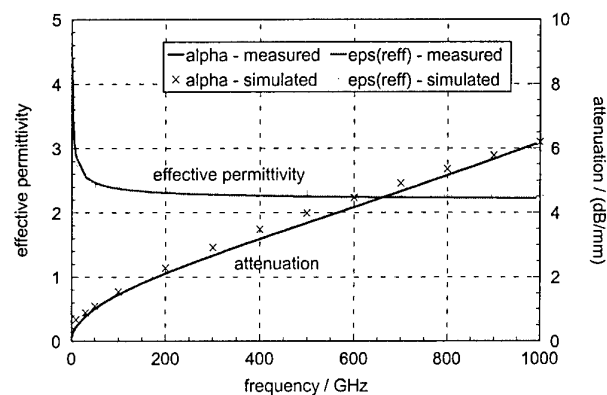


Fig. 2: Effective permittivity ϵ_{reff} and attenuation α as a function of frequency (50 Ω TFMSL according to Fig. 1 with strip width $w = 7.4 \mu\text{m}$, BCB layer with thickness $h_d = 2.7 \mu\text{m}$, $\tan\delta_e = 0.015$, and metal conductivity $\kappa = 30 \text{ S}/\mu\text{m}$; Si substrate with $\rho = 5 \Omega\text{cm}$; simulation data [1] and electro-optic measurements [2]).

Frank Schnieder and W. Heinrich are with the Ferdinand-Braun-Institut für Höchstfrequenztechnik (FBH), Albert-Einstein-Strasse 11, D-12489 Berlin / Germany. This work is supported by the Deutsche Forschungsgemeinschaft (DFG) under contract No. He 1676/10.

Effective permittivity $\epsilon_{\text{reff}} = (\beta/\beta_0)^2$ and attenuation α are plotted against frequency up to 1 THz. Effective permit-

tivity exhibits a negative slope at the lower frequency end, which is caused by metal loss, and then approaches a constant value. This demonstrates the quasi-TEM properties and the excellently low dispersion. The reasons are the small BCB thickness and strip width together with the low permittivity of the BCB ($\epsilon_r = 2.7$). On the other hand, the miniaturized conductor dimensions lead to attenuation values of about 5 dB/mm at 1 THz. However, for short connecting lines within a circuit, this is acceptable. Moreover, one can trade lower loss for higher dispersion by increasing the line dimensions.

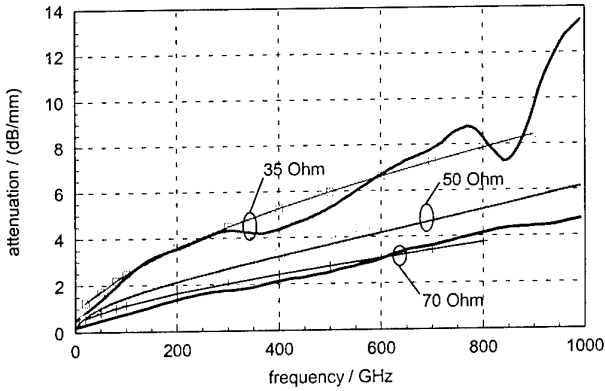


Fig. 3: Attenuation as a function of frequency for a 35 Ω , 50 Ω , and a 70 Ω line (all data as in Fig. 2, except for $w = 8 \mu\text{m}$, $h_d = 1.7 \mu\text{m}$ for the 35 Ω case, and $w = 8 \mu\text{m}$, $h_d = 5.4 \mu\text{m}$ for the 70 Ω line).

The characteristic impedance can be adjusted by choosing a suitable w/h_d ratio. Fig. 3 illustrates the attenuation curves for the 50 Ω TFMSL of Fig. 2 together with a 35 Ω and a 70 Ω geometry. Larger impedance values can be achieved by increasing h_d or decreasing w . One should note that, despite of the low- ϵ_r dielectric, the full impedance range down to 30 Ω can be realized within the common technological limitations.

III. COPLANAR WAVEGUIDE (CPW)

The CPW type most appropriate for sub-mm-wave applications is that with finite ground width and substrate thickness. Fig. 4 illustrates the cross-section. Only modes with even symmetry are considered (for analysis, a magnetic symmetry wall is placed in the center). As for the TFMSL, high-resistivity Si is used as a substrate. The substrate resistivity plays an important role in the CPW case, because, in contrast to the TFMSL, the fields penetrate deeply into the substrate and thus attenuation is strongly affected by substrate material loss. In order to keep dispersion and non-TEM effects low the ground-to-ground spacing $w+2s$ has to be scaled down with increasing frequency of operation.

Fig. 5 presents simulation results and electro-optic measurements [2] for such a miniaturized CPW in the frequency range up to 1 THz. The simulation data refers to a mode-matching approach [1], which considers conductor loss but neglects radiation, and FDTD calculations [6], which include radiation but assume lossless conductors. Thus, the realistic attenuation value is the sum of both

contributions, which closely fits the measured data. Two different ground-plane widths w_g of 160 μm and 16 μm are studied in Fig. 5.

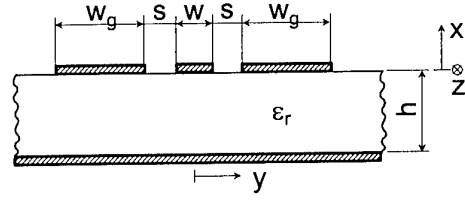


Fig. 4: The CPW geometry considered (substrate: high-resistivity Si with $\epsilon_r = 11.67$).

Generally, dispersion in ϵ_{eff} is small, but larger than for the TFMSL structures treated before. This can be attributed to the larger lateral line dimensions of the CPW (note that the CPW ground-to-ground spacing $w+2s$ in Fig. 5 is 40 μm compared to 8 μm strip width for the TFMSL in Figs. 2 and 3).

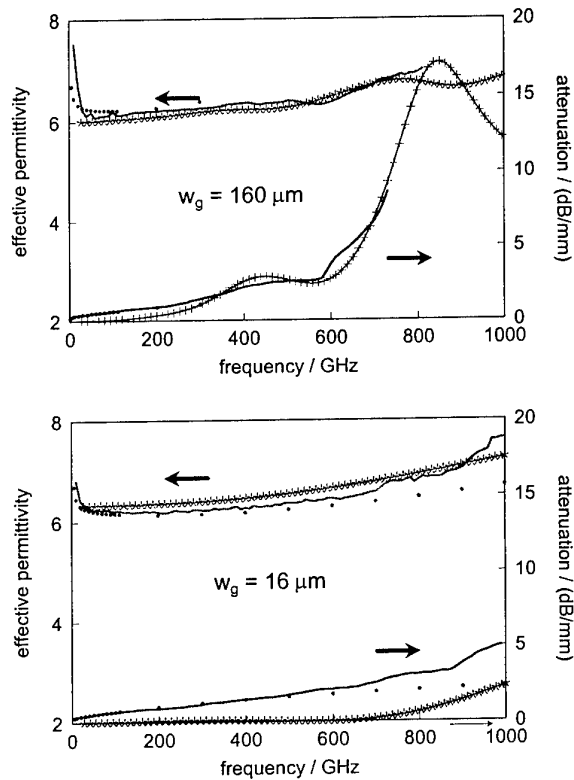


Fig. 5: CPW effective permittivity and attenuation as a function of frequency for two different ground-plane widths w_g (solid lines: electro-optic measurements [2], symbols: mode-matching analysis [1] for closed structure, curves with symbols: FDTD simulation [6]; for geometry and parameter see Fig. 4 with $w = 16 \mu\text{m}$, $s = 12 \mu\text{m}$; metal conductivity 35 S/ μm , 380 μm thick Si substrate).

Studying the ϵ_{eff} characteristics in Fig. 5 in more detail, a slight peak near 700 GHz is observed for the larger ground value. This will be explained in the context of Fig. 7. In the low GHz range, one has the typical increase

in ϵ_{reff} caused by conductor loss as observed for the TFMSL. More important, however, are the attenuation results. They show clearly that the reduced ground width leads to a considerably lower attenuation level.

In this context, it is interesting to study the differences between the two cases for finite and infinite ground width. In Fig. 6, simulation data [7] for $w_g = 80 \mu\text{m}$ (both infinite substrate thickness h and $h = 200 \mu\text{m}$) are plotted together with the well-known approximation of [3], which assumes infinite ground width and substrate. For the latter one, attenuation follows an f^2 rule, whereas finite w_g leads to an f^5 dependence. This finding supports the statement that w_g is indeed an important parameter regarding CPW radiation loss. Substrate thickness h , on the other hand, determines the onset of radiation, but does not exert a strong quantitative influence.

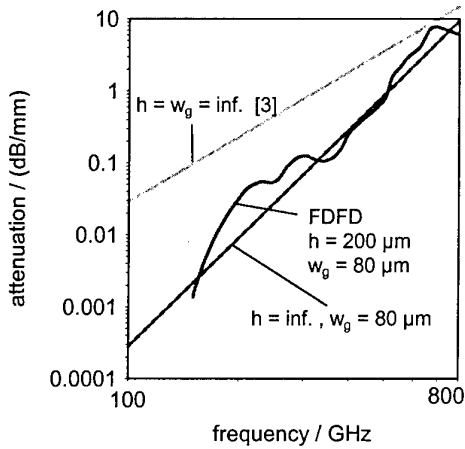


Fig. 6: CPW attenuation due to radiation against frequency (FDFD analysis [7] of the geometry in Fig. 4 with ideally conducting metalizations, $w = 16 \mu\text{m}$, $s = 12 \mu\text{m}$, $w_g = 80 \mu\text{m}$, and $h = 200 \mu\text{m}$ as compared to analytical formulas with $h = \infty$ for $w_g = \infty$ [3][5] and $w_g = 80 \mu\text{m}$ [7], respectively).

IV. CPW DESIGN RULES

In the CPW case, one has not only to account for dispersion and radiation of the CPW mode but also to consider higher-order modes, which may adversely affect propagation characteristics or cause parasitic effects in the packaged circuit (see, e.g., [4]). These higher-order modes are related to substrate thickness h and ground width w_g (see [7]). Fig. 7 presents the effective permittivity values for the 2 fundamental modes (CPW and PPL) and the first 3 higher-order ones (HM). The CPW structure of Fig. 5 is studied with a realistic w_g value of $80 \mu\text{m}$ and a $200 \mu\text{m}$ thick conductor-backed substrate.

First, one should note that the finite extent of the ground plane ($w_g < \infty$) shifts onset of radiation into lateral surface-wave modes to higher frequencies (one has $f = 0$ for $w_g = \infty$), but it does not prevent existence of a parallel-plate like (PPL) mode (sometimes referred to as the microstrip-like mode). This PPL mode is present in any case as long as conductor-backed substrates are used. In prac-

tical circuits, they form a parasitic bypass between discontinuities and interconnects, which reduces isolation and may cause instabilities in high-gain systems.

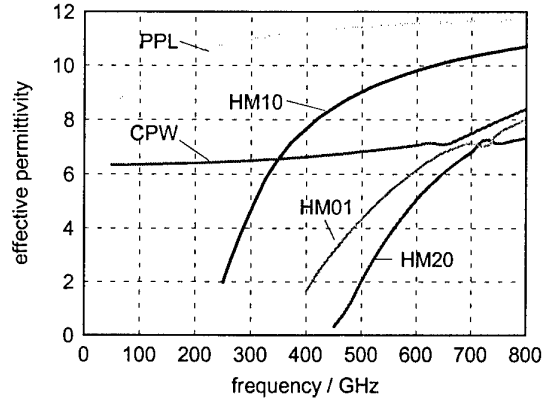


Fig. 7: Effective permittivity of fundamental modes (CPW, PPL) and higher-order modes (HM) against frequency (FDFD analysis of the geometry in Fig. 4 with ideally conducting metalizations, $w = 16 \mu\text{m}$, $s = 12 \mu\text{m}$, $w_g = 80 \mu\text{m}$, and $h = 200 \mu\text{m}$).

The PPL mode exhibits a microstrip-like dispersion behavior with a strong increase in ϵ_{reff} with growing frequency, whereas the CPW mode phase constant remains almost constant up to about 600 GHz in our case. Here, critical effects are not the non-TEM dispersion itself, but interaction with higher-order modes.

For the geometry studied in Fig. 7, the first higher-order mode (HM10) as well as HM20 are related to substrate thickness h , i.e., they can be shifted towards higher frequencies by reducing h . The second higher order mode, HM01, is due to the lateral line width, i.e., primarily ground-plane width w_g . Thus, one concludes that for reliable high-frequency operation, both h and w_g have to be chosen small enough to prevent the occurrence of higher-order modes. Introducing an approximate model one derives a simple formula providing the corresponding design values as a function of the maximum frequency f_{max} (see [7]):

$$\text{Max} \left\{ h, \frac{w}{2} + s + w_g \right\} \leq \frac{1}{f_{\text{max}} \cdot \sqrt{2\mu_0\epsilon_0(\epsilon_r - 1)}} \quad (1)$$

Using (1) one can easily adjust substrate thickness h and ground-width w_g to the desired frequency range. Note that a further reduction of w_g can be of advantage, because it reduces attenuation (see Section III).

V. CPW VERSUS TFMSL

As described in the preceding sections, CPW and TFMSL both are suitable sub-mm-wave transmission lines. So far, however, a direct comparison is missing. This is presented in Fig. 8. In order to obtain useful information from such a comparison, two structures are compared that provide the same characteristic impedance and are comparable in size. The latter condition involves some uncer-

tainties as to lateral line size. In the CPW case (see Fig. 4), the total line width ($w+2s+2w_g$) represents a good measure, also regarding the lateral spacing from neighboring lines required to prevent crosstalk. For the TFMSL, it is more difficult to define such a figure since the strip width w (see Fig. 1) is much smaller than the spacing needed because of crosstalk. A value of 5 times the dielectric thickness h_d gives good isolation so that the total width allocated by a TFMSL is approximately $10h_d+w$. Following these considerations, in Fig. 8 both for CPW line width ($w+2s+2w_g$) and TFMSL width ($10h_d+w$) the same value of $62\text{ }\mu\text{m}$ is chosen.

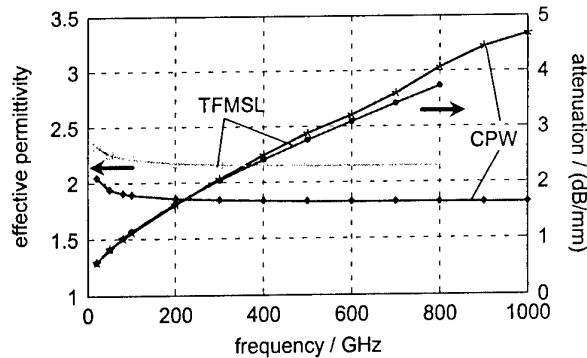


Fig. 8: Comparison of CPW and TFMSL ($70\text{ }\Omega$ lines of equivalent size): effective permittivity and attenuation against frequency (simulation data [1]); TFMSL dimensions as in Fig. 1 with $w = 8\text{ }\mu\text{m}$, $h_d = 5.4\text{ }\mu\text{m}$, CPW with $w = 13\text{ }\mu\text{m}$, $s = 3.5\text{ }\mu\text{m}$, $w_g = 21\text{ }\mu\text{m}$ on $25\text{ }\mu\text{m}$ thick BCB over $5\text{ }\Omega\text{cm}$ Si substrate (see Fig. 4 with layered substrate); Al metalization with $\kappa = 23.5\text{ S}/\mu\text{m}$, BCB: $\epsilon_r = 2.7$, $\tan\delta_e = 0.015$.

The results demonstrate that both line types show comparable attenuation. The same statement holds for dispersion characteristics, which is negligible up to at least 800 GHz . Naturally, effective permittivity for the CPW is lower than for the TFMSL, because in the latter case the field portion within the dielectric is larger. Briefly speaking, the differences with respect to dispersion and attenuation are minor and do not justify a clear preference for one of the line types.

There is one major difference, however, which is important for circuit design: The BCB dielectric with its low permittivity value is very beneficial in reducing dispersion. But, at the same time, it lowers characteristic impedance for a given conductor geometry. So, given a fixed impedance value, e.g., $50\text{ }\Omega$, one has to compensate for this by adjusting conductor dimensions accordingly. For the TFMSL, this is obtained easily (see Figs. 2 and 3). For the CPW, however, this requires a very small slot-to-strip width ratio s/w . This can be seen from the data in Fig. 8, where for a $70\text{ }\Omega$ CPW a slot width of only $3.5\text{ }\mu\text{m}$ is necessary. For a $50\text{ }\Omega$ CPW, situation is worse: assuming $40\text{ }\mu\text{m}$ ground-to-ground spacing (as treated in Sec. III) on a dielectric with $\epsilon_r = 3$ yields a center strip width w of $35\text{ }\mu\text{m}$ and a slot width $s = 2.5\text{ }\mu\text{m}$, which is beyond the technological limitations of the common processes.

VI. CONCLUSIONS

- Both TFMSL and miniaturized CPW are suitable for sub-mm-wave monolithic applications. Scaling down the dimensions yields excellent dispersion properties and low radiation, of course, at the expense of higher conductor loss. Attenuation levels are in the range of $5\text{--}10\text{ dB/mm}$ at 1 THz . Given the short line lengths in monolithic structures this is acceptable.
- While TFMSL and CPW achieve comparable performance in terms of dispersion and loss, there are differences in flexibility. The TFMSL properties do not depend on substrate quality and it covers a wider impedance range. The CPW impedance range, on the other hand, is restricted more severely by technological limitations, particularly the minimum slot width. This causes problems when realizing CPWs on low-permittivity dielectrics. Then the $50\text{ }\Omega$ value may be below the available impedance range.

VII. ACKNOWLEDGEMENTS

Part of this work was pursued in a collaboration with the RWTH Aachen, Lehrstuhl für Halbleitertechnik II (Prof. H. Kurz), where the TFMSL and CPW structures were fabricated and the electro-optic measurements were performed. The authors gratefully acknowledge this and would like to thank particularly H. Roskos, H.-M. Heiliger, and T. Pfeiffer for their contributions.

VIII. REFERENCES

1. W. Heinrich, "Full-wave analysis of conductor losses on MMIC transmission lines", IEEE Transactions MTT, vol. 38, 1990, pp. 1468-1472.
2. H.-M. Heiliger, M. Nagel, M. Setz, H. G. Roskos, H. Kurz, F. Schnieder, W. Heinrich, "Thin-film microstrip lines for mm and sub-mm-wave on-chip interconnects". 1997 IEEE MTT-S Int. Microwave Symp. Digest, vol. 2, pp. 421-424.
3. M.Y. Frankel, S. Gupta, J.A. Valdmanis, and G.A. Mourou, "Terahertz attenuation and dispersion characteristics of coplanar transmission lines," IEEE Trans. Microwave Theory Tech. vol. 39, pp. 910-915, June 1991.
4. H. Shigesawa, M. Tsuji, and A.A. Oliner, "Conductor-backed slot line and coplanar waveguide: dangers and full-wave analyses," 1988 Int. Microwave Symp. Digest, Vol. I, pp. 199-202.
5. D.B. Rutledge, D.P. Neikirk, and D.P. Kasilingam, in "Infrared and Millimeter Waves", vol. 10, "Millimeter Components and Techniques", chapt. 1: Integrated-circuit antennas", Editor: K.J. Button, New York, Academic Press, 1983.
6. N.-H. Huynh and W. Heinrich, "FDTD analysis of sub-millimeter wave CPW with finite-width ground metalization," IEEE Microwave and Guided Wave Letters, Vol. 7, No. 12, pp. 414-416, Dec. 1997.
7. W. Heinrich, F. Schnieder, and T. Tischler, "Dispersion and radiation characteristics of conductor-backed CPW with finite ground width," 2000 Int. Microwave Symp. Digest, vol. 3, pp. 1663-1666.

Tuneable Interferometric Bandpass and Bandstop Filters for Terahertz Applications

Otto Schwelb and István Frigyes

Abstract – Numerically simulated performance of a new type of tuneable bandstop and bandpass filter is presented. The filters use 2×2 couplers loaded by discontinuity-assisted ring resonators (DARR). The bandstop filter consists of one or several cascaded DARRs. Two bandstop filters separated by a cavity make up the bandpass filter. Tuning is achieved by varying the geometrical or material parameters of the ring resonators or the cavity. Alternatively, when the device is used as a sensor, environmental conditions are monitored by their detuning effect. Selectivity and tuning range are controlled by the coupling coefficient of the couplers, by the circumference of the rings and by the reflection coefficient of the discontinuities. The effects of coupler and waveguide loss have also been investigated.

I. INTRODUCTION

Quasi-optic tuneable bandstop and bandpass filters with bandwidths from the KHz to GHz range are key components in measurement, telecommunication and sensing. Analytical investigations show that a 2×2 coupler (lumped element or distributed parameter type) loaded by a ring resonator that incorporates a controlled amount of small reflective discontinuity can be a very effective bandstop filter subject to the strength of coupling. Using this circuit as a basic building block (BBB) we investigated several bandstop and bandpass filter configurations with remarkably selective properties. The bandstop filter, effectively a highly reflective composite mirror, is fabricated from one or several cascaded BBBs. The bandpass filter consists of two such mirrors, separated by a cavity, much like a Fabry-Perot resonator. The discontinuity built into the ring resonator can be a mismatch or a short length of waveguide with material or geometric properties slightly different from that of the ring.

The results have been obtained from a computer program using a lumped element model for the couplers; neither the fabrication technology of the resonant ring nor that of the discontinuity is addressed since they strongly depend on the band of operation. Some of our simulations have been carried out at 3THz, others at 194THz.

Tuning of the bandstop filter is achieved by modulating the parameters of the ring or that of the discontinuity. Tuning of the bandpass filter requires variation of the phase delay in the cavity between the mirrors. To obtain such a phase delay variation either the length or the refractive index of the cavity must be adjusted. Among the means to produce this adjustment are

micromechanical, piezoelectric, electrooptic and thermal. Conversely, environmental conditions can be monitored by their detuning effect. The technologies of tuning and modulation have not been here considered.

II. DISCONTINUITY-ASSISTED RING RESONATOR

The BBB of the filter is a 2×2 coupler loaded by a DARR as shown in Fig.1, where K is the power coupling coefficient of the coupler, γ its fractional power loss and r is the reflection coefficient of the discontinuity.

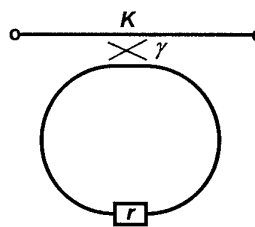


Fig.1. The basic building block of the filters: a 2×2 coupler loaded by a discontinuity-assisted ring resonator.

It is apparent that without the reflective discontinuity the circuit has an all-pass characteristic [1], i.e., the magnitude of the transmitted intensity in a lossless device is unity, and therefore without the reflective discontinuity the lossless circuit cannot be used as a frequency filter. (A lossy circuit without a discontinuity will still not reflect power back to the input, but its transmission will exhibit a notch near resonance.) Indeed, by exploiting the frequency dependency of its transmission *phase*, this circuit can be used as a group delay compensator [2].

While its reflectivity must be carefully controlled, the nature of the discontinuity embedded in the resonant ring is immaterial. It can consist of a small mismatch, a single step-index dielectric layer, a short shallow grating, etc. We assume a symmetric discontinuity, which is most conveniently represented by the scattering matrix [3]

$$S_d = \begin{bmatrix} r & jt \\ jt & r \end{bmatrix} \quad (1)$$

where $t = \sqrt{1-r^2}$ is the transmission coefficient of the discontinuity. In practice the reflection coefficient is small, in the order of 10^{-4} to 10^{-1} therefore, to obtain a high Q resonance, the power coupling coefficient K must be small as well, usually between 40dB and 10dB. Note also that it makes no difference for the operation of the DARR where inside the ring the discontinuity is located. Using a conventional model for the coupler [4] the two distinct elements of the scattering matrix of the BBB are

O. Schwelb is with the Department of Electrical and Computer Engineering, Concordia University, 1455 Demaisonneuve Blvd. West, Montréal, Québec, Canada H3G 1M8.

I. Frigyes is with the Dept. of Microwave Telecommunication, Budapest University of Technology and Economics, 1111 Budapest, Goldmann György tér 3, Budapest, Hungary

$$S_{11} = \frac{-a^2 r K \exp(jkL)}{\exp(j2kL) - a^2(1-K) - j2at\sqrt{1-K} \exp(jkL)} \quad (2)$$

and

$$S_{21} = a \frac{[\exp(j2kL) - a^2] \sqrt{1-K} - jat(2-K) \exp(jkL)}{\exp(j2kL) - a^2(1-K) - j2at\sqrt{1-K} \exp(jkL)} \quad (3)$$

where k is the wavenumber, L is the physical length of the ring and $a = (1-\gamma)^{1/2}$ is the amplitude loss coefficient of the coupler (γ is the fractional power loss).

Equations (2) and (3) reveal that the BBB is a bandstop filter whose behaviour is subject to the value chosen for K . Fig.2 depicts the wave intensity transmitted through the BBB as a function of detuning from the design frequency and as a function of K . (To convert from detuning to frequency multiply by c the free space velocity of light in mm/s.) The figure shows that at design frequency there is a critical value for K , denoted by K_c , where the transfer intensity is zero. For $K < K_c$ the resonator is undercoupled, showing two minima, increasingly separated as the value of K decreases. For $K > K_c$ the resonator is overcoupled showing one minimum which becomes increasingly shallow as the value of K rises. The relationship between K_c and r is:

$$K_c = \frac{2r}{1+r} \cong 2r \quad (4)$$

Important to notice is the second derivative of I_{21} with respect to frequency at centre wavelength. For an undercoupled DARR this is negative, whereas for an overcoupled DARR it is positive.

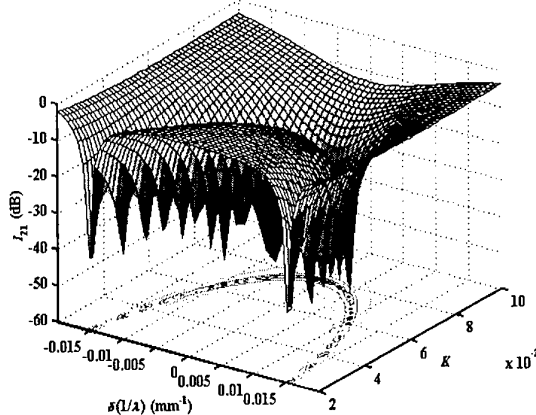


Fig.2. Intensity transfer through the BBB as a function of detuning and power coupling coefficient.

III. BANDSTOP FILTER CONSTRUCTION

Although the BBB offers large rejection levels, its skirt selectivity is not sufficiently steep. This can be improved upon by cascading several BBBs, separated by lengths of waveguides. To reinforce the reflection from each unit, the phase delay between consecutive BBBs must be such as to cause constructive interference at the entrance port,

much like in the case of reflected wavelets from each element of a Bragg grating in the stopband region [5]. Such constructive interference is achieved when the length of the waveguide separating the BBBs is an integral multiple of $\ell_\pi = \lambda_0/2n_e$, where λ_0 is the design wavelength and n_e the effective index of the guide. Fig.3 shows the transfer characteristics of N cascaded, undercoupled, identical BBBs. The bandwidth of the stopband of this composite mirror is proportional to r and inversely proportional to L_{eff} the effective length of the resonator (length \times effective index):

$$\Delta f \cong \frac{cr}{\pi L_{eff}} \quad (5)$$

This is in accordance with the fact that the group delay through the composite mirror at λ_0 is proportional to L_{eff} and inversely proportional to r . The performance characteristics of the composite mirror in the stopband region, including the group delay, are similar to those of a long Bragg grating [6]. By cascading undercoupled and overcoupled building blocks square well (flat bottom) stopband characteristics can be obtained.

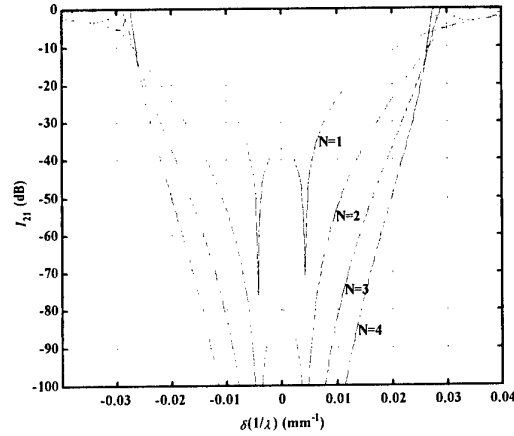


Fig.3. Intensity transfer as a function of detuning through N cascaded, undercoupled, identical BBBs.

IV. FABRY-PEROT TYPE BANDPASS FILTER

Since the transmission characteristic of a cascaded BBB is analogous to a composite mirror, one can build a Fabry-Perot type bandpass filter by inserting a waveguide between two identical chains of BBBs as shown in Fig.4.

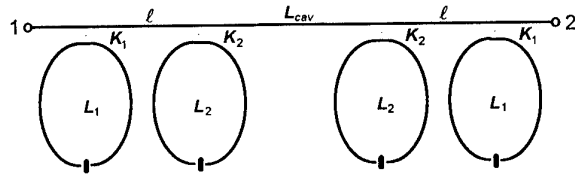


Fig.4. Fabry-Perot type bandpass filter consisting of two composite mirrors separated by a cavity.

If the length of the cavity (or defect, as it is sometimes called) is

$$L_{cav,n} = (n_{cav} + \frac{1}{2}) \frac{\lambda_0}{2n_{eff}}, \quad n_{cav} \text{ integer} \quad (6)$$

then the passband peak will fall in the middle of the stopband of the composite mirrors, i.e., on the design frequency. The maximum *continuous* tuning range within the mirror stopband, obtained by varying the cavity length is approximately $\Delta L_{cav} = 0.5\ell_\pi$, where ΔL_{cav} is the change in the physical length. Larger values of ΔL_{cav} to obtain the same tuning range can be realised by jumping from one n_{cav} to another, as implied by (6). When the cavity is tuned by refractive index variation the maximum tuning range is $\Delta n_c = n_c/(2n_{cav}+1)$. In either scheme the total phase delay while tuning the cavity from end of its range to the other is approximately $\Delta\phi = \pi/2$. Fig.5 shows the intensity transfer characteristics of the filter, centred at 3THz, using composite mirrors built with three unit cells having coupling coefficients $K_1=K_3=0.00103$ (29.9dB) and $K_2=0.00255$ (25.94dB), the reflection coefficient was $r = 0.001$. The solid lines are the bandpass curves corresponding to cavity lengths $L_{cav} = 100.58\ell_\pi$, $100.50\ell_\pi$ and $100.42\ell_\pi$, respectively, the dash-dotted line marks the flat-floor bandstop of the mirrors. The passband peaks rise from this floor; the lower the floor level the narrower are the passbands. A flat floor insures a constant bandwidth across the tuning range.

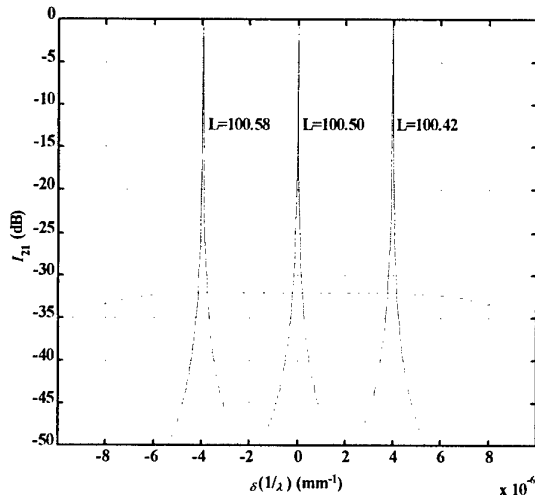


Fig.5. Transmission intensity as a function of detuning for three cavity lengths. The dash-dotted curve refers to the bandstop filters that comprise the mirrors.

V. THE EFFECT OF LOSS

The finite bandwidth and the corresponding finite Q of the bandpass filter fabricated with lossless components is an indication that the composite mirrors are partially transmitting. The smaller this transmission is, the larger is the Q :

$$Q = 2\pi \frac{L_{eff}}{\lambda_0 r I_{21}} \quad (7)$$

where I_{21} is the numerical value of the floor level transmission. Losses reduce the peak transmission and broaden the resonance curve.

In interferometric circuits one encounters coupler loss and ring resonator waveguide loss. These have demonstrably equivalent effect on the transmission and group delay characteristics of the filter. In comparison, waveguide losses in the connecting guides and in the cavity have insignificant effect on transmission. This is because a resonant ring 'magnifies' its losses (as well as its transmission group delay) proportional to $1/K$, usually a large number. Fig.6 is a surface plot of the bandpass peak in the vicinity of band centre as a function of fractional coupler loss. The plot shows the rapid deterioration of the passband characteristic with increasing γ . The parameters used to obtain Fig.6 are the same as those for Fig.5. An identical plot is obtained when instead of increasing γ from 0 to γ_{max} , the waveguide attenuation coefficient α is increased from 0 to $\alpha_{max} = \gamma_{max}/2L$, where α is in Np/mm and the length of the ring is in mm. Respecting the above law of equivalence between attenuation coefficient and fractional power loss, the two loss mechanisms are additive.

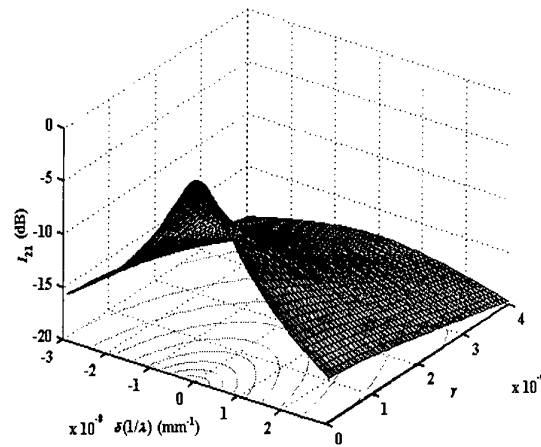


Fig.6. Surface plot of the intensity transfer as a function of detuning and fractional coupler loss.

Transmission levels of lossy filters also depend on K/K_c and the number of BBBs in the composite mirrors. This is illustrated in Fig.7, showing the transmitted intensity of bandpass filters at 3THz design frequency as a function of the relative coupling coefficient. The solid (dash-dotted) lines refer to $\gamma = 1 \times 10^{-6}$ ($\gamma = 1 \times 10^{-5}$), N represents the number of identical BBBs in each mirror and $\alpha = 0$. Observe how the transmission level for a given setting of γ drops as K approaches K_c and how sensitive this transmission is to N . The acute sensitivity of interferometric circuits based on resonant rings to loss might require inclusion of active elements that can provide the small amount of gain necessary to offset the losses.

VI. DESIGN PROCEDURE

The fundamental parameters and technological constraints given when designing a tuneable ring resonator based terahertz filter are: the centre wavelength, the tuning range, the stopband or passband width, the effective refractive index of the guides and the minimum,

or desirable length (circumference) of the rings. The minimum free spectral range (FSR) might also be specified, but its value is subject to the minimum ring radius.

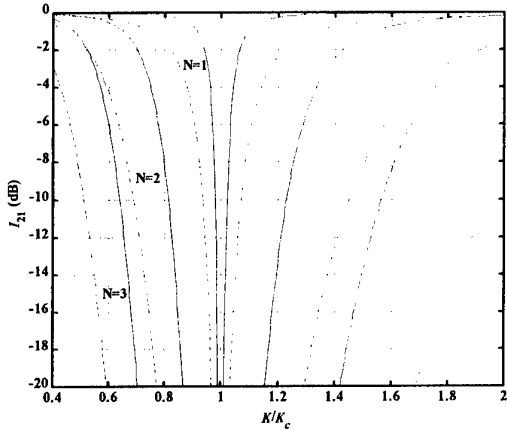


Fig.7. Transmission intensity vs. relative coupling coefficient of lossy bandpass filters using N identical BBBs in each mirror.

From (5) one can determine the reflection coefficient of the discontinuity r . When the discontinuity is a single defect layer, its refractive index n_a and length l_a are determined from

$$r = \left| \rho \frac{1 - \exp(-j2k_a l_a)}{1 - \rho^2 \exp(-j2k_a l_a)} \right| \quad (8)$$

where k_a is the wavenumber in the defect layer and

$$\rho = \frac{n_a - n_{eff}}{n_a + n_{eff}} \quad (9)$$

assuming $n_a > n_{eff}$. The maximum value of r provided by (8) is

$$r_{max} = \frac{2\rho}{1 + \rho^2} \quad (10)$$

and the relative index and length of the defect layer are, respectively

$$\frac{n_a}{n_{eff}} = \sqrt{\frac{1 + r_{max}}{1 - r_{max}}} \quad \text{and} \quad l_a = (2N + 1) \frac{\lambda_0}{4n_{eff}} \sqrt{\frac{1 - r_{max}}{1 + r_{max}}} \quad (11)$$

With the stopband width and the design wavelength we first determine the Q , then substituting the value of r and Q into (7) the floor level transmission intensity of the square well bandstop characteristics is computed. Next the coupling coefficients are adjusted to meet this requirement. The number of DARR loaded couplers is determined by the required filter skirt selectivity (and loss considerations), while the length of the guide separating the couplers within the composite mirror must be an integral multiple of ℓ_π . The length of the cavity at centre frequency is determined by (6). When the cavity is tuned

via index modulation, increasing the value of n_{cav} , as indicated above, can reduce the modulation depth necessary to tune through the stopband. The transmission and reflection characteristics of the bilaterally symmetric Fabry-Perot type bandpass filter are obtained from its scattering parameters:

$$S_{BP11} = S_{M11} \left[1 + \frac{S_{M21}^2 e^{-j2kl_{cav}}}{1 - S_{M11}^2 e^{-j2kl_{cav}}} \right] \quad (12)$$

and

$$S_{BP21} = \frac{S_{M21}^2 e^{-jkl_{cav}}}{1 - S_{M11}^2 e^{-j2kl_{cav}}} \quad (13)$$

where S_{M11} and S_{M21} are the scattering parameters of the composite mirrors on either side of the cavity. A computer code to follow through these steps has been developed.

VII. CONCLUSIONS

Simulated characteristics of a novel, tuneable bandstop and bandpass filter have been described. The bandstop filter, fabricated with one or several cascaded 2×2 couplers loaded by discontinuity-assisted ring resonators (DARR) is regarded as a composite mirror. The bandpass filter consists of two such mirrors in a Fabry-Perot configuration. The bandwidth is adjustable and can be made arbitrarily small. The effect of the parameters controlling the tuning range and the passband width, as well as the effect of waveguide and coupler loss has been investigated. A detailed design procedure has been described. The technological aspects of device fabrication and tuning have not been addressed.

ACKNOWLEDGMENT

The support of the Natural Sciences and Engineering Research Council of Canada and the Hungarian Foundation for Scientific Research (OTKA Project T-026277) is acknowledged.

REFERENCES

- [1] G.S. Pandian and F.E. Seraji, "Optical pulse response of a fibre ring resonator," *Proc. IEE, part J*, vol. 138, pp. 235-239, June 1991.
- [2] C.K. Madsen and G. Lenz, "Optical all-pass filters for phase response design with applications for dispersion compensation," *IEEE Photonics Technol. Lett.*, vol. 10, pp. 994-996, July 1998.
- [3] H.A. Haus, *Waves and Fields in Optoelectronics*. Englewood Cliffs: Prentice-Hall, Inc., 1984, Section 3.4.
- [4] O. Schwelb, "Generalized analysis for a class of linear interferometric networks. Part I: Analysis," *IEEE Trans. Microwave Theory Tech.*, vol. 46, pp. 1399-1408, Oct. 1998.
- [5] L.A. Coldren and S.W. Corzine, *Diode Lasers and Photonic Integrated Circuits*. New York: John Wiley & Sons, Inc., 1995, Section 3.5.
- [6] T. Erdogan, "Fiber grating spectra," *J. Lightwave Technol.*, vol. 15, pp. 1277-1294, Aug. 1997.

MICROMACHINED PLANAR ANTENNAS FOR D-BAND FREQUENCIES

KAREN DUWE ¹, STEFANIE HIRSCH ², ROLF JUDASCHKE ², JÖRG MÜLLER ¹

¹ Arbeitsbereich Halbleitertechnologie

² Arbeitsbereich Hochfrequenztechnik

Technische Universität Hamburg–Harburg

D–21073 Hamburg, Germany

Phone: +49 40 42878-2402, Fax: +49 40 42878-2396, E-mail: karen.duwe@tu-harburg.de

Abstract

The fabrication of different planar antenna structures using micromachining techniques is described. The antenna patches are based on thin dielectric HMDSN membranes deposited by plasma polymerization and fabricated by structuring the underlying silicon. Both antennas and CPW-feedlines are composed of two stacked KOH-etched silicon-layers. Different transitions from membrane-based coplanar waveguides to multi-layer antenna structures have been fabricated and characterized around 125 GHz.

Introduction

The structure of coplanar waveguides on thin dielectric membranes allows single-mode TEM wave propagation over a wide frequency range, almost negligible dispersion, and very low dielectric losses [4]. Coplanar waveguides on thin HMDSN-membranes have already been fabricated and characterized for D-band frequencies. They show a very low attenuation of about 0.1 dB/mm. A transition from membrane-based coplanar waveguide to rectangular waveguide has also been fabricated for D-band exhibiting low losses [1], [2]. Based on these results, two different planar antenna structures at D-band frequencies have been developed for power combining applications. The design and numerical results are presented in [3]. The manufacturing of the planar antennas on thin HMDSN-membranes is described below. The antennas consist of two stacked KOH-etched silicon layers fed by membrane-based coplanar waveguides. The membranes deposited from plasma-polymerized HMDSN were fabricated by structuring the 300 μm thick, low-resistive silicon below with micromachining techniques. The radiation pattern of a coplanar

fed microstrip probe horn antenna has been measured. Although the fabricated structure is based on a non-optimized design, it shows satisfactory far-field characteristics around 125 GHz.

Slot-Coupled CPW-Fed Patch Antenna

The structure is composed of two stacked micromachined silicon layers as shown in figure 1. The bottom layer contains the coplanar feedline which merges into a coupling slot. Both the coplanar feedline and the coupling slot are based on a 4 μm thin HMDSN-membrane.

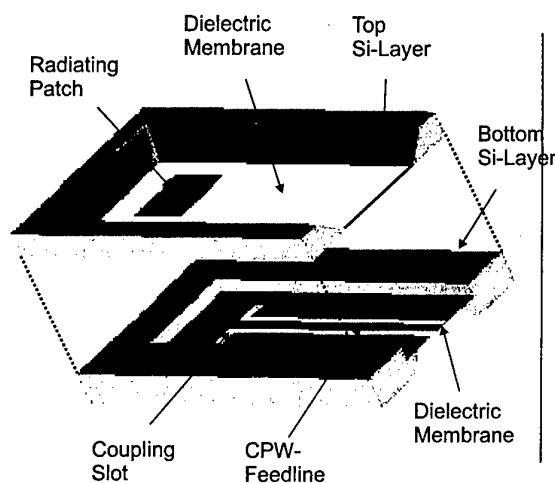


Figure 1: Structure of a slot coupled CPW-fed patch antenna.

The coplanar feedline is coupled to rectangular waveguide using the transition described in [1]. The membrane-based transition consists of two cascaded transitions, the first from rectangular waveguide to microstrip line followed by a taper from microstrip

to coplanar line. To form the ground plane of the membrane-based microstrip line the metallic surface of the test fixture is used. Therefore the height of the bottom layer has to be smaller than $100\text{ }\mu\text{m}$.

On the upper layer a radiating patch is placed on a $4\text{ }\mu\text{m}$ thin HMDSN-membrane. In the stacked structure, the radiating patch is centered exactly above the coupling slots. The gap between both layers is around $65\text{ }\mu\text{m}$. The gap is fabricated by structuring the upper side of the bottom silicon layer by plasma etching. Using low pressure chemical vapour deposition the silicon is cladded by a 200 nm thick Si_3N_4 -film. Subsequently, the $4\text{ }\mu\text{m}$ thick HMDSN film is grown by plasma-polymerization and annealed at 200°C . A 750 nm thick titanium/gold layer is sputtered and structured by wet chemical etching to form the coplanar waveguide and the coupling slot. The backside Si_3N_4 is opened by a plasma etching process serving as a mask on the silicon substrate.

Next the underlying silicon is etched to a depth of $100\text{ }\mu\text{m}$ in an alkaline KOH-solution. During this process the upper surface with the coplanar lines and the coupling slots is protected. Afterwards, the Si_3N_4 mask is removed by a plasma etching process. Employing the KOH-solution again, the silicon below the membrane is thinned to a few μm . During this fabrication step the upper surface is also protected. The remaining silicon and the Si_3N_4 are finally removed by a plasma etching process.

The upper layer is much easier to manufacture in comparison with the bottom layer, because the thickness of the substrate can be kept at $300\text{ }\mu\text{m}$. Furthermore, the upper surface of the layer is planar, because the gap between the layers is structured only in the bottom layer. The fabrication reduces to the evaporation of Si_3N_4 on a silicon substrate followed by the deposition and annealing of a $4\text{ }\mu\text{m}$ thick HMDSN film. Appropriate to the fabrication of the bottom layer described above, a titanium/gold film is sputtered and structured by wet chemical etching. Afterwards the Si_3N_4 is opened and the underlying silicon is removed up to a few μm in a KOH-solution while the upper surface is protected. At last the remaining silicon is removed by a plasma etching process.

Finally, the single manufactured layers are stacked and connected with fluid-silver.

CPW-Fed Microstrip Probe Micromachined Horn Antenna

Figure 2 shows a second type of planar antennas using thin dielectric membranes. The structure is based on the transition from coplanar waveguide on

thin HMDSN-membrane to conventional rectangular waveguide presented in [1]. The coplanar line is first tapered to a microstrip line. Afterwards, a transition from microstrip line to rectangular waveguide consisting of a nearly triangular patch placed in the E-plane of the coplanar waveguide is realized. To minimize the field distortion caused by the test fixture the direction of beam has to be perpendicular with respect to the test fixture surface. Therefore, a small KOH-etched, low-resistive silicon cuboid is used. The position of the bottom side of the cuboid is about $100\text{ }\mu\text{m}$ above the HMDSN-membrane, so this surface is used as ground plane of the microstrip line. The cavity sidewalls of the micromachined silicon substrate and the small silicon cuboid operate as a micromachined horn.

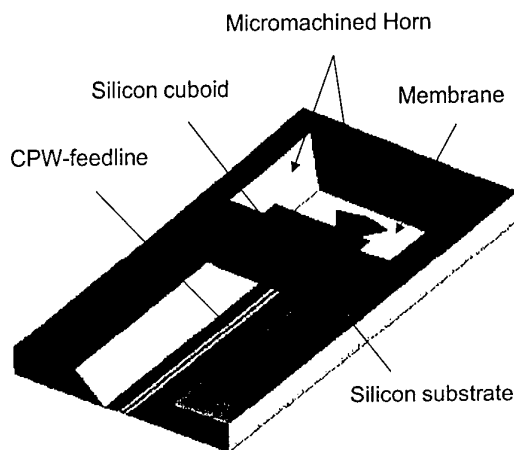


Figure 2: Structure of a microstrip probe micromachined horn antenna.

In principle, the fabrication of this antenna structure is identical compared with the fabrication of the upper layer of a slot coupled CPW-fed patch antenna described above. Figure 3 shows a photograph of the fabricated CPW-fed microstrip probe micromachined horn antenna.



Figure 3: Photograph of a microstrip probe micromachined horn antenna.

Characterization and Measurement

Both return loss and radiation pattern of a microstrip probe horn antenna have been measured. The results are shown in figures 4 and 5. Although the structure is based on a non-optimized design it shows satisfactory characteristics.

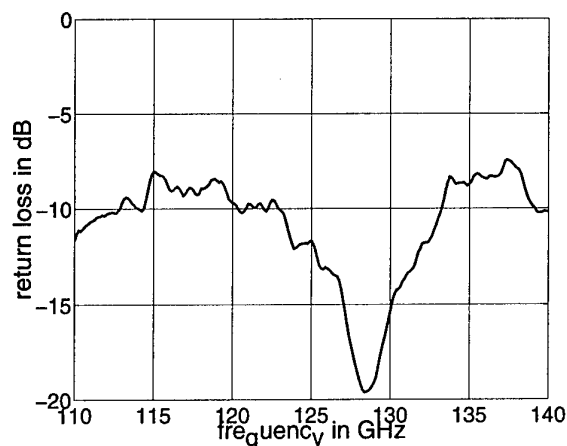


Figure 4: Measured return loss of a microstrip probe micromachined horn antenna.

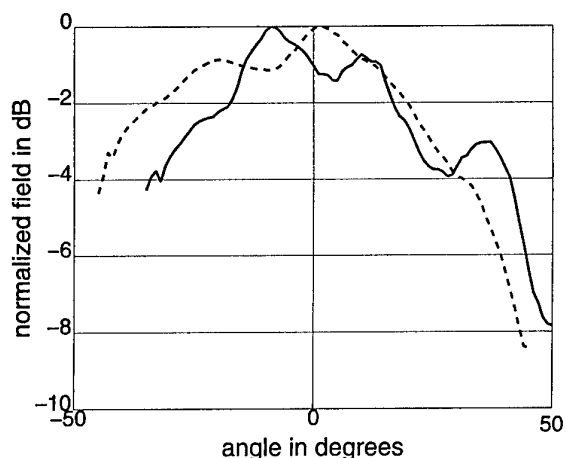


Figure 5: Measured radiation pattern of a microstrip probe micromachined horn antenna: E-plane (solid line) and H-plane (dashed line), $f = 125$ GHz.

Conclusions

Two different types of planar antennas based on thin HMDSN-membranes are presented. First measurements show satisfactory characteristics although the fabricated antenna is based on a non-optimized design. These results promise good performances for optimized structures. The antennas are fed by coplanar lines based on thin dielectric membranes. There-

fore, low-resistive silicon substrates can be used. Furthermore, the direction of maximum radiated power is perpendicular to the plane of the CPW-feedline indicating a good applicability for power combining applications. An integration of planar antennas and impatt oscillators to a multi-element power combining array will be part of future work.

Acknowledgement

The authors are indebted to the Deutsche Forschungsgemeinschaft for financial support.

References

- [1] S. Hirsch, K. Duwe, R. Judaschke, "A Transition from Rectangular Waveguide to Coplanar Waveguide on Membrane", to be presented in the *25th International Conference on Infrared and Millimeter Waves*, Sept 2000, Beijing, China
- [2] K. Duwe, S. Hirsch, R. Judaschke, J. Müller "Micromachined Coplanar Waveguides on Thin HMDSN-Membranes", to be presented in the *25th International Conference on Infrared and Millimeter Waves*, Sept 2000, Beijing, China
- [3] S. Hirsch, K. Duwe, R. Judaschke, "Coplanar Fed Micromachined Planar Antennas for Power Combining Applications at D-Band Frequencies", *this Conference*
- [4] L. P. Katehi, G. M. Rebeiz, "Novel Micromachined Approaches to MMICs Using Low-Parasitic, High-Performance Transmission Media And Environments", *IEEE MTT-S Digest*, 1996, pp. 1145-1148.
- [5] D. F. Filipovic, W. Y. Ali-Ahmad, G. M. Rebeiz "Millimeter-Wave Double-Dipole Antennas for High-Gain Integrated Reflector Illumination", *IEEE Transactions on Microwave Theory and Techniques*, 1992, vol. 40, No. 5, pp. 962-967.

Imaging Technologies in the Millimeter Wave Region

Koji Mizuno

Research Institute of Electrical communication, Tohoku University

Katahira, Aobaku-ku, Sendai 980-8577, Japan

Abstract - Imaging technologies using millimeter (mm) waves offer unique measurement means in many application areas. We discuss here mm-wave focal plane imaging technologies whose resolution is limited by diffraction and also mm-wave scanning near-field microscopy whose resolution is much smaller than operating wavelength. Results of our researches on both of these imaging technologies are presented.

1. MM-wave Imaging

Millimeter wave focal plane imaging [1] is able to provide image information through clouds, smoke, and dust when visible and IR systems are unusable. It can also be used in the fields of plasma measurement, remote sensing, etc. The resolution of the focal plane imaging is limited by diffraction and is the order of wavelength, while scanning near field microscopy achieves sub-wavelength resolution [2], which offers other applications of millimeter wave imaging technologies.

2. Focal plane imaging (Imaging arrays)

Conventional millimeter wave imaging relies mainly on the use of a single detector, with the optics mechanically scanned to obtain an image. The use of multiple detectors in an imaging array, however does not require mechanical scanning and makes real-time imaging possible. Figure 1 shows a 60 GHz imaging array [3,4] which consists of 2-element Yagi antennas with beam-lead Schottky diodes at the center of the antennas. The interval between the antennas was determined by the sampling theorem to obtain the diffraction-limited image.

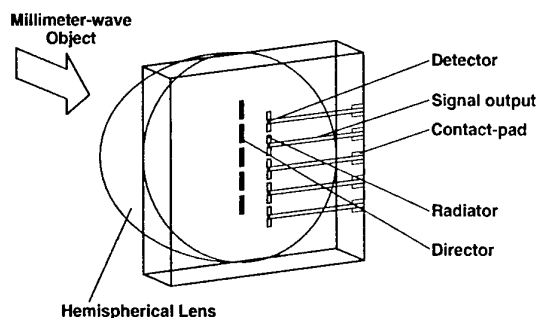


Fig. 1 Yagi-Uda antenna imaging array

i) Plasma diagnostics

The optics for mm-wave imaging radar systems can be designed using the ray tracing method. Figure 2 shows the 70 GHz optics designed for measuring 2-dimensional plasma density profile in a plasma machine for nuclear fusion research at the University of Tsukuba. Figure 3 shows measured time-revolution of 2-dimensional plasma density profile [5].

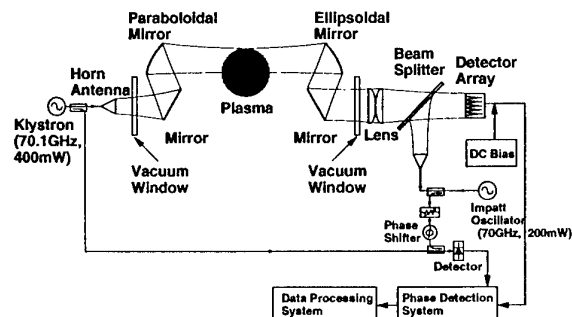


Fig. 2 Phase imaging system for plasma diagnostics

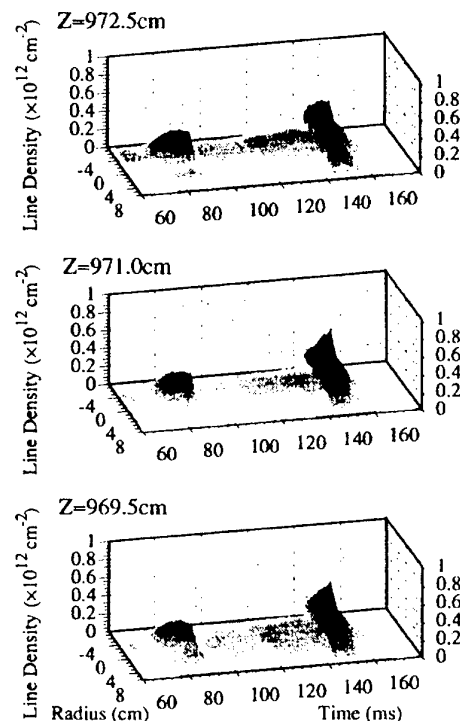


Fig. 3. Time evolution of line density radial profiles at three axial positions of a plasma at Tsukuba.

ii) Millimeter wave images and neural network processing

A neural network signal processing has been successfully introduced to recognize mm-wave images which were distorted by speckle and/or glint through coherent illumination [6].

Alphabetical letters made of aluminum foil were used as test objects for evaluating our mm-wave imaging system. Figure 4 (a) shows experimentally-obtained images for the letters A and J. The size of each object corresponds to about 8×8 pixels on the image plane. The images represent power distribution of scattered signals and are strongly distorted, mainly because of speckle and/or glint resulting from coherent illumination.

To recognize these images, a feed-forward neural network was used as a signal processor. The network consists of 10×10 input units, 60 hidden units and 26 output units. In Fig. 4 (b) the recognition rate is shown as a function of the number of "teach-data" required, when 10 alphabetical letters (A, H, J, L, O, P, S, T, V, and Z) which are dissimilar to each other were used as the objects. A high recognition rate of 98 % has been obtained using data from five teaching trials for each letter, which shows that neural network signal processing is a very powerful tool for recognition of mm-wave images.

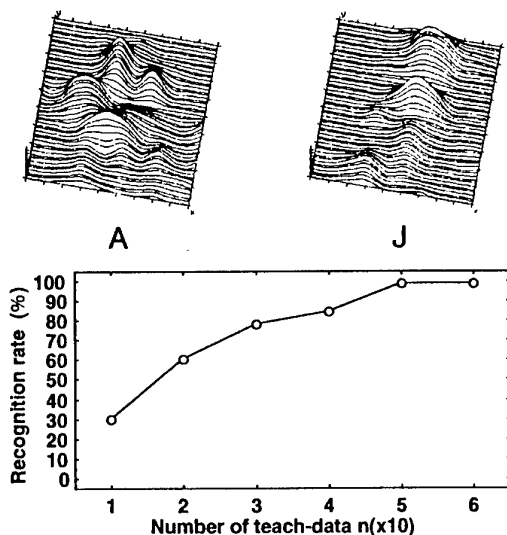


Fig. 4. Typical examples of MM-wave images for the letters A and J (above), and recognition rate as a function of the number of teach-data (below).

3. Scanning near-field microscopy

Diffraction limits the resolution of focal plane imaging and conventional microscopy to approximately $\lambda/2$. Sub-wavelength resolution has been demonstrated with scanning near-field microscopes. We proposed and demonstrated a new type of scanning near-field millimeter-wave microscopy using a metal slit at the end of a rectangular waveguide as a scanning probe [2, 7, 10].

The waveguide probe is shown in Fig. 5. A reduced-height waveguide forms the slit; the wide dimension of the slit and that of the waveguide are identical, but the waveguide height is reduced down to $\lambda/60$ ($80 \mu\text{m}$ at 60 GHz).

This probe is operated above the cutoff frequency for the fundamental waveguide mode and thus provides much stronger signals than point-type probes which operate below the cutoff frequency, resulting in improved sensitivity or resolution. For a 60 GHz band probe with the slit width of $80 \mu\text{m}$ the power transmission coefficient was estimated as 20 % which is much larger than that (10^{-5} %) for conventional metal-coated, tapered optical fiber probes. Also the slit type probe makes fast (but rough) scanning over a wide sample possible when it is useful.

To achieve sub-wavelength resolution for all directions with the slit-type probe, we have adopted an image reconstruction algorithm based on computerized tomographic imaging such as that used in the x-ray CT imaging.

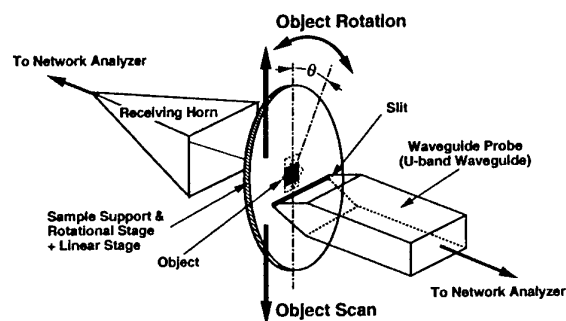


Fig. 5 Scanning near-field microscopy using a slit type probe.

We have successfully demonstrated an application of the microscope with a slit type probe in visualization of transition phenomena of photoexcited free carriers in a silicon substrate, i.e. time-resolved imaging of carrier distributions. For this demonstration a high-speed homodyne detection system at 60 GHz with a response time of 0.4 ns was constructed. The experimental setup of showing the probe and the substrate is depicted in Fig. 6. The object was a silicon on quartz (SOQ) substrate. The thickness of the silicon and quartz layers were $0.2 \mu\text{m}$ and 1.2 mm , respectively. Optical pulses from a Q-switched Nd:YAG laser passing through the quartz layer generated free carriers in the silicon layer. The photoexcited area was 0.5 mm in diameter. The density of free carriers generated was estimated to be as high as $10^{17} / \text{cm}^3$. Figure 7 shows the temporal evolution of the carrier distribution. Free carrier generation and diffusion processes are clearly imaged [8-10]. The images show that the carriers generated diffuse non-uniformly in the silicon layer, which suggests that the layer has some defect distribution along

the surface. The life time of carriers is affected and determined by the defect distribution. Animation of the images in Fig. 7 can be seen in our Web site [11].

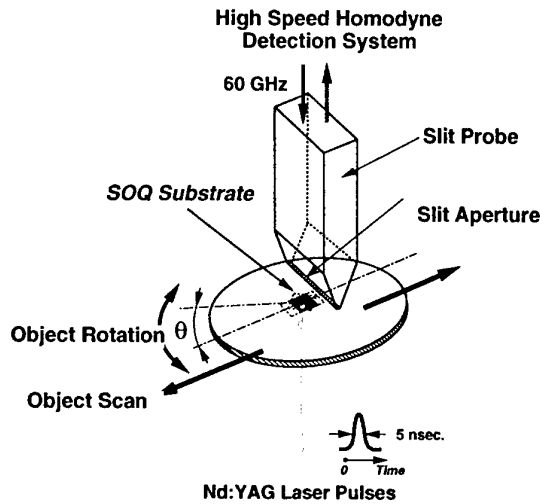


Fig. 6 Experimental scheme for measurement of photoexcited free carriers in a Silicon-On-Quartz substrate.

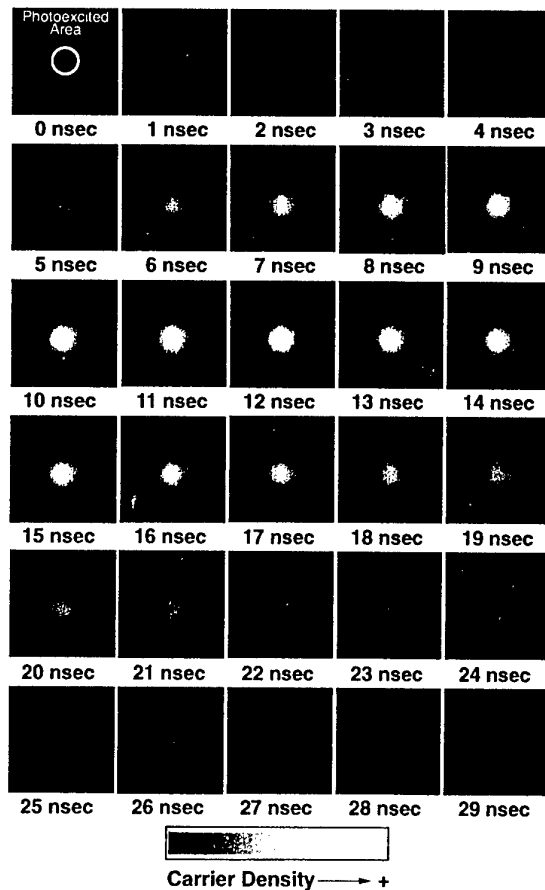


Fig. 7. Temporal evolution of photoexcited free carrier distribution. The time interval between the figures is 1 ns and the circle in the image at 0 ns shows the region illuminated by a laser.

4. Summary

As the proverb of "Seeing is believing" says, imaging technologies provide wide information. The unique characteristics of millimeter wave propagation make mm-wave imaging technologies very attractive.

A part of our research has been supported by the Public Participation Program for Frequency Resource Development from the Ministry of Posts and Telecommunications, and by a Grant-in-Aid for Scientific Research from the Ministry of Education, Science, Sports, and Culture, Japan.

REFERENCES

- [1] K. Mizuno, K. Watabe, J. Bae, T. Nozokido, and S. Sugawara, "Millimeter wave imaging technologies," 1997 Topical Symposium on Millimeter Waves (Invited), Hayama, Japan, July 1997.
- [2] T. Nozokido, J. Bae, T. Fujii, M. Itoh, and K. Mizuno, "Scanning near-field millimeter-wave microscopy using a Metal Slit as a Scanning Probe," in *Conf. Digest of 22nd Int. Conf. on Infrared and Millimeter Waves*, Wintergreen, Virginia, pp 302-303, 1997.
- [3] K. Mizuno, K. Uehara, H. Nishimura, T. Yonekura, and T. Suzuki, "Yagi-Uda array for millimeter-wave imaging," *Electron. Lett.*, vol. 27, pp. 108-109, 1991.
- [4] K. Uehara, K. Miyashita, K. Natsume, K. Hatakeyama, and K. Mizuno, "Lens-coupled imaging arrays for the millimeter and submillimeter regions," *IEEE Trans. Microwave Theory Tech.*, vol. 40, pp. 806-811, 1992.
- [5] N. Ohyama, A. Mase, T. Tokuzawa, K. Imamura, A. Itakura, T. Tamano, Y. Harada, and K. Mizuno, "Millimeter-wave two-dimensional imaging array for the GAMMA 10 tandem mirror," *Rev. Sci. Instrum.* vol. 68, pp. 500-503, 1997.
- [6] K. Watabe, K. Shimizu, M. Yoneyama, and K. Mizuno, "Millimeter-wave imaging using neural networks for object recognition," in *1996 IEEE MTT-S International Microwave Symposium Digest*, vol. 2, pp. 1135-1138, 1996.
- [7] J. Bae, T. Okamoto, T. Fujii, K. Mizuno, and T. Nozokido, "Experimental demonstration for scanning near-field optical microscopy using a metal micro-slit probe at millimeter wave lengths," *Appl. Phys. Lett.*, vol. 71, pp. 3581-3583, 1998.
- [8] T. Nozokido, H. Minamide, J. Bae, T. Fujii, M. Itoh, and K. Mizuno, "Visualization of photo-excited free carriers with a scanning near-field millimeter-wave microscope," in *Conf. Digest of 23rd Int. Conf. on Infrared and Millimeter Waves*, pp 382- 384, 1998. (Invited)
- [9] T. Nozokido, J. Bae, and K. Mizuno, "Visualization of photoexcited free carriers by scanning near-field millimeter-wave microscopy," *Appl. Phys. Lett.*, vol. 77, pp. 148-150, 2000.
- [10] T. Nozokido, J. Bae, and K. Mizuno, "Scanning near-field millimeter-wave microscopy using a metal slit as a scanning probe," *IEEE Trans. Microwave Theory Tech.*, to appear in 2000.
- [11] http://www.mizuno.riec.tohoku.ac.jp/nfnw/nfnw_anime.html

Imaging of Photoexcited Carrier Distribution in Semiconductors by THz Beams

Masanori Hangyo, Masatsugu Yamashita, Yoshiaki Kitoh, Masayoshi Tonouchi

Abstract – A terahertz (THz) wave imaging system using photoconductive antennas as an emitter and detector has been constructed and the focussing characteristics of the beam near the sample position has been investigated. By using this system, the images of photoexcited carrier distribution in silicon have been obtained with spatial resolution of 2.5 mm by measuring the transmission of the focused THz beams.

I. INTRODUCTION

The transmittance and reflectance of electromagnetic waves in the microwave and infrared regions are much affected by free carriers in semiconductors [1,2]. Fig. 1 shows the transmittance of electromagnetic waves in the THz region calculated for 400- μm thick silicon wafers with various carrier densities. In this calculation, multiple reflection in the sample is neglected since we can exclude the multiple reflection by cutting off the multiply reflected electromagnetic waves in the time domain. The transmittance is greatly affected by the carrier density, especially in the low frequency region. By measuring the transmittance or reflectance, the density and mobility of the free carriers can be obtained without contact to the samples [1]-[3]. The free carriers are generated also by optical excitation and the transmittance and reflectance of the electromagnetic waves are affected by these photoexcited carriers. The change of the reflectance of microwaves by the irradiation of light has been used to characterise semiconductors [4,5]. Since the photoinduced reflectance is influenced by the dark resistivity, recombination time

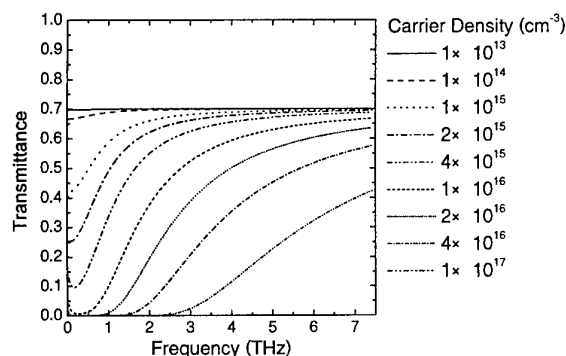


Fig. 1: Dependence of the transmittance of THz waves on the carrier density in silicon wafers

M. Hangyo, M. Yamashita, Y. Kitoh and M. Tonouchi are with the Research Center for Superconductor Photonics, Osaka University, 2-1 Yamadaoka, Suita, Osaka 565-0871, Japan

of photoexcited carriers, surface recombination velocity, and so on, versatile information on the free carriers and quality of the samples can be obtained.

Imaging of photoexcited carriers by using electromagnetic waves is important to evaluate the homogeneity of semiconductor samples. Recently, Nozokido *et al.* constructed a scanning near-field millimeter-wave microscope and applied it to visualising the photoexcited carrier distribution in silicon wafers and its time evolution with a spatial resolution of 110 μm [6]. In their system, the samples are placed very close to the tapered waveguide used as a probe. For introducing such noncontact evaluation systems in the fabrication process of semiconductor devices, it is preferable to separate samples and the probe widely. The imaging systems using THz waves are appropriate for this purpose [7].

In this paper, we constructed an imaging system using the focused THz beam generated and detected by photoconductive antennas and applied it to imaging the photoexcited carrier distribution in silicon wafers. The photoexcited carrier distribution is obtained with spatial resolution of ~ 2.5 mm.

II. THz IMAGING SYSTEM

Fig. 2 shows the schematic diagram of a THz imaging system. Optical pulses with a time width of ~ 80 fs, a wavelength of ~ 800 nm, and a repetition rate of 82 MHz from a mode-locked Ti:sapphire laser were used to excite a dipole-type photoconductive antenna on low-temperature grown GaAs (LT-GaAs) for generating THz wave pulses. The generated THz beam was focused on a sample by two paraboloidal mirrors (M_1 and M_2) and collected and focused by two paraboloidal mirrors (M_3 and M_4) into a dipole-type photoconductive antenna on LT-GaAs used as a detector. The focal length of M_1 and

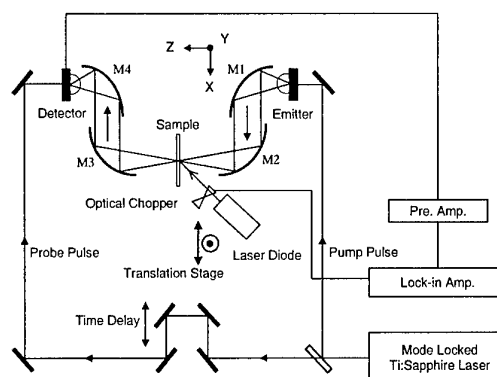


Fig. 2: Schematic diagram of the THz imaging system

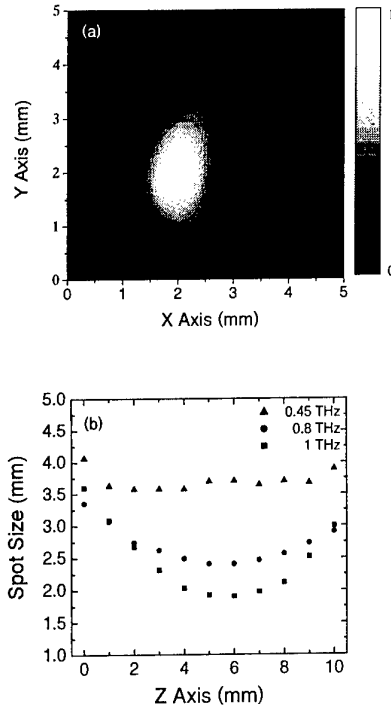


Fig. 3: (a) Maximum-amplitude distribution of THz waves in the X-Y plane at the focal point and (b) variation of the spot size along the beam direction at 0.45, 0.8 and 1 THz

M_4 was 7.6 cm and that of M_2 and M_3 was 11.9 cm. The detector was triggered by optical pulses divided from the exciting laser pulses after time delay.

The focusing characteristics of the THz beam near the focal point were measured by translating a metal mask with a pinhole of 1 mm diameter and taking a waveform in the time domain at each position. The exciting laser pulses were chopped at 2 kHz and the current induced by the THz electric field in the detector was lock-in detected. Fig. 3 (a) shows the distribution of the maximum amplitude of the waveform in the plane perpendicular to the beam direction at the focal point. The distribution is deformed from a simple Gaussian profile probably due to slight misalignment of optics. The full width at half maximum (FWHM) of the amplitude in the X and Y directions are 1.8 and 3.2 mm, respectively. Since the focussing characteristics are expected to be different for different frequencies, we calculated the Fourier spectrum of the waveform in the time domain at each position and fitted it with a Gaussian distribution function along the X axis at each frequency. The change of the FWHM of the amplitude thus obtained at 0.45, 0.8 and 1 THz along the Z axis (beam direction) is plotted in Fig. 3 (b). The FWHM at the focal point decreases with increasing frequency as expected from classical optics.

III. IMAGING OF PHOTOEXCITED CARRIERS

In order to see the effect of photoexcited carriers on the THz transmission for silicon wafers, the waveforms with and without CW laser diode illumination (800 nm, 100 mW) are measured. The silicon wafer is P-doped (2.5 Ω cm) and the thickness is 400 μ m. The diameter of the

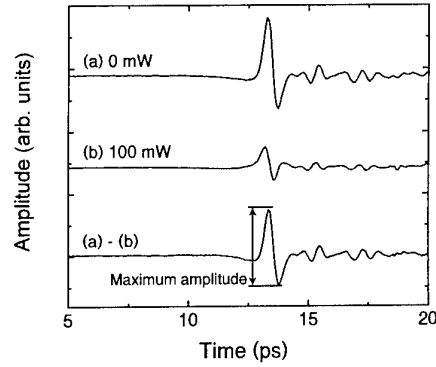


Fig. 4: Waveforms of the transmitted THz waves (a) without and (b) with CW laser diode illumination

laser spot on the sample is about 2 mm. Fig. 4 shows the waveforms (a) without and (b) with illumination of laser light. With the illumination of the laser light, the transmittance decreases due to the increase of the free carriers.

The position dependence of the THz transmission change is measured by translating the laser diode on an X-Y stage as shown in Fig. 2. Since the sample used is homogeneous, we are essentially measuring the position dependence of the THz transmission of the silicon wafer illuminated nonuniformly by the laser light. The CW light from the laser diode is chopped at 2 kHz instead of chopping the beam from the Ti:sapphire laser and the current induced by the THz electric field is lock-in detected. In this measurement, the photoinduced change of the THz waveform corresponding to (a) - (b) in Fig. 4 is measured.

The maximum-amplitude distribution of the waveforms in the X-Y plane at the focal point is shown in Fig. 5 (a). The FWHM's of the distribution are 3.9 mm for both X and Y axes. Since the spot size of the THz beam on the sample changes with frequency, the spatial resolution of the image of the photoexcited carriers will change with frequency. To confirm this, we Fourier transformed the waveform at each position and obtained the image at each frequency. The images at 300 GHz and 1.5 THz are shown in Figs. 5 (b) and (c), respectively. The FWHM's in the X and Y directions of the image at 300 GHz are 5.0 and 4.3 mm, respectively, and those at 1.5 THz are 3.6 and 3.5 mm, respectively. The spatial resolution increases with increasing frequency as expected [7].

Next, we show the dependence of the amplitude of the transmitted THz wave on the exciting laser intensity. Figs. 6 (a), (b) and (c) show the maximum-amplitude distribution for the exciting powers of 80, 160 and 250 mW, respectively. The amplitude increases with increasing the exciting laser power monotonically. Fig. 6 (d) shows the dependence of the amplitude on the exciting laser power. The amplitude increases linearly with increasing the laser power until ~ 150 mW and shows a trend of saturation with increasing the laser power further. This result indicates that the amplitude is proportional to the photoexcited carrier number when the exciting power is not too strong.

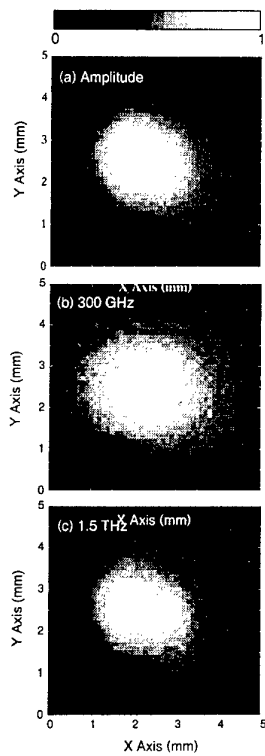


Fig. 5: Transmitted THz wave distribution for the silicon wafer illuminated by the laser diode corresponding to (a) the maximum amplitude, (b) the amplitude at 300 GHz and (c) the amplitude at 1.5 THz

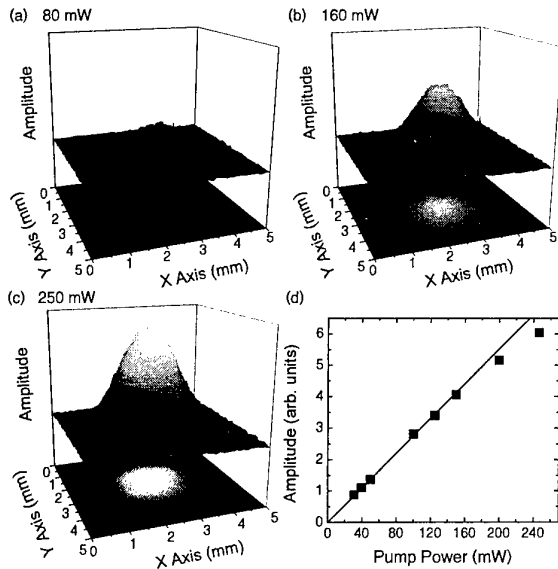


Fig. 6: Maximum-amplitude images of transmitted THz waves for (a) 80, (b) 160 and (c) 250 mW excitation, and (d) the dependence of the amplitude on the exciting laser power

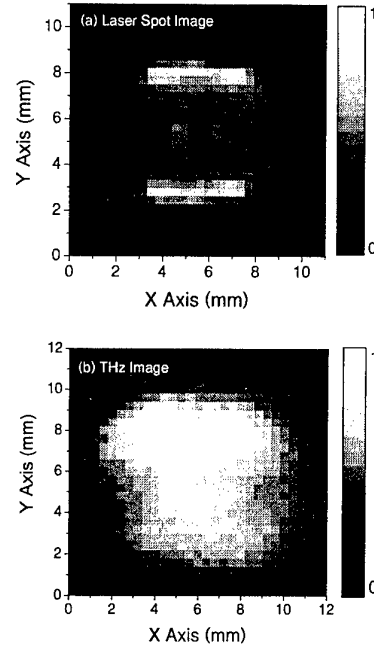


Fig. 7: (a) Distribution of the defocused exciting laser at the sample surface measured by the beam profiler and (b) its THz beam image

photoexcited carrier distribution corresponding to this defocused excitation condition. The intensity distribution of the defocused laser deviates from a Gaussian distribution considerably and this characteristic distribution is reflected in the THz maximum-amplitude image with decreased spatial resolution due to the THz beam spot size.

Since the photoexcited carrier distribution in silicon wafers depends on the chopping frequency of the exciting light due to the diffusion and recombination of the photoexcited carriers [8], the amplitude of the transmitted THz waves also changes with the chopping frequency. Fig. 8 (a) shows the change of the depth profile of the photoexcited carrier distribution in silicon with chopping frequency calculated assuming that the surface recombination velocity at the front surface can be neglected and the recombination time is 100 μ s.

The amplitude and penetration depth of the photoexcited carrier density oscillating with the chopping frequency decrease with increasing frequency. These changes of the distribution may cause the decrease of the THz amplitude with chopping frequency. Fig. 8 (b) shows the chopping frequency dependence of the THz amplitude. The amplitude decreases with increasing chopping frequency monotonically. Although the detailed calculation of the transmission of the THz wave is difficult because of the distribution of the photoexcited carriers, which causes the gradient of the complex refractive index in the sample, the amplitude may be approximately proportional to the total number of the photoexcited carrier oscillating with the chopping frequency. On this assumption, we calculate the frequency dependence of the amplitude and find that the

Fig. 7 shows the THz image of the photoexcited carrier for the case of the defocused excitation of the laser diode. Fig. 7 (a) shows the laser intensity distribution at the sample measured with the beam profiler and Fig. 7 (b) shows the maximum-amplitude THz image of the

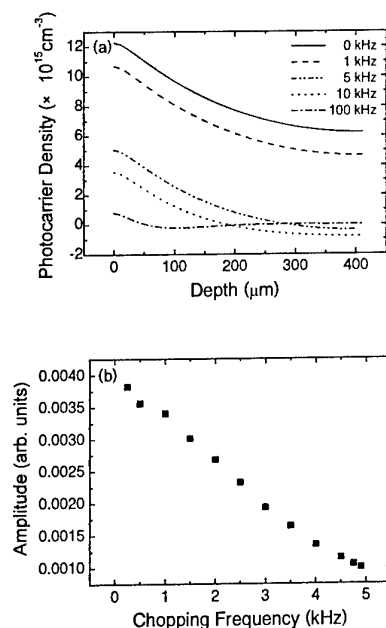


Fig. 8: (a) Calculated chopping frequency dependence of the photoexcited carrier distribution in silicon and (b) the measured chopping frequency dependence of the amplitude of the transmitted THz wave

result in Fig. 8 (b) is explained by assuming the recombination time to be $\sim 100 \mu\text{s}$.

IV. CONCLUSION

The THz wave imaging system using the photoconductive antennas as an emitter and detector is constructed. The beam waist at the sample is about 2.5 mm in our system, but it depends on frequency. The photoexcited carrier distribution in silicon wafers can be measured by using this imaging system with spatial

resolution of $\sim 2.5 \text{ mm}$. The THz imaging system in combination with photoexcitation will become a useful system for characterising semiconductor wafers under processing without electrical contact.

Acknowledgments

This work was partly supported by a Grant-in-aid for Scientific Research from the Ministry of Education, Science, Sports and Culture, Japan. This work was also partly supported by the public participation program for the promotion of creative info-communication technology R&D of Telecommunications Advanced Organization (TAO).

References

1. M. van Exter and D. Grischkowsky, "Carrier Dynamics of Electrons and Holes in Moderately Doped Silicon", *Phys. Rev. B*, Vol. 41, No. 17, pp. 12140-12149, 1990
2. T.-I. Jeon and D. Grischkowsky, "Characterization of Optically Dense, Doped Semiconductors by Reflection THz Time Domain Spectroscopy", *Appl. Phys. Lett.*, Vol. 23, No. 23, pp. 3032-3034, 1998
3. S. Nashima, O. Morikawa, K. Takata and M. Hangyo, "Temperature Dependence of Low Energy Carrier Dynamics of Silicon Studied by Terahertz Time Domain Spectroscopy", in this Proceedings
4. M. Kunst and G. Beck, "The Study of Charge Carrier Kinetics in Semiconductors by Microwave Conductivity Measurements", *J. Appl. Phys.*, Vol. 60, No. 10, pp. 3558-3566, 1986
5. M. Kunst and G. Beck, "The Study of Charge Carrier Kinetics in Semiconductors by Microwave Conductivity Measurements. II", *J. Appl. Phys.*, Vol. 63, No. 4, pp. 1093-1098, 1988
6. T. Nozokido, J. Bae and K. Mizuno, "Visualization of Photoexcited Free Carriers by Scanning Near-Field Millimeter-Wave Microscopy", *Appl. Phys. Lett.*, Vol. 77, No. 1, pp. 148-150, 2000
7. B. B. Hu and M. C. Nuss, "Imaging with Terahertz Waves", *Opt. Lett.*, Vol. 20, No. 16, pp. 1716-1718, 1995
8. S. M. Sze, *Physics of Semiconductor Devices*, 2nd ed., John Wiley & Sons, New York, 1981

THz Imaging of Carrier Concentration and Mobility in Silicon.

Michael Herrmann, Masahiko Tani, Kiyomi Sakai, Ryoichi Fukasawa

Abstract – Silicon samples have been imaged with THz radiation. The samples are n-type substrates, with half of one surface ion implanted with boron resulting in a $0.55\ \mu\text{m}$ thin strongly p-doped layer. Silicon reflects and absorbs the THz beam due to a plasma resonance, subsequently the additional layer results in strong image contrast depending on the implantation dosage. Spectra of these samples have been fit using a refractive index and extinction coefficient calculated from the plasmon resonance: carrier concentration and relaxation time are used as adjustable parameters. By the fitting spectra at every image position, THz images of the carrier concentration and carrier mobility in silicon can be obtained.

I. INTRODUCTION

Silicon is one of the technologically most important materials today. It is also one of the most cleanly produced materials, and consequently the characterisation of silicon is an essential part of the silicon production process securing the quality of a delicate product. With the plasmon frequency of silicon in the THz regime, THz radiation should be suitable for optically determining the electrical properties of silicon. Some recent studies on silicon and other semiconductor spectra in the THz regime can be found in Refs. 1 - 5.

In 1995 it was demonstrated that THz frequency beams can be used in combination with a scanning technique providing local resolution of samples [6 - 8]. THz Imaging (also called "T-ray Imaging") may among other prospective applications serve as a convenient tool for the non-destructive, contactless and locally resolved characterisation of silicon and other semiconductors. The use of THz Imaging for semiconductor characterisation was first proposed by Mittleman *et al.* [8, 9] in 1996. They used a specialised THz Imaging setup with a magnetic field and a double detector system that makes use of the rotation of the polarisation of THz light due to the "terahertz Hall effect".

In this paper, we propose the characterisation of silicon with a standard THz Imaging setup. We investigate n- and p-type silicon, and a "thick" wafer as well as thin ion-implanted layers. The measurements are compared to analytic and computer-supported calculations.

M. Herrmann, M. Tani and K. Sakai are with the Communication Research Laboratory, Kansai Advanced Research Center, 588-2 Iwaoka, Nishi-ku, Kobe 651-2401, Japan

R. Fukasawa is with Tochigi Nikon Corp., 770 Midori, Ohtawara-shi, Tochigi 324-8625, Japan

II. EXPERIMENTAL

The optical setup used for the experiments is shown in Fig. 1. The output of a Ti:Sapphire laser is split into a pump and probe beam. The pump beam hits the THz emitter, a dipole antenna on LT-GaAs. The emitted THz radiation is focused with parabolic mirrors on the sample, which is scanned in two directions vertical to the beam. The transmitted radiation is focused on the THz receiver, another dipole antenna, which is gated by the probe beam. When a THz pulse and a probe pulse arrive at the receiver simultaneously, a signal is generated and recorded with a lock-in amplifier. The probe pulse can be delayed with a delay stage. In this way a time-domain waveform is recorded at every image position.

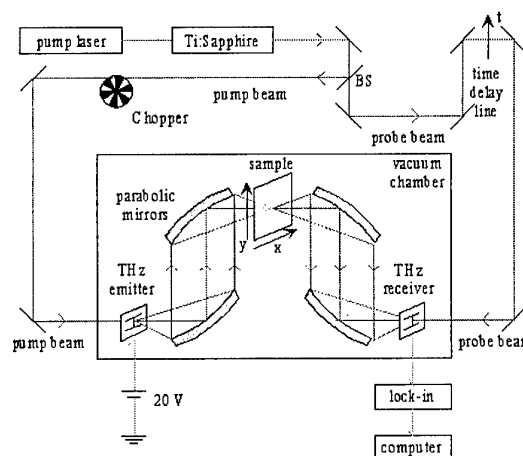


Fig. 1: Optical setup.

The samples are three specimen cut from a $380\ \mu\text{m}$ thick, phosphorus-doped n-type Si wafer with $4.5\ \Omega\text{cm}$ resistivity. Half of one surface of each sample has a $0.55\ \mu\text{m}$ thin p⁺-type layer produced by ion-implanting boron at a dosage of $5 \times 10^{13}\ \text{cm}^{-2}$, $5 \times 10^{14}\ \text{cm}^{-2}$ or $5 \times 10^{15}\ \text{cm}^{-2}$, respectively, and subsequent annealing.

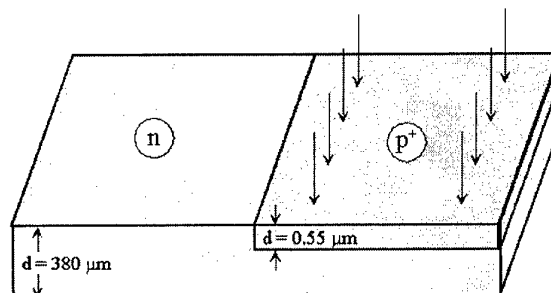


Fig. 2: Schematic of the sample. Half a surface has been ion-implanted with boron resulting in a p⁺-type layer.

III. INTENSITY-BASED IMAGES

In the intensity-based THz images, the non-implanted sides of the samples transmit between 40 to 50 % of the THz signal (i.e. electric field), and the implanted layers provide another drop in signal intensity that depends on the doping concentration. Fig. 3. shows a THz image of the $5 \times 10^{15} \text{ cm}^{-2}$ Si sample. On part of the image the THz beam was allowed to pass the sample. The corresponding (right-hand) part of the image is bright, representing maximum transmittance, or the reference level. The rest of the image shows two regions of different transmittance corresponding to the implanted (top) and the non-implanted (bottom) part of the sample. On all intensity-based images shown here, zero brightness (i.e. black) represents zero transmittance.

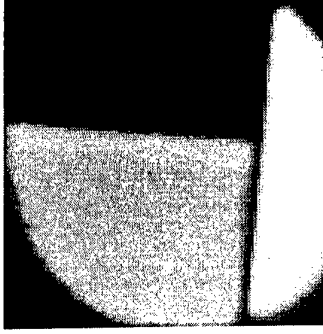


Fig. 3: THz image of the $5 \times 10^{15} \text{ cm}^{-2}$ Si sample. On the right-hand side the THz beam reaches the receiver directly, resulting in a strong signal. The sample (larger, left part of the image) reflects and absorbs the THz beam partly. The upper part of the sample is the implanted side. Image size is 20 mm \times 20 mm. The dark areas in the edges are shadows from the sample holder.

In Fig. 4 THz images of the three samples are compared. Their undoped sides look identical, but the doped sides differ according to doping concentration. The weakly implanted layer causes only a slight reduction in intensity, while the strongly doped layer reduces the THz signal by another factor 5. This is shown quantitatively in Fig. 5 which is based on vertical intersections through a set of images as those in Fig. 4.

IV. THEORY

The interaction between a semiconductor and electromagnetic radiation at THz frequencies is due to plasmon resonance and can be described by

$$\epsilon(\omega) = \epsilon_{\infty} - \frac{\epsilon_{\infty} \omega_p^2}{\omega^2 - i\omega\tau^{-1}} = \tilde{n}^2 = (n + ik)^2 \quad (1)$$

[10] where ω_p is the plasmon frequency with

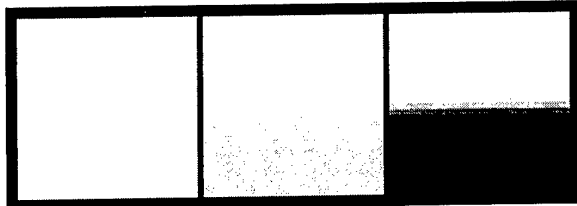


Fig. 4: Intensity-based THz images of three n-type Si samples the lower parts of which have been ion-implanted with boron, resulting in $0.55 \mu\text{m}$ thin p^+ -type layers. Implantation dosages (from left to right): $5 \times 10^{13} \text{ cm}^{-2}$, $5 \times 10^{14} \text{ cm}^{-2}$ and $5 \times 10^{15} \text{ cm}^{-2}$.

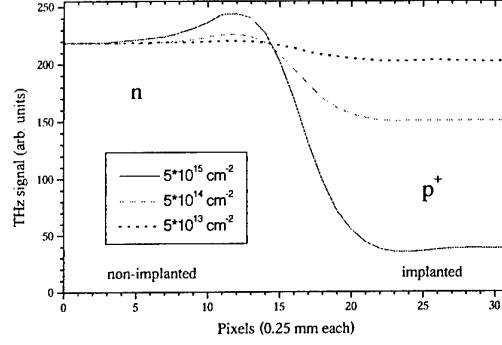


Fig. 5: Intersections through THz images of the three samples. While the 92 % of the THz electric field signal can transmit the weakly doped layer (dotted line), only 18 % pass through the strongly doped layer (solid line).

$$\omega_p^2 = \frac{Ne^2}{m^* \epsilon_0 \epsilon_{\infty}} \quad (2), \quad \tau = \frac{\mu m^*}{e} \quad (3) \text{ the relaxation or}$$

scattering time, ϵ (or ϵ_{∞}) the dielectric function (at infinite frequency, respectively), $\tilde{n} = n + ik$ the complex refractive index, and N , μ , m^* , e and ϵ_0 the carrier concentration, mobility, effective mass, electron charge and vacuum permittivity, respectively.

If the semiconductor properties are known, the complex refractive index can be calculated from Eq. 1, and transmittance through a single semiconductor layer can then be calculated using

$$t(\omega) = \frac{E_{\text{sample}}}{E_{\text{ref}}} = \frac{4\tilde{n}}{(\tilde{n}+1)^2} \times \frac{e^{i(\tilde{n}-1)\frac{\omega}{c}d}}{1 - \frac{(\tilde{n}-1)^2}{(\tilde{n}+1)^2} e^{2i\tilde{n}\frac{\omega}{c}d}} \quad (4)$$

[12] where the middle fraction describes reflection at the surfaces and in the right fraction the numerator represents bulk absorption and phase shift and the denominator takes account of multiple reflection.

For the implanted sides, a two-layer model has to be used as described by Eq. 5.

$$\frac{E_{\text{sample}}}{E_{\text{ref}}} = \frac{8\tilde{n}_1\tilde{n}_2}{(\tilde{n}_1+1)(\tilde{n}_1+\tilde{n}_2)(\tilde{n}_2+1)} \frac{e^{i(\tilde{n}_1-1)\frac{\omega}{c}d_1}}{1+\alpha_1+\alpha_2+\alpha_3} \frac{e^{i(\tilde{n}_2-1)\frac{\omega}{c}d_2}}{1+\alpha_1+\alpha_2+\alpha_3} \quad (5)$$

$$\text{with } \alpha_1 = \frac{(\tilde{n}_1-1)(\tilde{n}_2-\tilde{n}_1)}{(\tilde{n}_1+1)(\tilde{n}_2+\tilde{n}_1)} e^{2i\tilde{n}_1\frac{\omega}{c}d_1},$$

$$\alpha_2 = -\frac{(\tilde{n}_2-\tilde{n}_1)(1-\tilde{n}_2)}{(\tilde{n}_2+\tilde{n}_1)(1+\tilde{n}_2)} e^{2i\tilde{n}_2\frac{\omega}{c}d_2},$$

$$\alpha_3 = -\frac{(\tilde{n}_1-1)(1-\tilde{n}_2)}{(\tilde{n}_1+1)(1+\tilde{n}_2)} e^{2i\frac{\omega}{c}(\tilde{n}_1d_1+\tilde{n}_2d_2)}$$

[12]. However, much of what happens in the layer can also be understood from a thin-layer approximation of Eq. 4. For a given, constant implantation dosage N_{ar} , the carrier concentration $N = N_{ar}/d$ increases with decreasing thickness d , so that \tilde{n}^2 is proportional to $1/d$ in Eqs. 1 and 2. Using this and going towards zero thickness, Eq. 4 works out to

$$t_{thin}(\omega) = \frac{E_{sample}}{E_{ref}} = \frac{1}{1 + \frac{i}{2} \tilde{n}^2 \frac{\omega}{c} d} = \frac{1}{1 + \frac{N_{ar} e^2 \tau}{2cm^* \epsilon_0} (1 - i\omega\tau)} \quad (6)$$

In a strongly doped sample τ can drop to 10 fs and is then $\ll 1/\omega$ at THz frequencies, so that the imaginary part of Eq. 6 can be neglected in determining the absolute value of the transmittance. The phase shift can be calculated from Eq. 6 to be

$$\tan \varphi(\omega) = \frac{\text{Im}(t_{thin}(\omega))}{\text{Re}(t_{thin}(\omega))} = -\omega\tau, \quad (7)$$

in a further approximation valid for $N_{ar} \gg 10^{14} \text{ cm}^{-2}$ and thus at least for the strongly doped sample. Using these approximations the delay time in a thin layer equals minus the relaxation time, $\Delta t = \varphi(\omega)/\omega = -\tau$.

V. FITTING SPECTRA

Fig. 6 shows a three-parameter fit of THz transmittance for the non-implanted side using Eqs. 1 to 4. With $1960 \text{ cm}^2/\text{Vs}$ the resulting mobility is significantly higher than the literature value of $1450 \text{ cm}^2/\text{Vs}$ for intrinsic silicon. They are in fairly good agreement with those of van Exter *et al.* [1, 2] who also measure significantly increased values for μ . From the resulting values for N and μ , the resistivity is calculated to $\rho = 4.4 \text{ } \Omega\text{cm}$ which is in very good agreement with a value of $\rho = 4.5 \text{ } \Omega\text{cm}$ measured on this sample with spreading resistance technique.

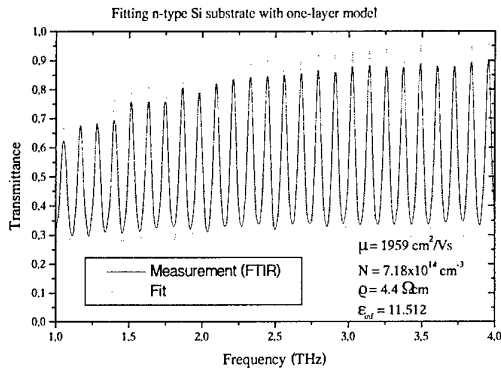


Fig. 6: A THz spectrum measured by Fourier Transform Infrared Spectrometry (FTIR) of the non-implanted side was fit using Eqs. 1 and 2.

In the thin layer approximation, the transmittance depends only on the product $N\mu$, not on N and μ separately (cf. Eqs. 3 and 6 with the imaginary part in Eq. 6 neglected). This is why only one of these two quantities can be fit from a transmittance spectrum. In order to fit the second quantity, phase information must be taken into account.

VI. TIME DELAY

Since the time delay is much smaller than the pulse duration, determining the time delay from specific features of the measured THz waveforms is questionable because even slight changes of pulse shape due to dispersion can change the result significantly. However, relatively good agreement is reached by Fourier

transforming the waveforms and calculating the time delay from the FFT phase shift at various frequencies. Fig. 7 shows a THz image based on time delay at 1.25 THz determined in this way. The delay of the implanted side relative to the non-implanted side amounts to -8.5 ± 2 fs. The calculated value is -6 fs. The calculation used Eq. 4 without the correction for multiple reflection for the non-implanted side and Eq. 5 for the implanted side. Multiple reflection in the substrate was excluded from the formulas, since the recorded time-domain waveforms were short and did not include pulses reflected through the substrate. Multiple reflection within the doped layer however was included.



Fig. 7: Time-delay THz image ($17 \text{ mm} \times 5 \text{ mm}$) of the strongly doped sample. The implanted region at the left appears dark representing earlier arrival time by 8.5 ± 2 fs. The dark vertical line in the middle is probably a diffraction effect.

VII. CONCLUSION

We have used a conventional THz Imaging system for investigating the local distribution of carrier concentration and mobility in silicon samples. n- and p-type silicon have been measured, and a "thick" wafer as well as thin ion-implanted layers. The measurements have been compared to analytic and computer-supported calculations. For a thick sample (i.e. $> \text{several } 10 \text{ } \mu\text{m}$), both carrier concentration and mobility can be determined by fitting transmission spectra. Mobility data is significantly increased against the literature value, but we see excellent agreement with the nominal value of sample resistivity. For a thin layer, either concentration or mobility can be determined in this way, the other quantity being accessible via time-delay information. The time-delay of a $0.55 \text{ } \mu\text{m}$ thin p⁺-type layer on n-type substrate has been determined to -8.5 ± 2 fs in fair agreement with calculations using a two-layer model. The method is non-destructive, does not need electric sample contacts and has a local lateral resolution of about 1 mm.

References

1. M. van Exter and D. Grischkowsky, "Carrier dynamics of electrons and holes in moderately doped silicon", *Phys. Rev. B* **41** (17), 12140 - 12142 (1989).
2. M. van Exter and D. Grischkowsky, "Optical and electronic properties of doped silicon from 0.1 to 2 THz", *Appl. Phys. Lett.* **56** (17), 1694 - 1696 (1990).
3. R. Fukasawa, K. Sakai and S. Perkowitz, "Far-Infrared Reflectance Study of Coupled Longitudinal-Optical Phonon-Hole Plasmon Modes and Transport Properties in Heavily Doped p-Type GaAs", *Jpn. J. Appl. Phys.* **36**, 5543 - 5548 (1997).
4. O. Morikawa, M. Tonouchi and M. Hangyo, "Sub-THz spectroscopic system using a multimode laser diode and photoconductive antenna", *Appl. Phys. Lett.* **75** (22), (1999).

5. O. Morikawa, M. Tonouchi and M. Hangyo, "A cross-correlation spectroscopy in sub-terahertz region using a incoherent light source", submitted to Appl. Phys. Lett. (2000).
6. B.B. Hu and M.C. Nuss, "Imaging with terahertz waves", Opt. Lett. **20**, 1716-1718 (1995).
7. Q. Wu, T.D. Hewitt and X.-C. Zhang, "Two-dimensional electro-optic imaging of THz beams", Appl. Phys. Lett. **69**, 1026-1028 (1996).
8. D.M. Mittleman, R.H. Jacobsen and M.C. Nuss, "T-ray Imaging", IEEE J. Quantum Electron. **2** (3), 679-692 (1996).
9. D.M. Mittleman, J. Cunningham, M.C. Nuss, "Noncontact semiconductor wafer characterisation with the terahertz Hall effect", Appl. Phys. Lett. **71** (1), 16-18 (1997).
10. Cf. textbooks that cover the interaction of light with matter, for instance Ref. 11.
11. D.F. Edwards, "Silicon (Si)", in E.D. Palik (ed.), "Handbook of Optical Constants of Solids", Academic Press, San Diego (1985, 1998).
12. Eqs. 4 and 5 can either be calculated from scratch using simple quantum mechanics for photons crossing a potential wall, or for instance using a formalism from M. Born and E. Wolf, "Principles of Optics", Cambridge University Press (1959, 1980).

Development of a mm-wave imaging system for the W7-AS fusion experiment

Stefan Bäuml, Georg Michel, Manuel Rodriguez-Gironés, Hans L. Hartnagel, Hans-Jürgen Hartfuß

Abstract – The intensity of the electron cyclotron emission (ECE) along a radial sightline of a magnetically confined fusion plasma can be used as a measure for the local temperature of the plasma electrons. The electron temperature is not constant in time but shows fast fluctuations with relative amplitudes of the order of less than 1% with a frequency spectrum extending into the MHz range of frequency. To get deeper insight in the physics of this plasma turbulence two-dimensional information about the fluctuating structures is indispensable. For the two-dimensional spatio-temporal characterization of these temperature fluctuations in the core of the W7-AS plasma an ECE imaging system is being developed.

As a first step an array of four vertically staggered sightlines is being built up with eight radial channels along each sightline. A mm-wave detector array acting as the front end of a multichannel heterodyne radiometer system consists of four channels of which each is made up of an antenna, a mixer, filters and the on-chip local oscillator power distribution for the individual mixers. This high frequency part is being developed in collaboration with TU Darmstadt. An alternative approach has already been installed using four conventional, separated mm-wave mixers allowing for first experiments.

I. INTRODUCTION

Electron cyclotron emission from a magnetically confined plasma is a direct consequence of the gyration motion of the electrons around the lines of the magnetic field. It occurs at the gyration frequency $\omega = n \cdot \frac{eB}{\gamma \cdot m_e}$

and its harmonics ($n=1,2,3,\dots$). ω is called the electron cyclotron frequency; e and m_e are the electron charge and mass, respectively, B is the magnetic induction and γ the relativistic factor with $\gamma = \frac{1}{\sqrt{1-\beta^2}}$. Radiometry of

electron cyclotron emission is used on many fusion devices as a standard diagnostic for radial profiles of the electron temperature by the spectral measurement of $I(\omega)$, the absolute mm-wave intensity¹. In a toroidal plasma configuration like a stellarator or a tokamak $B(R)$ along a radial sightline is monotonically varying, so that the spectral information of the ECE measurement transfers into spatial information.

If the fusion plasma is optically thick for all frequencies resonant inside the plasma torus, i.e. all radiation is absorbed by the electron resonance in a single pass of the

wave through the plasma, the plasma absorbs and by Kirchhoff's law also emits radiation I_{BB} as a blackbody radiator. In this case the radiation intensity depends only on the electron temperature. The blackbody intensity I_{BB} radiated power per unit area and unit solid angle is given

by Planck's law, $I_{BB}d\omega = \frac{\hbar\omega^3}{8\pi^3c^3} \frac{1}{e^{\hbar\omega/kT}-1} d\omega$, where

$d\omega$ denotes the observed frequency interval. For present day fusion plasmas $\hbar\nu < 1\text{meV}$, $kT > 10\text{eV}$, so that $\hbar\nu \ll kT$ and the Rayleigh-Jeans approximation holds:

$I_{BB}d\omega = \frac{\omega^2}{4\pi^2c^3} kT$. Here k denotes the Boltzmann

constant and c the speed of light in vacuum. So, if the electron velocity distribution perpendicular to the magnetic field has a Maxwellian distribution one can identify the apparent radiation temperature T with the temperature of the gyrating electrons $T=T_e$. Therefore spectrally resolved ECE measurements along one single radial sightline yield a radial profile of T_e .

It is the goal of ECE imaging systems to map several of these radial sightlines onto a two-dimensional ($m \times n$) array of detector elements in order to get a three-dimensional image of the plasma properties measured by the ECE diagnostic. By using filterbanks in the radiometric system of the ECE diagnostic T_e can be measured simultaneously in each of the planes at different radial positions, that correspond to different center frequencies of the filters in one filterbank and results in the third dimension of the image. The situation is illustrated in Fig. 1 for a $m \times n$ element array with eight filters in each filterbank.

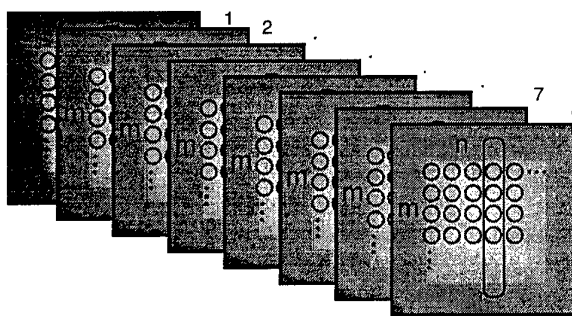


Fig. 1: Sketch of the mapping of $m \times n$ radial sightlines coming from an array of $m \times n$ detectors. The blue box marks a four element array as planned for W7-AS.

II. ELECTRON TEMPERATURE FLUCTUATIONS MEASURED BY ECE

In order to use an ECE-diagnostic as described above for measurements of the T_e fluctuations, some important preconditions concerning temporal and spatial resolution

S. Bäuml, G. Michel and H.-J. Hartfuß are with the Max-Planck-Institut für Plasmaphysik, EURATOM Ass., Wendelsteinstr. 1, 17491 Greifswald

M. Rodriguez-Gironés and H. L. Hartnagel are with the Institut für Hochfrequenztechnik, Merckstr. 25, 64283 Darmstadt

have to be fulfilled. The temporal resolution of a radiometric system is determined by the post-detection filter bandwidth B_V and can be made easily as high as a few MHz. The radial resolution is determined by the predetection bandwidth B_{IF} , which is about 300 MHz. The optical depth together with the relativistic broadening define a kind of natural lower limit for the radial resolution, which is about 0.5-1cm for typical fusion plasmas. The poloidal resolution is diffraction limited and determined by the type of optical arrangement used. Minimum reported values are 1-2 cm. Unwanted finite sample volume effects lead to increased phase velocities derived and restrict the wave number range of the fluctuation diagnostic.

The inherent intensity fluctuations of a thermal radiation source is denoted by $i(t)$ and is called wave or thermal noise. The ratio $i(t)/I_{BB}(t)$ in radiometry at high radiation temperatures is governed exclusively by these inherent intensity fluctuations superimposed to the mean intensity $I_{BB}(t)$ of the blackbody radiation of the plasma. It is determined by the radiometers bandwidth ratio of post- and pre-detection bandwidths:

$$\frac{\sqrt{\langle i(t)^2 \rangle}}{\langle I_{BB}(t) \rangle} = \sqrt{\frac{2B_V}{B_{IF}}},$$

which is about 5% for a typical ECE radiometer. This is the minimum level possible for a single mode heterodyne radiometer. This phenomenon sets a severe limit to fluctuation measurements burrying completely "true" temperature fluctuations below a relative level of 5%. This problem can be overcome by applying correlation techniques and making use of the coherence properties of the thermal radiation. In the past the existence of these T_e fluctuations was proven² and further investigations concerning their correlation with density fluctuations were made³.

III. SYSTEM SPECIFICATIONS

In a first step it is planned to build an antenna array consisting of four separated conventional antennas and harmonic mixers. In a second step a MMIC (monolithic microwave integrated circuit) mixer array with integrated antennas is being developed. The intermediate frequency (IF) parts of both systems are made up by filter banks which can be used for both of the systems.

To be able to do measurements at different radial positions along a single sightline simultaneously, a wideband single sideband detection scheme with fixed LO signal is chosen. The local oscillator (LO) frequency is 133 GHz for harmonic mixing and 67,5 GHz for subharmonic mixing using the MMIC array. The bandwidth of the working frequencies (RF) of both systems is about 10 GHz and centered around 146 GHz (2nd harmonic ECE), corresponding to the high field side of the electron temperature profile for 2,5 T.

The IF part consists of eight radial channels for each of the poloidally staggered antennas, which results in 32 radial channels for the ECE imaging systems. The intermediate frequency is chosen below 18 GHz to avoid additional complication with the detector array under development.

The first IF stage uses an amplifier with low noise figure (1.3 dB). After further IF amplification and signal splitting, the total signal bandwidth is reduced to 300 MHz by the eight bandpass filters which comprise the filterbank. Each center frequency of a filter marks a different radial position along the sightline of the corresponding poloidal antenna in the plasma. The bandwidth together with the center frequency of each filter determine the radial section along the chord. Finally the signals are detected with Schottky diode detectors and the output voltage of each video-channel is applied to the data acquisition.

IV. ECEI USING CONVENTIONAL IMAGING TECHNIQUES

A system of four identical radiometers comprises the ECEI approach using conventional focal plane imaging techniques. For the measurement of the 2nd harmonic ECE at about 146 GHz a Gaussian beam is formed by an elliptical mirror and a corrugated circular feed horn. The mirrors and the horns are placed inside the vacuum vessel. Fig. 2 shows the setup of the system inside the stellarator W7-AS.

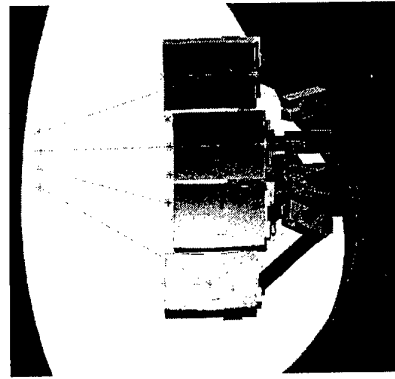


Fig. 2: CAD sketch of the four mirror-array showing the four elliptical mirrors together with the corrugated millimeter-wave horns inside the plasma vessel.

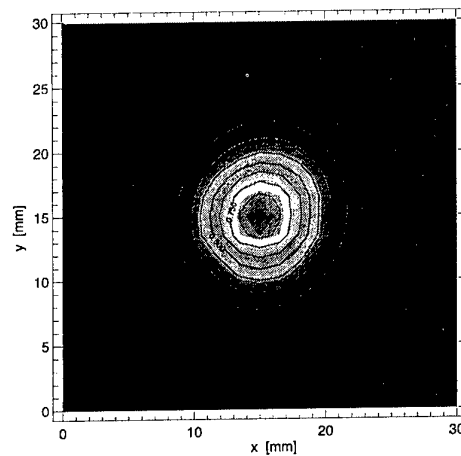


Fig. 3: Measurement of an antenna pattern. Plotted is the antenna pattern near the focal plane of the elliptical mirror of one of the four identical optical arrangements.

The beam waist, located near the center of plasma is about 5 mm. Fig.3 shows a normalized contour plot of the measurement of an intensity pattern at the beam waist of the optical system. The system shows no detectable sidelobes. The signal coming from the plasma is transmitted by the mirror, the horn and a fundamental waveguide outside the vessel towards the single sideband receiver system. After bandpass filtering and downconversion of the signal to frequencies below 18 GHz it gets processed at the following IF-part of the system described before.

In Fig. 4 the center-frequencies of each of the four sightlines inside the plasma together with the shape of the Gaussian beams, indicated by the errorbars, are shown.

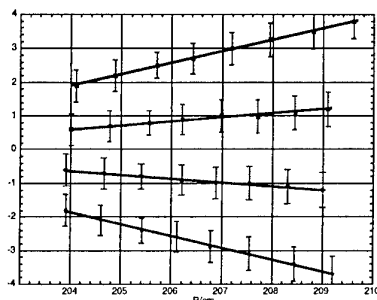


Fig. 4: Diagram of the calculated filter locations. Each of the datapoints along a sightline represents the place of the center frequency in real space (R,z). The vertical error bars indicate the beamwidths in z-direction.

The positions of the filters are chosen in a way, that the filters arranged one upon another are placed on the same magnetic flux surface. All filter positions are inside the so called Rayleigh lengths of the Gaussian beam, which is necessary for focal plane imaging systems.

Electron temperature fluctuations, their motion as well as their size inside the 50mm x 80mm detection volume will be revealed by using correlation techniques for neighbouring channels⁴. The system will also allow for investigations of coherent large scale fluctuations, so called MHD phenomena.

V. ECE IMAGING USING A MMIC ARRAY

The preceding section, especially Fig. 2, make clear, that for measurements of T_e fluctuations along a greater number of sightlines, which for example cover the whole plasma cross section, the spatial requirements of the optical arrangement at a fusion device are difficult to be fulfilled. Thanks to the miniaturization of the antenna and the mixer structures during the last decades it is possible to build small arrays made up of a number of these elements and allowing to map several sightlines on these arrays so that this problem can be overcome.

The development of two-dimensional detector arrays represents one of the main concerns of plasma diagnostics for 2D ECE imaging and also for applications in reflectometry and interferometry at fusion devices like TEXT-U⁵, GAMMA10^{6,7}, RTP⁸ and TEXTOR⁹.

Here a short description of the system under development for the stellarator W7-AS¹⁰ is given. The design of the fully MMIC 150 GHz subharmonic mixer array to be used for ECE imaging at W7-AS is discussed in detail on poster P.1 at this conference.

In a first step the system is planned to be made up of a four element array. Fig. 5 shows the layout of the four element receiver array. The four parallel subharmonic Schottky-diode mixers are realised on a microstrip line on a 70- μ m thick GaAs substrate. Rectangular patch antennas serve as RF receiving elements.

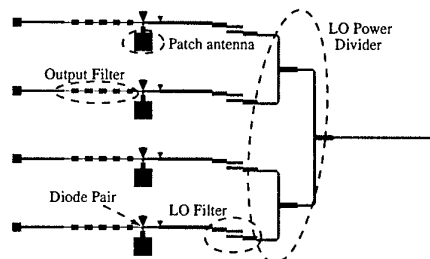


Fig. 5: Principal setup of two antennas mounted on a mixerblock. The RF signal from the plasma reaches the patch antennas. The LO signal is distributed on board. On the left hand side the IF stage follows.

As opposed to the receiver arrays on fusion devices mentioned above, which make use of quasi-optical techniques for the LO distribution^{5,6,7,8,9}, the circuit manufactured at the Technical University of Darmstadt distributes the local oscillator power directly on the chip.

The LO power gets fed to a 50 Ω microstrip line, thereby reducing significantly pumping power level requirements. The microstrip line acts as an LO filter and presents to the diodes a short circuit at IF and RF. Another structure on the other side acts as output filter. The RF antenna is also coupled to this structure. Cross-talk between channels is reduced by physical substrate separation to prevent propagation of substrate modes. To increase channel isolation further, the patch antennas can also be isolated. The circuit is designed to have 9 GHz RF- and IF-bandwidths. The diode pair has an anti-parallel structure, a configuration with well-known advantages^{11,12}. By reducing the pumping frequency to about 70 GHz, filtering is simplified, since the need to match an LO signal lying between RF and image bands is eliminated. This integrated circuit will be placed on the so called mixer. A backshort in the LO waveguide allows to carry out an optimisation of LO power distribution to the microstrip lines.

Simulations of the MMIC by using the method of moments predict excellent electrical attributes. The calculated conversion loss versus the output frequency for different values of pumping power available per channel indicates, that e.g. for a LO power of 8 dBm the conversion loss varies between 6 dB and 10 dB. Typical values of isolation between ports were also estimated. The LO-IF isolation is 31 dB. The LO power flowing towards the RF antenna is 41 dB below the injected LO level. The RF-IF isolation is 50 dB. Undesired down converted image signal at the IF port is between 10 and 30 dB below the desired IF frequency. This is due to the antenna acting as an image filter and to additional intended mismatching.

The optics for the MMIC ECEI system will be made up of a substrate lens and an additional elliptical mirror. Since only a circular vacuum port is available for the ECE imaging diagnostic at W7-AS, which is about 115

cm away from the plasma center, with only 10 cm in diameter, beam truncation would be the main problem for this diagnostic at W7-AS. The combination of these two concerns would make a refocussing of the beam necessary, but is prohibited by the limited space at this part of the vacuum vessel. It is planned to place the array in an immersion flange (see Fig. 6).

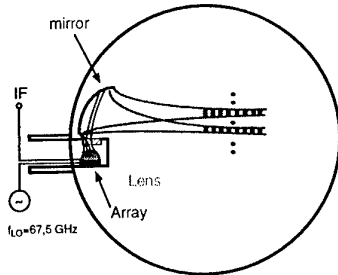


Fig. 6: Sketch of the planned W7-AS ECEI setup using a MMIC array placed in an immersion flange.

By a single focussing elliptical mirror inside the vessel, the radiation of the plasma will be focused onto the array, which is placed at atmospheric pressure together with another focussing lens. To ensure that the proper polarization is chosen, a polarizing grid is introduced into the sightline. LO power will be transmitted to the array by an oversized waveguide. The IF signal at the output of the array gets submitted to the IF section of the radiometer by coaxial cables.

Physical optics calculations were already performed in order to determine the expected E-field distribution coming from the rectangular patch antennas. Fig. 7 shows a contour plot of the amplitude of the electric field in front of the lens, which ends at $z=0$. Two of the sightlines are plotted.

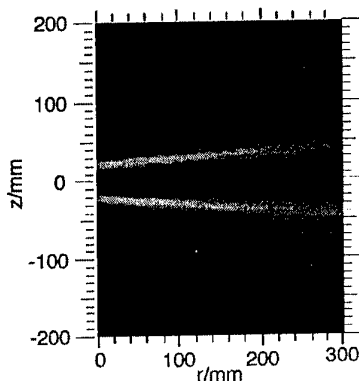


Fig. 7: Calculated sightlines of a two element array. Plotted is the E-field propagation along the radial sightline for two patch antennas in front of the lens, which is attached to the antennas.

The amplitude of the electric field in a plane perpendicular to the direction of propagation (z -direction) 10 cm away from the lens is plotted in Fig. 8. A separation of the two channels can clearly be identified. Simulations without using a substrate lens showed that the two sightlines cannot be separated any more.

But nevertheless, these encouraging simulations have to be verified by measurements. Especially the existence of sidelobes has to be tested in order to be able to use the

system for electron temperature fluctuation measurements.

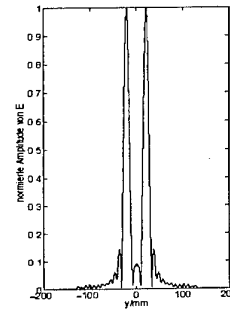


Fig. 8: Plot of the expected E-field distribution in z -direction 10 cm apart from the substrate lens of Fig. 7.

Acknowledgements

The authors would like to thank J.P. Pascual, M.L. de la Fuente and F. Lopez for their support at the MMIC array development. Acknowledgements also go to M. Bergbauer, M. Steffen and S. Radau for their assistance during the construction phase of the mixer block and their technical support for the setup of the conventional ECEI system.

References

1. H.J. Hartfuß, T. Geist, M. Hirsch, Plasma Phys. Control. Fusion, 39, 1693-1769 (1997)
2. S. Sattler, H.J. Hartfuß, W7-AS Team, Phys. Rev. Lett., 72, 653-656 (1994)
3. M. Häse, M. Hirsch, H.J. Hartfuß, Rev. Sci. Instrum., 70(1), 1014-1017 (1999)
4. B.H. Deng, D.L. Brower, G. Cima, C.W. Domier, N.C. Luhmann, Jr., C. Watts, Phys. Plasmas, 5, (12), 4117-4120 (1998)
5. R.P. Hsia, B.H. Deng, W.R. Geck, C. Liang, C.W. Domier, N.C. Luhmann, Jr., D. L. Brower, G. Cima, Rev. Sci. Instrum. 68(1), 488-491 (1997)
6. N. Oyama, A. Mase, H. Negishi, T. Tokuzawa, A. Itakura, T. Tamano, K. Yatsu, K. Watabe, K. Mizuno, Y. Nagayama, K. Kawahata, H. Matsuura, K. Uchida, A. Miura, Rev. Sci. Instrum. 70(1), 1003-1006 (1999)
7. N. Oyama, A. Mase, T. Tokuzawa, K. Imamura, A. Itakura, Y. Ito, T. Tamano, Y. Harada, K. Mizuno, Fus. Engineer. Design 34-35, 407-410 (1997)
8. B.H. Deng, R.P. Hsia, C.W. Domier, S.R. Burns, T.R. Hillyer, N.C. Luhmann, Jr., T. Oyevaar, A.J.H. Donne, and the RTP team, Rev. Sci. Instrum. 70(1), 998-1001 (1999)
9. C.W. Domier, B.H. Deng, A.J.H. Donne, P.L. Hsu, N.C. Luhmann, Jr., E. Mazzucato, H.K. Park, M.J. van de Pol, J. Wang, AP 20 at the 13th Topical Conference on High Temperature Plasma Diagnostics in Tucson, Arizona, 18-22 June 2000
10. S. Bäuml, M. Rodriguez, H.J. Hartfuß, ECE Imaging development at W7-AS, Proceedings of the 26th EPS Conference on Controlled Fusion and Plasma Physics, Maastricht, paper P4.055, 1999
11. M. Cohn, J.E. Degenford, B.A. Newman, IEEE trans. on MTT, 23, 667-673 (1975)
12. C.-I. Lin, et al, "Anti-Parallel Planar Schottky Diodes for subharmonically pumped 220 GHz mixer", 10th Int. Symp. On Space Terahertz Technology, Charlottesville, Virginia, 16-18 March 1999

Fourier Transform THz-Wave Spectrometer Using THz-Wave Parametric Generator

Jun-ichi Shikata, Kodo Kawase, Tetsuo Taniuchi, and Hiromasa Ito

Abstract—We have developed a THz-wave spectrometer with the combination of a bright THz-wave source of THz-wave parametric generator (TPG) and a Martin-Puplett interferometer. The TPG output was optimized by studying various configurations with LiNbO₃ crystals. THz-waves which span the 1-2THz region were emitted with the peak power of 280μW. The whole system, including the nitrogen-purge unit, was constructed in a table-top size. By use of the THz-wave spectrometer, absorption lines of water vapor were successfully obtained.

Index Terms—terahertz-wave, parametric generator, nanosecond, arrayed Si-prism coupler, Fourier transform spectrometer, spectroscopy

I. INTRODUCTION

There are increasing interests in experimental science and technology in the terahertz (THz)-wave region, where both generation and detection have been traditionally difficult. Recently, THz time-domain spectroscopy (THz-TDS) [1, 2] with a femtosecond laser attracted much attention, as the signal to noise ratio is much improved over that of conventional far-infrared Fourier transform spectrometers that use low-brightness incoherent sources and bolometric detectors. However, the conventional Fourier transform spectrometry, which directly measures the correlation of a THz-wave, has a vital importance as a standard method. In addition, considering the reflectivity measurements at the normal incident angle, it provides a simple and suitable experimental configuration [3]. Therefore, to improve S/N and to measure various samples with a large absorption, such as materials in biological tissues, the development of a compact and bright THz-wave source is essential.

In this paper, we describe the novel Fourier transform spectrometer, by combining a broad-band and bright source of THz-wave parametric generation (TPG) with a Martin-Puplett interferometer. The TPG is the single-pass version of the compact THz-wave parametric oscillator which we have studied [4-9]. Since THz-waves of a few-nanosecond pulsewidth are emitted, a long path difference of more than a few tens of centimeters and a high intensity are achieved.

The first half of this paper is devoted to the optimization of the TPG output by studying various experimental configurations. Next, spectroscopic data measured with the spectrometer are demonstrated.

II. PRINCIPLE OF THZ-WAVE PARAMETRIC GENERATION

The efficient generation of THz-waves is based on the parametric scattering of laser light from the lowest A₁-symmetry polariton mode in LiNbO₃ (stimulated polariton scattering). The scattering process involves both second- and third-order nonlinear processes, thus a strong interaction occurs among the pump, idler and polariton (THz) waves. As shown in Fig. 1, polaritons exhibit photon-like behavior in the non-resonant frequency region, where a signal photon at THz frequency (ω_p) and a near-infrared idler photon (ω_i) are created parametrically from a near-infrared pump photon (ω_p), according to the energy conservation law $\omega_p = \omega_i + \omega_t$ (p : pump, T : THz, i : idler). In the stimulated scattering process, the momentum conservation law $k_p = k_i + k_T$ (noncollinear phase-matching condition; see the insets of Fig.1) also holds. This leads to the angle-dispersive characteristics of the idler and THz-waves generated.

In spite of the efficient parametric interaction, most of the THz-wave generated is absorbed or totally reflected inside the LiNbO₃ crystal. This is due to the heavy absorption loss (more than several tens cm⁻¹) and the large refractive index (>5) in the THz range. To overcome the problem, we have proposed the Si-prism-output-coupler method [5], as shown in Fig. 2. Since the absorption

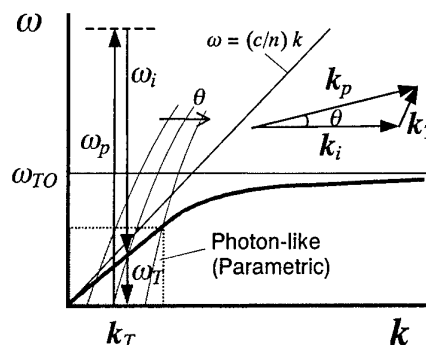


Fig. 1. Dispersion relation of the polariton, an elementary excitation generated by the combination of a photon and a transverse optical phonon (ω_{TO}). The inset shows the noncollinear phase-matching condition.

J. Shikata, T. Taniuchi, and H. Ito are affiliated with the Research Institute of Electrical Communication, Tohoku University, Sendai 980-8577, Japan.

K. Kawase is with Photo Dynamics Research Center, RIKEN, 519-1399 Aramaki Aoba, Aoba-ku, Sendai 980-0845, Japan.

H. Ito is also with Photo Dynamics Research Center, RIKEN.

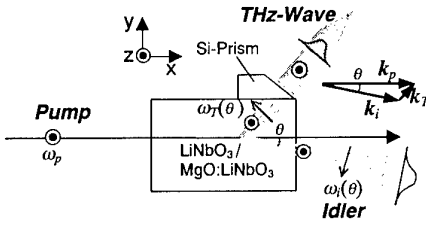


Fig. 2. Schematic diagram of single-pass THz-wave parametric generation (TPG) using a Si-prism-output coupler.

coefficient of Si is small ($\sim 0.6\text{cm}^{-1}$) and the refractive index is almost fixed to be 3.4 in the THz region, a THz-wave beam with a low divergence (less than a few degrees) is efficiently coupled out via Si-prism according to Snell's law.

III. OPTIMIZATION OF TPG OUTPUT

In order to obtain a stable high power THz-wave output, the single-pass TPG was studied with various configurations of LiNbO₃ crystals. The experimental setup is shown in Fig. 3. The pump source was a Q-switched Nd:YAG laser (New Wave MiniLase II, wavelength: $1.064\mu\text{m}$, pulse width: 7ns, typical output: 16mJ/pulse, spot size: 1mm), polarized along the z-axis of the crystal. 65mm-long undoped LiNbO₃ (LN) and 5mol% MgO:LiNbO₃ (MgO:LN) crystals [8] were used to generate THz-waves, and the end-surfaces of the crystals were anti-reflection coated for operation at around $1.07\mu\text{m}$. The pump path was set very close to the Y-surface of the crystal to reduce the absorption loss of THz-waves. An array of THz-wave output couplers [9] consisting of six Si-prisms fabricated from a high resistivity Si crystal ($\rho > 1\text{k}\Omega$, $\alpha \approx 0.6\text{cm}^{-1}$, total base length: 51mm) was introduced to obtain a high THz output. The angle of each prism was chosen as 39 degrees such that THz-waves were emitted almost normal to the prism surface. To obtain a high gain and a low threshold within the limitation of each crystal length (65mm), the crystals were arrayed in series along the x-axis with the prism coupler at the exit of the pump path (Fig. 3). The emitted THz-wave and near-infrared idler (Stokes) wave were measured with a 4 K Si-bolometer and a pyroelectric detector, respectively.

Optimization began with an examination of the gap between two LN crystals, as this will cause the decrease in the TPG output, due to the decrease in the interaction volume between the pump and the idler under the noncollinear phase-matching condition. As shown in Fig. 4, there was a monotonic decrease in the TPG output, but the power remains almost unchanged with the gap to around 5mm. In the experiment shown below, the gap of around 0.5mm was chosen.

Next, the input-output characteristics of the TPG-idler wave were studied. With the increase of the total crystal length, a monotonic increase in the idler output and a the monotonic decrease in the generation threshold were achieved, as shown in Fig. 5. It was also noted that MgO:LN [8] exhibited a better performance than undoped crystal. However, the THz-wave output did not correspond with the results of the idler, as shown in Fig. 6. Although the generation threshold decreased with the crystal length, the THz-wave power was saturated at the pump level of less than 16mJ when more than two crystals were used. The maximum THz-wave power and the highest stability was

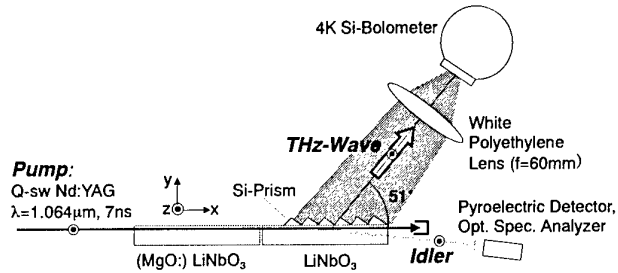


Fig. 3. Experimental setup for measuring TPG output

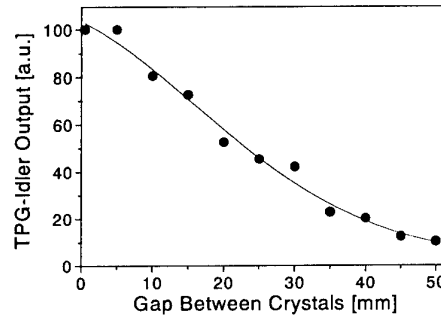


Fig. 4. Power dependence on the gap between two LiNbO₃ crystals.

Crystal(s)	Single Prism	Arrayed Prism	Enhancement Factor
LN (L=65mm)	0.8 μW	15.2 μW	$\times 19$
LN $\times 2$ (L=130mm)	1.4	272.8	$\times 195$
LN + MgO:LN (L=130mm)	1.4	279.2	$\times 199$
LN $\times 3$ (L=195mm)	1.9	224.0	$\times 118$
LN + MgO:LN $\times 2$ (L=195mm)	2.2	104.0	$\times 47$

Table 1. TPG-THz-wave output for various configuration (L: total crystal length, pump energy: 15.9 mJ).

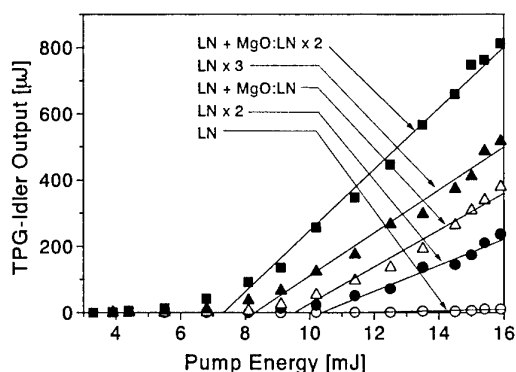


Fig. 5. Input-output characteristics of TPG-idler using LN and MgO:LN crystals.

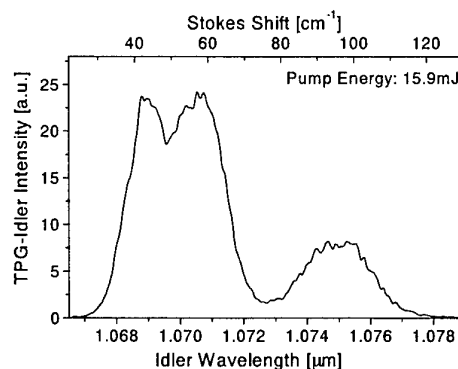


Fig. 7. Spectrum of TPG-idler generated with two LiNbO₃ crystals.

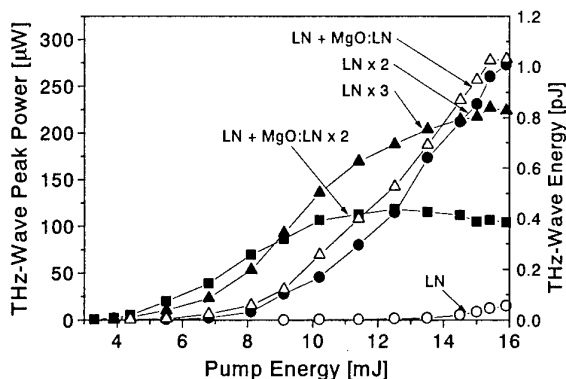


Fig. 6. Input-output characteristics of TPG-THz-wave using LN and MgO:LN crystals

achieved by use of two crystals at a pump energy of 15.9 mJ (conversion efficiency $\sim 5 \times 10^{-11}$). A comparison of the TPG THz-wave output with a single Si-prism output coupler (base length: 15mm) was also examined (Table 1). Power enhancement of more than two orders was obtained by introducing the arrayed Si-prism coupler.

To study further the saturation mechanism and the bandwidth of the THz-wave generated inside LN, the idler spectrum of two LN crystals was measured with an optical spectrum analyzer. The spectrum (frequency shift) extended from 30 to 120 cm^{-1} (0.9-3.6 THz), as shown in Fig. 7. The dip at 1.0696 μm corresponds to the frequency shift of 47 cm^{-1} , and therefore the spectral component around 1.075 μm (frequency shift: 94 cm^{-1}) represented the second Stokes component. Alternatively, low frequency resonances in LiNbO₃ were reported at 1.3THz ($\sim 43 \text{ cm}^{-1}$) and 2.4THz ($\sim 80 \text{ cm}^{-1}$) from the impulsive-response measurement [10]. However, these levels were slightly different from the dip position in our data (47, 75 cm^{-1}), and the linewidths were narrower. In particular, the Stokes component should not decrease with the resonance levels. Thus, this process was not dominant in our experiment.

IV. APPLICATION TO SPECTROSCOPY

Using the optimized TPG source with two LiNbO₃ crystals and an arrayed Si-prism coupler, a Martin-Puplett THz-wave spectrometer was developed in a table top size (Fig. 8). With the advantage of linear polarization characteristics of TPG, the interferometer simply requires two wire grid polarizers. In order to collimate the THz-wave beam, an aperture and an off-axis parabolic mirror were used. The linear stage has a maximum stroke of 20cm, and therefore a resolution of 0.025 cm^{-1} ($\sim 750 \text{ MHz}$) is possible. LabVIEW software was used to control the system.

Fig. 9 shows an example of interferograms measured with the purge of nitrogen, and the power spectrum obtained from the Fourier transform is shown in Fig. 10. In this experiment, the maximum path difference was 50mm, which corresponds to a resolution of 0.1 cm^{-1} . The dip positions in the spectrum were in good agreement with the absorption lines of water vapor [11]. The TPG-THz-wave output corresponded to the first-order Stokes component. To obtain the high frequency component of THz-wave ($\sim 100 \text{ cm}^{-1}$), further techniques to reduce the absorption loss in LiNbO₃ are required, which will be achieved by

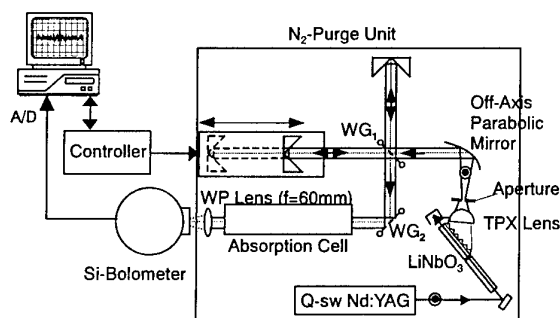


Fig. 8. Schematic diagram of a Fourier transform THz-wave spectrometer, combining a TPG-THz waves generator and a Martin-Puplett interferometer.

References

- [1] D. M. Mittleman, R. H. Jacobsen, and M. C. Nuss, "T-ray imaging," *IEEE J. Selected Topics in Quantum Electron.*, vol. 2, pp. 679-691, 1996, and references there in.
- [2] P. Y. Han, X.-C. Zhang, "Coherent, broadband midinfrared terahertz beam sensors," *Appl. Phys. Lett.*, vol. 73, pp. 3049-3051, 1998.
- [3] D. H. Martin, "Polarizing (Martin-Puplett) Interferometric Spectrometers for the Near- and Submillimeter Spectra," in *Infrared and Millimeter Waves*, vol. 6., Chapter 2, 1982.
- [4] K. Kawase, M. Sato, T. Taniuchi, and H. Ito, "Coherent tunable THz-wave generation from LiNbO₃ with monolithic grating coupler," *Appl. Phys. Lett.* vol. 68, pp. 2483-2485, 1996.
- [5] K. Kawase, M. Sato, K. Nakamura, T. Taniuchi, and H. Ito, "Unidirectional radiation of widely tunable THz-wave using a prism coupler under noncollinear phase matching condition," *Appl. Phys. Lett.*, vol. 71, pp. 753-755, 1997.
- [6] J. Shikata, M. Sato, T. Taniuchi, H. Ito, and K. Kawase, "Enhancement of terahertz-wave output from LiNbO₃ optical parametric oscillators by cryogenic cooling," *Opt. Lett.*, vol. 24, pp. 202-204, 1999.
- [7] A. Morikawa, K. Kawase, J. Shikata, T. Taniuchi, and H. Ito, "Optical parametric THz-wave generation using trapezoidal LiNbO₃," *Proc. SPIE*, vol. 3828, pp. 302-310, 1999.
- [8] J. Shikata, K. Kawase, K. Karino, T. Taniuchi, and H. Ito, "Tunable terahertz-wave parametric oscillators using LiNbO₃ and MgO:LiNbO₃," *IEEE Trans. MTT*, vol. 48, pp. 653-661, 2000.
- [9] K. Kawase, J. Shikata, H. Minamide, K. Imai, and H. Ito, "Arrayed silicon prism coupler for a THz-wave parametric oscillator," submitted to *Applied Optics*.
- [10] H. J. Bakker, S. Hunsche, and H. Kurz, "Investigation of anharmonic lattice vibrations with coherent phonon polaritons," *Phys. Rev. B*, vol. 50, pp. 914-920, 1994.
- [11] H. M. Pickett, R. L. Poynter, E. A. Cohen, M. L. Delitsky, J. C. Pearson, H. S. P. Muller, "Submillimeter, Millimeter, and Microwave Spectral Line Catalog," *JPL Publication 80-23*, Rev. 4, NASA, 1996; also, <http://spec.jpl.nasa.gov>.

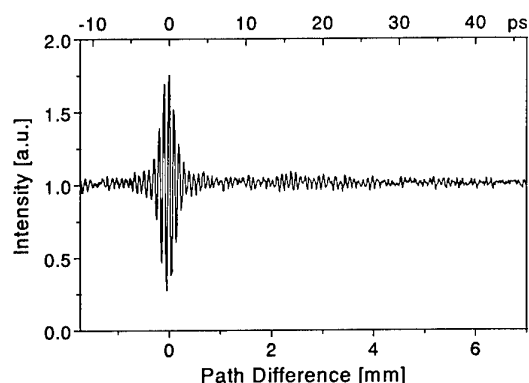


Fig. 9. Measured interferogram of TPG THz-wave in the nitrogen-purge unit.

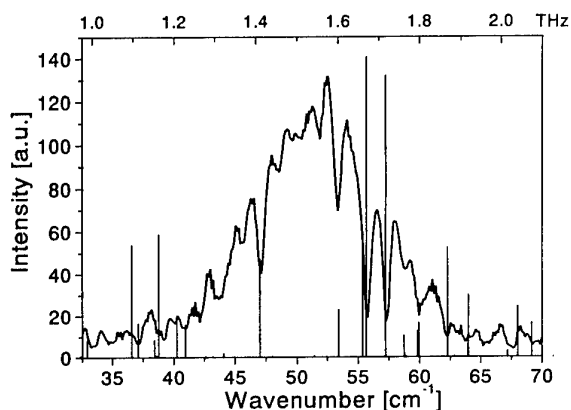


Fig. 10. TPG THz-wave spectrum obtained from the data shown in fig. 9, and the resolution is 0.1cm^{-1} . The absorption lines of water vapor are also indicated.

minimizing the propagation distance of the THz-wave using the total reflection of both the pump and the idler beam [7], or by cooling the crystal [6].

V. SUMMARY

We have described the characteristics of broad-band TPG-THz-wave generation, and its application in a Fourier transform spectrometer. This compact interferometer with bright source will be a powerful tool for spectroscopic studies of various materials in the THz region, such as solid state materials with strong absorption, biological tissues, and so on.

Acknowledgments

The authors are greatly indebted to C. Takyu and T. Shoji for their excellent work in coating and polishing. This work has been partly supported by the Grant-in Aid from the Ministry of Education, Science and Culture of Japan. Also, J. S. is supported by the Murata Science Foundation in Japan.

A 150 GHz Fully-Integrated MMIC Schottky-Mixer Array

M. Rodríguez-Gironés, J.P. Pascual, S. Bäuml, C.I. Lin, H.L. Hartnagel

Abstract¹ - The development of detector arrays for two dimensional imaging of electron cyclotron emission [1] is essential for the investigation of heat transport and turbulent confinement in fusion plasmas. A new approach to imaging techniques is presented in which the quasi-optical coupling of pumping power is substituted by a direct on-chip distribution scheme using a fully MMIC multi-channel mixer circuit. The system makes use of a subharmonic mixer array designed in multisubstrate technology to perform 6 to 8 dB conversion loss. Aperture coupled patch antennas are used for the reception of plasma signal, whereas pumping power is fed to the mixer through a waveguide-microstrip transition.

I. INTRODUCTION.

The achievement of spatially resolved measurements of electron-temperature fluctuations within the core of fusion plasmas has become a fundamental issue in plasma diagnostics [2]. The investigation of heat transport as well as of the turbulent confinement requires two-dimensional imaging of Electron Cyclotron Emission (2D-ECEI) radiated at the plasma core. Among the methods to perform Electron Cyclotron Emission (ECE) radiometry, heterodyne mixing plays an important role [1]. The development of detector arrays for 2D-ECEI [3] represents today therefore one of the main concerns of plasma diagnostics.

ECEI systems realised to date (e.g. [4]) rely on quasi-optical coupling of the pumping power, using the same antenna as for signal reception. Simple approximations presented below show that loss of local oscillator (LO) power can be improved by a factor of about 10 dB if the coupling is performed directly on-chip.

The circuit is realised on a multi-substrate technology and includes aperture-coupled patch antennas for the reception of the plasma signal. Cross-talking between channels may be reduced by physical substrate separation to prevent propagation of substrate modes. Also patch antennas can be isolated to increase channel isolation.

On-chip coupling of LO power requires the use of subharmonic pumping in order to minimise frequency-dependent attenuation in the microstrip circuit. Therefore, anti-parallel diode pairs are selected as mixer elements, which improve subharmonic performance [5]. The technology necessary for the fabrication of such anti-parallel diode pairs is available [6] and can be adapted to the fabrication of large-area integrated circuits.

The MMIC circuit is made of four parallel subharmonic Schottky-diode mixers realised on microstrip line on a 70- μm thick GaAs substrate. The circuit layout is shown in figure 1. Each channel receives RF signal (plasma radiation) in the band 144 - 153 GHz through a patch antenna coupled to the microstrip circuit. The specified circuit bandwidth should be 9 GHz also at the IF (9 GHz to 18 GHz). Local-oscillator power (at 67.5 GHz) is coupled to a 50- Ω microstrip line on the chip. The total size of the chip is about 10 x 6 mm². Simulated performance of the mixer systems show a minimum value of conversion loss between 6 and 8 dB for input LO powers ranging from 5 to 10 dBm per diode pair. The ripple throughout the IF band (9 to 18 GHz) is less than 4 dB.

II. SYSTEM CONCEPT

For each mixing channel, the patch antenna receives plasma radiation and delivers it through a slot in its ground plane to the microstrip circuit. In this way different substrates can be used for the patch antenna (fused quartz, $\epsilon_r = 3.4$, with good radiation properties) and for the microstrip circuit (GaAs, $\epsilon_r = 12.8$, with low radiation). Furthermore, the ground plane contributes to shield the mixer circuit, improving the circuit's isolation characteristics.

The multi-channel mixer system is mounted on a mixer block as shown in figure 1. The waveguide output of the LO source is coupled to the microstrip circuit and divided into four mixer channels. The intermediate frequency (IF) output is then coupled to coaxial cables before delivery to the IF section of the ECEI System.

An anti-parallel structure has been chosen for the diode configuration. This topology has well-known advantages ([7], [8]), in particular fundamental-mixing suppression and double LO mixing enhancement. It is still being employed for

¹ M. Rodríguez-Gironés, C.-I. Lin, and H. L. Hartnagel are with the Institut für Hochfrequenztechnik, Technische Universität Darmstadt, Merckstr. 25, 64283 Darmstadt, Germany
J.P. Pascual is with the Universidad de Cantabria, Avda. de los Castros, s/n, Santander, Spain
S. Bäuml is with the MaxPlanck Institute for Plasma Physics, Boltzmannstrasse 2, 85748 Garching bei München, Germany

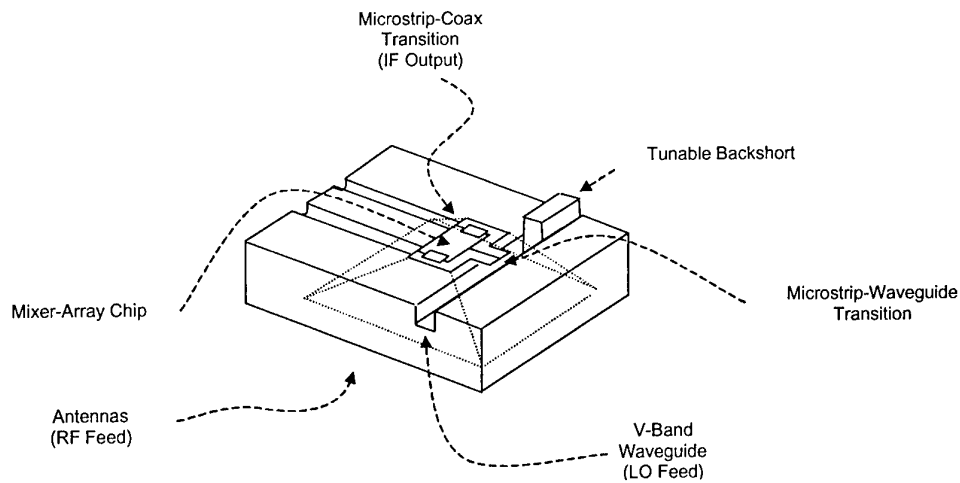


Fig. 1: Mixer block

different applications and at different frequency ranges [9], [10]. A lower pumping frequency simplifies the task of providing LO power (sources at about 70 GHz are more readily available than in the 150 GHz band). Furthermore, filtering of the image band is simplified as the need to match an LO signal lying between RF and image bands is eliminated.

I. ANTI-PARALLEL DIODES: DESIGN AND TECHNOLOGY

An equivalent circuit model has been used for the Schottky diodes. The linear part of the model was estimated from measurements and from the physical dimensions, and the non-linear part was based on measurements. This model is coherent with previous models electromagnetically de-embedded for such high frequency devices [11]. The values of diode parameters are shown in table 1.

Parameter	Value
I_{SAT} (saturation current)	2×10^{-17} A
Ideality factor	1.15
C_{j0}	4.5 fF
R_s (series resistance)	7 Ω
ϕ_{bi} (built-in potential)	1.03 V
L_f (parasitic inductance)	10 pH

Tab. 1: Values of the diode model

The technological process provides minimised parasitics, which allow high frequency operation. Single diodes were included to be characterised on wafer, making possible a more accurate post-simulation. The anti-parallel diode pairs used as mixer elements are an evolution of those described in [6]. The air bridge is substituted by an anode finger which runs above a 1.5 to 2- μ m thick passivation layer. This protects the diode further

from physical damage. The ohmic contact, in turn, is realised from the front side in order to simplify the technological process. Contact pads are not necessary since the diodes are integrated on the microstrip line, eliminating an important contribution to parasitic capacitance.

Diode dimensions (1.3 μ m anode diameter) are chosen to keep the parallel admittance of the junction capacitance ($2 \cdot 10^{-3} \Omega^{-1}$) low with respect to that of the average junction resistance. Furthermore, the absence of backside contacts suppresses one of the most important contributions to parasitic capacitance.

Fig. 2 shows a picture of a fabricated pair of diodes taken with an optical microscope.

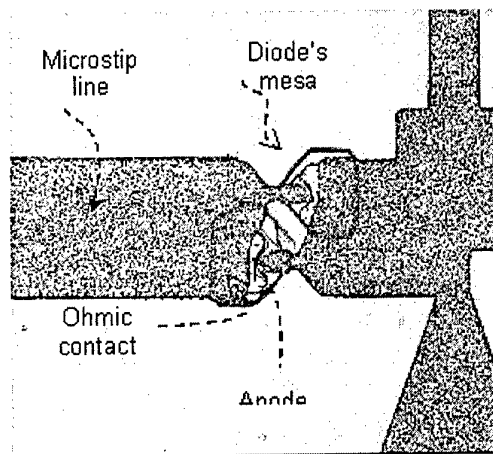


Fig. 2: Detail of the MMIC: Integrated Anti-parallel diodes

II. PLANAR PATCH ANTENNAS

Each channel receives plasma radiation in the band 144 to 153 GHz through a patch antenna coupled to the microstrip circuit by means of a slot on its ground plane. The antennas, about $400 \times 400 \mu\text{m}^2$ in size, are printed on a 150- μ m thick fused quartz

substrate using a thin-film technology. The radiation patterns calculated with the method of moments are typical for patch antennas. About 90 % of the radiated power is radiated for an angle of $\pm 45^\circ$.

III. MIXER DESIGN

The goal of the design is to obtain the smallest conversion loss, with rejection of unwanted harmonics (fundamental mixing, image) and good isolation between ports.

Using the harmonic balance technique [12], the most suitable LO pumping power range to have almost matched impedance showed by the grounded diodes was estimated. The impedance of the grounded diode pair at 67.5 GHz is shown in figure 3 for LO power values between 1 and 20 dBm.

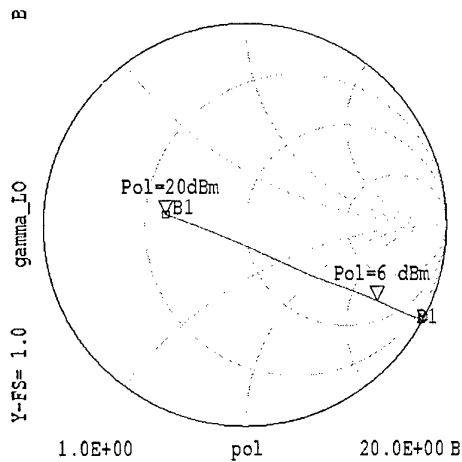


Fig. 3: LO impedance of the diode pair for several values of LO pumping power.

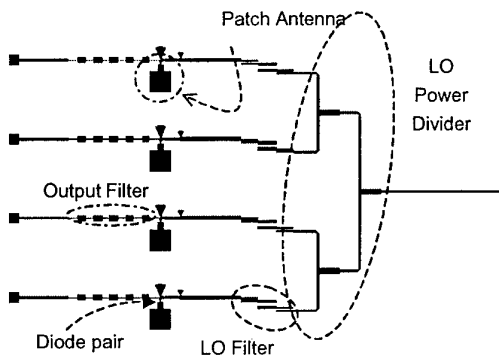


Fig. 4: Circuit layout

Performance of the mixer, especially in terms of conversion loss, is fixed by the design of the filtering and matching networks on each side of the diode pair [13]. The LO signal is injected through a microstrip structure which operates as LO filter and presents to the diodes a short circuit at IF and RF. Another structure on the other side acts as IF filter

and LO short. The RF antenna is also coupled to this structure.

The IF signal is extracted from the RF side to increase LO-IF isolation.

The microstrip parts have been simulated with the standard equivalent circuit models, but also with an electromagnetic simulator using the method of moments to take into account additional coupling effects [14]. This is crucial to prevent unwanted changes of the desired characteristics, more important at higher frequencies.

Fig. 4 shows the layout of the MMIC, whereas Fig. 5 shows a fabricated structure.

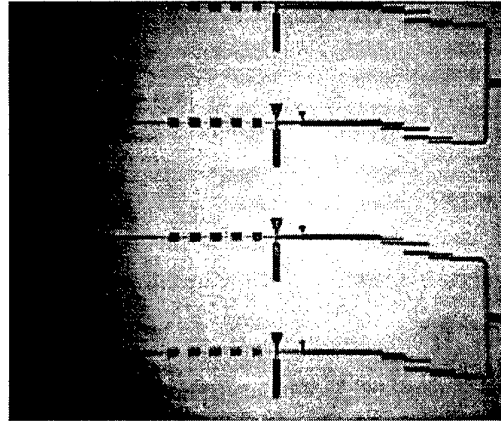


Fig. 5: Realised Microstrip MMIC

A procedure was applied to allow the simulation of RF power injection and the proper antenna impedance loading at the same time by using an Equivalent Large Signal Antenna. The reflection coefficient at the antenna input, previously obtained by electromagnetic simulation, is shown to the mixer circuit and at the same time RF power is flowing through towards the diodes, allowing the harmonic balance simulation of the mixer.

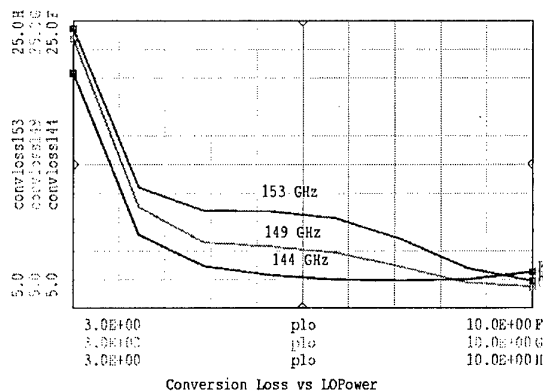


Fig. 5: Simulated conversion loss versus LO power for different values of RF frequency.

Conversion loss was evaluated in a single channel, using harmonic balance techniques in the whole RF band for several LO power values. The ripple across the RF band is less than 4 dB for each case.

Conversion loss saturate beyond 5 dBm pumping power per diode pair as it can be seen in figure 5 for three RF frequencies (lower, upper and middle band).

For LO available power ranging from 5 dBm to 10 dBm, best simulated values of conversion loss vary between 8 dB and 6 dB. This can be considered as an optimistic estimation.

Conversion loss versus IF frequency for several LO power values are shown in figure 6.

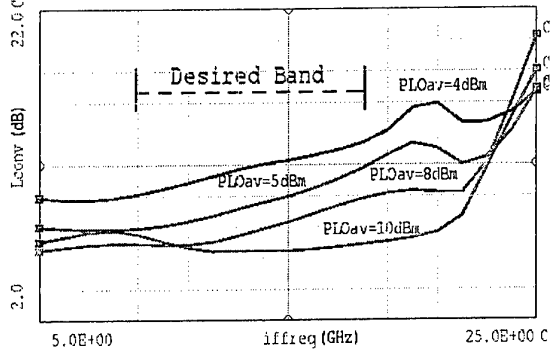


Fig. 6: Simulated conversion loss.

The goodness of the required shorts at IF, RF and OL frequencies at each side of the diodes was verified including the loading of the antenna and the LO power splitter.

Typical values of isolation between ports were also estimated. The LO-IF isolation is 31 dB. The LO power flowing towards the RF antenna is 41 dB below the injected LO level. The RF-IF isolation is shown in figure 9 for four values of LO available power. Because the antenna acts as an image filter, and also due to additional intended mismatching, down-converted image signal at the IF port is between 10 and 30 dB below the desired IF frequency. Optical filtering may improve image rejection if required.

The third-order interception point occurs for -6 dBm of output power: even on an optimistic value of -30 dBm of RF input power the third-order harmonic products at the output are more than 70 dB below the IF signal.

The double LO frequency at the output is negligible due to the anti-parallel diode properties to cancel it.

IV. CONCLUSIONS

A subharmonically pumped Schottky diode MMIC mixer has been designed for ECE plasma diagnostics applications. A Schottky diode high performance technology is used to allow fully integration on a single GaAs substrate, including also a patch antenna as RF port and an on-chip power distribution scheme. The design makes use of the anti-parallel diode structure advantages and it is strongly based on electromagnetic simulations of the planar microstrip structure. The first structures have been fabricated.

Acknowledgements.

The present work was partially financed by the European Commission through TMR contract number ERB FMRX CT-96 0050, and partially by the Max-Planck Institute for Plasma Physics at Garching, Germany.

References

- [1] H.J. Hartfuss, T. Geist and M. Hirsch, "Heterodyne methods in millimetre wave plasma diagnostics with application to ECE, interferometry and reflectometry", *Plasma Phys. Control. Fusion* 39 (1997), 1693-1769.
- [2] P.C. Liewer, *Nucl. Fusion* 25, 543 (1985).
- [3] H.J. Hartfuss and M. Tutter, "Fast multichannel heterodyne radiometer for electron cyclotron emission measurement on stellarator W VII-A", *Rev. Sci. Instrum.* 55 (9), September 1985.
- [4] N. Oyama et al, "Plasma diagnostics using millimetre wave two-dimensional imaging array", *Fusion Engineering and Design* 34-35 (1997), pp 407-410.
- [5] J.E. Degenford, B.A. Newman, "Harmonic Mixing with Antiparallel diode pair" *IEEE trans. on MTT*, Vol. 23, pp 667-673, Aug. 1975.
- [6] C.-I. Lin, et al, "Anti-Parallel Planar Schottky Diodes for Subharmonically-Pumped 220 GHz Mixer". 10th Intl. Symposium on Space Terahertz Technology, Charlottesville, Virginia, 16-18 March 1999.
- [7] M.V. Schneider, "Harmonically Pumped Stripline Down Converter," *IEEE Trans. on MTT*, vol. 23, pp 271-275, Mar. 1975.
- [8] M. Cohn, J.E. Degenford, B.A. Newman, "Harmonic Mixing with Antiparallel diode pair" *IEEE trans. on MTT*, Vol. 23, pp 667-673, Aug. 1975.
- [9] T. Jamaji, H. Tanimoto, H. Kokatsu, "An I/Q Active balance Harmonic Mixer with IM2 cancelers and a 45 degrees phase shifter." *IEEE Journal of Solid-State Circuits*. Vol. 33, No 12, pp 2240-2246, Dec. 1998.
- [10] C.I. Lin, M. Rodríguez-Gironés, A. Simon, J. Zhang, P.V. Pironen, V.S. Möttönen, H.L. Hartnagel, A.V. Räisänen, "Anti-Parallel Planar Schottky Diodes for Subharmonically-Pumped 220 GHz Mixer". 10th Intl. Symposium on Space Terahertz Technology, Charlottesville, Virginia, 16-18 March 1999.
- [11] J. Zhang, P.V. Pironen, V.S. Möttönen, J.T. Louhi, A.O. Lehto, A. Simon, C.I. Lin, A.V. Räisänen, "Wide-Band Equivalent Circuit of Quasi-Vertical Planar Schottky Diode for 650 GHz Subharmonic Mixers". THz Workshop 97. Grenoble, France.
- [12] Hewlett Packard's Microwave Design System, version B.07.10.
- [13] A. Madjar, M. Musia, "Design and Performance of a x4 Millimeter Wave Subharmonic Mixer". *Proc. of the 23rd European Microwave Conference*, September 1993, Madrid, Spain.
- [14] Hewlett Packard's MOMENTUM, version A.02.58

Laser Micromachining of THz Components

Christian Drouët d'Aubigny, Christopher Walker, Bryan Jones, Christopher Groppi, John Papapolymerou

Abstract – Laser micromachining techniques can be used to fabricate high-quality waveguide and quasi-optical components to micrometer accuracies. Successful GHz waveguide designs can be directly scaled to THz frequencies. We expect this promising technology to allow the construction of the first fully integrated THz heterodyne imaging arrays. At the University of Arizona, construction of the first laser micromachining system designed for THz waveguide components fabrication has been completed. Once we have tested and characterized our system we will use it to construct prototype THz 1x4 focal plane mixer arrays, AR coated silicon lenses, THz LO sources, phase gratings and more. The system can micromachine structures down to a few microns accuracy and up to 6 inches across in a short time. This paper discusses the design and performance of our laser micromachining system, and illustrates the type and range of components this exciting new technology will make accessible to the THz community.

INTRODUCTION

Laser processing offers many advantages over conventional machining of micrometer sized components [1]. Thanks to the ability to finely focus laser light, smaller features can be achieved with improved tolerances. Because chemically activated laser etching is a non contact process, there is no mechanically induced material damage, no hard to remove particulate residues, and no tool wear or machine vibration. Laser fabrication therefore yields finer finishes, improved accuracy, and lower process overheads. The chemical activation on which this process is based minimizes the etching energy requirement and therefore reduces the potential for cracking [1].

LASER MICROMACHINING PRINCIPLES

An Argon-Ion laser is used to heat a microscopic portion of the silicon substrate in a chlorine ambient. At the onset of melting, volatile silicon chlorides are formed. The highly non-linear activation energy of the process confines etching to a molten zone only a few microns across. Crystalline materials have the benefit that un-etched portions of the molten zone grow back epitaxially, allowing controlled shavings to be removed plane by plane. Structures can thus be built by limiting the etch depth at each scan plane, to typically 1 μm , (see Fig. 1).

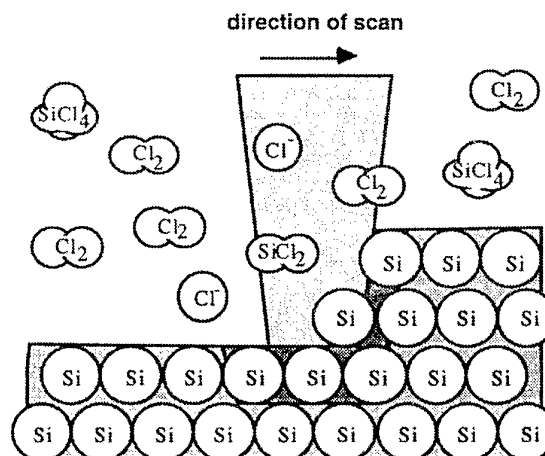


Fig. 1: Schematic representation of laser etching of silicon in chlorine ambient. Using high numerical aperture (NA) optics the reaction can be confined to a region only a few micrometer in size. The obvious trade off of high NA is a tapering of the beam that can be significant for some applications eg. Vertical walls [1].

At Steward Observatory we have built a laser micromachining system that follows the successful Lincoln Laboratory design and is optimized for THz applications.

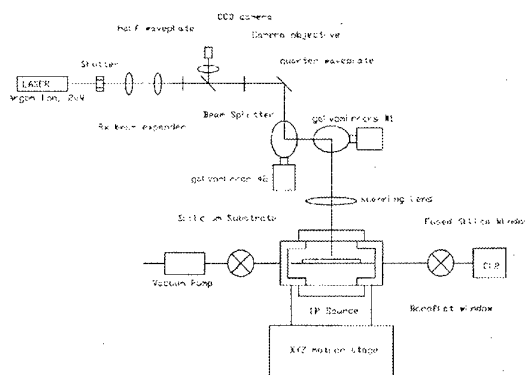


Fig. 2: Schematic of Steward Observatory's laser micromachining system

In our design the 18W Argon-Ion laser beam is expanded to 16mm, then deflected, using a commercial X-Y galvoscanner, onto achromatic scanning lens. The focused beam is then introduced through a fused silica window into a stainless steel reaction chamber containing the sample (see fig. 2).

C. Drouët d'Aubigny, C. Walker, B. Jones and C. Groppi are with Steward Observatory, The University of Arizona, Tucson, AZ 85721, USA

J. Papapolymerou is with The Department of Electrical and Computer Engineering, The University of Arizona, Tucson, AZ 85721, USA

The wafer surface is typically biased to 100°C using an IR illumination source shining through a second window on the back side of the reaction chamber (see Fig 3).

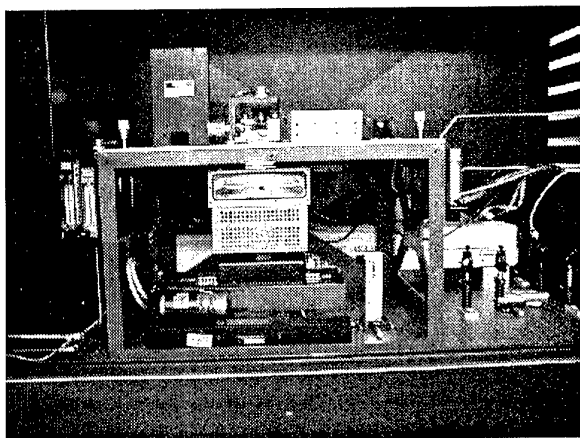


Fig. 3: Detailed view of the galvomirror scanner, reaction chamber, IR heater and X-Y-Z motion stages

The process is monitored through the focusing optics using a CCD with a plate scale of 7 μm per pixel. The scanning system is driven directly from computer generated patterns which can be constructed using Autodesk's AutoCAD. The ensemble is mounted on computer controlled X-Y-Z precision motion stages (see Fig. 3) allowing the stitching of large structures.

Before operation the cell is evacuated, then filled with 99.9 % pure chlorine gas to 100 Torr. After 2 hours of machining the remaining chlorine gas and silicon chlorides are vented through a scrubbing bubbler before release in the atmosphere. Figure 4 shows the system in our laboratory. The chlorine and nitrogen gas cylinders are stored in the gas cabinet on the right. The central hood houses the laser, reaction chamber, and optics. The vacuum pump and chlorine scrubbers are contained in the small gas cabinet on the left.

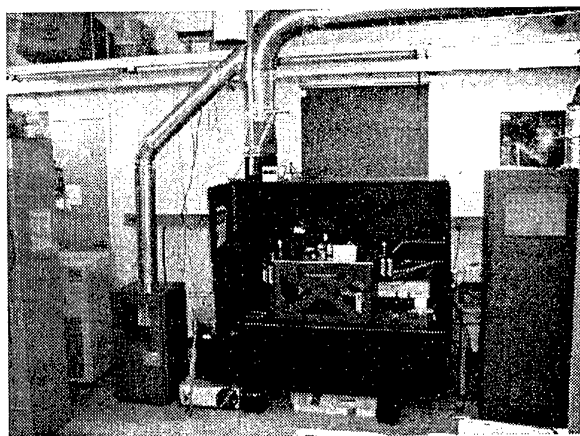


Fig. 4: Ensemble view of the Steward Observatory laser micromachining system

Figure 5 shows the electronic shutter and beam expander portion of the optical system with the laser turned on.



Fig. 5: Laser, shutter and beam expander assembly

RESULTS AND POSSIBLE APPLICATIONS

The laser micromachining system will permit the direct scaling of a wide variety of waveguide and optical structures to THz frequencies. One such device is a "Magic-T". Figure 6 is a conceptual design for a 0.85 THz mixer that coherently combines the signals from two independent telescopes using a Magic T before downconversion. The local oscillator is injected using a micromachined directional coupler. An array of such mixers is shown in Figure 6. We plan to propose to build such an instrument [3] for use on the Large Binocular Telescope now being constructed on Mount Graham, Arizona.

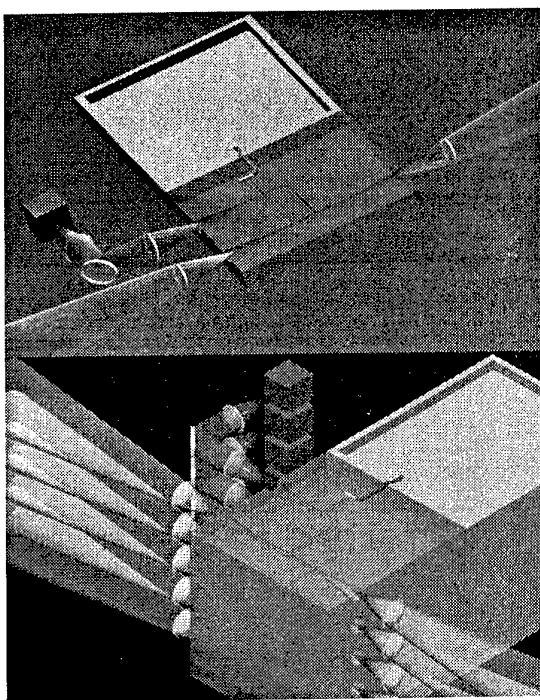
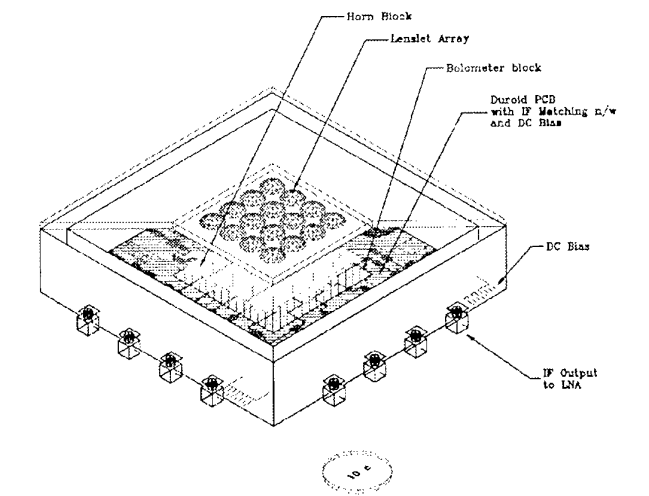


Fig. 6: Beam combiner and LO injection element design (top). Proposed beam combiner array for the LBT (bottom).

Figure 7 is a conceptual drawing of an integrated, micromachined, 2 THz array receiver being developed for SOFIA, the Stratospheric Observatory for Far Infrared Astronomy [3]. Test feedhorns for the array (Fig. 8) were fabricated using the parent laser micromachining system at Lincoln Laboratory and successfully tested at Steward Observatory [4].



STAR Mixer Assembly Diagram

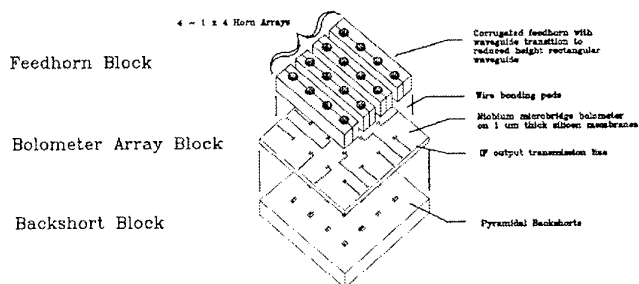


Fig. 7: SOFIA 2 THz, 4x4 array design

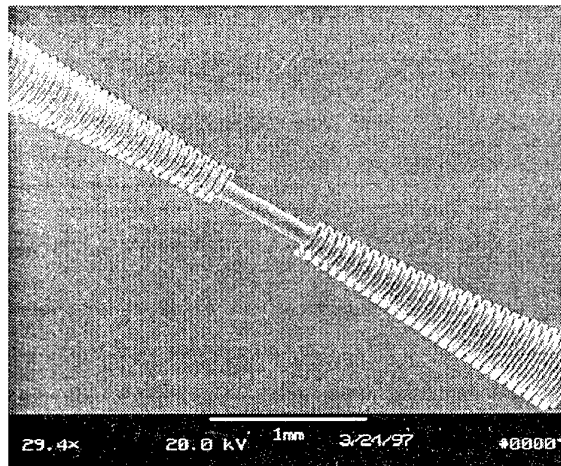


Fig. 8: Feedhorn produced at Lincoln Laboratories.

CONCLUSION

Laser etching not only makes the construction of THz waveguide arrays tractable but it is also ideally suited to make submillimeter phase gratings, high efficiency feedhorns to replace Winston cones in large bolometer arrays, AR grooving in silicon lenses and more. Optical diagrams, waveguide pictures and conceptual diagrams are available at:

<http://soral.as.arizona.edu/micromachining.html>

Acknowledgements

This project made possible by a Collaborative Research Agreement (CRDA) between the University of Arizona and MIT Lincoln Laboratory, was supported through NSF grant #9800260

References

1. Theodore M. Bloomstein, 1996, Ph-D Thesis, MIT
2. C. Y. Drouët d'Aubigny et al, 2000, SPIE Proceeding, "Radio Telescopes", Vol. 4015, p268
3. C. K. Walker et al, 2000, SPIE Proceeding, "Airborne Telescope Systems", Vol. 4014, p125
4. C. K. Walker et al, 1997, 8th Int. Symp. on Space Terahertz Technology, p358.

A One-Dimensional Photonic Bandgap System as High-Reflectivity Mirror for Microwave and THz Applications

Gerhard W. Schwaab

Abstract – A one-dimensional photonic bandgap mirror (PBM) has been designed consisting of periodically alternating planar quarter-wavelength layers of a high-refractive index dielectric and low-refractive index material (e.g. vacuum). A V-shaped folded Fabry-Perot-Interferometer was set up with two scaled PBMs and a spherical metal mirror to provide a stable resonator design. The PBMs consisted of polystyrene and air as dielectrics and were designed for a center frequency of 23.44 GHz. The transmission characteristics of the FPI was measured for different numbers of layers in the PBMs. The reflectivity of the PBMs was derived from the cavity's chromatic resolving power. The measured reflectivity and bandwidth are compared with theoretical expectations taking into account resonator losses and absorption in the dielectrics.

I. INTRODUCTION

The THz spectral range is especially important for spectroscopic applications since the lowest vibrational levels of large molecules (e.g. skeletal motions of biomolecules), the vibrational levels of small molecular clusters, and the energy states of molecules bound to a surface lie in that frequency region. Due to their low energies, THz photons are in general not able to break the bonds of weakly bound molecular systems. As radiation sources, several options are possible like BWOs (direct or multiplied), laser sidebands [1,2,3], optical mixers [4,5], or p-type Ge lasers [6]. The different sources strongly differ with respect to frequency range, output power, and spectral purity.

p-type Ge lasers provide the most promising aspects for an improved spectrometer for the frequency range between 1 and 4 THz, since they are solid state devices and they can easily be tuned by changing the magnetic field. p-type Ge lasers are characterized by their pulsed operation and a longitudinal mode spacing which is defined by the length of the laser crystal. To improve these systems, they have to be operated with an external resonator and anti-reflection coated front surfaces.

Pulsed lasers are even needed for cavity ringdown spectroscopy [7], where instead of directly measuring the absorption of a gas, the Q-factor of a resonator cavity is measured with and without an absorbing gas. Briefly, a high-Q resonator is illuminated by a short laser pulse. At the resonator output an exponentially decaying series of signal pulses appears whose decay time is a measure of the resonator quality. An absorbing gas in the resonator will change this decay time in a way that the absorption coefficient can be calculated.

Summarizing, to be able to develop a new type of TuFIR spectrometer, one major optical problem is the design of wideband high-reflectivity FIR mirrors.

II. THEORETICAL BACKGROUND

Wideband mirrors with high reflectivity (>99.5%) are well known in the optical and IR regions, where they serve for example as laser mirrors. They consist of a substrate that is coated with a stack of quarter wavelength layers with alternating high (n_h) and low (n_l) indices of refraction. The quality of such a mirror is determined by the number of layers, the ratio $n_{rel}=n_h/n_l$ and the absorption and diffraction losses within the different layers. The reflection and transmission of a multilayer optics can be calculated recursively by taking into account the reflections and transmissions at the boundaries between different layers and the phase delay within one layer. Weak dielectric absorption losses can be accounted for by using complex indices of refraction. Figure 1 shows a N-layer system with layer thickness d_i , index of refraction n_i , and propagation angle θ_i for the i-th layer. With the incident electric field E_i and the reflected electric field E_r , the total field reflection coefficient $\rho = \frac{E_r}{E_i}$ of layers $j+1$ through N can be calculated [8]. Within a real system additional losses occur. Most important are resonator losses and losses due

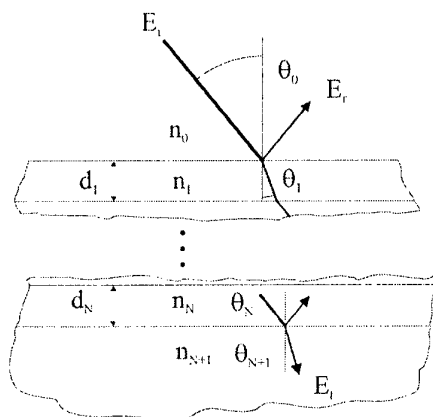


Fig. 1: Schematic of a N-layer optics with incident field E_i , reflected field E_r , and transmitted field E_t . Each layer is described by its thickness d , its refractive index n , and its propagation angle θ .

G. W. Schwaab is with the Lehrstuhl für physikalische Chemie II, Ruhr-Universität Bochum, Universitätsstrasse 150, 44780 Bochum

to misalignment which show a different frequency behavior than the dielectric losses. They can be accounted for [9] by modifying the one way phase shift $e^{i\delta_{j+1}}$ (with complex δ_{j+1}) to $e^{-r} e^{i\delta_{j+1}}$ with the additional loss factor e^{-r} . This leads to an electric field reflection coefficient of:

$$\rho_j = \frac{r_{j,j+1} + \rho_{j+1} e^{-2r} e^{2i\delta_{j+1}}}{1 + r_{j,j+1} \rho_{j+1} e^{-2r} e^{2i\delta_{j+1}}} \quad (1)$$

Here, $r_{j,j+1}$ represents the field reflection coefficient at the boundary of layers j and $j+1$, which is given by the Fresnel formulae [10] ρ_{j+1} the total field reflection coefficient of layers $j+2$ through N , i the $\sqrt{-1}$, and δ_{j+1} the phase delay in layer $j+1$. The phase delay is given by the relationship

$$\delta_j = 2 \pi \frac{\nu}{c} n_j d_j \cos \theta_j \quad (2)$$

with c the velocity of light and θ_j the propagation angle of the radiation in layer j . The θ_j can be calculated from the incident angle θ_i using Snellius' law.

The electric field transmission coefficient is given by

$$\tau_j = \frac{\frac{n_{j+1} \cos \theta_{j+1}}{n_j \cos \theta_j} t_{j,j+1} \tau_{j+1} e^{-r} e^{i\delta_{j+1}}}{1 + r_{j,j+1} \rho_{j+1} e^{-2r} e^{2i\delta_{j+1}}} \quad (3)$$

Here, $t_{j,j+1}$ represents the Fresnel field transmission factor at the boundary between layers j and $j+1$ as calculated by traversing from layer j into layer $j+1$. Please note, that for the transmission formula the layers are counted just opposite to the labeling in Figure 1 so that the numbers increase looking backward from the transmitted beam.

The power reflection and power transmission coefficients can be calculated from ρ_j and τ_j by taking the absolute square value, respectively. The phase shift is given by the overall argument of the expression.

To be able to theoretically study these problems, a Mathematica program has been developed, that includes iterative handling of multilayer optical problems and second order effective media theory to simulate artificial dielectrics.

III. WIDEBAND DIELECTRIC MIRRORS FOR HIGH-Q THZ RESONATORS

Since a quarter wavelength in the mm-wave to THz spectral regions is in the order of a few to a few hundred micrometers, such layers can currently not efficiently be fabricated by epitaxial or etching techniques. It is, however, possible to fabricate lambda quarter dielectric sheets from different materials ranging from polyethylene to silicon. The simplest possible way to build a high-reflectivity mirror is therefore to stack alternating $\lambda/4$ -layers of materials with high and low index of refraction (see Fig. 2, top).

Using air as the low index of refraction dielectric, best results are expected for low-loss dielectrics with a high index of refraction like high-purity Si ($n=3.42$), which

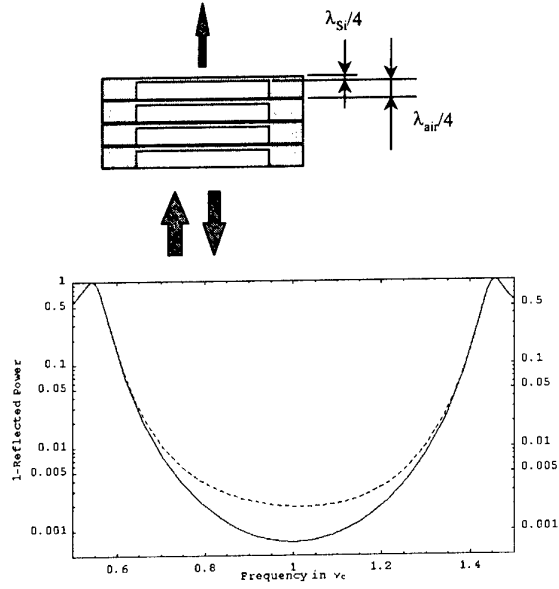


Fig. 2: top: Stack of four $\lambda/4$ doublets in air and Si as high-reflectivity THz mirror. bottom: 1-Reflectivity versus relative frequency for lossless Si (solid line) and Si with a loss tangent of 0.0012 (dashed).

shows low absorption in the design frequency range from 1-4 THz and can be grind down to a layer thickness of less than $7\mu\text{m}$.

Calculations were performed for four $\lambda/4$ -layers of Si separated by $\lambda/4$ -layers of air. Fig. 2, top, shows $1-\rho$ of such a system, ρ being the power reflection coefficient. For lossless material, reflectivities higher than 99.9 percent can be achieved with a relative bandwidth of more than 20%. Introducing a loss tangent of 12×10^{-4} as it has been described in the literature [11] leads to a reduced reflectivity of 99.8% maximum and a bandwidth of about 50% for reflectivities higher than 99.5%.

IV. A SCALED MICROWAVE DEMONSTRATOR

Due to the high cost of the ultrathin Si slices described above, a 100:1 scaled mirror model was built. It consisted of up to 10 layers of polystyrene sheets with a thickness of $d=2\text{ mm}$ and a length of 300 mm square. To prevent bending of the sheets and to keep the layer spacing constant over the full mirror area four $5 \times 5\text{ mm}^2$ evenly distributed cork spacers were glued to each sheet. The index of refraction of polystyrene is $n=1.6$. This corresponds to a design wavelength of $\lambda = 4nd = 12.8\text{ mm}$ or a design frequency of $\nu = c/\lambda = 23.4\text{ GHz}$. The size of the air gap between two adjacent polystyrene sheets was therefore chosen to be 3.2 mm. Literature values for the loss tangent of polystyrene [12] are in the order of $\tan\delta = 1 \times 10^{-4}$ to 1.2×10^{-3} . Expected reflectivities range from 99.97% (lossless material) to 99.5% ($\tan\delta = 1.2 \times 10^{-3}$).

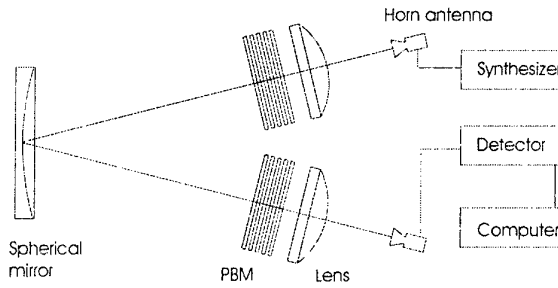


Fig. 3 V-shaped folded Fabry-Perot set-up to determine the reflectivity of the photonic bandgap mirrors.

To measure the mirror reflectivity, a folded confocal Fabry-Perot-interferometer (FPI) was designed (see Figure 3) with two PBMs as input and output ports and a single spherical aluminum mirror with a radius of curvature of 2400 mm and a diameter of 410 mm to re-focus the beam. The length of the FPI was adjustable and was fixed at 2.4 m. The angle between the two arms of the interferometer was 7°. The electric field distribution inside the interferometer can be described by Gaussian resonator modes, the TEM₀₀ mode being the strongest one (see Figure 5, right). The folding of the resonator leads to an astigmatism which results in slightly different beam waists for the beams parallel and perpendicular to the interferometer plane.

One arm of the FPI was irradiated by microwave radiation from a HP83640B synthesizer. A crystal detector was used to detect the transmitted output power. The data taking process was fully computerized. Two wideband rectangular horn antennas transformed the microwave radiation to free space. Plano-convex HDPE lenses with a diameter of 260 mm and a focal length of $f=480$ mm were used to match the interferometer input and output beams to the horn antennas.

Given the measured transmitted power P_m and the incident power P_0 and assuming identical mirrors at input and output of the interferometer, the frequency dependency $T[v]$ of the relative transmitted power $T=P_m/P_0$ around a transmission maximum is given by

$$T[v] = T_0 \frac{1}{1 + \frac{4\rho}{(1-\rho)^2} \sin^2\left[\frac{2\pi(v-v_0)}{2\Delta v}\right]} \quad (4)$$

Here, T_0 represents the maximum transmitted relative power, ρ the power reflectivity of a single mirror, v_0 the center frequency of the transmission maximum, and $\Delta v=c/2L$ the free spectral range of the interferometer.

The transmission spectrum of the interferometer was recorded from 20 to 26 GHz as a function of the number of dielectric layers (1 to 10 layers per mirror). The spectral resolution was chosen according to the expected transmission line width ranging from 1 MHz for a small number of layers to 0.05 MHz for a large number of layers.

The recorded power spectrum was linearized using calibration data for the power detector. Each TEM₀₀ transmission peak was fitted using a non-linear least square fit. To minimize cross-talk effects from higher

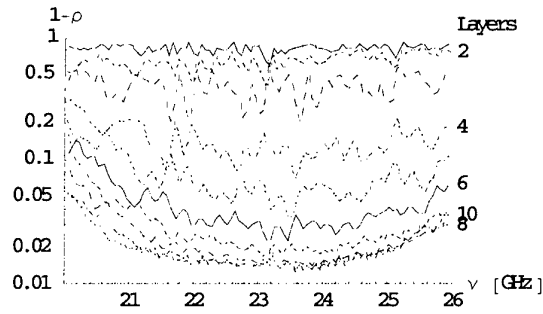


Fig. 4 Measured $1-\rho$ as function of the number of polyethylene layers per mirror versus frequency.

order Gaussian modes, only the frequency range close to the center frequency was used in the fit with the highest frequency coverage for small number of layers and a smaller frequency range for a large number of layers. The model was validated by using a theoretical transmission spectrum and by analysing it the same way than the measured spectra. The results obtained were compared with directly calculated power reflection coefficients and showed excellent agreement.

Figure 6 shows in logarithmic scale $1-\rho$, the measured power reflection coefficient, as a function of the number of dielectric layers. As expected, for $N_L=1$ to 7 the power reflection increases with increasing N_L . However, increasing N_L from 8 to 10, only little improvement in ρ can be observed. The maximum reflectivity obtained by this method was $\rho = 98.7\%$

V. DISCUSSION

The maximum achieved power reflectivity is considerably less than what is expected from theory, even taking loss factors as large as $\tan\delta=0.0012$ into account. This discrepancy between theory and experiment is at least partly due to resonator losses. A good measure to discuss resonator losses is the Fresnel number $N_f = a^2/(L\lambda)$ with $2a$ being the diameter of the resonator end mirrors, L the resonator length, and λ the wavelength of the radiation. An approximate formula for the resonator loss of a confocal resonator with circular end mirrors is given by [9]

$$\delta \approx 16 \pi^2 N_f \exp(-4 \pi N_f) \quad \text{for } N_f \geq 1. \quad (5)$$

That for a confocal resonator with square mirrors is given by

$$\delta \approx 8 \pi \sqrt{2 N_f} \exp(-4 \pi N_f) \quad \text{for } N_f \geq 0.5 \quad (6)$$

Although the resonator described here has planar end faces, due to the re-focusing mirror, the formulae for confocal mirrors apply. The definition of the relevant size a is ambiguous, however, because it is unclear, if the size of the spherical mirror or the size of the PBMs is the relevant dimension. Since the lateral dimensions of the PBMs leads to a smaller N_f and therefore larger resonator losses, we used the second formula to compare theoretical transmission spectra with the experimental results.

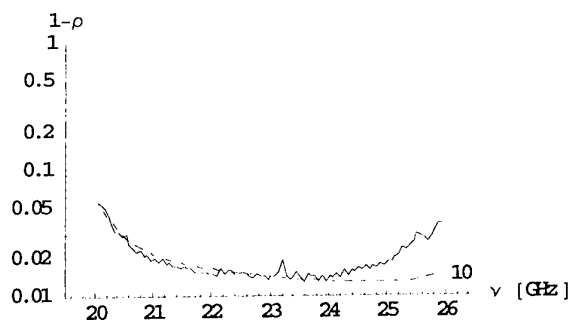


Fig. 5 $1-\rho$ as function of frequency for a photonic bandgap mirror with 10 polystyrene-air-layers (solid). The dashed curve shows theoretical values obtained assuming $N_f=0.833$ and an additional frequency independent loss of 0.4% per pass.

From this comparison, it is evident, that the critical dimension a is larger than 0.155 m. With a resonator length $L=2.4$ m and $\lambda=12.8$ mm, the Fresnel number for the folded Fabry-Perot interferometer is larger than 0.8 at band center. N_f and therefore δ are strongly frequency dependent leading to large losses at low frequencies, if a is underestimated. Thus taking only resonator losses into account cannot resolve the described discrepancy.

The theoretical data agree better with the experimental results, if an additional frequency independent loss of 0.4% per pass is included. But even then, the agreement is not perfect at the high frequency end of the reflectivity curve (see figure 6).

There are several mechanisms, that might be responsible for such a high frequency effect. The most important ones are the surface roughness of the metal mirror, deviations of the metal mirror surface from the ideal spherical shape, and spacing and shape deviations in the photonic bandgap mirrors. Currently, investigations are under way, which of these effects plays the most crucial role.

Recursive multilayer optics can be used to design high-reflectivity mirrors for advanced TuFIR spectrometers. The demonstration of the feasibility of high reflectivity FIR mirrors facilitates the design of new FIR resonators as they are needed for FIR cavity ringdown spectroscopy or for external resonators of p-type Ge lasers.

The next steps towards an advanced TuFIR spectrometer are the experimental clarification of the additional losses found in the scaled microwave model and the setup of a higher frequency system which can be used for spectroscopy. Eventually, the extension of the frequency and power range accessible to TuFIR spectroscopy will lead to an improved understanding of molecular systems as they can be found on earth and in space.

Acknowledgement

It is a pleasure to acknowledge the support of Dirk Plettemeier from the Institute of High Frequency Techniques at the Ruhr-Universität Bochum who supplied the wide-band horn antennas and the programming skills of Holger Krumm who considerably facilitated the measurement procedure.

References

1. D.D. Bicanic, B.F.J. Zuidberg, A. Dymanus, Appl. Phys. Lett. 32, 367 (1978).
2. P. Verhoeve, E. Zwart, M. Drabbels, J.J. ter Meulen, W. L. Meerts, A. Dymanus, D. B. McLay, Rev. Sci. Instrum. 61, 1612 (1990)
3. G.A. Blake, K.B. Laughlin, R.C. Cohen, K.L. Busarow, D.H. Gwo, C.A. Schmuttenmaer, D.W. Steyert, R.J. Saykally, Rev. Sci. Instrum. 62, 1701 (1991)
4. S. Matsuura, G.A. Blake, R.A. Wyss, J.C. Pearson, C. Kadow, A.W. Jackson, A.C. Gossard, Traveling-Wave Photomixers Based on Noncollinear Optical/Terahertz Phase-Matching, Proceedings of the 10th International Symposium on Space Terahertz Technology, Charlottesville, Virginia, 1999.
5. E. Duerr, K. McIntosh, S. Verghese, „Design of a Distributed Photomixer for Use as Terahertz Local Oscillator, . Proceedings of the 10th International Symposium on Space Terahertz Technology, Charlottesville, Virginia, 1999
6. E. Bründermann, D.R. Chamberlain, E.E. Haller, „Novel Design of Widely Tunable Germanium Terahertz Lasers“, IR Phys. & Techn. 40, 141-151 (1999)
7. J.J. Scherer, D. Voelkel, D.J. Rakestraw, J.B. Paul, C.P. Collier, R.J. Saykally, A.O. Keefe, Chem. Phys. Lett 245, 273-280 (1995)
8. D.H. Raguin, G.M. Morris, Appl. Optics 32, 1154 (1993)
9. A.E. Siegman, „Lasers“, Chapter 19, University Science Books, Mill Valley, California
10. Bergmann-Schaefer, Lehrbuch der Experimentalphysik Band III, Optik, 7th Edition, p. 452, Walter de Gruyter, Berlin 1978,
11. P.F. Goldsmith, „Quasioptical Systems“, Chapter 5.4, IEEE press, New York, 1998
12. A.J.Bur, “Dielectric properties of polymers at microwave frequencies: a review”, Polymer 26, 963-977, (1985)

An Analytical Solution to Diffraction Problems Involving Periodically Structured Objects

THORE MAGATH AND MAHMOOD AKBARI

Arbeitsbereich Hochfrequenztechnik
Technische Universität Hamburg-Harburg
D-21073 Hamburg, Germany

Phone: +49 40 42878-2758, FAX: +49 40 42878-2755, E-mail: magath@tuhh.de

Abstract

A rigorous analysis of diffraction by rectangularly profiled, dielectric gratings is presented. An analytical solution is obtained for the total electromagnetic field. The approach presented can readily be extended to computations for metallic gratings and arbitrarily shaped surface-relief gratings.

1 Introduction

Because of their many potential applications, two-dimensional (2-D) dielectric gratings are of great interest. In these applications the gratings typically assume functions of beam combiners, splitters, or shapers, etc. [1], [2].

The design of such gratings inherently is an inverse problem, in our case involving Maxwell's equations with boundary conditions. Genetic Algorithms (GA) have shown promise of coping with this kind of problem. In [3], an excellent overview is provided on the application of GA to engineering electromagnetics.

Genetic Algorithms are stochastic search and optimization techniques with many advantages. They tend to produce globally optimal results, and the target functions are not required to be continuous. Another remarkable property is the inherent parallelism of GA so that they are ideally suited for implementation on a parallel machine.

For a CAD tool to be useful in the design of 2-D gratings based on GA, an efficient method for analysis is needed. With further extensions, the method presented here has the required properties. Modified slightly, it has been successfully applied to analyze Multi-Quantum-Well DFB laser diodes in a three-dimensional manner as demonstrated in [4].

In [5], a system of second-order differential equations has been introduced to describe the total electromagnetic field within a rectangularly profiled, dielectric grating¹. This system can be regarded as a wave equation with propagation constant. In this paper, an analytical solution to this wave equation is presented. For the sake of convenience, the wave equation will be briefly derived.

¹... also called binary dielectric grating.

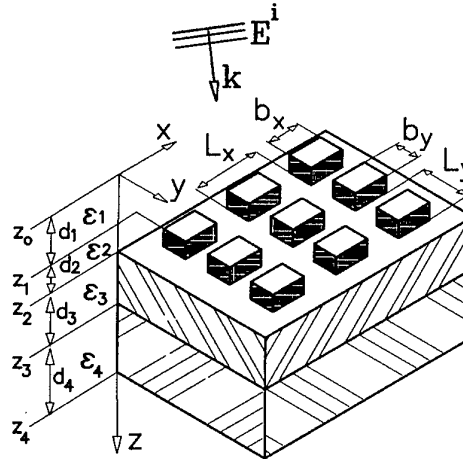


Figure 1: A binary, biperiodic grating exposed to the field of an incident plane wave.

2 Theory

In the scattering of a *homogeneous plane wave* $\mathbf{E}^i(\mathbf{r}) = \mathbf{E}_0 e^{-j\mathbf{k} \cdot \mathbf{r}}$, characterized by its polarization vector \mathbf{E}_0 and its wave number vector \mathbf{k} , by a biperiodically structured object, as illustrated in Fig.1, the total electromagnetic field obeys the Floquet theorem, i.e.

$$[\mathbf{E}(\mathbf{r} - \mathbf{r}_{mn}), \mathbf{H}(\mathbf{r} - \mathbf{r}_{mn})] = e^{j\mathbf{k} \cdot \mathbf{r}_{mn}} [\mathbf{E}(\mathbf{r}), \mathbf{H}(\mathbf{r})] \quad (1)$$

for any \mathbf{r} , where $\mathbf{r}_{mn} = mL_x \mathbf{u}_x + nL_y \mathbf{u}_y$. Hence the total field can be expressed by

$$\begin{bmatrix} \mathbf{E}(\mathbf{r}) \\ \mathbf{H}(\mathbf{r}) \end{bmatrix} = \sum_{m=-M}^M \sum_{n=-N}^N \begin{bmatrix} \mathbf{E}_{mn}(z) \\ \mathbf{H}_{mn}(z) \end{bmatrix} e^{-j\alpha_m x} e^{-j\beta_n y} \quad (2)$$

with $\alpha_m = \mathbf{k} \cdot \mathbf{u}_x + m2\pi/L_x$ and $\beta_n = \mathbf{k} \cdot \mathbf{u}_y + n2\pi/L_y$. L_x and L_y denote the periodicity in \mathbf{u}_x and \mathbf{u}_y direction, respectively. The vector expansion coefficients $\mathbf{E}_{mn}(z)$ and $\mathbf{H}_{mn}(z)$ are the unknowns which must be solved.

Slicing a scatterer in layers, the permittivity $\epsilon(x, y, z)$ of each layer at constant z can be expanded into a 2-D Fourier series

$$\epsilon(x, y, z) = \sum_{m=-M}^M \sum_{n=-N}^N \bar{\epsilon}_{mn}(z) e^{-jm \frac{2\pi}{L_x} x} e^{-jn \frac{2\pi}{L_y} y} \quad (3)$$

In a homogeneous layer, $\varepsilon(x, y, z)$ simply equals $\bar{\varepsilon}_{00}$. Note that in Eqs. (2) and (3), M and N approach infinity.

Substitution of expansions (2) and (3) into Maxwell's equations yields after some manipulations

$$0 = \frac{d^2}{dz^2} \mathbf{U}(z) + \omega_o^2 \mathbf{L} \mathbf{C} \mathbf{U}(z) \quad (4)$$

$$\mathbf{I}(z) = (-j\omega_o \mathbf{L})^{-1} \frac{d}{dz} \mathbf{U}(z) \quad (5)$$

where the following vectors

$$\mathbf{U}^T = [\mathbf{u}_x^T[\dots, \mathbf{E}_{\nu(m,n)}, \dots], \mathbf{u}_y^T[\dots, \mathbf{E}_{\nu(m,n)}, \dots]] \quad (6)$$

$$\mathbf{I}^T = [\mathbf{u}_x^T[\dots, \mathbf{H}_{\nu(m,n)}, \dots], -\mathbf{u}_y^T[\dots, \mathbf{H}_{\nu(m,n)}, \dots]] \quad (7)$$

with a bijective index transformation $\nu = (2N+1)(m+M)+n+N+1$ are defined. Further, denoting the Kronecker product with the symbol \otimes , the identity matrix by $\mathbf{1}$, and letting $k_o = \omega_o \sqrt{\mu_o \varepsilon_o}$, diagonal matrices

$$[\bar{\alpha}] = \frac{1}{k_o} [(\mathbf{k} \cdot \mathbf{u}_x) \mathbf{1} + \frac{2\pi}{L_x} \text{diag}([-M, \dots, M] \otimes \overbrace{[1, \dots, 1]}^{2N+1})] \quad (8)$$

$$[\bar{\beta}] = \frac{1}{k_o} [(\mathbf{k} \cdot \mathbf{u}_y) \mathbf{1} + \frac{2\pi}{L_y} \text{diag}(\overbrace{[1, \dots, 1]}^{2M+1} \otimes [-N, \dots, N])] \quad (9)$$

and the block matrices become

$$\mathbf{L} = \mu_o \begin{bmatrix} \mathbf{1} - [\bar{\alpha}] \mathcal{N}^{-2} [\bar{\alpha}] & -[\bar{\alpha}] \mathcal{N}^{-2} [\bar{\beta}] \\ -[\bar{\beta}] \mathcal{N}^{-2} [\bar{\alpha}] & \mathbf{1} - [\bar{\beta}] \mathcal{N}^{-2} [\bar{\beta}] \end{bmatrix} \quad (10)$$

$$\mathbf{C} = \varepsilon_o \begin{bmatrix} \mathcal{N}^2 - [\bar{\beta}]^2 & [\bar{\beta}] [\bar{\alpha}] \\ [\bar{\alpha}] [\bar{\beta}] & \mathcal{N}^2 - [\bar{\alpha}]^2 \end{bmatrix} \quad (11)$$

where the block Toeplitz-matrix

$$\mathcal{N}^2 = \begin{bmatrix} & & & & & \\ & & & & & \\ & \bar{\varepsilon}_0 & \bar{\varepsilon}_{-1} & \bar{\varepsilon}_{-2} & & \\ \cdots & \bar{\varepsilon}_{+1} & \bar{\varepsilon}_0 & \bar{\varepsilon}_{-1} & \cdots & \\ & \bar{\varepsilon}_{+2} & \bar{\varepsilon}_{+1} & \bar{\varepsilon}_0 & & \\ & & & & & \\ & & & & & \end{bmatrix} \quad (12)$$

with

$$\bar{\varepsilon}_m = \begin{bmatrix} & & & & & \\ & & & & & \\ & \bar{\varepsilon}_{m,0} & \bar{\varepsilon}_{m,-1} & \bar{\varepsilon}_{m,-2} & & \\ \cdots & \bar{\varepsilon}_{m,+1} & \bar{\varepsilon}_{m,0} & \bar{\varepsilon}_{m,-1} & \cdots & \\ & \bar{\varepsilon}_{m,+2} & \bar{\varepsilon}_{m,+1} & \bar{\varepsilon}_{m,0} & & \\ & & & & & \\ & & & & & \end{bmatrix} \quad (13)$$

is introduced in Eqs. (4) and (5).

Evidently, the diffraction of electromagnetic waves by objects with periodic structure can be modelled by coupled transmission lines [6], because they are also described by a wave equation of exactly the same form as given in Eqs. (4) and (5). It has to be pointed out that the definition of the matrix for the refractive index squared, \mathcal{N}^2 , allows this compact formulation.

As in transmission line theory, the square of a propagation constant in z -direction can be defined in Eq. (4):

$$[\gamma_z]^2 = -\omega_o^2 \mathbf{L} \mathbf{C} \quad (14)$$

Accordingly, a similar wave equation with propagation constant $-\omega_o^2 \mathbf{C} \mathbf{L}$ can also be deduced for the magnetic field.

Note, that the presented formulation is *exact*, because expansions (2) and (3) for $M, N \rightarrow \infty$ are both *rigorous*.

3 Analytical Solution

The system of second-order differential equations (4) can easily be solved by diagonalizing $[\gamma_z]^2$. If \mathbf{P} contains the right eigenvectors of $[\gamma_z]^2$, the propagation constants of the waves in the decoupled domain are given by the following diagonal matrix

$$[\tilde{\gamma}_z] = \pm \sqrt{\mathbf{P}^{-1} [\gamma_z]^2 \mathbf{P}} \quad (15)$$

A characteristic admittance and impedance can be defined as is also done in transmission line theory:

$$\mathbf{Y}_o = \mathbf{Z}_o^{-1} = \mathbf{P}^{-1} (j\omega_o \mathbf{L})^{-1} \mathbf{P} [\tilde{\gamma}_z] \quad (16)$$

$$= \mathbf{P}^{-1} (j\omega_o \mathbf{C}) \mathbf{P} [\tilde{\gamma}_z]^{-1} \quad (17)$$

The solutions to the wave equation (4) are exponential functions. After rearranging terms, the analytical solutions can assume the form

$$\begin{bmatrix} \mathbf{U}(z) \\ \mathbf{I}(z) \end{bmatrix} = \underbrace{\mathbf{T} \tilde{\mathbf{A}}(z) \mathbf{T}^{-1}}_{\mathbf{A}(z)} \begin{bmatrix} \mathbf{U}(z_0) \\ \mathbf{I}(z_0) \end{bmatrix} \quad (18)$$

where

$$\mathbf{T} = \begin{bmatrix} \mathbf{P} & \mathbf{0} \\ \mathbf{0} & \mathbf{P} \mathbf{Y}_o \end{bmatrix} \quad (19)$$

and

$$\tilde{\mathbf{A}}(z) = \begin{bmatrix} \cosh([\tilde{\gamma}_z]z) & \sinh([\tilde{\gamma}_z]z) \\ \sinh([\tilde{\gamma}_z]z) & \cosh([\tilde{\gamma}_z]z) \end{bmatrix} \quad (20)$$

Matrix \mathbf{A} denotes the chain matrix for one layer. For a homogeneous layer, the eigenvalues are explicitly given so that the chain matrix simplifies accordingly.

The electromagnetic field in a structure consisting of cascaded layers is easily obtained once the chain matrix of each layer has been computed. If \mathbf{A}_i corresponds to the chain matrix of layer i in Fig. 1, the electromagnetic field in a plane $z, z_3 \leq z \leq z_4$ is then given by the product of the respective chain matrices:

$$\begin{bmatrix} \mathbf{U}(z) \\ \mathbf{I}(z) \end{bmatrix} = \mathbf{A}_4(z - z_3) \mathbf{A}_3(d_3) \mathbf{A}_2(d_2) \mathbf{A}_1(d_1) \begin{bmatrix} \mathbf{U}(z_0) \\ \mathbf{I}(z_0) \end{bmatrix} \quad (21)$$

In the same manner, the total electromagnetic field in arbitrarily bi-periodic structures can be computed to any desired accuracy. This is achieved through slicing the bi-periodic region into layers which are constant in z , so that the above solution can be utilized; the thinner the layers the higher the accuracy. The overall chain matrix is again calculated as the product of the chain matrices of the respective layers.

4 Numerical Example

In Figs. 2 and 3, the magnitude of the x -component of the total electric field is illustrated for the case, that an incident Gaussian beam at 65GHz (beam waists $w_{ox} = w_{oy} = 10\text{mm}$) is splitted by a binary grating as shown in Fig. 1. The values of the design parameters are as follows: $\varepsilon_1 = \varepsilon_4 = 1$, $\varepsilon_2 = \varepsilon_3 = 2.25$, $d_1 = 8.7\text{mm}$, $d_2 = 5.8\text{mm}$, $d_3 = 15.0\text{mm}$, $d_4 = 30.5\text{mm}$, $L_x = 7.0\text{mm}$, $L_y = 8.3\text{mm}$, $b_x = 5.6\text{mm}$, $b_y = 3.3\text{mm}$. The incident beam has only an x -component, so that no y -component of the total electric field exists. The images have been produced by using a more elaborated version of the analysis presented here.

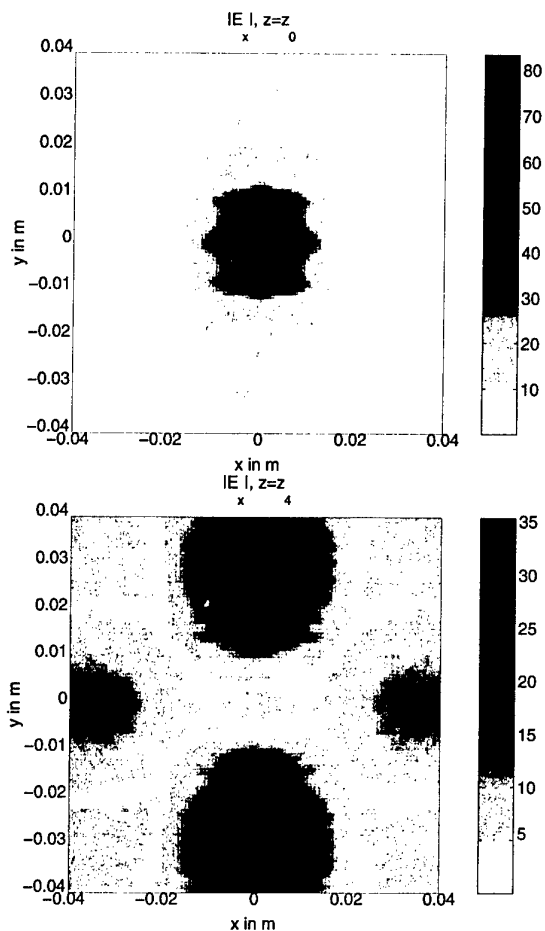


Figure 2: $|E_x|$ -component of the total electric field in planes $z = z_0$ and $z = z_1$

5 Conclusions

Since all techniques applied in transmission line theory can also be applied to the diffraction of electromagnetic fields at biperiodic structures, the analysis presented still incorporates many imaginable extensions of the theory. For instance, reflection and transmission coefficients in matrix form can be defined in a similar fashion as has been shown for the propagation constant and the characteristic admittance/impedance. By introducing a complex permittivity, the analysis presented here can also be extended to metallic gratings. Furthermore, the diffraction of electromagnetic beams can be treated, if they are periodically shifted [7].

To summarize, an efficient and compact analysis method has been presented which allows the analytical solutions known from transmission line theory to be applied to electromagnetic fields diffracted by objects with periodic structure in one, two, and three dimensions. As indicated, further generalizations of the theory are possible.

Acknowledgement

The authors appreciate the fruitful discussions with Prof. Schünemann and Dr. Shahabadi of Technische Universität Hamburg-Harburg.

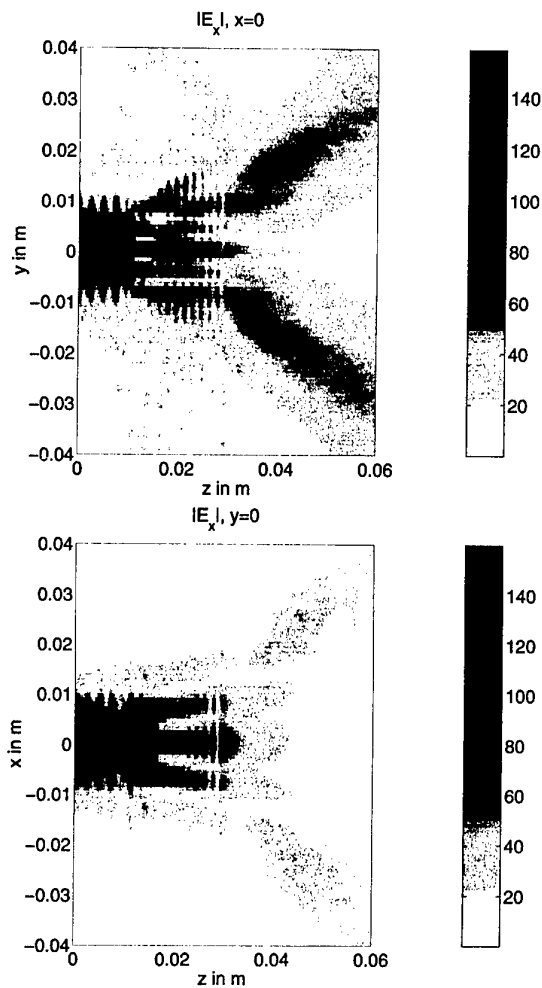


Figure 3: $|E_x|$ -component of the total electric field in planes $x = 0$ and $y = 0$

References

- [1] T.K. Gaylord, M.G. Moharam, *Proc. IEEE*, vol. 73, pp. 894-937, 1985
- [2] M. Shahabadi, K. Schünemann, H.-G. Unger, *IEEE MTT-Symposium*, Denver, USA, pp. 573-576, 1997.
- [3] J.M. Johnson, Y. Rahmat-Samii, *IEEE Ant. Prop. Mag.*, Vol. 39, No. 4, pp. 7-25, 1997
- [4] M. Akbari, K. Schünemann, H. Burkhard, *Optical and Quantum Electronics*, Bd. 32, pp. 991-1004, 2000
- [5] T. Magath, M. Akbari, *25th IRMMW*, Beijing, China, 2000
- [6] M. Shahabadi, K. Schünemann, H.-G. Unger, *20th IRMMW*, Orlando, USA, pp. 397-398, 1995.
- [7] M. Shahabadi, K. Schünemann *20th ESTEC Antenna Workshop on Millimeter Wave Antenna Technology and Antenna Measurement*, Noordwijk, Netherlands, pp. 99-104, 1997.

An optoelectronic cw THz source for imaging applications

Karsten Siebert, Gregor Segschneider, Holger Quast, Hartmut G. Roskos, Soenke Tautz, Peter Kiesel, Gottfried Döhler, Viktor Krozer

Abstract – We report on optoelectronic generation of continuous-wave (cw) THz radiation from a two-colour Ti:sapphire laser source. The laser emits two beams with a frequency difference between 1 GHz and 50 THz simultaneously. For the photomixing of the two frequencies, planar dipole and microstrip patch antennas based on low-temperature-grown (LT-)GaAs are examined. THz powers up to 60 nW at 450 GHz are achieved. Potential applications of this cw THz source for imaging are discussed.

I. INTRODUCTION

Application of optoelectronically generated THz radiation in imaging has recently been identified to be a realistic goal of research [1,2]. All THz imaging work up to now has been performed with femtosecond laser systems. However, cw THz systems can be advantageous because of the following reasons: (i) They can be operated with laser diodes which implies a reduction in cost, size and complexity of the laser source. From a commercial point of view this is the main advantage over conventional femtosecond-laser-based systems. (ii) In addition, cw systems have technological advantages such as their higher spectral brightness in combination with a better frequency resolution. The latter stems from the fact that the frequency stability of the emitted radiation and thus the spectral resolution of the cw system is limited by the frequency stability of the laser source (typically ~ 100 kHz), whereas for pulsed systems the frequency resolution is given by the scanned length of the delay line (the resolution is approx. 1 GHz for 15-cm scan length). (iii) Last but not least, data acquisition with cw systems has the prospect of being less time-consuming as no Fourier transformation or pattern recognition is needed to obtain information for a specific frequency. On the other hand, obtaining wide-band spectra is and remains the strong point of femtosecond-laser-based THz systems.

Heterodyne downconversion, or photomixing, of two infrared optical frequencies is a promising way to gener-

ate tunable cw electromagnetic radiation in the GHz and THz frequency bands. Previous investigations mainly focused on two independent laser sources [3,4] or two-colour diode lasers [5,6] for photomixing.

We present a Ti:sapphire laser which emits two near-infrared beams from a single cavity. Both beams can be tuned independently over a wavelength range of 100 nm which corresponds to difference frequencies from below 1 GHz up to 50 THz. The total output power is on the order of 250 mW at a pump power of 6 W. The photomixer is a planar photoconductive antenna with an ultrafast switch based on LT-GaAs and either a Hertzian dipole or a microstrip patch antenna as the radiating element.

We present an investigation of a measurement set-up basically suited (but not optimized yet) for cw THz imaging with a bolometer as a detector.

II. LASER SYSTEM

The two-colour laser is pumped by a single beam of an argon-ion laser operated in all-lines mode with an output power of 6 W. Figure 1 shows the linear, α -shaped resonator with a round-trip length of 1.36 m (corresponding to a 219.5-GHz spacing of the longitudinal modes).

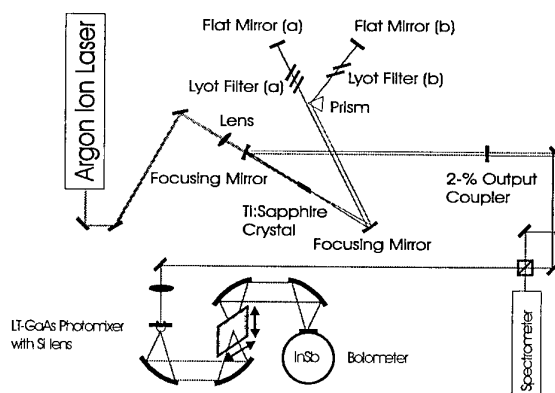


Fig.1: Two-colour Ti:sapphire laser with photomixing set-up in THz-imaging configuration

The laser cavity [7] consists of five mirrors, three of them being shared by both beams while two mirrors in the wavelength-selection segment are used by either beam only. Under all operation conditions, laser action with a circular TEM₀₀ Gaussian mode profile showing no sign of astigmatism is achieved. The two colours are emitted in parallel, but non-collinear beams. Beam (a) is

K. Siebert, G. Segschneider, H. Quast and H.G. Roskos are with the Physikalisches Institut der J.W. Goethe-Universität, Robert-Mayer-Str. 2-4, D-60054 Frankfurt.

S. Tautz, P. Kiesel and G. Döhler are with the Institut für Technische Physik I der Universität Erlangen, Erwin-Rommel-Str.1, D-91058 Erlangen.

V. Krozer is with the Fakultät für Elektrotechnik und Informationstechnik der TU Chemnitz, Reichenhainer Str. 70, D-09126 Chemnitz

tuned with a three-plate Lyot filter, beam (b) with a two-plate filter and a prism. The wavelength tuning curve is given in Fig. 2.

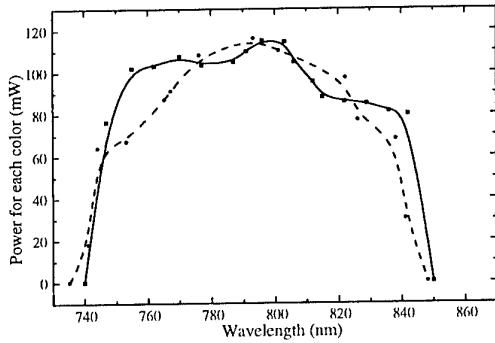


Fig. 2: Tuning spectrum of the two-color Ti:sapphire laser. Solid line: One frequency is fixed at 800 nm the other is tuned; Dotted line: Both frequencies are tuned with a fixed wavelength difference of 7 nm.

The solid line displays the tuning characteristics which can be achieved if one frequency is kept fixed at 800 nm. The dotted line is taken while both frequencies are tuned with a fixed wavelength difference of 7 nm between them. From interference measurements (see [7]), we obtain a FWHM width of each of the two optical lines of less than 150 MHz which suggests that the laser runs predominantly on a single longitudinal mode.

The data shown in Fig. 2 are obtained with a 2-% output-coupling mirror in the resonator. Replacing it with a 4-% output coupler increases the output power to 125 mW per beam in the central part of the spectrum.

III. PHOTOMIXING

For the first demonstration of photomixing applying the two-colour Ti:sapphire laser, we fabricated a planar Hertzian-dipole antenna on LT-GaAs. The antenna layout is shown schematically in Fig. 3. It is a design as often utilized in femtosecond THz systems.

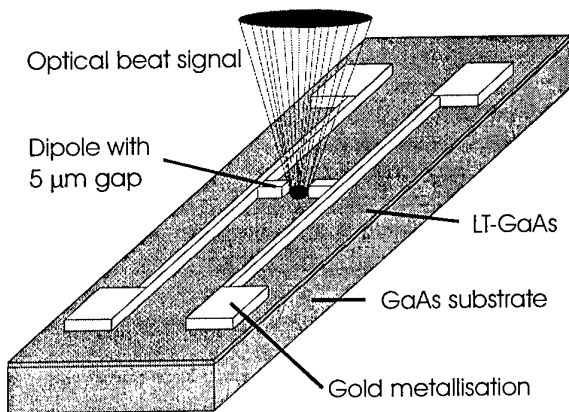


Fig. 3: Planar Hertzian-dipole photoconductive antenna on LT-GaAs

The antenna is made from thermally evaporated chromium/gold and patterned by photolithography and photo-

resist lift-off. The dipole length is chosen to be 50 μm yielding resonance of the antenna just above 1 THz. The dipole has a 5- μm -gap which serves as a photoconductive switch. On the substrate side of the antenna, a Si lens is mounted to collect the emission from the radiating structure. In order to drive the antenna at the optical beat signal, the two infrared beams emitted by the two-colour Ti:sapphire laser have to be overlapped on a beam combiner (see Fig. 1). The laser radiation is then focused with a 2-cm lens onto the photoconductive switch. For the detection of the THz radiation, we apply an InSb hot-electron bolometer.

Due to the bandwidth limitations of the InSb bolometer, THz signals can only be measured up to 460 GHz. This is far below the resonance frequency of the antenna. At 460 GHz, about 0.02 nW of THz power (calibration of the bolometer) is measured for an optical pump power of 55 mW and a bias voltage of 25 V applied to the switch.

A more promising device in terms of the emitted power was developed based on an emitter concept known from the very first experiments on the generation of GHz radiation by photomixing of two infrared beams by Brown et al. [8]. The layout of our device can be described as a microstrip patch antenna and is displayed in Fig. 4.

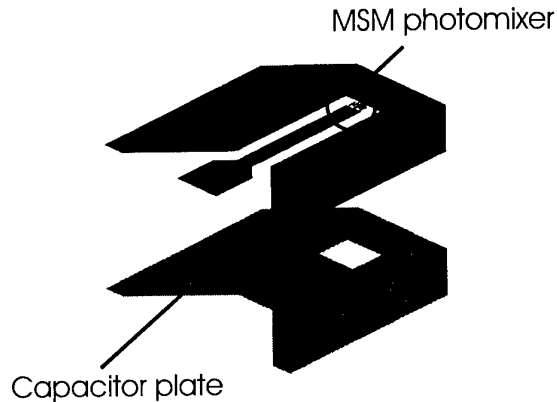


Fig. 4: Exploded view of the folded microstrip patch antenna with metal-semiconductor-metal (MSM) interdigitated photoconductive switch

In the work described in [8], operation of the photomixer was limited to frequencies up to 50 GHz due to constraints in the design and size of the device which were determined by the fact that the measurements were made with a HF spectrum analyser connected to the device via a coaxial cable. In contrast, we perform free-space measurements and are free from these limiting factors in the design.

While the emitter of [8] consists of a single planar metal structure, our emitter is based on a capacitor-like double-layer design. Details concerning the emitter can be found in [9]. Briefly summarized: The top layer is a coplanar waveguide structure whose centre conductor is in Ohmic contact with the bottom layer; otherwise, the two layers are separated from each other by a 1- μm -thick polyimide film. The photoconductive switch is located at one end of the coplanar waveguide. It consists of four-finger interdigitated electrodes which are defined on a LT-GaAs epi-

taxial layer transferred by lift-off technology from the GaAs growth substrate onto a glass substrate. The width of the metal fingers is 3 μm , the distance between adjacent fingers is also 3 μm .

When excited with the far-infrared beat signal, the device exhibits a pronounced resonance in the emission spectrum at 439 GHz (for the data, see [9]). The resonance curve has a FWHM of 55 GHz. The THz power emitted at resonance is on the order of 60 nW for 9-mW optical pump power and a bias of 20 V.

The patch antennas investigated so far were processed by epitaxial lift-off onto a glass substrate. As a result of the low heat conductivity of glass, the MSM switch was thermally damaged when the optical power exceeded 10 mW. If left on the semiconductor growth substrate, the MSM photomixers should sustain optical powers up to 70 mW [10]. This fact clearly points the way toward further improvements of the emitter.

The tunability of the device is clearly limited due to its resonant behaviour. For wide-band imaging applications, this may seem to be a disadvantage. One has to keep in mind, however, that a narrow-band emitter can be optimized for both higher maximum output power and better noise rejection than a wide-band radiator. With different mixers designed for various discrete frequencies of interest, one can achieve a broad wavelength coverage while keeping the advantages of a narrow-band emitter.

IV. CW THz IMAGING

For the first tests of THz imaging with a cw system we employ a set-up as shown in Fig. 1. Behind the photomixer, the divergent radiation is collimated and focused onto the sample with two off-axis paraboloidal mirrors. The radiation transmitted through the sample is collected by another set of paraboloidal mirrors and focused into the bolometer.

The object to be imaged can be raster-scanned in the focus of the THz beam with the help of a x-y-stage while recording the transmittivity at each pixel with the InSb bolometer. The first structures which we have examined are various objects consisting of THz-absorbing materials like metal and carbon (data to be published elsewhere). Our measurements indicate that intensity-contrast imaging with cw THz radiation is feasible and that it takes no more time to obtain an image than with femtosecond-laser-based systems.

Due to the relatively large wavelength at frequencies below 450 GHz, the spatial resolution is still rather poor. This will change, when higher frequencies are accessible upon replacement of bolometric detection by coherent homodyne detection, i.e., photoconductive [11] and electrooptic sampling [12].

V. CONCLUSIONS

We presented a two-colour Ti:sapphire laser which emits two near-infrared beams simultaneously with a maximum output power of 250 mW for both colours together. The difference frequency is tuneable from 1 GHz to 50 THz. We have demonstrated photomixing with a photoconductive switch integrated into either a Hertzian-dipole antenna or a microstrip patch antenna. For the patch antenna, we achieve a THz output power of 60 nW at 439

GHz, when pumped with 9 mW of optical power. Finally, the principal suitability of our cw measurement systems for THz imaging was corroborated.

References

1. B.B. Hu, M.C. Nuss, "Imaging with THz waves", *Optics Lett.*, Vol. 20, pp. 1716-1718, 1995
2. D.M. Mittleman, M. Gupta, R. Neelamani, R.G. Baraniuk, J.V. Rudd, M. Koch, "Recent advances in terahertz imaging", *Appl. Phys. B*, Vol. B 86, pp. 1085-1094, 1999
3. E.R. Brown, K.A. McIntosh, K.B. Nichols, C.L. Dennis, "Photomixing up to 3.8 THz in low-temperature-grown GaAs", *Appl. Phys. Lett.*, Vol. 66, pp. 285-287, 1995
4. K.A. McIntosh, E.R. Brown, K.B. Nichols, C.L. Dennis, O.B. McMahon, W.F. DiNatale, T.M. Lyszczarz, "Terahertz photomixing with diode lasers in low-temperature-grown GaAs", *Appl. Phys. Lett.* Vol. 67, pp. 3844-3846, 1995
5. P. Gu, M. Tani, M. Hyodo, K. Sakai, T. Hidaka, "Generation of cw-terahertz radiation using a two-longitudinal mode laser diode", *Jpn. J. Appl. Phys.*, Vol. 37, pp. L976-L978, 1998
6. P. Gu, F. Chang, M. Tani, K. Sakai, C.L. Pan, "Generation of coherent cw-terahertz radiation using a tunable dual-wavelength external cavity laser diode", *Jpn. J. Appl. Phys.*, Vol. 38, pp. L1246-L1248, 1999
7. F. Siebe, K. Siebert, R. Leonhardt, H.G. Roskos, "A fully tunable dual-color Ti:Al₂O₃ laser", *IEEE Journ. Quantum Electronics*, Vol. 35, No. 11, pp. 1731-1736, 1999
8. E.R. Brown, K.A. McIntosh, F.W. Smith, M.J. Manfra, C.L. Dennis, "Measurements of optical-heterodyne conversion in low-temperature-grown GaAs", *Appl. Phys. Lett.*, Vol. 62, No. 11, pp. 1206-1208, 1993
9. C. Steen, S. Tautz, P. Kiesel, G.H. Döhler, G. Segschneider, K. Siebert, H.G. Roskos, V. Krozer, "Observation of THz oscillations and efficient THz emission from contacted low-temperature-grown GaAs structures", see *Proceedings of 8th International THz Conference*, 2000
10. S. Verghese, K.A. McIntosh, E.R. Brown, "Optical and terahertz power limits in the low-temperature-grown GaAs photomixers", *Appl. Phys. Lett.*, Vol. 71, No. 19, pp. 2743-2745, 1997
11. S. Verghese, K.A. McIntosh, S. Calawa, W.F. Dinatale, E.K. Duerr, K.A. Molvar, "Generation and detection of coherent terahertz waves using two photomixers", *Appl. Phys. Lett.*, Vol. 73, No. 11, pp. 3824-3826, 1998
12. A. Nahata, J.T. Yardley, T.F. Heinz, "Free-space electro-optic detection of continuous-wave terahertz radiation", *Appl. Phys. Lett.*, Vol. 75, No. 17, pp. 2524-2526, 1999

Analysis and Design of Quasi-Optical Filters

Maurizio Bozzi and Luca Perregrini

Abstract – This paper presents an optimisation procedure for the automatic design of frequency selective surfaces. The optimisation tool is based on the genetic algorithm, and embeds an analysis method we recently developed. The implementation of the optimisation code and its application are described, and the major advantages of the method are discussed. An example is also reported, where the code is applied to the optimisation of frequency selective surfaces with circular holes.

I. INTRODUCTION

Metal screens perforated periodically with apertures are used as *Frequency Selective Surfaces* (FSSs) from the microwave to the infrared region [1,2]. Their design requires both a fast and flexible analysis code and an efficient optimisation tool, especially when tight electrical constraints are imposed.

Recently, we presented a novel algorithm for the analysis of FSSs, consisting of a thin [3] or thick [4] metal screen perforated periodically with arbitrarily shaped apertures (Fig. 1). This algorithm is based on the Method of Moments (MoM) and on the Boundary Integral-Resonant Mode Expansion (BI-RME) method [5], and has been implemented in a computer code. This code was widely applied to the analysis of FSSs both in the microwave [6] and in the THz region [7], showing its efficiency, flexibility and reliability. These capabilities make possible its use within a procedure aiming at the automatic design of FSSs.

The optimisation procedure requires the minimisation of a properly defined *cost function*, which represents the distance between the actual and the desired behaviour of the FSS. The minimisation of the cost function can be reached via either local or global search methods. The local search methods (*i.e.*, gradient descend methods) are usually very fast if the starting point is close to the final solution. However, they run the risk to be trapped in a local minimum, especially when the cost function is particularly uneven. On the contrary, the global search methods (*e.g.*, the evolutionary approaches) are able to investigate the whole space of the possible solutions, avoiding the local minimum problem. For this reason, we implemented an optimisation tool, based on the Genetic Algorithm (GA), intended for the automatic design of FSSs.

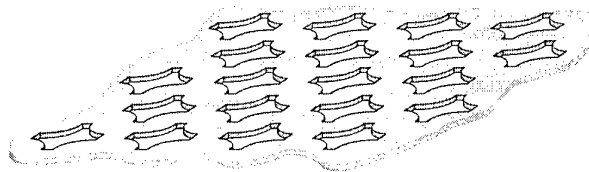


Fig. 1: A thick metal screen perforated periodically with arbitrarily shaped apertures.

In this paper, we briefly discuss the analysis algorithm and the optimisation procedure, and present the preliminary results in the optimisation of FSSs with circular holes. The investigation of this simple structure permits to better understand the capabilities of the GA, highlighting advantages and drawbacks intrinsic of this approach. Some final remarks indicate a possible improvement of the optimisation procedure that will permit to overcome the drawbacks, while keeping all the advantages of the GA approach.

II. MOM/BI-RME ANALYSIS OF FSSs

When considering FSSs whose overall dimensions are larger than the cross-section of the impinging electromagnetic wave (as usually happen when considering a focused beam), the analysis of the FSS can be carried out under the infinite array approximation. In fact, in that case, the contribution to the scattered wave due to the diffraction at the edges of the FSS is negligible. Under this hypothesis, and representing the impinging wave as a uniform plane wave, by using the Floquet theorem the study of the FSS reduces to the investigation of a single unit cell with periodic boundary conditions (Fig 2).

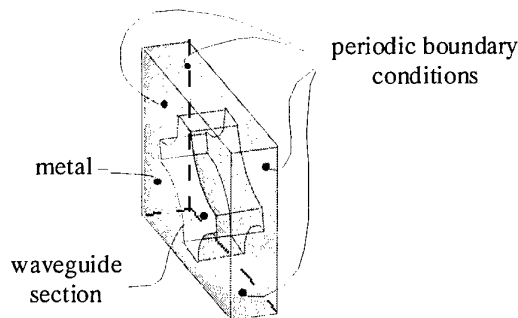


Fig. 2: Unit cell of the periodic structure of Fig. 1

The authors are with the Department of Electronics, University of Pavia, Via Ferrata 1, 27100 Pavia, Italy.
Phone: +39-0382505223, fax: +39-0382422583,
e-mail: m.bozzi@ele.unipv.it, l.perregrini@ele.unipv.it

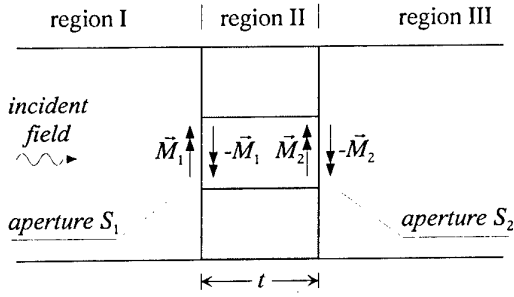


Fig. 3: Side view of the unit cell after the application of the equivalence theorem.

The analysis of the unit cell is based on the application of the equivalence theorem: the terminal cross-section of the waveguide section shown in Fig. 2 are closed by perfect metal sheets, and unknown magnetic current densities are considered over them to guarantee the continuity of the electric and magnetic fields across the apertures S_1 and S_2 (Fig. 3).

Thus, the fields in free-space (region I and III) are expressed as a combination of Floquet modes, whereas the fields in the waveguide (region II) are represented as a combination of the modal fields of the waveguide.

By enforcing the continuity of the tangential components of the electric and magnetic fields on S_1 and S_2 , two coupled integral equations are obtained, which are solved by the MoM (see [3,4], for more details).

The use of the MoM requires the choice of a suited set of basis and test functions to represent the (unknown) magnetic current and to test the integral equations. The choice of the basis functions greatly affect the accuracy, flexibility and efficiency of the method. The better choice is to consider entire domain basis functions, *i.e.*, functions that span the entire domain where the unknown quantities are defined and satisfy the proper boundary conditions. In our problem these functions are the electric modal fields of the waveguide shown in Fig. 2. In the past, entire domain basis functions were used only for circular or rectangular holes, since in these cases they are known analytically [1].

We extended the use of entire domain basis functions to the case of arbitrarily shaped aperture, exploiting the capabilities of the BI-RME method [5]. This method is very fast and flexible, and allows for calculating a large number of modes of an arbitrarily shaped waveguide in a few seconds.

Furthermore, the BI-RME method yields as a primary result the boundary values of the potentials of the TE and

TM waveguide modes. These results can be used for a direct calculation of the integrals involved in the MoM matrices, by reducing surface to line integrals [3,4].

The possibility of considering arbitrarily shaped apertures adds degree of freedom in tailoring the frequency response of the FSS, and, moreover, it allows for taking into account the unavoidable inaccuracies due to the fabrication process, *e.g.* rounding of edges or corners in the aperture shape [7].

III. EVOLUTIONARY OPTIMIZATION OF FSSS

Optimisation tools based on the Genetic Algorithm (GA) received particular attention in the last years [8,9,10,11].

The major advantage of the evolutionary approach with respect to standard optimisation tools (*e.g.*, gradient descent methods, Quasi-Newton methods) is the robustness: in fact, the evolutionary methods explore the whole space of solutions, with no risk of being trapped in a local minimum. Moreover, no initial guess or tentative solution is required to the user.

The basic idea of the evolutionary optimisation originates from the human genetics: the geometrical data of the FSS are coded as the genes of a chromosome (Fig. 4). Firstly, a population of chromosomes is randomly generated. A *fitness* value is calculated for each element of the population. The value of this parameter indicates how well the performance of the corresponding FSS satisfies the optimisation target. The target consists of a list of required transmission or reflection coefficient in a number of frequency points. The fitness depends on the Euclidean distance between the required and the achieved performance: the higher the fitness, the closer to the target. Then, new generations of the population are created, through the mechanisms of selection, cross-over and mutation [12]. Chromosomes are selected on the basis of favouring individuals with higher fitness, which reflects how well the individual fits the environment. After a number of generations, the best fitting chromosome is taken as the optimal solution of the problem.

Besides the optimal solution, the algorithm provides a population of chromosomes, which are *quasi*-optimal solutions. In fact, some of these chromosomes present a fitness slightly worse than the optimal one. Nevertheless, these solutions could be interesting from a mechanical or technological point of view, if they either guarantee better mechanical features (*e.g.*, stiffness) or are easier to fabricate.

We implemented a genetic optimisation routine, based on the GA library PGA-Pack [13]. This optimisation routine embeds our analysis code based on the BI-RME method. Even if the analysis code permits to manage with FSSs comprising arbitrarily shaped apertures, we preliminary limited the optimisation code to FSSs with circular holes. In this case, in fact, only five geometrical quantities are needed to characterise the FSS (Fig. 4a), and the check for the physical consistence of the structure is trivial. This allowed us for deeply investigating the effect of the GA parameters on the optimisation process. We decided to use chromosomes with five real genes (Fig. 4b), which are selected by a binary tournament or probabilistic tournament selection and combined through uniform cross-over; furthermore, a mutation rate ranging from 1% to 5% is applied.

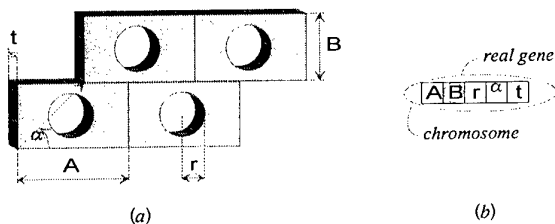


Fig. 4: Structure of a FSS with circular holes (a) and the corresponding chromosome (b).

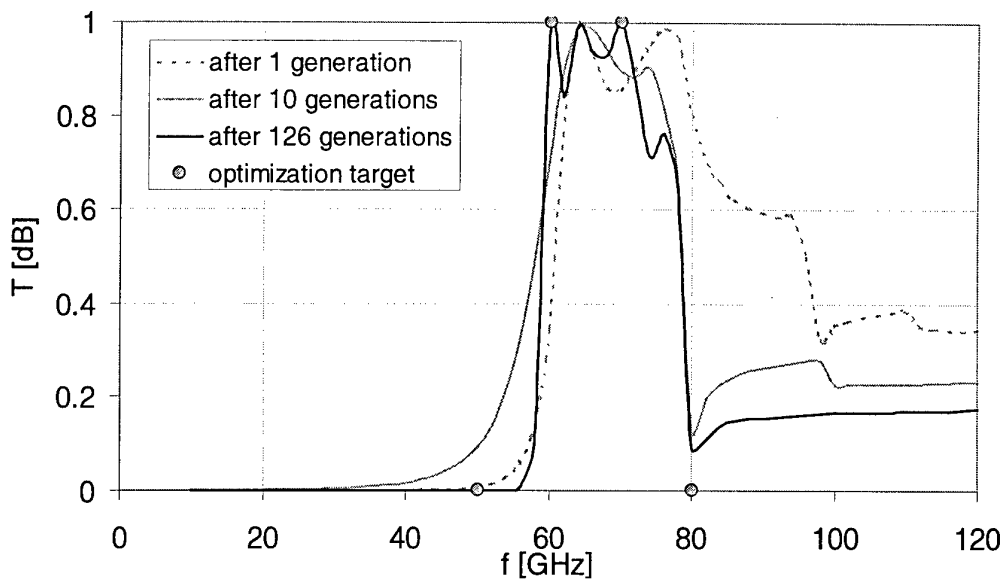


Fig. 5: Power transmittance of the FSS with circular holes vs. operation frequency (TM mode, normal incidence): best solution after 1, 10, and 126 generations.

IV. PRELIMINARY RESULTS

The example we present refers to the optimisation of an FSS with circular holes (Fig. 4a). This structure has been widely investigated for applications in the THz region [7,14], and empirical formulas for its design has been derived. Therefore, the choice of this test structure permits to gain an insight into the behaviour of the GA.

The optimisation targets are imposed in four frequency points: total reflection of the TM mode at 50 and 80 GHz, total transmission of the TM mode at 60 and 70 GHz (see the dots in Fig. 5). Normal incidence is considered.

The population size was fixed at 250 chromosomes. At each generation, 40 chromosomes were discarded and replaced by using probabilistic tournament selection, cross-over and 5% mutation rate.

Fig. 5 shows the frequency response of the FSS corresponding to the best chromosome of the population after 1, 10, and 126 generations. After 126 generation all the targets were practically satisfied, and no further significant improvement was observed.

To deeply understand the behaviour of the GA, we reported in Fig. 6 the historical evolution of the optimisation parameters (genes), as well as of the distance to target. It can be observed that some parameters (e.g., the radius R of the holes and the thickness t) converge rapidly to the final value. This fact is not surprising since these parameters determine the resonant frequency of the filter (the radius) and the slope of the transmission parameter (the thickness) [14].

The GA method always converges to the required solution, but, however, the rate of convergence becomes slow when approaching the target. This is an intrinsic drawback of the GA approach. In fact, at the beginning of the procedure, the mutation permits to rapidly investigate the space of the possible solutions, locating a set of solutions near to the target. On the contrary, the algorithm is not clever enough to rapidly refine these

solutions. For this reason, a better approach could consist in coupling the GA optimisation procedure with a local search minimisation method. We implemented this hybrid approach for the analysis of non-linear circuits [15], obtaining, in some case, a dramatic improvement of the efficiency of the code. This hybrid optimisation approach uses the GA for finding a reasonable initial guess and then a gradient based method for its refinement. With this approach we will keep unchanged the flexibility and reliability of the optimisation code (no initial guess required, convergence guarantee), while improving its efficiency.

V. CONCLUSION

In this paper, we presented the implementation of a GA optimisation code for FSSs. The code was preliminarily applied to the optimisation of metal screens perforated periodically with circular holes, with the aim of fully investigating the GA parameters. Although this tool allows for the automatic optimisation of FSS, without any need for human intervention or initial guess, the convergence rate becomes slow when approaching the target. For this reason, a better approach could be the coupling of the GA with a local search optimisation method. This hybrid optimisation approach, starting with the GA for finding a reasonable initial guess and then inserting a gradient based method, could strongly reduce the computing time.

VI. ACKNOWLEDGEMENT

The authors would like to express their acknowledgements to Dr. C. Zuffada for stimulating their interest in the Genetic Algorithm, and Dr. P. Gasparini for his help in the implementation of the code.

This work was supported by the University of Pavia under the FAR funding and the Young Researcher Programme.

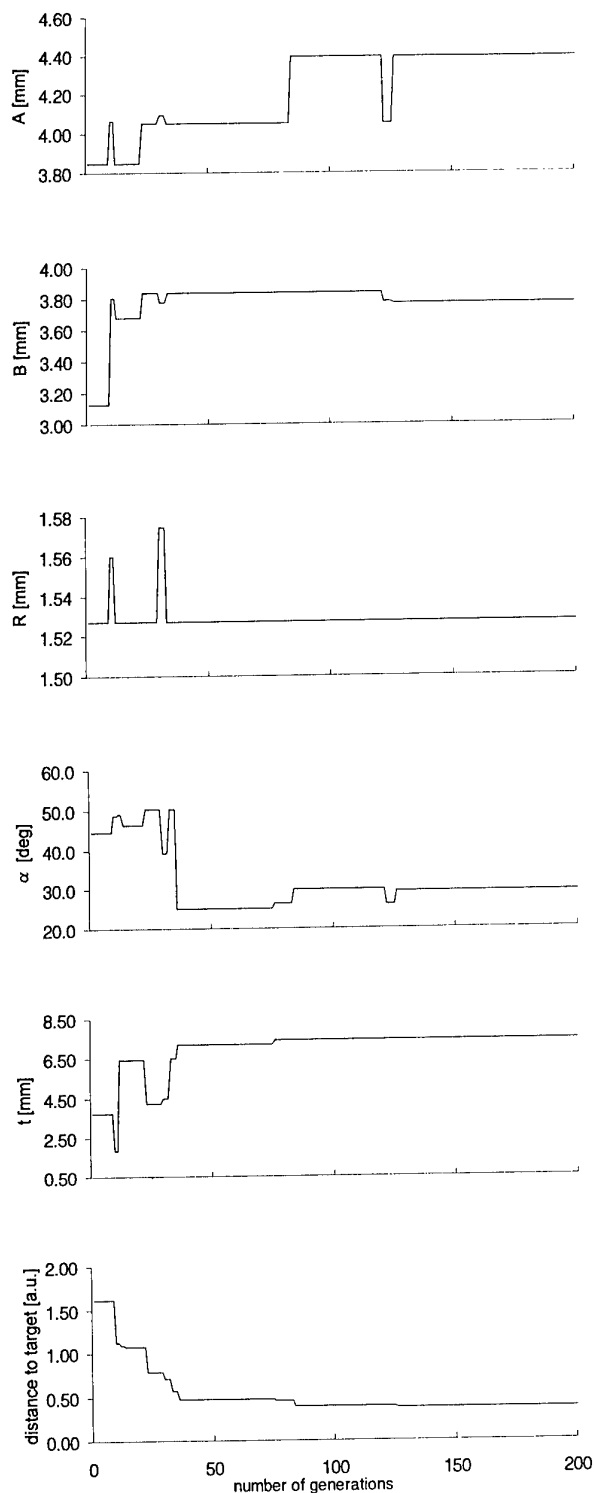


Fig. 6: Historical evolution of geometrical quantities (genes) and distance to target during the optimisation of FSS with circular holes.

VII. REFERENCES

1. T. K. Wu, *Frequency Selective Surface and Grid Array*, John Wiley and Sons, 1995.
2. J. C. Vardaxoglou, *Frequency Selective Surfaces*, John Wiley and Sons, 1997.
3. M. Bozzi and L. Perregrini, "Efficient analysis of thin conductive screens perforated periodically with arbitrarily shaped apertures," *IEEE Electronics Letters*, Vol. 35, No. 13, pp. 1085–1087, 24 June 1999.
4. M. Bozzi, L. Perregrini, J. Weinzierl, and C. Winnewisser, "Efficient Analysis of Quasi-Optical Filters by a Hybrid MoM/BI-RME Method," submitted to *IEEE Transactions on Antennas & Propagation*.
5. G. Concinauro, M. Guglielmi, R. Sorrentino, *Advance Modal Analysis, CAD Techniques for Waveguide Components and Filters*, John Wiley and Sons, Chap. 5, 1999.
6. M. Bozzi, L. Perregrini, P. Besso, P. Gianola, R. Maddè, S. Junker, "Design of an inductive frequency selective surface with cross shaped holes," *Proc. of the Millenium Conference on Antennas & Propagation (AP2000)*, Davos, Switzerland, April 9–14, 2000.
7. M. Bozzi, L. Perregrini, J. Weinzierl, and C. Winnewisser, "Design, Fabrication and Measurement of Frequency Selective Surfaces," *Optical Engineering*, Vol. 39, No. 8, Aug. 2000.
8. E. Michielssen and Y. Rahmat-Samii, *Electromagnetic Optimization by Genetic Algorithms*, John Wiley and Sons, 1999.
9. D.S. Weile and E. Michielssen, "Design of doubly periodic filter and polarizer structures using a hybridized genetic algorithm," *Radio Science*, Vol. 34, No. 1, pp.51–63, Jan.–Feb. 1999.
10. G. Manara, A. Monorchio, and R. Mittra, "Frequency selective surface design based on genetic algorithm," *IEEE Electronics Letters*, Vol. 35, No. 17, pp. 1400–1401, 19 Aug. 1999.
11. J. M. Johnson and Y. Rahmat-Samii, "Genetic Algorithms and Method of Moments (GA/MOM) for the Design of Integrated Antennas," *IEEE Transactions on Antennas & Propagation*, Vol. 47, No. 10, Oct. 1999.
12. D. E. Goldberg, *Genetic algorithm in search, optimization and machine learning*, Addison-Wesley Publishing Company, Inc., 1989.
13. D. Levine, *User guide to the PGAPack parallel genetic algorithm library*, ANL-95/18, Argonne National Laboratory, 1996. (Available via anonymous ftp from ftp.mcs.anl.gov in the file pub/pgapack/pgapack.tar.Z)
14. C. Winnewisser, F. Lewen, J. Weinzierl, and H. Helm, "Transmission features of frequency-selective components in the far infrared determined by terahertz time-domain spectroscopy," *Appl. Optics*, Vol. 38, pp. 3961–3967, 1999.
15. M. Bozzi, M. Saglam, M. Rodriguez-Girones, L. Perregrini, H. L. Hartnagel, "A novel evolutionary approach for the analysis and optimization of THz nonlinear circuits," *8th International Conference on Terahertz Electronics*, Darmstadt, Germany, 28–29 September 2000.

Attempt to Generate Narrow Linewidth, CW Terahertz Radiation by Using Optical Frequency Comb

S. M. Ifthiqar, Kiyomi Sakai, Masahiko Tani,
Bambang Widiyatmoko, Motonobu Kourogi, Motoichi Otsu

Abstract- We report on an attempt to generate highly stable continuous terahertz (THz) wave by using optical frequency comb (OFC). About 10-nm wide OFC has been generated through a deep phase modulation of a 852 nm laser line in lithium niobate crystal cavity. The multiple optical modes (side bands) of the OFC, which are equally separated from each other by the modulation frequency (=6 GHz) are taken as the frequency reference. When another semiconductor laser is frequency locked, the stability of the difference frequency between the master laser and the second laser is improved on the same order of the RF modulator. An ultra-narrow, line and tunable THz radiation source can be achieved by photomixing of this stable difference-frequency optical beat in a photoconductive antenna.

I. INTRODUCTION

Generation of submillimeter wavelength (THz) radiation through photomixing, or optical-heterodyne conversion of two single mode laser beams in a photoconductive antenna [1] is a promising approach in realizing a stable and tunable THz radiation source. The stability (linewidth) and tunability of this kind of radiation source is mostly determined by those of the optical pump source. Semiconductor lasers are good candidates as the excitation laser source because of its wide tunability, compactness, and the ease for the operation. In addition, the advanced diode laser technology is already available at hand. For example, two external grating-stabilized diode lasers were used as the photomixing source, and a wide tunability (0.6-3.2 THz) and a linewidth of ~5 MHz was achieved [2]. A Fabry-Perot cavity was used to further stabilize the diode lasers, and a linewidth about 1 MHz was achieved [3]. The Fabry-Perot cavity shows a optical frequency comb in transmission spectrum, whose mode separation corresponds to the FSR (Free Spectral Range) of the cavity. However, the linewidth of a mode ($\Delta\nu$), which is determined by the finesse of the Fabry-Perot cavity ($\Delta\nu = \text{FSR}/\text{finesse}$), is usually on a MHz order. The modes in such a passive optical device are also subject to mechanical and temperature instabilities.

With the recent advancement in the opto-electronics we can now generate an optical frequency comb by a deep phase modulation of a continuous-wave (cw) laser beam [4]. For example, some of the co-authors demonstrated an optical frequency comb generation with a bandwidth

of 4 THz (mode separation=5.8 GHz) and a mode stability about 30 Hz at 1.55 μm line from a diode laser by using a LiNbO_3 crystal cavity as the phase modulator [5]. In this work we have tried to stabilize two diode lasers by using an optical frequency comb (OFC).

The OFC is a result of a deep phase modulation of a laser beam and consists of many sidebands around the carrier line due to the phase modulation. It is equivalent to phase modulated (or phase locked) pulses, whose repetition frequency is corresponding to the RF modulation frequency (twice of it). Once such an OFC is achieved, a second laser can be frequency or phase locked to one of the OFC sideband. The difference frequency between the second laser and the master laser used for OFC (or a third laser locked to a different mode of the OFC) is stabilized to the order of the stability obtained by the RF modulator, for which a stability of $\Delta\nu = 10^{-10}$ is easily achieved. In addition to the good stability, the absolute difference frequency (ν_{dif}) can also be determined by the mode difference number (k) and the off-set frequency of the laser line to a mode of the OFC (ν_{offset}): $\nu_{\text{dif}} = \nu_{\text{offset}} + k\nu_{\text{mod}}$, where ν_{mod} is the modulation frequency. The mode difference number k can be determined from the relation that $\Delta\nu_{\text{dif}} = k\Delta\nu_{\text{mod}}$, where $\Delta\nu_{\text{mod}}$ is the variation in the modulation frequency and $\Delta\nu_{\text{dif}}$ is the change in the difference frequency (both are measurable values).

The narrow line and tunable THz radiation source is desired for the high-resolution molecular spectroscopy, because the vibrational and rotational transition in molecules or molecular radicals are observed in the THz frequency range. In astro-physics, there is a big demand for a compact and stable THz local oscillator for the heterodyne detection of millimeter and submillimeter wavelength radiation, for example, in VLBI [6] or satellite observatories for precise positioning of heavenly bodies and spectroscopy of interstellar molecular gases, respectively.

S. M. Ifthiqar, K. Sakai and M. Tani are with the Terahertz Optoelectronic Research Group, Kansai Advanced Research Center, CRL (MPT), 588-2 Iwaoka, Iwaoka-cho, Nishi-ku, Kobe, Hyogo 651-2401, Japan
B. Widiyatmoko, M. Kourogi and M. Otsu are with the Interdisciplinary Graduate School of Science and Technology, Tokyo Institute of Technology, 4259 Nagatsuta, Midori-ku, Yokohama, Kanagawa 226, Japan, & Kanagawa Academy of Science and Technology, KSP East building, Room 408, 3-2-1 Sakado, Takatsu-ku, Kawasaki, Kanagawa 213, Japan

II. : OPTICAL FREQUENCY COMB GENERATOR (OFCG)

A 852-nm diode laser beam is phase modulated in a lithium niobate (LiNbO₃) crystal with a monolithic Fabry-Perot cavity. One of the cavity mirrors is a plane mirror and the other is a spherical mirror with a radius of curvature of 50 mm. Details of the OFCG can be obtained in [7]. In our experiment the crystal length is 22 mm (along z-axis) with two high reflecting mirrors at the two ends whereas gold electrodes are deposited on two side surfaces normal to the c-axis. At 852-nm wavelength the refractive index of O-ray obtained through a Sellmeier equation and experimental data are 2.2410 and 2.2465, respectively. Thus, the obtained FSR is 3.03 GHz. Power reflectivity of the mirrors is 99.6 %. With this crystal cavity, a 10-watt RF power at 6.06 GHz has been applied to phase modulate the laser beam. A number of frequency sidebands are generated, which can briefly be described by the following equation in an ideal condition,

$$E_{pm} = E_0 \left\{ \sum_{k \geq 0} J_k(p) e^{ik\Omega t} + \sum_{k > 0} (-1)^k J_k(p) e^{-ik\Omega t} \right\} e^{i\omega t}, \quad (1)$$

where, J_k Bessel function of order k , Ω RF modulation frequency, p modulation depth.

The generated OFC with a band width of about 10 nm is shown in Fig. 1(a). Presently the used laser power is of 10 mW and obtained OFC output power is about 1 mW.

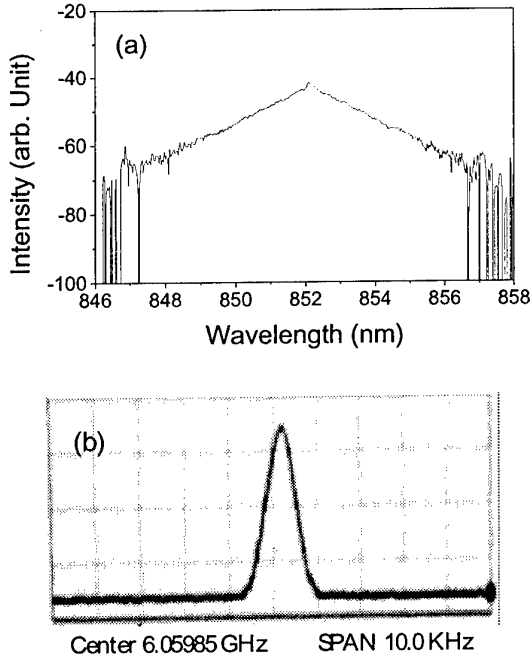


Fig.1(a): OFC generated around 852 nm carrier laser line, (b) Beat signal of OFC sidebands detected through RF spectrum analyzer.

The stability of the RF oscillator is 2×10^{-7} . This gives a RF frequency linewidth of 1.2 kHz at 6 GHz, which was confirmed by measuring the RF signal at 6.06 GHz as shown in Fig. 1(b). The stability of an optical beat between two modes in OFC is estimated from this RF oscillator stability. For mode difference $\Delta k=100$, the beat frequency is 606 GHz and the linewidth of the beat node is expected to be 121 kHz.

III. LASER STABILIZATION

We used two external-cavity diode lasers with a grating mirror on one end (Littrow mount), both of which can be tuned at around 852 nm. The first laser (LD1), that is used for OFC generation, has been frequency stabilized with a reference Fabry-Perot cavity. The finesse of the cavity is about 530 (FSR ~ 10 GHz). A low voltage modulation is given to a PZT element on one of the cavity mirrors, and transmission of the beam is detected by a photodetector. This signal has been used to frequency stabilize the LD1. This stabilization scheme is shown in Fig. 2. Since the RF oscillator frequency stability ($\Delta\nu/\nu$) is 2×10^{-7} , the difference frequency noise at the laser line (852 nm) of the first sideband will be the same as the RF frequency stability and is expected to be about 1 kHz. For the 165-th order sideband that corresponds to about 1 THz frequency separation from the carrier frequency (352 THz), the frequency noise will be about 165 kHz in an ideal case. This noise will be reflected in the emitted THz radiation as well.

A schematic diagram of the system for offset locking is shown in Fig. 2. At the photodiode PD2 a beat frequency is generated, which corresponds to the frequency separation between the LD2 and one of the OFC sideband. Since the estimated power of the 5 th sideband of the OFC is only 2.6 μ W, a higher power of the LD2 beam (about 5 mW out of 80 mw total power) is used to generate more intense beat signal. According to equation below the intensity of the beat signal depends on power of both the difference frequency components:

$$P_i = \eta \left\{ P_0 + 2(mP_1P_2)^{1/2} \cos(\omega_1 - \omega_2)t \right\}, \quad (2)$$

where, P_i PD output power, η PD efficiency ($\sim 45\%$ @ 850nm), $P_0 = P_1 + P_2$, P_1 OFC sideband power, P_2 power of LD2 beam used, ω_1 OFC side band frequency, ω_2 LD2 frequency, m mixing efficiency ($\sim 50\%$). Thus, $\sim 75 \mu$ W beat signal is expected to be generated at the PD2 photodiode, which is then amplified through a 30-dB preamplifier to detect the signal by a RF spectrum analyzer. This amplified beat signal is tuned to about 95 MHz by the PZT actuator mounted to the feed back grating of the LD2. Using a 100-MHz local oscillator with a -30 -dBm output power, an intermediate frequency between the beat signal and the local oscillator is generated in a double balanced mixer (DBM). The signal of the intermediate frequency from the DBM is then passed through an IF-voltage converter and low noise amplifier before feeding it to a lock in amplifier (LIA).

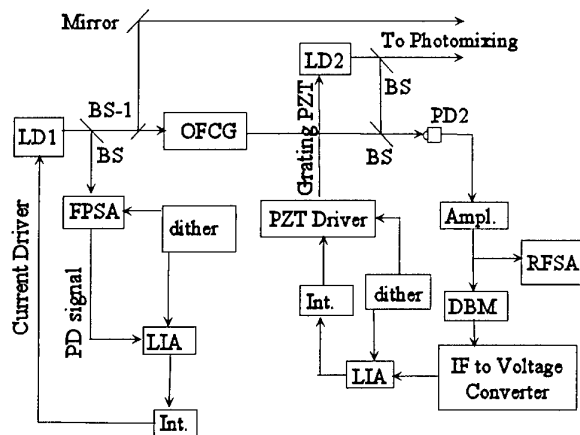


Fig.2: Schematic diagram of laser stabilization. BS; 90:10(T:R) beam splitter, BS-1; 40:60 beam splitter, LIA; lock in amplifier, Int.; Integrator, Ampl.; low noise amplifier, FPSA; Fabry-Perot spectrum analyzer, RFSA; RF spectrum analyzer, DBM; double balanced mixer, OFCG; optical frequency comb generator.

The LIA then generates the corresponding signal, which is fed back to the PZT actuator attached on grating of the LD2. The correction signal is generated when frequency of LD2 is modulated, through current modulation, of about 10 kHz and fed to the LD2.

IV. THz GENERATION

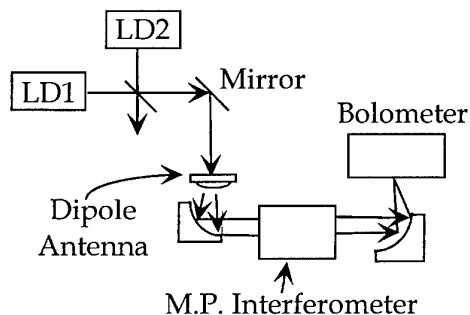


Fig. 3: Schematics of generation of THz radiation through Photomixing and detection through M.P. interferometer and Bolometer combination.

Major power of the laser beam from LD1 and LD2 are spatially coupled for photomixing. A 50:50 beam splitter/combiner has been used for this purpose, as shown in Fig. 3. A long dipole antenna with 1 mm antenna length and 5 μm antenna gap, fabricated on a low-temperature-grown GaAs, is used for the photomixing. A DC voltage bias is applied across the antenna gap. The generated THz radiation is then measured through a Martin-Puplett polarizing interferometer [8] with a liquid-helium cooled (4.2 K) InSb hot-electron bolometer.

Unfortunately, one of the lasers had a break-down during the experiment. The spectrum of the THz radiation is not available yet at this stage of our experiment. The data for the THz radiation spectrum will be presented at the Conference.

V. SUMMARY

We have demonstrated stabilization of two lasers for its relative frequency difference by using an optical frequency comb. With this laser system an optical beat and thus THz frequency radiation with the same stability of the RF oscillator used is achievable through the photomixing in a photoconductive antenna. Ultimate frequency stability better than 1 kHz is feasible at THz frequencies by using a RF oscillator with a stability of 10^{-10} (already commercially available) and the phase locking of the lasers to the OFC. The advantages of this system, in addition to the stability, are the tunability and the relative ease in determining the absolute frequency, which can be calculated from the number of mode difference and the off-set frequency.

References

1. S. Matsuura, M. Tani and K. Sakai, "Generation of coherent terahertz radiation by photomixing in dipole antennas", *Applied Physics Letter*, vol. 70, no. 5, pp. 559, 1997.
2. S. Matsuura, M. Tani, H. Abe, K. Sakai, H. Ozeki, and S. Saito, "High-resolution spectroscopy by a compact radiation source based on photomixing with diode lasers in a photoconductive antenna," *J. Mol. Spectrosc.* Vol. 187, pp.97-101, 1998
3. S. Matsuura, P. Chen, G. A. Blake, J. C. Pearson, and H. M. Pickett, "Simultaneous amplification of terahertz difference frequencies by an injection-seeded semiconductor laser amplifier at 850 nm," *International Journal of Infrared and Millimeter Waves*, Vol. 19, pp. 850-858, 1998
4. M. Kourogi, T. Enami and M. Ohtsu, "A monolithic optical frequency comb generator", *IEEE Photonics Technology Letters*, Vol. 6, No. 2, pp. 214, 1994
5. M. Kourogi, K. Nakagawa, M. Ohtsu, "Wide-span optical frequency comb generator for accurate optical frequency difference," *IEEE J. Quantum Electron.* Vol. 29, pp. 2693-2701, 1993
6. S. Sakamoto, M. Ishiguro, R. Kawabe, "The large millimeter and submillimeter array", 1999 IEEE Seventh International Conference on Terahertz Electronics, pp. 284, 1999
7. M. Ohtsu ed., "Frequency control of semiconductor lasers", John Wiley & Sons, Inc., pp. 95, 1996
8. D. H. Martin and E. Puplett, *Infrared Physics*, "Polarized interferometric spectrometry for the millimetre and submillimetre spectrum", Vol.10, pp. 105-109, 1969

Continuously Tunable THz-Wave Generation from GaP Crystal by Difference Frequency Mixing with a Dual-Wavelength KTP-OPO

Tetsuo Taniuchi, Jun-ichi Shikata, and Hiromasa Ito

Abstract- Tunable terahertz (THz)-wave generation has been achieved by difference frequency generation (DFG) in a GaP crystal, with a KTiOPO_4 (KTP) optical parametric oscillator (OPO). We have developed a dual signal-wave OPO with two KTP crystals of $\phi = 55^\circ$ to oscillate wavelengths from 980 nm to 990 nm, corresponding to the phase matching wavelength for DFG in GaP. Continuously tunable THz-waves were successfully generated in the 0.5 - 2.0 THz region, with the angle-tuning of the KTP crystal in the OPO cavity. The maximum power of 1.4 mW at the peak was achieved at 1.4 THz.

Index Term- terahertz-wave, optical parametric oscillator, difference frequency generation

I. INTRODUCTION:

A coherent tunable terahertz (THz) wave can be generated by difference frequency generation (DFG) or parametric oscillation in nonlinear-optic crystals. THz-wave (far infrared) generation by DFG has been reported by mixing two CO_2 lasers using GaAs [1], and two dye lasers using ZnTe [2] and LiNbO_3 [3]. THz waves have also been generated by THz parametric oscillation (TPO) in LiNbO_3 pumped by a Q-switched Nd:YAG laser [4], based on stimulated polariton scattering. Recently we successfully generated THz waves tunable from 1 to 3 THz in MgO doped LiNbO_3 , and we found that THz-wave output was nearly five times larger, compared to undoped LiNbO_3 [5]. The TPO has an advantage that it requires only one pump laser with a fixed wavelength, however, it has a threshold energy large than 10 mJ.

On the other hand, DFG has no threshold, and it potentially has wider tunability than TPO by selecting the DFG crystal and input wavelengths. The light sources for DFG must have slightly different wavelengths, with a separation of 0-10 nm, corresponding to the THz frequency.

Recently we have demonstrated THz-wave DFG in 4-N,N-dimethylamino-4'-N'-methyl-stilbazolium tosylate (DAST) [6] crystal using a type II KTiOPO_4 (KTP) optical parametric oscillator (OPO) with dual wavelengths near 1064 nm [7]. The organic crystal DAST has a large nonlinear-optic coefficient of

$d_{11}=290\text{pm/V}$ [8], which is 10 times larger than that of LiNbO_3 , and phase matching wavelength for collinear DFG is in the range of 1 - 1.15 μm . DAST is an effective material for generation of sub-THz-waves below 1THz, however, there is a large absorption band near 1.1THz, so that frequency range of DFG was limited to 0.2 - 1.2THz region.

To generate frequencies higher than 1 THz, low-loss crystals in the THz-wave region, such as GaP, ZnTe, or GaAs are useful for DFG interaction. Also, the nonlinear crystal is required to possess a large nonlinear coefficient at the two input optical frequencies. Therefore, GaP crystal is an attractive material for nonlinear interaction between optical wave and THz-wave due to wide transmission range of optical and THz waves [9,10]. In addition, we can easily obtain a large high quality GaP crystal with 2 inches diameter. The phase-matching for THz-DFG can be achieved in the wavelength range of 980-1000 nm in GaP crystal [11].

In this paper, we developed a dual signal-wave OPO using two KTP crystals in the same cavity as a source for THz-wave DFG with GaP. Using $\phi = 55^\circ$, $\theta = 90^\circ$ cut KTP crystals, we can easily obtain dual wavelengths with separation of 0-10 nm in the range 980 to 990 nm by angle-tuning the KTP crystals. Continuously tunable THz-wave generation in the range of 0.5 to 2.0 THz is demonstrated by tuning the angle of KTP.

II. DFG CHARACTERISTICS

Fig.1 shows a schematic diagram for generating THz waves by mixing two light waves from OPO, with slightly different wavelengths. For efficient DFG, the phase matching conditions in GaP is important, and they are given by;

$$\text{energy conservation: } \frac{1}{\lambda_1} - \frac{1}{\lambda_2} = \frac{1}{\lambda_3}$$

$$\text{momentum conservation: } \frac{n_1}{\lambda_1} - \frac{n_2}{\lambda_2} = \frac{n_3}{\lambda_3}$$

where λ_1 and λ_2 are the input wavelengths, λ_3 is the DFG wavelength, and n_1 , n_2 , n_3 are the refractive indices at each wavelength.

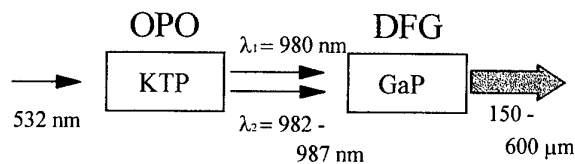


Fig. 1 THz-wave generation using a dual-wavelength OPO

T. Taniuchi, J. Shikata, and H. Ito are affiliated with the Research Institute of Electrical Communication, Tohoku University, Sendai 980-8577, Japan

The refractive indices n_1 , n_2 and n_3 of GaP in the optical and THz region were calculated using the Sellmeier equation [12].

$$n^2 = 2.81479 + \frac{6.27677\lambda^2}{\lambda^2 - 0.09116} + \frac{2.05549\lambda^2}{\lambda^2 - 762.1311}$$

Fig.2 shows measured refractive indices [13] and the calculation from the Sellmeier equation. The transmittance of GaP in the THz region is also shown in Fig.2. The GaP crystal is transparent below 2.7THz.

The coherence length L_c for DFG is obtained by:

$$L_c = \frac{1}{2 \left| \frac{n_1}{\lambda_1} - \frac{n_2}{\lambda_2} - \frac{n_3}{\lambda_3} \right|}$$

Fig. 3 shows the coherence length L_c as a function of the input wavelength λ_1 , calculated using the above equation. It shows that the collinear phase-matching can be achieved with input wavelengths near 980 - 990 nm in order to generate 0.5 to 2 THz frequencies. For example, 1.5 THz ($\lambda_3 = 200 \mu\text{m}$) can be generated with input wavelengths of 980 nm (λ_1) and 985 nm (λ_2).

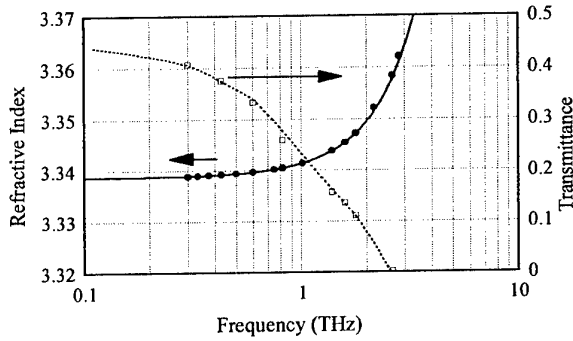


Fig.2 Characteristics of GaP in THz-wave region

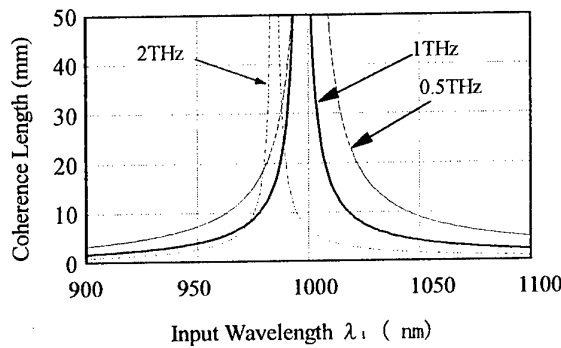


Fig.3 Coherence length for DFG vs input wavelength λ_1

III. EXPERIMENT

Fig. 4 shows a schematic diagram of the experimental arrangement for THz- wave generation in GaP by mixing dual wavelengths of KTP-OPO, which has two KTP crystals in the same cavity. The oscillating wavelengths can be independently controlled by the angle-tuning of KTP.

The pump source for the OPO was a frequency-doubled Q-switched Nd:YAG laser, with a pulse duration of 10 ns and 20 Hz-repetition rate. The OPO cavity was 150-mm long, which consisted of two 15mm-long KTP crystals and two highly reflective flat mirrors with 98% (input) and 82% (output). The threshold energy of the KTP-OPO was 3 mJ, and an output energy of 0.3 mJ was obtained with a pump energy of 4 mJ. In the KTP-OPO, it is possible to generate signal waves with relatively narrow bandwidths in the range of 980 to 990 nm by the angle-tuning from $\phi = 55$ to 59° as shown in Fig.5.

Fig. 6 shows typical output spectrum of generated signal waves. P_1 and P_2 are obtained power at λ_1 and λ_2 . P_2 is slightly lower than P_1 because of the pump depletion. The output power and the spectral bandwidth (0.2 nm) did not change throughout the tuning range.

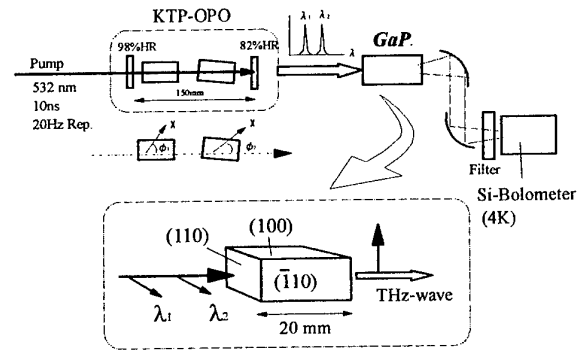


Fig. 4 Experimental arrangement for THz-DFG in GaP

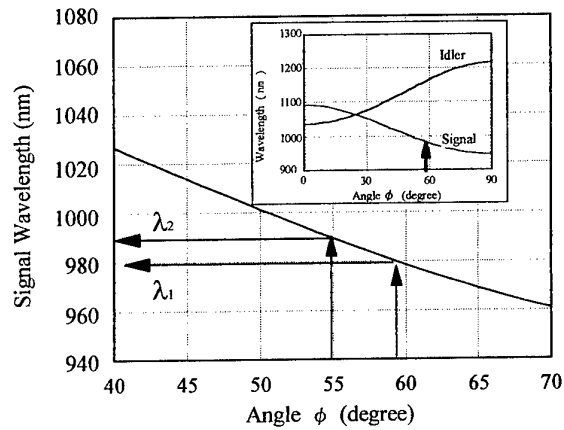


Fig.5 Signal wavelength vs KTP angle ϕ

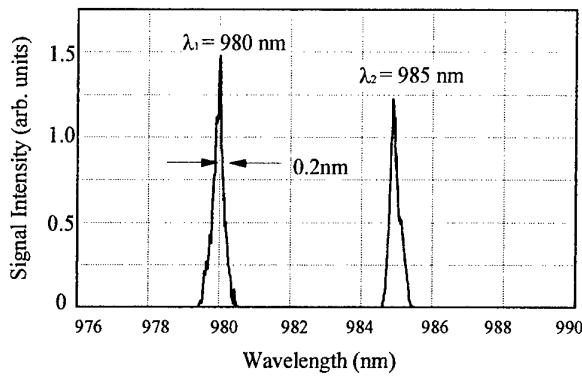


Fig.6 Signal spectrum of the dual signal-wave KTP-OPO

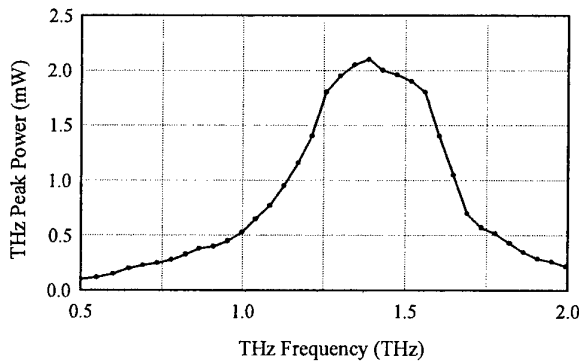


Fig.7 Frequency dependence of DFG output power

The DFG experiment was carried out with an undoped 20mm-long GaP crystal with high resistivity ($> 10^6 \Omega\text{cm}$). The direction of input waves was along $\langle 110 \rangle$ direction of the GaP crystal. The generated THz-wave was collimated with a parabolic mirror and detected using a Si bolometer (4.2 K), as shown in Fig.4. The maximum DFG output was obtained when the polarization of the incident optical waves was perpendicular to the $\langle 100 \rangle$ direction of the GaP crystal. The polarization of the generated THz-wave, measured by rotating the wire-grid polarizer, was parallel to the $\langle 100 \rangle$ direction of the GaP crystal.

A continuously tunable THz-wave was successfully generated in the range of 0.5 to 2.0 THz by angle-tuning the KTP crystals as shown in Fig. 7. In this experiment, the angle of the first KTP was fixed to generate signal wave at $\lambda_1 = 980 \text{ nm}$ and the second KTP was tuned at $\lambda_2 = 982 - 987 \text{ nm}$. The peak power of the THz-wave was about 1.4 mW at 1.4 THz, when input average power was 5 mW. The decrease in the generated THz-wave above 2 THz is due to the absorption in GaP. The bandwidth of the THz wave obtained was estimated to be about 60 GHz, corresponding to the optical spectral bandwidth of 0.2 nm. To generate a narrow THz wave, the spectral bandwidth of the KTP-OPO must be narrowed by inserting a grating element in the cavity.

Fig.8 shows the DFG output energy as a function of input energy. It is shown that DFG output energy increases proportional to square of input energy. We can

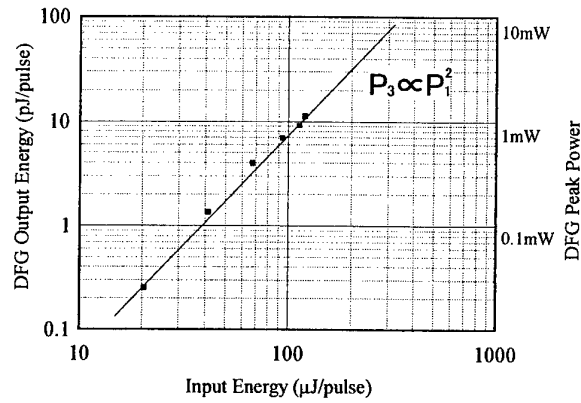


Fig.8 DFG output energy vs input energy

find that the photorefractive damage and the two photon absorption in the GaP crystal are small in the power range of 5mW(average).

IV. CONCLUSIONS

We have investigated THz-wave DFG in GaP crystal. Continuously tunable THz-wave generation was demonstrated using a dual-wavelength KTP-OPO. The frequency of the THz wave was tuned in the 0.5 to 2.0 THz range by varying the KTP crystal angle in the OPO cavity. Maximum peak power of 1.4mW was obtained at 1.4 THz. The dual-signal wave KTP-OPO presented here is a suitable light source for generating a widely tunable THz wave.

Acknowledgements

The authors are greatly indebted to Dr. K. Kawase for useful discussion about DFG crystals, and to C. Takyu of our institute for their excellent technical support.

References

- [1] R. L. Aggarwal, B. Lax, H. R. Fetterman, P. E. Tannenwald, and B. J. Clifton, "CW generation of tunable narrow-band far-infrared radiation", J. Appl. Phys., Vol.45, No.9, pp. 3972-3974 (1974)
- [2] N. Matsumoto and T. Yajima, "Far-infrared generation by self-beating of dye laser light", Jpn. J. Appl. Phys., Vol.12, No.1, pp. 90-97 (1973)
- [3] K. H. Yang, J. R. Morris, P. L. Richards, and Y. R. Shen, "Phase-matched far-infrared generation by optical mixing of dye laser beams". Appl. Phys. Lett., Vol. 23, No. 12, pp. 669-671 (1973)
- [4] M. A. Piestrup, R. N. Fleming, and R. H. Pantell, "Continuously tunable submillimeter wave source", Appl. Phys. Lett., Vol. 26, No. 8, pp. 418-421 (1975)
- [5] J. Shikata, K. Kawase, K. Karino, T. Taniuchi, and H. Ito, "Tunable terahertz-wave parametric oscillators using LiNbO₃ and MgO:LiNbO₃ crystals", IEEE

Trans. MTT, Vol.48, No.4, pp. 653-661 (2000)

- [6] H. Nakanishi, H. Matsuda, S. Okada, and M. Kato, "Organic polymeric ion-complexes for nonlinear optics", Proceedings of the MRS International Meeting on Advanced Materials, 1, pp.97-104 (1989)
- [7] T. Taniuchi, J. Shikata, and H. Ito, "Tunable THz-wave generation in DAST crystal with a dual-wavelength KTP optical parametric oscillator", to be published in Electronics Letters.
- [8] F. Pan, G. Knopke, Ch. Bosshard, S. Follonier, R. Spreiter, M. S. Wong, and P. Gunter, "Electro-optic properties of the organic salt 4-N, N-dimethylamino -4'-N'-methyl-stilbazolium tosylate", Appl. Phys. Lett., Vol. 69, No. 1, pp. 13-15 (1996)
- [9] D. D. Boyd, T. J. Bridges, M. A. Pollack, and E. H. Turner, "Microwave nonlinear susceptibilities due to electronic and ionic anharmonicities in acentric crystals", Phys. Rev. Lett., Vol.26, No.7, pp. 387-390 (1971)
- [10] F. De Martini, "Infrared generation by coherent excitation of polariton", Phys. Rev. B, Vol.4, No.12, pp. 4556-4578 (1971).
- [11] G. Herman, "Terahertz generation in high purity semiconductor via 3 wave DFG and Cross-Reststrahlen band PM", Proceedings of Advanced Solid-State Laser, WV3, pp. 574-575 (1999)
- [12] D. F. Parsons and P. D. Coleman, "Far infrared optical constants of Gallium Phosphide", Appl. Opt. Vol.10, No.7, pp.1683-1685 (1971)
- [13] A. Borghesi and G. Guizzetti, Handbook of optical Constants of Solids, Academic Press, pp. 445-464 (1985)

COPLANAR FED MICROMACHINED PLANAR ANTENNAS FOR POWER COMBINING APPLICATIONS AT D-BAND FREQUENCIES

STEFANIE HIRSCH, KAREN DUWE, ROLF JUDASCHKE

Abstract

Several transitions from coplanar waveguide on thin dielectric membrane to micromachined planar antennas have been investigated. The physical dimensions of the multi-layer planar antenna structures as well as the shape of the micromachined horns have been optimized for operation at 150 GHz. The calculated return losses are low and the direction of maximum radiated power is orthogonal to the plane of the CPW-feedline what indicates a good applicability for power combining array arrangements.

Introduction

Micromachined coplanar waveguides on thin dielectric membranes proved very satisfactory transmission properties for D-band frequencies because of the absence of substrate modes, low losses, and low dispersion [1]. Transmission lines with very good characteristics have already been fabricated. Micromachined shielded coplanar waveguides provide the advantage that neither via-holes as for microstrip applications nor air bridges as for conventional coplanar lines are needed. Unlike other approaches [1], low-resistive silicon substrates have been used which act as a shielding cavity without necessarily having to be coated with gold to ensure a sufficiently good RF short between the two ground planes. This fact implies the additional advantage of low production costs. The planar gold conductors of our structures are entirely based on dielectric membranes of thickness $4\mu\text{m}$ [2]. In order to radiate power into free space, broadband low loss transitions from coplanar waveguide to planar antenna elements are needed. Several approaches have been made for other frequency bands [3], [4]. Presented here are two different types of antennas which provide good impedance match and radiation characteristics adapted for power combining applications at D-band frequencies. For this purpose, a certain number of exactly identical antenna elements has to be arranged in a

quasi-optical power combining structure. That means that the mounting and power feeding components of each single element have to permit that the elements are collocated close to each other. Furthermore, the design must imply reproducibility in fabrication, i.e. the possibility for integrated fabrication by means of micromachining techniques. Both of these properties are provided by the CPW-configurations described in this paper. Beyond the aim of good impedance match and high gain it is important that the main lobe of the radiation pattern is perpendicular to the CPW-plane, and that sidelobes are suppressed as much as possible. These requirements have been optimized for operation at D-band frequencies. The numerical analysis of the investigated structures has been carried out by the field simulator HFSS and the optimization was done by means of empipe3d, both software tools by Agilent Technologies.

Slot-Coupled CPW-Fed Patch Antenna

The first one of the two investigated antenna types is a rectangular patch antenna fed by a coplanar waveguide on membrane as described for a lower frequency band in [3]. In this case, the coupling between the CPW feedline and the patch is performed by a rectangular coupling slot in the ground plane which is connected to the CPW either inductively or capacitively. Both couplings have been investigated but only the inductively coupled type has been optimized for D-band operation. The structure is composed of two stacked layers, one of which is carrying the CPW feedline and the coupling slot, and the other one is carrying the radiating patch. CPW and patch are both lying on dielectric membranes as described above. A schematic of the structure is shown in Fig. 1.

The parameters which have been varied during the optimization procedure were the length of the coupling slot, the dimensions of the radiating patch, and the distance between the patch and the CPW-plane. The calculated return loss $|S_{11}|$ and the radiation pattern

at 150 GHz for an optimized structure are shown in Fig. 2 and Fig. 3.

A return loss of -35 dB and an antenna gain of more than 9 dB at 150 GHz have been obtained. However, this type of antenna shows good performance only within a very narrow frequency band. Furthermore, the structure proved high sensitivity with respect to small variations in physical dimensions. Especially the length of the coupling slot that directly influences the center frequency is very critical as far as fabrication tolerances are concerned.

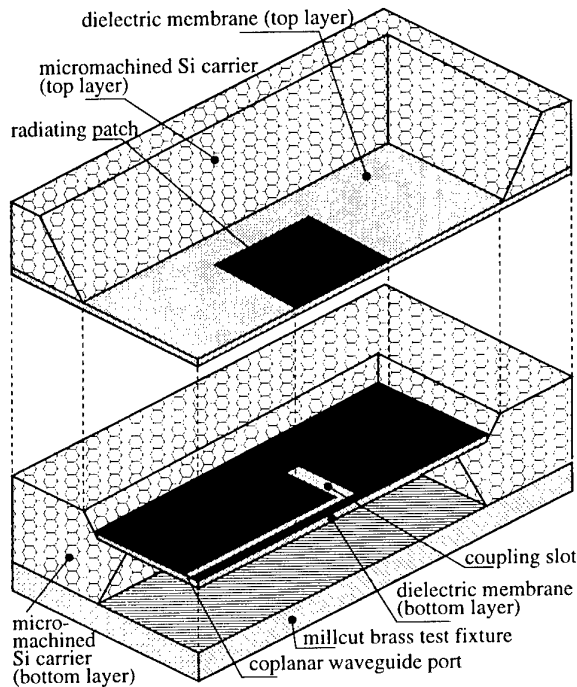


Figure 1: Schematic of the slot-coupled CPW-fed patch antenna (cut in half).

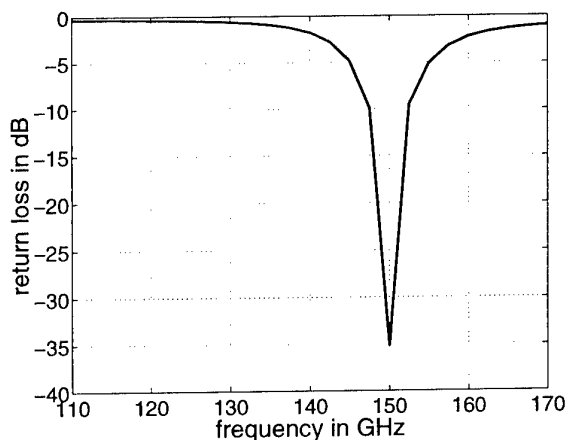


Figure 2: Simulated return loss of the slot-coupled CPW-fed patch antenna.

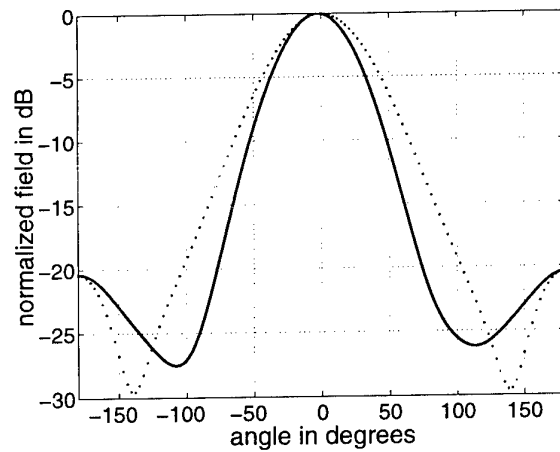


Figure 3: Simulated radiation pattern of the slot-coupled CPW-fed patch antenna: E-plane (solid line) and H-plane (dotted line).

CPW-Fed Microstrip Probe Micromachined Horn Antenna

For the purpose of an enhanced bandwidth another type of planar integrated antenna was investigated. This concept is very promising because it is based on a transition from CPW on membrane to conventional rectangular waveguide which has previously been published and successfully fabricated [5], [6]. This transition consists of a Klopfenstein taper [7] which transforms the coplanar waveguide into a microstrip line followed by a microstrip probe. The latter converts the electromagnetic field of the microstrip line into the TE_{10} -mode of a rectangular waveguide which on one side is shorted at a distance of approximately a quarter of a wavelength from the probe. The transition from the microstrip line to the rectangular waveguide is performed by a triangularly shaped microstrip patch placed in the E-plane of the rectangular waveguide. The membrane as well as the carrier substrate are located in this plane of the rectangular waveguide. Undesired higher order modes are suppressed by means of sufficiently small micromachined shielding cavities surrounding the CPW as well as the microstrip line. On the opposite side of the waveguide short, the rectangular waveguide is terminated by a small micromachined horn in the probe-plane. Fig. 4 shows a schematic of the structure.

The dimensions of the CPW-to-rectangular waveguide-transition have to be slightly modified for satisfactory antenna performance according to the requirements described in the introduction. Optimization parameters were both width and length of the microstrip patch as well as the position of point D in Fig. 4, optimization goals were the center

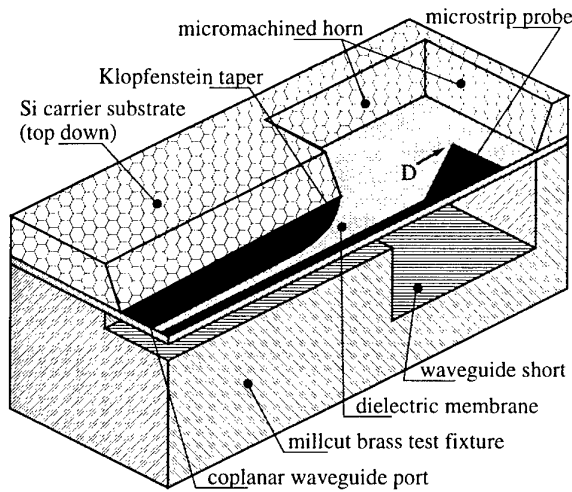


Figure 4: Schematic of the CPW-fed microstrip probe micromachined horn antenna (cut in half).

frequency and the broadband characteristics of the transition. Furthermore, the distance of the waveguide short from the probe has been optimized to improve impedance match. Fig. 5 and Fig. 6 show the calculated return loss $|S_{11}|$ and the radiation pattern at 150 GHz of the presented antenna. Return losses of less than -20 dB and a gain of more than 6 dB were achieved over a frequency range from 140 GHz to 160 GHz.

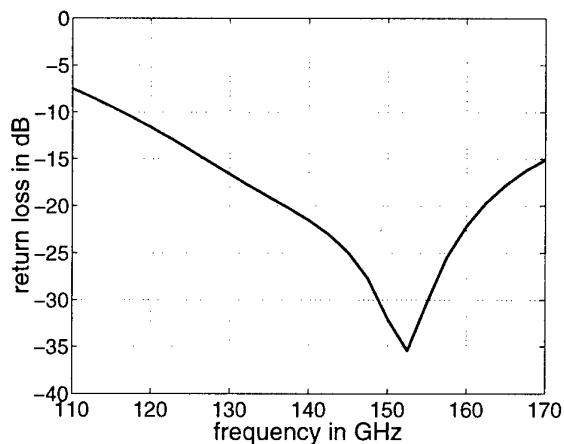


Figure 5: Simulated return loss of the microstrip probe micromachined horn antenna.

Experimental Results

The presented structures have not been fabricated yet, but very similar structures which have not been optimized show satisfactory characteristics what promises good operation for the optimized structures, too. Fig. 7 and Fig. 8 show the simulated and measured return

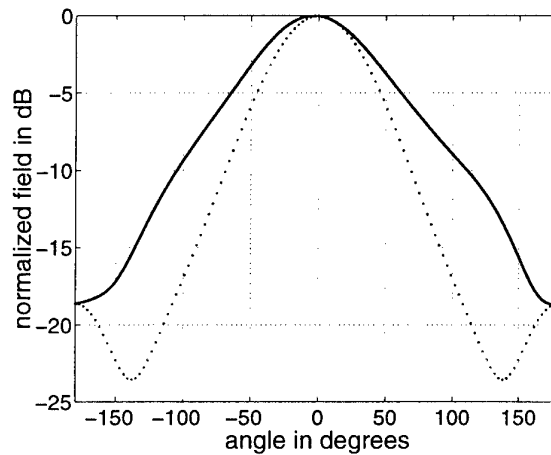


Figure 6: Simulated radiation pattern of the microstrip probe micromachined horn antenna: E-Plane (solid line) and H-Plane (dotted line)

loss $|S_{11}|$ and the radiation pattern for a microstrip probe micromachined horn antenna with a center frequency around 125 GHz.

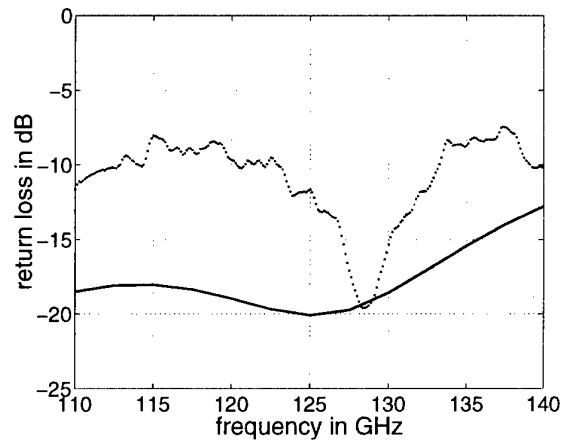


Figure 7: Simulated and measured return loss of a microstrip probe micromachined horn antenna.

Conclusions

Transmission line structures on thin dielectric membranes are a promising technique for applications at D-band frequencies. The simulated results presented in this paper promise low-cost and reproducible fabrication of antennas which may contribute to effective power combining array arrangements for D-band frequencies.

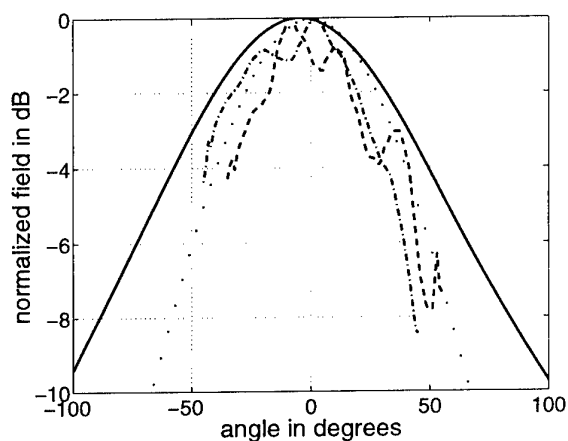


Figure 8: Simulated and measured radiation pattern of a microstrip probe micromachined horn antenna: E-Plane (solid line, dashed line) and H-Plane (dotted line, dash-dotted line)

Acknowledgement

The authors are indebted to the Deutsche Forschungsgemeinschaft for financial support.

References

- [1] N. I. Dib, W. P. Harokopus Jr., P. B. Katehi, C. C. Ling, and G. M. Rebeiz, "Study of a Novel Planar Transmission Line", *IEEE MTT-S Digest*, 1991, pp. 623-626.
- [2] K. Duwe, S. Hirsch, R. Judaschke, J. Müller, "Micromachined Planar Antennas for D-Band Frequencies", *this conference*.
- [3] W. Menzel, W. Grabherr, "A Microstrip Patch Antenna with Coplanar Feed Line", *IEEE Microwave and Guided Wave Letters*, 1991, vol. 1, no. 11, pp. 340-342.
- [4] R. Q. Lee, R. N. Simons, "Coplanar Waveguide Aperture-Coupled Microstrip Patch Antenna", *IEEE Microwave and Guided Wave Letters*, 1992, vol. 2, no. 4, pp. 138-139.
- [5] S. Hirsch, K. Duwe, R. Judaschke, "A Transition from Rectangular Waveguide to Coplanar Waveguide on Membrane", *25th International Conference on Infrared and Millimeter Waves*, Sept. 2000, Beijing, China.
- [6] K. Duwe, S. Hirsch, R. Judaschke, J. Müller, "Micromachined Coplanar Waveguides on Thin

HMDSN-Membranes", *25th International Conference on Infrared and Millimeter Waves*, Sept. 2000, Beijing, China.

- [7] S. V. Robertson, L. P. B. Katehi, and G. M. Rebeiz, "Micromachined W-Band Filters", *IEEE Trans. Microwave Theory Tech.*, April 1996, vol. MTT-44, pp. 598-606.

Design and Simulation of a 600 GHz RTD Oscillator using Commercial Harmonic Balance Software

John Muscat and Charles V. Sammut

Abstract – We report on the design and optimisation of a 600 GHz double barrier resonant tunnelling diode (RTD) oscillator. Using the simple Esaki equivalent circuit diode model and published DC experimental I-V data, a custom device model was developed and integrated within a commercial harmonic balance (HB) simulator. This technique utilises a spline interpolation algorithm as part of the device model to determine instantaneous values of device voltage and current when called from within the main HB software. The maximum oscillation frequency for a $5\ \Omega$ load was 1.6 THz, whilst optimisation at 600 GHz was achieved with a $15\ \Omega$ load, with an output power of 420 μ W. The present technique should facilitate and simplify simulation of both existent and novel non-linear devices in other configurations, such as multipliers, mixers, self-oscillating mixers, etc.

I. INTRODUCTION

During the past two decades, the RTD has been thoroughly investigated as a potential sub-millimetre wave source. To date, the best RTD oscillators were realised in the InGaAs/AlAs and InAs/AlSb material systems where the latter generated fundamental oscillations up to 712 GHz [1]. However, the highest reported power output of the RTD when used as a fundamental oscillator [2] still remained disappointingly low when compared to Schottky diode – based multipliers. Power combining was shown to bring about considerable improvement [3] while the series integration of RTDs [4,5] also seems promising. Yet, low power levels together with the inherent tendency for bias-circuit instabilities [6,7] have limited the use of RTDs in system applications.

Despite the current state of affairs, the RTD's potential as one of the fastest solid-state devices continues to attract interest in the scientific community. This is evidenced by a number of recent publications by various groups such as [4,5,8,9].

Novel oscillator designs based on device equivalent circuits are still being developed. To predict the performance of such oscillators, circuit simulations are necessary. Design techniques and analysis of RTD-based oscillators would benefit greatly from the implementation of commercial circuit simulators as this would speed up the optimisation process and also facilitate design and analysis of power combining schemes. In this type of work, a fundamental difficulty arises from incorporating essential non-linear current-voltage (I - V) and

capacitance-voltage (C - V) device characteristics using a satisfactory device model and making this compatible with the available CAD software. The following sections will describe the construction and validation of a user-defined model of a RTD followed by the design and optimisation of a 600 GHz RTD oscillator.

II. MODEL CONSTRUCTION

Recent research activity in the development of large signal models of RTDs suitable for SPICE-type CAD tools has been significant. The early models employed simplified versions of the I – V characteristic such as piecewise linear [10] or polynomial [11,12] fits. Subsequently, more complex expressions were introduced [13-17] mainly due to the recent SPICE capability of representing transcendental forms of voltage-controlled current sources. These models range from a purely physics-based equation [13] to a totally empirical curve-fitting procedure [17].

Empirical curve-fitting to generate analytical expressions does not always reproduce real device behaviour accurately over the *entire* voltage-/current-/frequency-range of interest and entails the use of elaborate routines to generate a number of parameters, most of which would not be related to device physics. Likewise, physics-based models are generally insufficient to accurately reproduce experimental behaviour. It is therefore often found necessary to allow physical parameters to depart from their 'theoretical' values to compensate for the necessary simplification of the model.

We believe that it is currently impossible to generate an analytic formula that faithfully reproduces device characteristics and that is easily adaptable from one device to another by simply specifying a number of RTD physical parameters. There are a number of reasons for this problem, but chiefly device characteristics change significantly even within small distances of the order of 1 mm on the same wafer. This is exacerbated by the fact that well-designed resonant tunnelling heterostructures exhibit strong negative differential resistance (NDR) effects in many material systems and over a wide range of current density [18]. The solution would be to characterise each actual device individually, if accuracy in system design and analysis is required.

The present technique was developed in order to circumvent these problems and is based on the use of device characteristics derived by cubic-spline interpolation of measured data. In contrast with piecewise-linear methods, cubic splines are continuous

J. Muscat and C. V. Sammut are with the Department of Physics, University of Malta, Msida MSD 06, Malta.

up to the second derivative and intrinsically smooth. Thus, most non-linear device characteristics may be represented faithfully with a number of data points not by far exceeding the number of parameters required for an equivalent representation in terms of analytic functions. In fact, only 16 data points were necessary to reproduce the experimental I - V curve from Brown *et. al.* [1], using a higher point density near the peak and valley to better reproduce the non-linearities. In the NDR region special care was taken to duplicate the maximum negative conductance of -64 mS at about 1.3 V as reported in Ref. [1].

This model was developed within the context of Microwave Harmonica [19], which employs the HB algorithm developed by Rizzoli and his co-workers [20]. Specific FORTRAN code was developed to automate the process of constructing user defined models from external I - V data files. The generated subroutine is then linked to the main commercial simulator. During analysis, the main program calls the subroutine, which determines instantaneous device voltage and current by spline interpolation. These are fed back to the main program for the successive iterations in the HB procedure. We have also generated a more complex model that allows for capacitance variation with device voltage based on data published in [21]. This will be reported elsewhere.

III. MODEL VALIDATION

Figure 1 shows a simplified equivalent circuit of an oscillator with a RTD connected to a bias circuit and load. In the case of RTD oscillators, the active device provides the capacitance and negative differential conductance required. Therefore, the resonator only has to show inductive behaviour. As a first approximation, lumped element inductances L_B and L_R were assumed. The circuit of figure 1 was analysed using the commercial HB simulator. The parameters used were $V_b = 1.35$ V, $R_s = 3$ Ω , $C_d = 2.8$ fF, $L_B = 1$ μ H, $L_R = 25$ pH and $R_L = 12$ Ω . R_s and C_d were obtained from data published in [1] while L_R was chosen to provide resonance conditions at 600 GHz. At this point no effort

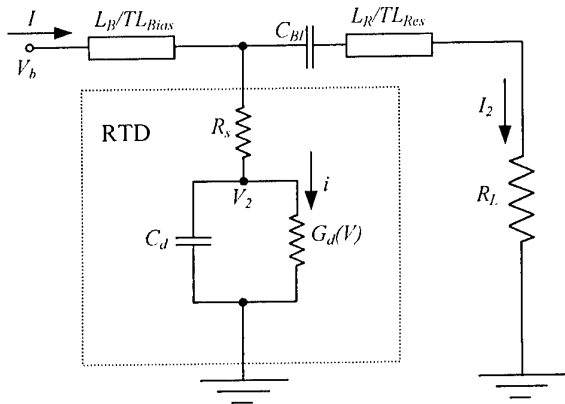


Fig. 1 : Equivalent circuit model of an RTD oscillator. L_B and L_R are lumped inductances used in model validation, whilst TL_{Bias} and TL_{Res} are transmission line lengths used in the 600 GHz oscillator design. Introduction of C_{BI} was necessary in the latter case.

was made to optimise the bias circuit and load. Basically, the aim of the exercise was to compare the output of the commercial simulator with the time domain solution. The output voltage waveforms across the load resistance R_L are shown in figure 2. These oscillations are nearly sinusoidal in nature and have a fundamental frequency of 530 GHz.

The time domain solution is obtained by solving a set of differential equations governing the behaviour of the circuit in figure 1:

$$\frac{dI}{dt} = \frac{V_b - IR_s + I_2 R_s - V_2}{L_B} \quad (1)$$

$$\frac{dI_2}{dt} = \frac{V_2 + IR_s - (R_s + R_L)I_2}{L_R} \quad (2)$$

$$\frac{dV_2}{dt} = \frac{I - i(V_2) - I_2}{C_d} \quad (3)$$

Equations (1) – (3) were solved using MATLAB [22]. Before the integration was carried out, the variable units were scaled to avoid numerical instabilities arising from small values of L_R and C_D in the denominator. To evaluate the right hand side of equation (3), the program used spline interpolation within the same data set as for the HB simulation. Figure 2 shows the time-domain voltage waveforms across the resistive load R_L compared to those obtained by the commercial simulator. Clearly, the two are in excellent agreement once the steady state is reached. Other simple circuits that demonstrate bistability, hysteresis and relaxation oscillations were also simulated successfully to confirm the validity of the RTD model within Harmonica. Section IV describes how this technique was employed in the optimum design of a 600 GHz oscillator.

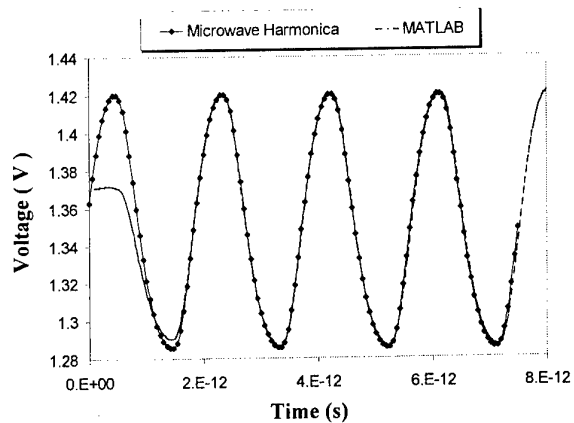


Fig. 2: Time domain voltage curves across load resistance R_L .

IV. DESIGN OF A 600 GHz RTD-BASED OSCILLATOR

The oscillator shown in figure 1 employs the series resonance circuit technique where transmission line lengths TL_{Bias} and TL_{Res} are now used instead of L_B and L_R to fulfil the resonance requirement at the desired

frequency. The negative resistance of the RTD allows oscillations in the circuit while the blocking capacitor C_{BI} and the quarter wavelength transmission line TL_{Bias} constitute the biasing circuit. This topology follows Sigurdardóttir [8]. An optimum bias voltage of 1.4 V was determined by a procedure similar to that described by Boric *et al* [12]. The other elements of the device model were a series resistance $R_s = 3 \Omega$ and a device capacitance $C_d = 2.8 \text{ fF}$ [1].

The output power and oscillation frequency depend on transmission line length and load resistance. This dependence was investigated for transmission line lengths varying from $20 \mu\text{m}$ to $200 \mu\text{m}$ and with two different loads of impedance 5Ω and 20Ω . The corresponding results are shown in figure 3. The maximum oscillation frequency was about 1.6 THz for the 5Ω load, whilst with the 20Ω load oscillations occurred only at frequencies below 550 GHz. This may be due to the transformation of the terminating impedance to capacitive at the device port, thereby annihilating the resonant circuit at a lower frequency. This general behaviour was also observed in [8] with similar orders of magnitude as regards oscillation frequency and power.

Finally, figure 3 suggests that the optimal transmission line length for a 600 GHz oscillator should lie between 70 and $90 \mu\text{m}$.

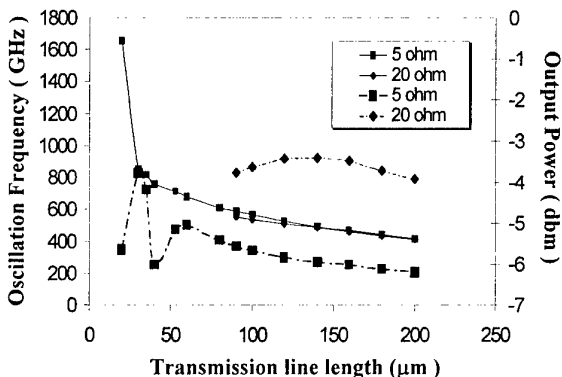


Fig. 3: Oscillation frequency (solid line) and output power (dashed line) as a function of transmission line length.

Figure 4 shows the available output power as a function of load resistance R_L .

The load resistance was varied from 2Ω to 18Ω while the transmission-line length was varied from $74 \mu\text{m}$ to $86 \mu\text{m}$. It transpired that a load resistance of 15Ω and a corresponding transmission line length of $78 \mu\text{m}$ deliver the maximum power of $421.6 \mu\text{W}$ at 600 GHz at a bias voltage of 1.4 V. This is much higher than the $0.3 \mu\text{W}$ reported in [1] and would correspond to the absolute maximum power that can be delivered from that particular single InAs/AlSb RTD, assuming the simple Esaki diode model of fig. 1.

V. CONCLUSION

This work was motivated in part by the need to model and optimise the behaviour of RTDs in the submillimetre

region, and by the usefulness of simple equivalent circuit models based on measurement data. We have reported a novel implementation of a spline interpolation algorithm within a commercial HB analysis package. To the best of the authors' knowledge, this is the first time that cubic spline interpolation of experimental data was incorporated into commercial HB software for the analysis of RTD-based microwave circuits. The technique reported here allows automated generation of custom device models and offers some attractive advantages over established analytic or semi-analytic

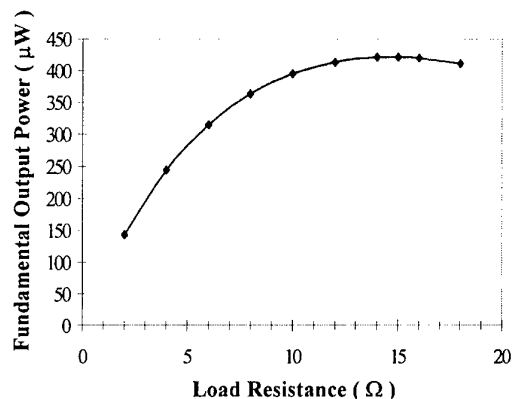


Fig. 4: Output power as a function of load resistance R_L .

techniques:

- virtually any device or device model may be incorporated into commercially available HB, or other non-linear analysis packages, providing the software allows definition of custom models, a feature which is becoming increasingly common;
- software implementation does not require construction of analytic functions with various parameters chosen to fit typical data. Instead, an *actual* device may be modelled, rather than a *typical* one, without the need of employing complicated curve fitting schemes.
- most non-linear device characteristics may be represented faithfully with a number of data points not by far exceeding the number of parameters required for an equivalent representation in terms of analytic functions. The computation time is not adversely effected since interpolation within a restricted set of data points is usually not significantly more computationally intensive than evaluating cumbersome analytic functions.

Acknowledgement

This work was supported by the University of Malta through research grant No. 73542.

References

- E. R. Brown, J. R. Söderström, C. D. Parker, L. J. Mahoney, K. M. Molvar and T. C. McGill, "Oscillations up to 712 GHz in InAs/AlSb resonant tunneling diodes," *Appl. Phys. Lett.*, Vol. 58, pp. 2291–2293, 1991.

2. E. R. Brown, C. D. Parker, A. R. Calawa, M. J. Manfra, and K. M. Molvar, "A quasi-optical resonant-tunneling-diode oscillator operating above 200 GHz," *IEEE Trans. Microwave Theory Tech.*, Vol. 41, pp. 720-722, 1993.
3. K. D. Stephan, S. C. Wong, E. R. Brown, K. M. Molvar, A. R. Calawa, and M. J. Manfra, "5-mW parallel-connected resonant tunneling diode oscillator," *Electron. Lett.*, Vol. 28, pp. 1411-1412, 1992.
4. C. C. Yang and D. Pan, "Theoretical Investigations of a Proposed Series Integration of Resonant Tunneling Diodes for Millimeter-Wave Power Generation," *IEEE Trans. Microwave Theory Tech.*, Vol. 40, No. 3, March 1992.
5. R. Sun, O. Boric-Lubecke, D. S. Pan and T. Itoh, "Considerations and Simulations of Subfrequency Excitation of Series Integrated Resonant Tunneling Diodes Oscillator," *IEEE Trans. Microwave Theory Tech.*, Vol. 43, No. 10, pp. 2478-2485, October 1995.
6. C. Y. Belhadj, K. P. Martin, S. B. Amor, J. J. L. Rascol, R. J. Higgins, R. C. Potter, H. Hier, and E. Hempfling, "Bias circuit effects on the current - voltage characteristic of double - barrier tunnelling structures. Experimental and theoretical results," *Appl. Phys. Lett.*, Vol. 57, pp. 58 - 60, 1990.
7. C. V. Sammut, "An investigation of the microwave properties of resonant tunnelling devices," *Ph.D. Thesis*, University of Bath, 1992.
8. A. Sigurdardóttir, A. Megej, K. Beilenhoff, and H. L. Hartnagel, "Oscillator Circuit-Simulations Using a Novel, Mathematically Robust Large-Signal Equivalent Model for DBRTD," in *29th European Microwave Conf. Proc.*, Vol. 1 of 3, Oct. 1999, pp. 270-273.
9. R. Sun, L. Peng and D. S. Pan, "Analytical Theory for the Subfrequency Excitation of a Parametric Series-Integrated RTD Oscillator," *IEEE Trans. Microwave Theory Tech.*, Vol. 47, No. 10, Oct. 1999.
10. Z. X. Yan And M. J. Deen, "A New Resonant-Tunnel Diode-Based Multivalued Memory Circuit Using Mesfet Depletion Load," *IEEE J. Solid-State Circuits*, Vol. 27, No. 8, pp. 1198-1202, 1992.
11. O. Boric-Lubecke, D. S. Pan and T. Itoh, "DC Instability of the Series Connection of Tunnelling Diodes," *IEEE Trans. Microwave Theory Tech.*, Vol. 44, No. 6, pp. 936-943, June 1996.
12. O. Boric-Lubecke, D. S. Pan and T. Itoh, "Large signal Quantum-well Oscillator Design," in *Proc. 23rd Europe. Microwave Conf.*, Madrid, pp. 817-818, September 1993.
13. J. N. Schulman, H. J. De Los Santos and D. H. Chow, "Physics-Based RTD Current-Voltage Equation," *IEEE Elec. Dev. Lett.*, Vol. 17, No. 5, pp. 220-222, May 1996.
14. E. R. Brown, O.B. McMahon, L.J. Mahoney and K.M. Molvar, "SPICE Model of the Resonant - Tunnelling Diode," *Elec. Lett.*, Vol. 32, No. 10, pp. 938 -940, May 1996.
15. C. E. Chang, P. M. Asbeck, K. C. Wang and E. R. Brown, "Analysis of Heterojunction Bipolar Transistor/Resonant Tunnelling Diode Logic for Low-Power and High-Speed Digital Applications," *IEEE Trans. on Elec. Dev.*, Vol. 40, No. 4, pp. 685-690, April 1993.
16. M. T. Abuelma'atti and A. R. Ali, "Modelling Tunnel Diodes for Computer Aided Design," *Int. Journal of Infrared and Millimeter Waves*, Vol. 14, No. 6, pp. 1293-1297, 1993.
17. Z. Yan and M. J. Deen, "New RTD Large-Signal DC Model Suitable for PSPICE," *IEEE Trans. on CAD of Integrated Circuits and Systems*, Vol. 14, No. 2, pp. 167-172, February 1995.
18. J. R. Soderstorm, D. H. Chow, and T.C. McGill, "InAs/AlSb Double-Barrier Structure with Large Peak-to-Valley Current Ratio: A Candidate for High Frequency Microwave Devices," *IEEE Elec. Dev. Lett.*, Vol. 11, pp. 27, 1990.
19. *Microwave Harmonica Reference Manual*, Compact Software, Inc., Paterson, NJ
20. V. Rizzoli, A. Lipparini, and E. Marazzi, "A General-Purpose Program for Nonlinear Microwave Circuit Design," *IEEE Trans. Microwave Theory Tech.*, Vol. 31, No. 9, pp. 762-770, September 1983.
21. C. V. Sammut and N. J. Cronin, "Comparison of Measured and Computed Conversion Loss from a Resonant Tunneling Device Multiplier," *IEEE Microwave and Guided Wave Lett.*, Vol. 2, No. 12, pp. 486-488, Dec. 1992.
22. "MATLAB", The Math-Works Inc., MA.

A new method to measure the shape of short THz pulses: Differential Electronic Gating

J.N. Hovenier, R.W. van Es, T.O. Klaassen, W.Th. Wenckebach
Department of Applied Physics, Delft University of Technology, The Netherlands.
P.O. Box 5046, 2600 GA Delft, The Netherlands.

M. Krätschmer, F. Klappenberger, E. Schomburg, and S. Winnerl
Institut für Experimentelle und Angewandte Physik, Universität Regensburg, Germany.

G.M.H. Knippels and A.F.G. van der Meer,
FOM Institute for Plasma Physics, Nieuwegein, The Netherlands.

Abstract - A simple experimental method has been developed to determine the shape of repetitive picosecond THz pulses in the presence of jitter in the trigger signal. This method, a modification of the recently reported Differential Optical Gating (DOG) method, is based on the femtosecond electronic gating of a high-frequency sequential oscilloscope. Preliminary tests have been performed on pulses from the free electron laser FELIX as well as on pulses from a mode locked p-Ge laser.

I. INTRODUCTION

In the visible and near infrared spectral region many non-linear detection techniques are used to determine the shape of picosecond optical pulses by measuring the pulse intensity auto-correlation. At THz frequencies, some work has been done in this field. For instance, using two-photon absorption in p-type $\text{Hg}_x\text{Cd}_{(1-x)}\text{Te}$, the width of picosecond pulses of the free electron laser FELIX for a wavelength range from $20\text{ }\mu\text{m}$ to $40\text{ }\mu\text{m}$ has been studied [1]. Recently, it was demonstrated that a GaAs/AlAs superlattice detector could be used as an autocorrelator for intense THz pulses in the 1 – 7 THz frequency band [2, 3]. However, the intensity auto-correlation has, in principle, the disadvantage that any asymmetry in the pulse shape can not be determined. Also, general use of non-linear detection techniques at THz frequencies is not feasible due to the small optical susceptibilities of materials and/or low pulse intensities in this wavelength region.

Two *linear* techniques to analyze short THz pulses already exist. These use high intensity femtosecond optical pulses to *create* as well as to *detect* - through optical or electronic gating - broadband THz pulses [4, 5]. The intrinsic synchronization between a THz and a gating pulse results in a very good time resolution. Other

sources for the creation of short THz pulses, such as the free electron laser and the mode locked p-Ge laser, however, do not rely on optical pumping. The use of a gating technique, therefore, causes serious problems to synchronize the THz and gating pulses, strongly deteriorating the temporal resolution with which the THz pulse can be determined.

Recently, Rella et al. [6] developed the "Differential Optical Gating" (DOG) method, that enables the study of THz pulses with a good time resolution, *also* in the absence of an adequate synchronization between THz and gating pulse. A disadvantage of this technique is that, in order to obtain a time resolution of the order of picoseconds, a mode-locked Ti:Sapphire laser system is needed.

We have developed a simple technique, based on the DOG principle, that does not rely on optical, but on *electronic* gating. This work was started in order to determine the precise pulse width of our mode-locked p-Ge THz laser, which, until now was impossible because

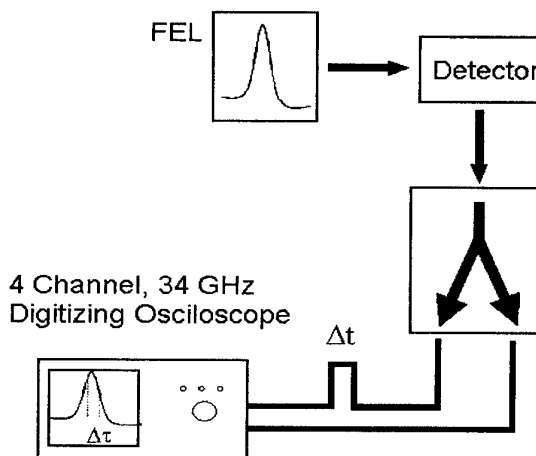


Fig. 1: Principal setup for the DEG method.

of the limited bandwidth of the 6 GHz single-shot oscilloscope used. We show that, with this "Differential Electronic Gating" (DEG) method together with an ultrafast room temperature detector, a time resolution in the picosecond range is possible.

II. PRINCIPLE OF THE DIFFERENTIAL TECHNIQUE

In the DEG technique the THz pulse is detected by one fast detector. The signal is *electronically* gated and recorded at two slightly different times t and $t + \Delta t$. In that way, both the average intensity

$\bar{I} = [I(t + \Delta t) + I(t)]/2$ and the time derivative of the intensity $F(\bar{I}) = [I(t + \Delta t) - I(t)]/\Delta t$ are determined. For a series of THz pulses, this yields a set of derivative *versus* intensity data, $\{F(\bar{I}) - \bar{I}\}$, which is *not* influenced by jitter in the trigger, as time as explicit variable has been eliminated. The actual pulse intensity as a function of time can now be reconstructed by integration:

$\int_{\bar{I}_0}^{\bar{I}_1} d\bar{I} / F(\bar{I}) = t(\bar{I}_1) - t(\bar{I}_0)$. It must be noted that

this integral is only well defined, if $F(\bar{I})$ does not contain any zeros. But at the pulse maximum the derivative will always be zero. Therefore, without additional assumptions it is only possible to reconstruct rising and falling edges of a pulse shape. In order to obtain the pulse duration, one can take advantage of the fact that the density of data points indicates the relative amount of time spent in a given part of the $F - \bar{I}$ curve.

By comparing the density in the peak region ($\bar{I} = \max$, and $F = 0$) with the density in the region, where $F \neq 0$, the time duration of the pulse peak can be inferred.

III. EXPERIMENTAL

We have tested the DEG technique (the principle of our experiment is shown in Fig.1), using either pulses at a wavelength of 150 μm from the free electron laser "FELIX", set at a 4 μs long macropulse and a micropulse repetition frequency of 1 GHz, or pulses at 175 μm from our mode-locked p-Ge THz laser. The light is focused on a fast room temperature superlattice detector [3] consisting of a GaAs/AlAs superlattice mounted in a corner cube reflector with a long wire antenna. The video output of the detector was amplified with a 28 ps rise time amplifier and split by a Picosecond Pulse Labs. Model 5335 high frequency power splitter. One signal is delayed with respect to the other, using two coaxial lines with a slightly different length. (see fig. 1) The signals $I(t + \Delta t)$ and $I(t)$ are measured at the same time on two different channels of a HP 54120B gating oscilloscope with 54123A front-end, featuring a 34 GHz bandwidth

and a 200 fs electronic gate width. Pulse shapes have also been studied using a single shot 6 GHz bandwidth Tektronix 7250 oscilloscope. The time delay between the channels, that determines the time scale of the reconstructed pulse, is measured by sending the scope's TDR pulse into the power splitter, and comparing the time delay of the signals on the two channels. At the

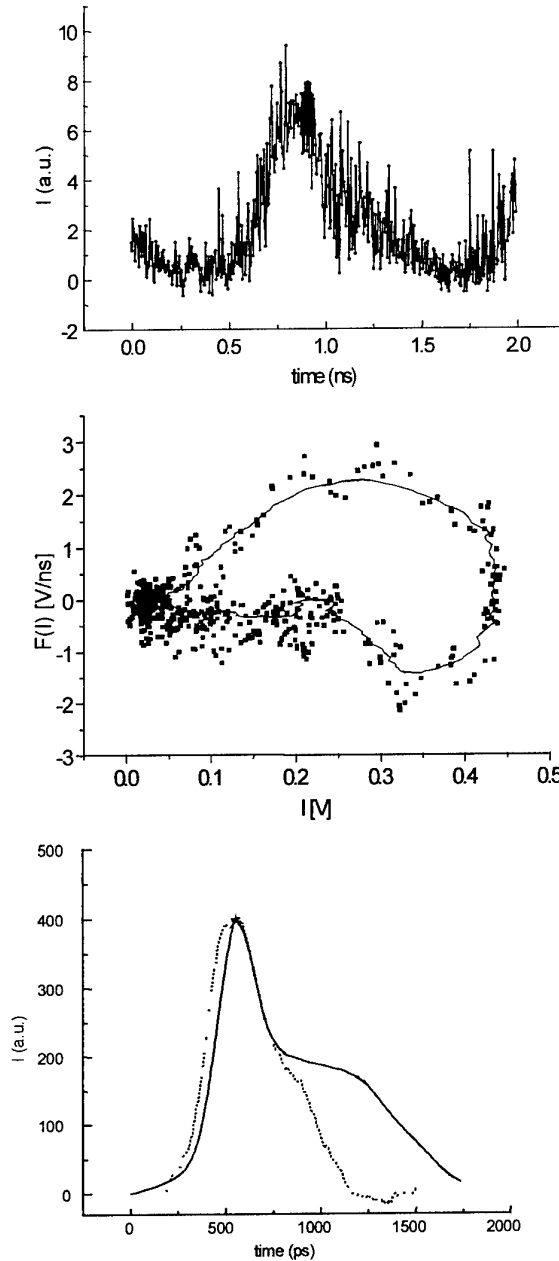


Fig. 2: Mode-locked p-Ge laser output:

- a: Sequential data with optical trigger.
- b: F versus I plot with $\Delta t = 40$ ps.
- c: Reconstructed pulse (solid line) and averaged sequential signal (dotted line).

same time the accuracy of the power splitting is checked. Using the normal sequential data collection routine of the oscilloscope, a set of data $\{I(t+\Delta t), I(t)\}$ is taken at each macropulse, with a 0.2 ps stepwise increase of the time delay between external trigger and electronic gate.

IV. RESULTS

The first experiment was performed using the output of our mode-locked p-Ge THz laser [8]. Earlier experiments using a 6 GHz bandwidth single shot oscilloscope proved that that source was able to produce 60 ps FWHM pulses. In view of the 50 ps overall rise time of that electronic system, clearly a way to improve the time resolution had to be found! In this experiment we used a 40 ps time delay between the two channels, and the optical signal itself was used as a trigger. In fig. 2^a the sequential data from two channels are shown, whereas in fig. 2^b the F versus I plot of a large data set is given. The reconstructed shape is shown in fig. 2^c, together with a pulse shape obtained from an averaged sequential scan. Although the FWHM value of the reconstructed pulse is slightly smaller, the overall shape is even worse than that obtained from the direct scan. Clearly this method does not work properly in this case. The reason for that is the strong shot to shot variation of the intensity and shape of the pulse resulting from strong mode beating of the laser.

To test the technique with a well controlled source with a reproducible pulse shape, experiments were started at the FELIX free electron laser. For this experiment, the laser was slightly detuned to create a double pulse structure [9]. In a first test we used $\Delta t=13$ ps and the optical signal itself was taken as a (very good) trigger. In fig. 3^a the resulting data sets for the two channels show a well defined double pulse structure. Fig. 3^b gives the same data set, but now plotted as F versus I ; a double loop curve is seen, characteristic for pulse structure with two unequal pulses. The reconstructed shape is given in fig. 3^c and compared to the direct signal of fig. 3^a. Because of the finite overlap between the two pulses, no zero intensity region in between the pulses occurs, and thus the distance between the pulses can be unambiguously determined from the experimental data. The two shapes match quite well and the FWHM value of the first peak in both cases is about 50 ps, mainly set by the amplifier rise time. For the second test $\Delta t=7$ ps was taken and the macropulse trigger was used with a jitter of about 1 ns; two orders of magnitude larger than the FWHM of the pulse. In the data from the first channel given in fig. 4^a, therefore, no pulse shape can be distinguished at all. In

Fig. 4^b the full data set $F-I$ plot is shown and the reconstructed double pulse is given in Fig. 4^c. The FWHM of the largest pulse is about 40 ps, slightly smaller than before, due to the smaller value of the time delay Δt used.

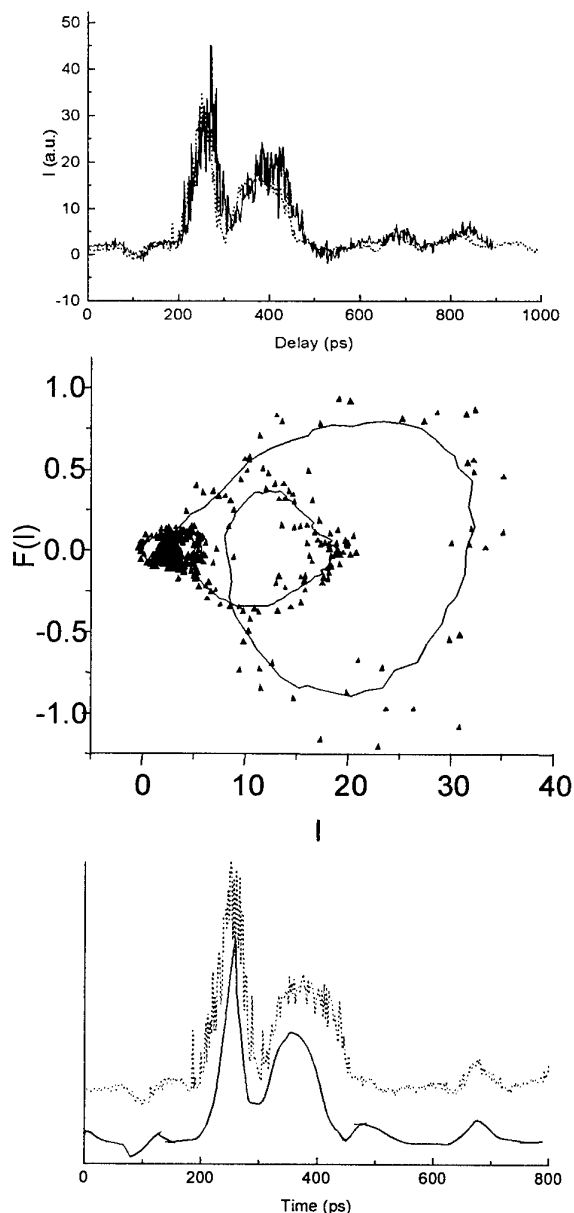


Fig. 3: FELIX double pulse:

- a: Sequential data with optical trigger: two channels with $\Delta t = 13$ ps.
- b: F versus I plot with double loop contour.
- c: Reconstructed pulse (solid line) compared with sequential pulse shape.

V. CONCLUSIONS

We have shown that the use of the differential electronic gating (DEG) method enables the detection of repetitive picosecond THz pulses, even when the jitter of the synchronization signal is much larger than the width of the pulse. The time resolution of this method is limited

by the electronic rise time of optical detector and electronics. The shot to shot reproducibility of the pulse shape, however, has to be good - like in all sequential recording techniques - in order to obtain an optimal result.

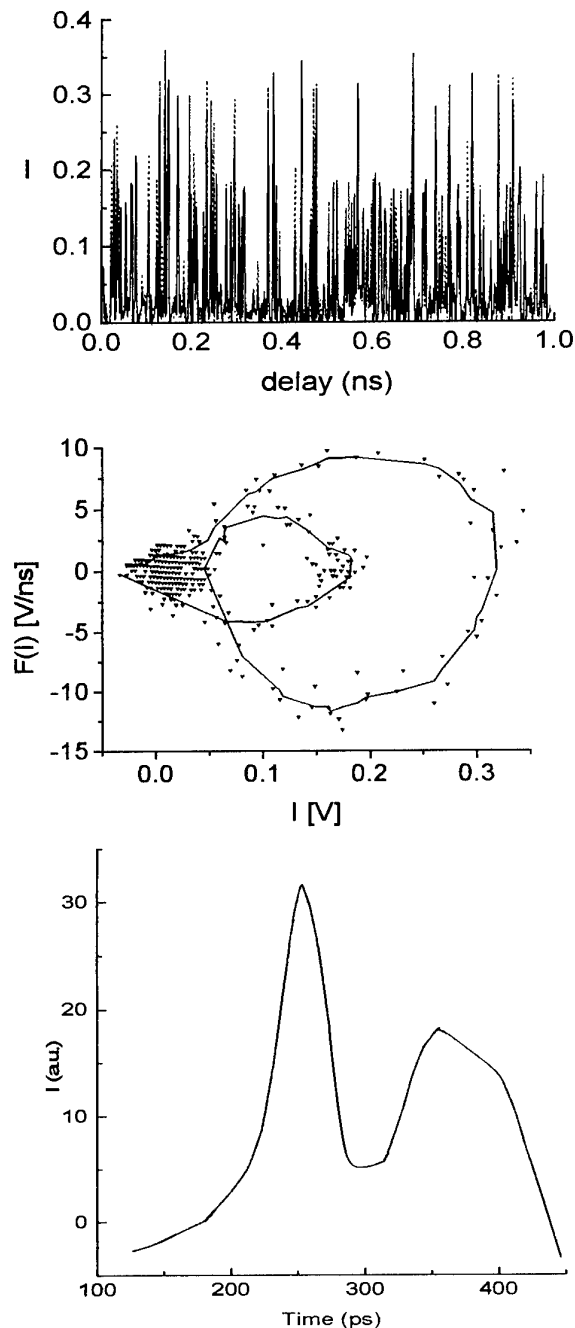


Fig. 4: FELIX double pulse:
a: Sequential data with macropulse trigger; two channels with $\Delta t = 7$ ps.
b: F versus I plot.
c: Reconstructed pulse with 40 ps FWHM.

Acknowledgments

The authors thanks M.J.W. Vermeulen from the Delft Interfaculty Reactor Institute for the use of the 6 GHz oscilloscope and W.Wegscheider for the sample growth.

References

1. J. Burghoorn, V.F. Anderegg, T.O. Klaassen, W.Th. Wenckebach, R.J. Bakker, A.F.G. van der Meer, D. Oepts, P.W. van Amersfoort, *Appl. Phys. Lett.* 61, 2330 (1992).
2. S. Winnerl, S. Peschl, E. Schomburg, J. Grenzer, K.F. Renk, H.P.M. Pellemans, A.F.G. van der Meer, D.G. Pavel'ev, Yu. Koschurinov, A.A. Ignatov, B. Melzer, V. Ustinov, S. Ivanov and P.S. Kop'ev, A GaAs/AlAs superlattice autocorrelator for picosecond THz radiation pulses, *Superlattices and Microstructures* 25, 57 (1999).
3. S. Winnerl, W. Seiwerth, E. Schomburg, J. Grenzer, K.F. Renk, C.J.G.M. Langerak, A.F.G. van der Meer, D.G. Pavel'ev, Yu. Koschurinov, A.A. Ignatov, B. Melzer, V. Ustinov, S. Ivanov, and P.S. Kop'ev, *Appl. Phys. Lett.* 73, 2983 (1998).
4. M. van Exter, D.R. Grischkowsky, *IEEE transactions on Microwave Theory and Techniques* 38, 1684 (1990).
5. X.-C. Zhang, Y. Jin, X.F. Ma, *Appl. Phys. Lett.* 61, 2764 (1992).
6. C.W. Rella, G.M.H. Knippels, D.V. Palanker, H.A. Schwettman, *Optics Communications* 157, 335 (1998).
7. S. Winnerl, E. Schomburg, J. Grenzer, H.-J. Regl, A.A. Ignatov, A.D. Semenov, K.F. Renk, D.G. Pavel'ev, Yu. Koschurinov, B. Melzer, V. Ustinov, S. Ivanov, S. Schaposchnikov, and P.S. Kop'ev, *Phys. Rev. B* 56, 10303 (1997).
8. J.N. Hovenier, T.O. Klaassen, W.Th. Wenckebach, A.V. Muravjov, S.G. Pavlov, V.N. Shastin, *Appl. Phys. Lett.* 72 (1998) 1140.
9. G.M.H. Knippels, X. Yan, A.M. MacLeod, W.A. Gillespie, M. Yasumoto, D. Oepts, A.F.G. van der Meer, *Phys. Rev. Lett.* 83, 1578 (....)

Electrical Detection of THz Frequencies by Asymmetrically Shaped n-n⁺-GaAs Diodes

Algirdas Suziedelis, Jonas Gradauskas, Steponas Asmontas, Gintaras Valusis,
Hartmut G. Roskos

Abstract – We propose a planar diode based on a thin asymmetrically-shaped n-n⁺-GaAs junction prepared on an elastic polyimide film as THz detector. The device can be used to detect electromagnetic radiation in the range from 0.129 THz up to 2.5 THz at room temperature. The principle of operation of the device is based on non-uniform carrier heating effects caused by both the asymmetrical shape of the structure and the presence of the n-n⁺-junction. An estimate of the sensitivity of the device based on a phenomenological approach for the description of the physical processes gives good agreement with the experimental data within the studied range of frequencies.

I. INTRODUCTION

Detection of terahertz radiation usually relies on optical techniques employing mainly either photoconducting dipole antennas [1] or free-space electro-optic sampling [2]. Despite of a very high sensitivity and attractive frequency band features (with electro-optic THz detection it is possible to measure coherent transients spanning frequencies from 100 GHz to over 30 THz [3] if the sensor crystals is selected properly), the detection system requires coherence between the optical and the THz radiation and thus is suited only for detection of THz signals generated by optical means.

As an alternative, electrical methods for THz detection can be utilized. For instance, it was determined that THz radiation produces a strong modulation of the photocurrent due to intrasubband THz absorption in coupled quantum well diodes [4]. Very recently, voltage-tunable THz detectors for 2-5 THz have been demonstrated [5]. Here, the principle of operation is based on the convolution of the THz absorption coefficient and the effect of carrier heating on the photocurrent.

This communication presents a n-n⁺-junction GaAs diode which can be used for electrical detection of electromagnetic radiation from frequencies from 100 GHz up to 2.5 THz at room temperature. The device operation relies on non-uniform free-carrier heating effects in asymmetrically necked n-n⁺-junctions under external THz illumination, causing a voltage drop over the ends of the sample. Hence, a bias voltage is not required for device operation. The planar geometry enables us to avoid undesirable design-induced effects such as parasitic capacitances and layer contact resistances due to the small

size of the Ohmic contacts which are inherent for whisker-contacted diodes.

II. DEVICE FABRICATION TECHNOLOGY

Fig. 1 shows the asymmetrically shaped diode fabricated photolithographically on the basis of a n-n⁺-GaAs epitaxial structure. For metal contacts to the diodes Ge-Ni-Au thermal evaporation was used. The metallisation patterns were formed using direct lift-off technique. The metal contacts were then annealed in inert gas atmosphere. Further, the semiconductor structures were covered with polyimide material by spin-on technique and cured at 250⁰ C for one hour in order to obtain an elastic polyimide film with a thickness of 10 μm serving as mechanical support layer for the finished device. After thinning the semiconductor substrate to a desirable thickness, the semiconductor wafer was completely removed by wet etching at the metal contacts. As a result of the technological procedures, an array of diodes each with a length of 500 μm, thickness of 3 μm and width at the neck of about 10 μm was obtained.

Fig. 1 shows the layout of the device. It should be noted that the doping in the n-region is close to 10¹⁵cm⁻³, while it is about 2·10¹⁸cm⁻³ in the n⁺-region. The high doping of the narrower part of the semiconductor structure is desirable in order to improve the impedance matching of the diode.

III. MEASUREMENT TECHNIQUES

The device frequency characteristics was examined over a wide range of THz frequencies at room temperature.

In the range of 0.129÷0.143 THz we employed clystrons generating pulsed signals with a duration of several microseconds and a repetition rate of 40 Hz. In this kind of experiments the detector diodes were placed in rectangular waveguides.

In the range of frequencies from 0.693 THz up to 2.52 THz we used a CO₂-pumped CW THz laser. Here, a teflon lens served to concentrate the incident field on the freely-mounted sample. The signal was measured by lock-in amplifier at a chopper frequency of 40 Hz.

In all experiments, the electric field was oriented along the sample.

IV. THEORETICAL ANALYSIS

The operation of the device and its voltage sensitivity were analyzed in the warm-electron range using a phenomenological approach including equations for the

A. Suziedelis, J. Gradauskas and S. Asmontas are with the Semiconductor Physics Institute, A.Gostauto 11, LT-2600 Vilnius
G. Valusis and H. G. Roskos are with Physikalisches Institut der Universität, Robert-Mayer Str. 2-4, D-60054 Frankfurt

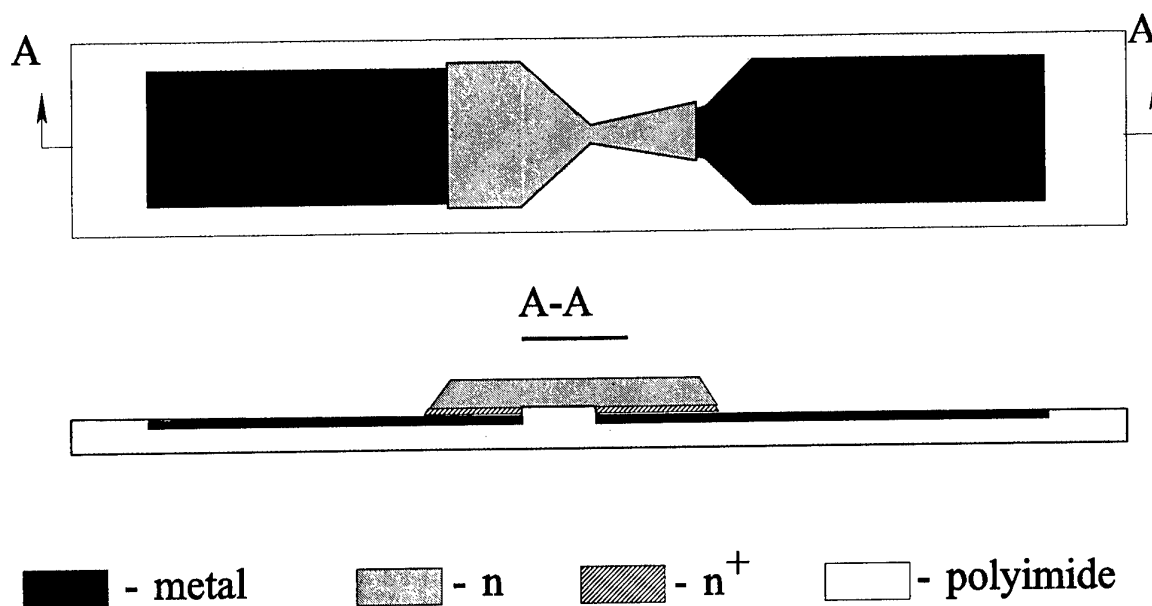


Fig. 1: Schematic view of the asymmetrical n-n⁺-GaAs diode

current density, heat balance, heat flow density and the electric field. Further details can be found in [6].

V. EXPERIMENTAL RESULTS AND DISCUSSION

The principle of the diode operation is based on thermoelectromotive forces of hot carriers under the influence of the external THz radiation. First, due to the asymmetrical shape of the diode, the gradients of the electric field at different sides of the diode are different, consequently, non-uniform carrier heating occurs. As a result, this so-called bi-gradient effect of hot carriers [7] induces a voltage signal along the sample. Second, since the structure contains a n-n⁺-junction, a conventional thermoelectromotive force of hot carriers also arises in the diode in addition to the bi-gradient one. Therefore, the increased doping of the some of the necked part of the diode not only allows to get better matching of the sample resistance with the impedance of the waveguide, which is especially important for application of these diodes in microwaves [8], but also enhances the voltage sensitivity of the device.

Fig. 2 presents the theoretical prediction (solid line) and the measured data (circles) of the voltage sensitivity of the device as a function of frequency in the THz range. It is seen that this dependence is nearly independent on frequency up to 0.3 THz. The observed decrease at higher frequencies is due to electron momentum relaxation.

As is evident from Fig.2, the experimental values of the voltage sensitivity are in a good agreement with the theoretical calculations within the studied range of frequencies. It should be pointed out here, how the experimental values of the voltage sensitivity have been determined. We have proceeded in the following way: The voltage response as a function of the THz power

absorbed in the active region of the device can be deduced from the static I-V-curve. What remains unknown, however, is the power absorbed in a specific measurement geometry. The absorbance in the active region has to be estimated in a careful way as described in detail in ref. [8]. For our free-space detection geometry covering the range from 0.693 THz to 2.52 THz, it is estimated that only a fraction of 10^{-4} of the incident power contributes to carrier heating in the active area and thus to the voltage signal.

The detected signal was found to be linearly proportional to the incident power in all studied frequencies (power-voltage characteristics are not given in this communication). This illustrates the suitability of the proposed device for the electrical detection and power measurement of THz frequencies over a broad frequency range.

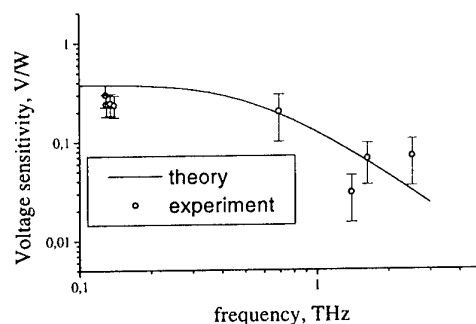


Fig. 2: Voltage sensitivity at THz frequencies

Despite a number of advantages, such as the wide frequency band of operation, the fact that no bias voltage

is needed, and the room-temperature operation, it is evident that the device suffers from rather low voltage sensitivity, which around 0.1 THz it is close to 0.3 V/W while at 2.5 THz it amounts to 0.06 V/W. Clearly, for direct applications higher values are desirable. Theory [8] shows two ways to solve his problem: Firstly, since the sensitivity is proportional to the mobility of the carriers, semiconductor material with high mobility values should be found to be more suitable for the production of the device; secondly, since the sensitivity is inversely proportional to the square of the size of the necked part of the diode [8], it should be possible to achieve a voltage sensitivity reaching 100 V/W at the range of frequencies below 0.5 THz by narrowing the neck down to 300 nm size.

VI. CONCLUSION

We proposed a wide-band THz detector based on asymmetrically necked GaAs structures containing a $n-n^+$ junction. The origin of the voltage signal arising over the sample is the result of nonuniform heating of free electrons caused by external illumination. The experiments indicate that the bigradient and the thermoelectric effects of hot carriers can be successfully employed for THz-frequency detection and encourage to look for better designs of the device in order to increase its voltage sensitivity.

Acknowledgement

The authors express their sincere acknowledgements to Dr. Bernd Wolf, Steffen Schmidt and Dr. Holger Schwenk for the professional help in the THz experiments. Also, we are greatly indebted to Robert Sachs, Vitaly Ksenevich, Torsten Löffler, Pablo Richter

and Tobias Bauer for enlightening discussions. We sincerely thank Herbert Hassenpflug for help with the improvements of the experimental set-up. G.V. acknowledges Alexander von Humboldt-Stiftung for financial support.

References

1. P. R. Smith, D. H. Auston, and M. C. Nuss, "Subpicosecond Photoconducting Dipole Antennas", *IEEE Journ. Quantum Electr.*, Vol. 24, No. 2, pp. 255-260, 1988
2. Q. Wu and X.-C. Zhang, "Free-Space Electro-Optic Sampling of Terahertz Beams", *Appl. Phys. Lett.*, Vol. 67, No. 24, pp. 3523-3525, 1995
3. P. Y. Han and X.-C. Zhang, "Coherent, Broadband, Midinfrared Terahertz Beam Sensors", *Appl. Phys. Lett.*, Vol. 73, No. 21, pp. 3049-3051, 1998
4. R. J. Stone, J. G. Michels, S. L. Wong, C. T. Foxon, R. J. Nicholas, and A. M. Fox, "Detection of Terahertz Radiation by Hot Electron Effects in Coupled Quantum Well Photodiodes", *Appl. Phys. Lett.*, Vol. 69, No. 23, pp. 3569-3571, 1996
5. A. M. Tomlinson, C. C. Chang, R. J. Stone, R. J. Nicholas, A. M. Fox, M. A. Pate, and C. T. Foxon, "Intersubband Transitions in GaAs Coupled-Quantum-Wells for Use as a Tunable Detector at THz Frequencies", *Appl. Phys. Lett.*, Vol. 76, No. 12, pp. 1579-1581, 2000
6. S. Asmontas, J. Gradauskas, A. Suziedelis, "Wide Frequency Band Radiation Detector", *Int. Conf. on Millimeter and Submillimeter Waves and Applications, SPIE Proc.*, Vol. 2842, pp. 434-441, 1996
7. S. Asmontas, "Electrogradient phenomena in Semiconductors, (Mokslas, Vilnius, 1984), p.183. (in Russian)
8. S. Asmontas, A. Suziedelis, "New Microwave detector", *Inter. Journ. Infrared and Millimet. Waves*, Vol. 15, No. 3, pp. 525-538, 1994

Fast Physical Optics Simulation of the Dual-Reflector Submillimetre-Wave Telescope on the ESA PLANCK Surveyor

Vladimir Yurchenko, John Anthony Murphy, Jean-Michel Lamarre

Abstract – We present physical optics simulations of the dual-reflector submillimetre-wave telescope on the ESA PLANCK surveyor. The telescope is of a non-conventional Gregorian configuration, with two ellipsoidal reflectors providing a very large field of view at the focal plane where the array of 76 horn antennas feeding low-temperature detectors is located. We analyse defocusing effects of the system, polarization characteristics of the telescope, and the optical performance of high-frequency channels based on special multi-mode horns operating at 545 and 857 GHz.

I. INTRODUCTION

ESA PLANCK surveyor is being designed for imaging the temperature anisotropies and polarization characteristics of the cosmic microwave background over the whole sky with unprecedented sensitivity, accuracy and angular resolution using nine frequency channels ranging between 25 and 1000 GHz [1].

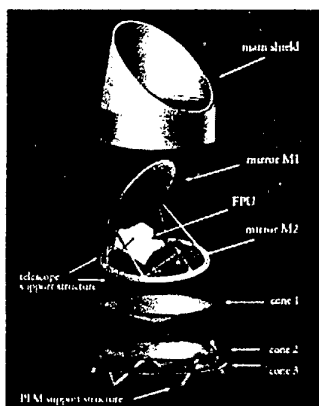


Fig. 1: A general view of the Planck telescope

To achieve this goal, the PLANCK surveyor utilizes a special dual-reflector submillimetre-wave telescope of a non-conventional Gregorian configuration. Both the design and simulation of such a telescope are extremely challenging. Firstly, the telescope is electrically large, the primary mirror having a projected aperture diameter of

Vladimir Yurchenko is with the Institute of Radiophysics and Electronics, National Academy of Sciences of Ukraine, 12 Proskura St., Kharkiv, 61085, Ukraine

Vladimir Yurchenko is also with the National University of Ireland, Maynooth, Co. Kildare, Ireland

John Anthony Murphy is with the National University of Ireland, Maynooth, Co. Kildare, Ireland

Jean-Michel Lamarre is with the Institut d'Astrophysique Spatiale, Université de Paris XI, bat.121, 91405, Orsay Cedex, France

D=1500 mm while the minimal wavelength involved is only about $\lambda=0.3$ mm (i.e., $D/\lambda=5000$). Secondly, it is an axially asymmetric system that consists of two essentially defocused ellipsoidal reflectors providing a very large field of view at the focal plane where the array of 76 horn antennas feeding low-temperature detectors is located. To add to the complexity, 14 channels operating at the highest frequencies of 545 and 857 GHz, are based on the multi-mode horns [2] designed for receiving maximum microwave power within the required angular resolution of 5 arcminutes on the sky. Polarization characteristics of the microwave background should be measured in different channels as well.

Among various simulation techniques appropriate for such a design, physical optics is the most adequate one for the given problem [3, 4]. However, conventional implementations of the technique are unacceptably slow. Our implementation overcomes the limitations of a generic approach for large multi-reflector systems and can perform typical simulations of the telescope in the order of minutes.

II. GEOMETRY OF THE TELESCOPE AND DETECTOR UNIT

A general view of the Planck telescope is shown in Fig.1 and a view of the entrance horns of High-Frequency Instrument (HFI), as seen from the telescope, is given in Fig.2 [5].

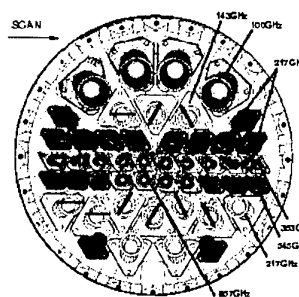


Fig. 2: A view of the entrance horns of HFI

In this paper, we consider power patterns, polarization characteristics and defocusing effects of two beams that correspond to the horns H-143-4 ($f=143$ GHz) and H-545-1 ($f=545$ GHz), the ones on the extreme left in the second and in the fourth rows from the bottom in Fig.2 (notations in Fig.2 and some parameters referenced in [1] are out of date).

H-143-4 is a Gaussian horn with the electric field at the aperture being linearly polarized and given by the formula

$$\vec{E}(r) = E_0 \exp(-r^2/w_0^2) \vec{e}_0 \quad (1)$$

where r is the radial coordinate, $w_0 = 3.289$ mm is the half-waist of the beam, $a = 5$ mm is the aperture radius and \vec{e}_0 is the polarization vector. H-545-1 is a multi-mode conical horn, with the electric field at the aperture given by the set of six modes ($m = 1..6$) defined as follows

$$\vec{E}_m(r) = E_{0m} J_n(p_m r/a) \exp(iqr^2) \vec{e}_m(\varphi) \quad (2)$$

where $J_n(\cdot)$ is the Bessel function, $n = 0, 1, 2$ when $m = 1$ or 6 , 2 or 3 , and 4 or 5 , respectively, $p_1 = 2.405$, $p_2 = p_3 = 3.831$, $p_4 = p_5 = 5.136$, $p_6 = 5.520$, $q = \pi/\lambda L$, $L = 28$ mm is the length of the horn, $a = 4.1$ mm is the aperture radius, and $\vec{e}_m(\varphi)$ is the polarization vector depending on the azimuthal angle, $\vec{e}_{1,6} = \hat{j}$, $\vec{e}_{2,3} = \pm \sin(\varphi)\hat{i} + \cos(\varphi)\hat{j}$, and $\vec{e}_{4,5} = \sin(2\varphi)\hat{i} \pm \cos(2\varphi)\hat{j}$. Amplitudes E_0 and E_{0m} in (1) and (2) are normalized so that each mode has the total power $P = 1$. Horn positions and orientations are specified with respect to the reference detector plane P defined as a plane normal to the chief

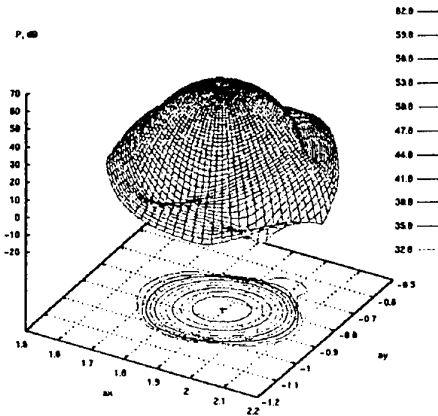


Fig. 3: Power pattern of the beam H-143-4

ray at the (0,0) point that is the paraxial focus of the telescope. When studying defocusing effects, we have the horn axis fixed. The geometrical focus of the horn, F, is specified by the refocus parameter R_F defined as a distance from the plane P to the point F measured along the horn axis, with $R_F > 0$ when moving towards the secondary mirror. Optimum 'geometrical' values of R_F have been provided as a result of the previous design performed with the ray tracing software. For the horns H-143-4 and H-545-1, they are $R_F = 10.5$ mm and $R_F = 5.526$ mm, respectively.

III. BEAM FROM THE GAUSSIAN HORN H-143-4

Fig.1 shows the power pattern of the telescope beam from the Gaussian horn H-143-4 as projected on the plane normal to the telescope line-of-sight at (0, 0) point (α_x and α_y are the horizontal and vertical axes on the plane, respectively, measured in degrees). The beam is perfectly shaped down to -30 dB below the maximum, with the beam width being about 8 arcmin at -3 dB. The polarization of the beam is, generally, elliptical except at the very axis where it remains linear. In order to achieve the required orientation of the polarization pattern in the sky, we should orient the polarization

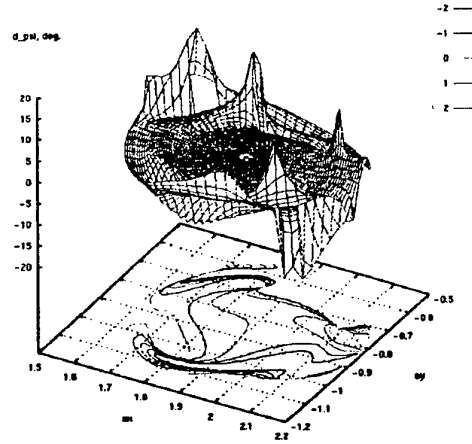


Fig. 4: Deviation of the major axis of polarization ellipse from the local meridian as a function of the observation point within the beam

vector \vec{e}_0 properly on the horn aperture. For immediate comparison of polarizations measured by different horns when scanning through the sky, we should use easily aligned directions in the sky as equivalent reference polarization axes for different beams. Such directions are the meridians in the spherical frame of the telescope, with the telescope spin axis being the pole (the meridians define local verticals at various observation points). Also, we should properly define the reference axis for polarization vectors \vec{e}_0 of differently tilted horns. We define the reference axis as the direction of \vec{e}_0 in the aperture plane that is projected on the vertical axis in the detector plane P. Orientation of \vec{e}_0 is specified by the angle φ_e in the aperture plane measured from this reference clockwise when looking from the horn to the secondary mirror.

Using these definitions, we find that the beam from the horn H-143-4 is vertically polarized on the axis (the electric field is directed along the meridian) if the horn polarization vector \vec{e}_0 is specified by the angle $\varphi_e = 3.04$ deg.

The deviation of the major axis of the polarization ellipse from the local meridian as a function of the observation point within the beam is shown in Fig.4.

When the polarization is properly adjusted, the cross-polarized component of the field measured with respect to the given direction is minimized. For example, in the case of the vertical polarization discussed above, the power pattern of the cross-polarized component measured as the horizontal component of the electric field, is shown

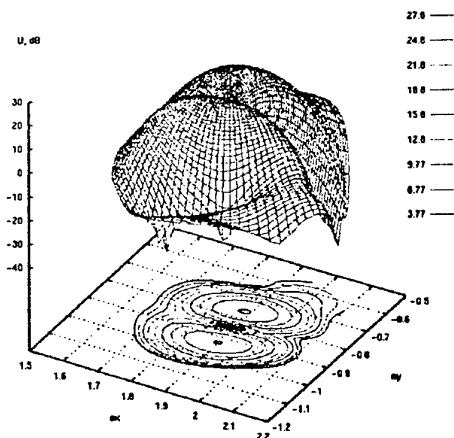


Fig. 5: Power pattern of cross-polarized (horizontal) component of the vertically polarized beam from the Gaussian horn H-143-4

in Fig. 5. It resembles very much the power pattern of the minor axes of polarization ellipses, being only somewhat greater in magnitude at the points where the polarization ellipse is more tilted with respect to the local meridian. Observing Figs. 3 and 5, we can see that the cross-polarized component in this case is about -35 dB below the co-polarized one that constitutes the main power of the beam. For comparison, if the polarization vector \vec{e}_0 is not properly adjusted ($\varphi_c = 0$), the cross-polarized component is 10 dB greater than possible minimum.

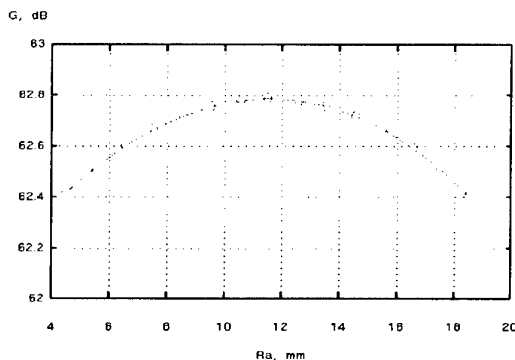


Fig. 6: Defocusing effect of the horn H-143-4

Finally, Fig. 6 shows the defocusing effect of the horn on the gain function G defined as

$$G = 10 \log_{10} (4\pi P(0) / P) \quad (3)$$

where $P(0)$ is the power flux on the beam axis and $P = 1$ is the total power of the beam. The position of the horn is specified by the refocus parameter R_A similar to

R_F but measured to the centre of the horn aperture. For the Gaussian horn with the plane phase front at the aperture, the optimum value of R_A is expected to be about R_F . Indeed, Fig. 6 shows that the optimum position is only 1 mm = 0.5λ ahead of the geometrical focus R_F , and the variation of G is sufficiently small, being only 0.4 dB within the range of ± 7 mm = $\pm 3.5\lambda$ around the optimum point.

IV. BEAM FROM THE MULTI-MODE HORN H-545-1

Multi-mode horns are designed for receiving maximum microwave power within the required angular resolution consistent with the requirements on the beam taper at the secondary mirror at the level of -30 dB, with the aspect angle of 20 degrees. These are rather restrictive and contradictory requirements resulting in a rather big aperture area of the corrugated conical horns.

Since the phase front of the horn aperture field is convex, the effective focal centre is located inside the horn at the distance R_C from the aperture. For the horn H-545-1, assuming the shape of the beam approximately Gaussian, R_C is estimated as $R_C = 25.8$ mm. It is expected that the horn is properly focused if the aperture refocus parameter R_A is $R_A = R_F + R_C = 31.3$ mm. In this case, since the total field of the horn is quite uniform within the aperture and rapidly decays outside the horn, one should expect the far-field pattern of the telescope beam to be just a map of the aperture field, with the beam being perfectly shaped. The full beam width is estimated $W = 2Ma = 14$ arcmin where $M = 1.72$ arcmin/mm

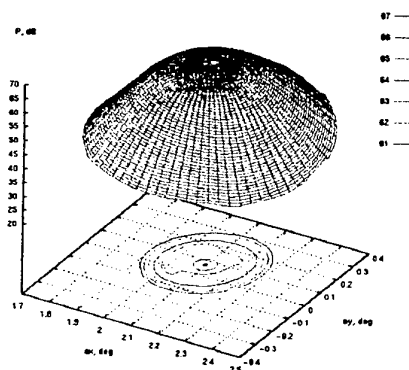


Fig. 7: Power pattern of the multi-mode horn H-545-1 placed 'in-focus' ($R_A = 31.3$ mm)

is the magnification of the telescope and $a = 4.1$ mm is the horn aperture radius.

The power pattern of the telescope beam computed in this case is shown in Fig. 7. The beam is quite symmetrical, well shaped and has a flat top but it is too wide compared to the requirements. The edge of the flat top is about -3 dB below the maximum, and the beam width at the edge is approximately 17 arcmin that is quite close to the estimate above but more than three times greater compared to the required resolution of 5 arcmin.

In order to find the optimum position of the horn, we studied defocusing effect in a wide range of the refocusing parameter R_A , Fig. 8.

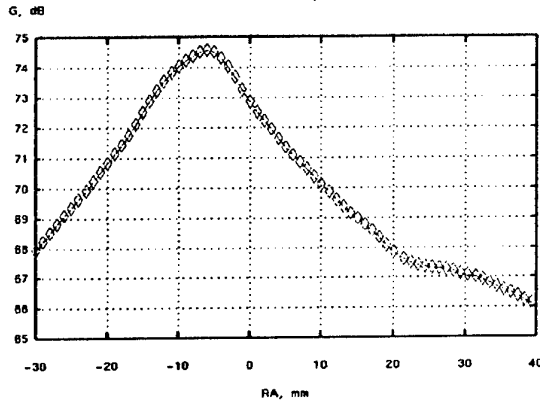


Fig. 8: Defocusing effect of the horn H-545-1

In terms of the gain G defined in (3) where $P(0)$ is the flux along the beam axis of the total power of all the modes in both polarizations and $P = 1$ is the power of a single mode, the maximum gain is achieved when $R_A = -6$ mm.

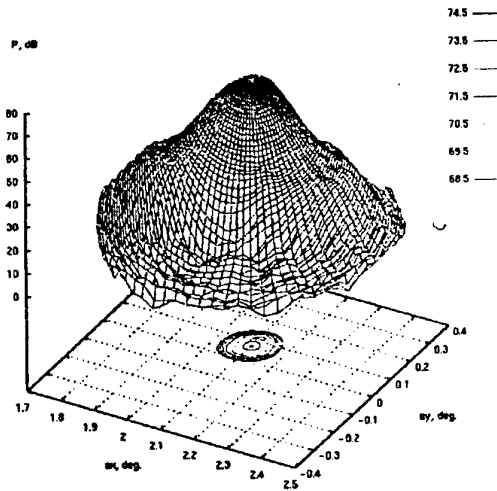


Fig. 9: Power pattern of the horn H-545-1 placed at the position of $R_A = -6$ mm providing the maximum gain $G = 74.5$ dB

The beam pattern computed in this case is shown in Fig. 9. As one can see, the total power of the beam is concentrated in a much smaller area resulting in a significant increase in the gain G . The beam is still slightly flat topped, although not so perfect, being of elliptical shape. The effective width of the beam at the edge of the flat top (at -3 dB) varies from $W_{\min} = 6$ arcmin to $W_{\max} = 7.5$ arcmin that is just slightly greater than the desired angular resolution of the telescope at the

given frequency. Power patterns of different modes composing the beam are shown in Fig. 10.

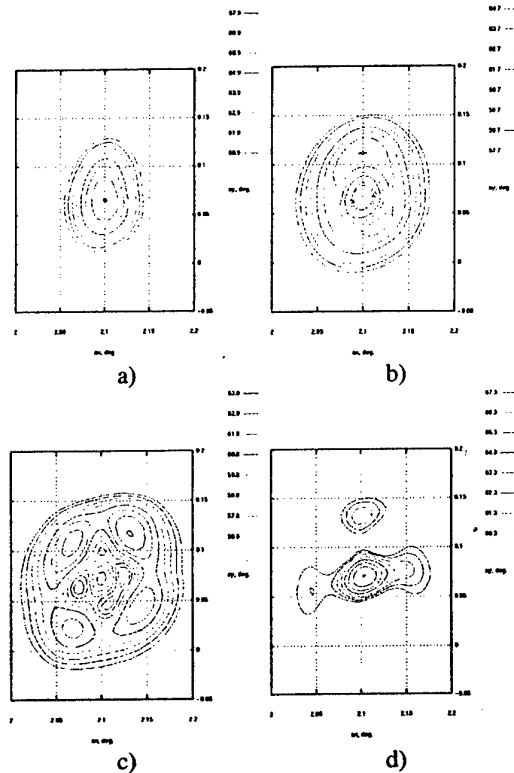


Fig. 10: Power patterns of different modes: (a) $m=1$; (b) $m=2,3$; (c) $m=4,5$; (d) $m=6$

V. CONCLUSION

Fast physical optics simulator has been developed for the analysis of the dual-reflector submillimetre-wave telescope on the ESA Planck Surveyor. Study of the power patterns, polarization, defocusing effects and modal structure of the telescope beams from both the Gaussian and multi-mode horns operating at 143 and 545 GHz, respectively, has been performed.

Acknowledgement

The authors are grateful to Yuying Longval for providing updated positions and aiming angles of the high-frequency horns. V.Y. and J.A.M. would like to acknowledge the support of Enterprise Ireland.

References

1. <http://astro.estec.esa.nl/Planck>
2. R. Colgan, J. A. Murphy, B. Maffei, C. O'Sullivan, R. Wylde, P. Ade, "Modelling Few-Mode Horns for Far-IR Space Applications", to appear in Eleventh Int. Symp. on Space Terahertz Technology, 2000
3. L. Diaz, T. Milligan, Antenna Engineering Using Physical Optics: Practical CAD Techniques and Software, Artech House, London, 1996
4. C. Scott, Modern Methods of Reflector Antenna Analysis and Design, Artech House, London, 1990
5. http://astro.estec.esa.nl/Planck/pictures/pictures_top.html

Few-Cycle THz Generation from Semiconductor Quantum Structures

R. Bratschitsch, T. Müller, R. Kersting, G. Strasser, K. Unterrainer

Abstract – During the past years several groups showed that ultrafast photoexcitation of semiconductors generates coherent THz radiation. We present a new emission process which overcomes the limitations of the conventional generation schemes (intensity, frequency, tuning). We use n-doped GaAs layers where extrinsic electrons are confined between the substrate and the surface depletion field. In addition, modulation doped parabolic quantum wells are used where the THz emission frequency can be designed by the well dimensions. In our experiments, the THz radiation is generated by excitation of the GaAs structures with femtosecond laser pulses. Auto correlation data of the pulses are recorded using a Michelson interferometer and a Si-bolometer detector.

From the n-doped layers we observe intense, coherent THz radiation. The THz emission is generated by coherent plasma oscillations of the extrinsic electrons inside the layer. Femtosecond laser excitation of the GaAs leads to an ultrafast screening of the surface depletion field. Thus, the extrinsic electrons respond to the fast field change by starting coherent plasma oscillations. The frequency of the THz emission increases with higher doping - according to the square root dependence of the plasma frequency on the carrier concentration $/1/$. Since the emission spectrum shows no dependence on excitation density we conclude that the emission results exclusively from the coherent oscillation of the extrinsic electrons. In all experiments we observe temporally and spatially coherent THz radiation with intensities of up to 100 nW.

The dephasing time of the plasma oscillation is limited to <1 ps due to the mobility of the electrons in the layer. A longer dephasing time can be achieved by modulation doping. We used modulation doped, parabolic GaAs/AlGaAs quantum wells with widths in the range of 1200 - 2000 Å and carrier sheet densities of 1.7×10^{11} - $5 \times 10^{11} \text{ cm}^{-2}$. The spectrum of the emitted THz radiation consists of two components, a broad one around 0.8 THz and a narrow one (FWHM: 0.3 THz) with a center frequency of 2.54 THz $/2/$. The narrowband emission results from the intersubband plasmon oscillation of the carriers inside the PQW. The observed frequency corresponds very

well to the designed frequency given by $\omega_0 = \sqrt{\frac{8\Delta}{L^2 m^*}}$,

where Δ is the depth, and L is the width of the well. The dephasing times are increased by about one order of magnitude compared to the "bulk" GaAs layers.

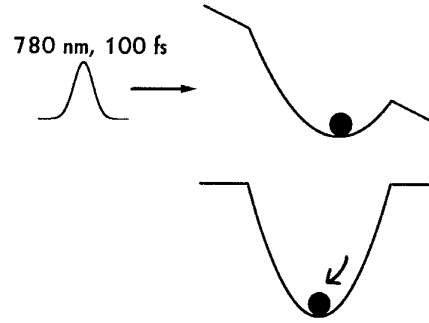


Fig.1: Schematic drawing of the excitation mechanism: an oscillation of the carriers in the parabolic potential is initiated by ultrafast field screening.

Using these new THz generators we perform THz time domain spectroscopy to investigate transitions between quantized states in semiconductor nanostructures. $/3/$

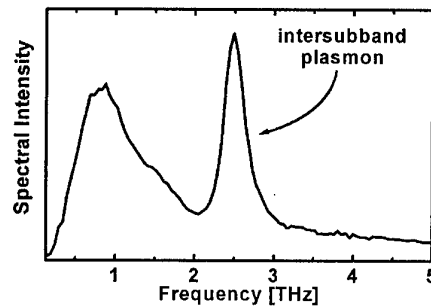


Fig. 2: THz emission spectrum of the 1400 Å PQW excited by 780 nm, 100fs laser pulses.

REFERENCES

1. R. Kersting, K. Unterrainer, G. Strasser, H.F. Kauffmann, E. Gornik, Phys. Rev. Lett., **79**, 3038 (1997).
2. R. Bratschitsch, T. Müller, R. Kersting, G. Strasser, and K. Unterrainer, Appl. Phys. Lett., (June 2000).
3. R. Kersting, R. Bratschitsch, G. Strasser, K. Unterrainer, J. N. Heyman, Opt. Lett., **25**, 272 (2000).

At the time of publication the final manuscript was not available.

From Honey-Comb to SMMIC: Schottky Diodes at TU Darmstadt

Chih-I Lin¹, Victoria Ichizli, Manuel Rodríguez-Gironés,
Mustafa Saglam, Paweł Szeliga, Hans L. Hartnagel

Abstract – GaAs Schottky diode proved itself to be one the main semiconductor device used in THz-electronics. This contribution describes the evolution of THz-devices from honey-comb whisker-contacted Schottky diodes to sub-millimetre monolithically integrated circuits (SMMIC) at University of Technology (TU) Darmstadt. Short description of each device and integration type is given together with pointing technological and device particularities.

I. INTRODUCTION

The interest to THz radiation grows with enormous speed due to the wide range of frequencies and their suitable applicability to various fields, from atmospheric, earth, medical and biological studies to automobile and industrial involvement. The main units in heterodyne mixer systems are the local oscillator and the mixer. Mixing and frequency multiplying in THz region requires the use of very fast non-linear devices with high cut-off frequency. GaAs Schottky diodes represent ones of the fastest electronic semiconductor devices known nowadays due to the high electron mobility, absence of minority carriers and very simple structure. Due to the non-linearity of the current-voltage-characteristics and the capacitance-voltage-characteristics, GaAs Schottky diodes are often used in heterodyne mixers and frequency multipliers in the THz region, respectively. Their device configuration varies from single diodes for hybrid integration to monolithically integrated circuits. In this contribution we will discuss the device configuration of GaAs Schottky diodes available at TU Darmstadt, and consequently the evolution of their technology.

II. SINGLE SCHOTTKY DIODES

Schottky varactor diodes are the key element for all-solid-state local oscillator sources at frequencies higher than 100 GHz. A single Schottky diode represents itself as a highly efficient for varactor applications. For hybrid integration, both whisker-contacted and single planar Schottky diodes are successfully used. Although planar diode technology improved substantially, whisker contacted Schottky diodes still provide the highest efficiencies and output powers at frequencies above 300 GHz. The conventional form of whisker-contacted diodes was modified into a substrateless device configuration [1] by reducing the odd part of n^+ -GaAs from hundreds to only a few micrometers. There is a large number of advantages of the latter against the conventional one, among which: less influence of skin effect, better heat sink, small semiconductor volume, and vertical current flow.

All that leads to significant improvements in performance, which were shown from RF-measurements for frequency multipliers and mixers using substrateless diodes [2]. As a logical sequence of vertical configuration is the Quasi-Vertical structure of planar Schottky diode (QVD), developed at TU Darmstadt. Fig. 1 presents schematically the technology evolution from the conventional whisker-contacted diode to QV-configuration of a planar diode.

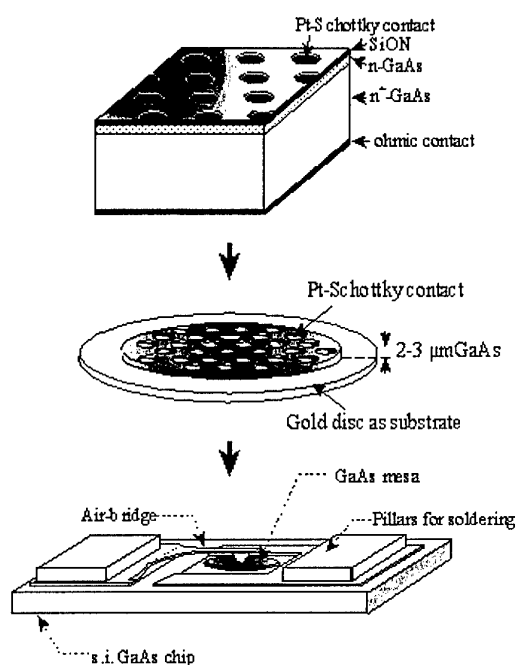


Fig.1: The way from a whisker-contacted diode to a quasi-vertical planar Schottky diode

Fig. 2 offers some examples of substrateless and planar Schottky diode fabricated according to the principle described above. Let us attend your attention here for some details of device particularities and parameters of both substrateless and planar Schottky diodes.

A. Substrateless Whisker-Contacted Schottky Diode

Substrateless Schottky diodes, proposed in 1995 [1], offer the prospect to increase the power handling capabilities and to receive a minimum series resistance. Compared with the conventional diode chip the thickness of the n^+ -GaAs (gallium arsenide) substrate is strongly reduced from 100 μm to 2 μm .

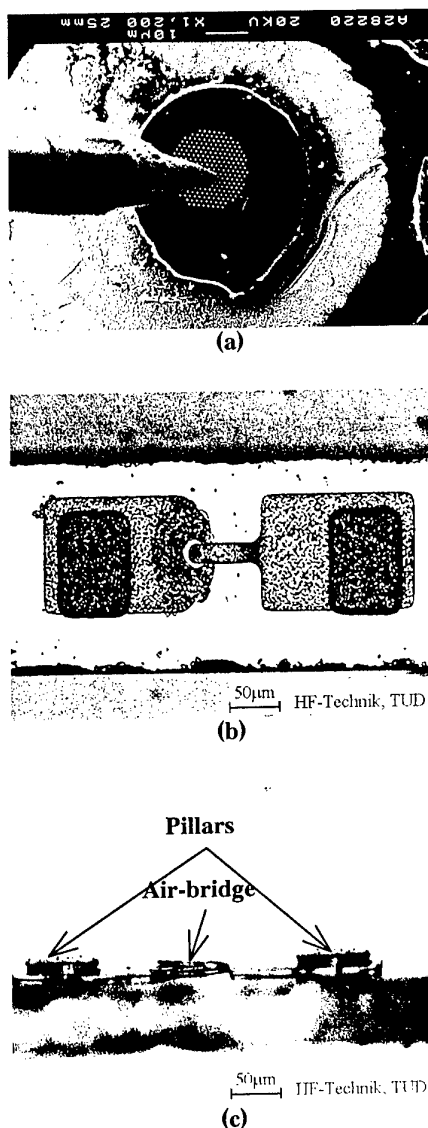


Fig.2: (a) Anode array placed in a honey-comb manner on a gold disk and contacted with a NiAu-whisker. (b) Top-view and (c) side view of a single planar Schottky-diode chip

A 5-10 μm thick gold disk promotes the mechanical stability of the device and simplifies the handling. Due to the reduced geometry, substrateless Schottky diodes offer several advantages compared with a conventional whisker contacted Schottky diodes. Due to minimised dimensions the structure is less affected by the skin effect [2]. The n^+ -substrate thickness is reduced to a few microns reducing its contribution to the resistance. Small distance between the active n-layer and the backside metal provides a good heat sink. Therefore, substrateless Schottky diodes can operate more reliably at high current densities without thermal degradation and the contribution to the system noise is reduced. Reduced semiconductor surface area decreases the leakage current. Reduced device volume allows a better coupling of the input signal into the diode within the waveguide. Due to these advantages substrateless Schottky diodes give a prospect to attain improved performance of mixers and frequency multipliers in the sub-millimetre wave regime.

In co-operation with the research group by Prof. Brand at the University of Erlangen-Nürnberg, a 2.5 THz corner cube mixer using substrateless whisker contacted diode is realised. Fig. 2 (a) shows a picture of a substrateless diode with an anode diameter of 0.5 μm contacted with a whisker in the corner cube mixer set-up. Different diodes were under investigation of the video sensitivity. The best one with a doping level of $3 \times 10^{17} \text{ cm}^{-3}$ and an anode diameter of 0.5 μm was applied to further rf measurement. A mixer noise temperature of 16000 K at 2.5 THz was achieved which is even little lower than the best result published in 1999, which is measured in a waveguide mixer and had a noise temperature of 16500 K [3]. Some of multipliers built with substrateless varactor diodes yielded record output power and efficiency. The efficiency of a tripler of almost 19% has been achieved at frequencies close to 300 GHz. With optimised complex doping structures we could achieve a very high capacitance modulation ratio. Recently, the doubler efficiency of 40% that has been achieved with this diode is the highest reported value for a single diode multiplier.

B. Planar Single Schottky Diode

Like substrateless diodes, the QVD's possess also the geometrical advantages as the substrateless ones and are expected to be very promising for applications in the THz regime. Fig. 2 (b) and (c) show top and side view of a single planar Schottky diode after separation from the substrate. Within the ESA/ESTEC-Kasimir project we co-operate with Radiometer Physics GmbH (RPG) to build a 650 GHz waveguide mixer using planar Schottky diodes. Single quasi-vertical planar Schottky mixer diodes were used for this purpose. The diodes with doping level $5 \times 10^{17} \text{ cm}^{-3}$ and anode diameter 0.8 μm have shown series resistance of 16 Ω , zero junction capacitance C_{j0} of 1.2 fF, saturation current of $2 \times 10^{-17} \text{ A}$, ideality factor of 1.15, and finally, breakdown voltage of -4 V. The diodes were submitted to noise measurements at 1.5 GHz. The mixer noise temperature was of $T_{\text{mixer}}^{\text{DSB}} = 2500 \text{ K}$ with a conversion loss of $L_{\text{mixer}}^{\text{DSB}} = 10 \text{ dB}$ which proves the high quality of the diode.

III. MONOLITHICALLY INTEGRATED CIRCUITS FOR THZ APPLICATIONS

Using planar techniques it is possible to integrate several diodes and other elements for special applications. The first step to integration is to produce chips with a number of diodes connected or placed together in one unit. Such integration of diodes permits to avoid parasitic effects introduced by not-reproducible hybrid techniques and ensures acceptable circuit performance. In this section, we will discuss different types of integration performed at TU Darmstadt.

A. Anti-Parallel Diode

One of the elementary integration methods is to connect a few diodes together in parallel or in series in dependence of the purpose of their use. For mixing, two diodes should be connected in anti-parallel manner, so that at least one diode is always forward-biased. This regime is for frequency mixing. An anti-parallel diode pair performed according to the Quasi-Vertical approach is shown in Fig. 3. The noise temperature measurements at 1.4 GHz

carried out on each diode of the mounted diode pair at different biases were reported in Ref. [4]. At a typical bias current of 500 μA for a single mixer diodes, the noise temperature was determined as 350 K which is comparable to whisker-contacted diodes.



Fig. 3. Anti-parallel planar diodes pair

B. Schottky-Diode Array for Quasi-Optical Frequency Multipliers

For frequency multipliers, Schottky diodes can be put in series in order to increase the total breakdown voltage of the circuit, which is important for efficient performance of a frequency multiplier. Monolithically integrated balanced groups of Schottky diodes of various number and dimensions are currently produced and investigated at TU Darmstadt. Another possibility to integrate diodes for frequency multiplication in the THz-range is to fabricate a non-linear element array for quasi-optical frequency multiplier [5].

Monolithic Integration of several non-linear elements offers the possibility to increase the efficiency of quasi-optical frequency multipliers. At the University of Technology Darmstadt, several of such systems have been fabricated. In one approach, an array of non-linear elements are fabricated on a ground plane, and slot antennas are used to feed them. This represents an advanced integration, where the chip contains apart Schottky diodes also other elements such as antennas and filters.

Another example of such integration is strip-line technology. In this case electrical dipoles are used to feed the non-linear elements, which in turn deliver the multiplied signal to a further electrical dipole, orthogonal to the first. Orthogonal polarisation is used for incoming and outgoing power. Fig. 4 shows such a circuit featuring seven Schottky diodes with their corresponding dipole antennas for reception of fundamental signal and emission of the second harmonic.

C. Integrated Circuits of Atmospheric Observations

Another field in which monolithic integration can have many advantages is in atmospheric sensing. Traditional heterodyne receivers use waveguide mixers fed by horn antennas incorporating waveguide-mounted single diodes. The integration of the front-end in one single chip should have not only the electrical advantages mentioned above but also lower the costs.

The possibility to realise microstrip structures adequate for very high frequencies on the same chip as the Schottky diode suggested the system [5] pictured in Fig. 5. A microstrip-fed double-slot antenna supplies the diode with the signal to be detected as well as with pumping power.

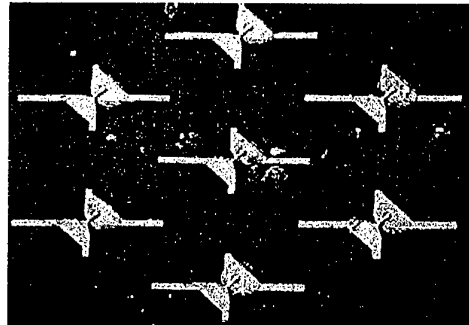


Fig. 4: SEM image of a 7-Schottky diode array for Frequency Doubling

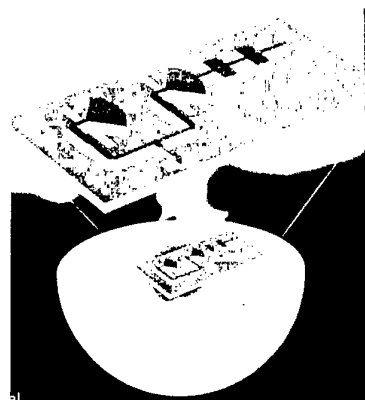


Fig. 5: Sketch of an integrated front-end for atmospheric observation

D. Integrated Multi-Channel Mixer Circuits for Imaging Applications

Monolithic integration of THz circuits may also find a very promising application in the development of detector arrays for imaging of electron cyclotron in fusion plasmas.

The basic problem presented here is the high pumping power requirements in a system with several mixer diodes. The LO loss can be reduced by a factor of about 10 dB in a system with on-chip LO-power distribution as opposed to quasi-optically fed systems, which might be the best solution for single-receiver systems.

On-chip coupling of LO power may be improved through the use of sub-harmonic pumping, which brings about a significant reduction of the attenuation in the microstrip. Therefore, antiparallel diode pairs are selected as mixer elements to improve sub-harmonic performance [6].

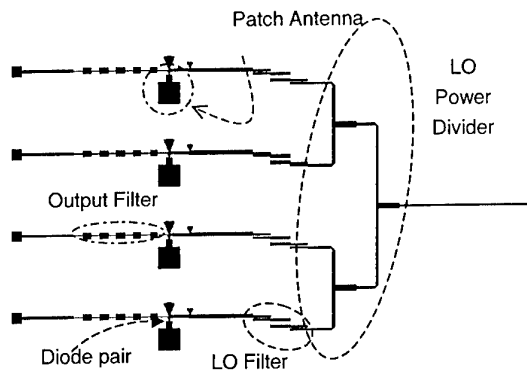


Fig. 6: Layout of a 4-receiver array for imaging of electron temperature in fusion plasmas

The circuit, sketched in Fig. 6, is realised on a multi-substrate technology and includes aperture-coupled patch antennas for the reception of the plasma signal. Cross-talking between channels may be reduced by isolation of patch antennas through trench etching.

System calculations show a minimum expectable value of conversion loss between 6 and 8 dB for input LO powers ranging from 5 to 10 dBm per diode pair. The ripple throughout the IF band (9 to 18 GHz) is less than 4 dB.

IV. CONCLUSION

In the THz range, both single devices as whisker contacted and planar Schottky diodes to partially integrated circuits and SMMIC techniques are essential to satisfy high requirements of complex designs and reproducible characteristics of modern science, electronics and research. In this paper, the present research activities in the THz region at Darmstadt are highlighted. Fabrication technologies as well as simulation techniques are being further optimised in order to match the high demands of THz Electronics.

ACKNOWLEDGEMENTS

Under support from ESA/ESTEC (Noordwijk) and DFG, TUD establishes a well-defined fabrication process for Pt/n-GaAs Schottky diodes for the THz applications. The authors would like also to express their acknowledgements to Dr. H. Grothe and Dr. J. Freyer, both from the Technical University of Munich, Germany, and Dr. Walther from EpiNova, Freiburg i. Br. for supplying high-quality epitaxial material.

REFERENCES

1. A. Simon, A. Grüb, M. Rodriguez-Gironés and H. L. Hartnagel, "A Novel Micron-Thick Whisker Contacted Schottky Diode Chip", Sixth Int. Symp. on Space Terahertz Technology, pp 5-12, 1995
2. C.I. Lin, A. Simon, M. Rodriguez-Gironés, H.L. Hartnagel, P. Zimmermann, R. Zimmermann, "Substrateless Schottky Diodes for THz Applications", Eighth Int. Symp. on Space Terahertz Technology, pp 224-229, 1997
3. P. H. Siegel, R. P. Smith, M. C. Gaidis, S. C. Martin, "2.5 THz GaAs Monolithic Membrane-Diode Mixer", IEEE Trans. Microwave Theory Tech., Band MTT-47, No. 5, pp. 595-604, 1999
4. C.I. Lin, A. Simon, J. Zhang, P.V. Piironen, V.S. Möttönen, H.L. Hartnagel, A.V. Räisänen, "Anti-Parallel Planar Schottky Diodes for Subharmonically Pumped Mixer", 23rd International Conference on Infrared and Millimeter Waves, pp. 90-91 (1998)
5. J. Mees, et al. "Open Structure Integrated Schottky Receiver for Space Applications", Proc. 20th ESTEC Antenna Workshop on Millimeter Wave Antenna Technology and Antenna Measurements, ESA/ESTEC, Noordwijk, June, 1997.
6. M.Cohn, J.E.Degenford, B.A.Newman, "Harmonic Mixing with Antiparalell diode pair", IEEE MTT Trans., Vol .23, pp. 667-673, 1975

[†] All authors belong with the Institut für Hochfrequenztechnik, TU Darmstadt, Merckstr. 25, 64283 Darmstadt, Germany;
E-mail address: thzuser@hrz2.hrztu-darmstadt.de
Web-page: <http://www.hfz-technik.tu-darmstadt.de/thz.html/>

High duty cycle germanium lasers and continuous terahertz emission from germanium

Erik Bründermann, Danielle R. Chamberlin, Eugene E. Haller

Abstract – We have measured laser emission from beryllium-doped germanium crystals with small inter-contact distances. An improved heat sink allowed a two-fold increase of the laser duty cycle to 5%. Non-thermal terahertz emission was found for conventional, continuously excited beryllium-doped germanium crystals with a volume of 0.5 mm³. Experimental and theoretical investigations of germanium lasers headed for continuous wave operation will be discussed. Major emphasis is placed on the electric field uniformity. We present experimental results of lasers utilizing a planar contact geometry. A planar laser structure with a thin active layer seems to be a very good candidate for a high power and continuous wave terahertz laser.

I. INTRODUCTION

The germanium laser has become an interesting candidate for far-infrared and time-resolved spectroscopy due to the recent improvement of germanium laser material [1,2] combined with technological advances in the laser operation, e.g., using permanent magnets in a closed cycle refrigerator [3,4,5] and mode-locking [6,7].

Germanium lasers provide high power emission which is widely tunable from 1 to 4 THz [8] with narrow line widths below 1 MHz [9]. Linear polarization is achieved in the Voigt configuration [4]. The pulse length can be several tens of picoseconds [6,7] to several tens of microseconds [10].

The pulsed output power can reach 5-10 W [11,12]. An even higher peak power can be expected with mode-locking and cavity dumping. Laser emission is normally observed at temperatures from 4 to 40 K [10] but higher temperatures (65 K and 80 K) were also reported [13].

We have also demonstrated pulsed laser emission from smaller crystals that only consume 4 W of electrical power [10].

In the continuous wave mode an output power of several tens of μ W to tens of mW can be expected. The theoretical conversion efficiency of 0.5% [14] can lead to a generated output power of 5 mW at an electrical pump power of 1 W. Modern closed cycle refrigerators easily cool a heat load of 1 W to 4.2 K.

II. HIGH DUTY CYCLE AND CONTINUOUS EXCITATION OF GERMANIUM CRYSTALS

Previously, we have used oxygen free high conductivity copper with a purity of 99.95% as a heat sink for our

lasers [10]. The heat sinks were attached to the ohmic contacts of the lasers. However, the heat conductivity of this copper material is lower than that of germanium laser material below 20 K (see Table 1, germanium values for an acceptor concentration of $N_A = 10^{14} \text{ cm}^{-3}$).

Table 1: Heat conductivity of different materials at low temperatures.

T [K]	99.999% Cu [Wcm ⁻¹ K ⁻¹]	99.95% Cu [Wcm ⁻¹ K ⁻¹]	Ge [Wcm ⁻¹ K ⁻¹]	In [Wcm ⁻¹ K ⁻¹]	He [Wcm ⁻¹ K ⁻¹]
4	70	3.2	8	8	2.6E-4
10	135	8	18	4	1.7E-4
20	90	13	15	2	2.6E-4
30	40	14	10.5	1.2	3.4E-4

We have therefore replaced these heat sinks with high-purity copper material with a purity of 99.999%. Thin indium layers were also omitted in contrast to previous studies [1,3].

Because of these new heat sinks the duty cycle of a larger laser of 162 mm³ volume was doubled and the time-averaged input power was raised from 8 to 17 W [13].

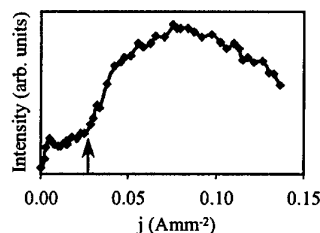


Fig. 1: Laser emission of a Ge:Be laser vs the current density j at a duty cycle of 5%. The arrow indicates the laser threshold.

Using the high-purity copper heat sinks we have studied Ge:Be lasers with small inter-contact distances. Figure 1 shows the laser emission of a crystal of 20 mm³ volume with a contact distance of 0.8 mm. The ohmic contacts of 24.5 mm² area allowed sufficient cooling. The laser threshold current was 600 mA, and the threshold voltage was 31 V. Hence, the input power during the pulse was 19 W. The latter corresponds to an average input power of 0.95 W for the duty cycle of 5%. The two-fold increased repetition rate of 5% (previously 2.5% in ref. [10]) was only limited by the available pulse generator. Non-thermal emission has also been found for small *continuously* excited Ge:Be crystals with a volume of 0.5

E. Bründermann is with Ruhr-Universität Bochum, Physical Chemistry II - NC 7/68, D-44780 Bochum, Germany.
E-mail: Erik.Bruendermann@ruhr-uni-bochum.de
<http://homepage.ruhr-uni-bochum.de/Erik.Bruendermann/>
D.R. Chamberlin and E.E. Haller are with Lawrence Berkeley National Laboratory and University of California, Berkeley, California 94720, USA.

mm³ (Fig. 2) [15]. These devices only need 1 to 4 W electrical input power.

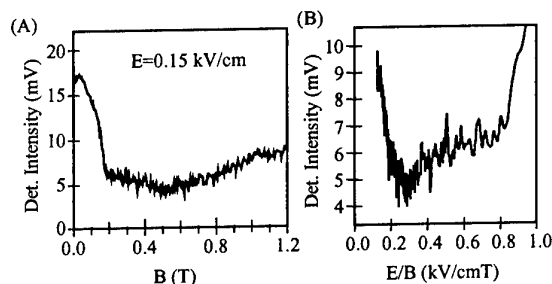


Fig. 2: Continuously excited Ge:Be laser material at $E = 0.15$ kV/cm (A) vs the magnetic field and (B) vs the E/B -ratio. Emission above 0.5 T could be related to cyclotron resonance emission of light holes. Emission from intervalence band transitions is expected below 0.2 T.

Recently, we obtained a modern closed cycle refrigerator (SRDK-408D made by Sumitomo Heavy Industries, Ltd., Japan) and measured a temperature of 4.2 K and 20 K at heat loads of 1 W and 42 W, respectively. Future experiments will use this machine to deliver the required continuous cooling power for a continuous wave laser.

III. ELECTRIC FIELD UNIFORMITY

The formation of a population inversion in the germanium crystal requires uniform magnetic and electric fields which have to be perpendicular to each other. However, the electric field distribution of common lasers is very non-uniform due to the Hall electric field. This non-uniformity largely depends on the chosen crystal dimensions and the geometry of the ohmic contacts. Advanced germanium laser material [2] allows a variety of laser shapes [16]. Subsequently, there are multiple possibilities to dramatically improve the field uniformity and enhance the laser conversion efficiency.

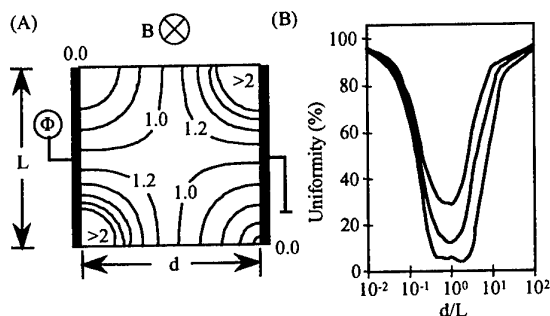


Fig. 3: (A) Electric field distribution in a laser crystal with a square cross-section in kV/cm for an applied field of 1 kV/cm. (B) Calculation of the electric field uniformity as a percentage of the crystal volume. The set of three lines corresponds to an electric field deviation $\Delta E_T/E_T$ of 1%, 10%, and 40%.

The field uniformity is very important because the lifetime of the carriers in the upper laser states strongly depends, *i.e.*, by many orders of magnitude for deviations of only 1%, on the electric field strength.

This lifetime also strongly depends on the field orientation with respect to the crystallographic axes. This orientation varies across the laser cross-section but will not be discussed here.

Figure 3A shows a calculation of the electric field distribution perpendicular to the magnetic induction B in a laser crystal with a square cross-section. Commonly used germanium lasers have a cross-section which is very close to a square cross-section.

Figure 3B displays a calculation of the electric field uniformity as a percentage of the crystal volume and a function of the cross-section dimension ratio d/L . The set of three lines corresponds to an electric field deviation $\Delta E_T/E_T$ of 1%, 10%, and 40% with respect to the total electric field E_T in the crystal center. For example, the electric field deviates by more than 1% from the center field in 94% of the crystal volume for a d/L -ratio of 0.5, which has been used for high duty cycle lasers (dc = 2.5%).

A high d/L -ratio and therefore a high uniformity (Fig. 3B) can be obtained by using a planar device structure [16,17]. In this case the electric field is uniform between the contacts.

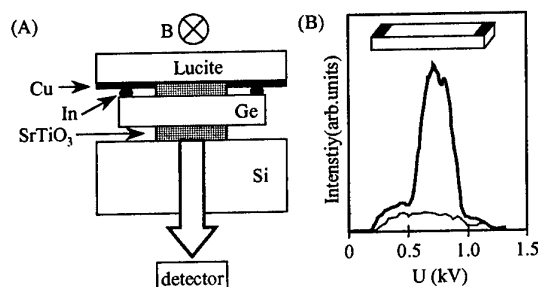


Fig. 4: (A) Planar germanium laser using SrTiO_3 mirrors. The coplanar ohmic contacts (see inset in Fig. 4B) are connected via indium (In) to copper foils glued to Lucite. A Ge:Al photoconductor detects the laser emission through the silicon heat sink. (B) Emission of a Ge:Be planar laser as a function of the applied voltage with (upper, thick line) and without (lower, thin line) SrTiO_3 mirrors.

Figure 4 shows a planar germanium laser with two dielectric mirrors made from SrTiO_3 . This material has a high reflectivity in the far infrared due to reststrahlen bands. Dielectric materials are also advantageous because they do not disturb the electric field distribution in contrast to commonly used metal mirrors. The sample thickness between the mirrors was only 2.2 mm, and the contact distance was 10 mm ($d/L = 4$).

Beryllium-doped germanium seems to be the laser material of choice which allows one to construct relatively arbitrary shapes because the generated photons are not absorbed by impurity related transitions. Unexcited germanium material within the laser sample is transparent in the far infrared and it can act as a heat sink.

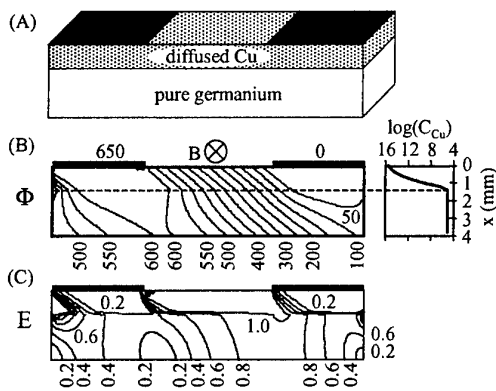


Fig. 5: (A) Potential continuous wave laser with coplanar ohmic contacts. A thin active layer is formed by copper diffusion. (B) Calculation of the potential lines (Φ) perpendicular to a magnetic induction B for a calculated copper diffusion profile of concentration C_{Cu} . The potentials on the two contacts are 0 and 650 V. (C) Electric field distribution in 0.2 kV/cm intervals for a contact spacing of 10 mm.

A laser consisting of a thin active, doped layer introduced by diffusion in a larger pure germanium substrate seems to be an ideal candidate for a continuous wave terahertz laser.

Copper is easily diffused in germanium in a relatively short time. A 1 mm thick, active layer is fabricated within a few hours (Fig. 5). In this device structure we can naturally obtain a very large d/L -ratio (in Fig. 5, $d/L = 10$) and find a uniform electric field region between the ohmic contacts (Fig. 5C). Beryllium diffuses much slower than copper in germanium. Therefore, very thin active layers can be fabricated, e.g., a 25 μm active layer is formed within 3 days at 800°C.

IV. CONCLUSION

Although the germanium laser material was optimized for bulk germanium crystals [2] little work has been done to optimize the laser device with respect to geometry.

Especially, the high non-uniformity was not considered to be crucial. We have shown that remarkable field improvements can result if planar lasers are used. They can dramatically improve the power conversion efficiency.

Dielectric materials can serve as mirrors in planar laser structures. They do not disturb the electric field distribution in contrast to commonly used metal mirrors.

Nevertheless, laser emission at high duty cycles and non-thermal emission at continuous excitation were observed for non-optimized lasers using d/L -ratios close to unity.

A thin active layer within a pure germanium substrate seems to be a good candidate for a high power and continuous wave terahertz laser. A large d/L -ratio is naturally obtained. The high-purity and undoped germanium substrate can act as an efficient heat sink and heat conductor without a thermal interface to the active layer.

Future applications of germanium lasers in far-infrared spectroscopy of chemical and biological species [18] will

certainly show the uniqueness and the value of this tunable semiconductor laser source in the far infrared.

Acknowledgments

This work was supported by the Director, Office of Science, Office of Basic Energy Sciences, Division of Materials Sciences of the U.S. Department of Energy under Contract No. DE-AC03-76SF00098.

One of the authors, EB, acknowledges support by the Alexander-von-Humboldt Foundation through a Feodor-Lynen Fellowship and by the Center for Particle Astrophysics at UC Berkeley. D.R.C. acknowledges the NASA Office of Space Science Fellowship No. S99-GSRP-070 for their support.

References

1. E. Bründermann, A.M. Linhart, L. Reichertz, H.P. Röser, O.D. Dubon, W.L. Hansen, G. Sirmain, and E.E. Haller, "Double acceptor-doped Ge: A new medium for inter-valence-band lasers," *Appl. Phys. Lett.* **68**, pp. 3075-3077 (1996).
2. U.S. Patent 6,011,810 (January 4, 2000), E.E. Haller and E. Bründermann, "Doping of germanium and silicon crystals with non-hydrogenic acceptors for far infrared lasers," (to The Regents of the University of California, Oakland, CA).
3. E. Bründermann and H.P. Röser, "First operation of a far-infrared p-germanium laser in a standard closed-cycle machine at 15 K," *Infrared Phys. Technol.* **38**, pp. 201-203 (1997).
4. E. Bründermann, A.M. Linhart, L.A. Reichertz, G. Sirmain, H.P. Röser, O.D. Dubon, D.R. Chamberlin, W.L. Hansen, and E.E. Haller, "Tunable THz-laser for applications in FIR astronomy," *Proc. 8th Int. Symp. Space Terahertz Technology*, Harvard, Boston, March 1997, pp. 430-435 (1997).
5. K. Park, R. E. Peale, H. Weidner, and J. J. Kim, "Submillimeter p-Ge laser using a Voigt-configured permanent magnet," *IEEE J. Quantum Electron.* **32**, pp. 1203-1210 (1996).
6. J.N. Hovenier, A.V. Muravjov, S.G. Pavlov, V.N. Shastin, R.C. Strijbos, and W.T. Wenckebach, "Active mode locking of a p-Ge hot hole laser," *Appl. Phys. Lett.* **71**, pp. 443-445 (1997).
7. A. V. Muravjov, R. C. Strijbos, C. J. Fredricksen, H. Weidner, W. Trimble, S. H. Withers, S. G. Pavlov, V. N. Shastin, and R. E. Peale, "Evidence for self-mode-locking in p-Ge laser emission," *Appl. Phys. Lett.* **73**, pp. 3037-3039 (1998).
8. L.A. Reichertz, O.D. Dubon, G. Sirmain, E. Bründermann, W.L. Hansen, D.R. Chamberlin, A.M. Linhart, H.P. Röser, and E.E. Haller, "Stimulated far-infrared emission from combined cyclotron resonances in germanium," *Phys. Rev. B* **56**, pp. 12069-12072 (1997).
9. E. Bründermann, H.P. Röser, A.V. Muravjov, S.G. Pavlov, and V.N. Shastin, "Mode fine structure of the FIR p-Ge intervalenceband laser measured by heterodyne mixing spectroscopy with an optically pumped ring gas laser," *Infrared Phys. Technol.* **36**, pp. 59-69, (1995).
10. E. Bründermann, D.R. Chamberlin, and E.E. Haller, "Thermal effects in widely tunable germanium terahertz lasers," *Appl. Phys. Lett.* **73**, pp. 2757-2759 (1998).
11. F. Keilmann, V.N. Shastin, and R. Till, "Pulse buildup of the germanium far-infrared laser," *Appl. Phys. Lett.* **58**, pp. 2205-2207 (1991).
12. A. A. Andronov, I.V. Zverev, V. A. Kozlov, Yu. N. Nozdin, S. A. Pavlov, and V. N. Shastin, "Stimulated emission in the long-wavelength IR region from hot holes in Ge in crossed electric and magnetic fields," *Pis'ma Zh. Eksp. Teor. Fiz.* **40**, pp. 69-71 (1984). [*Sov. Phys.-JETP Lett.* **40**, pp. 804-807 (1984)].

13. L. E. Vorob'ev, S. N. Danilov, Yu. V. Kochegarov, D. A. Firsov, and V. N. Tulupenko, "Characteristics of a far-infrared germanium hot-hole laser in the Voigt and Faraday field configurations," *Fiz. Tekh. Poluprovodn.* **31**, pp. 1474-1481 (1997). [*Semiconductors* **31**, pp. 1273-1279 (1997)].
14. E.V. Starikov and P. N. Shiktorov, "Numerical simulation of far infrared emission under population inversion of hole sub-bands," *Opt. Quantum Electron.* **23**, pp. S177-S193 (1991).
15. E. Bründermann, D.R. Chamberlin, and E.E. Haller, "High duty cycle and continuous terahertz emission from germanium," *Appl. Phys. Lett.* **76**, pp. 2991-2993 (2000).
16. E. Bründermann, D.R. Chamberlin, and E.E. Haller, "Novel design concepts of widely tunable germanium terahertz lasers," *Infrared Phys. Technol.* **40**, pp. 141-151 (1999).
17. D.R. Chamberlin, E. Bründermann, and E.E. Haller, "Planar contact geometry for far-infrared germanium lasers," *Appl. Phys. Lett.* **74**, pp. 3761-3763 (1999).
18. Updates on: [//homepage.ruhr-uni-bochum.de/Erik.Bruendermann/](http://homepage.ruhr-uni-bochum.de/Erik.Bruendermann/)

III-V Material Systems for Heterostructure Barrier Varactors

M. Saglam, A. Megej, J. Sigmund, M. Rodríguez-Girones, K. Mutamba, V. Ichizli, C.I Lin, H. L. Hartnagel

Abstract— This paper presents the lattice matched and pseudomorphic $\text{Al}_{0.7}\text{Ga}_{0.3}\text{As}/\text{GaAs}$ and $\text{In}_{0.52}\text{Al}_{0.48}\text{As}/\text{In}_{0.53}\text{Ga}_{0.47}\text{As}/\text{InP}$ material systems for HBVs. HBVs with different mesa diameters have been fabricated and their DC characteristics have been measured. A comparison of the DC characteristics are presented for the two material systems.

I. INTRODUCTION

Heterostructure barrier varactor is an ideal device for direct tripling since the C-V characteristic is evenly symmetric and I-V characteristics is anti-symmetric and only odd harmonic generation occurs under large signal excitation. An undoped high band gap semiconductor is sandwiched between two moderately n-doped smaller band gap semiconductors. The high band gap semiconductor behaves like a barrier which prevents electrons passing through the device.[1]

II. DEVICE DESIGN AND GROWTH

Several different material systems have been proposed since the invention of the HBV. The most promising material system is $\text{In}_{0.52}\text{Al}_{0.48}\text{As}/\text{In}_{0.53}\text{Ga}_{0.47}\text{As}/\text{InP}$. [2] It offers a large conduction band offset, especially when AlAs layers are inserted between the two moderately doped InGaAs layers. High multiplier efficiencies with this material system has been recently reported. [3]

Table I: $\text{Al}_{0.7}\text{Ga}_{0.3}\text{As}/\text{GaAs}$ HBV material structure

Material	Thickness	Doping
GaAs	300 nm	$5 \times 10^{18} \text{ cm}^{-3}$
GaAs	250 nm	$8 \times 10^{16} \text{ cm}^{-3}$
GaAs	3.5 nm	Undoped
$\text{Al}_{0.7}\text{Ga}_{0.3}\text{As}$	20 nm	Undoped
GaAs	3.5 nm	Undoped
GaAs	500 nm	$8 \times 10^{16} \text{ cm}^{-3}$
GaAs	3.5 nm	Undoped
$\text{Al}_{0.7}\text{Ga}_{0.3}\text{As}$	20 nm	Undoped
GaAs	3.5 nm	Undoped
GaAs	250 nm	$8 \times 10^{16} \text{ cm}^{-3}$
GaAs	2000 nm	$5 \times 10^{18} \text{ cm}^{-3}$
$\text{Al}_{0.7}\text{Ga}_{0.3}\text{As}$	500 nm	Undoped
GaAs	50 nm	Undoped
GaAs S.I Substrate		

This work is supported by DFG under the MEMSTIC Project.

M. Saglam, A. Megej, J. Sigmund, M. Rodríguez-Gironés, K. Mutamba, V. Ichizli, C. I Lin, and H. L. Hartnagel are with the Technical University of Darmstadt, Institut für Hochfrequenztechnik, Merckstr. 25, 64283 Darmstadt

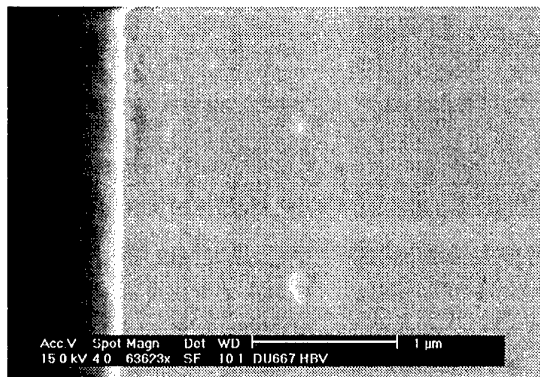


Fig. 1: SEM picture of the two barrier InP-based HBV epitaxial layer grown in University of Duisburg.

The $\text{Al}_{0.7}\text{Ga}_{0.3}\text{As}/\text{GaAs}$ material system grown on GaAs substrate has considerable attention due to simple process and cheapness of the substrate. The drawback of this material system is high conduction current due to self-heating and Gamma-X transition. [4] Table I shows the layer structure of double barrier $\text{Al}_{0.7}\text{Ga}_{0.3}\text{As}/\text{GaAs}$ HBV. Fig. 1 shows a SEM picture of a double barrier InP-based HBV structure where the double barriers are clearly seen.

III. DEVICE FABRICATION

The $\text{Al}_{0.7}\text{Ga}_{0.3}\text{As}/\text{GaAs}$ and $\text{InAlAs}/\text{InGaAs}/\text{InP}$ HBV structures which are grown with Molecular-Beam Epitaxy are fabricated using standard photolithography techniques for isolation and ohmic contact patterning, and wet chemical etching of mesa isolation. The Ni/AuGe/Ni and Ti/Pt/Au ohmic contacts are evaporated for GaAs and InP HBVs, respectively. The HBVs with diameters of 10, 20 and 40 μm are fabricated in the form of two columns with a total of four barriers, as shown in Fig. 2.

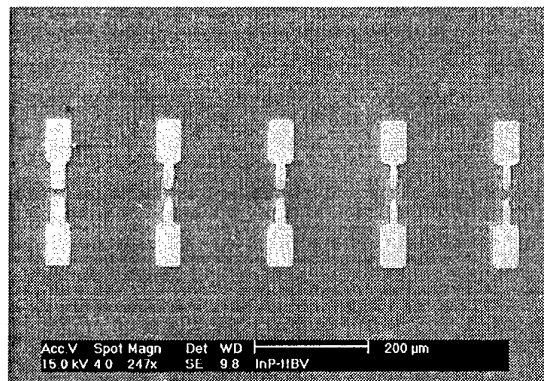


Fig. 2: SEM picture of the two-column four-barrier $\text{In}_{0.52}\text{Al}_{0.48}\text{As}/\text{In}_{0.53}\text{Ga}_{0.47}\text{As}/\text{InP}$ HBVs.

IV. DC MEASUREMENTS

The measured I-V and C-V characteristics of the HBVs are shown in Fig. 3 and 4, respectively. It is seen that the devices show extremely symmetrical characteristics which proves the quality of the epitaxial growth. The devices with $\text{Al}_{0.7}\text{Ga}_{0.3}\text{As}/\text{GaAs}$ material system exhibit a leakage current of $2.3 \mu\text{A}/\mu\text{m}^2$ whereas $\text{InAlAs}/\text{InGaAs}/\text{InP}$ material system exhibit much lower leakage current of $0.23 \mu\text{A}/\mu\text{m}^2$. The $C_{\text{max}}/C_{\text{min}}$ ratio in the voltage handling ratio of 10 V for InP and GaAs HBVs are 3.5 and 2.5, respectively.

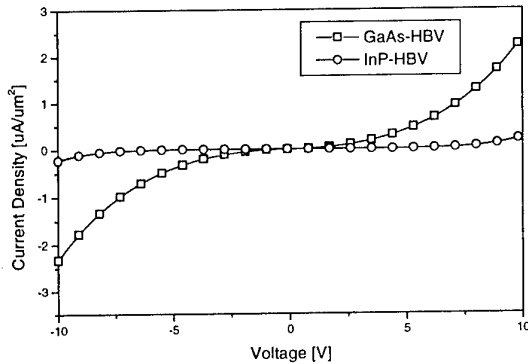


Fig. 3: Measured I-V characteristics of the AlGaAs/GaAs and InAlAs/InGaAs/InP HBVs.

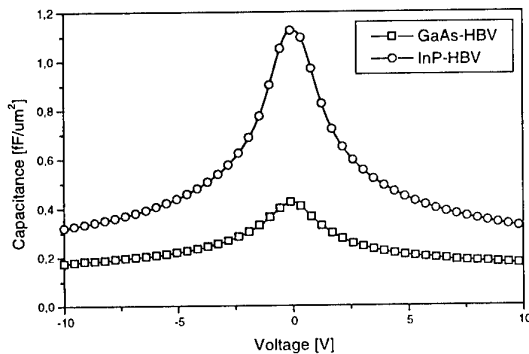


Fig. 4: Measured C-V characteristics of the AlGaAs/GaAs and InAlAs/InGaAs/InP HBVs.

V. CONCLUSION

We demonstrated the DC performances of the two different epitaxial designs of the HBVs. It is obviously seen that InP based HBVs have a great potential for the future development of the varactors. The next generation HBVs should increase the power capability and bandwidth of operation frequencies.

ACKNOWLEDGEMENT

The authors would like to thank Chiaki Domoto of ATR, Japan and Uwe Auer of University of Duisburg, Germany for the high quality epitaxial layers.

REFERENCES

- [1] A. Rydberg, H. Gronqvist, and E. Kollberg, "Millimeter- and submillimeter-wave multipliers using quantum-barrier-varactor (QBV) diodes," *IEEE Electron Device Letters*, vol. 11, pp. 373 - 375, 1990.
- [2] E. Lheurette, P. Mounaix, P. Salzenstein, F. Mollot, and D. Lippens, "High performance InP-based heterostructure barrier varactors in single and stack configuration," *Electronics Letters*, vol. 32, pp. 1417 - 1418, 1996.
- [3] X. Melique, A. Maestrini, E. Lheurette, P. Mounaix, M. Favreau, O. Vanbesien, J. M. Goutoule, G. Beaudin, T. Nahri, and D. Lippens, "12% efficiency and 9.5 dBm output power from InP-based heterostructure barrier varactor triplers at 250 GHz," presented at 1999 IEEE MTT-S International Microwave Symposium Digest, 1999.
- [4] J. Stake, L. Dillner, S. H. Jones, C. Mann, J. Thornton, J. R. Jones, W. L. Bishop, and E. Kollberg, "Effects of self-heating on planar heterostructure barrier varactor diodes," *IEEE Transactions on Electron Devices*, vol. 45, pp. 2298 - 2303, 1998.

IF Bandwidth of YBCO Thin Film Hot-Electron Bolometer Mixers

Konstantin Ilin, O. Harnack, M. Siegel, Boris S. Karasik, William R. McGrath, Gert de Lange

Abstract – The hot-electron bolometer (HEB) mixer made from a high-TC superconductor (HTS) thin film was introduced recently as an alternative to a Schottky mixer at THz frequencies. We report on a systematic study of the influence of length, thickness, temperature, and local oscillator (LO) frequency on the 3dB intermediate frequency (IF) bandwidth of YBCO HEB mixers on MgO and CeO₂/sapphire substrates. At temperatures close to the superconductive transition temperature the IF bandwidths

increases to unexpected high values of about 2-6 GHz. As discovered recently, the IF bandwidth also depends strongly on the bias voltage in this regime. However, these effects gradually vanish as the LO frequency was increased from 1 GHz to 100 GHz, 300 GHz and 480 GHz. We attribute these effects to the dynamics of magnetic vortices in the microbridge. The impact of the YBCO thin film and buffer layers properties, and device geometry on the value of the 3dB IF bandwidth of HTS mixer will be discussed.

Institute of Thin Film and Ion Technology, Research Center Juelich, 52425 Juelich, Germany

Center for Space Microelectronics Technology, Jet Propulsion Laboratory California Institute of Technology, Pasadena, CA, USA

Space Research Organization of the Netherlands, Division Sensor Research and Technology, 9700 AV Groningen, The Netherlands

At the time of publication the final manuscript was not available.
--

An InGaAs/InAlAs superlattice oscillator for frequencies above 100 GHz

R. Scheuerer, E. Schomburg, A. Ignatov, K.F. Renk,
D.G. Pavelev, Yu. Koschurinov
V.M. Ustinov, A.E. Schukov, A. Kovsh, P.F. Kopev

Abstract – We present an InGaAs/InAlAs superlattice oscillator at 150 GHz. With a superlattice device mounted in a waveguide and biased at a voltage of 1.3 V (current 15 mA), radiation of a power of 0.1 mW was generated. In the doped superlattice, the electron motion is governed by miniband transport, leading to a negative differential conductance due to Bragg reflection of the electrons at the miniband boundary. As a consequence, propagating charge carrier domains are formed giving rise to microwave generation with the frequency determined by the domain velocity. By using superlattices with thinner layers it should be possible to reach higher domain velocities, and hence higher oscillation frequencies.

I. INTRODUCTION

Semiconductor superlattices, i.e. heterostructures which consist of alternating layers of two different semiconductors, have been shown to generate microwave power either in a resonant [1] or non-resonant circuit [2,3]. The microwave generation in the superlattice is caused by travelling charge domains, which form due to the negative differential mobility of the electrons in the lowest miniband.

II. DEVICE STRUCTURE

Our superlattice consisted of alternating layers of $\text{In}_{0.53}\text{Ga}_{0.47}\text{As}$ and $\text{In}_{0.52}\text{Al}_{0.48}\text{As}$ with thicknesses of 44 Å and 6 Å, respectively, and had 120 periods. The layers were uniformly n-doped with Si ($8 \cdot 10^{16} \text{ cm}^{-3}$). The superlattice was sandwiched between two heavily Si-doped InGaAs buffer layers with a doping concentration of $5 \cdot 10^{18} \text{ cm}^{-3}$. In order to avoid the formation of a n^+n heterojunction at the interface between the superlattice and the buffer layers, regions with increasingly larger thicknesses and higher doping were introduced inbetween. The superlattice was grown on a n-doped InP substrate by MBE.

From the superlattice wafer, a quasi-planar SuperLattice Electronic Device (SLED, Fig. 1a) was structured with two mesas of different cross section (area $7 \mu\text{m}^2$ and $8000 \mu\text{m}^2$, respectively) which were, on the bottom side, electrically connected via the n^+ buffer, and, on the top side, to different Au beams (mechanically supported by polyimide). The SLED was mounted in a waveguide structure (Fig. 1b) with one beam grounded via the metal

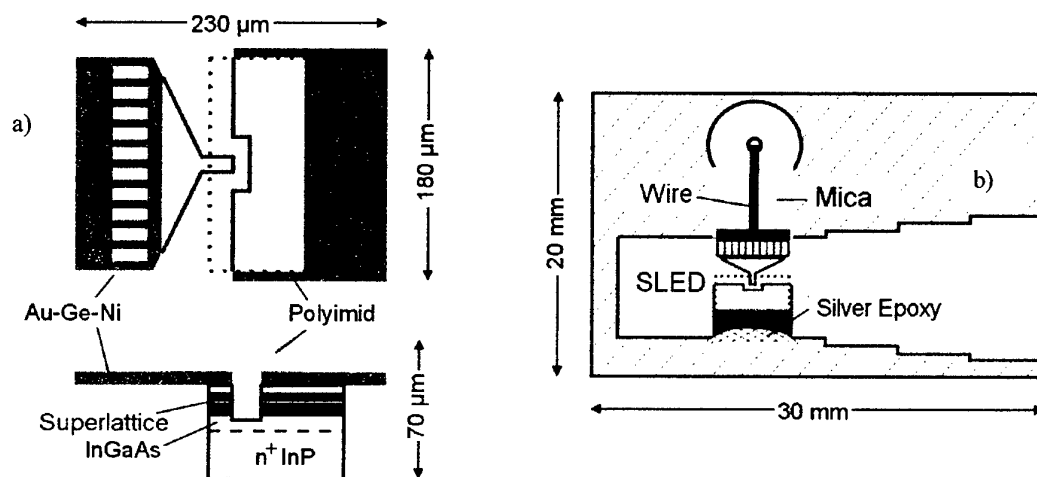


Fig. 1: Planar superlattice device SLED (a) mounted in waveguide structure (b).

R.Scheuerer, E.Schomburg, A.Ignatov, K.F.Renk are with the Institut für Exp. und Angew. Physik, Univ. Regensburg, 93053 Regensburg
D.G.Pavelev, Yu.Koschurinov are with the Institute for Radiophysics, Nizhny Novgorod, Russia

V.M.Ustinov, A.E.Schukov, A.Kovsh, P.F.Kopev are with the Ioffe Institute, St. Petersburg, Russia

waveguide, the other soldered to the inner wire of a coaxial bias line. Microwave radiation was guided (with a WR-7 waveguide) to a spectrum analyzer

III. DC AND MICROWAVE MEASUREMENTS

The current-voltage characteristic (Fig.2) of the oscillator exhibits negative differential conductance. After an

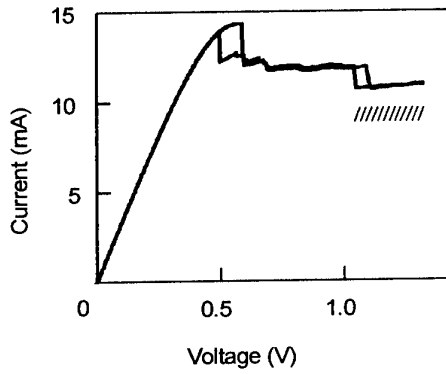


Fig. 2: Current voltage characteristic of the oscillator.

ohmic region at small bias voltages the current goes through a maximum (15 mA) at 0.5 V and shows current jumps for higher voltages. In our quasi-planar device, the current-voltage characteristic is mainly determined by the small area mesa, while the large area mesa acts as a series resistance with a small voltage drop. In the bias range between 1.1 and 1.4 V (hatched in Fig. 2) microwave generation was observed.

Fig. 3 shows the emission spectrum for a bias of 1.3 V. The spectrum indicates an emission line centered at 147 GHz. The line had a halfwidth of 7 MHz. The power at the line center was 0.1 mW, which corresponds to an efficiency of 0.6 % for the conversion of dc power to microwave power. With increasing the bias voltage, the center frequency varied between 143 GHz and 148 GHz in several steps. Between the steps, tuning over about 100 MHz was possible. The output power varied only slightly.

IV. DISCUSSION AND PROSPECTIVES

We attribute the microwave generation to travelling electron domains through the superlattice. The oscillation frequency is given by the ratio of the domain velocity and the superlattice length, L . From the peak current, the cross section of the small mesa, and the doping concentration a peak-drift velocity, v_p , of $150 \cdot 10^5$ m/s follows. The measured oscillation frequency equals

$0.6 v_p / L$, indicating that the domain velocity was $0.6 v_p$. This is consistent with computer simulations [4].

Higher oscillation frequencies may be reached either by reducing the superlattice length, or by increasing the peak drift velocity. The latter seems possible by reducing the thicknesses of the single semiconductor layers: due to the stronger coupling of wavefunctions of neighbouring

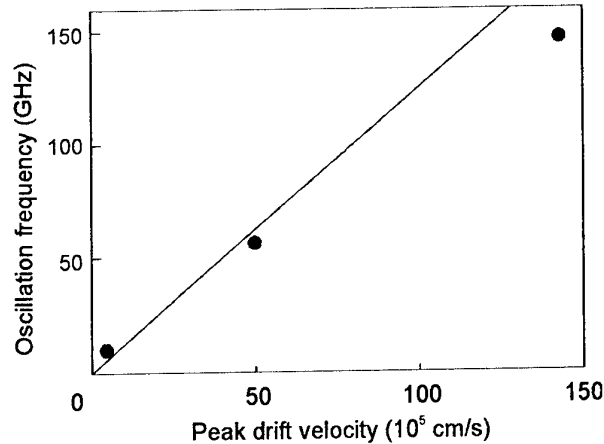


Fig. 4: Relation between peak drift velocity and oscillation frequency in three InGaAs/InAlAs superlattices with different layer thicknesses.

layers, the peak-drift velocity increases as predicted by Esaki and Tsu [5]. A corresponding behaviour was found for lower frequencies: two other InGaAs/InAlAs superlattices with $47 \text{ \AA}/23 \text{ \AA}$ and $41 \text{ \AA}/12 \text{ \AA}$ layer thicknesses had peak-drift velocities of $18 \cdot 10^5$ m/s and $53 \cdot 10^5$ m/s showed oscillations at 15 GHz and 55 GHz, respectively (Fig 4.).

The upper frequency limit of the negative differential mobility, and therefore the domain formation, is given by the time in which the electrons react on electric field changes, i.e. by the relaxation time. The negative differential mobility stems from electrons in the lowest

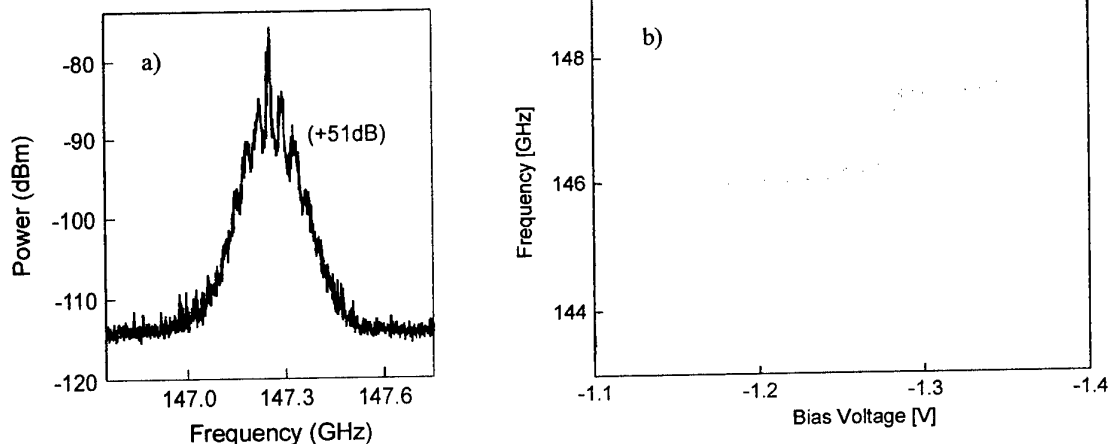


Fig. 3: Microwave spectrum at 1.3 V (a) and variation of oscillation frequency with bias (b).

miniband being Bragg reflected at the Brillouin zone boundary, and hence is a intra(mini)band effect. We suggest that the relaxation time lies in the order of 200 fs. This time has been extracted by an analysis of the static transport taking into account elastic scattering.

Compared to InP Gunn oscillators with a inter-valley relaxation time of about 0.75 ps, for which fundamental mode operation up to 165 GHz has been reported [6], superlattice oscillators up to 500 GHz seem possible.

V. CONCLUSION

We have presented a superlattice oscillator at 150 GHz with an output power of 0.1 mW (efficiency 0.6 %). According to the fast relaxation process, superlattice oscillators up to a frequency of 500 GHz seem feasible.

References

1. J.F. Cadiou, J. Guena, P. Legaud, C. Minot, J.F. Palmier, H. LePerson and J.C. Harmand, *Electron. Lett.* **30**, 1690 (1994)
2. K. Hofbeck, J. Grenzer, E. Schomburg, A.A. Ignatov, K.F. Renk, D.G. Pavelev, Yu. Koschurinov, B. Melzer, S. Ivanov, S. Schaposchnikov and P.S. Kopev, *Phys. Lett A* **218**, 349 (1996)
3. E. Schomburg, R. Scheuerer, S. Brandl, K.F. Renk, D.G. Pavelev, Yu. Koschurinov, V. Ustinov, A. Zhukov, A. Kovsh, and P.S. Kopev, *El. Lett.* **35**, 17 (1999)
4. T. Blomeier, E. Schomburg, K. Hofbeck, J. Grenzer, S. Brandl, I. Lingott, A.A. Ignatov, K.F. Renk, D.G. Pavelev, Yu. Koschurinov, B. Melzer, V. Ustinov, S. Ivanov and P.S. Kopev, *Phys. Stat. Solidi B* **204**, 485 (1997)
5. L. Esaki, R. Tsu, *IBM J. Res. Dev.* **14**, 61 (1970)
6. H. Eisele, G.I. Haddad, *IEEE Trans. Microwave Theory Tech.* **MTT-46**, 6 (1998)

Integrated 150 GHz Silicon IMPATT Diodes for Power Combining Applications

M. Luschas*, R. Judaschke*, K. Schünemann*, J.-F. Luy*

* Arbeitsbereich Hochfrequenztechnik, TU Hamburg-Harburg, Germany

* DaimlerChrysler Research Center, FT2/HM, Ulm, Germany

Abstract - This paper describes the manufacturing process of integrated Si-IMPATT diodes for power combining applications at 150 GHz.

A computer optimized doping profile is grown by molecular beam epitaxy (MBE) on high resistivity Si-substrate. The new technology process that realizes the integration of a diode and its housing is explained in detail. The device is thermo-compression bonded in a single step onto a diamond heat sink. Measurements are made in a rectangular, reduced height waveguide resonator.

The integrated IMPATT device is designed for high reproducibility. Variations that were formerly introduced by multiple bonding steps in the fabrication of quartz ring housings are eliminated. The single bonding step used here results in the improved diode matching required for power combining applications.

I. INTRODUCTION

Limited DC-power dissipation and a suitable packaging technology are barriers to building high power IMPATT diodes. Especially at millimeter-wave frequencies, optimization of both doping profile and mounting of the diode is important.

The most efficient doping profile is a double Read (DLHL) structure which reduces the operating voltage. This allows a higher current density through the diode compared to a flat double drift (DD) design. The doping profile is computer optimized for a low breakdown voltage and high negative resistance using an existing simulation tool that is based on a hydro-dynamic model.

The integration of active device and housing in a single technology process is desirable to eliminate manual adjustments in the μm range that are currently involved in the manufacturing process of conventional IMPATT diodes. Three thermo-compression bonding steps are necessary to fabricate a beamlead diode with a surrounding quartz ring on a heat sink. This leads to problems

in reproducible manufacturing which is mandatory for power combining applications.

II. DIODE DESIGN

Optimization of RF-output power around the desired frequency of 150 GHz is the main goal. Hence, the design requires a low breakdown voltage in order to drive the diode with a high DC-current. This results in a high negative resistance. The limiting factor is the dissipated DC-power, which depends mostly on the quality of the bonding contact of the diode on the diamond heat sink. This leads to a DLHL diode design.

The doping levels and dimensions of the high field and drift regions are computer optimized with respect to their feasibility by the MBE. The minimum resolution of the growth rate and doping gradient of the MBE is close to the spike dimensions in the avalanche region of a DLHL profile for 150 GHz.

For simulation purposes, an in-house simulation tool [1] which is based on a hydro-dynamic carrier transport model is used. Simulations are carried out with a DC-current of 250 mA and a RF-voltage amplitude of 6 V at a 500K operating temperature. Results show that a diode diameter of 23 μm is a good compromise between high RF-output power and high impedance levels. The breakdown voltage gets as low as 8.5 V for the doping profile given in Tab. 1 with a maximum RF-output power of 220 mW at 150 GHz. The theoretical figures of RF-output power with and without considering series resistances of the diode are shown with measured RF-output power values in Fig. 5.

Tab. 1: Doping profile of integrated IMPATT diodes

150 GHz DLHL doping profile	doping concentration [cm^{-3}]	length [nm]
p - drift region	$2.2 \cdot 10^{17}$	140
p ⁺ - spike	$1.4 \cdot 10^{18}$	25
intrinsic		60
n ⁺ - spike	$1.5 \cdot 10^{18}$	25
n - drift region	$1.2 \cdot 10^{17}$	150

III. TECHNOLOGY PROCESS

The outstanding results obtained in [2,3] suggest a modification of the introduced beamlead diode process to fabricate housing and active device in a single technology process.

In [4], a successful realization of integrated IMPATT devices has been introduced for GaAs.

Instead of a low resistivity n⁺-Si substrate, a high resistivity p⁺-SIMOX (Separation by Implanted Oxygen) substrate is used. This Si-substrate has a buried oxide layer, which acts primarily as an etch stop layer. It also improves isolation between the upper and the lower diode contact.

The active layer is grown by MBE on a 4" SIMOX wafer. The top is protected by an evaporated and electroplated 2 μ m Ti/Au layer. This wafer is mechanically thinned and polished to a thickness of 100 μ m. It is separated in 18x18 mm² pieces for better handling. The pieces are subsequently thinned by wet chemical etching in hot, aqueous KOH to a thickness of 30 μ m.

The active layer then has to be contacted from the substrate side (n⁺-contact). The following is a closer look at this critical process step.

A 370 nm thick, buried Si-oxide layer between the IMPATT diode layer and the Si-substrate is used as an etch stop layer. High etching selectivity for Si and SiO₂ in hot, aqueous KOH is reported in [5]. A Ti/Au etch mask with a thickness of 500 nm is structured lithographically, as shown in Fig. 1.

The via holes with a (111) crystal plane slope of 54.7 deg. are etched in the 29 μ m thick Si-substrate in approximately 30 min. The etching process is basically stalled once the Si-oxide layer is reached.

For the buried oxide, an etch rate of about 5 nm/min is measured. This corresponds to the Si/SiO₂ etch selectivity given in [5] of about 250.

To make sure that the etch stop layer has been reached over the whole wafer, it is etched for another 10 min.

The etch-stop can be verified very easily with the microscope. The bottoms of the via-holes become green to blue once the oxide layer is reached. The Si-oxide is etched in buffered hydrofluoric acid. Only the Si-buffer layer and the active layer beneath it remain.

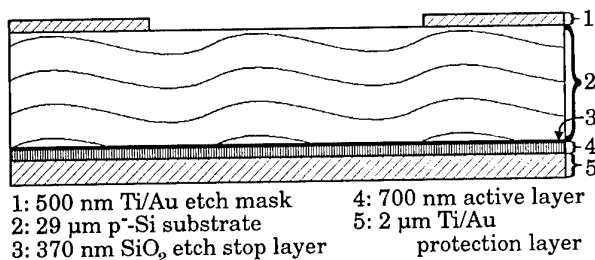


Fig. 1: Schematic of a wafer before via hole etching

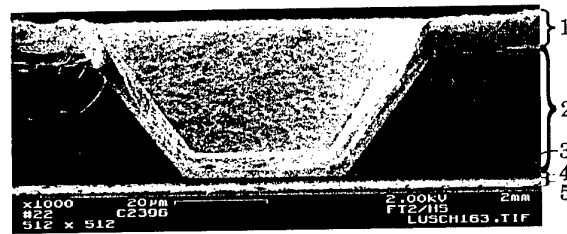


Fig. 2: SEM-picture of an etched and electroplated via hole

The Si-Buffer layer and parts of the oversized n⁺-contact are removed by plasma etching to get deep into the n⁺-contact region of the IMPATT diode.

Next, the top contact of the diode at the bottom of the via hole is defined.

This is achieved by evaporating a 300 nm thick Ti/Au-contact layer on the substrate side of the wafer. The devices are lithographically structured on the substrate side. The metal contact is then electroplated to a thickness of at least 15 μ m to add stability to the thin wafer. This makes handling easier during the remaining process.

The thick metal layer is also needed to guarantee a good bond contact. The mesa diode is attached only to the upper gold contact. Thus, the bonding pressure that the diode experiences is determined by the thickness of the gold contact layer and the maximum pressure that the substrate is able to withstand.

The processed substrate side of the wafer is shown in a cross-section SEM picture in Fig. 2.

On the epitaxial side of the wafer mesas are defined by plasma etching using the lithographically structured contact metallization of the diode as an etch mask. As shown in Fig. 3, the active layer is utilized for two different purposes.

It is structured as a mesa diode and as a stand-off along the edges of the device. The stand-off is responsible for overall device stabilization on the heat sink and for diode protection. It seals the diode hermetically from the environment and prevents any exposure to mechanical stress.

In a last step, the wafer is plasma etched to separate the devices. The upper gold metallization is used as an etch mask.

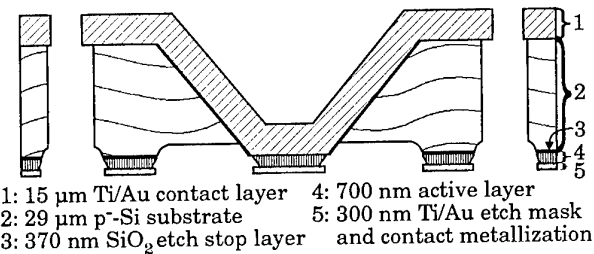


Fig. 3: Schematic of a cross-section view of the processed IMPATT device

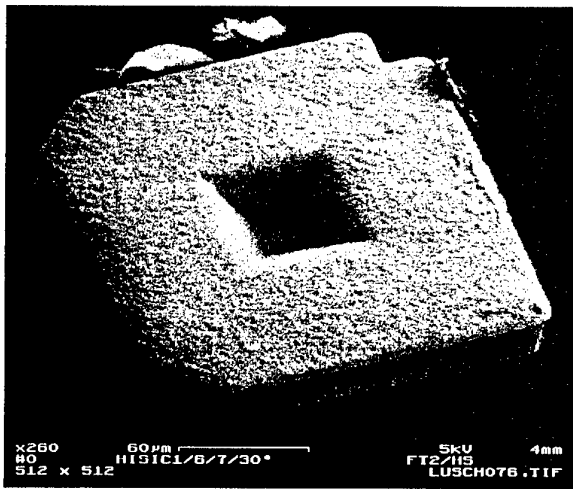


Fig. 4: SEM-picture of a top view of an integrated Si-IMPATT device for operation at 150 GHz

A SEM-picture of the final device is shown in Fig. 4. It is designed for operation at 150 GHz. It includes a diode with a diameter of $23\text{ }\mu\text{m}$ on the back side of the via-hole. The dimensions of the device are $200 \times 200\text{ }\mu\text{m}^2$ with a height of $45\text{ }\mu\text{m}$.

IV. BONDING OF INTEGRATED DEVICES

The integrated diode is thermocompression bonded with a flat bondhead onto a diamond heat sink in a single step. The bond pressure has to be chosen carefully. On the one hand, it has to be high enough to assure a good bond contact and, thus, a good thermal connection between the IMPATT diode and the diamond. On the other hand, it must not exceed the maximum pressure that the Si-substrate is able to withstand. Tests show that bond pressures up to 2 bar can be applied without destroying the device. However, no major difference in the thermal resistance of devices that are bonded with 1.4 bar, 1.6 bar and 2 bar can be measured. They all show a thermal resistance of about 50 K/W . Bond contacts made with a lower pressure show higher values. For example, for a contact bonded with 1.2 bar a thermal resistance of 65 K/W is measured.

The following results are obtained with integrated diodes that are bonded with 1.4 bar for 15 sec. The typical thermal resistance measured with the method described in [6] is around 50 K/W .

V. MEASUREMENT RESULTS

RF characterization is carried out in a D-band waveguide resonator which is tuned at the reduced height end with a sliding short. The heat sink with diode is mounted in the waveguide resonator. Its position relative to the bottom of the waveguide can be varied with a micrometer screw. The diode

is contacted by a choke from the top of the waveguide. Thin metal disks are put directly on top of the integrated device to match the impedance level of the diode to the resonator impedance. For tuning the frequency, disks with different diameters are used. Oscillations above 140 GHz require disks with diameters of 0.7 mm or smaller. Usually, for a fixed DC-current two diode positions with maximum RF-output power can be found. The diode is either elevated almost to the top of the waveguide or lowered about the height of the waveguide in its hole.

In Fig. 5, the measured results are shown. Additionally, the simulated theoretical RF-output power (—), which has a value of about 220 mW at 150 GHz, and the simulated RF-output power with series resistances of 1.0 (---) and 1.5 Ohms (—) is plotted. The RF-output power is reduced by more than 3 dB to 90 mW at 150 GHz when a series resistance of 1 Ohm is taken into account. A reduction of almost 10 dB to only 25 mW RF-output power at 150 GHz is the result of a series resistance of 1.5 Ohms. The latter corresponds to the measured series resistances of the characterized devices.

The series resistance needs to be improved during the next process runs to take full advantage of the potential of this doping profile. From experiences with the beamlead diode process a reduction to values between 1.0 and 0.5 Ohms is expected.

The actual measured values of several devices are marked with triangles. Test parameters are set to match the simulation results. The DC-current is 250 mA and only diodes with diameters of $23\text{ }\mu\text{m}$ are characterized.

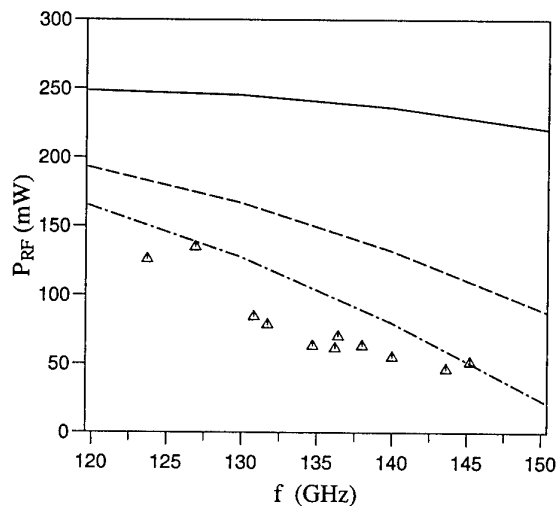


Fig. 5: Simulated and measured RF-output power of integrated IMPATT diodes; $I_D=250\text{ mA}$; $U_i=6\text{ V}$; $T=500\text{ K}$; $d=23\text{ }\mu\text{m}$; —: simulated diode RF-power without the inclusion of losses; ---: simulated diode RF-power with 1.0 Ohms series resistance; —: simulated diode RF-power with 1.5 Ohms series resistance; single triangles: measured oscillator RF-output power

In the region around 135 GHz the RF-output power is about 65 mW, above 140 GHz 50 mW can be achieved. This is in good agreement with the simulation values with a 1.5 Ohms series resistance. The minor differences between the measured power levels and the simulation results are due to surface resistance losses in the waveguide resonator setup.

The results show the desired progress in reproducibility. For unchanged current and tuning of the waveguide resonator, the operating points of the devices are close together.

VI. CONCLUSION

Integrated Si-IMPATT diodes for power combining applications at 150 GHz have been designed using computer optimization tools. The active layer is grown by MBE on a high resistivity SIMOX substrate. A new technology process for the fabrication of Si-IMPATT devices has been introduced in great detail. The process integrates the active element and its housing. The elimination of manual adjustments in the bonding of IMPATT diodes minimizes variations of device parameters caused during manufacturing. This makes the new integrated devices ideal candidates for power combining applications.

Simulation and measurement results of the integrated diodes have been presented. The measurement results show the desired match of the integrated devices. The low RF-output power of the devices from the first process run has to be blamed on series resistances introduced by the new process. A future challenge is the reduction of these series resistances.

Another topic is the design of a waveguide resonator that enables an exact and reproducible positioning of heat sinks for diode matching characterizations.

VII. ACKNOWLEDGEMENT

This work has been done at the DaimlerChrysler Research Center, FT2/HM, in Ulm, Germany, in cooperation with the Arbeitsbereich Hochfrequenztechnik of the Technische Universität Hamburg-Harburg, Germany. It is part of the Deutsche Forschungsgemeinschaft Forschergruppe "Submillimeterwellen-Schaltungs-technologie".

The authors are indebted to the Deutsche Forschungsgemeinschaft for financial support.

VIII. REFERENCES

- [1] M. Curow. *Konsistente Simulation von Millimeterwellen-Oszillatoren mit Gunn-Elementen und IMPATT-Dioden*. Technische Universität Hamburg-Harburg, Hamburg, 1996
- [2] M. Wollitzer. *Planare Silizium-IMPATT-Oszillatorschaltungen bei 140 GHz*. Fortschritt-Berichte VDI, Nr. 286, ISBN 3-18-328609-2, 1998
- [3] M. Wollitzer, J. Büchler, F. Schäffler, J.-F. Luy, "D-band Si-IMPATT diodes with 300 mW CW output power at 140 GHz," *Electronic Letters*, 32, pp. 122-123, Feb. 1996
- [4] M. Tschernitz. *Optimierung von GaAs-Lawinenlaufzeitdioden mit Hilfe einer neuartigen monolithischen Einbautechnik*. Lehrstuhl für allgemeine Elektrotechnik und angewandte Elektrotechnik der Technischen Universität München, München, 1995
- [5] H. Seidel, L. Csepregi, A. Heuberger, H. Baumgärtel, "Anisotropic Etching of Crystalline Silicon in Alkaline Solutions, I. Orientation Dependence and Behavior of Passivation Layers," *J. Electrochem. Soc.*, 137, pp. 3612-3625, Nov. 1990
- [6] R. H. Haitz, H. L. Stover, N. J. Tolar, "A Method for Heat Flow Resistance Measurements in Avalanche Diodes," *IEEE Trans. Electron Devices*, Vol. ED-16, No. 5, 438-444, May 1969

Submillimeter-Wave Nonreciprocal Propagation Characteristics in Transversely Magnetized Image Guide and Two-Layer Parallel-Plate Waveguide Containing *p*- or *n*-InSb Slab

Shinichi Yodokawa and Tetsuo Obunai

Abstract - The magnetic field dependence of 526 GHz and 671 GHz submillimeter-wave propagation in waveguides containing InSb slab was studied in detail varying the ambient temperature. It was shown that, at the liquid nitrogen temperature, submillimeter-wave propagation loss is very small, typically 0.3 dB/mm, and that a submillimeter-wave image guide employing *p*-InSb slab may be possible. At the dry ice temperature, slow surface wave resonance clearly appeared, and a nonreciprocity of at least 15 dB was obtained with an insertion loss of 5 dB. The possibility of constructing electrically controllable nonreciprocal devices in submillimeter-wave monolithic integrated circuits is presented.

I. INTRODUCTION

In a previous paper, [1] we reported that the propagation loss of a 70 GHz millimeter-wave dielectric image guide consisting of a *p*-type InSb slab is extremely small, typically about 0.43 dB/mm, and that the propagation characteristics of this structure can be controlled by generating plasma in the InSb material by means of light irradiation. Our recent results of numerical calculations predict that the submillimeter-wave propagation loss of such a *p*-InSb image guide is far smaller than the above-mentioned value. These results suggest that it is possible to apply this waveguide configuration to the transmission line in the submillimeter-wave range. In this paper, we report the preliminary results of nonreciprocal propagation characteristics of InSb dielectric waveguides. The possibility of constructing nonreciprocal devices embedded in one body in the dielectric waveguide material and of controlling their nonreciprocal propagation characteristics electrically by varying the plasma density are suggested.

II. EXPERIMENTAL PROCEDURE AND APPARATUS

A. Submillimeter-Wave Measuring System

In this work, the characteristics of transmission through the two structures shown in Fig.1 are studied. Fig.1(a) shows a rectangular metal waveguide with the cross-sectional dimensions of 0.3 mm \times 1.5 mm where a thin InSb slab of thickness *b* is inserted as a plasma material with a vacuum gap of thickness *a*. Fig.1(b) shows an image guide employing an InSb slab in stead of the conventional dielectric material. Transverse static magnetic field *B* is applied to these waveguides, the direction of which is defined as indicated by *B*⁺ and *B*⁻ in Fig.1. The length *L* of the InSb sample slab is typically 3.4 mm.

The experimental setup is outlined in Fig.2. The submillimeter-wave source used is a conventional CO₂-excited submillimeter-wave gas laser, and submillimeter outputs of 526 GHz and 671 GHz are obtained by exciting CH₃OH and CH₃I by the 9P16 line and 10P18 line of the CO₂ laser, respectively. The submillimeter laser output is

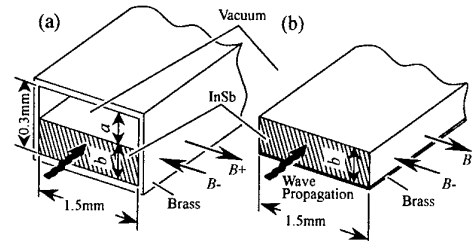


Fig. 1. Two-layer parallel-plate waveguide (a) and image guide structure (b) used in experiments.

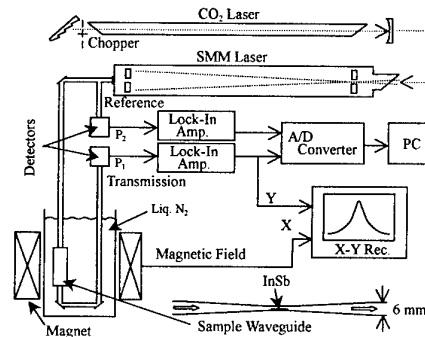


Fig. 2. Schematic of the measurement setup.

introduced into the cryostat through a copper light pipe of 6 mm diameter, and supplied to the sample waveguide through a long taper. In the following, the *B*-dependence of the transmission, which is defined by the ratio of the outputs of pyrodetectors *P*₁ and *P*₂, is mainly discussed for various values of the sample temperature *T* as the parameter.

B. Carrier Density and Carrier Mobility of Sample

Slabs of *p*-type and *n*-type single-crystalline InSb were used as the solid-plasma material. The hole density *n*_{h0} and the hole mobility μ_{h0} of the *p*-type material at 77 K are $1.1 \times 10^{20} \text{ m}^{-3}$ and $0.7 \text{ m}^2/(\text{V}\cdot\text{s})$, respectively. The electron density *n*_{e0} and the electron mobility μ_{e0} of the *n*-type material at 77 K are $1.55 \times 10^{21} \text{ m}^{-3}$ and $50.0 \text{ m}^2/(\text{V}\cdot\text{s})$, respectively.

First, the temperature dependences of carrier density and carrier mobility of the *p*-InSb material determined from the Hall coefficient are plotted in Fig.3. The experimental value of the electron density *n*_e shows reasonable agreement, especially in the *T*-region above 200 K, with the empirical expression given by Hrostowski et al. [2]:

$$n_e = n_h = [3.6 \times 10^{41} T^3 \exp(-0.26/kT)]^{1/2}. \quad (1)$$

On the other hand, the theoretical values of the electron and hole mobilities were calculated by assuming $T^{-3/2}$ dependence and by setting their theoretical values at 77 K to be equal to their experimental ones of $\mu_{e0} = 50 \text{ m}^2/(\text{V}\cdot\text{s})$ and $\mu_{h0} = 0.7 \text{ m}^2/(\text{V}\cdot\text{s})$. The measured value of the carrier mobility shows reasonable agreement with the theoretical values of the holes at *T* < 120 K, and of the electrons at *T* > 170 K. Taking these results into account, the electron density and the hole density employed for *p*-InSb used in the following theoretical work

The authors are with Department of Electrical and Electronic Engineering, Faculty of Engineering and Resource Science, Akita University, Akita 010-8502, Japan.

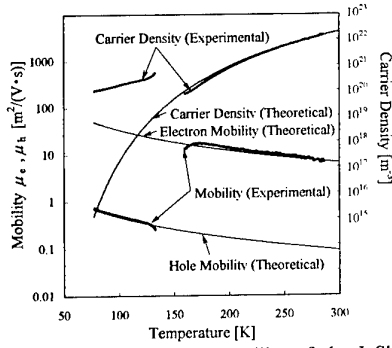


Fig. 3. Carrier density and carrier mobility of the InSb sample as a function of temperature.

were assumed to be equal to n_c and $n_h + n_{h0}$, respectively, over the whole temperature range, where n_c and n_h represent the empirical values given by eq.(1). Similarly, the electron density and the hole density for n -InSb material were assumed to be equal to $n_c + n_{c0}$ and n_h , respectively. As for the electron and hole mobilities, theoretical values were employed over the entire temperature range. The electron effective mass $m_e^* = 1.23 \times 10^{-32}$ kg, the hole effective mass $m_h^* = 3.99 \times 10^{-31}$ kg and the lattice dielectric constant of InSb $\epsilon_l = 16.0$ were employed in the following calculations.

III. RESULTS AND DISCUSSIONS

A. Transmission Characteristics of Two-Layer Structure

1) Two-Layer Structure with p -InSb Slab

The results of the two-dimensional analysis reveal that, for $B = 0$, the two-layer structure containing the p -InSb slab with $a = 0.220$ mm and $b = 0.08$ mm supports two separate propagation modes, as shown in Fig.4, where their attenuation constant α and phase constant β are plotted on the phase plane of α versus β with the ambient temperature T as the parameter. At 77 K, one of the modes, denoted M1, has a field distribution similar to that of a higher-order mode of the transverse magnetic (TM) image guide mode, as shown in Fig.5(a). The other mode, denoted M2, has a field distribution similar to that of the fundamental image guide mode [see Fig.5(b)]. Since the attenuation constant α of M2 is more than one order greater than that of M1 over whole temperature range, as shown in Fig.4, only M1 is surmised to appear experimentally.

First, the experimentally observed temperature dependence of the 526 GHz submillimeter-wave transmission is plotted for $B = 0$ in Fig.6, for $a = 0.220$ mm and $b = 0.080$ mm. The corresponding theoretical variation for M1 is also presented in the same figure by a solid line such that the theoretical and experimental values coincide at 77 K. The experimental results are generally in good quantitative agreement with the theoretical variation for the M1 mode. The results in Fig.6 are explained as follows. First, at a sufficiently low temperature, the only existing carrier is holes, which negligibly move, regardless of the submillimeter-wave fields. Thus, in this T -region, the p -InSb slab acts as a dielectric material with the dielectric constant of 16.0, and the wave propagation experiences very small attenuation. On the other hand, the InSb material becomes intrinsic near room temperature, and it acts as a poor conductor. Consequently, the electromagnetic fields are driven out of the InSb slab and concentrate mostly in the vacuum region. Thus, the InSb slab again induces only small attenuation. In contrast, in the intermediate temperature range, electrons in InSb dissipate considerable energy, and consequently a minimum appears in the transmission curve at a certain T -value.

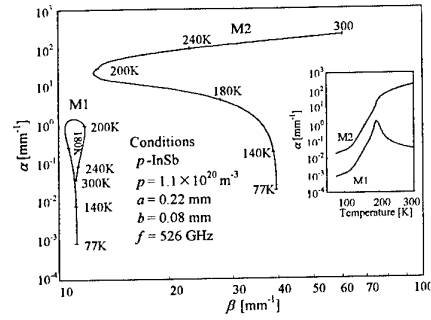


Fig. 4. Loci of $\gamma (= \alpha + j\beta)$ for the two propagation modes with varying temperature (two-layer parallel-plate waveguide structure containing p -InSb at 526 GHz).

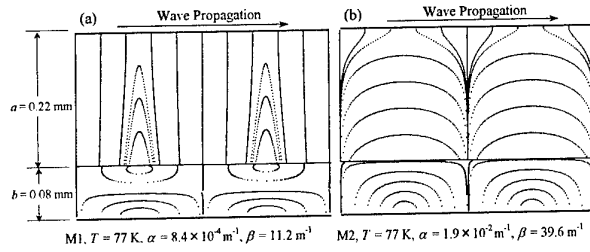


Fig. 5. Electric field distributions of the two propagation modes (two-layer parallel-plate waveguide structure containing p -InSb at 526 GHz).

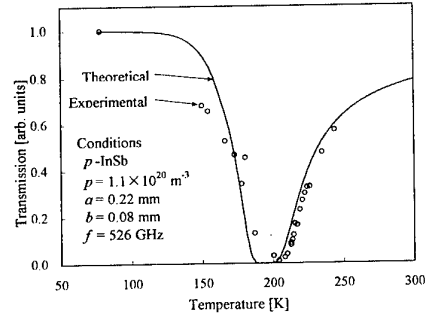


Fig. 6. Variation of the transmission for $B = 0$ as a function of temperature (two-layer parallel-plate waveguide structure containing p -InSb at 526 GHz).

The experimentally observed insertion loss of the InSb slab is about 0.3 dB/mm for $B = 0$ T and $T = 77$ K, which is much greater than the theoretical prediction of 7.3×10^{-3} dB/mm. The discrepancy is attributed to the reflection of the wave at the end of the sample slab. The theoretical value of the propagation loss of the image guide mode M2 is also very small, and is calculated to be 0.16 dB/mm for $B = 0$ T and $T = 77$ K, although no corresponding experimental data have been obtained. This indicates that the construction of image-guide-type transmission lines in the submillimeter-wave frequency range is possible by using p -type InSb slabs. Indeed, results of calculations show that a p -InSb image guide with a thickness of 0.05 mm has a 526 GHz propagation loss of 0.19 dB/mm at 77 K.

Except for the case where T is very near the liquid nitrogen temperature, a maximum and a minimum appear in the B -dependence of the transmission. They are classified into two classes arising from different origins.

Figures 7(a) to (c) show the B -dependence of the 526 GHz submillimeter transmission for various ambient temperatures in the T -region $T < 190$ K for both $B+$ and $B-$ directions. Corresponding theoretical values for M1 are calculated using the electron and hole densities and their mobilities at each

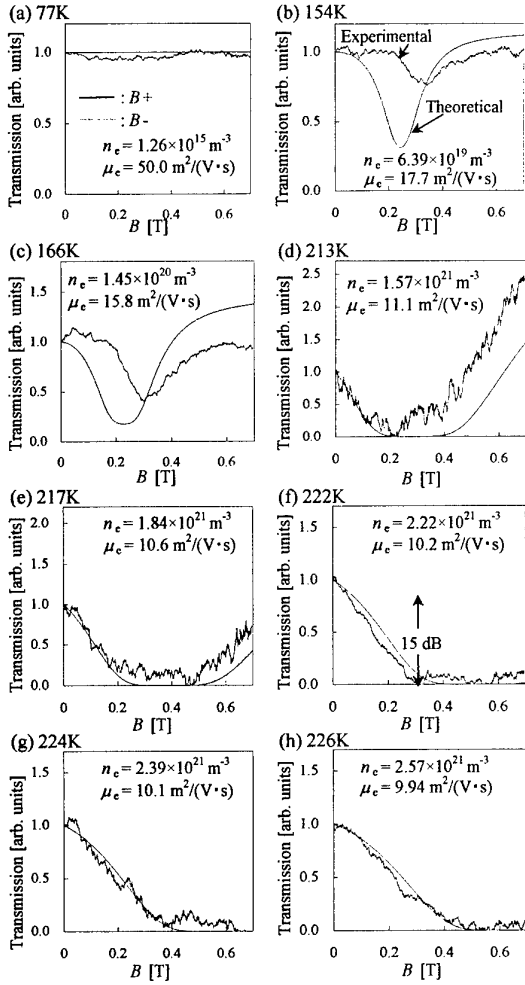


Fig. 7. Variations of the transmission as a function of B for various temperatures [two-layer parallel-plate waveguide structure containing p -InSb ($b = 0.08$ mm) at 526 GHz].

temperature, and are also plotted in the figure as thin lines such that the experimental and theoretical values coincide at $B = 0$ T.

First, at 77 K, both theoretically and experimentally, the transmission is almost independent of the magnetic field, as shown in Fig.7(a). This is clearly because the holes in InSb can move only negligibly, regardless of the submillimeter-wave fields.

Next, at $T = 154$ K [Fig.7(b)], a small dip appears on the theoretical and experimental transmission curves at $B = 0.24$ T and at $B = 0.3$ T, respectively, for both $B+$ and $B-$ directions. They originate from the electron cyclotron resonance caused by the rotating electric field in the InSb slab. The discrepancy between the magnetic fields that cause the experimental and theoretical dips is explained by nonuniform energy intervals between succeeding Landau levels of InSb arising from the nonparabolic feature of the conduction band.

As the temperature further increases, the magnetic field that causes the minimum transmission considerably decreases for both $B+$ and $B-$ direction. This indicates that the resonance became a hybrid one whose resonant magnetic field B_r is given by $eB_r/m_e = (\omega^2 - \omega_{pe}^2/\epsilon_r)^{1/2}$, where ω_{pe} denotes the electron plasma frequency $\omega_{pe}^2 = n_e e^2/m_e \epsilon_0$. The experimental results are in agreement with the theoretical ones only qualitatively.

As the sample temperature increases over 200 K, the propagation characteristics vary drastically. Large dips clearly

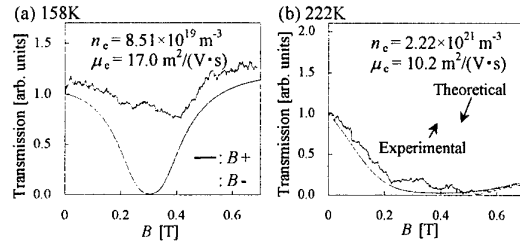


Fig. 8. Variations of the transmission as a function of B for various temperatures [two-layer parallel-plate waveguide structure containing p -InSb ($b = 0.026$ mm) at 671 GHz].

appear again on the theoretical and experimental transmission curves for both B -directions, as shown in Figs.7(d) to (h). The magnetic field giving the minimum transmission greatly increases for both $B+$ and $B-$ directions as the carrier density increases with increasing T . The dip in the $B-$ direction occurs at a higher magnetic field than that in the $B+$ direction. The experimental results indicate very good quantitative agreement with the theoretical prediction. These variations in the present temperature region originate from the slow surface wave resonance which has already been reported for the 70 GHz millimeter-wave frequency range and for n -type InSb[3]. The slow surface wave resonant magnetic field B_s is given by the relation

$$B_s = (m_e^*/e) \{ \omega_{pe}^2 / [\omega (\epsilon_r + 1)] - \omega \} \quad (2)$$

It should be noted that the T -value of 200 K corresponds to the electron density at which the above B_s -value vanishes. Thus, the surface wave resonance appears only for the T -region higher than 200 K. It is interesting from the viewpoint of device application that, in the submillimeter-wave region, the slow surface wave resonance is observed at the dry ice temperature with p -type material. In addition, it is to be noted that this surface wave resonance exhibits large nonreciprocal characteristics. For example, it is indicated in Fig.7(f) that, at the temperature of 222 K, a nonreciprocity of more than 15 dB is obtained with an insertion loss of 5 dB at a moderate magnetic field of 0.3 T. This result indicates that our two-layer structure with a p -InSb slab functions as a submillimeter-wave nonreciprocal device which operates at the dry ice temperature. It is surmised that the wave propagation in p -InSb at 77 K can be made to have a nonreciprocal nature by injecting plasma in an appropriate part of the material in the presence of an externally applied magnetic field, and can be easily controlled by varying the plasma density.

Next, the magnetic field dependence of the transmission of 671 GHz submillimeter waves through the p -InSb two-layer waveguide are presented in Fig.8 for $a = 0.274$ mm and $b = 0.026$ mm. The situation is quite similar to the case of Fig. 7. As a consequence of the increase in frequency, the magnetic field that induces cyclotron resonance in the case shown in Fig.8(a) is larger than that in the case shown in Fig.7(b). On the other hand, the theoretical value of the surface wave resonant magnetic field in the case of Fig.8(b) is 0.396 T, which is somewhat smaller than that in the case of Fig.7(f) (0.526 T). The experimental results are consistent with the theory.

2) Two-Layer Structure with n -InSb Slab

Figure 9 shows the 526 GHz transmission characteristics of a two-layer waveguide containing an n -InSb slab with the electron density $1.55 \times 10^{21} \text{ m}^{-3}$ and electron mobility $50.0 \text{ m}^2/(\text{V}\cdot\text{s})$. Since the electron density is sufficiently large, even at 77 K, in this case, the B_s -value of eq.(2) remains positive. Thus surface wave resonance clearly appears even at 77 K, in

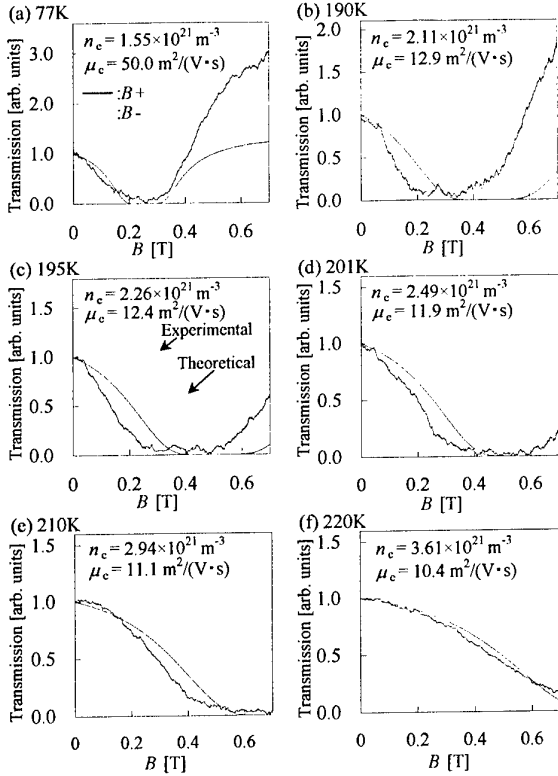


Fig. 9. Variations of the transmission as a function of B for various temperatures [two-layer parallel-plate waveguide structure containing n -InSb ($b = 0.09$ mm) at 526 GHz].

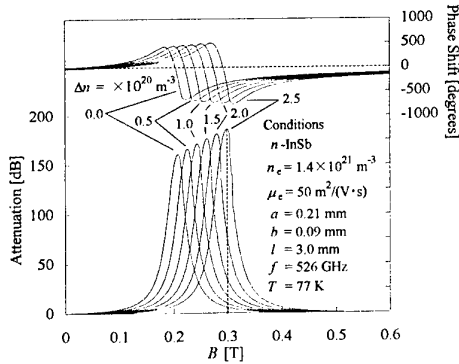


Fig. 10. Variations of the attenuation and phase shift as functions of B for various values of the injected plasma density [two-layer parallel-plate waveguide structure containing n -InSb ($b = 0.09$ mm) at 526 GHz].

contrast with the case of p -InSb. The resonance in this case is very sharp, and large nonreciprocity, 15 dB at $B = 0.25$ T, is obtained because of the high electron mobility. As the electron density increases with T , the magnetic field giving the minimum transmission considerably increases, which is again consistent with eq.(2), and simultaneously, the resonance becomes very broad because of the reduction of the electron mobility.

The dependence of the surface wave resonance on the injected plasma density Δn is calculated and presented in Fig.10 for an n -InSb slab with the initial electron density of $1.40 \times 10^{21} \text{ m}^{-3}$ and electron mobility of $50.0 \text{ m}^2/(\text{V}\cdot\text{s})$. The surface wave resonant magnetic field, which is defined as the B -value corresponding the peak of the attenuation, increases with increasing plasma density. This result shows that, at $B = 0.3$ T, the submillimeter-wave transmission theoretically varies over 150 dB with $\Delta n = 2.5 \times 10^{20} \text{ m}^{-3}$. This indicates the possibility of applying our configuration to a submillimeter-wave variable attenuator.

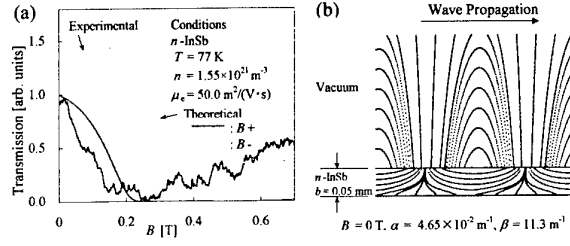


Fig. 11 (a) Variations of the transmission as a function of B and (b) electric field distributions [image guide structure containing n -InSb ($b = 0.05$ mm) at 526 GHz].

B. Transmission Characteristics of Image guide

For the case where a sufficiently dense plasma is injected into the p -InSb image guide shown in Fig.1(b), we present here the transmission characteristics of the image guide made of an n -InSb slab. This guide also supports, as presented below, a slow surface wave resonance similar to the one observed for the two-layer structure. Figure 11(a) shows the experimentally observed B -dependence of the 526 GHz transmission through the n -InSb image guide depicted in Fig.1(b). For the $B+$ direction, transmission first decreases with magnetic field, and then becomes minimum at $B = 0.35$ T. For $B-$, transmission initially increases and becomes maximum at $B = 0.15$ T. It then decreases and becomes minimum at $B = 0.4$ T. These variations are similar to those for the two-layer structure, and are the characteristic of slow surface wave resonance. As seen in the results, nonreciprocity of 8.4 dB also appears in this configuration at $B = 0.13$ T. The electric field for $B = 0$ of this propagation mode is shown in Fig.11(b). In contrast to the case of p -InSb where the image guide mode propagates, this mode in n -InSb is the well-known Zenneck surface wave.

IV. CONCLUSIONS

The magnetic field dependence of 526 GHz and 671GHz submillimeter-wave transmission characteristics through a two-layer waveguide containing a p - or n -InSb slab was studied in detail theoretically and experimentally at various ambient temperatures. For p -InSb, submillimeter-wave propagation loss at 77 K is very small, at most 0.3 dB/mm, which suggests that the construction of dielectric transmission lines, such as an image guide using p -InSb material, is possible. For $T > 200$ K, slow surface wave resonance occurs, and nonreciprocity of more than 15 dB appears at $B = 0.3$ T at the dry ice temperature, which indicates the possibility of applying our waveguide configuration to submillimeter-wave nonreciprocal devices. The resonance occurs also in the n -InSb image guide. The possibility of controlling these nonreciprocal propagation characteristics easily by injecting plasma was also revealed. Experimental study on this point is now under way.

ACKNOWLEDGEMENT

This work was supported in part by a Grant-in-Aid for Scientific Research from the Ministry of Education, Science, Sports and Culture.

REFERENCES

- [1] S. Yodokawa and T. Obunai: Jpn. J. Appl. Phys. **36** (1997) 2101.
- [2] H. J. Hrostowski, F. J. Morin, T. H. Geballe and G. H. Wheatley: Phys. Rev. **10** (1955) 1672.
- [3] T. Obunai and T. Sekiguchi: Jpn. J. Appl. Phys. **13** (1974) 93.

NANOTEXTURIZATION OF III-V COMPOUNDS FOR THz-WAVE GENERATION

I.M. Tiginyanu, S. Langa, K. Hjort, J. Monecke, H.L. Hartnagel

Abstract – Being low loss semiconductors, GaP and GaAs are promising materials for generating THz-wave by difference frequency generation (DFG). In particular, CW generation of tunable narrow-band THz radiation was achieved in GaAs by mixing two laser beams [J. Appl. Phys. 45 (1974) 3972]. In this work we analyze the possibility to increase the nonlinear response by nanotexturization of III-V compounds. MeV and GeV heavy-ion implantation with subsequent electrochemical etching of samples is shown to

result in the formation of parallel pores, their density being defined by the implantation dose. We succeeded to fabricate optically-homogeneous uniaxial free-standing membranes of GaP and GaAs with the thickness up to tens of micrometers. These membranes prove to be superior for electromagnetic frequency conversion in comparison with the bulk materials.

Laboratory of Low-Dimensional Semiconductor Structures, Technical University of Moldova, 2004 Chisinau, Moldova;
Materials Science Dep., Uppsala University, S-751 21 Uppsala, Sweden;
Institut für Theoretische Physik, Technical University Freiberg, 09596 Freiberg, Germany;
Institut für Hochfrequenztechnik, Technical University Darmstadt, 64283 Darmstadt, Germany

At the time of publication the final manuscript was not available.

Phase Noise Estimation for THz Radiation from RTDs and other Solid-State Sources

Peter H. Handel

Physics Dept., Univ. of Missouri, St. Louis, MO 63121, USA

Abstract - For imaging and remote sensing applications, the phase noise of the THz generator must be minimized. This can be done as part of the optimization process on the basis of a properly chosen figure of merit. For this, the present paper provides an analytical phase noise expression as a function of the device parameters and operation point. The quantum $1/f$ theory is used to calculate from first principles the $1/f$ noise present in the device parameters and in the resulting system frequency from resonant tunneling diodes (RTDs), super-electronic lattice devices (SLEDs), Gunn devices (TEDs), and transit time diodes. In general, quantum $1/f$ fluctuations in the dissipative elements lead to a Q^{-4} dependence of the spectral density of fractional frequency fluctuations and of the corresponding phase noise, where Q is the quality factor.

I. INTRODUCTION

Fluctuations with a spectral density proportional to $1/f$ are found in a large number of systems in science, technology and everyday life. These fluctuations are known as $1/f$ noise in general. They have first been noticed by Johnson in early amplifiers, have limited the performance of vacuum tubes in the thirties and forties, and have later hampered the introduction of semiconductor devices.

The present paper is focused on the general origin of fundamental $1/f$ noise as a universal form of chaos, and on the cause of its ubiquity. It starts with a *special case* of the general $1/f$ noise phenomenon, the Quantum $1/f$ Effect (with its conventional and coherent contributions) which is as fundamental as time and space. The $1/f$ fluctuations are a necessary consequence of the mathematical homogeneity of the dynamical (or physical) equations describing the motion of an arbitrary chaotic or stochastic nonlinear system. A sufficient criterion was derived by the author. It indicates if an arbitrary system governed by a given system of nonlinear integro-differential equations will exhibit $1/f$ noise. The criterion was applied to several particular systems, and is used to predict the fundamental quantum $1/f$ effect as a *special case*.

II. CONVENTIONAL QUANTUM $1/f$ EFFECT

This effect¹⁻⁶ is present in any cross section or process rate involving charged particles or current carriers. The physical origin of quantum $1/f$ noise is easy to understand. Consider for example Coulomb scattering of current carriers, e.g., electrons on a center of force. The scattered electrons reaching a detector at a given angle away from the direction of the incident beam are described by DeBroglie waves of a frequency corresponding to their energy. However, some of the electrons have lost energy in the scattering process, due to the emission of bremsstrahlung. Therefore, part of the outgoing DeBroglie waves is shifted to slightly lower frequencies. When we calculate the probability density in the scattered beam, we obtain also cross terms, linear both in the part scattered with and without bremsstrahlung. These cross terms oscillate with the same frequency as the frequency of the emitted bremsstrahlung photons. The emission of photons at all frequencies results therefore in probability density fluctuations at all frequencies. The corresponding current density fluctuations are obtained by multiplying the probability density fluctuations by the velocity of the scattered current carriers. Finally, these current fluctuations present in the scattered beam will be noticed at the detector as low frequency current fluctuations, and will be interpreted as fundamental cross section fluctuations in the scattering cross section of the scatterer. While incoming carriers may have been Poisson distributed, the scattered beam will exhibit super-Poissonian statistics, or bunching, due to this new effect which we may call quantum $1/f$ effect. The quantum $1/f$ effect is thus a many-body or collective effect, at least a two-particle effect, best described through the two-particle wave function and two-particle correlation function.

Let us estimate the magnitude of the quantum $1/f$ effect semiclassically by starting with the classical (Larmor) formula $2q^2a^2/3c^3$ for the power radiated by a particle of charge q and acceleration a . The acceleration can be approximated by a delta function $a(t) = \Delta v \delta(t)$ whose Fourier transform

$\Delta \mathbf{v}$ is constant and is the change in the velocity vector of the particle during the almost instantaneous scattering process. The one-sided spectral density of the emitted bremsstrahlung power $4q^2(\Delta \mathbf{v})^2/3c^3$ is therefore also constant. The number $4q^2(\Delta \mathbf{v})^2/3hfc^3$ of emitted photons per unit frequency interval is obtained by dividing with the energy hf of one photon. The probability amplitude of photon emission $[4q(\Delta \mathbf{v})^2/3hfc^3]^{1/2}e^{i\gamma}$ is given by the square root of this photon number spectrum, including also a phase factor $e^{i\gamma}$. Let ψ be a representative Schrödinger catalogue wave function of the scattered outgoing charged particles, which is a single-particle function, normalized to the actual scattered particle concentration. The beat term in the probability density $\rho=|\psi|^2$ is linear both in this bremsstrahlung amplitude and in the non-bremsstrahlung amplitude. Its spectral density will therefore be given by the product of the squared probability amplitude of photon emission (proportional to $1/f$) with the squared non-bremsstrahlung amplitude which is independent of f . The resulting spectral density of fractional probability density fluctuations is obtained by dividing with $|\psi|^4$ and is therefore

$$|\psi|^{-4}S_{|\psi|^2}(f) = 8q^2(\Delta \mathbf{v})^2/3hfc^3 = 2\alpha A/fN = j^2S_j(f), \quad (1)$$

where $\alpha = e^2/hc = 1/137$ is the fine structure constant and $\alpha A = 4q^2(\Delta \mathbf{v})^2/3hfc^3$ is known as the infrared exponent in quantum field theory, and is known as the quantum $1/f$ noise coefficient, or Hooke constant, in electrophysics.

The spectral density of current density fluctuations is obtained by multiplying the probability density fluctuation spectrum with the squared velocity of the outgoing particles. When we calculate the spectral density of fractional fluctuations in the scattered current j , the outgoing velocity simplifies, and therefore Eq. (1) also gives the spectrum of current fluctuations $S_j(f)$, as indicated above. The quantum $1/f$ noise contribution of each carrier is independent, and therefore the quantum $1/f$ noise from N carriers is N times larger; however, the current j will also be N times larger, and therefore in Eq. (1) a factor N was included in the denominator for the case in which the cross section fluctuation is observed on N carriers simultaneously.

The fundamental fluctuations of cross sections and process rates are reflected in various kinetic coefficients in condensed matter, such as the mobility μ and the diffusion constant D , the surface and bulk recombination speeds s , and recombination times τ , the rate of tunneling j_t and the thermal diffusivity in semiconductors. Therefore, the

spectral density of fractional fluctuations in all these coefficients is given also by Eq. (1).

When we apply Eq. (1) to a certain device, we first need to find out which are the cross sections σ or process rates which limit the current I through the device, or which determine any other device parameter P , and then we have to determine both the velocity change $\Delta \mathbf{v}$ of the scattered carriers and the number N of carriers simultaneously used to test each of these cross sections or rates. Then Eq. (1) provides the spectral density of quantum $1/f$ cross section or rate fluctuations. These spectral densities are multiplied by the squared partial derivative $(\partial I/\partial \sigma)^2$ of the current, or of the device parameter P of interest, to obtain the spectral density of fractional device noise contributions from the cross sections and rates considered. After doing this with all cross sections and process rates, we add the results and bring (factor out) the fine structure constant α as a common factor in front. This yields excellent agreement with the experiment in a large variety of samples, devices and physical systems.

Eq. (1) was derived in second quantization, using the commutation rules for boson field operators. For fermions one repeats the calculation replacing in the derivation the commutators of field operators by anticommutators, which yields¹⁻⁶

$$\rho^{-2}S_\rho(f) = j^{-2}S_j(f) = \sigma^{-2}S_\sigma(f) = 2\alpha A/f(N-1) \quad (2)$$

This causes no difficulties, since $N \geq 2$ for particle correlations to be defined, and is practically the same as Eq. (1), since usually $N \gg 1$. Eqs. (1) and (2) suggest a new notion of physical cross sections and process rates which contain $1/f$ noise, and express a fundamental law of physics, important in most high-technology applications.

We turn now to the connection to the coherent Quantum $1/f$ Effect, essentially caused by the uncertainty of the electron mass, by the coherent state of the field of the electron. The coherent state has an uncertain energy. The coherent state in a conductor or semiconductor sample is the result of the experimental efforts directed towards establishing a steady and constant current, and is therefore the state defined by the collective motion, i.e. by the drift of the current carriers. It is expressed in the Hamiltonian by the magnetic energy E_m , per unit length, of the current carried by the sample. In very small samples or electronic devices, this magnetic energy

$$E_m = \int (B^2/8\pi) d^3x = [nevSc/c^2] \ln(R/r) \quad (3)$$

is much smaller than the total kinetic energy E_k of the drift motion of the individual carriers

$$E_k = \sum_i m_i v^2/2 = nSmv^2/2 = E_m/s. \quad (4)$$

Here we have introduced the magnetic field B , the carrier concentration n , the cross sectional area S and radius r of the cylindrical sample (e.g., a current carrying wire), the radius R of the electric circuit, and the "coherence ratio"

$$s = E_m/E_k = 2ne^2S/mc^2 \ln(R/r) = 2e^2N'/mc^2, \quad (5)$$

where $N' = nS$ is the number of carriers per unit length of the sample and the natural logarithm $\ln(R/r)$ has been approximated by one in the last form. We expect the observed spectral density of the mobility fluctuations to be given by a relation of the form

$$(1/\mu^2)S_\mu(f) = [1/(1+s)][2\alpha A/fN] + [s/(1+s)][2\alpha/\pi fN] \quad (6)$$

which can be interpreted as an expression of the effective Hooke constant if the number N of carriers in the (homogeneous) sample is brought to the numerator of the left hand side. In this equation $\alpha A = 2\alpha(\Delta v/c)^2/3\pi$ is the usual nonrelativistic expression of the infrared exponent, present in the familiar form of the conventional quantum $1/f$ effect¹⁻⁶. This equation is limited to quantum $1/f$ mobility (or diffusion) fluctuations, and does not include the quantum $1/f$ noise in the surface and bulk recombination cross sections, in the surface and bulk trapping centers, in tunneling and injection processes, in emission or in transitions between two solids.

Note that the coherence ratio s introduced here equals the unity for the critical value $N' = N'' = 2 \cdot 10^{12}/\text{cm}$, e.g. for a cross section $S = 2 \cdot 10^{-4} \text{ cm}^2$ of the sample when $n = 10^{16}$. For small samples with $N' \ll N''$ only the first term survives, while for $N' > N''$ the second term in Eq. (6) is dominant.

III. DERIVATION OF MOBILITY QUANTUM $1/f$ NOISE IN N^+-P DIODES

For a diffusion limited n^+-p junction the current is controlled by diffusion of electrons into the p -region over a distance of the order of the diffusion length $L = (D_n\tau_n)^{1/2}$ which is shorter than the length w_p of the p -region in the case of a long diode. If $N(x)$ is the number of electrons per unit length and D_n their diffusion constant, the electron current at x is

$$I_{nd} = -eD_n dN/dx, \quad (7)$$

where we have assumed a planar junction and taken the origin $x = 0$ in the junction plane. Diffusion constant fluctuations, given by kT/e times the mobility fluctuations, will lead to local current fluctuations in the interval Δx

$$\delta I_{nd}(x,t) = I_{nd} \Delta x \delta D_n(x,t)/D_n. \quad (8)$$

The normalized weight with which these local fluctuations representative of the interval Δx contribute to the total current I_d through the diode at $x = 0$ is determined by the appropriate Green function and can be shown to be $(1/L)\exp(-x/L)$ for $w_p/L \gg 1$. Therefore the contribution of the section Δx is

$$\delta I_d(x,t) = (\Delta x/L) \exp(-x/L) I_{nd} \delta D_n(x,t)/D_n, \quad (9)$$

with the spectral density

$$S_{\Delta I_d}(x,f) = (\Delta x/L)^2 \exp(-2x/L) I_{nd}^2 S_{D_n}(x,f)/D_n^2 \quad (10)$$

For mobility and diffusion fluctuations the fractional spectral density is given by $\alpha_{Hnd}/fN\Delta x$, where α_{Hnd} is determined from quantum $1/f$ theory according to Sec II. With Eq. (7) we obtain then

$$S_{\Delta I_d}(x,f) = (\Delta x/L^2) \exp(-2x/L) (eD_n dN/dx)^2 \alpha_{Hnd}/fN \quad (11)$$

The electrons are distributed according to the solution of the diffusion equation, i.e.

$$N(x) = [N(0) - N_p] \exp(-x/L); \quad dN/dx = -\{[N(0) - N_p]/L\} \exp(-x/L). \quad (12)$$

Substituting into Eq. (11) and simply summing over the uncorrelated contributions of all intervals Δx , we obtain

$$S_{Id}(f) = \alpha_{Hnd} (eD_n/L^2)^2 \int [N_0 - N_p]^2 e^{-4x/L} dx / \{[N(0) - N_p] e^{-x/L} + N_p\} \quad (13)$$

The integral is from 0 to w . We note that $eD_n/L^2 = e/\tau_n$. With the expression of the saturation current $I_0 = e(D_n/\tau_n)^{1/2} N_p$ and of the current $I = I_0[\exp(eV/kT) - 1]$, we can carry out the integration from 0 to 1

$$S_{Id}(f) = \alpha_{Hnd} (eI/f\tau_n) \int du/(au + 1) = \alpha_{Hnd} (eI/f\tau_n) F(a). \quad (14)$$

Here we have introduced the notations

$$u = \exp(-x/L), \quad a = \exp(eV/kT) - 1, \quad F(a) = 1/3 - 1/2a + 1/a^2 - (1/a^3) \ln(1+a) \quad (15)$$

Eq. (14) gives the diffusion noise as a function of the quantum $1/f$ noise parameter α_{Hnd} . A similar result can be derived for the quantum $1/f$ fluctuations of the recombination rate r in the bulk of the p -region, the only difference being the presence of α_{Hnr} instead of α_{Hnd} in Eq. (14). The total noise is then given by Eq. (14) with α_{Hnd} replaced by the sum $\alpha_{Hnd} + \alpha_{Hnr}$

$$S_{Id}(f) = (\alpha_{Hnd} + \alpha_{Hnr}) (eI/f\tau_n) F(a). \quad (16)$$

IV. 1/f FLUCTUATIONS IN RTDs

Resonant tunneling diodes have been proposed as generators of THz oscillations and radiation. They consist of two potential barriers enclosing a quantum well. Electrons penetrating the potential barriers by tunneling are controlled by the quasistationary energy levels defined by the potential well. If their energy is close to the first energy level in the well, resonance occurs, and a peak I_p of the current through the diode occurs. This corresponds to an applied bias voltage V_p . If, however, the applied voltage increases further, only a negligibly small non-resonant current trickle remains at the voltage $V=V_v$ and a broad valley is observed in the I/V characteristic. Scattering processes that reduce the energy of the carriers to a value close to eV_p will always be present, generating a finite current minimum I_v at V_v . Between V_p and V_v there is a negative differential conductance

$$G = -(I_p - I_v) / (V_v - V_p) \quad (17)$$

on the I/V curve, that is used to generate oscillations.

1/f noise in I_v is given by Eqs. (1)-(2) with

$$(\Delta v/c)^2 = 2eV_v/m. \quad (18)$$

Taking for instance $V_p = 0.4$ V, $I_p = 2.5 \cdot 10^8$ A/m², $V_v = 0.6$ V, $I_v = 4 \cdot 10^7$ A/m², we obtain with $m_{eff} = 0.068 m_0$,

$$NI_v^{-2} S_{I_v}(f) = 2\alpha A/f = 7.4/0.068 \cdot 10^{-9} = 1.3 \cdot 10^{-7} \quad (19)$$

N is given by

$$N = \tau I_v / e, \quad (20)$$

where τ is the life time of the carriers. With a cross-sectional area of 10^{-6} cm² and $\tau = 10^{-10}$, we obtain $N = 2.5 \cdot 10^6$.

Finally, the quantum 1/f frequency fluctuations can be obtained from the formula

$$\omega^2 = -G^3 L_c / C_D^3 (R_L + R_s), \quad (21)$$

which is obtained by equating the RF circuit-limited output power with the DC bias circuit-limited power. Here L_c is the inductance in the bias circuit, C_D is the diode capacitance, R_L the resistance introduced by the RF circuit inductance, and R_s is the diode series resistance. From Eq. (17) the fluctuations in G caused by I_v are calculated and substituted into the linearized form of Eq. (21).

V. 1/f FREQUENCY FLUCTUATIONS FROM 1/f NOISE IN RF DISSIPATIVE ELEMENTS

RF resonant circuits can be described as a harmonic

oscillator with losses

$$dx/dt + \gamma dx/dt + \omega_o^2 x = F(t) \quad (22)$$

The quantum 1/f fluctuations are present in the loss coefficient γ . They are given by an expression of the form

$$S_{\delta\gamma/\gamma}(f) = \Lambda/f \quad (23)$$

where Λ is a quantum 1/f coefficient characterizing the elementary loss process.

The resonance frequency is given by

$$\omega_r^2 = \omega_o^2 + \gamma^2 \quad (24)$$

The quantum 1/f fluctuations in the resonance frequency are given by $\omega_r \delta\omega_r = -2\gamma\delta\gamma$, or

$$\delta\omega_r/\omega_r = -2(\gamma/\omega_r) \delta\gamma/\gamma = -(1/2Q^2)(\delta\gamma/\gamma) \quad (25)$$

where $Q = \omega_r/2\gamma$ is the quality factor. Squaring, averaging and particularizing Eq. (25) for the unit frequency interval, we obtain the Q^{-4} law

$$S_y(f) = \langle (\delta\omega_r/\omega_r)^2 \rangle_f = (1/4Q^4) \langle (\delta\gamma/\gamma)^2 \rangle_f = \Lambda/4fQ^4, \quad (26)$$

where y is the fractional frequency fluctuation $\delta\omega_r/\omega_r$. This law is also applicable to quartz resonators⁵. The examples in the last two sections show how the phase noise is to be found in other solid state sources of THz radiation.

References

1. P.H. Handel: "The Quantum 1/f Effect and the General Nature of 1/f Noise", *Archiv für Elektronik und Übertragungstechnik (AEÜ)* **43**, 261-270 (1989);
2. A. van der Ziel, "Unified Presentation of 1/f Noise in Electronic Devices; Fundamental 1/f Noise Sources", *Proc. IEEE* **76**, 233-258 (1988 review paper); "The Experimental Verification of Handel's Expressions for the Hooke Parameter", *Solid-State Electronics* **31**, 1205-1209 (1988); "Semiclassical Derivation of Handel's Expression for the Hooke Parameter", *J. Appl. Phys.* **63**, 2456-2455 (1988); **64**, 903 (1988);
3. A. van der Ziel et. al., "Extensions of Handel's 1/f Noise Equations and their Semiclassical Theory", *Phys. Rev. B* **40**, 1806-1809 (1989);
4. P.H. Handel: "Fundamental Quantum 1/f Noise in Small Semiconductor Devices", *IEEE Trans. on Electr. Devices* **41**, 2023-2033 (1994).
5. P.H. Handel: "Nature of 1/f Frequency Fluctuation in Quartz Crystal Resonators", *Solid-State Electronics* **22**, 875-876 (1979).
6. P.H. Handel: "Coherent and Conventional Quantum 1/f Effect" *Physica Status Solidi* **b194**, 393-409 (1996)

Power Generation in Waveguide and Quasi-Optical Technologies Using Hybrid Circuits at Millimetre Waves

A. Pédén, D. Bourreau

LEST UMR CNRS n° 6616 - ENST de Bretagne - BP 832 - 29285 BREST CEDEX

E-mail : Daniel.Bourreau@enst-bretagne.fr Tel : (33) 2 29 00 13 14 - Fax : (33) 2 29 00 13 43

E-mail : Alain.Peden@enst-bretagne.fr Tel : (33) 2 29 00 10 92 - Fax : (33) 2 29 00 13 43

Abstract - Terahertz applications require specific components and technologies. To study and develop systems at this frequency range, a preliminary investigation at much lower frequency is often undertaken. This paper presents some results on signal generation using classical hybrid technologies in the X and Ka bands, and some investigations using a quasi-optical technology in the W band are also presented.

A cavity oscillator at 9.15 GHz with 16 dBm output power and -110 dBc/Hz @ 10kHz phase noise is first described. Power combining is then carried out in a cavity oscillator and also in free space for spatial or "quasi-optical" combining.

The design and measurement of an hybrid varactor frequency multiplier in the millimetre wave range with 12 dB measured conversion losses at 62 GHz and the investigations on a quasi-optical frequency doubler are presented.

I. INTRODUCTION

For sub-millimetre wave applications, like FIRST and SOFIA programs [1], local oscillators at very high frequencies (up to 1 THz) are required for heterodyne receivers. A solution for providing power with low phase noise at sub-millimetre waves associates a low frequency oscillator with one - or more - frequency multipliers. This high frequency oscillator must have sufficient power for efficient driving of the down converter. Waveguide techniques are still widely used for millimetre and sub-millimetre radiometers but planar circuits (hybrid or MMIC) could allow the drawbacks of wave-guide whisker contacted diode multipliers (losses, fragility...) to be overcome. However, no tuning can be done on planar multipliers and accurate modelling of the circuit is required. The Quasi-optical technology could provide a solution to waveguide and planar techniques, but at the same time introduces new challenges.

II. WAVEGUIDE AND PLANAR TECHNOLOGIES FOR POWER GENERATION

A- Cavity oscillator and power combining (in cavity)

Local oscillator characteristics (i.e. output power, phase noise, stability and reliability) are very important for the heterodyne receiver performances. Compared with the

vacuum tube technology (klystron,...), solid state components are very attractive in terms of size, weight, reliability and can be mass produced. But for optimum performances and high output power, impedance matching of the active component and power combining are to be achieved.

The oscillator uses a GUNN diode coupled through a circular patch antenna to a cylindrical cavity. A non linear electrical model of the diode was extracted using a load-pull setup ([2]) and electromagnetic simulations of the cavity with the circular patch were carried out to obtain its equivalent impedance at the connection point of the diode. The simulations lead to a cavity TE_{121} resonant mode and the oscillator Harmonic Balance simulation gives a 12.3 dBm output power at 9.17 GHz. Experimental results are shown in fig. 1. Fig. 2 gives the oscillator phase noise measurement.

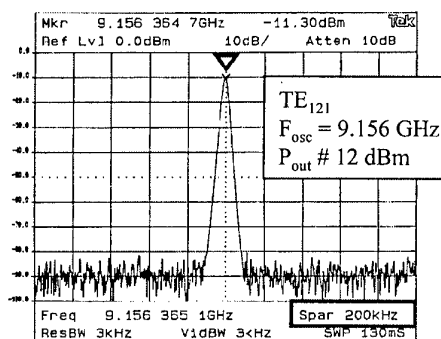


Fig.1: Output spectrum of the cavity oscillator

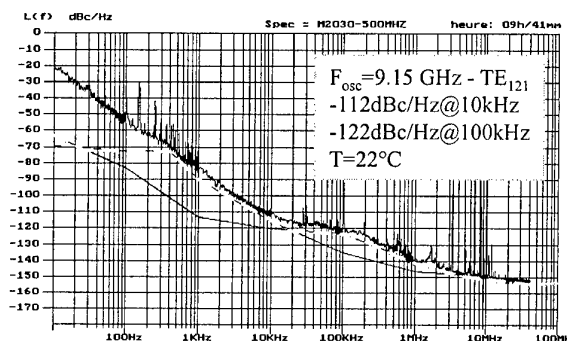


Fig. 2: Phase noise measurement

For power combining, a second diode and its coupling patch antenna was added in the cavity. For optimum oscillation stability and output power, a TE_{113} resonant mode of the cavity was chosen. The oscillation frequency and the output power are given in the table I.

Table I: Oscillation frequency and output power of the oscillator with 1 or 2 diodes in the cavity

	TE_{113} Cavity Mode	TE_{121} Cavity Mode
1 GUNN diode	9.98 GHz 16.8 dBm	9.15 GHz 12 dBm
2 GUNN diodes	10.0 GHz 19.4 dBm	No synchronization as expected in simulation

B- Frequency multiplier in planar technology

The source and load impedances and the working conditions of the multiplier are initialized with the Penfield and Rafuse equations [3]. Non-linear simulations are then used to optimize the results and calculate the output power at fundamental and harmonic frequencies.

Realisations at lower frequencies and sensitivity simulations give other informations. First, only radial stubs are used to short-circuit the second harmonic at the input and the fundamental frequency at the output in a very large frequency band. Classical planar technologies such as microstrip or coplanar technologies lead to very low and very high impedance transmission line sections for the diode matching, inducing high losses. So, a technology [4] with microstrip and multilayer coplanar lines was adopted. To obtain very low characteristic impedances, a small substrate thickness is used. But at the same time, high values are required. The multilayer technology (see fig. 3) allows to retain approximately the same central conductor width throughout the circuit, cutting the ground plane under the inductive transmission line sections. Classical coplanar lines are used at the accesses for coaxial probe measurements.

Experimental results (see fig. 4) show that the optimal input frequency is 30.8 GHz for maximum output power (10.8 dBm) and efficiency, but is 28.25 GHz for optimal fundamental rejection (as expected in simulations for output power, efficiency and fundamental rejection).

III. QUASI-OPTICAL TECHNOLOGY FOR POWER GENERATION

The spatial or quasi optical technology is very attractive because it enables a substantial reduction in propagation losses, higher power as well as reliability are obtained by combining the power produced from many solid-state devices and there is no need of a physical connection between the quasi optical components, the source and the load. Some tuning is also possible by moving the parallel

quasi optical components (slab, array,...), each in relation to the others.

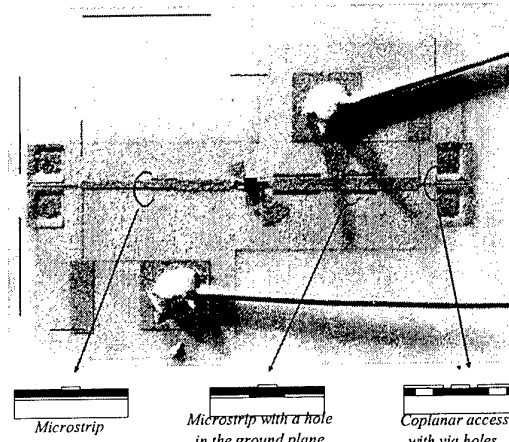


Fig. 3: multilayer technology process

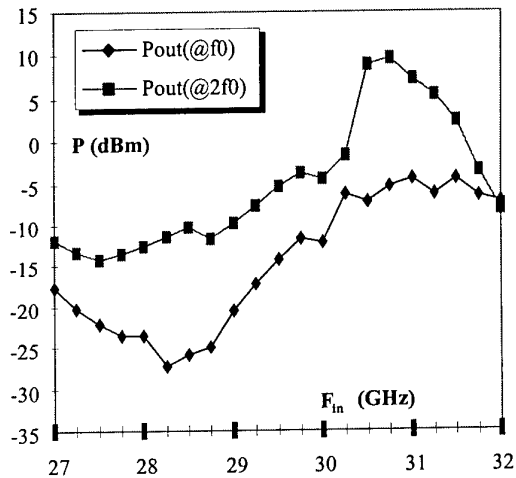


Fig. 4: Output power at fundamental and second harmonic for $P_{in}=20$ dBm and $V=-9$ V.

A- Quasi-optical test bench design and its validation

For quasi-optical element characterisation and modelling, two test benches were carried out with Gaussian Optic Lens Antennas (GOLA) in the Ka ([5]) and W band ([6]). These benches were validated for S parameter measurements of passive quasi-optical elements such as polarizer, filter and dielectric slab. The complex permittivity of dielectric slabs is also extracted with high precision ([5]).

Tests were also carried out for simple cascaded quasi-optical functions and well compared with simulations made on classical CAD software (such as HP-MDS) ([5], [6]). So, active quasi-optical functions were then investigated.

B- Oscillators and power combining

For free space combining, a 2 and a 3 diode oscillator combiner using a Whispering Gallery Mode circular dielectric resonator was tested. The structure of the oscillator is shown in fig. 5. The oscillation frequency is 13.51 GHz with 2 diodes as expected from the 13.55 GHz WGH_{438} mode of the resonator and with 3 diodes, the frequency is 13.12 GHz with the 13.25 GHz WGH_{428} mode of the resonator (see fig 6). The output power spectrum is given in fig.7.

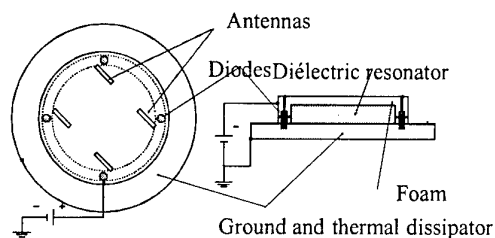


Fig. 5: Quasi-optical structure of the WGM resonator oscillator



Fig. 6: E field intensity for the WGM resonator

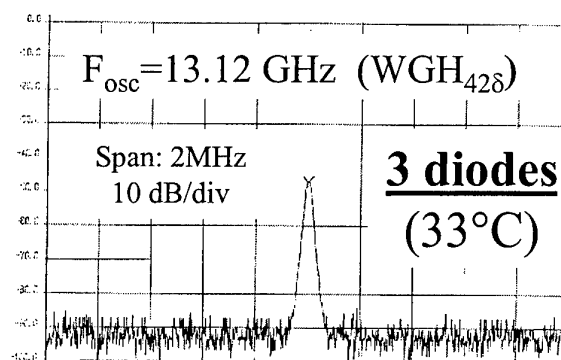


Fig. 7: The WGM resonator oscillator output spectrum measurement.

C- Quasi-optical frequency multiplier

An example of a quasi-optical frequency multiplier is shown in fig.10 with its active grid, polarizers and

dielectric slabs. A 38 GHz/76 GHz multiplier was designed and tested with a Ka band GOLA for the 38 GHz input signal, a W band GOLA for the 76 GHz output signal. A Ka band travelling wave tube amplifier (10W) was also used. The active grid is depicted in fig. 8 and fig. 9.

For this first investigation, 9 diodes were mounted on the array but with so few diodes, the performances are not very attractive. The conversion efficiency is less than -40dB at the 76 GHz output frequency. To explain these poor results, it must be pointed out that the 1.7 cm active area diameter with 9 diodes on the grid is too small in comparison with the 8 cm waist diameter of the input Gaussian beam. So, too little power is intercepted by the active area that is, by the 9 dipole antennas connected to the diodes (see fig. 9). Most of the incident power is not transferred to the active device and the efficiency is very low.

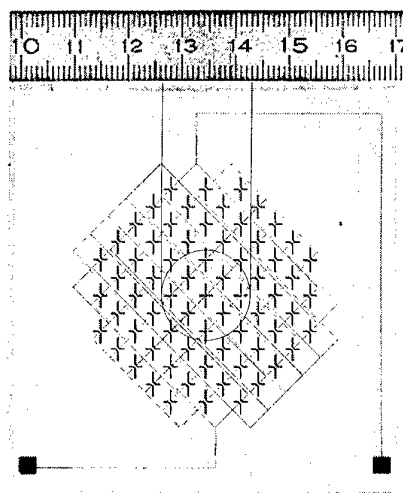


Fig. 8. Photograph of the active grid (dimension in cm).

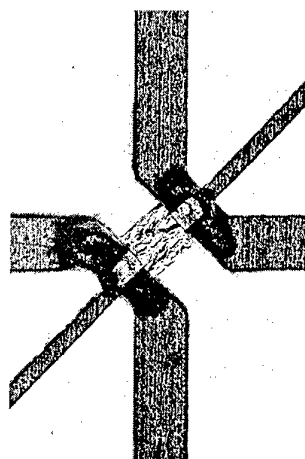


Fig. 9. Detail of the diode connected to dipole antennas.

Non-linear simulations of the whole quasi-optical frequency multiplier were investigated and are still under study. The precise modelling of the component access through the antenna (dipole,...) is very important and rather difficult because it has to take into account all the modes in the structure, the cross-polarisation and the multiple accesses (quasi-optical and active components).

VI. CONCLUSION AND PERSPECTIVES

Power generation at millimeter waves with different techniques and technologies has been presented. Waveguide and planar technology can be used for direct generation with good low noise performance (at lower frequency) or for multiplier with low conversion losses (at high frequency).

Investigations at millimeter waves for spatial or quasi-optical power generation and frequency multiplication have been presented too. This technology is very attractive and promising for combining solid state components, tuning circuits and adding power. At the same time, it introduces new challenges for the

realization and the global simulation of active non-linear functions.

References

- [1] N. Erickson, "THz Frequency Multiplier for FIRST and SOFIA", Proc. of the 2nd ESA Workshop on Millimeter Wave Technology and Applications, May 1998, Espoo, pp. 423-428.
- [2] B. Deschamps, D. Bourreau, A. Peden, S. Toutain "Gunn Diode Modelling through a New Load-Pull Characterization Method", Proc. of the 28th EuMC, Amsterdam 6-8 oct. 98, pp. 328-330
- [3] P. Penfield and R.P. Rafuse, "Varactor Applications", MIT Press, 1962.
- [4] E. Rius et al., "Integration of Various Types of Compensated Dielectric Bridges for Millimeter Coplanar Applications", IEEE MTT Symp. Digest, 1996
- [5] M. Legoff, J.L. Le Bras, B. Deschamps IEEE MTT Symp. Digest, 1996., D. Rozuel, D. Bourreau, A. Peden, "Ka Band Quasi-Optical Test bench using Focusing Horns", Proc. of the 29th EuMC, Munich 5-7 oct. 99, vol. 2, pp 240-243
- [6] J.L. Le Bras, M. Le Goff, B. Deschamps, A. Peden and D. Bourreau, "Quasi-Optical Circuit Measurement Method in the W Band", Proc. of the 2nd ESA Workshop on Millimeter Wave Technology and Applications, May 1998, Espoo, pp. 453-457.
- [7] J.L. Le Bras, M. Le Goff, B. Deschamps, F. Le Pennec, A. Peden, D. Bourreau and S. Toutain, "High Efficiency Planar Frequency Multiplier at Millimetre Waves and Quasi-Optical Investigations for (sub)millimetre Applications", Proc. of the 29th EuMC, Munich 5-7 oct. 99, vol. 2, pp 105-108

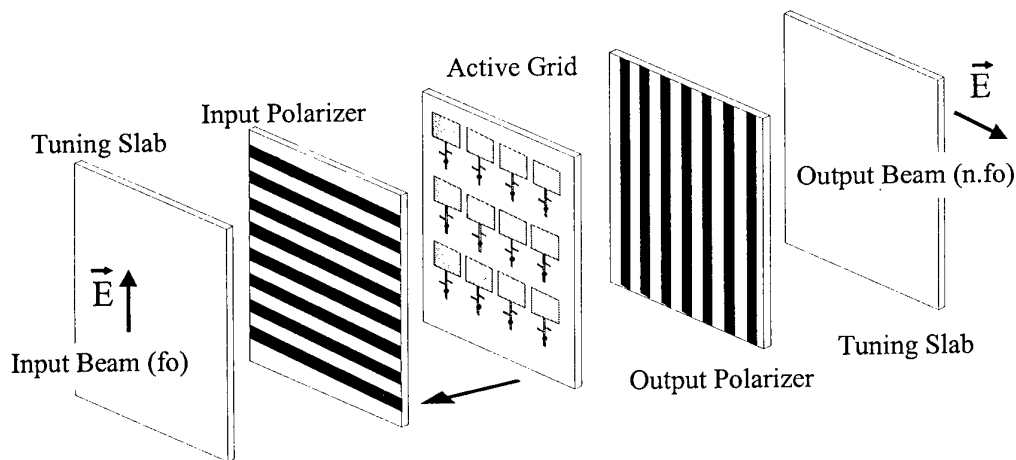


Fig. 10: Quasi-Optical frequency multiplier

Ridged Waveguide Bandpass Filter for Terahertz Applications

George Goussetis and Djuradj Budimir

Abstract – In this paper a CAD procedure for the design of ridged waveguide E-plane filters for THz applications is presented. The transverse resonance technique has been applied for the rigorous analysis of modal propagation in ridged waveguide. Mode matching method has then been used to derive scattering parameters for the discontinuities involved in a ridged waveguide filter. In order to exhibit the performance of the developed CAD, three bandpass filters at 0.270, 0.550 and 1.340 THz have been designed, simulated and presented.

I. INTRODUCTION

The cross-sectional shape of the ridge waveguide is shown in Fig. 1. Firstly proposed in [1], ridge waveguide propagation has been rigorously studied in [2], [3] and is well known to combine the advantages of lower cutoff frequency of the dominant mode, wider bandwidth free from higher modes and low characteristic impedance. Furthermore, the guided wavelength as well as the characteristic impedance in ridged waveguide propagation varies with the ridges height. Therefore, with no particular constructing difficulty, this type of waveguide permits altered propagation characteristics.

Due to these properties, it is believed that the use of sections of ridged waveguide as resonators in an all-metal E-plane filter may optimize its performance in terms of second passband attenuation; all the waveguide sections will be resonant at a single fundamental frequency, but not simultaneously resonant at any higher frequencies, due to different guide wavelengths in the different filter sections [4]. In order to analyze the proposed filter (Fig. 2), a rigorous analysis of the ridged waveguide propagation is necessary, that can calculate the cutoff frequency as well as the field distribution of each mode. Mode-matching technique will then be applied in order to study the ridged waveguide to metal insert discontinuity.

The generalized transverse resonance method, as described in [3] is appropriate for such demands.

II. THEORY

The analysis of the electromagnetic propagation in a ridged waveguide is based on the generalized transverse resonance technique and implementation of field matching. Since the cross-sectional distribution of the field is independent of the frequency [5], we may analyse the field distribution for a waveguide mode at its cutoff frequency, assuming standing waves along the transverse

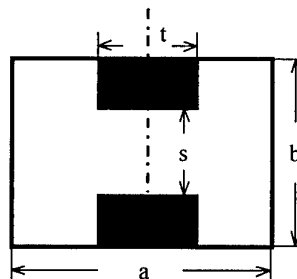


Fig. 1: Cross-section of a ridged waveguide

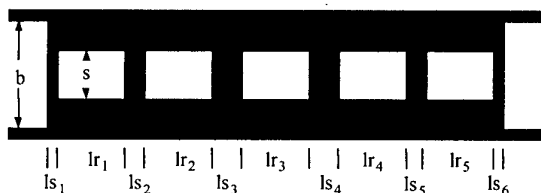
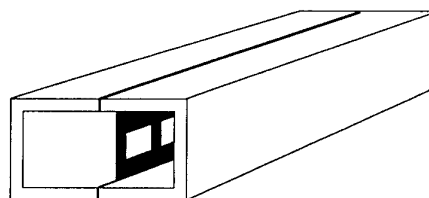


Fig. 2: Ridged waveguide bandpass filter

coordinates and no propagation along the longitudinal axis (transverse resonance). The concept of field matching lies into theoretical division of the cross section under consideration into discrete regions where it will be easy to formulate the x - and y -dependence of the fields. The interface relation (continuity of tangential fields) is then applied. Due to the x -symmetry of the structure, the analysis can be carried out assuming only half of the structure's cross-section. In order to account for all possible cases, along the symmetry plane we should consider both an electric and a magnetic wall [2]. Odd modes however have been proven to be sufficient for the characterisation of the discontinuities under consideration[3].

The authors are with the Wireless Communications Research Group, University of Westminster, London W1M 6JS, UK

Mode Matching Method makes use of the orthogonality of the modal solution of the field distribution.

Tangential fields, expressed in terms of vector potentials [5] are matched in their common surface and using the orthogonality properties, the generalised scattering matrix can be obtained. Even though transmission matrix representation will lead to an easier formulation for the characterisation of cascaded discontinuities, this procedure is potentially unstable due to exponentials with positive arguments. Therefore the scattering matrix representation is used throughout [7].

The design procedure is based on the method proposed by Rhodes [4, 8]. Once the prototype filter has been chosen, the equivalent K-inverter representation with half waveguide wavelength resonators is easily obtained according to [9]. Using the expressions given by Levy [10], the equivalent K value for each septum discontinuity can be obtained from its scattering matrix. Hence the lengths of the metal septa are determined. The resonator lengths are then calculated as half the guide wavelength adding or subtracting the necessary electrical length in order to ensure the K-inverter behaviour of the septa [10].

III. RESULTS

In order to demonstrate the performance of the presented CAD, three ridged waveguide filters have been designed. 20 TE and 20 TM modes were used for the design of each one, which lasted less than one minute on a Pentium Pro with 96MB RAM.

IV. CONCLUSION

An efficient CAD procedure for the design of ridged waveguide filters for THz applications has been presented. The efficiency of the procedure has been exhibited by designing three filters at 270, 550 and 1340 GHz.

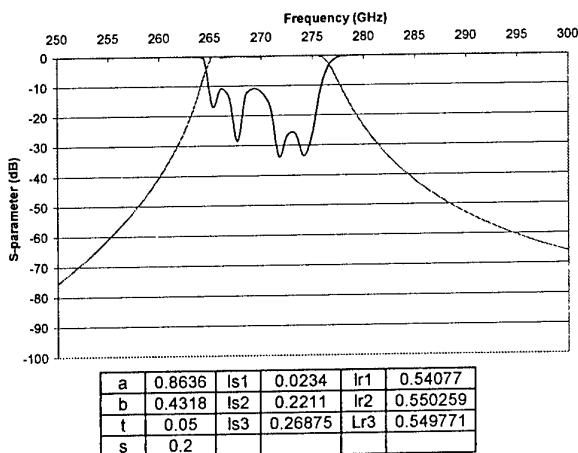


Fig. 3: Dimensions and performance of 270GHz bandpass filter

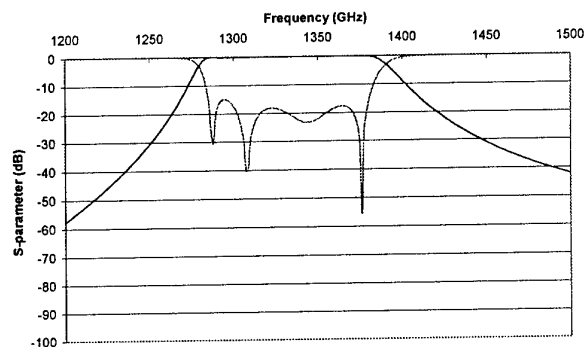
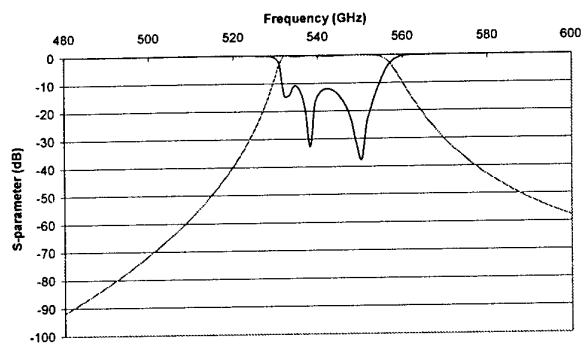


Fig. 4: Dimensions and performance of 550 and 1340 GHz ridged waveguide bandpass filters

Acknowledgement

This work was supported by the Engineering and Physical Sciences Research Council by means of a research grant (GR/K58634), UK

References

1. S. B Cohn., "Properties of Ridge Wave Guide", Proc IRE, Vol 35, August 1947, pp.783-788
2. J.P. Montgomery, "On the complete eigenvalue solution of ridged waveguide", IEEE Trans. Microwave Theory and Techniques, MTT-19, 457-555 (1971)
3. J. Bornemann, "Comparison between different formulations of the Transverse Resonance Field-Matching Technique for the three-dimensional analysis of metal-finned waveguide resonators", International Journal of Numerical Networks, Devices and Fields, Vol. 4, 63-73 (1991)
4. D. Budimir, Generalized Filter Design by Computer Optimization, Artech House, 1998
5. W. J. Getsinger, "Ridge Waveguide Field Description and Application to Directional Couplers", IRE Trans. On Microwave Theory and Techniques, MTT-10, p. 42-50 (1962)

6. R. E Collin., Field Theory of Guided Waves, IEEE Press, 1990
7. Uher, Bornemann, Rosenberg, "Waveguide Components for Antenna Feed Systems: Theory and CAD", Artech House, 1993
8. J.D. Rhodes, "Microwave circuit realizations", in *Microwave Solid State Devices and Applications*, D.V. Morgan and M.J. Howes, Eds. England: Peregrinus, 1980, pp.49-57
9. G. Matthaei, L. Young, E.M.T. Jones, Microwave Filters, Impedance Matching Networks and Coupling Structures, Artech House, Dedham, MA 1980
10. R. Levy, "The Generalized Design Technique for Practical Distributed Reciprocal Ladder Networks", IEEE Transactions Microwave Theory and Techniques, vol. MTT-21, pp. 1-15, 1987

Slot-Antenna Coupled Microbolometer Arrays for THz Radiation

Yoshizumi Yasuoka, Yukihiro Hiraga, and Yasuhiko Abe

Abstract – New type of slot antenna coupled microbolometer arrays were fabricated, and the receiving properties for 2.5THz-CH₃OH laser radiation were investigated at room temperature. The detected voltage of the device increased in proportion to the number of slots, but the receiving pattern was independent of the number of slots when the slots in the device were arranged with a space of $0.5\lambda_d$ (λ_d : dielectric wavelength).

I. INTRODUCTION

Recently, the millimeter and submillimeter wave frequency regions have attracted considerable attention as the remaining frequency resource for applications such as communications and remote sensing, and much research has been done to develop electronic devices for realizing these applications. A microbolometer is one of the notable candidates for electronic devices to use in the far-infrared frequency region, because of its room-temperature operation and easy fabrication [1-3].

A conventional bolometer has been used as a thermal detector for infrared radiation, making use of the change of bolometer resistance with an increase in its temperature by absorbing the irradiation power directly or by absorbing the heat power from the radiation absorbers [4]. Therefore, the detection properties strongly depend on the receiving area of the bolometer (size of the bolometer) and the heat capacity of the bolometer including the radiation absorbers. An increase in the size of the bolometer introduces a decrease of the responsivity of the bolometer [5]. The routes of the power absorbed by the antenna coupled microbolometer are different from those of the conventional one. In the case of the antenna coupled microbolometer [1], the irradiation power received by the antenna, then the induced current on the antenna passes through the microbolometer, and finally the resistance of the bolometer changes with the Joule heating. Then, the responsivity of the antenna coupled microbolometer depends on the effective aperture (gain) of the antenna, and is independent of the size of the bolometer (different from the conventional bolometer). In the previous paper, we fabricated a bow-tie antenna coupled microbolometer and receiving properties were investigated at 2.5THz [5]. However, the responsivity was still low.

One of the ways to improve the detection properties of the device is to increase the effective aperture of the antenna by making the antenna array. In this paper, we fabricate a new type of array-coupled with a microbolometer, which is called an antenna-coupled microbolometer array, and investigate the detection

properties at 2.5THz. In the new device, each antenna has a microbolometer (for example, the five-antenna coupled microbolometer array has five antennas and five microbolometers), and each bolometer is connected in series.

II. CONFIGURATION OF THE SLOT ANTENNA COUPLED MICROBOLOMETER

One of the planar antennas for an antenna coupled microbolometer in the submillimeter wave region is the slot antenna. This slot antenna has a simple configuration and is suitable for microfabrication. Since the radiation is in the direction normal to the substrate, the antenna is suitable for antenna arrays. In addition, since a large ground plane exists, the use of electron beam lithography is possible for fabrication of a microbolometer on the antenna. Figure 1 (a) shows the configuration of the single slot antenna coupled microbolometer. The microbolometer is placed in the center of the slot which is the feeding point. DC cuts (narrow slit lines) are made on the ground plane for supplying DC bias and DC output terminals. Figure 1(b) shows the configuration of the slot-antenna coupled microbolometer array. By placing each bolometer in series, we anticipated that the detected voltage would increase in proportion to the number of slots.

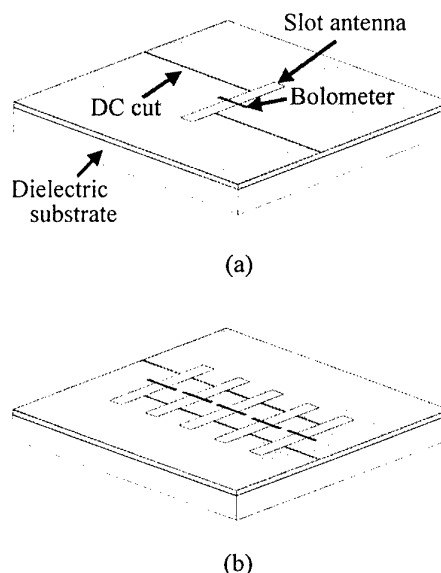


Fig.1 Structure of the slot antenna coupled microbolometer.

Figure 2 shows the configuration and equivalent circuits of the slot antenna coupled microbolometer array. When the millimeter or submillimeter wave is irradiated

Y. Yasuoka, Y. Hiraga and, Y. Abe are with Department of Electronic Engineering, National Defense Academy, Yokosuka 239-8686, Japan (E-mail: yasuoka@cc.nda.ac.jp).

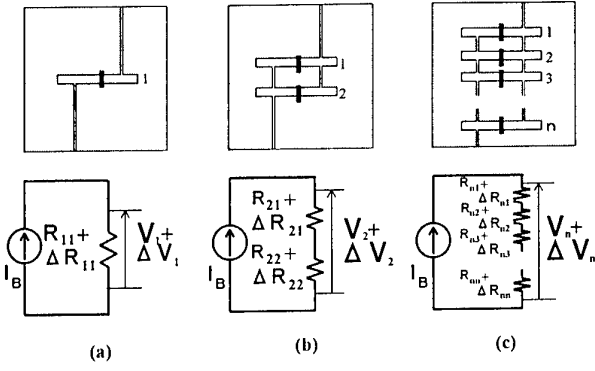


Fig.2 Configuration and equivalent circuits of the slot antenna coupled microbolometer array.

to a single slot antenna coupled microbolometer as shown in fig. 2(a), the power received by the antenna is supplied to the bolometer, and the resistance (R_{11}) of the bolometer changes into $R_{11} + \Delta R_{11}$. The voltage (V_1), which is generated by the (I_B), of the bolometer changes into $V_1 + \Delta V_1$. The detected voltage is shown by

$$\Delta V_1 = I_B \cdot \Delta R_{11} = I_B \cdot \frac{dR}{dT} \cdot \frac{dT}{dP} \cdot P_{11} \quad (1)$$

where dR/dT is the slope of resistance as a function of temperature, and dT/dP is the thermal resistance. Both depend on the material and shape of the microbolometer. P_{11} is the power supplied to the microbolometer from the antenna. In the case of a two slot antenna coupled microbolometers placed in series as shown in Fig. 2(b), the detected voltage (ΔV_2) is written as follows,

$$\Delta V_2 = I_B \cdot (\Delta R_{21} + \Delta R_{22}) \quad (2)$$

If the bolometer's characteristics are the same for each slot, then equation(2) leads to

$$\Delta V_2 = I_B \cdot \frac{dR}{dT} \cdot \frac{dT}{dP} \cdot (P_{21} + P_{22}) \quad (3)$$

and the detected voltage of the slot antenna coupled microbolometer n -array as shown in Fig. 2(c) is written as

$$\begin{aligned} \Delta V_n &= I_B \cdot (\Delta R_{n1} + \Delta R_{n2} + \dots + \Delta R_{nn}) \\ &= I_B \cdot \frac{dR}{dT} \cdot \frac{dT}{dP} \cdot (P_{n1} + P_{n2} + \dots + P_{nn}) \end{aligned} \quad (4)$$

The power $P_{n1} \sim P_{nn}$ supplied to each bolometer in equation (4) are generally dependent on each antenna gain. Each antenna's gain is affected by the reciprocity of other antennas in the array, so there is the possibility that each antenna's gain can become a different value. Therefore, it is necessary to investigate the receiving properties of the slot antenna array, such as its receiving pattern and antenna gain, when we fabricate the slot antenna coupled microbolometer arrays.

III. EXPERIMENTS IN THE MICROWAVE REGION

In order to see the interaction between the slots in a slot antenna coupled microbolometer array, the antenna pattern and the power gain were observed as functions of the space between the slots and the number of slots. The experiments were carried out at 4.7GHz. Each slot array

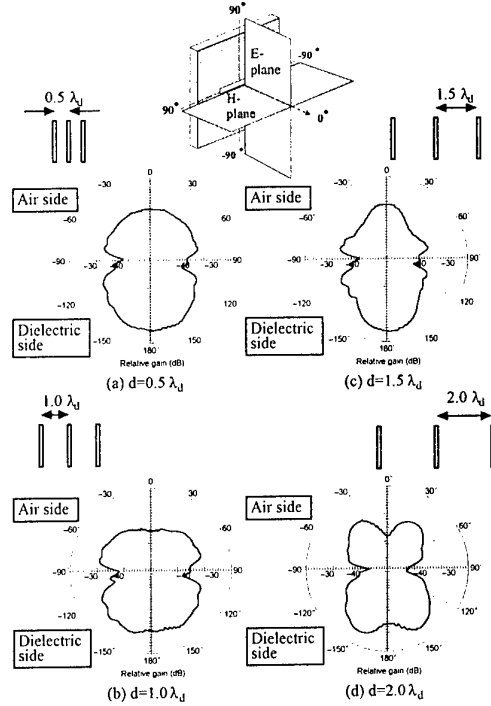


Fig.3 The receiving patterns of the three-slot array at 4.7GHz. The separation of the slots "d" was changed.

element was connected by semi-rigid cable, and the receiving signal was measured using this cable. The relative dielectric constant of the substrate was $\epsilon_r = 4.5$. The length and width of the slots were 0.72 and $0.08\lambda_m$, respectively, in order to operate as a one wavelength slot antenna with impedance 50Ω [6], where λ_m is the mean wavelength [7] shown by $\lambda_m = \lambda_0 / \{(\epsilon_r + 1)/2\}^{1/2}$ in terms of the free space wavelength λ_0 . Each slot was loaded with a resistance of 50Ω instead of the bolometer.

Figure 3 shows the E-plane pattern of the three-slot array for 4.7GHz radiation. The patterns are the sum of the measurements obtained by three slots. The distance between the slots (d) was changed from $0.5\lambda_d$ to $2.0\lambda_d$ by $0.5\lambda_d$ step, where λ_d is the wavelength in the dielectric substrate given by $\lambda_d = \lambda_0 / \epsilon_r^{1/2}$. Figure 3 shows that the antenna pattern obtained from the three-slot array was received by the different interactions from the space between the slots. The antenna patterns shown in figs. 3(a) and (c) are more suitable for our purpose than the ones shown in figs. 3(b) and (d), because the antenna patterns shown in figs. 3(b) and (d) have a dent in the direction perpendicular to the substrate. Figures 3(a) and (c) show that the three-slot array arranged with a space of $1.5\lambda_d$ has a receiving power 1dB higher than that of the three-slot array arranged with a space of $0.5\lambda_d$ at a perpendicular angle to the substrate. However, if we rearrange the slots with a space of $0.5\lambda_d$ using the same area as the three-slot array arranged with a space of $1.5\lambda_d$, then we can include seven slots in the same space. The seven slot array arranged with a space of $0.5\lambda_d$ has a receiving power 3dB higher than that of the three-slot array arranged with a space of $1.5\lambda_d$. These facts show that the suitable space between the slots for our purpose is $0.5\lambda_d$.

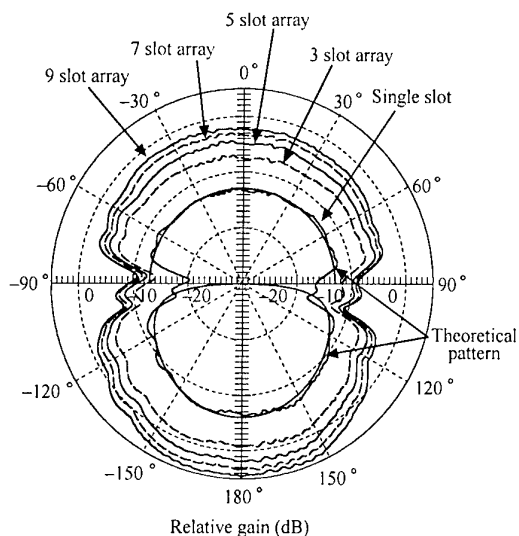


Fig.4 E-plane patterns of slot array at 4.7GHz.

Figure 4 shows E-plane patterns of the single slot and n-slot arrays ($n=1, 2, 3, 4, 5, 6, 7, 8$ and 9) arranged with a space of $0.5\lambda_d$. In the figure, the theoretical pattern of a single slot antenna is also shown for comparison. From this figure, it became clear that the receiving power increased with an increase in the number of slots, however the pattern is independent of the number of slot as long as the slots are arranged with a space of $0.5\lambda_d$.

IV. RECEIVING PROPERTIES OF THE SLOT ANTENNA COUPLED MICROBOLMETER ARRAYS

The slot antenna coupled microbolometers were fabricated using microfabrication techniques. The fabrication process is shown in fig. 5. Following completion of the fabrication process, Cr and Au were evaporated on the fused quartz substrate [(a),(b)], and positive electron beam resist was spin-coated on the substrate (c). The shape of the antennas was formed using an electron beam lithographic method (d). The areas of the Au and Cr film not covered with the resist were removed by dry etching (e). Removing the resist completed the antenna part of the process [(f), (g)]. The shape of the bolometer was formed using a photolithographic method [(h), (i)]. Then Bi, which is the material of the bolometer, was evaporated on this resist (j). Finally, the resist was lifted-off to complete the slot antenna coupled microbolometer array (k). Figure 6 shows the SEM photograph of the fabricated 15-slot antenna coupled microbolometer array detector for 2.5THz-CH₃OH laser radiation. The length and width of the slots are 85μm and 10μm.

Figure 7 shows the schematic diagram of the measuring system at 2.5THz. The fabricated slot antenna coupled microbolometer array was placed on a rotating stage, and the bolometer was biased with a current source. A CH₃OH laser was used as a 2.5THz submillimeter wave source. The laser beam was mechanically chopped at 1KHz and radiated to the slot antenna coupled microbolometer array. The detected voltage of the slot antenna coupled microbolometer array was measured with a lock-in amplifier by changing the angle of

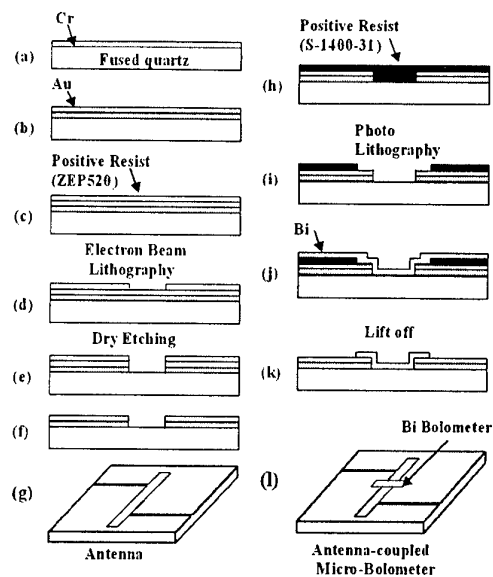


Fig.5 Fabrication process.

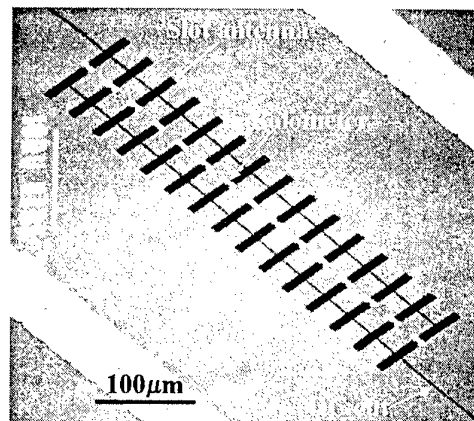


Fig.6 SEM photograph of the fabricated slot antenna coupled microbolometer array for 2.5THz-CH₃OH laser radiation.

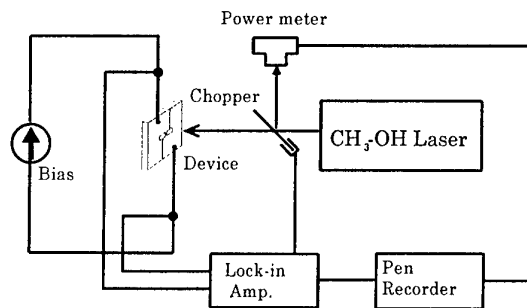


Fig.7 Measurement system for 2.5THz-CH₃OH laser radiation.

incidence.

Figure 8 shows the receiving patterns of the seven-slot antenna coupled microbolometer array using 2.5THz-CH₃OH laser radiation. The laser beam was irradiated from the air side. The symbols ● and ○ show the E- and H-plane experimental patterns, and the broken and the solid curves show the E- and H-plane theoretical antenna patterns of a single slot antenna. The experimental data of the seven-slot antenna coupled microbolometer array

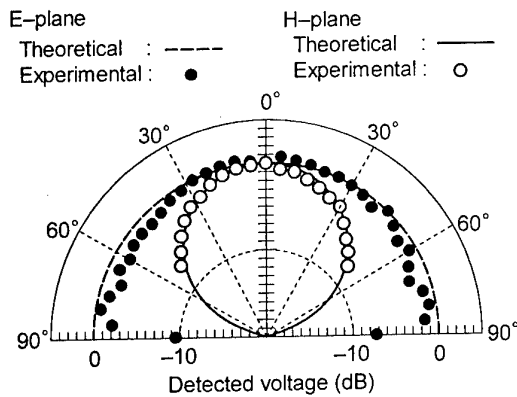


Fig.8 Receiving pattern of the seven-slot antenna coupled microbolometer array, when irradiating a 2.5THz-CH₃OH laser radiation from the air side.

agree with the theoretical antenna pattern of the single slot antenna. From fig. 8, it is found that the receiving patterns of the slot antenna coupled microbolometer array are independent of the number of slots, and are the same as the receiving antenna patterns of the single slot antenna as expected from the results obtained at the microwave band.

The relationship between the number of slots and the detected voltage of the one-dimensional slot antenna arrays is shown by the symbol ● in Fig. 9. The detected voltages increased in proportion to the number of slots. In the figure, the detected voltages of a two-dimensional 5 × 3 slot antenna coupled microbolometer array and a two-dimensional 6 × 3 slot antenna coupled microbolometer array are shown by the symbol △. Figure 9 shows that the detected voltage increases in proportion to the number to slots regardless of the dimension of the arrangement.

V. CONCLUSION

In order to improve the detection sensitivity of far-infrared radiation detectors, a new type of slot antenna coupled microbolometer arrays was fabricated. The antenna and detection properties were investigated at 4.7GHz and 2.5THz, and the following results were obtained:

- (1) The optimum distance between the slots in the slot antenna coupled microbolometer array is $0.5\lambda_d$ (λ_d : dielectric wavelength).
- (2) The detected voltage of the slot antenna coupled microbolometer array increased in proportion to the number of slots.

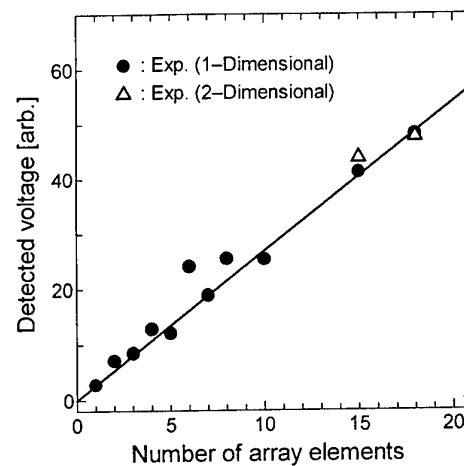


Fig.9 Relationship between number of slots and the detected voltage of the slot antenna coupled microbolometer arrays at 2.5THz.

- (3) The receiving pattern of the slot antenna coupled microbolometer array was the same as the antenna pattern of the single slot antenna, and independent of the number of slots.

References

1. T. L. Hwang, S. E. Schwarz, and D. B. Rutledge, "Microbolometers for Infrared Detection," *Appl. Phys. Lett.*, Vol. 34, pp.773-776, Jun.1979.
2. D. F. Filipovic, W. Y. Ali-Ahmad, and G. M. Rebeiz, "Millimeter-Wave Double Dipole Antennas for High-Gain Integrated Reflector Illumination," *IEEE Trans. Microwave Theory Tech.*, Vol. 40, No. 5, pp.962-967, May 1992.
3. S. M. Wentworth and D. P. Neikirk, "Composite Microbolometers with Tellurium Detector Elements," *IEEE Trans. Microwave Theory Tech.*, Vol. 40, No. 2, pp.196-201, Feb.1992.
4. P. W. Kruse, L. D. McGlauchlin and R. B. McQuistan, *Elements of Infrared Technology*. New York: John Wiley & Sons, 1962, pp.345.
5. T.Shimizu, H.Moritsu, Y.Yasuoka, and K.Gamo, "Fabrication of Antenna-Coupled Microbolometers," *Jpn. J. Appl. Phys.*, Vol. 34, No. 12A, pp.6352-6357, Dec.1995.
6. T.Shimizu, Y.Abe, and Y.Yasuoka, "Thin-Film Slot Antenna for 700 GHz Submillimeter Wave Radiation," *IEICE Trans. Electron.*, Vol.E78-C, No. 8, pp.1002-1006, Aug.1995.
7. M. Kominami, D. M. Pozar, and D. H. Schaubert, "Dipole and Slot Elements and Arrays on Semi-Infinite Substrates," *IEEE Trans. Antennas Propag.*, Vol. 33, No. 6, pp.600-607, Jun.1985.

Spatial pattern formation of optically excited carriers in photoconductive THz antennas

M. Bieler, G. Hein, K. Pierz, U. Siegner, M. Koch, M. W. Feise, D. S. Citrin

Abstract—

We have investigated the role of spatio-temporal carrier dynamics in photoconductive THz antennas. To this end, the photoluminescence from a GaAs/AlGaAs quantum well has been spatially resolved after femtosecond laser excitation for different electric bias fields applied in the plane of the well. The photoluminescence patterns demonstrate substantially different electron-hole dynamics across the excitation laser spot. The density dependence of screening combines with the lateral variation of the carrier density to produce the observed effects. The experimental data are compared to a self-consistent calculation of the drift-diffusion equation for electrons and holes and Poisson's equation for the electric field in both space and time. Our results prove that the spatial variation of the carrier dynamics should be taken into account for further optimization of THz antennas.

I. INTRODUCTION

Photoconductive dipole antennas are widely used to generate pulsed THz radiation [1]. These semiconductor antennas basically consist of a piece of semiconductor onto which coplanar metallic microstriplines are deposited. An ultrashort laser pulse injects carriers into the semiconductor gap between the metallic electrodes. An applied bias field accelerates electrons and holes towards the electrodes. The resulting photocurrent gives rise to the emission of a THz pulse.

Considerable experimental effort has been made to optimize photoconductive dipole antennas for THz power and bandwidth [2]. Moreover, the temporal evolution of the photocurrent was numerically modeled by a Drude-Lorentz approach [3]. Although this model describes the experimental results quite well, one fundamental problem has not been addressed so far, namely the *spatio*-temporal dynamics of the optically created carriers. It is obvious that the field-induced motion of all optically excited electrons and holes determines the shape of the current pulse and thus the THz bandwidth.

The carrier motion is determined by the local field which, in turn, is constantly modified by screening resulting from the carrier displacement. Due to the non-uniformity of the Gaussian excitation spot, we can expect different carrier dynamics in its center and at its edges. Since the carrier density is lower at the edges, electrons and holes have to separate further in order to screen the bias field. As these carriers have to move a larger distance, it can be

expected that their contribution to the total current persists for a longer time as compared to the current contribution resulting from the carriers in the center of

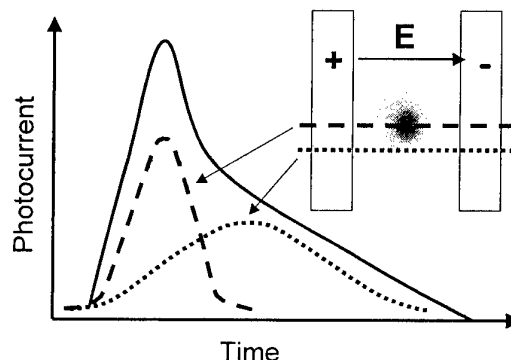


Fig. 1: Schematic of the photocurrent pulse.

the excitation spot (see schematic drawing in Fig. 1). The shape of the current pulse is given by the integral of all partial currents.

In this paper, we address the complex problem of the spatio-temporal pattern formation in an optically excited photoconductive THz antenna. We have performed temporally integrated but spatially resolved luminescence experiments on a biased semiconductor. The results are compared to numerical solutions of the drift-diffusion equation. The comparison confirms that the carrier dynamics spatially varies over the excitation spot and yields first quantitative information on the spatio-temporal carrier dynamics.

II. EXPERIMENT

The sample consists of 30 GaAs/AlGaAs quantum wells with a thickness of 12 nm. It is excited with 150 fs Ti:sapphire laser pulses at 800 nm. The full width at half maximum of the focused laser spot, which is centered between two Ni-Au/Ge-Ni electrodes (see inset of Fig. 2), is approximately 25 μm . The luminescence, which peaks at 860 nm, is imaged onto a two dimensional charged coupled device (CCD). In front of the CCD camera an interference filter is introduced to suppress reflected pump light. The spatial resolution of our setup is close to the diffraction limit. All experiments are carried out at room temperature.

Without field, we observe a Gaussian luminescence spot following the Gaussian intensity profile of the laser beam. When an electric field is applied, the overall luminescence intensity drops [4], the luminescence profile becomes narrower and the position of the peak is slightly displaced towards the anode [5]. These effects result from the motion of the electrons towards the anode

M. Bieler, G. Hein, K. Pierz and U. Siegner are with the Physikalisch-Technische Bundesanstalt, Bundesallee 100, D-38116 Braunschweig, Germany

M. Koch is with the Institut für Hochfrequenztechnik, Technische Universität Braunschweig, Schleinitzstrasse 22, D-38106 Braunschweig, Germany

M. W. Feise and D. S. Citrin are with the Department of Physics, Washington State University, Pullman, WA 99164, USA

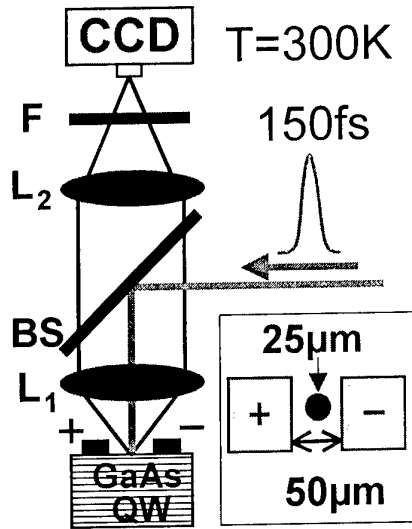


Fig. 2: Experimental setup. BS: beam splitter; F: interference filter; L1, L2: lenses; CCD: charged coupled device. The inset shows the ohmic Ni-Au/Ge-Ni contacts.

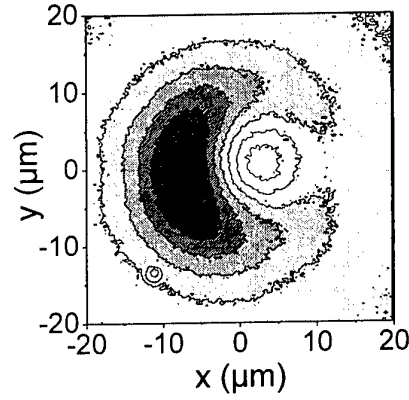


Fig. 3: Normalized luminescence without field minus normalized luminescence with field (differential luminescence) shown as a contour plot. The bias field is 4 kV/cm and the spatially averaged carrier density is about $7 \times 10^{11} \text{ cm}^{-2}$.

while the holes hardly move. The effect of the field induced carrier motion is visualized most clearly when plotting the normalized luminescence pattern with electric field subtracted from the normalized luminescence pattern without field. This “differential luminescence” pattern is shown in Fig. 3 for a bias field of 4 kV/cm and a spatially averaged carrier density of $7 \times 10^{11} \text{ cm}^{-2}$. The field is applied in x-direction and the anode is on the right-hand side. The center of the excitation laser spot is at (0,0). Dark colors mark a strong field-induced reduction of the luminescence (white: enhancement of the normalized luminescence). Zero is indicated by the grey tone in the lower left corner of the contour plots.

In all experiments, even with lower excitation densities, we observe a characteristic crescent-shaped pattern. When increasing the electric field from 1 to 4 kV/cm the crescent becomes more pronounced and almost encircles the white region. From a comparison with simple analytical expressions [5], we conclude that different carrier dynamics occur in the center and at the edges of the excitation spot. The carrier density dependence of screening is at the origin of this result [5]. In the following we present more elaborate numerical calculations.

III. CALCULATION

We describe the motion of the charge carriers in the framework of the drift-diffusion model [6]. The carriers are represented as 2-dimensional densities of electrons and holes located in a single GaAs quantum well. Scattering processes and the band structure of the material are approximated by an effective mobility and diffusion coefficient. The equation of motion for the charge carriers reads:

$$\frac{\partial f_{h,e}}{\partial t} = D_{h,e} \nabla_{x,y}^2 f_{h,e} \mp \mu_{h,e} \nabla_{x,y} \cdot (f_{h,e} \vec{E}) + \frac{(G-R)}{e}$$

Here f is the particle density, D the diffusion coefficient, μ the carrier mobility, and e the elementary charge. Moreover, E is the local electric field that consists of the uniform external field and the screening field. The latter is self-consistently determined through Poisson's equation. G is the position and time dependent generation term that describes the electron-hole pair creation by the laser pulse. The band-band recombination of electrons and holes is given by $R = r f_h f_e$ where r is the recombination coefficient. This recombination term leads to a non-exponential decay of the charge carriers and does not allow the definition of a constant recombination time [7].

We solve the equation using a finite difference technique [8]. The motion of the charges is constrained to the plane of the quantum well whereas the electric field is calculated in three dimensions. We assume the following boundary conditions: (i) No charge carriers are injected into the quantum well by the applied voltage. (ii) Carriers in the quantum well can enter the electrodes and then no longer contribute to screening of the external field. (iii) In the direction normal to the external field, where no electrodes provide a boundary for the carriers, we extend the computational region far enough to ensure that the numerical boundaries have only negligible influence on the results.

To solve Poisson's equation, one can first treat the direction normal to the quantum well analytically and then solve for the potential in the plane of the quantum well self-consistently at each time step. The electrodes are assumed to be held at a constant potential. In this approach, the voltage change induced by the moving free charges in the quantum well is compensated by the voltage source. In the in-plane direction normal to the external field, we extend the calculation until the

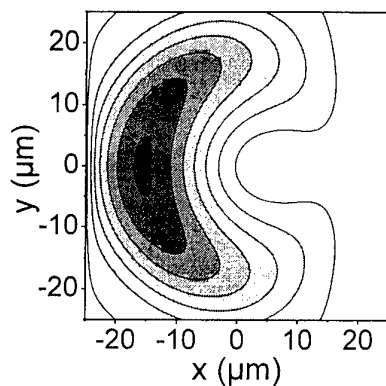


Fig. 4: Calculated differential luminescence for a bias field of 4 kV/cm and a carrier density of $3 \times 10^{11} \text{ cm}^{-2}$. The integration time and the recombination coefficient are 24 ns and $5 \times 10^{-3} \text{ cm}^2/\text{Vs}$, respectively. The electron and hole mobilities are $100 \text{ cm}^2/\text{Vs}$ and $5 \text{ cm}^2/\text{Vs}$, respectively. Temperature 300 K.

potential is close to the value of the potential with no net charge in the computational region.

Figure 4 shows the calculated differential luminescence for parameters comparable to the experiment; see caption for details. The characteristic crescent-shaped pattern is well reproduced by the drift-diffusion model.

IV. CONCLUSION

In summary, we have performed luminescence experiments on a photoconductive THz antenna. The experimental results demonstrate different carrier dynamics at the center and the edges of the excitation spot. The results are in qualitative agreement with first numerical calculations based on the drift-diffusion equation. The comparison between experiment and

theory can provide quantitative information on carrier dynamics. This information provides the basis for the further optimization of photoconductive THz antennas taking into account spatial effects.

Acknowledgement

The authors would like to thank E. O. Göbel for many fruitful discussions and H. Lecher and H. Marx for expert technical assistance.

References

1. X.-C. Zhang and D. H. Auston, "Optically induced THz electromagnetic radiation from planar photoconducting structures", *J. Electron. Wave Appl.*, Vol. 6, pp 85-106, 1988
2. Y. Cai, I. Brener, J. Lopata, J. Wynn, L. Pfeiffer and J. Federici, "Design and performance of singular electric field terahertz photoconducting antennas", *Appl. Phys. Lett.*, Vol. 71, pp 2076-2078, 1997
3. P. Uhd Jepsen, R. H. Jacobsen and S. R. Keiding, "Generation and detection of terahertz pulses from biased semiconductor antennas", *J. Opt. Soc. Am. B*, Vol. 13, pp 2424-2436, 1996
4. M. Koch, M. Bieler, G. Hein, K. Pierz and U. Siegner, "Photoconductive Switches: The Role of Spatial Effects in Carrier Dynamics", *phys. stat. sol.*, in press
5. M. Bieler, G. Hein, K. Pierz, U. Siegner and M. Koch, "Spatial pattern formation of optically excited carriers in photoconductive switches", *Appl. Phys. Lett.*, in press
6. S. M. Sze, "Physics of Semiconductor Devices", John Wiley & Sons, New York, 1981
7. Bimolecular recombination was experimentally verified.
8. W. H. Press, B. P. Flannery, S. A. Teukolsky and W. T. Vetterling, "Numerical Recipes: The Art of Scientific Computing", Cambridge University Press, Cambridge, 1989

Temperature Dependence of Low Energy Carrier Dynamics of Silicon by Terahertz Time Domain Spectroscopy

Shigeki Nashima, Osamu Morikawa, Kazue Takata, Masanori Hangyo,

Abstract – The complex conductivity of moderately P-doped silicon wafers ($1.1 \pm 0.2 \Omega\text{cm}$) at various temperatures has been deduced by using a terahertz time-domain (THz-TDS) spectroscopy. The characteristic dispersion of the complex conductivity is observed in the THz region. Temperature dependence of the complex conductivity changes dramatically around ~ 120 K, which is interpreted in terms of enhancement of mobility and the freezing of the carrier. The experimental data at low temperatures slightly deviates from the simple Drude model, which causes the underestimation of the mobility and overestimation of the carrier density.

I. INTRODUCTION

It is well known that the optical properties of semiconductors from microwave to infrared regions are greatly influenced by the dynamics of free carriers of semiconductors[1]-[6]. Dispersion of the complex conductivity ($\sigma_1 - i\sigma_2$) depends on the carrier density and scattering time, which is explained by the simple Drude model. Such a model conversely provides a simple method of calculating optical constants in the far infrared region from the carrier density and mobility. However, the optical properties in this region at low temperatures have not been discussed so much before. The terahertz time-domain spectroscopy (THz-TDS) is used to measure the complex conductivity of samples at THz frequencies without the need of the Kramers-Kronig transformation[6]. In this letter, the complex conductivity of a moderately doped silicon wafer is deduced at various temperatures by using the THz-TDS. We obtain the carrier density and mobility of the sample at low temperatures and compare them with the results obtained from the Hall measurement and four-point contact resistivity.

II. EXPERIMENTAL

An *n*-type silicon wafer doped with phosphorus was used as a sample in this study. The resistivity at room temperature and the thickness of the sample were $1.1(\pm 0.2) \Omega\text{cm}$ and $400 \mu\text{m}$, respectively. A conventional THz-TDS system was used wherein the pump and the trigger beams were derived from a mode-locked Ti:sapphire laser which produces optical pulses with a

width of 50 fs and a wavelength of 790 nm at a repetition rate of 82 MHz[4][5]. The sample was mounted on a sample holder of a closed-cycle He refrigerator specially designed to avoid mechanical vibrations and was inserted between a set of paraboloidal mirrors. In this measurement, a 5- μm gap bowtie-type photoconductive antenna was used as a THz emitter and detector. The frequency range of this system was limited by the absorption property of a 3-mm-thick fused quartz windows of the He refrigerator and was estimated to be less than 1.5 THz.

III. RESULTS AND DISCUSSION

We calculate the complex refractive index \tilde{n} from experimental transmittance and phase shift obtained by the Fourier transformation of the THz pulse waveforms before and after inserting the sample. The complex conductivity is obtained from the complex refractive index from the relation,

$$\tilde{n}^2 = \tilde{\epsilon}(\omega) = \epsilon_{\text{Si}} + i\tilde{\sigma}(\omega)/\omega\epsilon_0, \quad (1)$$

where $\tilde{\epsilon}(\epsilon_1 - i\epsilon_2)$ is the complex dielectric constant, ϵ_{Si} is the dielectric constant of undoped silicon and ϵ_0 is the free-space permittivity. We used the expression $\epsilon_{\text{Si}} = (3.415)^2$ [1]. Frequency dependence of the complex conductivity of the sample at 300 K, 120 K, 70 K, and 16 K is shown in Figs. 2(a)-(d), respectively. At room temperature the value of σ_1 decreases monotonically with increasing frequency. The value of σ_2 at room temperature increases from zero with increasing frequency until ~ 0.6 THz and decreases monotonically with increasing frequency further. At 0.6 THz, a crossover of the two curves is observed. Frequency dependence of the complex conductivity becomes pronounced with decreasing temperature until ~ 120 K. The value of σ_1 in the low frequency region increases and that in the high frequency region decreases with decreasing temperature. The temperature dependence of σ_2 also becomes pronounced with decreasing temperature. The crossover point of the two curves shifts to the lower frequency region with decreasing temperature. The dispersion of the complex conductivity decreases rapidly with decreasing temperature below 120 K and the values of σ_1 and σ_2 at 16 K are almost zero over the entire frequency region.

S. Nashima, O. Morikawa, K. Takata, M. Hangyo are with Reserch Center for Superconductor Photonics, Osaka University, 2-1 Yamadaoka, Suita, Osaka 565-0871, Japan

Solid lines in Fig. 1 show the fitting curves to σ_1 and σ_2 at each temperature using the simple Drude model. According to the simple Drude model, in which the collision damping is independent of the carrier energy, the frequency-dependent complex conductivity in SI units is given by

$$\tilde{\sigma} = i\epsilon_0\omega_p^2 / (\omega + i\Gamma), \quad (2)$$

where $\Gamma=1/\tau$ is the carrier damping rate and τ is the average collision time. The plasma frequency ω_p is defined by $\omega_p^2 = N_c e^2 / \epsilon_0 m^*$, where N_c is the number density of carriers, e is the electronic charge and m^* is the effective carrier mass. The expression $m^*=0.26 m_0$ is also used, where m_0 is the free-electron mass[7]. Our fitting procedure effectively optimizes the values of N_c and τ , from which the mobility μ given by $\mu = e\tau/m^*$ is determined. The two parameters are determined by fitting the complex conductivity data between 0.2 and 1 THz.

Figure 2 (a) shows the temperature dependence of the mobility obtained from the fitting (open circles). Solid and dashed lines show the data obtained from previous Hall measurements on two samples with smaller and larger resistivities ($\rho=0.66 \Omega\text{cm}$, $4.76 \Omega\text{cm}$) than the present sample, respectively[8]. Error bars show the uncertainties associated with temperature. At room temperature the value of μ and ρ ($=1/\sigma(0)$) is estimated to be $1560 \text{ cm}^2/\text{Vs}$ and $1.06 \Omega\text{cm}$ for the present sample, respectively, which agree on the whole with that obtained by Hall measurement and four-point contact resistivity measurement[9]. The value of μ increases dramatically with decreasing temperature until 150 K. The increasing rate gradually decreases with decreasing temperature. However, the value of μ obtained by the simple Drude fit at various temperatures is a little smaller than that of the silicon with lower resistivity obtained from the Hall measurement.

Figure 2 (b) displays the temperature dependence of the carrier density (open circles) of the sample obtained from the simple Drude fit. According to the Fermi-Dirac distribution, the carrier density of moderately doped silicon at various temperatures satisfies the following equation,

$$\frac{N_c^2}{N_D - N_c} = N_v \cdot \left(\frac{2\pi m_n k_B T}{h^2} \right)^{3/2} \exp\left(-\frac{\Delta E_D}{k_B T}\right), \quad (3)$$

where N_D is the donor density, N_v is the number of the valley at the X point, m_n is the effective mass, k_B is the Boltzman constant, T is the temperature, h is the Planck constant, and ΔE_D is the donor ionization energy of the phosphorus dopant. The value of N_v is 6. The values, $N_D=3.4 \times 10^{15} \text{ cm}^{-3}$ (solid lines) and $5 \times 10^{15} \text{ cm}^{-3}$ (dashed lines), are used corresponding to $\rho=1.1+0.2 \Omega\text{cm}$ and $1.1-0.2 \Omega\text{cm}$ (the positional fluctuation of the resistivity of the present sample)[10]. The expression $m_n=(m_l^2 m_t)^{1/3}=0.32 m_0$ is also used, where m_l and m_t are longitudinal and transverse masses at the X point, respectively. At room temperature, the experimentally

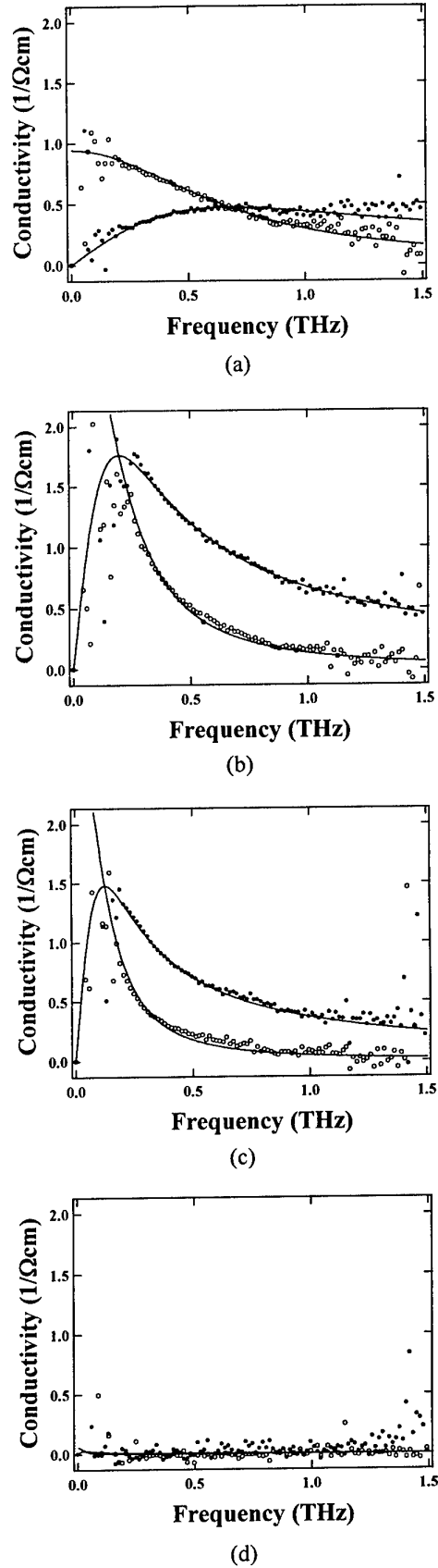
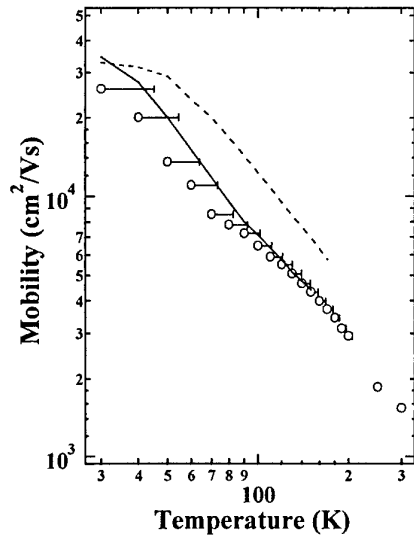
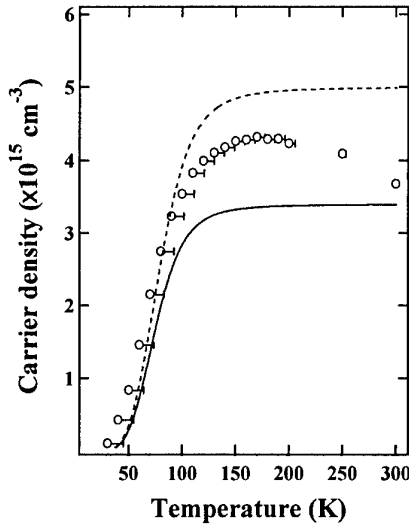


Fig. 1. Temperature dependence of the complex conductivity σ_1 (open circles) and σ_2 (solid circles) at (a) 300 K, (b) 120 K, (c) 70 K, and (d) 16 K. Solid lines show the simple Drude model.



(a)



(b)

Fig. 2. Temperature dependence of (a) mobility and (b) carrier density deduced from the simple Drude fit to the complex conductivity obtained from the THz-TDS measurement. The solid and dashed lines in (a) show the results from Hall measurements for silicon with resistivity of 0.66 Ωcm and 4.76 Ωcm , respectively. The solid and dashed lines in (b) show the carrier density calculated using Eq. (3) assuming $N_D = 3.4 \times 10^{15} \text{ cm}^{-3}$ and $5 \times 10^{15} \text{ cm}^{-3}$ as a function of temperature, respectively.

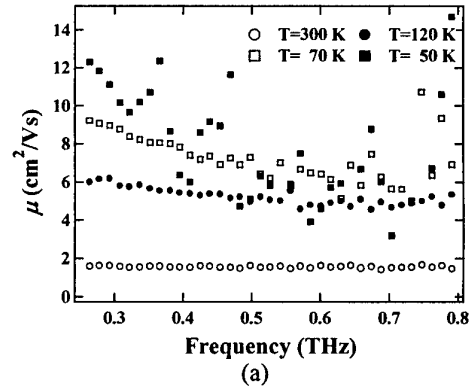
obtained N_c is found to be $3.7 \times 10^{15} \text{ cm}^{-3}$ for the present sample. The experimentally obtained value of N_c increases slightly with decreasing temperature until 150 K and rapidly drops to zero. Below 30 K, the accurate estimation of the carrier density from the experimental results is difficult because of small frequency dependence of complex conductivity compared to the noise level. At room temperature, the results obtained from THz-TDS agree well with the simple Drude model. However, the deviation from the simple Drude model is observed at

low temperatures as shown in Figs. 1(a)-(d). The value of σ_1 at low frequency region obtained from THz-TDS is smaller than that obtained from the simple Drude model, which is similar to the results reported by Exter *et al*[4]. Deviation from the simple Drude model becomes more pronounced with decreasing temperature. We calculate $\mu(\omega)$ and $N_c(\omega)$ from the experimental complex dielectric constant at each frequency at various temperatures by the following equations[2].

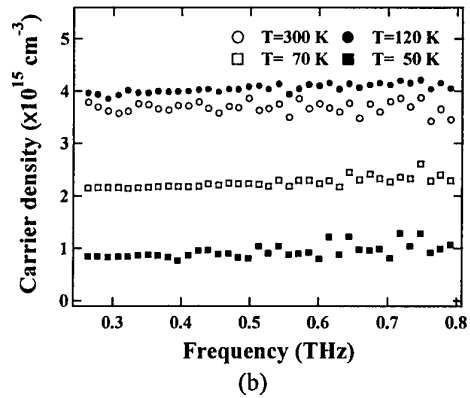
$$\mu(\omega) = \frac{e}{m^*} \frac{\epsilon_\infty - \epsilon_1}{\omega \epsilon_2}, \quad (4)$$

$$N_c(\omega) = \frac{m^* \omega}{e^2 \tau} \left\{ \epsilon_0 \epsilon_2 (1 + \omega^2 \tau^2) \right\}, \quad (5)$$

The dispersion of $\mu(\omega)$ and $N_c(\omega)$ at various temperatures are plotted in Figs. 3 (a) and (b), respectively. At room temperature, the value of $\mu(\omega)$ is constant over the entire frequency region, which indicates that the experimental results agree well with the simple Drude model. However, the values of $\mu(\omega)$ at low temperatures decrease with increasing frequency, which means disagreement with the simple Drude model. This dispersion is also observed at 90 K in the millimeter wave region and is explained by the calculation based on the Boltzman transport equation[3]. The dispersion of $\mu(\omega)$ becomes more



(a)



(b)

Fig. 3. The dispersion of (a) μ and (b) N_c obtained from the experimental dispersion of ϵ_1 and ϵ_2 at 300 K (open circles), 120 K (solid circles), 70 K (open squares), and 16 K (solid squares).

pronounced with decreasing temperature. Below 50 K $\mu(\omega)$ is difficult to estimate because of small frequency dependence compared to the noise level. These results indicate that $\mu(\omega=0)$ is larger than μ obtained from the simple Drude fitting in the entire frequency region. Although the value of $N_c(\omega)$ at room temperature is also constant as well as $\mu(\omega)$, the change of $N_c(\omega)$ with frequency is observed at low temperatures. The value of $N_c(\omega)$ slightly increases with increasing frequency, which predicts that N_c at low temperatures obtained from the simple Drude model estimates a slightly larger than that obtained from $N_c(\omega=0)$.

IV. CONCLUSION

The THz-TDS system is used to measure the complex conductivity of *n*-type silicon wafer at temperatures from 16 K to room temperature. The measured complex conductivity is well fitted by the simple Drude model at room temperature and the experimentally obtained carrier density and mobility agree on the whole with Hall measurement and four-point contact resistivity. This result indicates that the THz-TDS measurement is an effective method for electric noncontact characterization of doped silicon. The change of the temperature dependence of the complex conductivity around ~120 K is observed and slight deviation from the simple Drude model is found at low temperatures. This deviation causes the calculation of the mobility and carrier density using the simple Drude model in the entire frequency region to be slightly underestimated and overestimated, respectively.

Acknowledgment

This work was partially supported by a Grant-in-Aid for the Scientific Research from the Ministry of Education,

Science, Sports, and Culture. This work was partly supported by the Public Participation Program for Promotion of Creative Infocommunications Technology R&D of the Telecommunications Advanced Organization of Japan (TAO). S. Nashima acknowledges the Japan Society for the Promotion of Science for financial support. The help and support of M. Tonouchi and A. Quema over many years are also acknowledged.

References

1. J. D. Holm and K. S. Champlin, "Microwave Conductivity of Silicon and Germanium", *J. Appl. Phys.*, Vol. 39, pp. 275-284, 1968
2. E. Barta, "Determination of Effective Mass Values by A Kramers-Kronig Analysis for Various Doped Silicon Crystal", *Infrared Physics*, Vol. 17, pp. 111-119, 1977
3. M. Hangyo, S. Nakashima, N. Hasegawa, T. Hattori, and K. Sakai, "Carrier Dynamics in Doped Silicon Crystals Studied by Dispersive Interferometric Spectrometers in the Millimeter Wave Region", *Digests 18th Int. Conf. on Infrared and Millimeter Waves*, pp.168-169, 1993
4. M. van Exter and D. Grischowsky, "Carrier Dynamics of Electrons and Holes in Moderately Doped Silicon", *Phys. Rev. B*, Vol. 41, No. 17, pp. 12140-12149, 1990
5. P. G. Huggard, J. A. Cluff, G. P. Moore, C. J. Shaw, S. R. Andrews, S. R. Keiding, E. H. Linfield, and D. A. Ritchie, "Drude Conductivity of Highly Doped GaAs at Terahertz Frequencies", *J. Appl. Phys.*, Vol. 87, No. 5, pp. 2382-2385, 1999
6. K. P. Cheung and D. H. Auston, "A novel technique for measuring far-infrared absorption and dispersion", *Infrared Phys.* Vol. 26, No. 20, pp. 23-27, 1986
7. S. M. Sze, *Physics of Semiconductor Devices*, Wiley, New York, 1981
8. P. Norton, T. Braggins, and H. Levinstein, "Impurity and Lattice Scattering Parameters as Determined from Hall and Mobility Analysis in n-Type Silicon", *Phys. Rev. B*, Vol. 8, No. 12, pp. 5632-5653, 1973
9. C. Jacoboni, C. Canali, G. Ottaviani, and A. Alberigi Quaranta, "A Review of Some Charge Transport Properties of Silicon", *Solid State Electron.* Vol. 20, No. 1, pp. 77-89, 1977
10. W. F. Beadle, J. C. C. Tsai, and R. D. Plummer, Eds., *Quick Reference Manual for Semiconductor Engineers*, Wiley, New York, 1985

THz Wave Generation by Difference Frequency Mixing in Photonic Crystal Cavity

Masahiko Tani, Ping Gu, Kiyomi Sakai, Hideaki Kitahara, Masanori Suenaga, and Mitsuo Wada Takeda

Abstract – It is known that a defect mode within a photonic band gap is localized in the photonic crystal. This suggests that a high-Q and loss-less cavity for an electromagnetic wave can be realized, and that it is possible to make an efficient and compact oscillator using such a photonic crystal cavity. In this paper we report observation of defect modes in a pseudo-simple-cubic lattice ($d=0.4$ mm) generated by excitation of a nonlinear crystal (defect layer) embedded in the photonic crystal with femtosecond pulses. The observed defect modes show different magnitudes and frequencies for defect layers with different thickness, suggesting a layer-thickness dependence of the defect modes. For the purpose of an efficient generation of narrow band THz radiation by difference frequency mixing (DFM) in the photonic crystal cavity, an experimental scheme using a chirped pulse beating is proposed.

I. INTRODUCTION

The periodic dielectric structures, so-called as photonic crystals, are attracting much attention because of their peculiar optical properties [1-4]. The most striking one is the photonic band gap (PBG), where no propagating electro-magnetic mode exists. When a defect is introduced in a photonic crystal, local electromagnetic modes can occur within the forbidden band gap. The photonic crystal acts as a high-Q cavity for such local modes. In terahertz (THz) frequency range, a high-Q cavity has been difficult to realize due to a serious loss/absorption in the cavity. However, it is now feasible to achieve unprecedentedly high-Q cavity in the THz frequency range by using defect modes in a photonic crystal. Such a high-Q cavity can be used, for example, in a parametric or solid-state oscillator, a frequency filter for THz radiation, etc.

In this report we investigate defect modes in square-air-rod pseudo-simple-cubic lattice [5] formed in Si by using the THz time-domain spectroscopy (TDS). The defect modes were introduced by inserting a dielectric layer between the two photonic crystals. Nonlinear crystal (<110>-cut ZnTe crystal) substrates with different thickness were used as the dielectric defect layers so that THz radiation can be generated by the difference frequency mixing (DFM) within the defect layer. Firstly, we measure the transmission spectra of the photonic crystal with a defect layer by a standard THz TDS measurement. It revealed the existence of several defect modes within the PBG region. Secondly, we excited the nonlinear crystal with femtosecond laser pulses and

generated THz radiation within the photonic crystal. By detecting THz radiation emitted from the photonic crystal, we can investigate dynamics of the defect modes and the effect of photonic crystal on the nonlinear process of the difference frequency mixing.

II. PHOTONIC CRYSTAL STRUCTURE

Fig.1 shows the structure of the pseudo-simple-cubic photonic crystal made with Si ($\epsilon_d=11.4$). The lattice constant is 0.4 mm, and the filling factor is about 0.82. The detailed fabrication process and dimension of the lattice was described in the previous paper of this

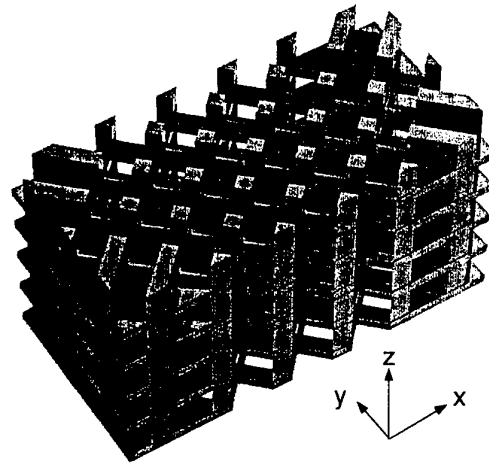


Fig. 1: Structure of the pseudo-simple-cubic lattice structure. The lattice constant is 0.4mm.

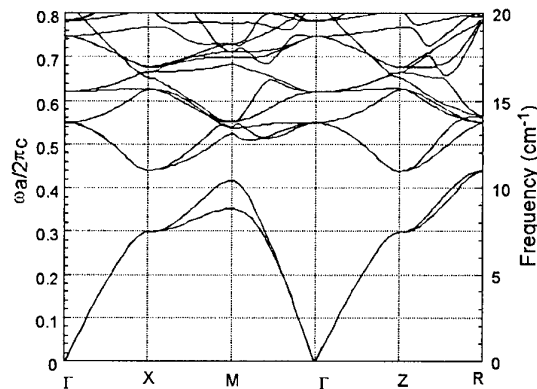


Fig. 2: Photonic band structure of a infinite, pseudo-simple -cubic lattice composed of parallel square air-rods formed in silicon($\epsilon_d=11.4$).

Masahiko Tani, Ping Gu, and Kiyomi Sakai are with Kansai Advanced Research Center, CRL, 588-2 Iwaoka, Kobe 651-2492, Japan
Hideaki Kitahara, Masanori Suenaga, and Mitsuo Wada Takeda are with Department of Physics, Faculty of Science, Shinshu University, Matsumoto 390-8621, Japan

Conference [6]. The band structure of the photonic crystal calculated by the plane-wave expansion method is illustrated in Fig. 2.

III. THZ TIME DOMAIN SPECTROSCOPY OF THE PHOTONIC CRYSTAL

In order to investigate spectroscopic characteristics of the photonic crystal, we carried out the THz TDS in a conventional scheme using low-temperature-grown (LTG) GaAs photoconductive antennas as the THz emitter and detector. The detailed description of the spectroscopic system is the same as that of in ref [6]. The measured transmission spectrum and phase shift for a ten-layer photonic crystal in Γ -Z direction are shown in Fig. 3 and the calculated ones (for eight layers) by using transfer matrix method are shown in Fig. 4, respectively. The experimental and calculated spectra show a good agreement between them. The experimental data shows a clear stop band from 6.5 to 10.2 cm^{-1} ($1 \text{ cm}^{-1} = 30 \text{ GHz}$), which is very close to the first PBG calculated as shown in Fig. 4. The phase shift also shows a close

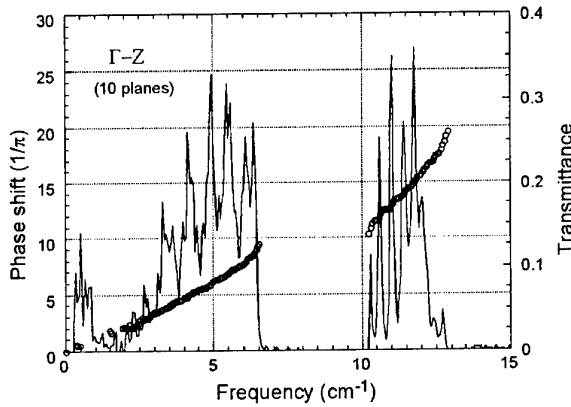


Fig. 3: Transmission amplitude (solid line) and phase shift (open circle) spectra of the pseudo-simple-cubic photonic crystal observed along the Γ -Z direction

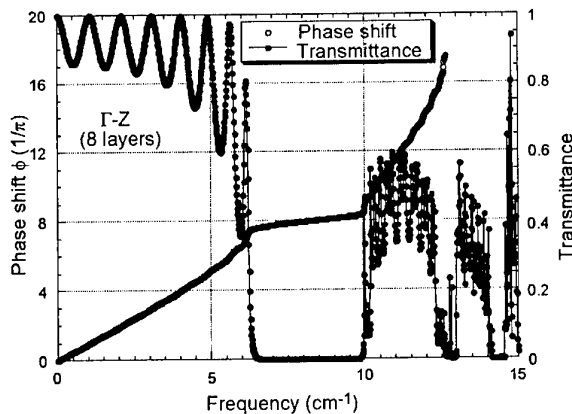


Fig. 4: Transmission (solid circle) and phase shift (open circle) spectra of the pseudo-simple-cubic photonic crystal calculated by the transfer matrix method along the Γ -Z direction for a sample with 8 layers.

correspondence between the experimental data and the calculation. For the experimental phase shift in the second transmission band of Fig. 3 we included a π phase change across the PBG. The periodic spectral peaks observed both in the experiment and calculation originated from the Fabry-Perot effect in the finite size of the photonic crystal [6].

In order to introduce defect modes in the photonic crystal, a $\langle 110 \rangle$ -cut ZnTe substrate was sandwiched by the photonic crystals with 4 layers. We prepared samples with different thickness of the defect layer: $d = 0.3, 1.0, 1.3 \text{ mm}$. These samples were measured by the THz TDS. The results are shown in Fig. 5. In the PBG region non-zero transmission is observed for all the cases. We observe strong spectral peaks near 7 cm^{-1} for the defect layer thickness of 0.3 mm and 1.3 mm, while for the 1.0-mm thick defect the peak is not so distinct. There are also several sub-peaks in the band gap region (6.5-10.2 cm^{-1}). These peaks can be attributed to defect modes induced by the defect layer.

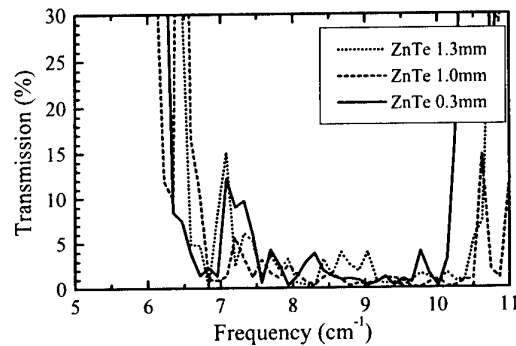


Fig. 5: The transmission spectra for photonic crystals with a defect layer inside. The thickness of the defect layers was 0.3 mm (solid line), 1.0 mm (dashed line) and 1.3 mm (dotted line), respectively.

IV. EXCITATION OF DEFECT MODE WITH FEMTOSECOND LASER PULSES

We tried to excite defect modes within the photonic crystals with a defect layer of thickness $d=0.3 \text{ mm}$ and 1.3 mm by excitation with femtosecond laser pulses. The defect layer is a $\langle 110 \rangle$ -cut ZnTe, which is known as an efficient emitter of THz radiation. The THz radiation is generated in the ZnTe crystal due to the optical rectification effect. This excitation process is also explained by the difference frequency mixing between different frequency components in the broad optical frequency spectrum of the femtosecond pulse.

The excitation pulses were delivered from a mode-locked Ti: sapphire laser, whose pulse width, repetition rate, and the center wavelength were 80 fs, 82 MHz, and 810 nm, respectively. The laser beam was focused by a lens ($f=250 \text{ mm}$) to the defect layer through an air hole in the photonic crystal in direction of the z-axis. The radiation emitted from the opposite side of the sample was

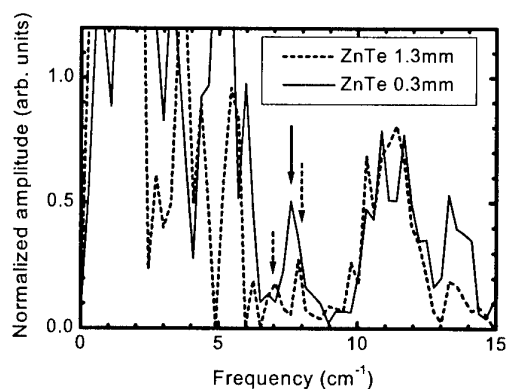


Fig. 6: Emission spectra from photonic crystals with defect layer of 0.3-mm thick (solid line) and 1.3-mm (dashed line) ZnTe. Defect modes observed are indicated by vertical arrows.

collected and focused on to an LTG-GaAs photoconductive dipole antenna (50- μm long) by using a pair of off-axis parabolic mirrors. The THz emission spectra normalized by that without photonic crystals are shown in Fig. 6. For the defect layer with 1.3-mm ZnTe, we observe peak spectra at 7.0 cm^{-1} and 7.8 cm^{-1} (indicated by dashed vertical arrows). The former peak corresponds to the peak observed in the transmission spectrum at 7.0 cm^{-1} . The latter peak observed at 7.8 cm^{-1} also coincides well with a peak at 7.7 cm^{-1} observed in the transmission spectrum. For the defect layer with 0.3-mm thick ZnTe, a strong peak at 7.6 cm^{-1} (indicated by a solid vertical arrow) is observed. This mode is not clear in the transmission spectrum in Fig. 5. The reason why we observe a defect mode that is not observed in transmission measurement is not clear for present. One possibility is the difference of the symmetry for the transmission and excited modes: in the transmission spectrum we can only observe even modes regarding to the mirror symmetry for the z-y or z-x plane because the electromagnetic oscillations are symmetric for a plane, which is along z-axis and vertical to the polarization direction. On the other hand the electrical polarization generated by the optical rectification is not necessarily symmetric with respect to the z-axis, and thus can excite non-symmetric modes.

Although the femtosecond laser excitation is useful for investigation of defect modes generated in the photonic crystal, the enhancement of generation of THz emission due to the cavity effect is not strong because of the short coherence length of the femtosecond pulse ($\sim 30\text{ }\mu\text{m}$ in free space). To observe enhancement of THz radiation at defect modes, it is better to use an optical beat whose beat frequency is tuned to the defect mode frequency. However, in a completely continuous wave DFM, the peak intensity of the generated THz wave is expected to be weak and thus it is difficult to achieve peak intensity needed for THz wave to interact with the strong pump beam. To obtain a strong peak intensity of the THz radiation we can use optical beating pulses or pulse trains by using chirped femtosecond laser pulses. An efficient way for generation of an optical beat and generation of

narrow band THz radiation by the use of the chirped pulses was demonstrated by Weling *et al* [7], recently. The optical beat can be generated by superimposing two chirped femtosecond pulses with different time-delay. The difference frequency between the two chirped pulses is kept constant over the chirped pulse duration when the chirping rate is constant. Figure 7 shows the waveforms of THz radiation generated by excitation of a photoconductive antenna with such chirped beating pulses. By changing the delay-time between the two chirped pulses, the beat frequency can be tuned arbitrarily. Three waveforms excited with beat frequencies at around 150, 230 and 500 GHz are shown in Fig. 7(a). Figure 7(b) shows their corresponding FFT spectra. The spectral bandwidth of the radiation generated by the optical beat is about several tens GHz. The experiment to observe narrow band THz radiation from defect modes by excitation with the chirped optical beating pulses is now under way.

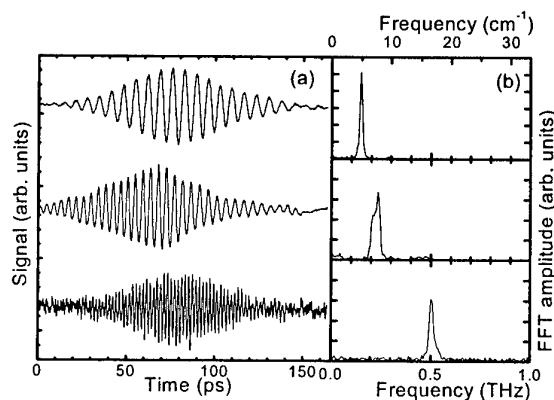


Fig. 7: (a) THz waveforms generated by excitation of a photoconductive antenna with chirped beating pulses, and (b) their FFT spectra.

V. CONCLUSION

We have demonstrated generation of THz radiation from defect modes in a pseudo-simple-cubic photonic crystal by excitation of the ZnTe defect layer with femtosecond laser pulses. Several defect modes were clearly observed, whose frequency and amplitude were depending on the thickness of the defect layer. This is the first observation of THz wave generation due to the defect modes of a photonic crystal.

Acknowledgement

This work was supported by a Grant of Aid for Scientific Research of Priority Areas, "Photonic Crystal", and by that for General Scientific Research from the Ministry of Education, Science, Sport, and Culture of Japan, and also supported by Research Foundation for Opto-Science and Technology.

References

1. K. Ohtaka, "Energy band of photons and low-energy photon diffraction," *Phys. Rev.* **B19**, 5057 (1979).

2. E. Yablonovich, "Inhibited spontaneous emission in solid-state physics and electronics," *Phys. Rev. Lett.* **58**, 2059 (1987).
3. C. M. Bowden, J. P. Dowling, and H. O. Everitt, Special Issue on "Development and Applications of Materials Exhibiting Photonic Band Gaps," *J. Opt. Soc. Am.* **B10**, (1993).
4. Mitsuo Wada, Yoshiyuki Doi, Kuon Inoue, and J. W. Haus "Far-infrared transmittance and band-structure correspondence in two-dimensional air-rod photonic crystals," *Phys. Rev.* **B55**, 10443 (1997).
5. H. S. Sözüer and J. W. Haus, "Photonic bands: simple-cubic lattice," *J. Opt. Soc. Am.* **B10**, 296 (1993).
6. T. Aoki, M. W. Takeda, J. W. Haus, Z. Yuan, M. Tani, K. Sakai, N. Kawai, and K. Inoue, "The photonic dispersion relation of the pseudo-simple-cubic lattice revealed by THz time-domain measurements," 7th International Conference on Terahertz Electronics, P37, pp.256-259 (1999).
7. A. S. Weling and D. H. Auston, "Novel sources and detectors for coherent tunable narrow-band terahertz radiation in free space," *J. Opt. Soc. Am.* **B13**, 2783 (1996).

Nonlinear response of a superlattice

Flå, T., Birnir, B., and Allen Jr., S.J.

Abstract— In this work we study the nonlinear dc and ac response of a superlattice. We develop asymptotic theories for the I-V curve and ac gain valid in both the very low frequency quasistatic limit, the intermediate frequency limit and high frequency limit. We also explore the I-V curve and ac gain for a quite extensive parameter regime. Parameter regimes which have gain and positive differential conductivity are identified for sufficiently high ac amplitudes. These parameter regimes will be important to understand the nonlinear state of solid state sources in the THz range.

I. INTRODUCTION

We will in this work report on nonlinear ac and dc conductivities in a superlattice favorable for a THz source [1]. Esaki and Tsu [1] proposed to use a semiconductor superlattice to achieve a device with a current-voltage characteristic with negative differential conductivity (NDC) above a certain critical dc-bias proportional to the geometric mean collision frequency (ν_g). Subsequently, Ktiterov et al.[2] gave a simple model for the miniband electron distribution function for a superlattice including both momentum and energy relaxation. They showed that for dc-bias in the NDC-regime and linear ac-drive that there was ac-gain for frequencies slightly below the resonant Bloch frequency. We will further investigate Ktiterov's theory into the nonlinear ac-drive regime. It turns out that the problem of calculating currents in Ktiterov's Boltzmann model, can be reduced to studying the momentum equation and en-

ergy equation[3, 4]. The electron density equation for homogenous E-field is simply $\rho_0 = \text{const}$.

The model we will concentrate on is based on the fluid moments of the Ktiterov's Boltzmann equation, but in a nondimensional form where the essential parameters of the theory is stressed from the beginning. This emphasis has simplifying implications for scaling of theoretical, simulation and experimental results and parameters. Our goal is to find conditions under which a dc-biased and nonlinearly ac-driven superlattice can have both gain and positive differential conductivity. The coincidence of the regime of gain of small amplitude oscillations and negative differential conductivity imply that domain formation is an obstacle to the construction of a superlattice THz source. The ac E-field is assumed to give rise to such high electric fields in the medium that the dc and ac conductivities in the superlattice is nonlinearly modified. We want to explore conditions under which the dc conductivity is locally of the positive differential type and at the same time that the nonlinear conductivity give rise to gain. The model we choose to investigate is the momentum $\rho_0 v$ and energy $\rho_0 \epsilon$ fluid moments of a Boltzmann equation with a simple energy and momentum collision operator. We find the following equations in agreement with several earlier works :

$$\begin{aligned} \left(\frac{\partial}{\partial t} + \nu_p\right)v + \frac{ed^2 E}{\hbar^2}(\epsilon - \frac{\Delta_1}{2}) &= 0, \\ \frac{\partial}{\partial t}\epsilon + \nu_\epsilon(\epsilon - \epsilon_{T0}) - eEv &= 0, \\ \epsilon_{T0} &\equiv \frac{\Delta_1}{2} \left(1 - \frac{I_1(\frac{\Delta_1}{2k_B T_0})}{I_0(\frac{\Delta_1}{2k_B T_0})}\right) \end{aligned} \quad (1)$$

By introducing new variables $v_\epsilon = (\epsilon - \epsilon_{T0})d/\hbar$, $v_\epsilon^0 \equiv (\frac{\Delta_1}{2} - \epsilon_{T0})d/\hbar = (\Delta_1 d/2\hbar) \frac{I_1(\frac{\Delta_1}{2k_B T_0})}{I_0(\frac{\Delta_1}{2k_B T_0})}$ and defining the Bloch frequency $\omega_B = edE/\hbar$, we find the alternative description

$$\left(\frac{\partial}{\partial t} + \nu_p\right)v_p + \omega_B v_\epsilon = \omega_B v_\epsilon^0, \quad (2)$$

$$\left(\frac{\partial}{\partial t} + \nu_\epsilon\right)v_\epsilon - \omega_B v = 0 \quad (3)$$

These equations can now be put into a nondimensional

form by scaling the velocities by v_ϵ^0 (alternatively by $d\omega_{B0}$ or $d\omega$) and time and frequency by the background Bloch frequency $\omega_{B0} = \frac{edE_0}{\hbar}$ (alternatively ω or the the geometric mean collision frequency which we also will discuss below). We then find the following nondimensional form of the equations with frequencies and time scaled with respect to the dc Bloch frequency. Here we have by abuse of notation used the same symbols for the variables $\omega_B \rightarrow \omega_B/\omega_{B0}, \nu_{\epsilon,p} \rightarrow \nu_{\epsilon,p}/\omega_{B0}, t \rightarrow t\omega_{B0}, (v_\epsilon, v) \rightarrow (v_\epsilon, v)/v_\epsilon^0$

$$\left(\frac{\partial}{\partial t} + \nu_p\right)v + \omega_B v_\epsilon = \omega_B, \quad (4)$$

$$\left(\frac{\partial}{\partial t} + \nu_\epsilon\right)v_\epsilon - \omega_B v = 0. \quad (5)$$

An alternative useful scaling of frequencies and times of this equation are given in terms of units of the geometric mean collision frequency (c.f. discussion below) $\nu_g = (\nu_\epsilon \nu_p)^{0.5}$ which means $t \rightarrow \bar{t} = t\nu_g$; $\nu_{\epsilon,p} \rightarrow \kappa_{\epsilon,p}, \frac{1}{\kappa_{\epsilon,p}}; \omega_{B0} \rightarrow \omega_0 = \frac{\omega_{B0}}{\nu_g}; \omega_B \rightarrow \bar{\omega}_B = \frac{\omega_B}{\nu_g}; \omega \rightarrow \bar{\omega} = \frac{\omega}{\nu_g}, \kappa_{\epsilon,p} = \left(\frac{\nu_\epsilon}{\nu_p}\right)^{0.5}$.

The dc-solutions of these equations for a given constant E-field $E_0 = V_0/L$ corresponding to a constant Bloch frequency ω_{B0} is given in these scaled variables by

$$v_0 = \kappa_{ep}\omega_0/(1 + \omega_0^2) = \sigma_0\omega_0; v_{\epsilon 0} = \omega_0^2/(1 + \omega_0^2) \quad (6)$$

Here we have introduced the scaled dc conductivity σ_0 . We have also introduced the relative Bloch frequency in units of the geometric mean collision frequency ω_0 which is normalized to 1 at the maximum of the I-V curve. Another quantity we will be interested in is the linear response of the velocity and energy due to a harmonic perturbation in the E-field drive corresponding to $\omega_B = 1 + \varepsilon\omega_{B1}(t), \omega_{B1}(t) = -\omega_1 \cos(\omega t) = -\frac{\omega_1}{2} \exp(-i\omega t) + c.c.$ ε is just an ordering parameter. We now find the $O(\varepsilon)$ scaled ac-response (the dc and ac response for a nonlinear ac drive is too long to be included explicitly) in agreement with Khiterov's model ac-conductivity

$$\hat{\mathbf{v}}_1 = \begin{pmatrix} \hat{v}_1 \\ \hat{v}_{\epsilon 1} \end{pmatrix} = -\frac{\omega_1\omega_0}{2} \begin{pmatrix} \sigma_1(\omega) \\ \sigma_{\epsilon 1}(\omega) \end{pmatrix} \quad (7)$$

$$\begin{pmatrix} \sigma_l \\ \sigma_{\epsilon l} \end{pmatrix} = \frac{\sigma_0}{\omega_0^2 + 1 - (\omega\omega_0)^2 - i\omega\omega_0(\kappa_{ep} + 1/\kappa_{ep})} \quad (8)$$

$$\begin{pmatrix} 1 - \omega_0^2 - i\omega\omega_0/\kappa_{ep} \\ \omega_0(2/\kappa_{ep} - i\omega\omega_0) \end{pmatrix}. \quad (9)$$

$$\hat{\omega}^2 = \frac{1}{\hat{\nu}_\epsilon \hat{\nu}_p}, \quad \hat{\nu}_\epsilon = \nu_\epsilon - i\omega, \quad \hat{\nu}_p = \nu_p - i\omega \quad (10)$$

We immediately see that there is a resonance in the ac-conductivity at frequency $\omega_r = \pm(1 - \nu_d^2)^{1/2}$

($\nu_d = (\nu_p - \nu_\epsilon)/2 = \hat{\nu}_d/\omega_0, \hat{\nu}_d = (1/\kappa_{ep} - \kappa_{ep})/2 \approx 0.35$) which for high enough ω_0 is close to the normalized Bloch frequency 1. For fixed Bloch frequency (ω_0) or fixed frequency ($\bar{\omega}$) this resonance translate to $\bar{\omega}_r = \pm(\omega_0^2 - \hat{\nu}_d^2)^{0.5}$ or $\omega_{0r} = \pm(\bar{\omega}^2 - \hat{\nu}_d^2)^{0.5}$ respectively. A short calculation will show that there is linear gain, i.e. $\sigma_1 = \text{Re}(\sigma_l) < 0$ only if $\omega_0 > 1$ and in the frequency regime $\omega < \omega_z < \omega_{0c} = 1$. Here ω_z (near to ω_r) is the crossover frequency from gain to no gain. Consequently there is no coincidence between gain and PDC in the linear limit $\bar{\omega}_1 \rightarrow 0$. We remark that no resonance is found for $\nu_d (\simeq .35/\omega_0) > 1$, i.e. $\omega_0 < \hat{\nu}_d$ or $\bar{\omega} < \hat{\nu}_d$ respectively. If we assume that the ratio of the collision frequencies are reasonably fixed, we see that the description of the dc and ac response can be given in terms of the three nondimensional parameters $\bar{\omega}_1 = \omega_1\omega_0, \bar{\omega} = \omega\omega_0$ and ω_0 which is nothing but the ac-drive amplitude, frequency and Bloch frequency measured in units of the geometric mean collision frequency. These three variables are also reasonable to use since for given geometric mean collision frequency they correspond to fixed frequency and ac-amplitude as we vary the dc bias.

II. AC AND DC CONDUCTIVITIES WITH A NONLINEAR AC-DRIVE

We summarize our theoretical (there is no space to give the theory) and numerical investigation below (see some of the results of I-V curves and ac response in Fig. 2a,b). This has eventually to be substantiated by experimental results.

1. The solution of our model in the high frequency limit approaches a limit cycle with a timescale $\tau = O(1/\bar{\nu})$ and with leading order oscillation frequency and renormalized resonance given as $\omega_l = (1 - \bar{\nu}_d)^{1/2}$ if $\bar{\nu}_d = \nu_d J_0(2\omega_1/\omega) < 1$. For $\bar{\omega}_1 \geq O(1)$ there is a narrow layer of PDC and gain in the domain $\omega_0 \in [\bar{\omega} - \delta, \bar{\omega}]$ where $\delta = o(1)$ and similar indications near the second resonance $\lesssim 2\bar{\omega}$ for $\bar{\omega}_1 \gg 1$. There is a change in signature of the I-V curve for small ω_0 and near $\bar{\omega}_1/\bar{\omega} = 2.405$ ($J_0(\frac{\bar{\omega}_1}{\bar{\omega}}) = 0$). The corrections of $O(\nu_d)$ is quantitatively important in our theory in contrast to many authors who use a model with only one collision frequency.

2. The quasistatic theory and intermediate frequency theory $\omega < O(\nu_d)$ is characterized by a decay with timescale τ (no oscillations) to the limit cycle, a linear shift of the maximum of the I-V curve $\omega_{0c} \sim \bar{\omega}_1$ and a small region of coinciding gain and PDC for $\bar{\omega}_1 > 1$.

The limit cycle can be described in a three-dimensional phase space plot of $\{\omega_B(t), \mathbf{v}(t)\}$. Since we will basically be interested in conductivities, we will study the projection of the limit cycle on the Bloch frequency-

velocity plane, $\{\omega_B(t), v(t)\}$. The limit cycle will have a basic period of $T = 2\pi/\omega$, but can have a complex behavior with one or several loops at high frequencies $\bar{\omega} \gg 1$ and will due to the stiffness of the system have a tendency to align along the I-V curve in the quasistatic limit for small $\bar{\omega}$.

A. I-V curves

The averaged velocity $v_0 = \frac{1}{T} \int_0^T v dt$ over a basic period $T = 2\pi/\omega$ of the limit cycle is the dc component of the periodic velocity. DC I-V curves (see examples in Fig. 2a) in this context is nothing else than a graph of $v_0(\omega_0; \bar{\omega}_1, \bar{\omega})$ as a function of the Bloch frequency with the amplitude and frequency of the drive as parameters. To measure this property for a nonlinearly driven superlattice numerically one has to wait until all transients has died out such that the solution sticks to the limit cycle. For the parameter regime and the collision frequencies we are interested in, it is sufficient to wait 4-5 periods before one do the averaging around one period of the limit cycle. The collision frequency for a GaAs superlattice has been estimated by a fit to I-V measurements for a specific sample given on the Quantum Institute homepage (J. Scott) to be $1/\nu_\epsilon \approx 0.3ps$ and $1/\nu_p \approx 0.15ps$. For a InAs/AlSb superlattice a reasonable guess for collision frequencies are $1/\nu_\epsilon \approx 0.6ps$ and $1/\nu_p \approx 0.2 - 0.4ps$. Therefore estimates of the collision frequency ratio are $\kappa_{ep}(GaAs) \approx 0.707$ and $\kappa_{ep} \in [0.6, 0.8]$. The geometric mean of the collision frequencies are therefore estimated as $\nu_g(GaAs) \approx 4.7THz$ and $\nu_g(InAs/AlSb) \in [2, 3]THz$. With these parameters given, the Bloch frequency can be deduced, i.e. $\omega_0, \bar{\omega}, \bar{\omega}_1 = 1$ corresponds to the physical frequencies $\omega_{B0}, \omega, \omega_1 = \nu_g$. To help the reader we give the following table which scale our nondimensional theoretical and numerical results to different type of superlattice experimental settings.

$\omega_{B0}(\omega_{B1})$	$4.7\omega_0(\text{or } \bar{\omega}_1)(\frac{\nu_g}{4.7THz})THz$
$V_0(V_1)$	$0.294(\frac{N}{100})\frac{\nu_g}{4.7THz}\omega_0(\text{or } \bar{\omega}_1)eV$
$f = \frac{\nu_g\omega}{2\pi}$	$0.748(\frac{\nu_g}{4.7THz})\bar{\omega}THz$
$v_{\epsilon 0}$	$\frac{\Delta_1}{20meV} \frac{d}{10nm} F(\kappa) 3.79 \times 10^6 m/s$
$\kappa = \frac{\Delta_1}{2k_B T}$	$0.3868(\frac{\Delta_1}{20meV})(\frac{T}{300K})^{-1}$
σ	$(\frac{N}{100})^{-1} \frac{n_0}{10^{16}cm^{-3}} \frac{S}{20(\mu m)^2} \frac{L_{mf}}{0.1615\mu m} \bar{\sigma}$

Tab.1 Scaling of some physical quantities from nondimensional ones. Here $\bar{\sigma} = \sigma_0 0.393 mho$ and $\sigma = \frac{e^2 n_0 L_{mf} S \sigma_0}{Nh}$. For scaling of physical σ_{1p} with nondimensional σ_1 interchange $\sigma \rightarrow \sigma_1$ and $\sigma_0 \rightarrow \sigma_{1p}$.

Here $F(\kappa) = I_1(\kappa)/I_0(\kappa)$ is plotted in Fig.1 and can also be used to infer the nonlinear temperature dependence of the dc-bias and ac-field given data for the nonlinear mean energy through our simulation (we

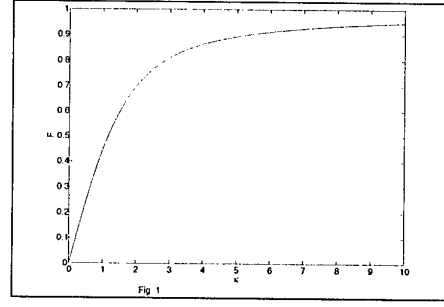


Figure 1 - Here we have plotted the function $F(\kappa) = I_1(\kappa)/I_0(\kappa)$ where the nondimensional parameter $\kappa = \frac{\Delta_1 d}{2k_B T}$. The scaling of this parameter for different superlattices is given in Tab. 1.

do not discuss the energy/temperature results here) or by experimental means. $v_{\epsilon D}(\bar{\omega}, \bar{\omega}_1, \omega_0) = \frac{\Delta_1 d}{2h} F(\kappa) \Rightarrow T(\bar{\omega}, \bar{\omega}_1, \omega_0) = \frac{2k_B}{T_0} F^{-1}(\frac{2h}{\Delta_1 d} v_{\epsilon D})$.

This nonlinear temperature might be an important parameter to determine selfconsistent models of collision frequencies, especially for temperature regimes where kinetic energy is comparable to the phonon energy. We have also defined a characteristic collision length $L_{mf} = \nu_{\epsilon 0}/\nu_g$ for superlattices. The dc current given for a nondimensional conductivity σ_0 in a superlattice with electron density n_0 , transversal crosssection of the mesa S and length $L = Nd$ now scales as a function of dc voltage V_0 , ac electric field $E_1 = V_1/L$ and frequency f by $I_{dc} = \sigma V_0$ ($[I] = \text{Ampere}$ if $[V_0] = \text{Volt}$). The ac-current and conductivity scale the same way given an ac nondimensional conductivity.

B. Nonlinear ac response

We will now measure the nonlinear ac response (see examples in Fig. 2b) of the superlattice velocity and energy at the first harmonic of the limit cycle. The first harmonic can be determined directly through a discrete fouriertransform of velocity and energy data from a complete period of the limit cycle. Alternatively, the real part or cosine component of the first harmonic can be determined by averaging the superlattice equations over one period assuming again that we are at the limit cycle such that periodicity can be assumed, i.e. $v(t) = v(t + T)$. This leads to the averaged equations

$$\nu_p v_D + v_{\epsilon D} - \frac{\omega_1}{2} v_{1c} = 1, \quad (11)$$

$$\nu_\epsilon v_{\epsilon D} - v_D + \frac{\omega_1}{2} v_{\epsilon 1c} = 0. \quad (12)$$

The interaction terms $\mp \frac{\omega_1}{2} v_{1c, \epsilon 1c}$ has an interesting physical interpretation as the rescaled averaged

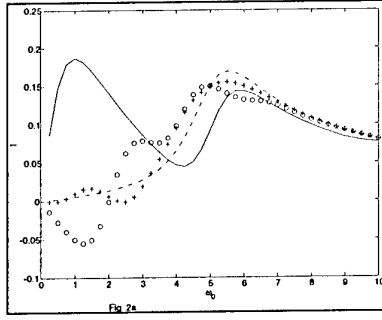


Figure 2 – In Fig. 2a we have plotted the normalized dc I-V curve parameterized by the velocity averaged over one period of the limit cycle as a function of normalized Bloch frequency $\omega_0 \in [0, 10]$ and for a fixed nonlinear ac-drive amplitude $\bar{\omega}_1 = 5.0$. These normalized I-V curves can be scaled to I-V curves for different experimental parameters by the scaling laws given in Tab.1 and the relation $v_0 = \sigma\omega_0$. The curves are labelled as: dash-dotted curve $\rightarrow \bar{\omega} = 0.1$, curve of +’s $\rightarrow \bar{\omega} = 1.0$, curve of o’s $\rightarrow \bar{\omega} = 2.079 = \bar{\omega}_1/2.405$, and solid curve $\rightarrow \bar{\omega} = 5.0$. The case $\bar{\omega}_1/2.405$ corresponds to the degenerate case of the first zero of the zeroth order Bessel function $J_0(\frac{\bar{\omega}_1}{\bar{\omega}})$.

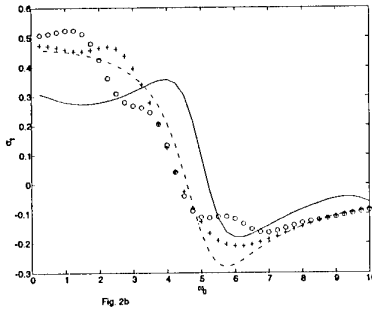


Figure 3 –

Lorentz force and averaged radiation power gain due to the first harmonic. Now, we can deduce that $v_{1c} = -\frac{2}{\bar{\omega}_1}\sigma_1 A_0 \Delta v_D$, where we have defined $A_0 = \begin{pmatrix} \frac{1}{\kappa_{ep}} & \omega_0 \\ -\omega_0 & \kappa_{ep} \end{pmatrix}$, $v_{1c} = \begin{pmatrix} v_{1c} \\ v_{\epsilon 1c} \end{pmatrix}$, $\Delta v_D = v_D - v_0 = \begin{pmatrix} v_D - v_0 \\ v_{\epsilon D} - v_{\epsilon 0} \end{pmatrix}$.

We can deduce the ac gain through either of the two equivalent relations $\sigma_1(\omega) = -v_{1c}(\omega)/\bar{\omega}_1 = -\text{real}(\hat{v}_1(\omega))/(\bar{\omega}_1/2)$. Here $v_{1c}(\omega)$ and $\hat{v}_1(\omega)$ are the first harmonic cosine and real coefficient of the Fourier expansion of the limit cycle time series of the velocity. The scaling of each value of this nondimensional version nonlinear ac conductivity to a whole continuum of experimental parameters can be found through Tab. 1.

Therefore, given that there are resonances in $v_{1c}(\bar{\omega}, \bar{\omega}_1, \omega_0)$ at $n\bar{\omega} = \omega_0$ and that the peak of the I-V curve without ac-drive is at $\omega_0 = 1$ in units of the geometric mean collision frequency, we can only expect effects of the first resonance on the I-V characteristic in the form of additional bumps if $\bar{\omega} > 1$. Moreover, we qualitatively deduce that if v_{1c} is slowly varying with $\bar{\omega}_1$ in the quasistatic regime $\bar{\omega} \ll 1$ that one can expect an approximate linear shift in v_D with increasing $\bar{\omega}_1$. E.g., a linear shift in the position of the maximum of the I-V curve can be expected.

REFERENCES

- [1] Esaki, L. and Tsu, R. , IBM J. Res. Dev. 14, 61(1970).
- [2] Ktitorov, S.A., Simin, G.S., and Sindalovskii, V. Ya , Fiz. Tverd. Tela 13,2230(1971) [Sov. Phys. Solid State 13, 1872(1972).
- [3] Ignatov, A.A. and Shashkin, V.I. , Phys. Lett. 94A, 169(1983).
- [4] Ignatov, A.A., Renk, K.F., and Dodin, E.P. Phys. Rev. Lett. 70, 1996(1993).

AUTHOR LIST

Author	Presented Papers	Author	Presented Papers
Y. Abe	P.27	C. Groppi	P.2
M. Akbari	P.4	P. Gu	SI.4, D.2, P.30
I.V. Altukhov	SI.4	E.E. Haller	SI.5, P.17
D. Arslan	SI.1	P.H. Handel	P.24
S. Asmontas	P.12	M. Hangyo	I.2, P.29
S. Bäuml	I.4, P.1	O. Harnack	P.19
M. Bieler	P.28	H.J. Hartfuß	I.4
D. Bourreau	P.25	H. Hartnagel	SI.1, Mul.4, Mi.2, I.4, P.1, P.16, P.18, P.23
M. Bozzi	Mul.4, P.6	H. Hasegawa	D.1
H. Brand	Mi.2	G. Hein	P.28
R. Bratschitsch	P.14	W. Heinrich	Pa.3
E. Bründemann	SI.5, P.17	M. Herrmann	I.3
D. Budimir	P.26	J. Hesler	Mi.5, Mi.3
M. Carter	Mi.3	Y. Hiraga	P.27
J.M. Chamberlain	SI.2	S. Hirsch	Pa.5, P.9
D.R. Chamberlin	SI.5, P.17	K. Hjort	P.23
G. Chattopadhyay	Mi.4, Mul.5	M. Hoeft	Q.1
D.S. Citrin	P.28	J.N. Hovenier	SI.5, P.11
M. Claassen	Mul.2	Q. Hu	SI.2
Th. Crowe	Pa.1	K. Huber	Mi.2
S.U. Dankowski	SI.3	H.W. Hübers	Mi.4, Mi.3
L. Dillner	Mu.1	E.J. Huq	SI.2
Y.Y. Divin	D.4	V. Ichizli	Mi.2, P.16, P.18
T. Dobbertin	Q.2	S.M. Iftiqar	P.7
G.H. Döhler	SI.3, P.5	A.A. Ignatov	D.3, P.20
K. Dramura	SI.1	K. Ilin	P.19
C. Drouet d'Aubigny	P.2	M. Ingvarson	Mu.1
K. Duwe	Pa.5, P.9	H. Ishizuka	SI.1
H. Endert	SI.2	H. Ito	I.5, P.8
R.W. Es	P.11	B. Jones	P.2
J. Faist	SI.1	R. Judaschke	Pa.5, Q.1, P.9, P.21
R. Feinäugle	Mi.3	M.S. Kagan	SI.4
M.W. Feise	P.28	B. Karasik	P.19
J.R. Fletcher	SI.2	K. Kawase	I.5
J. Freyer	Mul.2	U.D. Keil	SI.3
I. Frigyes	Pa.4	R. Kersting	P.14
R. Fukasawa	I.3	P. Kiesel	SI.3, P.5
M. Gaidis	Mi.1	H. Kitahara	P.30
J.J. García	SI.2	Y. Kito	I.2
E. Gershenzon	Mi.4	T.O. Klaassen	SI.5, P.11
G. Goltsman	Mi.4	F. Klappenberger	D.3, P.11
E. Gornik	SI.1	R.M. de Kleijn	SI.5
Y.P. Gousev	SI.4	G.M. Knippels	P.11
G. Goussetis	P.26	P. Knobloch	Q.2
J. Gradauskas	P.12	M. Koch	Q.2, P.28
J. Grajal	Mul.3	E. Kollberg	Mu.1
		Sh. Kono	SI.4, D.2
		W. Kooi	Mi.4

P.S. Kopev	P.20	H. Ohtake	SII.2
Y. Koschurinov	P.20	H.K. Olsson	SI.4
M. Kourogi	P.7	S. Ono	SII.2
A. Kovsh	P.20	C. O'Sullivan	Q.3
M. Krach	Mul.2	M. Otsu	P.7
M. Krätschmer	D.3, P.11		
V. Krozer	SIII.3, Mul.3, P.5		
		J. Papapolymerou	P.2
D. Lamarre	Mil.1	J.P. Pascual	P.1
J.M. Lamarre	P.13	D.G. Pavelev	P.20
J.F. Lampin	SII.3	V.V. Pavlovskii	D.4
S. Langa	P.23	A. Peden	P.25
G. de Lange	P.19	L. Perregrini	Mul.4, P.6
J. Langen	Mil.1	E. Peytavit	SII.3
B. Lazareff	Mil.3	T.G. Phillips	Mil.4
M. Lee	D.5	K. Pierz	P.28
C.T. Li	D.5	U. Poppe	D.4
Ch.I. Lin	Mil.2, P.1, P.16, P.18	D. Pukala	Mul.5
Ch.C. Lin	Mil.1		
D. Lippens	SII.3	H. Quast	P.5
M. Luschas	P.21		
J.F. Luy	P.21	K.F. Renk	D.3, P.20
		M. Rodríguez-Gironés	Mil.2, Mul.4, I.4, P.1, P.16, P.18
P. de Maagt	Mil.1	H.G. Roskos	SIII.3, P.5, P.12,
A. Maestrini	Mul.5	V. Ryzhii	SI.3
T. Magath	P.4		
F. Maiwald	Mul.5	M. Saglam	Mil.2, Mul.4, P.16, P.18
C.M. Mann	SIII.2	K. Sakai	D.2, SIII.4, I.3, P.7, P.30
L. Marchand	Mil.1	Ch.V. Sammut	P.10
P. Masselin	SII.3	N. Sarukura	SII.2
F. Mattiocco	Mil.3	R. Scheuerer	P.20
W.R. McGrath	P.19	R. Schieder	Mil.4
A. Megej	P.18	E. Schlecht	Mul.5
I. Mehdi	Mul.5	L.P. Schmidt	Mil.2
M. Melloch	SI.2	F. Schnieder	Pa.3
G. Michel	I.4	E. Schomburg	D.3, P.11, P.20
R.E. Miles	SIII.2	J. Schubert	Mil.4
H. Mimura	SI.1	K. Schünemann	P.21
K. Mizuno	I.1	G.W. Schwaab	P.3
F. Mollot	SII.3	O. Schwelb	Pa.4
J. Monecke	P.23	G. Segschneider	SIII.3, P.5
D. Moreno	Mul.3	A. Semenov	Mil.4
O. Morikawa	P.29	J.-I. Shikata	I.5, P.8
P. Mounaix	SII.3	M. Shur	SI.3
G. Mouret	SII.3	K. Siebert	SIII.3, P.5
J. Müller	Pa.5	M. Siegel	P.19
T. Müller	P.14	U. Siegner	P.28
J.A. Murphy	Q.3, P.13	I. Sigmund	P.18
J. Muscat	P.10	V.P. Sinis	SI.4
C.K. Mutamba	P.18	Jan Stake	Mul.1
		D.P. Steenson	SIII.2
A. Nakanishi	SII.2	Ch. Stehen	SIII.3
T. Närhi	Mil.1	M.L. Stock	SII.2
S. Nashima	P.29	G. Strasse	P.14
S. Nishizawa	SII.2	G. Strasser	SII.1
		M. Suenagan	P.30
T. Obunai	P.22	Y. Suyuki	SII.2
		A. Suziedelis	P.12

P.	Szeliga	MiI.2, P.16	B.	Voronov	MiI.4
K.	Takata	P.29	C.	Walker	P.2
M.	Takeda	P.30	K.L.	Wang	SI.4
M.	Tani	SIII.4, D.2, I.3, P.7, P.30	W.	Wegscheider	D.3
T.	Taniuchi	I.5, P.8	W.	Wenckebach	SI.5, P.11
S.	Tautz	SIII.3, P.5	S.	Whithington	Q.3
M.	Thielman	MiI.4	B.	Widiyatmoko	P.7
S.G.	Thomas	SI.4	B.S.	Williams	SI.2
I.M.	Tiginyanu	P.23	S.	Winnerl	P.11
M.	Tonouchi	I.2	B.	Xu	SI.2
T.	Tsukamoto	SII.2	M.	Yamashita	I.2
D.	Turchinovich	Q.2	Y.	Yasuoka	Pa.2, P.27
			O.	Yilmazoglu	SI.1
			S.	Yodokawa	P.22
J.	Ulrich	SII.1	K.	Yokoo	SI.1
K.	Unterrainer	SII.1, P.14	M.	Yoshida	SII.2
K.	Urban	D.4	L.V.	Yurchenko	SII.4
V.M.	Ustinov	P.20	V.B.	Yurchenko	SII.4, P.13
G.	Valusis	P.12	A.E.	Zhukov	P.20
A.F.	van de Meer	P.11	P.	Zimmermann	Mul.1
O.Y.	Volkov	D.4	R.	Zobl	SII.1

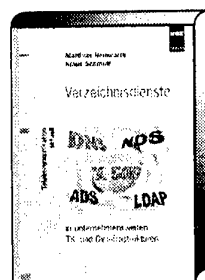
Sichern Sie Ihren Unternehmenserfolg!

VDE
VERLAG



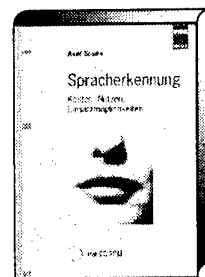
Willimowski, I.
Telekommunikation aktuell
**FMC – Konvergenz von
Fest- und Mobilfunknetzen**
Ein Tutorial

2000, 108 S., DIN A5, kart.
ISBN 3-8007-2536-3
39,- DM / 36,- sFr / 285,- öS / 19,94 €*
In dem neuen Fachbuch geht es hauptsächlich um die FMC-Begriffsdefinition, die möglichen Szenarien und Formen von FMC (Fixed Mobile Convergence) sowie die Rahmenbedingungen und wichtigsten Schlüsseltechnologien.



Schmidt, K. / Reinwarth, M.
Telekommunikation aktuell
Verzeichnisdienste
in unternehmensweiten TK- und
DV-Infrastrukturen

Herausgeber: Badach, A.
1999, 248 S., DIN A5, kart.
ISBN 3-8007-2373-5
59,- DM / 53,50 sFr / 431,- öS / 30,17 €*
Verzeichnisdienste spielen im Bereich der technischen Infrastruktur für Netzwerke als Konfigurations- und Managementkomponente eine immer wichtigere Rolle.



Susen, A.
Spracherkennung
Kosten, Nutzen, Einsatzmöglichkeiten
1999, 229 S., DIN A5, kart., mit CD-ROM
ISBN 3-8007-2323-9
42,- DM / 39,- sFr / 307,- öS / 21,47 €*
Das Werk behandelt die verschiedenen Aspekte der Sprachverarbeitung sowie technische und anwendungsbezogene Schwierigkeiten bei der praktischen Umsetzung.

Thaller, E.
EDV-Praxis
Software-Qualität

Der Weg zu Spitzenleistungen in der Software-Entwicklung
2000, ca. 250 S., DIN A5, kart.
ISBN 3-8007-2494-4
ca. 55,- DM / ca. 50,- sFr / ca. 402,- öS / ca. 28,12 €* (In Vorbereitung)

Ein unverkennbarer Trend unserer Tage ist das Vordringen von Software in alle Bereiche der Technik und des menschlichen Lebens. Deshalb hat die Qualität der Software eine ganz besondere Bedeutung.

Wilde, A.
Telekommunikation aktuell
SDH in der Praxis – Grundlagen,
Systemkomponenten, Einsatzmöglichkeiten
Herausgeber: Badach, A.
1999, 220 S., DIN A5, kart.
ISBN 3-8007-2446-4
38,- DM / 35,- sFr / 277,- öS / 19,43 €*
Das Fachbuch gibt einen Einblick in die Thematik der Hochgeschwindigkeitsnetze, insbesondere des SDH. Ein Abschnitt ist dem Thema WDM und dessen Einsatz in SDH-Netzen gewidmet.

Hüffmann, P.
Der Vertriebsingenieur
2000, ca. 165 S., DIN A5, kart.
ISBN 3-8007-2466-9
ca. 45,- DM / ca. 41,50 sFr / ca. 329,- öS / ca. 23,01 €* (In Vorbereitung)

Das Buch liefert Denkanstöße und Verfahren, die zahlreichen Zeichen und Impulse des Vertriebsalltages zu deuten und für gezielte Methoden und Verfahren zu verwenden.

Coupon für Ihre direkte Bestellung per Post oder Fax

Lieferanschrift:

Anzahl	ISBN	Titel
	3-8007-	
	3-8007-	
	3-8007-	
	3-8007-	

Außerdem kostenlos:

- ☐ Verlagsverzeichnis 2000
☐ Katalog der Normen (auf CD-ROM)
☐ Prospekt „Informations- und Nachrichtentechnik“
☐ Prospekt „Fachzeitschriften“

VDE VERLAG

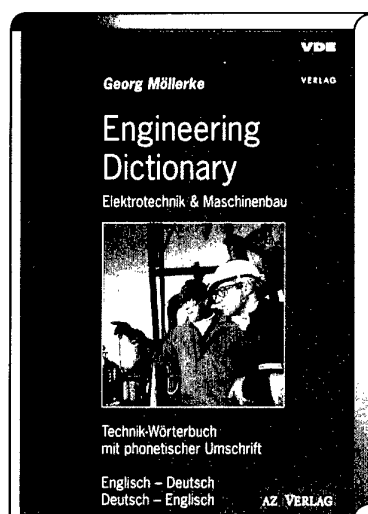
Werb-Nr. 000846

Postfach 12 01 43 · 10591 Berlin
Telefon: (030) 34 80 01-0 · Fax: (030) 341 70 93
E-Mail: vertrieb@vde-verlag.de
Internet: www.vde-verlag.de

Firma _____
Abteilung/Besteller (oder Name bei Privatschrift) _____
Branche _____
UST-IdNr. _____ VDE VERLAG-Kundennr. _____
VDE-Mitgliedsnr./Bezirksverein _____
Straße/Nr. _____
Postleitzahl/Ort _____
Telefon/Fax _____
E-Mail _____
Datum/Unterschrift _____

English for engineers

VDE
VERLAG



Möllerke, G.

Engineering Dictionary

Electrical & Mechanical Engineering

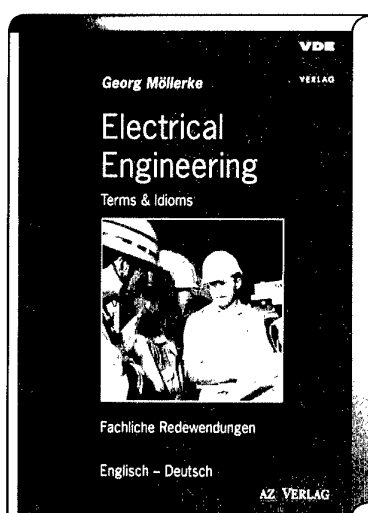
English – German

German – English

2nd edition 2000, 220 pages, 12 x 17,5 cm,
paperback

ISBN 3-8007-2526-6

32,- DM / 29,50 sFr / 234,- öS / 16,36 €



Electrical Engineering

Terms & Idioms

English – German

2000, 160 pages, 12 x 17,5 cm, paperback

ISBN 3-8007-2388-3

32,- DM / 29,50 sFr / 234,- öS / 16,36 €

Prices and information are valid at time of going to press but are subject to change.

VDE VERLAG

P.O. Box 12 01 43 · 10591 Berlin

Phone: ++/ 30/ 34 80 01-0 / Fax: ++/ 30/ 341 70 93

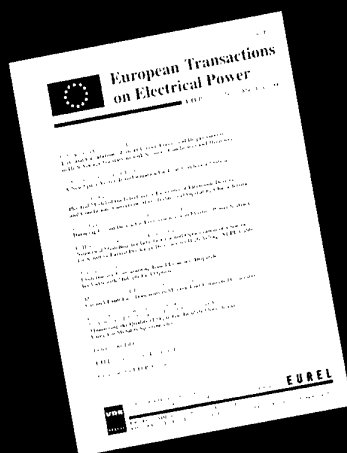
E-Mail: vertrieb@vde-verlag.de

Internet: www.vde-verlag.de

Take advantage of Europe's and the World's accumulated knowledge in the field of electrical power engineering

VDE

VERLAG



E T E P

**The international technical magazine
ETEP provides you with the latest
research and development findings
from industry, research institutes
and universities.**

E T E P

*is an international forum for research and
development in the field of electrical power
engineering supported by an international body
consisting of well-known experts from European
electrical engineering associations.*

*In recent years, informative and professional articles
by competent authors from industry and research
have made ETEP a respected, outstanding scientific
magazine.*

VDE VERLAG

Bismarckstraße 33 · 10625 Berlin · Germany

Phone: ++49 30 / 34 80 01-225 · Fax: ++49 30 / 34 80 01-88

E-Mail: abo-service@vde-verlag.de · Internet: www.ETEP.de

Werb-Nr. 000906

ISBN 3-8007-2580-0



9 783800 725809

ISBN 3-8007-2580-0